Springer Proceedings in Physics 223

Leonid A. Bulavin
Limei Xu *Editors*

Modern Problems of the Physics of Liquid Systems

Selected Reviews from the 8th International Conference "Physics of Liquid Matter: Modern Problems", Kyiv, Ukraine, May 18–22, 2018

Springer

Springer Proceedings in Physics

Volume 223

Indexed by Scopus

The series Springer Proceedings in Physics, founded in 1984, is devoted to timely reports of state-of-the-art developments in physics and related sciences. Typically based on material presented at conferences, workshops and similar scientific meetings, volumes published in this series will constitute a comprehensive up-to-date source of reference on a field or subfield of relevance in contemporary physics. Proposals must include the following:

- name, place and date of the scientific meeting
- a link to the committees (local organization, international advisors etc.)
- scientific description of the meeting
- list of invited/plenary speakers
- an estimate of the planned proceedings book parameters (number of pages/articles, requested number of bulk copies, submission deadline).

More information about this series at http://www.springer.com/series/361

Leonid A. Bulavin · Limei Xu
Editors

Modern Problems of the Physics of Liquid Systems

Selected Reviews from the 8th International Conference "Physics of Liquid Matter: Modern Problems", Kyiv, Ukraine, May 18–22, 2018

Springer

Editors
Leonid A. Bulavin
National Academy of Sciences
of Ukraine
Kyiv, Ukraine

Taras Shevchenko National
University of Kyiv
Kyiv, Ukraine

Limei Xu
International Center for Quantum
Materials and School of Physics
Peking University
Beijing, China

ISSN 0930-8989 ISSN 1867-4941 (electronic)
Springer Proceedings in Physics
ISBN 978-3-030-21754-9 ISBN 978-3-030-21755-6 (eBook)
https://doi.org/10.1007/978-3-030-21755-6

This Springer imprint is published by the registered company Springer Nature Switzerland AG
The registered company address is: Gewerbestrasse 11, 6330 Cham, Switzerland

Preface

The physics of liquid matter has crucial importance for many disciplines such as material science, chemical engineering, and biological systems. For better understanding and broader discussion of the properties of liquid matter, the 8th International Conference "Physics of Liquid Matter: Modern Problems" (PLMMP-2018) was organized by the Taras Shevchenko National University of Kyiv, Institute for Safety Problems of Nuclear Power Plants and Bogolyubov Institute for Theoretical Physics of the National Academy of Sciences of Ukraine. The conference program focused on the most recent developments in liquid matter physics, and was organized in a way to follow the whole diversity of the liquid systems that can be illustrated by the classification of liquid matter developed earlier by Leonid A. Bulavin (Fig. 1). It covered subjects of broad disciplines, such as liquids, solutions, soft polymers, biological molecules, colloids, and liquid crystals as well as a rich variety of theoretical and experimental techniques, ranging

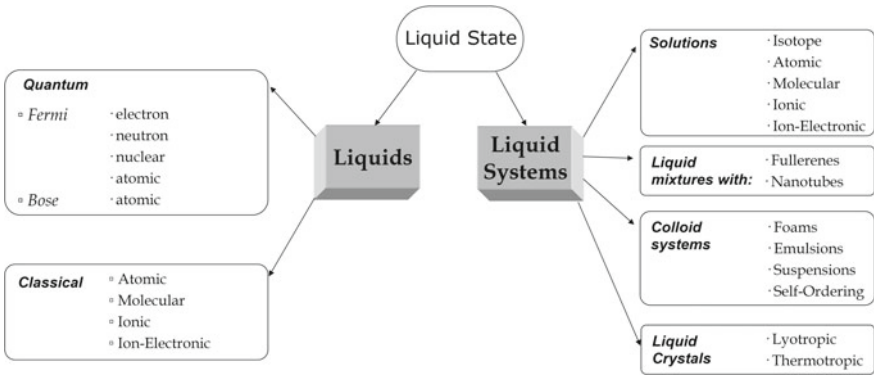

Fig. 1 Classification of liquid matter (Adapted from: Leonid A. Bulavin, Neutron diagnostics of the liquid state of matter: a monograph. National Academy of Sciences of Ukraine, Institute for Safety Problems of Nuclear Power Plants.—Chornobyl (Kyiv. region.): Institute for Safety Problems of NPP, 2012. p. 532)

from Quasi-Elastic Neutron Scattering (QENS), Small-Angel Scattering (SAS), vibrational spectroscopy, etc.

This book consists of invited contributions presented at the PLMMP-2018, held during May 18–22, 2018 in Kyiv, Ukraine. It covers four general topics of the properties of liquid matter, including (i) Water and water systems; (ii) Physics–chemistry properties of liquid systems; (iii) Aggregation in liquid systems; (iv) Biological aspects in liquid systems. It is intended for scientific researchers as well as for engineers, teachers, students, and all those readers interested in modern problems of the physical sciences of liquid matter.

On behalf of the Organizing Committee of the PLMMP-2018 Conference, we would like to thank all the plenary and invited speakers as well as all the participants for their valuable contributions and brainstorming discussions, the International Advisory Board and Local Organizing Committee for assistance in organizing and realization of the scientific program of the PLMMP-2018 Conference, and the Springer International Publishing for helping to organize the publication of the book "Physics of Liquids: Modern Problems" in Springer Proceedings in Physics.

Kyiv, Ukraine — Leonid A. Bulavin
Beijing, China — Limei Xu

Contents

Contributors

V. L. Aksenov Frank Laboratory of Neutron Physics, Joint Institute for Nuclear Research, Dubna, Moscow Region, Russia;
National Research Centre "Kurchatov Institute", Moscow, Russia

Wagner A. Alves Departamento de Química Inorgânica, Instituto de Química, Universidade Federal do Rio de Janeiro, Rio de Janeiro, RJ, Brazil

M. V. Avdeev Frank Laboratory of Neutron Physics, Joint Institute for Nuclear Research, Dubna, Moscow Region, Russia

Greta Babakhanova Advanced Materials and Liquid Crystal Institute, Kent State University, Kent, OH, USA;
Chemical Physics Interdisciplinary Program, Kent State University, Kent, OH, USA

Leonid A. Bulavin Department of Molecular Physics, Taras Shevchenko National University of Kyiv, Kyiv, Ukraine;
Institute for Safety Problems of Nuclear Power Plants, National Academy of Sciences of Ukraine, Kyiv, Ukraine

Guillaume Castanet LEMTA, CNRS-UMR7563, Université de Lorraine, ENSEM, Vandoeuvre les Nancy, France

Kostyantyn Cherevko Faculty of Physics, Taras Shevchenko National University of Kyiv, Kyiv, Ukraine

O. P. Dmytrenko Faculty of Physics, Taras Shevchenko National University of Kyiv, Kyiv, Ukraine

Andrew Erwin School of Materials Science and Engineering, Georgia Institute of Technology, Atlanta, GA, USA

Dmytro Gavryushenko Faculty of Physics, Taras Shevchenko National University of Kyiv, Kyiv, Ukraine

Michel Gradeck LEMTA, CNRS-UMR7563, Université de Lorraine, ENSEM, Vandoeuvre les Nancy, France

Maryana A. Gumenna Institute of Macromolecular Chemistry of the National Academy of Sciences of Ukraine, Kyiv, Ukraine

Mykola Isaiev LEMTA, CNRS-UMR7563, Université de Lorraine, ENSEM, Vandoeuvre les Nancy, France;
Faculty of Physics, Taras Shevchenko National University of Kyiv, Kyiv, Ukraine

N. Jargalan Institute of Physics and Technology, Mongolian Academy of Sciences, Ulaanbaatar, Mongolia

O. D. Kachkovsky Institute of Bioorganic Chemistry and Petrochemistry, NAS of Ukraine, Kyiv, Ukraine

Nina S. Klimenko Institute of Macromolecular Chemistry of the National Academy of Sciences of Ukraine, Kyiv, Ukraine

V. K. Koltover Institute of Problems of Chemical Physics, Russian Academy of Sciences, Chernogolovka, Moscow Region, Russian Federation

Volodymyr F. Korolovych School of Materials Science and Engineering, Georgia Institute of Technology, Atlanta, GA, USA

M. P. Kulish Faculty of Physics, Taras Shevchenko National University of Kyiv, Kyiv, Ukraine

M. O. Kuzmenko Frank Laboratory of Neutron Physics, Joint Institute for Nuclear Research, Dubna, Moscow Region, Russia;
Faculty of Physics, Taras Shevchenko National University of Kyiv, Kyiv, Ukraine

Oleg D. Lavrentovich Advanced Materials and Liquid Crystal Institute, Kent State University, Kent, OH, USA;
Chemical Physics Interdisciplinary Program, Kent State University, Kent, OH, USA;
Department of Physics, Kent State University, Kent, OH, USA

Nikolai Lebovka Department of Physical Chemistry of Disperse Minerals, Biocolloidal Chemistry Institute, Kyiv, Ukraine

Hansol Lee School of Materials Science and Engineering, Georgia Institute of Technology, Atlanta, GA, USA

Fabrice Lemoine LEMTA, CNRS-UMR7563, Université de Lorraine, ENSEM, Vandoeuvre les Nancy, France

Ming-Ru Li The Key Laboratory of Beam Technology and Material Modification of Ministry of Education, College of Nuclear Science and Technology, Beijing Normal University, Beijing, China;
Beijing Radiation Center, Beijing, China

Longin Lisetski Institute for Scintillation Materials of STC "Institute for Single Crystals", NAS of Ukraine, Kharkiv, Ukraine

N. P. Malomuzh Department of Theoretical Physics, Odessa I.I.Mechnikov National University, Odesa, Ukraine

Emily Mikan School of Materials Science and Engineering, Georgia Institute of Technology, Atlanta, GA, USA

N. V. Obernikhina Department of Bioorganic and Biological Chemistry, Bogomolets National Medical University, Kyiv, Ukraine

O. L. Pavlenko Faculty of Physics, Taras Shevchenko National University of Kyiv, Kyiv, Ukraine

Lars G. M. Pettersson Department of Physics, AlbaNova University Center, Stockholm University, Stockholm, Sweden

Ya. O. Prostota Institute of Bioorganic Chemistry and Petrochemistry, NAS of Ukraine, Kyiv, Ukraine

V. A. Sendiuk Faculty of Physics, Taras Shevchenko National University of Kyiv, Kyiv, Ukraine

K. S. Shakun Department of Physics and Chemistry, National University "Odessa Maritime Academy", Odesa, Ukraine

Valery V. Shevchenko Institute of Macromolecular Chemistry of the National Academy of Sciences of Ukraine, Kyiv, Ukraine

Oleh O. Sobko Institute of Macromolecular Chemistry of the National Academy of Sciences of Ukraine, Kyiv, Ukraine

Alexandr V. Stryutsky Institute of Macromolecular Chemistry of the National Academy of Sciences of Ukraine, Kyiv, Ukraine

Volodymyr Sysoev Physics Faculty, Taras Shevchenko National University of Kyiv, Kyiv, Ukraine

Konstantinos Termentzidis CETHIL UMR5008, CNRS, INSA-Lyon, Université Claude Bernard Lyon 1, Villeurbanne, France

O. V. Tomchuk Faculty of Physics, Taras Shevchenko National University of Kyiv, Kyiv, Ukraine;
Frank Laboratory of Neutron Physics, Joint Institute for Nuclear Research, Dubna, Moscow Region, Russia

T. V. Tropin Frank Laboratory of Neutron Physics, Joint Institute for Nuclear Research, Dubna, Moscow Region, Russia

Vladimir V. Tsukruk School of Materials Science and Engineering, Georgia Institute of Technology, Atlanta, GA, USA

Tetiana Vlasenko Institute for Safety Problems of Nuclear Power Plants, National Academy of Sciences of Ukraine, Kyiv, Ukraine

Nan Zhang The Key Laboratory of Beam Technology and Material Modification of Ministry of Education, College of Nuclear Science and Technology, Beijing Normal University, Beijing, China;
Beijing Radiation Center, Beijing, China

Feng-Shou Zhang The Key Laboratory of Beam Technology and Material Modification of Ministry of Education, College of Nuclear Science and Technology, Beijing Normal University, Beijing, China;
Beijing Radiation Center, Beijing, China;
National Laboratory of Heavy Ion Accelerator of Lanzhou, Center of Theoretical Nuclear Physics, Lanzhou, China

Part I
Water and Water Systems

Chapter 1
A Two-State Picture of Water and the Funnel of Life

Lars G. M. Pettersson

Abstract Here I show that experimental and simulation data on liquid water using vibrational (infrared and Raman) and X-ray (absorption and emission) spectroscopies, as well as recent data from X-ray scattering, are fully consistent with a two-state picture of water. At ambient conditions there are fluctuations between a dominating high-density liquid (HDL) and a low-density form (LDL). These are related to the two forms of amorphous ice at very low temperature, high-density amorphous (HDA) and low-density amorphous (LDA), which interconvert in a first-order-like transition. This transition line is assumed to continue into the so-called "No-man's land" as a liquid-liquid transition and terminate in a critical point with very large fluctuations between the two liquid forms. These fluctuations extend in a funnel-like region up to ambient temperatures and pressures and give water its unusual properties which are fundamental to life. With this picture we find simple, intuitive explanations of the anomalous properties of water, such as the density maximum at 4 °C, why ice floats, and why the compressibility and heat capacity grow as the liquid is cooled. We summarize by noting that in this picture, water is not a complicated liquid, but two normal liquids with a complicated relationship.

1.1 Introduction

Our planet Earth is often called "The Blue Planet" due to the large part of its surface covered by oceans, which appear blue from space. Water is considered a prerequisite for life and it thus becomes important not only to know both the extent and quality of the water resources that are available, but also to understand the properties of water in order to efficiently produce the fresh water that is necessary for an increasing population of humans on Earth. A recent illustration from the US Geological Survey [1], based on the estimates by Shiklomanov [2], shows the total amount of available

L. G. M. Pettersson (✉)
Department of Physics, AlbaNova University Center, Stockholm University, 106 91 Stockholm, Sweden
e-mail: lgm@fysik.su.se

L. A. Bulavin and L. Xu (eds.), *Modern Problems of the Physics of Liquid Systems*, Springer Proceedings in Physics 223,
https://doi.org/10.1007/978-3-030-21755-6_1

water in, on and above the Earth as a sphere of about 1,385 km in diameter, which is quite small in comparison with that (12,742 km) of the Earth. However, the dominating fraction is salty ocean water and, when this is excluded, the sphere representing the remainder (trapped in glaciers and ice caps, groundwater, swamp water, rivers, and lakes) has shrunk to a sphere only 272.8 km in diameter. Most of this fresh water is inaccessible. When only easily accessible surface water in lakes and rivers is included, the diameter of the corresponding sphere is a mere 56.2 km. Clearly, fresh water is a limited resource and we will need to develop efficient approaches to large-scale desalination to supply the needs for fresh water for the growing human population, for agriculture, for industry and to abate desertification in view of global climate change. To achieve this, a profound understanding of water's properties is a prerequisite. The overarching question then is: How well do we understand water?

Water is often referred to as "the most anomalous liquid" [3] due to the number of physical and chemical properties in which it deviates from the behavior of normal simple liquids [4]. Examples of these anomalies include that the solid (ice) is less dense than the liquid and that the density of the liquid is maximum at 4 °C. These properties of water make aquatic life in temperate zones possible, since lakes and oceans freeze over from the top, providing an insulating layer, while the temperature at the bottom remains at 4 °C. The specific heat of the liquid (4.18 J/g K), i.e. how much energy is needed to change the temperature by one degree, is about twice that of the solid and significantly higher than for the simple liquid ethanol (2.44 J/g K). This provides the basis for water as an efficient medium to redistribute energy over the Earth, as exemplified by the Gulf Stream. The specific heat (C_P) depends on fluctuations in entropy, while the compressibility at constant temperature (κ_T) of the liquid depends on fluctuations in the density. At higher temperatures both decrease in magnitude with decreasing temperature, as expected for any normal liquid as thermal motion slows down. However, water exhibits a minimum at 35 °C (C_P) and 46 °C (κ_T) after which both C_P and κ_T seem to go towards infinity near a temperature of −45 °C upon further cooling. This behavior is clearly anomalous in that fluctuations thus dramatically *increase* as the liquid is cooled below 0 °C [5–9].

Another example of anomalous behavior is given by the boiling point of water at +100 °C which, if extrapolated based on decreasing molecular mass along the group 6A dihydrides (H_2Te, H_2Se, H_2S and H_2O), should rather be closer to −66 °C. The boiling point of water is thus ~160 °C higher than expected from comparable liquids (Fig. 1.1). Also the melting point, when extrapolated in the same manner, is around 90 °C higher than expected [4]. As final examples we note the unusually high surface tension and self-diffusivity, i.e. molecular mobility, where the latter is observed to *increase* with applied pressure when the liquid is cooled below the minimum in compressibility at 46 °C. Clearly, the origin of the anomalous properties must be sought in how the water molecules interact with each other, and what types of local arrangements they can form under different conditions.

A two-state picture of water provides a simple and intuitive understanding of the origin of water's many anomalous properties by considering the liquid under ambient temperatures and pressures as balancing between two local forms. One form favors order, through maximizing hydrogen-bond (H-bond) formation, which limits the

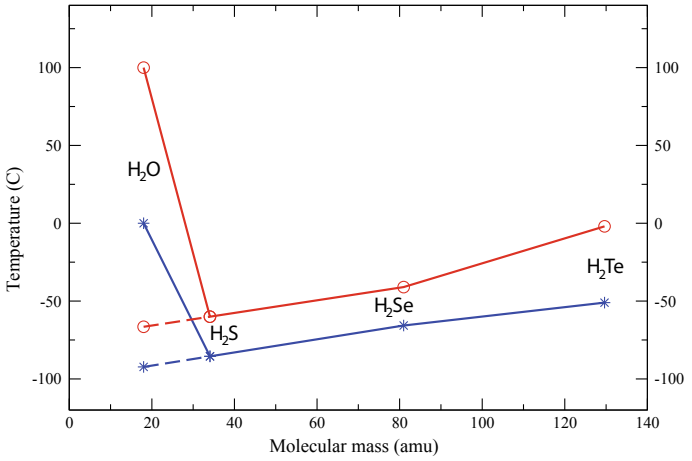

Fig. 1.1 Melting point (blue line, stars) and boiling point (red line, circles) of the group 6A dihydrides as function of molecular mass. Dashed curves show straight line extrapolations to H_2O using the trend from H_2Se to H_2S. H_2Po (mass 211, melting point −36 °C, boiling point 37 °C) is not shown in order to better focus on the region around water. Temperatures in °C

number of neighbors and leads to a local low-density liquid (LDL) environment. The other form favors disorder, squeezing the molecules tighter (close-packing) by breaking or distorting H-bonds, thus leading to a local high-density liquid (HDL) [10–25]. The two forms are clearly incompatible and at ambient conditions the HDL form dominates, but with local fluctuations into the LDL form as it is lower in energy.

The two forms of the liquid (LDL, HDL) have been connected to the two forms of amorphous solid water, i.e. low-density amorphous (LDA) and high-density amorphous (HDA) ice, which differ in density by ~20% and exhibit a first-order-like transition between them [26, 27]. By heating HDA to above −163 °C (110 K), i.e. into the ultra-viscous regime, it has recently been possible to follow the transition between the two forms (HDL to LDL) using wide-angle X-ray scattering (WAXS) and simultaneously measuring diffusion through X-ray photon correlation spectroscopy (XPCS) [28]. Through this combination of techniques the transition was shown to proceed from HDA into HDL, that subsequently converted into LDL, i.e. a liquid-liquid transition [28]. Thus, the existence of, and transformation between, the hypothesized two forms of liquid water seems clear, albeit only in deeply supercooled and pressurized form.

A coexistence line between two phases, e.g., gas and liquid, may terminate in a critical point where fluctuations grow beyond bounds. Beyond the coexistence line and critical point extends a funnel-like region of fluctuations between the two forms. The fluctuations become less intense the farther away one moves into the one-phase region beyond the critical point where one can no longer distinguish the two phases. A remaining question thus concerns whether the coexistence line between the two liquids, HDL and LDL, also is terminated by a critical point, which could explain the

seeming divergence of compressibility and heat capacity as water is deeply supercooled [16, 23, 29]. Experimentally, the probable location of such a critical point around 800 bar [8] and significantly below the temperature of homogeneous ice nucleation, makes it very challenging to unambiguously determine its existence. However, also far away from such a critical point, one would expect local fluctuations between the two forms. This would lead to two-state behavior with fluctuations on some characteristic length- and time-scale. The magnitude of such fluctuations would depend both on temperature and pressure, as these two thermodynamic quantities determine the distance from the hypothesized liquid-liquid critical point (LLCP). If such structural fluctuations can be shown to exist also for ambient water it would provide very simple and intuitive explanations of all of water's anomalous properties.

Molecular dynamics (MD) computer simulations have contributed significantly to the present understanding of the liquid, based on both classical force-field interactions [30] and quantum mechanical techniques, e.g., [31–34]. Impressive agreement with experiment has been obtained for many properties, such as the radial distribution functions, molecular self-diffusion, proton transport, and many more. Even the challenging problem of the difference in density between simulated liquid and ice has been resolved using advanced simulation techniques [31, 32]. These are properties that depend on averaging, while for properties that depend on fluctuations the picture is different (Fig. 1.2), which suggests that further developments are needed.

In Fig. 1.2a we compare the experimental isothermal compressibility, which was recently measured down to −46 °C (227 K) [8], with results from a range of force-field models [9]. The dramatic increase of the compressibility in the experiment is not captured by any of the studied models. It is clear that the magnitude of fluctuations seen in experiment is severely underestimated in the simulations, though many other properties are reproduced quite accurately.

In Fig. 1.2b we compare the X-ray emission (XES) spectrum from experiment (top) with a computed spectrum from simulations using path-integral MD (PIMD) for nuclear quantum effects, in combination with the opt-PBE-vdW van der Waals corrected density functional [35]. XES measures the valence electronic structure and the experiment shows a clear two-peak structure in the lone-pair region (526–527 eV). The simulation, however, does not reproduce the split observed experimentally, but rather gives an average. Finally, we compare the experimental Raman spectrum of water (Fig. 1.2d) with that (Fig. 1.2c) obtained from simulations using the MB-pol force-field [36], which includes up to three-body interactions fitted to a large set of structures computed at the quantum chemical gold-standard CCSD(T) level. The overall shift to lower frequencies with decreasing temperature is reproduced, but not the bimodality observed in experiment. Some effect thus seems to be missing in the description of water that could enhance fluctuations (Fig. 1.2a) and cause a stricter bimodality in simulated XES (Fig. 1.2b) and Raman (Fig. 1.2c) spectra. What can be the character of such fluctuations? Clearly, since they increase with decreasing temperature, their origin and driving force must be different from normal, random thermal fluctuations in the liquid.

In the following, we will present and discuss evidence from different experimental techniques and theoretical simulations, which point to fluctuations between

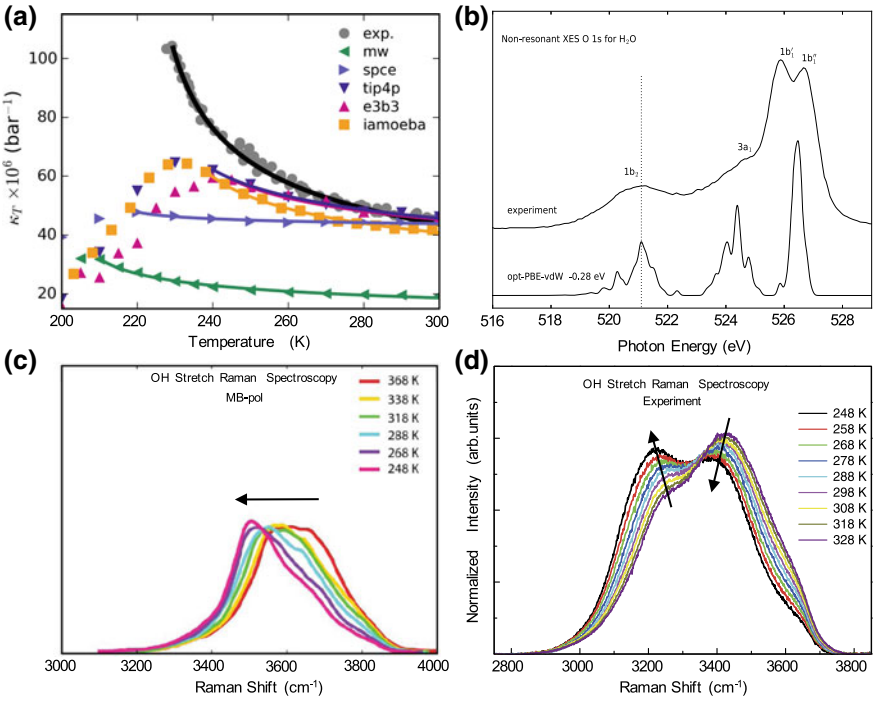

Fig. 1.2 **a** Comparison of the temperature-dependent isothermal compressibility from experiment [8] (grey) and the mW, SPCE, TIP4P/2005, E3B3 and iAMOEBA simulation models. Solid lines are power-law fits to the rising part of each set of data points. Although accurate in many other respects all here tested simulation models severely underestimate structural fluctuations leading to the strong enhancement observed in experiment (Figure adapted from [9]). **b** Experimental XES spectrum of H_2O (top) compared with computed spectra from PIMD simulations using opt-PBE-vdW (bottom) [35]. **c** Simulated H_2O Raman spectrum using MB-pol [36] compared with **d** experiment [37, 38]. Reprinted with permission from [35]

two well-defined local environments. Before embarking on this endeavor, however, we first point out that two-state behavior has been shown to be fully consistent with thermodynamics and a prerequisite for a theory that describes the anomalies of water [17–19, 39–43]. Secondly, we note that the two-state picture of water has a long history [44–49], and may be considered required to explain the properties of supercooled water [13]. For ambient water the picture of the liquid as a continuum distribution around mainly tetrahedral H-bonding is still prevalent, however, very much due to the influence of MD simulations. These typically result in a continuum picture, but severely underestimate the magnitude and specificity of the fluctuations inferred from experiment as indicated in Fig. 1.2.

We will begin by discussing the structure of water based on scattering techniques [X-ray and neutron diffraction and extended X-ray fine-structure (EXAFS)] and continue with information from spectroscopic [IR, Raman, X-ray absorption (XAS) and emission (XES)] techniques. We will follow up by discussing MD simulations and

what aspects may need improvement in order to reproduce, in particular, structural fluctuations in the liquid. In the discussion section we will explain the origin of many of water's properties in terms of fluctuations between local HDL and LDL structures and speculate about how a deeper understanding of water can help desalination efforts.

1.2 Scattering Techniques

X-ray (XRD) and neutron (ND) diffraction provide the most direct measurement of structure in the liquid, where the split in the first peak of the oxygen-oxygen scattering structure factor is a measure of tetrahedrality in the liquid. X-rays interact with the electronic charge density where the diffraction pattern is equivalent to the Fourier transform of the charge-density distribution in the liquid. As such, X-ray diffraction provides mainly information on the O–O and O–H correlations, while the small charge density on the hydrogens results in low information-content as regards H–H correlations. Neutrons, on the other hand, scatter against the nuclei, with highest sensitivity to the light particles (hydrogen or deuterium), such that XRD and ND provide complementary information-content on the structural arrangement. Scattering from the liquid gives the typical angularly-symmetric rings, with intensity depending on the momentum (q) transfer (distance from the center of the ring). This is then integrated over the 2π angle to obtain the structure factor as function of momentum transfer, which can subsequently be directly transformed to a real-space correlation function, provided that a sufficient interval in q has been measured.

Since XRD and ND, measured on a single sample, give insufficient data to disentangle the three correlations (O–O, O–H and H–H), one typically adds a sample containing a different isotope with different neutron scattering length [50]. In order to avoid uncertainties due to somewhat different structure for H_2O and D_2O [51–53], as well as the inelastic corrections due to the lighter hydrogen isotope, the contrast between ^{17}O and ^{18}O can be used [54]. Here we will focus on to what extent the H-bonding arrangement in the liquid is determined by the combination of XRD and ND.

The two dominating techniques to extract structural data, beyond the three individual pair-correlation functions from the XRD and ND scattering patterns, are empirical potential structure refinement (EPSR) [55] and reverse Monte Carlo (RMC) [56, 57]. The goal for both is to develop structural models that are consistent with the scattering data, and from which further information can be obtained. In EPSR, an initial potential from some force-field description of water is used in Monte Carlo simulations of the diffraction data. The potential is then successively perturbed, based on the difference between simulated and measured data, to give agreement with the experiment [58, 59]. In this approach, one thus purposely relies on a model force-field to constrain the simulation to physically acceptable solutions. This then relies on the data to correct any unintentional bias that the force-field may have introduced. Drawbacks of this approach are that, in situations where many different structural

solutions are possible, still only one final potential corresponding to a specific solution is obtained, and also that the data may be insufficient to correct possible biases inadvertently introduced by the force-field.

The RMC approach, on the other hand, performs Monte Carlo atomistic moves to generate a distribution of solutions, which are maximally disordered within the constraints imposed by the experimental data, and by possible additional constraints set by the simulator [56, 57]. As an illustrative example of limitations on the information content in the scattering data, we mention that with the RMC approach, unless the simulation is constrained to molecular H_2O (or D_2O), the stoichiometry is obeyed only on average, i.e. one finds a distribution of H_xO entities where only the average of x is two. The approach is thus completely driven by the data and one may use constraints to drive the solutions in different directions and thus explore what bounds the data actually set on possible solutions. By adding more and more experimental data from different techniques that are sensitive to different structural aspects, these bounds can then be made more and more rigorous.

In the 2004 paper by Wernet et al. [60], XAS and X-ray Raman scattering (XRS) data were interpreted as a dominant fraction of the molecules in the liquid being very asymmetrically H-bonded, with only one well-defined donated and accepted H-bond, consistent with molecules in chains or rings. This was in contrast to the distorted, mainly tetrahedral picture of the liquid that was accepted based on earlier analyses of, e.g., scattering data [61, 62], and has caused significant debate [63–70].

Leetmaa et al. [71, 72] used RMC on ND data for five different isotope compositions together with XRD to investigate whether a large number of broken H-bonds would be contradicted by the data. To this end, an H-bond criterion was added and the program was set to fit the experimental data combined with maximizing the number of intact donated H-bonds. This resulted in 74% double H-bond donors (DD) and 21% single donors (SD). Maximizing instead the number of broken H-bonds gave 81% SD and 18% DD, while still reproducing the experimental data, and losing only 0.7–1.8 kJ/mole interaction energy as measured using a range of force-fields [71]. Diffraction data thus allow a tetrahedral model, but does not exclude models with a large fraction (81%) with one broken donated H-bond as proposed by Wernet et al. [60]. In terms of H-bond-connectivity in the liquid, diffraction data thus allow a large range, and complementary experimental data must be applied to narrow this range.

1.2.1 Extended X-Ray Absorption Fine-Structure (EXAFS)

In 2007, Bergmann and coworkers [73, 74] reported an O–O pair-correlation function based on EXAFS, which was markedly different from that from XRD with a significantly sharper and higher first peak at shorter distance than obtained from XRD. In EXAFS an X-ray photon ejects an inner-shell (O 1*s*) electron as a spherical wave, which is back-scattered against atoms in the environment. This gives oscillations in the scattering cross-section that depend on interatomic distance and number of scatterers; the process can be likened to a particle in a box, for which

specific resonances occur when multiples of its half-wave-length coincide with the box dimensions. Could the EXAFS and XRD data be reconciled in terms of a single structural solution?

To answer this question, theoretical EXAFS signals must be computed, including multiple scattering to account for the presence of the positive hydrogens between two oxygens in an H-bond. Such calculations take too long for a standard RMC procedure based on hundreds of millions of atomistic moves, where the properties in question are recomputed after every move. To overcome this difficulty, the SpecSwap-RMC procedure [75] was developed and implemented [76]. This builds on precomputing the data for a large variety of structures that are then used to reproduce the experimental data in an RMC fashion; instead of atomistic moves, the exchanges are made among library structures based on their contributions to the fit to the experimental data. Applying this to a simultaneous fit of EXAFS signal and XRD O–O pair-correlation function resolved the discrepancy, and structural solutions that reproduced both EXAFS and XRD could be obtained [77].

EXAFS is particularly sensitive to short interatomic distances, which enhance the back-scattering signal, and furthermore to the presence of a positively-charged hydrogen between the two oxygens. The positive charge acts as a lens that focuses the outgoing spherical wave onto the accepting oxygen, as well as back onto the oxygen from which the electron was emitted. This results in a strong enhancement of the EXAFS signal, which becomes additionally enhanced if the environment is symmetric with all neighboring oxygens at similar (short) distance. EXAFS is thus particularly sensitive to a subclass of molecules in very tetrahedral environment with short and well-defined H-bonds, while XRD sees all situations with similar probability. Including a subset of molecules in very well-defined, tetrahedral local environment, with the remainder in more disordered structures, thus resolved the seeming discrepancy and emphasized the importance of using complementary experimental information when deducing structure in the H-bonding network [77].

1.2.2 Wide-Angle X-Ray Scattering (WAXS)

By using very high-energy X-ray photons it is possible to extend the measured q-range in XRD to high-enough values that a direct Fourier transform can be applied to extract the O–O correlation function with very small uncertainty [78, 79]. The O–H contribution must still be removed, but once this is done, a high-accuracy O–O pair-correlation function for ambient water [79] and, in particular, the temperature-dependence of the various peaks, can be reliably determined [78, 80]. Most notably, it was found that the second correlation (at ~4.5 Å) becomes well-established only below the compressibility minimum at 46 °C [78] and that this is accompanied by the growth of specific correlations at 8.5 and 11 Å, as well as weaker radial correlations out to ~17 Å [80]. The peak at 4.5 Å is associated with tetrahedral H-bonding and the association with growth of the additional peaks at longer distance indicates the appearance and growth of collective fluctuations into tetrahedral structures, which

can be associated with the increased compressibility below 46 °C. As further indication of a change in behavior around the compressibility minimum, there are changes in slope with temperature for properties as varied as, e.g., the thermal conductivity (64 °C), the refractive index (60 °C), and the conductance (53 °C) as compiled by Maestro et al. [81].

1.2.3 Small-Angle X-Ray Scattering (SAXS)

Extending the q-range instead to lower values towards zero q-transfer in small-angle X-ray scattering (SAXS) gives information on larger-scale fluctuations through the inverse relation between momentum space and real space. This was used by Huang et al. [20, 82] who estimated the typical size of tetrahedral fluctuations in ambient water to be around 10 Å. The suggested local heterogeneity in terms of tetrahedral fluctuations in a predominantly high-density environment was criticized [63, 64, 70, 83, 84], but is in good agreement with the observed temperature-dependent correlations in the O–O pair-correlation function [80] discussed above, as well as with the spectroscopic evidence to be discussed below. The conclusion is furthermore supported by MD simulations [85, 86] using the TIP4P/2005 force-field [87], although it should be noted that the enhancement of the low-q scattering upon deep supercooling is severely underestimated by the simulations [86].

Extending the low-q scattering measurements of the structure factor, $S(q)$, to zero q-transfer at different temperatures gives information on the temperature-dependent isothermal compressibility, κ_T, through the thermodynamic relationship $S(0) = k_B T n \kappa_T$, where k_B is the Boltzmann constant, T is the temperature (in Kelvin), and n the number density. Since κ_T is related to density fluctuations, the underestimated enhancement of $S(0)$ in the simulations at low temperatures [86] indicates that structural fluctuations at low temperatures are underestimated in the simulations.

The connection to the isothermal compressibility provides an entrance to exploit SAXS to determine κ_T to lower temperatures than previously possible. This was recently achieved by performing SAXS measurements on micron-sized water droplets that are cooled ultrafast in vacuum and measured using femtosecond coherent pulses from an X-ray free-electron laser (XFEL) [8, 9]. These measurements are extremely challenging considering that the kilometers-long, linear electron-accelerator generates "bullets" of X-rays with diameter ~3 μm ($3 \cdot 10^{-6}$ m) which have to hit water droplets of ~10 μm while they fall in vacuum. However, the technical difficulties could be overcome and the SAXS signal measured on liquid water down to −46 °C (227 K) [8, 9]. At these low temperatures, significantly below the previously established temperature of homogeneous ice nucleation, the water droplets crystallize on a sub-millisecond time-scale, which necessitates the ultra-fast probing that has become possible with the availability of XFELs.

As result of these measurements, it could be shown that the isothermal compressibility exhibits a maximum at −44 °C (229 K) [8], rather than the divergence that had

been proposed based on extrapolation from higher temperatures [7]. A divergence is expected upon approaching a critical point, while a maximum is expected along the continuation of the coexistence line into the one-phase region beyond a critical point, the so-called Widom line. This line in the phase diagram separates regions dominated by either species (HDL or LDL) and along this line fluctuations are maximal as it corresponds to a 50:50 average composition in terms of the fluctuating species [88]. The magnitude of the maximum in κ_T depends on the distance to the critical point and, by comparison with simulations using the iAMOEBA model [89], the LLCP in water was proposed to lie at ~800 bar pressure [8].

To summarize the observations from scattering measurements, the pure HDL and LDL liquids and transformation between them have been identified in the ultraviscous regime using a combination of WAXS and XPCS upon heating HDA at ambient pressure [28]. A maximum has been observed in the temperature dependence of κ_T, consistent with a Widom line that indicates the presence of an LLCP at higher pressure [8]. The proposed LLCP has thus been approached both from below the crystallization temperature by starting from amorphous ice and from above the temperature of homogeneous ice nucleation by using micron-sized water droplets.

Using XRD with a very high q-range, a change towards more well-developed tetrahedral fluctuations below the minimum in κ_T was found [78], which could furthermore be connected to the growth of well-defined correlations out to ~11 Å [80], that indicate the appearance of collective fluctuations [90]. This is consistent with earlier determinations of the spatial magnitude of density heterogeneities due to tetrahedral fluctuations using SAXS [20, 21]. We note finally, that the combination of XRD and EXAFS, as well as XES (see below), requires a minority subset of structures in the ambient liquid, with very well-defined tetrahedrality and short H-bonds that connect the participating molecules [77].

1.3 Spectroscopic Techniques

1.3.1 Raman Spectroscopy

The temperature-dependent Raman spectrum of liquid neat water is bimodal with a transfer of intensity from the high-energy side to that at low energy upon cooling (Fig. 1.2d) [37, 38, 91–95]. Scherer et al. [91] used the polarization dependence to show that molecules contributing to the low-energy side of the spectrum are in a highly symmetrical, tetrahedral environment with two donated and two accepted hydrogen bonds, while the local environment of molecules contributing to the high-energy peak is highly disordered. This is consistent with the expected temperature-dependence of H-bond formation, with more disorder and broken or distorted H-bonds at higher temperature. It is also consistent with the effects on the spectra from applying pressure [95], which inhibits fluctuations into low-density tetrahedral structures and reduces the intensity on the low-energy side of the Raman spectrum.

Walrafen et al. [93] showed furthermore that, upon heating the liquid, the integrated intensity-gain above the isosbestic point (point where the intensity is independent of temperature, see Fig. 1.2d) at 3425 cm^{-1} [1] in the OH-stretch vibration very closely matches the intensity-loss integrated below this point, i.e. fully consistent with temperature-dependent conversion between two specific types of H-bonded species.

1.3.2 Infrared Spectroscopy

Further compelling evidence for interconversion between two specific local structures in the liquid is provided by Maréchal [96], who showed that the temperature-dependent (0–80 °C) IR spectrum (0–4000 cm^{-1}) can be decomposed as a temperature-dependent linear combination of two temperature-*independent*, complete spectra. Since the IR spectrum is sensitive to H-bond structure, this provides a strong indication of the existence of two rather specific classes of H-bond situations in the liquid, tetrahedral (LDL) and disordered (HDL), consistent with the analysis based on polarized Raman OH-stretch data [91] and the XRD, EXAFS and XES data above.

1.3.3 X-Ray Spectroscopies

X-ray spectroscopies in absorption (XAS) and emission (XES) measure the electronic structure locally around the probed molecule in the liquid or solid [22, 97–100]. In absorption, an X-ray photon is used to excite an O 1*s* core-electron into empty valence and continuum states. XES is connected to XAS as the decay of a valence electron from an occupied level to fill the 1*s* core-hole, with the released energy carried away by an X-ray photon. Since the 1*s* orbital is strongly localized, and an overlap between the initial and final levels is required for a transition, both spectroscopies provide very local probes of the electronic structure—unoccupied states in XAS and occupied in XES—which depends on the H-bonding situation [35, 101]. Both spectroscopies obey the dipole selection-rule, which makes them sensitive only to the local *p*-character of the unoccupied (XAS) and occupied (XES) states due to the spherical symmetry of the 1*s* core level. XAS is thus particularly sensitive to donated H-bonding due to the *p*-character in the internal O–H antibonding states, which are located mainly on the hydrogens, while in XES the highest intensity comes from the doubly-occupied 2*p* lone-pairs.

From the traditional picture of liquid water as mainly tetrahedrally H-bonded, an XAS spectrum similar to that of ice would be expected, but broadened and smeared out by disorder since the excitation is into antibonding states whose energy position depends on the bond distance. Instead, the dominant post-edge at 540 eV of ice is all but lost and a main-edge at 537 eV and sharp pre-edge at 535 eV become prominent

[60, 98, 99, 102, 103]. This was interpreted by Wernet et al. [60] as most molecules in the liquid being in an asymmetric H-bonding situation with only one well-defined donated and accepted H-bond, indicating chains or larger rings in the liquid [60].

1.3.4 XES

The core-hole-state generated by XAS is very highly excited (~540 eV) and decays on a time-scale of the order 4 fs [104]. When this decay occurs through emission of an X-ray photon, it may be detected in XES and give a direct measurement of the atomic $2p$ character in the occupied orbitals on the probed molecule. We focus on the non-bonding $1b_1$ lone-pair, which does not get vibrationally excited and remains sharp [20, 105–111]. Hydrogen-bonding in crystalline ice shifts the peak to ~1.5 eV lower energy compared to gas phase. Interestingly, liquid water shows *two* sharp lone-pair peaks that interconvert, but do not broaden with increasing temperature (Fig. 1.2b); the peak at low emission energy (close to the position in ice) goes down in intensity, but remains in fixed position at higher temperature, while the peak at high energy increases in intensity and disperses towards the gas-phase position [20, 23, 106, 112]. This is consistent with the existence of two specific types of local structures, very tetrahedral (LDL) and very disordered (HDL), in the liquid [20, 22, 106–109]. However, removing a screening $1s$ electron effectively converts the oxygen to a fluorine ($Z+1$ approximation [113, 114]) which generates strong vibrational excitations through core-hole-induced dynamics, that can even lead to dissociation [115]. An alternative interpretation of the peaks has been proposed as due to, respectively, intact and dissociated molecules [105, 111, 116–118]. This interpretation has recently, through direct measurement of the contribution from dissociation [119], been shown to be inconsistent, which favors the picture of interconversion between two specific local structures in the liquid, as also concluded from the IR and Raman studies above.

As seen from Fig. 1.2b, typical MD simulations result in a single peak at the lone-pair position in XES when computing the contribution from all molecules in a snapshot of the simulation [35]. Experiment, however, shows a rather sharp double-peak feature with energy separation and relative intensity depending on the temperature [20, 100, 105–109, 112, 120]. The peak position in the simulations is intermediate between the two peaks observed experimentally, which indicates that the instantaneous structure in the simulated liquid is somehow intermediate between two more well-defined structures in the real liquid [35]. This is similar to the simulated Raman spectrum in Fig. 1.2c, which exhibits the trend towards lower energy with decreasing temperature, but not the clear bimodality and intensity transfer between two peaks that is observed experimentally (Fig. 1.2d).

The lone-pair peak position in XES, computed for local structures in the simulated liquid depends on the local H-bonding, where fully H-bonded molecules in tetrahedral environment were found to contribute at lower emission energy than molecules in asymmetrical environments with some broken or weakened H-bonds [35]. How-

ever, applying this criterion by itself when computing the spectrum resulted in a significantly too small computed split between the peaks in comparison with the experiment (Fig. 1.3, top). The computed peaks are very broad, however, and, by restricting H-bond distances within each class (tetrahedral and asymmetrical), it was found that the computed split is rather sensitive to this parameter (Fig. 1.3, middle and bottom): in order to obtain a split comparable to experiment it was found necessary to restrict the class of tetrahedral species to molecules with very short (<2.68 Å) and well-defined H-bonds. The asymmetrical species, on the other hand, were found to require long (>2.8 Å) H-bonds, as also expected for an HDL local structure which squeezes in a fifth neighbor between the first and second coordination shells [35]. We thus have a consistent interpretation of XRD, EXAFS and XES in terms of a subset of molecules in very well-defined tetrahedral LDL-like environment, while the majority at ambient conditions prefer a more HDL-like environment, with expanded first coordination shell to accommodate a fifth neighbor and some broken or weakened H-bonds. MD simulations do contain such structures, but they constitute a minority with most molecules in local structures that constitute more an average between these situations. In Sect. 1.4 we will discuss requirements on simulations to remedy this situation.

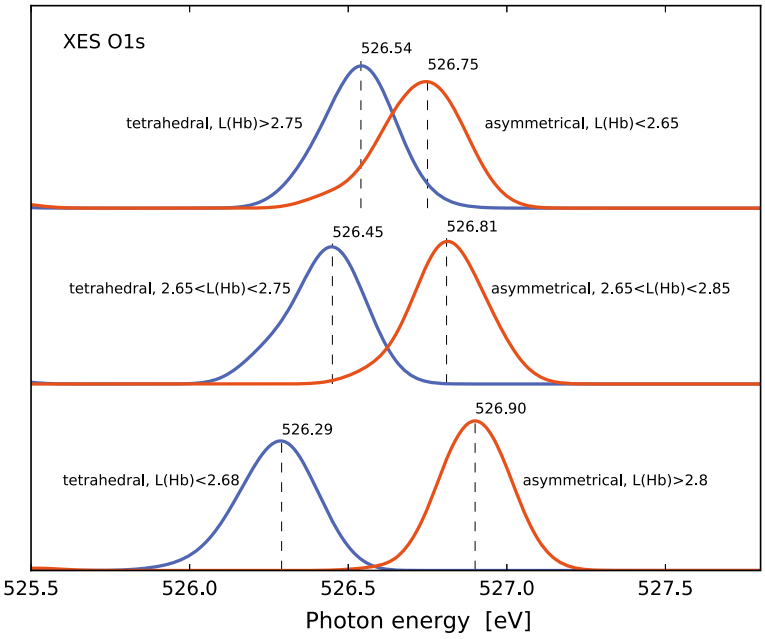

Fig. 1.3 Computed lone-pair XES peak positions as function of H-bond symmetry (tetrahedral and asymmetrical) and H-bond distances. The split increases toward the experimentally observed by considering a subclass of very tetrahedral molecules with short H-bonds and asymmetrically H-bonded with long H-bonds. Reprinted with permission from [35]

1.3.5 Connecting XAS and XES and Raman Spectroscopy

By selecting different energies for creating the core-hole in XAS, the absorption features in XAS can be connected to emission features in XES [20]. By exciting at the post-edge in XAS, which contains significant contributions from tetrahedrally H-bonded molecules, the emission peak assigned to tetrahedral species is enhanced [20]. Excitation at the sharp pre-edge, which grows in intensity as the liquid is heated and has been assigned to weakly coordinated OH-groups, results in only the peak due to disordered species appearing in XES, consistent with only these species contributing to the sharp pre-edge. By tuning the XAS excitation energy it is thus possible to select specifically-coordinated species in the liquid for study [20].

XES is thus connected to XAS through energy-selective excitation, but there is more information to be obtained by connecting also to vibrational spectroscopy. XES is an energy-loss spectroscopy, in which a photon is scattered from the system, losing part of its energy; this is similar to optical Raman spectroscopy. By resolving losses due to vibrational excitations in XES, it is possible to directly measure the OH-stretch energy for the different species selected through the XAS process [111, 121, 122].

The energy of the OH-stretch vibration of the proposed weakly H-bonded OH-group of the disordered species (HDL), contributing to the pre-edge, is found to be 0.45 eV, which is close to the gas-phase symmetric (0.453 eV) and asymmetric (0.465 eV) stretch energies, thus confirming the assignment of the pre-edge as due to very weakly H-bonded OH-groups [122]. By scanning over the XAS spectrum and monitoring the vibrational loss features, a direct connection between species selected in XAS and their contribution to the Raman spectrum could be established, where, e.g., the post-edge with mainly tetrahedrally coordinated molecules contributes to the low-energy part of the Raman spectrum, while pre-edge excitation contributes on the high-energy side [121]. There is thus a full consistency and direct experimental connection between the X-ray spectroscopies (XAS and XES) and IR and Raman vibrational spectroscopies for water.

To summarize the spectroscopic information, we note that both vibrational Raman and electronic XES exhibit clear bimodality in terms of two peaks and intensity transfer from one to the other with changes in temperature. The peak on the low-energy side of the Raman spectrum (left in Fig. 1.2d) has been shown experimentally, using symmetry-resolving techniques [91], to be due to molecules in tetrahedral local environment, which is also consistent with this peak growing in intensity as the liquid is cooled. In the same study, the peak at higher energy (right in Fig. 1.2d) was shown to be due to molecules in asymmetric H-bonding environment. This is fully consistent with the assignment of XAS and XES, as demonstrated through selective probing of different local H-bonding structures in the liquid and connecting to the Raman spectrum [121, 122]. The observed bimodality in terms of spectral features indicates that the molecules in the liquid spend more time in the corresponding H-bonded environments than in structures intermediate between them. This is further underlined

by the decomposition of the IR spectrum in terms of a temperature-dependent linear combination of two temperature-independent complete spectra.

1.4 MD Simulations

In Fig. 1.4 we illustrate different possible situations that are consistent with the experimental data discussed above, and which can be valid for water at different combinations of temperature and pressure. Going from the bottom to the top in the figure corresponds to a combination of going from high to low pressure and from low to high temperature. At the bottom (Fig. 1.4a) we have the two different pure forms of liquid water, for which the transformation from HDL to LDL has recently been observed (LDL in blue and HDL in yellow) [28]. Beyond the proposed LLCP there are large fluctuations into the minority species, which is LDL on the HDL-dominated side (right) and HDL on the LDL-dominated side (left) of the Widom line (dashed in the figure). At the Widom line the distribution is 50:50 on average [88]. Based on the bimodality observed in IR, Raman and XES, structures representing a structural average in between the two extremes, indicated with fuzzy green, constitute a small fraction. The HDL and LDL structural species rearrange into each other through fluctuations on a time-scale longer than the H-bond lifetime. The farther away from the LLCP one moves (Fig. 1.4b–d) the wider the fluctuating region becomes, while the length-scale of the fluctuations diminishes. It should be noted that, the high-precision temperature-dependent XRD data [78, 80], as well as the SAXS data [20, 82], indicate that the cross-over from the situation in Fig. 1.4d (right) to that in Fig. 1.4c (right) occurs around 50 °C, i.e. collective structural fluctuations appear at temperatures and pressures that are relevant to life. Figure 1.4e, finally, illustrates the simple liquid situation, where the liquid only encompasses a homogeneous single structural environment with normal thermal fluctuations. These involve only very local structural variations reminiscent of LDL and HDL, while most of the molecules are in H-bonded structures that are intermediate between the two extremes.

There are two simple pictures that can account for the observed bimodality in the dynamics of the fluctuations in the heterogeneous case (Fig. 1.4b, c). One is that the fluctuations behave similar to the motion of a classical pendulum moving between two turning points: the velocity is zero at the turning points and at a maximum at the point in the middle. In this picture the molecules of the liquid will spend most of the time at the extreme points and little time in between as they convert. This leads to an extreme heterogeneous situation, where two well-defined structural classes develop on a temperature-dependent length and time scale. The interfacial region between the end-points (local HDL/LDL) would contain few molecules, since only a short time is spent in this region. Another hypothesis may be that the LDL structural fluctuations appear as attempted, but frustrated, growth around specific, more long-lived templates that begin to form below ~+50 °C. Here a number of authors have pointed out the favorable stability of clathrate structures, e.g., [45, 46, 95, 123].

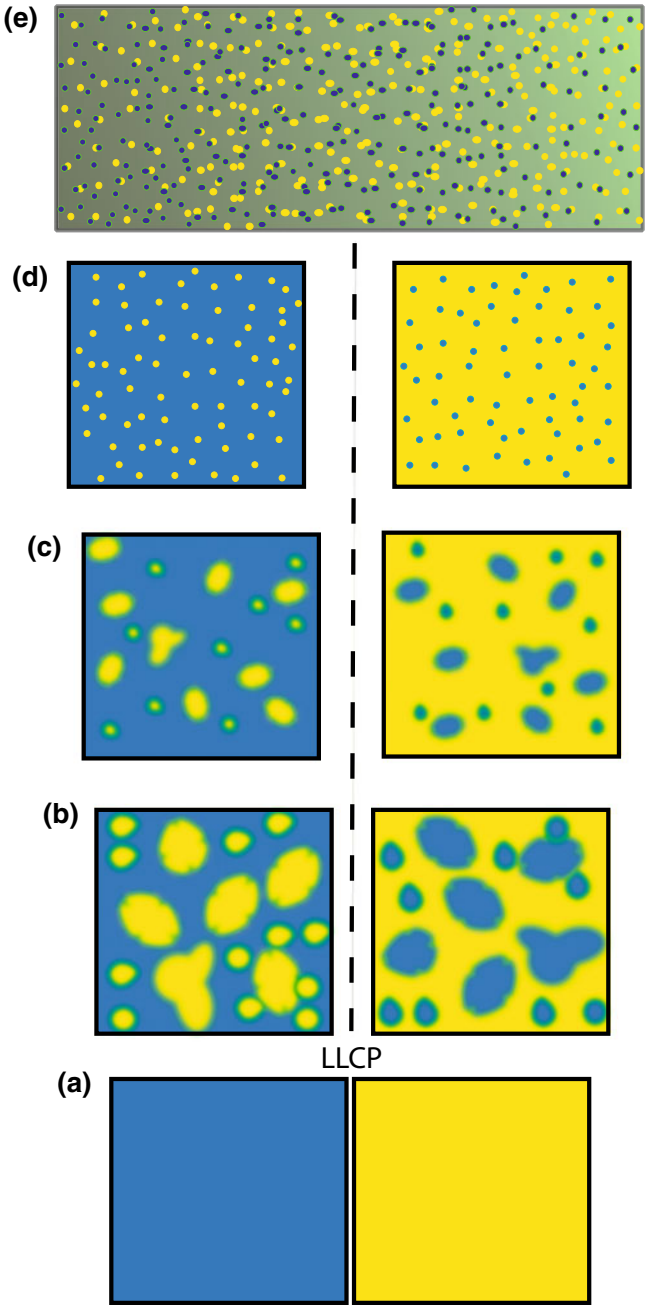
(e)
(d)
(c)
(b)
LLCP
(a)

◀**Fig. 1.4** Illustration of different possible scenarios for fluctuations in liquid water at different temperatures and pressures. Blue illustrates LDL and yellow HDL. **a** The pure liquid forms as observed using WAXS and XPCS in the ultraviscous regime [28] with the coexistence line separating them. Beyond the proposed LLCP there are **b** large fluctuations in the one-phase region where on one side of the Widom line (dashed) LDL dominates and on the other HDL. The fuzzy green borders indicate the transition region between the two local forms. **c** Moving farther from the LLCP, the one-phase region becomes broader while fluctuations diminish and **d, e** sufficiently far away, the fluctuations become small enough to represent an ideal mixture

The similarity in frequency of the OH-stretch maximum in Raman measurements of highly supercooled liquid water to that in clathrates was noted by Walrafen et al. [95] and Pauling proposed that many water properties could be understood based on clathrate structures in the liquid [45]. X-ray diffraction of supercooled water has also been interpreted as indicating the presence of clathrate structures [124], although, as shown by the RMC modeling discussed in Sect. 1.2 above [71, 72], XRD allows a multitude of structural solutions.

Clathrates are built from open, ball-like structures, largely based on pentagonal rings, which leads to favorable angular correlations [123], but a low density, which has been taken as argument against such structures in the liquid. However, considering both HDL and LDL as simple liquids [23] that each has increasing density with decreasing temperature, the density maximum is easily understood as the point where low-density tetrahedral fluctuations overcome the density increase of the HDL component that dominates at higher temperatures. Similarly, there should then also be a density minimum when the liquid has been converted to LDL, for which the density also increases upon further cooling. This density minimum has indeed been observed for water in confinement [125, 126] and in MD simulations of deeply supercooled water, e.g., [86]. The density of an LDL component should thus be closer to that at the density minimum than to that of ambient water. Fluctuations involving clathrate-like components can thus not be excluded based on density arguments. They have been proposed based on careful analysis of experimental Raman spectra [95], but have not been directly structurally identified in the liquid.

A hypothetical clathrate-like structure, built from fused dodecahedra, is shown in Fig. 1.5 as an illustration. It is clear from the figure that, if such structures appear, the core region could be expected to be stabilized by favorable H-bonding. It is also clear that the growth of such hypothetical structures would be hindered through the increased angular strain in outer layers, which could give rise to a narrow surrounding region of intermediate H-bonded structures as molecules from the HDL environment attempt to attach to the template, but become unstable and return to HDL. Clathrate-like structures have not been reported in MD simulations of ambient or supercooled water, which, however, does not exclude that such structures could still be relevant for real water.

Water does represent a severe challenge to theoretical simulations, not only due to the delicate balance between different counteracting interactions of similar magnitude, but also due to the emergent character of the resulting properties, which requires

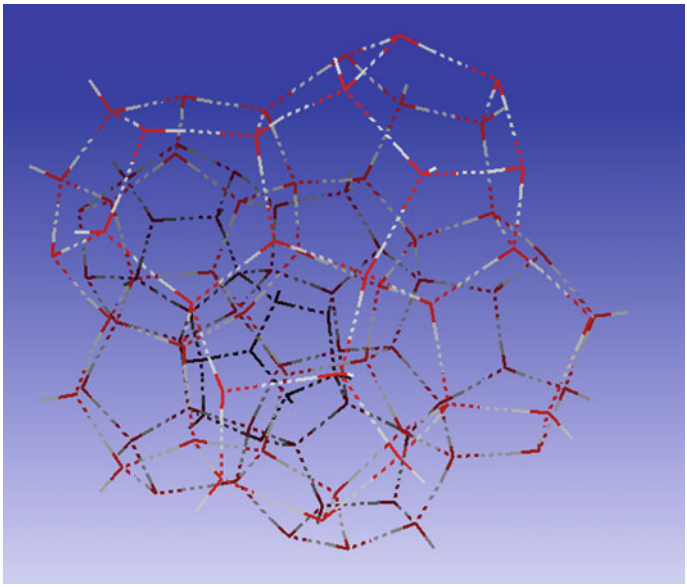

Fig. 1.5 Illustration of a clathrate-like structure built from fused dodecahedra (20 molecules each). Dashed lines indicate H-bonds between molecules which are located at the vertices of the connecting lines. The internal OH bond in each molecule is indicated by solid sticks colored red-grey

a large number of molecules to develop. It is clear that highly accurate computational approaches are needed to reliably capture this balance and significant progress has been made in terms of many properties, such as the RDFs. Recent developments with parameterization of up to three-body interactions at the CCSD(T) level of quantum chemical accuracy hold promise [30], but the resulting structure is still unimodal, both in terms of computed XES [35] and Raman spectra (Fig. 1.2c) [36]. In another approach, VandeVondele and coworkers [31] have exploited algorithmic and computer developments to perform fully ab initio periodic MP2 quantum chemical Monte Carlo simulations of 64 water molecules, but considering the experimental observation of an eighth *radial* coordination shell at ~17 Å, significantly larger simulation boxes will be necessary, which will be a challenge to this approach. Simulations based on DFT [127, 128] scale better with size of the system, but a simulation box size of 30–40 Å still represents a severe challenge, although impressive progress is being made [32, 129–131]. Nuclear quantum effects (NQE) are furthermore important [132–134] and have been proposed to be decisive in determining the difference in entropic contribution from HDL and LDL [21]. The expense of including NQE has been significantly reduced by developments in terms of colored noise Langevin thermostats [135] and quantum ring-polymer contraction [136].

In Fig. 1.6 the local structure index [137], LSI, is used as order parameter to demonstrate that, even in simulations with classical force-fields, the *inherent structure* (Fig. 1.6, right) is perfectly bimodal [88]; the inherent structure is obtained

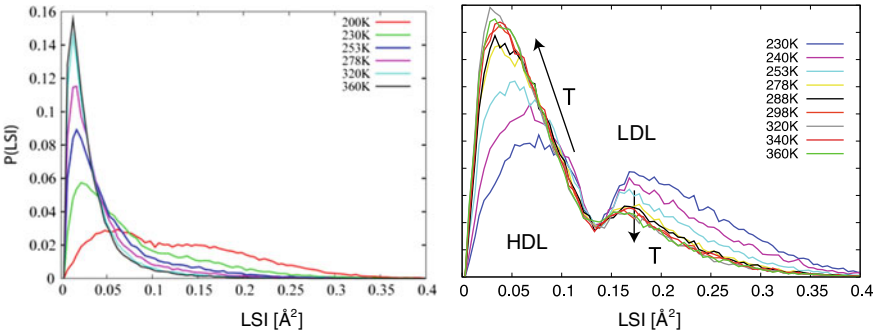

Fig. 1.6 LSI distributions obtained from (left) the real structure and (right) energy-minimized "inherent structures" in simulations of TIP4P/2005 water as function of temperature. An isosbestic point is seen around LSI = 0.13–0.14 Å^2 and is present at all temperatures in the inherent structure, but only as a weak minimum at the lowest temperature in the real structure

by quenching the instantaneous structure into the nearest local minimum on the underlying potential energy surface, thus removing thermal motion [138]. In the real structure (Fig. 1.6, left), including temperature, the bimodality is lost except at the lowest simulated temperature (200 K). The LSI reflects the degree of order in the first and second coordination shells and gives a high value for tetrahedrally strongly ordered local coordination (LDL) and a low value for close-packed, disordered local coordination (HDL).

The bimodality in the inherent structure implies that the multidimensional potential energy surface, on which the simulation evolves, contains two qualitatively different types of projections relating to *local* configurations of molecules in agreement with XAS [60, 98, 99] and XES [106, 112] experimental data, as well as with IR [96] and Raman [38, 91, 92, 94]. We note that the populations at ambient conditions in the inherent structure, ~25% high-LSI (LDL-like) and 75% low-LSI (HDL-like) [88], reflect closely the experimental estimates [20, 84, 106] of the two components in XES and XAS/XRS [60, 98], as well as those of Taschin et al. [139] based on the optical Kerr effect and Xu et al. [140] from IR data on confined water. We observe further, that the behavior of the two peaks in the LSI distribution matches what is observed from XES, where the lone-pair feature, assigned as due to tetrahedral species (LDL-like), only loses intensity with increasing temperature, but shows no dispersion; this is also seen for the high-LSI distribution in Fig. 1.6 (right). The other peak in XES, close to the gas phase position and assigned as due to disordered species (HDL-like) gains intensity and disperses toward the gas phase peak position with increasing temperature; this is closely matched by the low-LSI distribution in Fig. 1.6 (right).

We thus have a direct correspondence between the two LSI components and the spectroscopic observations. However, including temperature removes the bimodality. The simulation exhibits the prerequisites for generating a bimodal spectroscopic signal in that the underlying potential energy surface on which it evolves does con-

tain two minima, consistent with the interpretation of the spectra. The minima are, however, seemingly too shallow such that, when a finite temperature is included, an average structure is obtained. In this picture the two minima would thus need to be deeper to constrain the simulation more closely to either minimum.

An alternative is to remove thermal energy by simulating deeply supercooled and pressurized water. In this case, many different water models have indicated the existence of an LLCP associated with a liquid-liquid transition [12, 13, 15, 16, 24, 29, 39, 42, 141–152]. However, since the LLCP in the models is located at very low temperature, these simulations are challenging and require very long equilibration times. Since ice is significantly more stable in this metastable region, the interpretation in terms of a liquid-liquid transition in the ST2 force-field model of water [16] was challenged by Chandler and Limmer in a series of papers [153–155] and claimed to instead be a liquid-solid transition. Debenedetti and coworkers [12, 147] used the same model and, in contrast, found unequivocal evidence of a reversible transition between two basins corresponding to LDL and HDL in the free-energy landscape, as well as locating the transition to ice. Since they used the same model as Chandler and Limmer, but with different results, this led to a heated exchange [147, 156, 157], which was only resolved when it was shown that the Chandler and Limmer simulation code had conceptual problems [142, 158]. Thus, it is now clear that the ST2 model of water, as well as many other water models, supports a liquid-liquid transition but, when simulating *ambient* water, the experimentally observed bimodality and structural fluctuations, that would be expected from the existence of an LLCP, become washed out.

Figure 1.7 illustrates in a simplified picture what effects need to be considered and improved in simulations in order to better represent the bimodality in structural fluctuations that the experimental data above suggest also for ambient liquid water. Since we discuss bimodality, we will illustrate the result of adding specific interactions through a one-dimensional free-energy surface condensed to two basins representing LDL and HDL at ambient conditions; the 9N (N being the number of molecules) degrees of freedom have thus been condensed into one, qualitatively illustrating the free-energy balance between LDL- and HDL-like environments.

Figure 1.7a illustrates the qualitative behavior in a classical force-field simulation, where the minima are present, but not deep enough to constrain the simulation to either of the two wells; the resulting distribution (red) becomes an average due to the available thermal energy (dashed).

Electronic structure cooperativity in H-bond formation, which strengthens individual H-bonds if a more extended tetrahedral network is created [159, 160], is not included in common classical non-polarizable force-fields. Extending the description to ab initio MD simulations, using DFT at the generalized gradient level, enhances the minimum corresponding to tetrahedral or LDL-like structures, as indicated in Fig. 1.7b. The balance is, however, shifted too much towards tetrahedral H-bonding and LDL as demonstrated by the melting temperature of ice, which is found to be around 420 K when simulated using the PBE or BLYP functionals [161].

The non-directional van der Waals interaction can offset the too strong directional H-bonding as illustrated in Fig. 1.7c. HDL is a more close-packed structure, which is

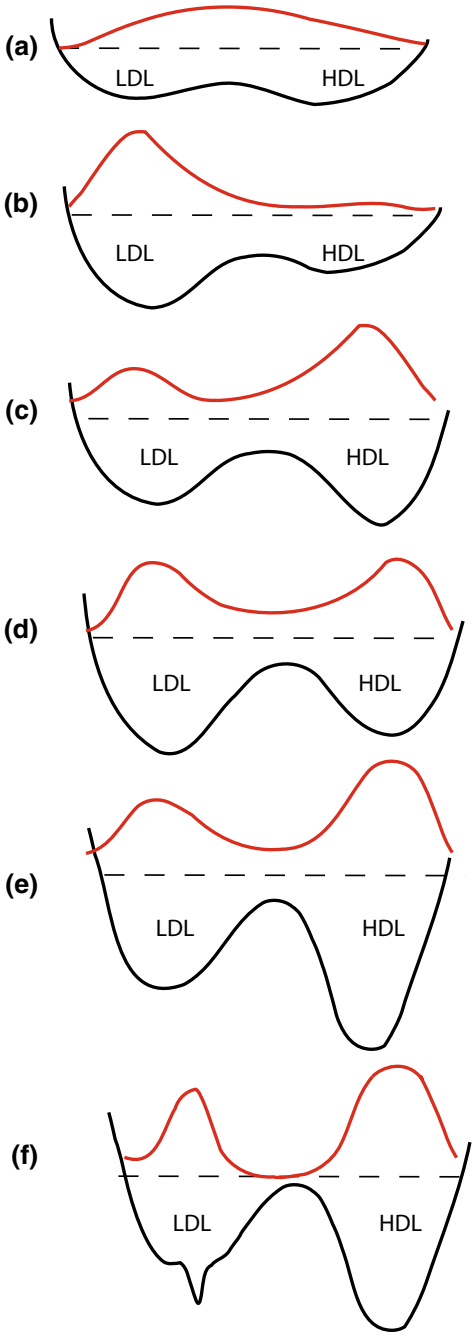

Fig. 1.7 Illustration of the effect of various contributions on the balance between HDL and LDL. **a** Classical force-field. **b** Add electronic cooperativity through DFT. **c** Add van der Waals interaction. **d** Increase the box size. **e** Add nuclear quantum effects. **f** Allowing enough time for the simulation to find preferred templates for tetrahedral LDL fluctuations

favored by more non-directional interactions. Including the van der Waals interaction thus enhances the other, HDL-like, minimum in the simulations, as shown by the melting point of BLYP ice being lowered by 60° to 360 K when van der Waals interactions are included [162]. MD simulations using functionals including van der Waals interactions fully ab initio [32, 163–165] have reported that the very overstructured, LDL-like O–O RDF obtained with GGA functionals becomes a very feature-less, HDL-like RDF when instead applying the vdW-DF2 or optPBE-vdW non-local correlation functionals [164]; the recent work by Del Ben et al. [32], investigating a range of techniques to include non-local correlation, underlines the importance of a proper balance between H-bonding and non-directional van der Waals interactions.

The size of the simulation box is of particular importance for the LDL-like fluctuations, as illustrated in Fig. 1.7d. The analysis of the temperature-dependent extended O–O RDF's by Schlesinger et al. [80] revealed shell structure out to around 17 Å becoming evident upon cooling. Since the RDF describes the *radial* distribution, then a box size greater than ~35 Å would be needed to allow fluctuations into *one* such tetrahedral patch to fully develop; a standard 64 molecules ab initio MD simulation at experimental density uses a box of 12.42 Å side.

Figure 1.7e illustrates the importance of nuclear quantum effects [166] that have been proposed to discriminate between LDL and HDL [21, 167], since it is only when the stiffer modes in tetrahedral coordination (LDL) are fully quantized that these modes become thermally inaccessible and their contribution to the entropy eliminated. The less restricted motion in the HDL environment, with broken or weakened H-bonds, leads to softer vibrational motion and thermally accessible quantized energy levels at ambient temperatures which contribute to the entropy.

Finally, until now only up to short-range three-body interactions have been included in developing the force-fields that hold the potential to span both the spatial and temporal range necessary to fulfill the requirements outlined above. Figure 1.7f illustrates the potential effect of specific clathrate-like templates as basis for fluctuations, which could generate the rather sharp bimodality observed from IR, Raman and XES spectroscopies by forming a core template for fluctuations as they attempt to grow. This is indicated by the sharp specific well and absence of significant intensity in the transition region between the HDL and LDL basins.

However, even for as simple a structure as a 20-molecules dodecahedron there are 30,026 different ways to organize the same number of H-bonds, while still obeying the ice-rules [168]; these span a significant range in energetic stability depending on the topology of the H-bond network and would be only the simplest building-block in pentagon-based, clathrate-like templates for fluctuations. Even if all the above requirements are fulfilled in terms of description of the interactions, size of simulation box and inclusion of nuclear quantum effects, it will likely require a presently unattainable computer time for such templates to appear simply through statistical motion in the simulation box. This is qualitatively illustrated by the rather sharp local minimum in the potential energy surface in Fig. 1.7f.

One additional, strictly quantum mechanical effect may also be of importance for obtaining the correct instantaneous structure of the liquid. The overall wave

function for a system of protons must be antisymmetric with respect to exchange of the two protons since they are fermions, while for deuterons (being bosons) it must be symmetric. An antisymmetric spin wave function for the two protons thus enforces a symmetric spatial wave function for a system of protons (*para*-H_2O), while the opposite is true for the symmetric spin case (*ortho*-H_2O). The spatial wave function of the two protons relates to rotations, such that an *ortho* water molecule cannot be in the lowest rotational state. The energy difference in gas phase is small [169]. 23.8 cm^{-1}, but in condensed phase rotations become hindered with potentially larger energy differences when the relevant modes become librations and translations. Interestingly, the spin statistics give a 1:3 *para* to *ortho* ratio similar to what is found for the LDL to HDL ratio in the inherent structure in TIP4P/2005 water [88], as well as experimentally proposed from X-ray spectroscopy [20, 60].

Although significant efforts have been made to take into account wave function aspects of both electrons and light nuclei [170–176], the restrictions on the nuclear wave functions because of requirements on exchange of identical fermions have not been specifically treated. Notably, triplet-coupled (*ortho*) water molecules cannot be in the rotational ground state, which could make it unfavorable for *ortho* molecules to participate in fluctuations into tetrahedral, LDL-like environments. Similar requirements pertain for the bosonic wave functions of D_2O water.

It is not clear to what extent the requirements on the proton (deuteron) wave function affect the energetics and dynamics in the liquid. Is spin conversion through hyperfine interactions and proton (deuteron) exchange rapid enough to follow the picosecond dynamics of H-bond formation and breaking or will the wave function requirements induce preferences in the conversion between local structures? For water molecules confined in C_{60} fullerenes the time-constants for interconversion at room temperature was determined as 16–30 s (depending on oxygen isotope) [177] and, in a very recent experimental study [178] it was shown that *ortho*- and *para*-water exhibit different reactivity in a prototype reaction.

There are thus significant challenges remaining to simulators aiming to obtain all properties of this fundamental liquid correctly from a single, fully consistent simulation. These concern both developing accurate descriptions of the molecular interactions and a fundamental understanding of the quantum properties of the light particles in terms of proton delocalization, as well as wave function properties through nuclear spin-coupling. These must, furthermore, be possible to efficiently scale up to length-scales of tens or possibly hundreds of thousands of molecules and extended to time-scales that are sufficient for a fully ergodic sampling of the distribution of LDL fluctuations. The latter may occur based on structural templates that live on a very different time-scale than the normal H-bond dynamics in the liquid, which will further complicate the life of the simulator aiming for the "ultimate description" of water.

Having said this, a large number of properties are indeed well-described by present models [30, 34], although it is clear that earlier conclusions from Raman data [91–93, 95, 179] and more recent IR data [96], as well as from XAS and XES data [22, 23, 35, 97, 99, 106, 112] and scattering [8, 9, 86], are not well-described and indicate possibilities for improvement of the simulation models.

1.5 Discussion and Conclusions

We have presented a range of experimental data that indicate that the local structure of normal liquid water under ambient conditions is dominated by HDL-like environments with fluctuations into strongly tetrahedral environments with very well-defined and short H-bonds. The isosbestic point observed in the temperature-dependent OH-stretch Raman signal [37, 38, 92, 94], the split between the two lone-pair peaks in XES [35], as well as the decomposition of the temperature-dependent full IR spectrum as two temperature-independent spectra [96], indicate that structures intermediate between HDL-like and LDL-like do not contribute significantly. This could be due to rapid transitions between the two endpoints, i.e. HDL and LDL environments, with more time spent at either endpoint than in the transition between them.

An alternative explanation of the bimodality could be that specific clathrate-like templates form, where the core could be more long-lived. Intermediate structures then appear in the interfacial region only as molecules attempt to attach to such templates before these collapse. We note that, although the life-time of individual H-bonds is of the order of a picosecond, there is currently no experimental information on the time-scale of *structural* transformations between HDL-like and LDL-like.

Assuming HDL to be chain-like [60], H-bond breaking and formation could simply correspond to exchanging which of the hydrogens that is H-bonded and which is free, which doesn't change the structure. Similarly, for a fully tetrahedrally H-bonded molecule in a tetrahedral environment, more than one bond must be simultaneously broken for the structure to break apart. There may thus exist dynamics on several time-scales in the liquid.

From a thermodynamic point of view, LDL is favored by the gain in energy from H-bond formation, but the high degree of local order that this enforces leads to loss of entropy. The HDL, on the other hand, is favored by entropy through more broken and distorted H-bonding. The loss in energy of directional H-bonds for HDL is compensated by packing the molecules closer, which gives more favorable van der Waals interaction [164]. However, maximal H-bond-order and structural disorder are mutually exclusive, which leads to a balance between the two and fluctuations in the liquid. Indeed, such a two-state picture, with a balance between competing thermodynamic contributions, has been shown to lead to a consistent description of liquid water across its phase diagram in terms of temperature and pressure [13, 17, 18, 39–43].

Experimentally, HDL and LDL as pure liquids and the transition between them have been observed, but only in the ultraviscous regime [28]. The isothermal compressibility, κ_T, has been shown to exhibit a maximum at −44 °C (229 K) [8, 9], which is what is expected in the one-phase region beyond a critical point [180]. However, the location of the proposed critical point lies inside what is called "No-man's land", which is the region bounded from above by the temperature (T_H) of homogeneous ice nucleation and from below by the temperature (T_X) of crystallization (see Fig. 1.8). In this "No-man's land" the liquid is extremely unstable and conversion to ice cannot be hindered. This makes locating a possible critical point in a liquid-liquid transition

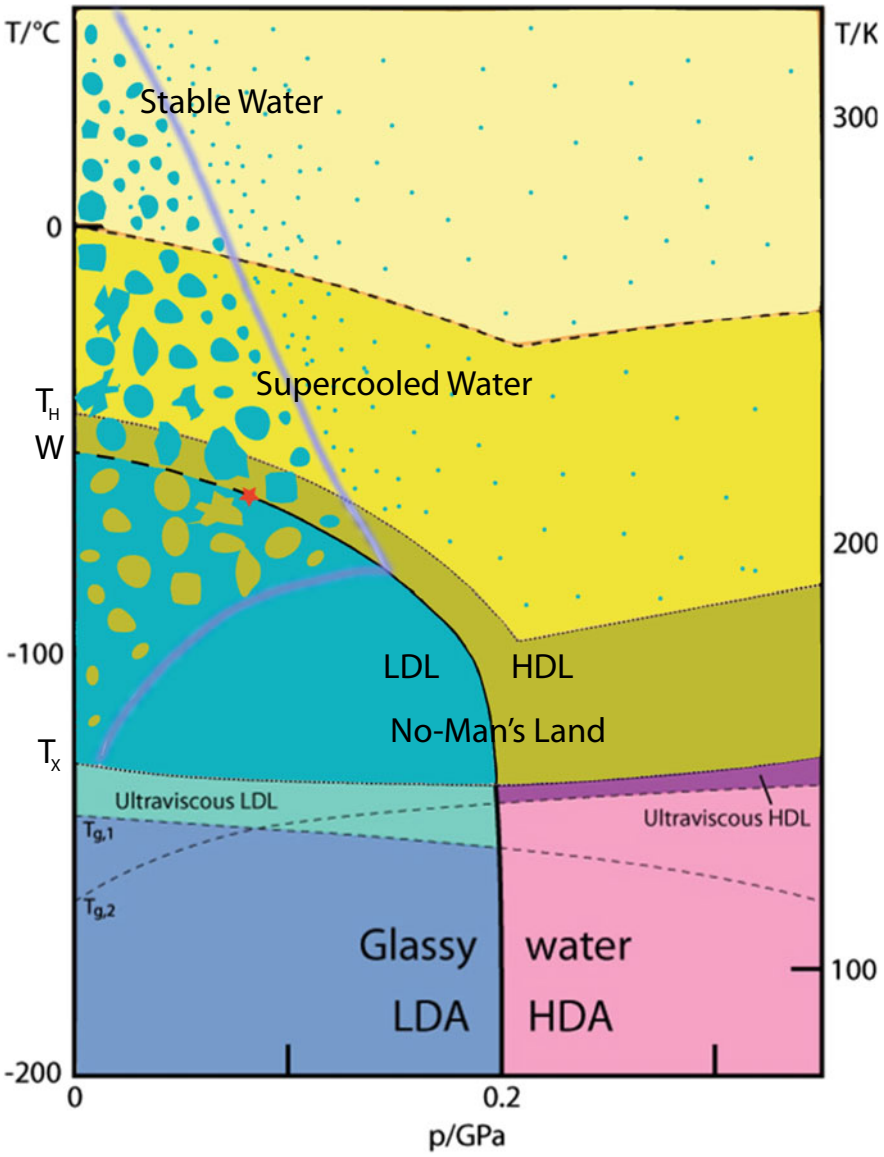
T/°C
T/K
Stable Water
300
0
Supercooled Water
T_H
W
200
-100
LDL
HDL
No-Man's Land
T_X
Ultraviscous LDL
Ultraviscous HDL
T_g,1
T_g,2
Glassy
water
LDA
HDA
100
-200
0
0.2
p/GPa

◀**Fig. 1.8** Illustrative phase diagram of liquid water in terms of pressure (x-axis) and temperature (y-axis). At the bottom there are the two forms of glassy water, LDA at low pressure and HDA at high pressure. T_X indicates the crystallization limit as one heats the amorphous ices. The "No-man's land" region is subdivided into pure LDL and pure HDL regions by the coexistence line (full black line) and terminated at the critical point (red star) beyond which the separation breaks down and large-scale fluctuations between the two forms appear. Below the Widom line (W, dashed), LDL (turquoise) dominates but with fluctuations into HDL regions (mustard), while above it, HDL dominates with fluctuations into LDL regions. The anomalous region, where correlated fluctuations occur and give deviations from simple liquid properties, lies in the funnel (hazy lines) extending from the region of the critical point. The farther away from the critical point one moves, the smaller the fluctuations become, as indicated by the size of the blobs. Outside the funnel, at higher temperatures, only local fluctuations occur in the otherwise HDL-dominated liquid (indicated by small blue dots on the yellow background). T_H marks the temperature of homogeneous ice nucleation, below which the liquid will convert to ice, and 0 °C marks the equilibrium line between liquid and solid

in this region extremely challenging. However, even the "virtual" existence of such a critical point would have a large influence also on water at conditions relevant for life. This would be a consequence of the two forms of liquid water, their coexistence and the mutual exclusivity of the thermodynamic contributions that favor each of them.

In Fig. 1.8 we illustrate in the form of a phase diagram in temperature and pressure the picture of liquid water that has emerged from recent and older data. At the bottom, at very low temperatures, we have the two forms, LDA and HDA, of amorphous ice that are known to interconvert in a first-order-like transition [26, 27, 181, 182]. The coexistence line is assumed to continue into the "No-man's land" as indicated by the full black line in Fig. 1.8. This line is assumed to separate the pure HDL and LDL forms of the liquid. It should be noted that crystalline ice is far more stable at these temperatures and pressures than either of the liquid forms, so that, if one could still generate either liquid, it would quickly crystallize.

The red star in Fig. 1.8 indicates the proposed critical point terminating the coexistence line between HDL and LDL, while the dashed line, continuing the coexistence line beyond the critical point, indicates the Widom line (W). This is a line of maxima in correlation length (a measure of spatial extent of correlations), or isothermal compressibility (κ_T) or specific heat (C_P); there is thus more than one line of maxima beyond the critical point, but they all converge to the critical point [183].

The latter two properties, κ_T and C_P, depend on fluctuations in, respectively, density and entropy, with the spatial extent of such fluctuations being greatest in the vicinity of the critical point (red star), as indicated by the size of the mustard and turquoise blobs in the illustration. It should be noted that, although this region beyond the critical point is a single-phase region where one can no longer speak of HDL and LDL, there will be fluctuations between the two structural species. The Widom line separates the region (turquoise) where LDL dominates, with HDL fluctuations, from that where HDL dominates, with LDL fluctuations (turquoise blobs). At the Widom line the ratio is 50:50 [88], leading to maximum values of properties depending on fluctuations, such as κ_T and C_P.

From the vicinity of the critical point there is a funnel-like region extending with structural fluctuations surviving also at temperatures and pressures far away from the critical point. This is indicated by the grey fuzzy lines extending as a funnel to lower and higher temperatures in the illustration and which delimit the region of correlated structural fluctuations between HDL and LDL. We define these lines as the onset of anomalous behavior of water properties, which thus occurs already around 50 °C for water at ambient pressure, as seen from the minimum of the isothermal compressibility (46 °C) and the associated structural changes evidenced by the temperature-dependent peaks in the O–O RDF [78, 80]. This is the temperature and pressure region of life and we may thus be said to live within this funnel of water's structural fluctuations. This is a region where there is a fine balance between the strength of H-bonding being sufficient to survive thermal fluctuations in H-bonded proton-transport chains in enzymes, but not so strong as to inhibit flexibility in other aspects. The minimum in the heat capacity, C_P, is at 35 °C, which is close to the body temperature of large mammals like humans. Although the derivative of a function near its minimum is small, one may speculate that evolution has found an advantage in placing body temperature close to that at which it requires more energy to change it to higher or lower temperatures. This could be another aspect of "the funnel of life".

From the picture of ambient liquid water as being within "the funnel of life", we can now in very simple terms understand the anomalous properties of water. Since ambient liquid water is dominated by the HDL structure and ice is more like the LDL liquid, it is no wonder that the solid has lower density and floats on the HDL-dominated liquid. We can view both HDL and LDL as normal liquids, which have their density increasing with decreasing temperature. At high temperatures water is dominated by HDL, but in the region of the funnel, water cannot decide which form is preferred. With more and more correlated LDL fluctuations appearing as water is cooled below 50 °C, it is clear that at some point the increasing appearance of lower-density structures should overcome the densification and a density maximum appear as the LDL fluctuations take over. For water this happens at 4 °C, which then is the temperature at the bottom of lakes and the oceans.

The high heat capacity of ambient liquid water can similarly be understood from the additional *structural* flexibility, added through the fluctuations into LDL-like structures in the HDL-dominated liquid. For normal, simple liquids, only random thermal fluctuations contribute, so the structural fluctuations in water add an extra dimension that increases the heat capacity and makes water a very efficient transporter of heat on our planet.

How does this picture relate to water as a solvent? The dipole moment of the water molecule makes water an excellent solvent for salts, but less so for non-polar solutes. The effects on the structure of water from dissolving salts (alkali fluorides, chlorides, bromides and iodides, e.g., LiCl, NaCl, KCl, RbCl and CsCl) have been investigated using XAS [184]. The anions, except for the large iodide, were found to not significantly affect the water spectrum, while the pre-edge and main-edge in the spectra, associated with HDL-like structures, were enhanced by the cations. In conjunction with the loss of intensity at the post-edge (associated with LDL-like

structures), this was interpreted as a change in the balance between HDL and LDL fluctuations, inhibiting the latter [184]. The effect on water structure from addition of salts was, furthermore, shown to be similar to heating water [23, 37, 184], which is known to break H-bonds, as well as to the effect of applying pressure [185], which would inhibit fluctuations into more voluminous LDL-like structures. The latter effect is seen directly from XRD on water at high pressures, which is found to reduce and eliminate the second shell in the O–O RDF that is associated with tetrahedrality [186].

Gases, such as N_2 and O_2, are small, non-polar molecules that do not interact strongly with the water molecules. We speculate that, in the choice between fitting into the dominating, compact HDL environment and a more spacious, open LDL-like environment, these molecules prefer the latter. Indeed, the solubility of these and similar gases increases strongly as water is cooled below 60 °C (333 K). This coincides with the appearance of correlated LDL-like fluctuations in the HDL-dominated liquid, and the solubility rises even more quickly as water is cooled further below ~20 °C (293 K). Furthermore, the solubility of, e.g., oxygen in seawater is lower than in fresh water, which might be connected to the effect of salts to reduce the occurrence of tetrahedral LDL-like fluctuations.

When considering how such a fluctuating picture of ambient water can affect efforts to purify water, the time-scale of structural fluctuations becomes essential. This is presently not known. If it is of the order of H-bond breaking and reformation, such fluctuations could be expected not to affect how water penetrates a separation membrane. If tetrahedral fluctuations are based on more long-lived structural templates, efficiency might be improved by working at higher temperatures, where the frequency of such fluctuations is reduced. This is highly speculative and would also depend on how water structure is affected by the presence of the membrane.

Figure 1.8 illustrates a picture of water, where two mutually exclusive contributions lead to two preferred arrangements in the liquid as close-packed HDL (favored by higher temperature and pressure) and the lower-density LDL. The proposed liquid-liquid critical point (red star in the figure) corresponds to the tipping point beyond which water cannot decide which form to prefer and fluctuations arise. These extend as a funnel-like region up to temperatures and pressures that are relevant to life and give rise to the numerous anomalous properties of the liquid that have caused scientists to refer to water as “the most anomalous liquid”.

However, in the picture presented here, water is *not* a complicated liquid, but rather two simple liquids with a complicated relationship.

Acknowledgements This chapter summarizes work from the literature and from experimental and modeling work from our group. Special thanks are due Anders Nilsson for many years of collaboration and discussions.

References

1. https://water.usgs.gov/edu/earthhowmuch.html (2016)
2. I. Shiklomanov, in *Water in Crisis: A Guide to the World's Fresh Water Resources*, ed. by P.H. Gleick (Oxford University Press, New York, 1993)
3. L.G.M. Pettersson, R.H. Henchman, A. Nilsson, Introduction: water the most anomalous liquid. Chem. Rev. **116**, 7459–7461 (2016)
4. M.F. Chaplin, http://www.lsbu.ac.uk/water/index.html (2017)
5. C.A. Angell, W.J. Sichina, M. Oguni, Heat capacity of water at extremes of supercooling and superheating. J. Phys. Chem. **86**, 998–1002 (1982)
6. H. Kanno, C.A. Angell, Water: anomalous compressibilities to 1.9 kbar and correlation with supercooling limits. J. Chem. Phys. **70**, 4008 (1979)
7. R.J. Speedy, C.A. Angell, Isothermal compressibility of supercooled water and evidence for a thermodynamic singularity at −45 °C. J. Chem. Phys. **65**, 851–858 (1976)
8. K.-H. Kim, A. Späh, H. Pathak, F. Perakis, D. Mariedahl, K. Amann-Winkel, J.A. Sellberg, J.H. Lee, S. Kim, J. Park et al., Maxima in the thermodynamic response and correlation functions of deeply supercooled water. Science **358**, 1589–1593 (2017)
9. A. Späh, H. Pathak, K.-H. Kim, F. Perakis, D. Mariedahl, K. Amann-Winkel, J.A. Sellberg, J.H. Lee, S. Kim, J. Park et al., Apparent power-law behavior of water's isothermal compressibility and correlation length upon supercooling. Phys. Chem. Chem. Phys. **21**, 26–31 (2019)
10. P.G. Debenedetti, Supercooled and glassy water. J. Phys. Cond. Matt. **15**, R1669–R1726 (2003)
11. J.R. Errington, P.G. Debenedetti, Relationship between structural order and the anomalies of liquid water. Nature **409**, 318–321 (2001)
12. J.C. Palmer, F. Martelli, Y. Liu, R. Car, A.Z. Panagiotopoulos, P.G. Debenedetti, Metastable liquid-liquid transition in a molecular model of water. Nature **510**, 385–388 (2014)
13. P. Gallo, K. Amann-Winkel, C.A. Angell, M.A. Anisimov, F. Caupin, C. Chakravarty, T. Loerting, A.Z. Panagiotopoulos, J. Russo, H. Tanaka et al., Water: a tale of two liquids. Chem. Rev. **116**, 7463–7500 (2016)
14. A. Geiger, H.E. Stanley, Low-density, "Patches" in the hydrogen-bonded network of liquid water: evidence from molecular dynamics computer simulations. Phys. Rev. Lett. **49**, 1749–1752 (1982)
15. T.A. Kesselring, G. Franzese, S.V. Buldyrev, H.J. Herrmann, H.E. Stanley, Nanoscale dynamics of phase flipping in water near its hypothesized liquid-liquid critical point. Sci. Reps. **2**, 474 (2012)
16. P.H. Poole, F. Sciortino, U. Essmann, H.E. Stanley, Phase-behavior of metastable water. Nature **360**, 324–328 (1992)
17. J. Russo, H. Tanaka, Understanding water's anomalies with locally favoured structures. Natl. Commun. **5**, 3556 (2014)
18. R. Shi, J. Russo, H. Tanaka, Common microscopic structural origin for water's thermodynamic and dynamic anomalies. J. Chem. Phys. **149**, 224502 (2018)
19. H. Tanaka, Bond orientational order in liquids: towards a unified description of water-like anomalies, liquid-liquid transition, glass transition, and crystallization. Eur. Phys. J. E **35**, 113 (2012)
20. C. Huang, K.T. Wikfeldt, T. Tokushima, D. Nordlund, Y. Harada, U. Bergmann, M. Niebuhr, T.M. Weiss, Y. Horikawa, M. Leetmaa et al., The inhomogeneous structure of water at ambient conditions. Proc. Natl. Acad. Sci. (USA) **106**, 15214–15218 (2009)
21. A. Nilsson, C. Huang, L.G.M. Pettersson, Fluctuations in ambient water. J. Mol. Liq. **176**, 2–16 (2012)
22. A. Nilsson, L.G.M. Pettersson, Perspective on the structure of liquid water. Chem. Phys. **389**, 1–34 (2011)
23. A. Nilsson, L.G.M. Pettersson, The structural origin of anomalous properties of liquid water. Natl. Commun. **6**, 8998 (2015)

24. M.J. Cuthbertson, P.H. Poole, Mixturelike behavior near a liquid-liquid phase transition in simulations of supercooled water. Phys. Rev. Lett. **106**, 115706 (2011)
25. C.A. Angell, Supercooled water two phases? Natl. Mater. **13**, 673–675 (2014)
26. O. Mishima, Reversible first-order transition between two H_2O amorphs at ~0.2 GPa and ~135 KJ. Chem. Phys. **100**, 5910–5912 (1994)
27. O. Mishima, L.D. Calvert, E. Whalley, An apparently 1st-order transition between 2 amorphous phases of ice induced by pressure. Nature **314**, 76–78 (1985)
28. F. Perakis, K. Amann-Winkel, F. Lehmkühler, M. Sprung, D. Pettersson, J.A. Sellberg, H. Pathak, A. Späh, F. Cavalca, D. Schlesinger et al., Diffusive dynamics during the high- to low-density transition in amorphous ices. Proc. Natl. Acad. Sci. (USA) **114**, 8193–8198 (2017)
29. H.E. Stanley, L. Cruz, S.T. Harrington, P.H. Poole, S. Sastry, F. Sciortino, F.W. Starr, R. Zhang, Cooperative molecular motions in water: the liquid-liquid critical point hypothesis. Phys. A **236**, 19–37 (1997)
30. G.A. Cisneros, K.T. Wikfeldt, L. Ojamäe, J. Lu, Y. Xu, H. Torabifard, A.P. Bartók, G. Csányi, V. Molinero, F. Paesani, Modeling molecular interactions in water: from pairwise to many-body potential energy functions. Chem. Rev. **116**, 7501–7528 (2016)
31. M. Del Ben, M. Schönherr, J. Hutter, J. VandeVondele, Bulk liquid water at ambient temperature and pressure from MP2 theory. J. Phys. Chem. Lett. **4**, 3753–3759 (2013)
32. M. Del Ben, J. Hutter, J. VandeVondele, Probing the structural and dynamical properties of liquid water with models including non-local electron correlation. J. Chem. Phys. **143**, 054506 (2015)
33. R.Z. Khaliullin, T.D. Kühne, The nature of the asymmetry in the hydrogen-bond networks of hexagonal ice and liquid water. J. Am. Chem. Soc. **136**, 3395–3399 (2014)
34. M.J. Gillan, D. Alfè, A. Michaelides, Perspective: how good is DFT for water? J. Chem. Phys. **144**, 130901 (2016)
35. I. Zhovtobriukh, N.A. Besley, T. Fransson, A. Nilsson, L.G.M. Pettersson, Relationship between X-ray emission and absorption spectroscopy and the local H-bond environment in water. J. Chem. Phys. **148**, 144507 (2018)
36. S.K. Reddy, D.R. Moberg, S.C. Straight, F. Paesani, Temperature-dependent vibrational spectra and structure of liquid water from classical and quantum simulations with the MB-pol potential energy function. J. Chem. Phys. **147**, 244504 (2017)
37. Q. Sun, Raman spectroscopic study of the effects of dissolved NaCl on water structure. Vib. Spectrosc. **62**, 110–114 (2012)
38. Q. Sun, Local statistical interpretation for water structure. Chem. Phys. Lett. **568–569**, 90–94 (2013)
39. J.W. Biddle, R.S. Singh, E.M. Sparano, F. Ricci, M.A. González, C. Valeriani, J.L.F. Abascal, P.G. Debenedetti, M.A. Anisimov, F. Caupin, Two-structure thermodynamics for the TIP4P/2005 model of water covering supercooled and deeply stretched regions. J. Chem. Phys. **146**, 034502 (2017)
40. D.A. Fuentevilla, M.A. Anisimov, Scaled equation of state for supercooled water near the liquid-liquid critical point. Phys. Rev. Lett. **97**, 195702 (2006)
41. V. Holten, M.A. Anisimov, Entropy-driven liquid–liquid separation in supercooled water. Sci. Reps. **2**, 713 (2012)
42. R.S. Singh, J.W. Biddle, P.G. Debenedetti, M.A. Anisimov, Two-state thermodynamics and the possibility of a liquid-liquid phase transition in supercooled TIP4P/2005 water. J. Chem. Phys. **144**, 144504 (2016)
43. H. Tanaka, Simple physical model of liquid water. J. Chem. Phys. **112**, 799–809 (2000)
44. W.C. Röntgen, Concerning the structure of liquid water. Ann. Phys. **45**, 91–97 (1892)
45. L. Pauling, in *Hydrogen Bonding,* ed. by D. Hadži (Pergamon Press, New York, 1959)
46. R.J. Speedy, Self-replicating structures in water. J. Phys. Chem. **88**, 3364–3373 (1984)
47. J. Urquidi, C.H. Cho, S. Singh, G.W. Robinson, Temperature and pressure effects on the structure of liquid water. J. Mol. Struc. **485–486**, 363–371 (1999)
48. J. Urquidi, S. Singh, C.H. Cho, G.W. Robinson, Origin of temperature and pressure effects on the radial distribution function of water. Phys. Rev. Lett. **83**, 2348–2350 (1999)

49. M. Vedamuthu, S. Singh, G.W. Robinson, Properties of liquid water—origin of the density anomalies. J. Phys. Chem. **98**, 2222–2230 (1994)
50. A.K. Soper, Joint structure refinement of X-ray and neutron diffraction data on disordered materials: application to liquid water. J. Phys. Cond. Mat. **19**, 335206 (2007)
51. U. Bergmann, D. Nordlund, P. Wernet, M. Odelius, L.G.M. Pettersson, A. Nilsson, Isotope effects in liquid water probed by X-ray Raman spectroscopy. Phys. Rev. B **76**, 024202 (2007)
52. A.K. Soper, C.J. Benmore, Quantum differences between heavy and light water. Phys. Rev. Lett. **101**, 065502 (2008)
53. K.-H. Kim, H. Pathak, A. Späh, F. Perakis, D. Mariedahl, J.A. Sellberg, T. Katayama, Y. Harada, H. Ogasawara, L.G.M. Pettersson et al., Temperature-independent nuclear quantum effects on the structure of water. Phys. Rev. Lett. **119**, 075502 (2017)
54. A. Zeidler, P.S. Salmon, H.E. Fischer, J.C. Neuefeind, J.M. Simonson, H. Lemmel, H. Rauch, T.E. Markland, Oxygen as a site specific probe of the structure of water and oxide materials. Phys. Rev. Lett. **107**, 145501 (2011)
55. A.K. Soper, Empirical potential Monte Carlo simulation of fluid structure. Chem. Phys. **202**, 295–306 (1996)
56. R.L. McGreevy, Reverse Monte Carlo modelling. J. Phys. Cond. Mat. **13**, R877–R913 (2001)
57. R.L. McGreevy, L. Pusztai, Reverse Monte Carlo simulation: a new technique for the determination of disordered structure. Mol. Simul. **1**, 359–367 (1988)
58. A.K. Soper, Tests of the empirical potential structure refinement method and a new method of application to neutron diffraction data on water. Mol. Phys. **99**, 1503–1516 (2001)
59. A.K. Soper, Partial structure factors from disordered materials diffraction data: an approach using empirical potential structure refinement. Phys. Rev. B **72**, 104204 (2005)
60. P. Wernet, D. Nordlund, U. Bergmann, M. Cavalleri, M. Odelius, H. Ogasawara, L.Å. Näslund, T.K. Hirsch, L. Ojamäe, P. Glatzel et al., The structure of the first coordination shell in liquid water. Science **304**, 995–999 (2004)
61. T. Head-Gordon, G. Hura, Water structure from scattering experiments and simulation. Chem. Rev. **102**, 2651–2670 (2002)
62. G. Hura, D. Russo, R.M. Glaeser, T. Head-Gordon, M. Krack, M. Parrinello, Water structure as a function of temperature from X-ray scattering experiments and ab initio molecular dynamics. Phys. Chem. Chem. Phys. **5**, 1981–1991 (2003)
63. G.N.I. Clark, C.D. Cappa, J.D. Smith, R.J. Saykally, T. Head-Gordon, The structure of ambient water. Mol. Phys. **108**, 1415–1433 (2010)
64. G.N.I. Clark, G. Hura, J. Teixeira, A.K. Soper, T. Head-Gordon, Small-angle scattering and the structure of ambient liquid water. Proc. Natl. Acad. Sci. (USA) **107**, 14003–14007 (2010)
65. T. Head-Gordon, M.E. Johnson, Tetrahedral structure or chains for liquid water. Proc. Natl. Acad. Sci. (USA) **103**, 7973–7977 (2006)
66. T. Head-Gordon, M.E. Johnson, Correction. Proc. National Acad. Sci. (USA) **103**, 16614 (2006)
67. T. Head-Gordon, S.W. Rick, Consequences of chain networks on thermodynamic, dielectric and structural properties for liquid water. Phys. Chem. Chem. Phys. **9**, 83–91 (2007)
68. J.D. Smith, C.D. Cappa, K.R. Wilson, B.M. Messer, R.C. Cohen, R.J. Saykally, Energetics of hydrogen bond rearrangements in liquid water. Science **306**, 851 (2004)
69. A. Nilsson, P. Wernet, D. Nordlund, U. Bergmann, M. Cavalleri, M. Odelius, H. Ogasawara, L.-Å. Näslund, T.K. Hirsch, L. Ojamäe, et al., Comment on "Energetics of hydrogen bond network rearrangements in liquid water". Science **308**, 793a (2005)
70. A.K. Soper, Recent water myths. Pure Appl. Chem. **82**, 1855–1867 (2010)
71. M. Leetmaa, K.T. Wikfeldt, M.P. Ljungberg, M. Odelius, J. Swenson, A. Nilsson, L.G.M. Pettersson, Diffraction and IR/Raman data do not prove tetrahedral water. J. Chem. Phys. **129**, 084502 (2008)
72. K.T. Wikfeldt, M. Leetmaa, M.P. Ljungberg, A. Nilsson, L.G.M. Pettersson, On the range of water structure models compatible with X-ray and neutron diffraction data. J. Phys. Chem. B **113**, 6246 (2009)

73. U. Bergmann, A. Di Cicco, P. Wernet, E. Principi, P. Glatzel, A. Nilsson, Nearest-neighbor oxygen distances in liquid water and ice observed by X-ray Raman based extended X-ray absorption fine structure. J. Chem. Phys. **127**, 174504 (2007)
74. U. Bergmann, A. Di Cicco, P. Wernet, E. Principi, P. Glatzel, A. Nilsson, Erratum: Nearest-neighbor oxygen distances in liquid water and ice observed by X-ray Raman based extended X-ray absorption fine structure. [J. Chem. Phys. **127**, 174504 (2007)]; J. Chem. Phys. **128**, 089902 (2008)
75. M. Leetmaa, K.T. Wikfeldt, L.G.M. Pettersson, SpecSwap-RMC: a novel reverse Monte Carlo approach using a discrete configuration space and pre-computed properties J. Phys. Cond. Mat. **22**, 135001 (2010)
76. M. Leetmaa, SpecSwap-RMC download. https://github.com/leetmaa/SpecSwap-RMC (2013)
77. K.T. Wikfeldt, M. Leetmaa, A. Mace, A. Nilsson, L.G.M. Pettersson, Oxygen-oxygen correlations in liquid water; addressing the discrepancy between diffraction and EXAFS using a novel multiple—data set fitting technique. J. Chem. Phys. **132**, 104513 (2010)
78. L.B. Skinner, C.J. Benmore, J.C. Neuefeind, J.B. Parise, The structure of water around the compressibility minimum. J. Chem. Phys. **141**, 214507 (2014)
79. L.B. Skinner, C. Huang, D. Schlesinger, L.G.M. Pettersson, A. Nilsson, C.J. Benmore, Benchmark oxygen-oxygen pair-distribution function of ambient water from X-ray diffraction measurements with a wide Q-range. J. Chem. Phys. **138**, 074506 (2013)
80. D. Schlesinger, K.T. Wikfeldt, L.B. Skinner, C.J. Benmore, A. Nilsson, L.G.M. Pettersson, The temperature dependence of intermediate range oxygen-oxygen correlations in liquid water. J. Chem. Phys. **145**, 084503 (2016)
81. L.M. Maestro, M.I. Marqués, E. Camarillo, D. Jaque, G. Solé, J.A. Gonzalo, F. Jaque, J.C. del Valle, F. Mallamace, H.E. Stanley, On the existence of two states in liquid water: impact on biological and nanoscopic systems. Int. J. Nanotechnol. **13**, 667–677 (2016)
82. C. Huang, T.M. Weiss, D. Nordlund, K.T. Wikfeldt, L.G.M. Pettersson, A. Nilsson, Increasing correlation length in bulk supercooled H_2O, D_2O and NaCl solution determined from small angle X-ray scattering. J. Chem. Phys. **133**, 134504 (2010)
83. A.K. Soper, J. Teixeira, T. Head-Gordon, Is ambient water inhomogeneous on the nanometer-length scale? Proc. Natl. Acad. Sci. (USA) **107**, E44 (2010)
84. C. Huang, K.T. Wikfeldt, T. Tokushima, D. Nordlund, Y. Harada, U. Bergmann, M. Niebuhr, T.M. Weiss, Y. Horikawa, M. Leetmaa, et al., Reply to Soper et al. "Fluctuations in water around a bimodal distribution of local hydrogen bonded structural motifs". Proc. Natl. Acad. Sci. (USA) **107**, E45 (2010)
85. S.D. Overduin, G.N. Patey, Understanding the structure factor and isothermal compressibility of ambient water in terms of local structural environments. J. Phys. Chem. B **116**, 12014–12020 (2012)
86. K.T. Wikfeldt, C. Huang, A. Nilsson, L.G.M. Pettersson, Enhanced small-angle scattering connected to the Widom line in simulations of supercooled water. J. Chem. Phys. **134**, 214506 (2011)
87. J.L.F. Abascal, C. Vega, A general purpose model for the condensed phases of water: TIP4P/2005. J. Chem. Phys. **123**, 234505 (2005)
88. K.T. Wikfeldt, A. Nilsson, L.G.M. Pettersson, Spatially inhomogeneous bimodal inherent structure in simulated liquid water. Phys. Chem. Chem. Phys. **13**, 19918–19924 (2011)
89. L.-P. Wang, T. Head-Gordon, J.W. Ponder, P. Ren, J.D. Chodera, P.K. Eastman, T.J. Martinez, V.S. Pande, Systematic improvement of a classical molecular model of water. J. Phys. Chem. B **117**, 9956–9972 (2013)
90. A. Nilsson, L.G.M. Pettersson, B. Hammer, T. Bligaard, C.H. Christensen, J.K. Nørskov, The electronic structure effect in heterogeneous catalysis. Catal. Lett. **100**, 111 (2005)
91. J.R. Scherer, M.K. Go, S. Kint, Raman spectra and structure of water from −10 to 90°. J. Phys. Chem. **78**, 1304–1312 (1974)
92. G.E. Walrafen, Raman spectral studies of water structure. J. Chem. Phys. **40**, 3249–3256 (1964)

93. G.E. Walrafen, M.R. Fisher, M.S. Hokmabadi, W.-H. Yang, Temperature dependence of the low- and high-frequency Raman scattering from liquid water. J. Chem. Phys. **85**, 6970–6982 (1986)
94. G.E. Walrafen, M.S. Hokmabadi, W.-H. Yang, Raman isosbestic points from liquid water. J. Chem. Phys. **85**, 6964–6969 (1986)
95. G.E. Walrafen, W.-H. Yang, Y.C. Chu, Raman evidence for the clathratelike structure of highly supercooled water. ACS Symp. Ser. **676**, 287–308 (1997)
96. Y. Maréchal, The molecular structure of liquid water delivered by absorption spectroscopy in the whole IR region completed with thermodynamics data. J. Mol. Struct. **1004**, 146–155 (2011)
97. M. Leetmaa, M.P. Ljungberg, A.P. Lyubartsev, A. Nilsson, L.G.M. Pettersson, Theoretical approximations to X-ray absorption spectroscopy of liquid water and ice. J. El. Spec. Rel. Phen. **177**, 135–157 (2010)
98. S. Myneni, Y. Luo, L.-Å. Näslund, M. Cavalleri, L. Ojamäe, H. Ogasawara, A. Pelmenschikov, P. Wernet, P. Väterlein, C. Heske, et al., Spectroscopic probing of local hydrogen bonding structures in liquid water. J. Phys. Condens. Matter **14**, L213–L219 (2002)
99. A. Nilsson, D. Nordlund, I. Waluyo, N. Huang, H. Ogasawara, S. Kaya, U. Bergmann, L.-Å. Näslund, H. Öström, P. Wernet et al., X-ray absorption spectroscopy and X-ray Raman scattering of water; an experimental view. J. El. Spec. Rel. Phen. **177**, 99–129 (2010)
100. A. Nilsson, T. Tokushima, Y. Horikawa, Y. Harada, M.P. Ljungberg, S. Shin, L.G.M. Pettersson, Resonant inelastic X-ray scattering of water. J. Electron Spectrosc. Relat. Phenom. **188**, 84–100 (2013)
101. D. Nordlund, H. Ogasawara, K.J. Andersson, M. Tatarkhanov, M. Salmerón, L.G.M. Pettersson, A. Nilsson, Sensitivity of X-ray absorption spectroscopy to hydrogen bond topology. Phys. Rev. B **80**, 233404 (2009)
102. U. Bergmann, P. Wernet, P. Glatzel, M. Cavalleri, L.G.M. Pettersson, A. Nilsson, S.P. Cramer, X-ray Raman spectroscopy at the oxygen K edge of water and ice: Implications on local structure models. Phys. Rev. B **66**, 092107 (2002)
103. M. Cavalleri, H. Ogasawara, L.G.M. Pettersson, A. Nilsson, The interpretation of X-ray absorption spectra in water and ice *Chem*. Phys. Lett. **364**, 363 (2002)
104. M. Neeb, J.E. Rubensson, M. Biermann, W. Eberhardt, Coherent excitation of vibrational wave-functions observed in core hole decay spectra of O_2, N_2 and CO. J. El. Spec. Rel. Phen. **67**, 261–274 (1994)
105. O. Fuchs, M. Zharnikov, L. Weinhardt, M. Blum, M. Weigand, Y. Zubavichus, M. Bär, F. Maier, J.D. Denlinger, C. Heske et al., Isotope and temperature effects in liquid water probed by X-ray absorption and resonant X-ray emission spectroscopy. Phys. Rev. Lett. **100**, 027801 (2008)
106. T. Tokushima, Y. Harada, O. Takahashi, Y. Senba, H. Ohashi, L.G.M. Pettersson, A. Nilsson, S. Shin, High resolution X-ray emission spectroscopy of liquid water: the observation of two structural motifs. Chem. Phys. Lett. **460**, 387–400 (2008)
107. K.M. Lange, R. Könecke, S. Ghadimi, R. Golnak, M.A. Soldatov, K.F. Hodeck, A. Soldatov, E.F. Aziz, High resolution X-ray emission spectroscopy of water and aqueous ions using the micro-jet technique. Chem. Phys. **377**, 1–5 (2010)
108. K.M. Lange, R. Könnecke, M. Soldatov, R. Golnak, J.E. Rubensson, A. Soldatov, E.F. Aziz, On the origin of the hydrogen-bond-network nature of water: X-ray absorption and emission spectra of water-acetonitrile mixtures. Angew. Chem. **123**, 10809–10813 (2011)
109. K.M. Lange, M. Soldatov, R. Golnak, M. Gotz, N. Engel, R. Könnecke, J.-E. Rubensson, E.F. Aziz, X-ray emission from pure and dilute H_2O and D_2O in a liquid microjet: hydrogen bonds and nuclear dynamics. Phys. Rev. B **85**, 155104 (2012)
110. L. Weinhardt, A. Benkert, F. Meyer, M. Blum, R.G. Wilks, W. Yang, M. Bär, F. Reinert, C. Heske, Nuclear dynamics and spectator effects in resonant inelastic soft X-ray scattering of gas-phase water molecules. J. Chem. Phys. **136**, 144311 (2012)

111. A. Pietzsch, F. Hennies, P.S. Miedema, B. Kennedy, J. Schlappa, T. Schmitt, V.N. Strocov, A. Föhlisch, Snapshots of the fluctuating hydrogen bond network in liquid water on the sub-femtosecond timescale with vibrational resonant inelastic X-ray scattering. Phys. Rev. Lett. **114**, 088302 (2015)
112. T. Tokushima, Y. Harada, Y. Horikawa, O. Takahashi, Y. Senba, H. Ohashi, L.G.M. Pettersson, A. Nilsson, S. Shin, High resolution X-ray emission spectroscopy of water and its assignment based on two structural motifs. J. El. Spec. Rel. Phen. **177**, 192–205 (2010)
113. N. Mårtensson, A. Nilsson, On the origin of core level binding energy shifts. J. El. Spec. Rel. Phenom. **75**, 209 (1995)
114. F.A. Delesma, M. Van den Bossche, H. Grönbeck, P. Calaminici, A.M. Köster, L.G.M. Pettersson, A chemical view on X-ray photoelectron spectroscopy: the ESCA molecule and surface-to-bulk XPS shifts. ChemPhysChem **19**, 169–174 (2018)
115. M. Odelius, H. Ogasawara, D. Nordlund, O. Fuchs, L. Weinhardt, F. Maier, E. Umbach, C. Heske, Y. Zubavichus, M. Grunze et al., Ultrafast core-hole-induced dynamics in water probed by X-ray emission spectroscopy. Phys. Rev. Lett. **94**, 227401 (2005)
116. O. Fuchs, M. Zharnikov, L. Weinhardt, M. Blum, M. Weigand, Y. Zubavichus, M. Bär, F. Maier, J.D. Denlinger, C. Heske et al., Reply to comment on "Isotope and temperature effects in liquid water probed by X-ray absorption and resonant X-ray emission spectroscopy". Phys. Rev. Lett. **100**, 249802 (2008)
117. M. Odelius, Molecular dynamics simulations of fine structure in oxygen K-edge X-ray emission spectra of liquid water and ice. Phys. Rev. B **79**, 144204 (2009)
118. M. Odelius, Information content in O[1s] K-edge X-ray emission spectroscopy of liquid water. J. Phys. Chem. A **113**, 8176–8181 (2009)
119. K. Yamazoe, J. Miyawaki, H. Niwa, A. Nilsson, Y. Harada, Measurements of ultrafast dissociation in resonant inelastic X-ray scattering of water, 2018, Manuscript
120. T. Fransson, Y. Harada, N. Kosugi, N.A. Besley, B. Winter, J. Rehr, L.G.M. Pettersson, A. Nilsson, X-ray and electron spectroscopy of water. Chem. Rev. **116**, 7551–7569 (2016)
121. Y. Harada, J. Miyawaki, H. Niwa, K. Yamazoe, L.G.M. Pettersson, A. Nilsson, Probing the OH stretch in different local environments in liquid water. J. Phys. Chem. Lett. **8**, 5487–5491 (2017)
122. Y. Harada, T. Tokushima, Y. Horikawa, O. Takahashi, H. Niwa, M. Kobayashi, M. Oshima, Y. Senba, H. Ohashi, K.T. Wikfeldt et al., Selective probing of the OH or OD stretch vibration in liquid water using resonant inelastic soft-X-ray scattering. Phys. Rev. Lett. **111**, 193001 (2013)
123. M. Mandziuk, From the trimer, through the pentamer, to liquid water. J. Mol. Struct. **1177**, 168–176 (2019)
124. H. Yokoyama, M. Kannami, H. Kanno, Existence of clathrate-like structures in supercooled water: X-ray diffraction evidence. Chem. Phys. Lett. **463**, 99–102 (2008)
125. Y. Zhang, A. Faraone, W.A. Kamitakahara, K.-H. Liu, C.-Y. Mou, J.B. Leão, S. Chang, S.-H. Chen, Density hysteresis of heavy water confined in a nanoporous silica matrix. Proc. Natl. Acad. Sci. (USA) **108**, 12206–12211 (2011)
126. D. Liu, Y. Zhang, C.-C. Chen, C.-Y. Mou, P.H. Poole, S.-H. Chen, Observation of the density minimum in deeply supercooled confined water. Proc. Natl. Acad. Sci. (USA) **104**, 9570 (2007)
127. L. Kong, X. Wu, R. Car, Roles of quantum nuclei and inhomogeneous screening in the X-ray absorption spectra of water and ice. Phys. Rev. B **86**, 134203 (2012)
128. Q. Wan, L. Spanu, G.A. Galli, F. Gygi, Raman spectra of liquid water from ab initio molecular dynamics: vibrational signatures of charge fluctuations in the hydrogen bond network. J. Chem. Theory. Comp. **9**, 4124–4130 (2013)
129. S. Andermatt, J. Cha, F. Schiffmann, J. VandeVondele, Combining linear-scaling DFT with subsystem DFT in Born-Oppenheimer and Ehrenfest molecular dynamics simulations: from molecules to a virus in solution. J. Chem. Theory Comput. **12**, 3214–3227 (2016)
130. J. VandeVondele, U. Borštnik, J. Hutter, Linear scaling self-consistent field calculations with millions of atoms in the condensed phase. J. Chem. Theory Comput. **8**, 3565–3573 (2012)

131. T.D. Kühne, Second generation Car-Parrinello molecular dynamics. WIREs Comput Mol. Sci. **4**, 391–406 (2014)
132. D. Marx, M.E. Tuckerman, J. Hutter, M. Parrinello, The nature of the hydrated excess proton in water. Nature **397**, 601–604 (1999)
133. S. Habershon, T.E. Markland, D.E. Manolopolous, Competing quantum effects in the dynamics of a flexible water model. J. Chem. Phys. **131**, 024501 (2009)
134. M. Ceriotti, W. Fang, P.G. Kusalik, R.H. McKenzie, A. Michaelides, M.A. Morales, T.E. Markland, Nuclear quantum effects in water and aqueous systems: experiment, theory, and current challenges. Chem. Rev. **116**, 7529–7550 (2016)
135. M. Ceriotti, G. Bussi, M. Parrinello, Langevin equation with colored noise for constant-temperature molecular dynamics simulations. Phys. Rev. Lett. **102**, 020601 (2009)
136. C. John, T. Spura, S. Habershon, T.D. Kühne, Quantum ring-polymer contraction method: Including nuclear quantum effects at no additional computational cost in comparison to ab initio molecular dynamics. Phys. Rev. E **93**, 043305 (2016)
137. E. Shiratani, M. Sasai, Growth and collapse of structural patterns in the hydrogen bond network in liquid water. J. Chem. Phys. **104**, 7671–7680 (1996)
138. P.G. Debenedetti, F.H. Stillinger, Supercooled liquids and the glass transition. Nature **410**, 259–267 (2001)
139. A. Taschin, P. Bartolini, R. Eramo, R. Righini, R. Torre, Evidence of two distinct local structures of water from ambient to supercooled conditions. Natl. Commun. **4**, 2401 (2013)
140. L. Xu, F. Mallamace, Z. Yan, F.W. Starr, S.V. Buldyrev, H.E. Stanley, Appearance of a fractional stokes-Einstein relation in water and a structural interpretation of its onset. Nat. Phys. **5**, 565–569 (2009)
141. S. Harrington, R. Zhang, P.H. Poole, F. Sciortino, H.E. Stanley, Liquid–liquid phase transition: evidence from simulations. Phys. Rev. Lett. **78**, 2409–2412 (1997)
142. J.C. Palmer, P.H. Poole, F. Sciortino, P.G. Debenedetti, Advances in computational studies of the liquid–liquid transition in water and water-like models. Chem. Rev. **118**, 9129–9151 (2018)
143. P.H. Poole, S.R. Becker, F. Sciortino, F.W. Starr, Dynamical behavior near a liquid-liquid phase transition in simulations of supercooled water. J. Phys. Chem. B **115**, 14176–14183 (2011)
144. F. Sciortino, I. Saika-Voivod, P.H. Poole, Study of the ST2 model of water close to the liquid-liquid critical point. Phys. Chem. Chem. Phys. **13**, 19759–19764 (2011)
145. L. Xu, P. Kumar, S.V. Buldyrev, S.-H. Chen, P.H. Poole, F. Sciortino, H.E. Stanley, Relation between the Widom line and the dynamic crossover in systems with a liquid–liquid phase transition. Proc. Natl. Acad. Sci. (USA) **102**, 16558–16562 (2005)
146. Y. Liu, J.C. Palmer, A.Z. Panagiotopoulos, P.G. Debenedetti, Liquid-liquid transition in ST2 water. J. Chem. Phys. **137**, 214505 (2012)
147. J.C. Palmer, R. Car, P.G. Debenedetti, The liquid-liquid transition in supercooled ST2 water: a comparison between umbrella sampling and well-tempered dynamics. Faraday Disc. **167**, 77–94 (2013)
148. Y. Li, J. Li, F. Wang, Liquid-liquid transition in supercooled water suggested by microsecond simulations. Proc. Natl. Acad. Sci. (USA) **110**, 12209–12212 (2013)
149. J.L.F. Abascal, C. Vega, Widom line and the liquid–liquid critical point for the TIP4P/2005 water model. J. Chem. Phys. **133**, 234502 (2010)
150. G. Franzese, G. Malescio, A. Skibinsky, S.V. Buldyrev, H.E. Stanley, Generic mechanism for generating a liquid-liquid phase transition. Nature **409**, 692–695 (2001)
151. T.A. Kesselring, E. Lascaris, G. Franzese, H.E. Stanley, Finite-size scaling investigation of the liquid-liquid critical point in ST2 water and its stability with respect to crystallization. J. Chem. Phys. **138**, 244506 (2013)
152. G. Malescio, G. Franzese, G. Pellicane, A. Skibinsky, S.V. Buldyrev, H.E. Stanley, Liquid-liquid phase transition in one-component fluids. J. Phys. Cond. Mat. **14**, 2193 (2002)
153. D.T. Limmer, D. Chandler, The putative liquid-liquid transition is a liquid-solid transition in atomistic models of water. J. Chem. Phys. **135**, 134503 (2011)

154. D.T. Limmer, D. Chandler, The putative liquid-liquid transition is a liquid-solid transition in atomistic models of water II. J. Chem. Phys. **138**, 214504 (2013)
155. D.T. Limmer, D. Chandler, Time scales of supercooled water and implications for reversible polyamorphism. Mol. Phys. **113**, 2799–2804 (2015)
156. D. Chandler, Metastability and no criticality. Nature **531**, E1–E2 (2016)
157. J.C. Palmer, F. Martelli, Y. Liu, R. Car, A.Z. Panagiotopoulos, P.G. Debenedetti, Palmer et al. reply Nature **531**, E2–E3 (2016)
158. J.C. Palmer, A. Haji-Akbari, R.S. Singh, F. Martelli, R. Car, A.Z. Panagiotopoulos, P.G. Debenedetti, Comment on "The putative liquid–liquid transition is a liquid-solid transition in atomistic models of water" [Parts I and II: J. Chem. Phys. **135**, 134503 (2011); J. Chem. Phys. **138**, 214504 (2013)] J. Chem. Phys. **148**, 137101 (2018)
159. L. Ojamäe, K. Hermansson, An ab initio study of cooperativity in water chains: interaction energies and anharmonic frequencies. J. Phys. Chem. **98**, 4271 (1994)
160. A. Nilsson, H. Ogasawara, M. Cavalleri, D. Nordlund, M. Nyberg, P. Wernet, L.G.M. Pettersson, The hydrogen bond in ice probed by soft X-ray spectroscopy and density functional theory. J. Chem. Phys. **122**, 154505 (2005)
161. S. Yoo, X. Zeng, S.S. Xantheas, On the phase diagram of water with density functional theory potentials: the melting temperature of ice I with the Perdew–Burke–Ernzerhof and Becke–Lee–Yang–Parr functionals. J. Chem. Phys. **130**, 221102 (2009)
162. S. Yoo, S.S. Xantheas, The effect of dispersion corrections on the melting temperature of liquid water. J. Chem. Phys. **134**, 121105 (2011)
163. J. Wang, G. Román-Pérez, J.M. Soler, E. Artacho, M.-V. Fernández-Serra, Density, structure, and dynamics of water: the effect of van der Waals interactions. J. Chem. Phys. **134**, 024516 (2011)
164. A. Møgelhøj, A. Kelkkanen, K.T. Wikfeldt, J. Schiøtz, J.J. Mortensen, L.G.M. Pettersson, B.I. Lundqvist, K.W. Jacobsen, A. Nilsson, J.K. Nørskov, Ab initio van der Waals interactions in simulations of water alter structure from mainly tetrahedral to high-density-like. J. Phys. Chem. B **115**, 14149–14160 (2011)
165. F. Corsetti, E. Artacho, J.M. Soler, S.S. Alexandre, M.V. Fernandez-Serra, Room temperature compressibility and diffusivity of liquid water from first principles. J. Chem. Phys. **139**, 194502 (2013)
166. X.-Z. Li, B. Walker, A. Michaelides, Quantum nature of the hydrogen bond. Proc. Natl. Acad. Sci. (USA) **108**, 6369–6373 (2011)
167. L.G.M. Pettersson, A. Nilsson, The structure of water; from ambient to deeply supercooled. J. Non-Cryst. Solids **407**, 399–417 (2015)
168. A. Lenz, L. Ojamäe, A theoretical study of water clusters: the relation between hydrogen-bond topology and interaction energy from quantum-chemical computations for clusters with up to 22 molecules. Phys. Chem. Chem. Phys. **7**, 1905–1911 (2005)
169. R. Sliter, M. Gish, A.F. Vilesov, Fast nuclear spin conversion in water clusters and ices: a matrix isolation study. J. Phys. Chem. A **115**, 9682–9688 (2011)
170. S.P. Webb, T. Iordanov, S. Hammes-Schiffer, Multiconfigurational nuclear-electronic orbital approach: incorporation of nuclear quantum effects in electronic structure calculations. J. Chem. Phys. **117**, 4106–4118 (2002)
171. A. Sirjoosingh, M.V. Pak, S. Hammes-Schiffer, Multicomponent density functional theory study of the interplay between electron-electron and electron-proton correlation. J. Chem. Phys. **136**, 174114 (2012)
172. Y. Yang, K.R. Brorsen, T. Culpitt, M.V. Pak, S. Hammes-Schiffer, Development of a practical multicomponent density functional for electron-proton correlation to produce accurate proton densities. J. Chem. Phys. **147**, 114113 (2017)
173. M. Hoshino, H. Nishizawa, H. Nakai, Rigorous non-Born-Oppenheimer theory: combination of explicitly correlated Gaussian method and nuclear orbital plus molecular orbital theory. J. Chem. Phys. **135**, 024111 (2011)
174. H. Nishizawa, Y. Imamura, Y. Ikabata, H. Nakai, Development of the explicitly correlated Gaussian-nuclear orbital plus molecular orbital theory: Incorporation of electron-electron correlation. Chem. Phys. Lett. **533**, 100–105 (2012)

175. R. Flores-Moreno, E. Posada, F. Moncada, J. Romero, J. Charry, M. Díaz-Tinoco, S.A. González, N.F. Aguirre, A. Reyes, LOWDIN: the any particle molecular orbital code. Int. J. Quant. Chem. **114**, 50–56 (2014)
176. E. Posada, F. Moncada, A. Reyes, The any particle molecular orbital grid-based Hartree-Fock (APMO-GBHF) approach. J. Chem. Phys. **148**, 084113 (2018)
177. B. Meier, K. Kouřil, C. Bengs, H. Kouřilová, T.C. Barker, S.J. Elliott, S. Alom, R.J. Whitby, M.H. Levitt, Spin-isomer conversion of water at room temperature and quantum-rotor-induced nuclear polarization in the water-endofullerene $H_2O@C_{60}$. Phys. Rev. Lett. **120**, 266001 (2018)
178. A. Kilaj, H. Gao, D. Rösch, U. Rivero, J. Küpper, S. Willitsch, Observation of different reactivities of *para* and *ortho*-water towards trapped diazenylium ions. Natl. Commun. **9**, 2096 (2018)
179. G.E. Walrafen, Argon-ion-laser-Raman studies of effects of pressure on water structure. Appl. Spectrosc. **22**, 237 (1968)
180. H.E. Stanley, *Introduction to Phase Transitions and Critical Phenomena* (Oxford University Press, New York, 1971)
181. O. Mishima, H.E. Stanley, The relationship between liquid, supercooled and glassy water. Nature **396**, 329–335 (1998)
182. S. Klotz, T. Strässle, R.J. Nelmes, J.S. Loveday, G. Hamel, G. Rousse, B. Canny, J.C. Chervin, A. Saitta, Nature of the polyamorphic transition in ice under pressure. Phys. Rev. Lett. **94**, 025506 (2005)
183. P. Gallo, D. Corradini, M. Rovere, Widom line and dynamical crossovers as routes to understand supercritical water. Natl. Commun. **5**, 5806 (2014)
184. I. Waluyo, D. Nordlund, U. Bergmann, D. Schlesinger, L.G.M. Pettersson, A. Nilsson, A different view of structure-making and structure-breaking in alkali halide aqueous solutions through X-ray absorption spectroscopy. J. Chem. Phys. **140**, 244506 (2014)
185. R. Leberman, A.K. Soper, Effect of high-salt concentrations on water-structure. Nature **378**, 364–366 (1995)
186. A.V. Okhulkov, Y.N. Demianets, Y.E. Gorbaty, X-ray scattering in liquid water at pressures of up to 7.7 kbar: test of a fluctuation model. J. Chem. Phys. **100**, 1578 (1994)

Chapter 2
Current Problems in the Quasi-elastic Incoherent Neutron Scattering and the Collective Drift of Molecules

Leonid A. Bulavin, N. P. Malomuzh and K. S. Shakun

Abstract The determination of the self-diffusion coefficient D_s is one of well known applications of the quasi-elastic incoherent neutron scattering. Here we will show that the half-width of the neutron peak considered as a function of wave vector can be used for the determination of (1) the residence time τ_0 for water molecules and (2) the very important ratio D_c/D_s where D_c is the collective part of the self-diffusion coefficient, caused by its drift in the field of thermal hydrodynamic fluctuations. The applicability region for the simplest diffusion approximation is discussed in details. The influence of the rotational motion of water molecules on spectra of the intermediate scattering function (ISF) is studied. A new type of the high-frequency asymptote for the ISF-spectra is predicted.

2.1 Introduction

The quasi-elastic incoherent neutron scattering (QEINS) is usually applied for the determination of the self-diffusion coefficient D_s [1–3]. In works [4, 5] it had been shown that the half-width of the neutron peak considered as a function of wave vector can be used for the determination of (1) the residence time τ_0 for water molecules [6–9] and (2) the rotational one τ_r for them. Unfortunately, the magnitude of the last does not correlate with its estimate τ_d following from the dielectric relaxation

L. A. Bulavin
Department of Molecular Physics, Kyiv Taras Shevchenko National University,
2 Academic Glushkov Ave., Kyiv 03680, Ukraine
e-mail: bulavin221@gmail.com

N. P. Malomuzh
Department of Theoretical Physics, Odessa I.I.Mechnikov National University,
2 Dvoryanskaja str., Odesa 65026, Ukraine
e-mail: mnp@onu.edu.ua

K. S. Shakun (✉)
Department of Physics and Chemistry, National University "Odessa Maritime Academy",
8 Didrikhson str., Odesa 65043, Ukraine
e-mail: gluon@meta.ua

L. A. Bulavin and L. Xu (eds.), *Modern Problems of the Physics of Liquid Systems*, Springer Proceedings in Physics 223,
https://doi.org/10.1007/978-3-030-21755-6_2

experiments [10–13]. Therefore, the manifestation of rotational motion in spectra of QEINS is needed in additional study.

The main goal of our work is to investigate the spectral properties of the intermediate scattering function (ISF):

$$F_s(\vec{k}, \omega) = \frac{1}{\pi} \int_0^\infty F_s(\vec{k}, t) \cos \omega t \mathrm{d}t, \tag{2.1}$$

where

$$F_s(\vec{k}, t) = < e^{i\vec{k} \cdot \Delta \vec{r}(t)} >, \tag{2.2}$$

$\Delta \vec{r}(t) = \vec{r}(t) - \vec{r}(0)$ is the displacement of a molecule during time t, $\vec{k}$ is the transferring wave vector. The behavior of $F_s(\vec{k}, t)$ will be modeled with the help of computer simulations. We will consider the peculiarities of the spectral density $F_s(\vec{k}, \omega)$ in the three characteristic cases: (1) $|\vec{k}|a \ll 1$; (2) $|\vec{k}|a \sim 1$ and $|\vec{k}|a \gg 1$, where a is the average interparticle spacing. The special attention will be also focused on the $\vec{k}$-dependence of the half-width $\gamma(\vec{k}^2)$ on the spectral peak on its half-height of the:

$$F_s(\vec{k}, \gamma(\vec{k}^2)) = \frac{1}{2} F_s(\vec{k}, \omega)\Big|_{\omega=0}. \tag{2.3}$$

We will also show that the description of experimental data for the case $|\vec{k}|a \ll 1$ with the help of the diffusion approximation

$$F_s(\vec{k}, \omega) \sim \frac{D_s \vec{k}^2}{\omega^2 + \left(D_s \vec{k}^2\right)^2} \tag{2.4}$$

is quite correct only for $0 < \omega \leq D_s \vec{k}^2$, i.e. the applicability region of the diffusion approximation is strongly restricted. The high-frequency asymptote of $F_s(\vec{k}, \omega)$ for the same values of wave vectors is the more surprising:

$$F_s(\vec{k}, \omega) \sim \exp\left(-(\omega \tau(k))^{2/3}\right), \quad \omega \gg D_s \vec{k}^2, \quad |\vec{k}|a \ll 1, \tag{2.5}$$

i.e. it is radically different from that, $F_s(\vec{k}, \omega) \sim \frac{D_s \vec{k}^2}{\omega^2}$, following from the diffusion approximation.

Comparing the $\vec{k}$-dependence of the half-widths for water and argon for $|\vec{k}|a > 1$ we will be able to establish that the rotational motion of water molecules practically does not influence on characteristic details of $\gamma(\vec{k}^2)$. This result is very important for correct description of the role of molecular rotation.

2.2 Cross-Section for the Quasi-elastic Incoherent Neutron Scattering

In general the displacement $\Delta\vec{r}(t)$ of a molecule can be represented as the sum of two terms

$$\Delta\vec{r}(t) = \Delta\vec{r}^{(\upsilon)}(t) + \Delta\vec{r}^{(d)}(t), \tag{2.6}$$

where the first of them is caused by vibration modes and the latter—by the irreversible thermal drift from the one temporary equilibrium position to another. Since these contributions are statistically independent, the intermediate function (2.2) transforms to the product

$$F_s(\vec{k}, t) \leq \exp(i\vec{k} \cdot \Delta\vec{r}^{(\upsilon)}(t)) > < \exp(i\vec{k} \cdot \Delta\vec{r}^{(d)}(t)) > . \tag{2.7}$$

Since vibration displacements $\Delta\vec{r}^{(\upsilon)}(t))$ are limited: $|\Delta\vec{r}^{(\upsilon)}(t))| < b \ll a$

$$|\vec{k}|b \ll 1 \tag{2.8}$$

we can write:

$$< \exp(i\vec{k} \cdot \Delta\vec{r}^{(\upsilon)}(t)) \geq \exp(-2W), \quad W = \frac{1}{12}\vec{k}^2 < \left(\Delta\vec{r}^{(\upsilon)}(t)\right)^2 >, \tag{2.9}$$

i.e. they generate the standard Debye-Waller factor [1–3].

Now we pass to the consideration of $< \exp(i\vec{k} \cdot \Delta\vec{r}^{(d)}(t)) >$ in the simplest case of the diffusion approximation: $|\vec{k}|a \ll 1$ for argon (Sects. 2.1 and 2.2) and water (Sects. 2.3 and 2.4).

2.2.1 Diffusion Approximation for Argon

In this case translational displacements $\Delta\vec{r}^{(d)}(t)$ of a molecule are described by the distribution function:

$$W\left(\Delta\vec{r}^{d}(t)\right) = \left(\frac{3}{2\pi\Gamma(t)}\right)^{3/2} \exp\left(-3\left(\Delta\vec{r}^{d}(t)\right)^2/(2\Gamma(t))\right), \tag{2.10}$$

which leads together with (2.7) and (2.9) to the result:

$$F_s(\vec{k}, t) = \exp(-2W)\exp\left(-\frac{1}{6}\vec{k}^2\Gamma(t)\right). \tag{2.11}$$

Here $\Gamma(t)$ is the mean square displacement (MSD) of a molecule. In accordance with [14, 15], $\Gamma(t)$ can be represented as the sum:

$$\Gamma(t) = \Gamma_{\mathrm{r}}(t) + \Gamma_{\mathrm{c}}(t), \tag{2.12}$$

where

$$\Gamma_{\mathrm{r}}(t) = 6D_{\mathrm{r}}t + C_{\mathrm{r}} \tag{2.13}$$

is the contribution to the MSD caused by displacements on molecular scales (nanoscales) and

$$\Gamma_{\mathrm{c}}(t) = 6D_{\mathrm{c}}t - B\sqrt{t} + \cdots, \quad B = \frac{k_{\mathrm{B}}T}{\rho(\pi\nu)^{3/2}} \tag{2.14}$$

is caused by the collective transport of molecules in the field of thermal hydrodynamic fluctuations (meso-scales) [14–16]. Here k_{B} is the Boltzmann constant, ρ is the mass density, ν is the kinematic shear viscosity and D_{c} is the collective part of self-diffusion coefficient [16].

It is clear from (2.12)–(2.14) that the Debye-Waller factor takes the form:

$$\exp(-2W) = \exp\left(-\frac{1}{6}\vec{k}^2 C_{\mathrm{r}}\right) \tag{2.15}$$

that allows to estimate $\exp(-2W)$ with the help of computer simulations.

As it had been shown in [15] the collective contribution to the self-diffusion coefficient D_{c} is determined by the expression:

$$D_{\mathrm{c}} = \frac{k_{\mathrm{B}}T}{10\pi\eta\sqrt{\nu\tau_{\mathrm{M}}}}, \tag{2.16}$$

where τ_{M} is the Maxwell relaxation time. The last is determined by the equation:

$$\frac{\partial\vec{u}}{\partial t} + \tau_{\mathrm{M}}\frac{\partial^2\vec{u}}{\partial t^2} = \nu\Delta\vec{u} \tag{2.17}$$

for the transversal hydrodynamic velocity field (see details in [17]).

One can show [18] that the MSD of a molecule can be represented in the form:

$$\Gamma(t) = C_{\mathrm{r}} + 6D_{\mathrm{s}}t\left[1 - \frac{10}{3\pi^{1/2}}\frac{D_{\mathrm{c}}}{D_{\mathrm{s}}}\left(\frac{\tau_{\mathrm{M}}}{t}\right)^{1/2} + \cdots\right], \tag{2.18}$$

where the self-diffusion coefficient D_{s} is the sum of D_{c} and D_{r}:

$$D_{\mathrm{s}} = D_{\mathrm{c}} + D_{\mathrm{r}}. \tag{2.19}$$

If we will use in (2.18) the MSD obtained with the help of computer simulations, we can estimate the relative value of the collective self-diffusion coefficient:

$$\frac{D_c}{D_s} = \frac{3\pi^{1/2}}{10} x^{1/2}\left[1 - \frac{\tilde{\Gamma}(x) - \tilde{c}}{x}\right] + o(1/x^{1/2}), \tag{2.20}$$

where $x = t/\tau_M$, $\tilde{\Gamma}(x) = \Gamma(t)/6D_s\tau_M$ and $\tilde{c} = C_r/6D_s\tau_M$. Since the inequality $x^{1/2} \gg 1$ is consistent with $\tilde{\Gamma}(x) \gg \tilde{c}$, the last equation can be simplified:

$$\frac{D_c}{D_s} = F_{MD}(x), \tag{2.21}$$

where $F_{MD}(x) = \frac{3\pi^{1/2}}{10} x^{1/2}\left[1 - \frac{<\tilde{\Gamma}_{MD}(x)>}{x}\right]$ and $\tilde{\Gamma}_{MD}(x)$ is the MSD determined in computer experiments. The angular brackets in $< \tilde{\Gamma}_{MD}(x) >$ denote the averaging operation on different realizations of $\tilde{\Gamma}_{MD}(x)$ over 6 different initial configurations. Here it is supposed that x satisfies the inequality: $1 \ll x \ll x_u$, where x_u is the upper limit for the applicability of computer simulation modeling. The reliability of such an estimate for the ratio $\frac{D_c}{D_s}$ is naturally verified by its comparison with that calculated as the ratio of D_c given by (2.16) to D_s that is determined experimentally.

Using the Einstein formula for the self-diffusion coefficient: $D_s = \frac{k_B T}{6\pi\eta r_p}$, we can attach the ratio D_c/D_s the following view:

$$\frac{D_c}{D_s} = \frac{3}{5}\frac{r_p}{\sqrt{\nu\tau_M}}, \tag{2.22}$$

where r_p is the effective radius for a molecule.

To find the ratio $\frac{D_c}{D_s}$ according to (2.20) it is necessary to find (1) the time dependence of the MSD and (2) the Maxwell relaxation time.

2.2.2 The Spectrum of the ISF for $|\vec{k}|a \ll 1$

From (2.11) it follows that the spectral density for the ISF is determined by the expression:

$$F_s(\vec{k}, \omega) = \frac{1}{\pi}\exp\left(-\frac{1}{6}\vec{k}^2 C\right)\int_0^\infty \exp\left(-\frac{1}{6}\vec{k}^2\Gamma(t)\right)\cos\omega t\, dt, \tag{2.23}$$

where $\Gamma(t)$ in accordance with (2.12)–(2.14) and (2.19) equals to

$$\Gamma(t) = 6D_s t - B\sqrt{t} + \cdots. \tag{2.24}$$

Since the first term in (2.24) plays the leading role for all $t > t_0$, where $t_0 = \left(\frac{B}{6D_s}\right)^2 \sim 10^{-13}$ s, the spectral density of the ISF can be represented in the form (see [19]):

$$F_s(\vec{k},\omega) = \exp\left(-\frac{1}{6}\vec{k}^2 C\right)\frac{1}{\pi}\mathrm{Re}\frac{1}{-i\omega + \gamma(\vec{k}^2,\omega)}, \tag{2.25}$$

where the half-width reduces to

$$\gamma(\vec{k}^2,\omega) = D_s\vec{k}^2\left(1 + \gamma_1(\vec{k}^2,\omega)\right) \tag{2.26}$$

and

$$\gamma_1(\vec{k}^2,\omega) = -\frac{b}{2}\sqrt{\pi(1 - i\tilde{\omega})}, \quad \tilde{\omega} = \frac{\omega}{D_s\vec{k}^2}, \quad b = \frac{B}{6\sqrt{D_s}}\left|\vec{k}\right|. \tag{2.27}$$

In low-frequency limit ($\tilde{\omega} \ll 1$) the half width tends to the value:

$$\gamma(\vec{k}^2,\tilde{\omega}) = D_s\vec{k}^2\left(1 - (b/2)\sqrt{\pi}\right), \tag{2.28}$$

i.e. the correction term is proportional to the cubic degree of the wave vector. In the opposite case let us introduce the function:

$$I(\tilde{\omega},b) = \mathrm{Re}\frac{\tilde{\omega}^2}{-i\tilde{\omega} + 1 + \gamma_1(\vec{k}^2,\tilde{\omega})} - 1, \tag{2.29}$$

having the following high-frequency asymptote:

$$I(\tilde{\omega},b) \underset{\tilde{\omega}\gg 1}{\Rightarrow} \frac{b}{2\sqrt{2}}\sqrt{\pi\tilde{\omega}}. \tag{2.30}$$

Taking into account the expression (2.27) for b and using the equality $B = \frac{20}{\pi^{1/2}}D_c\sqrt{\tau_M}$, from (2.30) we get:

$$\frac{D_c}{D_s} = R_D(\tilde{\omega}), \tag{2.31}$$

where

$$R_D(\tilde{\omega}) = \frac{6}{5}\left(\frac{2}{\tau_M D_s\vec{k}^2}\right)^{1.2}\frac{I(\tilde{\omega},b)}{\sqrt{\tilde{\omega}}}. \tag{2.32}$$

Equation (2.31) has the very important value since it allows us to determine in principle the relative value of the collective self-diffusion coefficient using the incoherent neutron scattering data for $\tilde{\omega} \gg 1$.

2.2.3 The Spectrum of the ISF for Water

The thermal motion of molecules in water essentially differ from that in argon due to clusterization effects. Near the triple point of water it can be represented as the vibrational motion during the residence time τ_0 and the consequent movement during time τ_1 to a new temporary equilibrium position. By order of magnitude: $\tau_1 \sim a/\upsilon_T \approx 3 \cdot 10^{-13}$ s, where υ_T is the average value of the thermal velocity of a molecule. If $\tau_1 \ll \tau_0$ it is accepted to say that the thermal motion has the crystal-like character. It is necessary to note that the residence time takes the same order of magnitude as the life time τ_H for an H-bond. In accordance with [20–22] $\tau_H \sim$ several *ps* at the room temperature.

The characteristic change of the ISF is occurred during time $\tau_0 + \tau_1 \approx \tau_0$ therefore we can write:

$$\frac{\partial F_s(\vec{k}, t)}{\partial t} = \frac{1}{\tau_0}\Big(F_s(\vec{k}, t + \tau_0) - F_s(\vec{k}, t)\Big). \tag{2.33}$$

In order to find the difference: $F_s(\vec{k}, t + \tau) - F_s(\vec{k}, t)$ as a function of t, τ_0 and $\vec{k}^2$, let us represent the displacement $\Delta\vec{r}(t)$ of a molecule as the sum:

$$\Delta\vec{r}(t) = \Delta\vec{r}(t_{1,2}) + \Delta\vec{r}(t_{2,3}) + \ldots + \Delta\vec{r}(t_{N-1,N}) \tag{2.34}$$

of consecutive displacements: $\Delta\vec{r}(t_{i-1,i}) = \vec{r}(t_i) - \vec{r}(t_{i-1})$ during τ_0 considered also as a time of an elementary diffusion act. Taking into account that:

$$\Delta\vec{r}(t_{i-1,i}) = \Delta\vec{r}^{(\upsilon)}(t_{i-1,i}) + \Delta\vec{r}^{(d)}(t_{i-1,i}) \tag{2.35}$$

and supposing that displacements $\Delta\vec{r}(t_{i-1,i})$ and $\Delta\vec{r}(t_{j-1,j})$ for $j \neq i$ are statistically independent we obtain for the ISF the following equation:

$$F_s(\vec{k}, t_N) \Rightarrow \exp(-2W) F_d(\vec{k}, t_N), \tag{2.36}$$

where

$$F_d(\vec{k}, t_N) = \Big(f_1(\vec{k}^2)\Big)^N, \quad f_1(\vec{k}^2) = < \exp\Big(i\vec{k} \cdot \Delta\vec{r}^{(d)}(t_{1,2})\Big) > . \tag{2.37}$$

It is not difficult to verify that $F_d(\vec{k}, t_m)$, $1 \leq m \leq N$, satisfies the equation:

$$\left.\frac{\partial F_{\mathrm{d}}(\vec{k},t)}{\partial t}\right|_{t=t_m} = -\frac{1}{\tau_0}F_{\mathrm{d}}(\vec{k},t_m)(1-f_1(\vec{k}^2)), \tag{2.38}$$

which leads to the solution:

$$F_{\mathrm{d}}(\vec{k},t) = \exp\left(-\frac{(1-f_1(\vec{k}^2))}{\tau_0}t\right). \tag{2.39}$$

From (2.36)–(2.39) it follows that the spectral density of the ISF equals to

$$F_{\mathrm{s}}(\vec{k},\omega) = \exp(-2W)\frac{1}{\pi}\frac{\gamma(\vec{k}^2)}{\omega^2+\gamma^2(\vec{k}^2)}, \tag{2.40}$$

where the half-width of the Lorentzian takes the value:

$$\gamma(\vec{k}^2) = \frac{1-f_1(\vec{k}^2)}{\tau_0}. \tag{2.41}$$

To construct the evident view of $f_1(\vec{k}^2)$ we take into account that the shift $\Delta\vec{r}_m^{(d)}$ of a molecule during the time τ_0 can be represented as the sum of two independent contributions:

$$\Delta\vec{r}_m^{(d)} = \Delta\vec{r}_m^{(c)} + \Delta\vec{r}_m^{(r)}, \tag{2.42}$$

where the first of them describes the collective drift of a molecule in the velocity field of thermal hydrodynamic fluctuations and the second—the displacement of a molecule about its nearest neighbors [18, 23]. This displacement has also the collective character and it arises due to small displacements of the nearest neighbors. In other words the first displacements are characterized by meso-scales and the second—by nano-scales. As a result we can write:

$$f_1(\vec{k}^2)) = f_1^{(c)}(\vec{k}^2)\cdot f_1^{(r)}(\vec{k}^2), \tag{2.43}$$

where

$$f_1^{(c)}(\vec{k}^2) = <\exp(i\vec{k}\Delta\vec{r}_m^{(c)})>, \quad f_1^{(r)}(\vec{k}^2) = <\exp(i\vec{k}\Delta\vec{r}_m^{(r)})>. \tag{2.44}$$

In accordance with [14–16, 24] the collective transport is caused by the transversal modes in liquids and it has the diffusion character. Due to this the main contribution to $f_1^{(c)}(\vec{k}^2)$ can be written in the view:

$$f_1^{(c)}(\vec{k}^2) = \exp(-6D_{\mathrm{c}}\vec{k}^2\tau_0), \tag{2.45}$$

where D_c is the collective contribution to the self-diffusion coefficient [14–16].

Writing the function $f_1^{(r)}(\vec{k}^2)$ in the equivalent form:

$$f_1^{(r)}(\vec{k}^2) = \left\langle \frac{\sin k|\Delta\vec{r}_m|}{k|\Delta\vec{r}_m|} \right\rangle \tag{2.46}$$

and averaging $\Delta\vec{r}_m$ by the Gaussian:

$$W(\Delta\vec{r}_m) = \left(\frac{\gamma}{\pi}\right)^{3/2} \exp(-\gamma(\Delta\vec{r}_m)^2), \quad \gamma = \frac{1}{4l_0^2}, \tag{2.47}$$

where l_0 is the typical displacement of a molecule during $\tau_0 + \tau_1 \approx \tau_0$, we get:

$$f_1^{(r)}(\vec{k}^2) = \exp\left(-\vec{k}^2 l_0^2\right). \tag{2.48}$$

In [25] it had been shown that $l_0 \approx a$. Since $|\vec{k}|\, l_0 \sim |\vec{k}|\, a \ll 1$ the function is very close to

$$f_1^{(r)}(\vec{k}^2) \approx \frac{1}{1 + \vec{k}^2 l_0^2} \tag{2.49}$$

characteristic for the model of the jump-like diffusion [22]. Here we should stress that the model of the jump-like self-diffusion is incorrect in water as well as in argon near their triple points since the structural voids in them are absent. Elementary displacements of molecules are mainly caused by circulator motions (see [18]).

The final result for $f_1^{(r)}(\vec{k}^2)$ becomes equal to:

$$\gamma(\vec{k}^2) = \frac{1}{\tau_0}\left(1 - \frac{\exp(-D_c\vec{k}^2\tau_0)}{1 + \tau_0 D_r\vec{k}^2}\right), \tag{2.50}$$

where we use the change $\vec{k}^2 l_0^2 \rightarrow \tau_0 D_r\vec{k}^2$ consistent with our reasons presented above.

This expression is close to that:

$$\gamma_D^{(SS)}(\vec{k}^2) = \frac{1}{\tau_0}\left(1 - \frac{\exp(-2W)}{1 + \tau_0 D_s\vec{k}^2}\right), \tag{2.51}$$

obtained in [8, 26]. However main assumptions made in [8] cannot be justified from the physical point of view.

The applicability region of our results is restricted by the inequality $\tau_0 D_r\vec{k}^2 \ll 1$, or $l_0^2\vec{k}^2 \ll 1$, therefore the half-width (2.50) of the diffusion peak can be expanded in the series:

$$\gamma(\vec{k}^2) \approx D_s\vec{k}^2 - \tau_0 D_r\vec{k}^4 + \tau_0^2 D_r^3\vec{k}^6 + \cdots . \tag{2.52}$$

where $D_s = D_r + D_c$ is the full self-diffusion coefficient.

It is necessary to note, that the representation of $\gamma(\vec{k}^2)$ by the expansion of type (2.52) is only correct from the mathematical point of view. Therefore, the expression for $\gamma(\vec{k}^2)$ in [8] is not quite satisfactory and can be lead to considerable errors.

Thus, remaining within the framework of the diffusion approximation, $a^2\vec{k}^2 \ll 1$ and fitting experimental data for the half-width with the help of (2.52), we can determine the self-diffusion coefficient D_s, its collective part D_r caused by local chaotic displacements and the residence time τ_0. Their temperature dependences are very important especially of the residence time. They had been in details investigated for water in [4, 5, 15]. Values of $D_c = D_s - D_r$ satisfy the inequality $D_c < (\ll) D_s$ that is one of criteria testifying in the favor of the proposed approach.

Here we add that the crystal-like character of thermal motion in water leading to (2.52) is only observed for $T \leq T_H = 315\,\mathrm{K}$. For higher temperatures it becomes inapplicable and the thermal motion in water approaches to argon-like one. Some important details will be presented in the Discussion.

2.3 Modeling of the VACF According to Computer Simulations

In order to construct the VACF for a molecule of argon and water were used the NVT-ensemble including $1 \cdot 10^6$ argon atoms and NVT-ensemble of 512,000 water molecules. In the second case the realistic flexible TIP4P/F water model [27] was used. In a case of argon atoms ensemble particles interacting by means of the Lenard-Jones potential

$$U(r) = 4\varepsilon\left[\left(\frac{\sigma}{r}\right)^{12} - \left(\frac{\sigma}{r}\right)^{6}\right] \tag{2.53}$$

with parameters $\sigma = 0.3409$ nm and $\varepsilon/k_B = 120.04$ K [28].

Molecules in water ensemble interacting via potential:

$$U(r,\theta) = U_{LJ}(r) + U_c(r) + U_{\text{intra}}(r,\theta), \tag{2.54}$$

$$U_{\text{intra}}(r,\theta) = \sum_{i=1,2} d_r\left(1 - \exp\left[-\beta\left(r_{OH_i} - r_0\right)\right]\right)^2 + \frac{1}{2}K_\theta(\theta - \theta_0)^2, \tag{2.55}$$

where $U_{LJ}(r)$—Lenard-Jones contribution, $U_c(r) = kq_1q_2/r^2$—component, that describes coulomb interaction and $U_{\text{intra}}(r,\theta)$—the part describing intramolecular interaction, taking into account the OH length and HOH angle vibrations. Here $\varepsilon/k_B = 93.2$ K, $\sigma = 0.3164$ nm, $q_H = 0.5564e$, $r_0 = 0,0942$ nm, $\beta = 22.8\,\mathrm{nm}^{-1}$, $d_r = 432.6$ kJ/mol, $\theta_0 = 107.4°$, $K_\theta = 367.8\ \mathrm{kJ/(mol\,rad^2)}$ [27].

For all molecular dynamic tasks, the Gromacs 5.13 software environment [29, 30] was used.

The velocity Verlet algorithm for integration of Newton's equations was used. The time step is $4 \cdot 10^{-16}$ s. For Van der Waals and electrostatic interaction calculations the PME method [31] was applied. At the beginning of calculations molecules are arranged within a cell with interparticle spacing corresponding to a considered density. The periodic boundary conditions are applied. The following requirements are carried out in our calculation procedure:

- the cell edge length (l_e) is much greater than the doubled radius (r_I) of the intermolecular interaction ($l_e \gg 2r_I$);
- the characteristic time $\tau_c = l_e/c$, where c is the longitudinal sound velocity, is greater than the simulation time τ_s ($\tau_c > \tau_s$);
- the cut-off distance is $r_I = 9\sigma$;
- the equilibrium value of pressure at given density and temperature is close to the experimental one;
- values of the self-diffusion coefficients obtained from the study of mean square displacement of a molecule and from the expression of the Green-Kubo type are close to each other.

At the initial simulation stage (up to 120 ps), a system is considered as NVE ensemble. After this a system is described as NPT ensemble using the chain of Nose-Hoover thermostats [32, 33] and MTTK barostat [34, 35]. To avoid large oscillations of pressure the high value of "time constant for coupling" [36] is used. As a result, the temperature and pressure of a system are supported to be consistent with their initial values.

The time dependence of the velocity autocorrelation function (VACF) $\phi_V(t) \leq \vec{v}(t)\vec{v}(0) >$ for a molecule is constructed with the help of simulation data on the last stage. Values of the VACF are obtained by averaging over $1.5 \cdot 10^6$ time steps and 6 independent initial configurations. The relative error of MD calculations averaged over $[3 \div 8]$ ps $\varepsilon = 0.168$ (the relative error for two different initial configurations (i and j) is determined as $\varepsilon = 2\,average\left(\frac{|\phi_i(t)-\phi_j(t)|}{|\phi_i(t)+\phi_j(t)|}\right)$. For larger time intervals the relative error significantly increases, for example, $\varepsilon = 0.363$ for $(20 \div 30)$ ps.

The dynamic memory time (τ_d) [37, 38] in our simulation procedure is about 23 ps for argon and 16 ps for water ensemble. For times that are $t > \tau_d$ parasitic noise contributions to the VACF become comparable with useful signal. In order to overcome partially this problem the Savitzky-Golay spline filter [39] is used (the window width takes 80 points).

2.4 The Determination of the MRT

In this Section we consider some general requirements made for the MRT and present a new method for its determination.

2.4.1 General Requirements for the MRT

In this subsection we establish the important inequality for the MRT. We start from the standard Maxwell definition:

$$\tau_{\mathrm{M}} = \eta / G_{\infty}, \tag{2.56}$$

where η is the dynamic shear viscosity and G_{∞} is the high-frequency shear modulus for liquid system. Value of G_{∞} are well known for crystal and amorphous phase of many systems [40]. Therefore the approximate value of the MRT can be estimated as

$$\tau_{\mathrm{M}} = \eta / G_{\mathrm{cr}} \text{ or } \tau_{\mathrm{M}} = \eta / G_{\mathrm{am}}. \tag{2.57}$$

The value for the amorphous phase is preferable since structures of a system in its amorphous and liquid states are closer to each other.

However, the elastic properties of a system essentially change at the melting and consequent its heating that is connected with decrease of the density. The first fact is clearly illustrated on the example of the longitudinal sound velocity c_l for water. In this case, according to [41, 42] near the melting point we have:

$$c_l^{(\mathrm{cr})} = 3.84 \cdot 10^5 \mathrm{cm/s} \text{ and } c_l^{(\mathrm{liq})} \approx 1.4 \cdot 10^5 \text{ cm/s} . \tag{2.58}$$

So noticeable change is also expected for high-frequency transversal sound velocity, although the corresponding estimates for $c_t^{(\mathrm{liq})}$ are absent.

It is evident that (2.57) can be rewritten in the form:

$$\tau_{\mathrm{M}}(T) = \nu(T)/c_t^2(T), \quad c_t^2(T) = G_{\mathrm{am}}/\rho_{\mathrm{am}}, \tag{2.59}$$

where $\nu(T)$ is the kinematic shear viscosity: $\nu(T) = \eta/\rho$. Since the high-frequency transversal and longitudinal sound velocities satisfy the inequality: $c_t < c_{\mathrm{l}}$, we conclude that the MRT should obey the inequality:

$$\tau_{\mathrm{M}} > \nu / c_{\mathrm{l}}^2. \tag{2.60}$$

Comparative values of the MRT for Argon taken from several sources and its lower limit $\tau_{\mathrm{M}}^{(l)} = \nu/c_l^2$ are presented in the Table 2.1.

Unfortunately, only values of the MRT from [45] satisfy to the inequality (2.60). It is clear that such distinctions of numerical values for the MRT reflects defects of methods used for the determination of τ_{M}.

The MRT should also satisfy the second inequality:

$$\zeta(T) > 1, \quad \zeta(T) = 2\sqrt{\nu(T)\tau_{\mathrm{M}}(T)}/\sigma_p, \tag{2.61}$$

Table 2.1 Values of the MRT for liquid Argon on its coexistence curve

T (K)	90	100	110	120	130	140	150
$\tau_M \cdot 10^{13}$ (s) [43]	≈2.28	–	–	–	–	–	–
$\tau_M \cdot 10^{13}$ (s) [44]	1.68	–	1.58	1.57	1.66	1.73	–
$\tau_M \cdot 10^{13}$ (s) [45]	–	–	≈21	≈22	–	–	–
$\tau_M^{(l)} \cdot 10^{13}$ (s)	2.68	2.51	2.45	2.75	3.3	4.85	–

where σ_p is the molecular diameter. Here we take into account that the combination $2\sqrt{\nu\tau_M}$ has meaning of the suitable radius for the Lagrange particle [15, 24]. In other words it is the size of a liquid particle drifting in the fluctuation hydrodynamic velocity field. It is clear that this size should exceed the molecular size and the interparticle spacing having the same order of magnitude.

The characteristic temperature T_*, higher which the MRT loses its meaning, is determined by the equation:

$$\zeta(T_*) = 1. \tag{2.62}$$

2.4.2 MRT for Water

The general view of the VACF for water molecule at $T = 274$ K is presented in the Fig. 2.1.

One can show that (1) the small peak centered at $t_d = 0.15$ ps corresponds to the dimer longitudinal vibrations, only observed for $T < 400$ K; (2) the more large and deep oscillation is genetically connected with elastic transversal and longitudinal

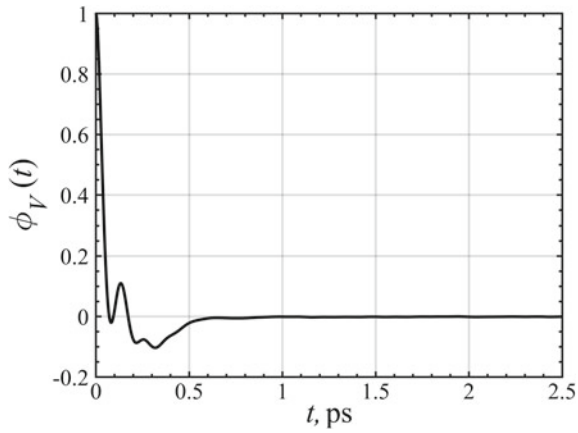

Fig. 2.1 The time dependence of the VACF for a water molecule at 274 K

modes of the hydrodynamic velocity field. This range of negative values for the VACF disappears later, for $T > 450$ K.

In [14, 15, 24] it had been shown that the low-frequency asymptote for the spectral density of the VACF for $T > 450$ K is determined by diffusion transversal modes and it is described by the expression:

$$\phi_{\vec{V}}^{(D)}(\omega) = 3D_c\left[1 - \frac{4}{3}\sqrt{2\pi\omega\tau_M}\left(1 - \frac{3}{2}\omega\tau_M + \frac{3}{8}(\omega\tau_M)^2\right) + \cdots\right]. \tag{2.63}$$

The full correspondence of the last to the VACF-spectrum for $T > 450$ K is demonstrated in the Fig. 2.2.

Near the triple point the important details of the VACF-spectrum are determined by elastic transversal and longitudinal modes. In accordance with [24] their contributions are determined by the formulas:

$$\phi_V(\omega) = \frac{1}{2\pi}\int_0^\infty dt e^{i\omega t}\left(\phi_V^{(t)}(t) + \phi_s^{(l)}(t)\right), \tag{2.64}$$

where

$$\phi_V^{(t)}(t) = \frac{3}{\pi^2}\frac{k_B T}{m_L}\int_0^\infty \frac{du}{u^2}\left(\cos u - \frac{\sin u}{u}\right)^2 \times \left[e^{\frac{t}{2\tau_M}\sqrt{p}} + e^{-\frac{t}{2\tau_M}\sqrt{p}} + \frac{e^{\frac{t}{2\tau_M}\sqrt{p}} - e^{-\frac{t}{2\tau_M}\sqrt{p}}}{\sqrt{p}}\right], \tag{2.65}$$

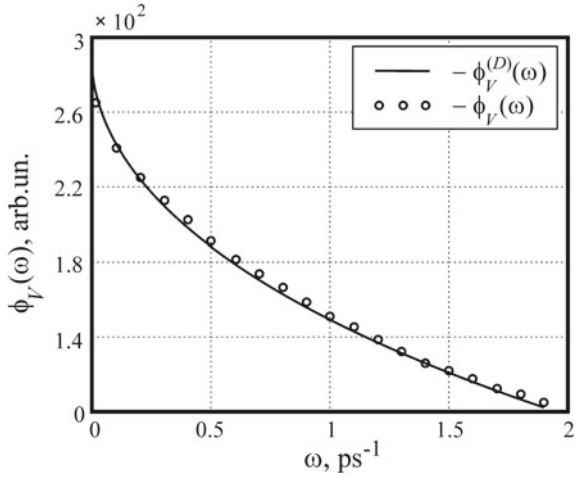

Fig. 2.2 The fitting of the VACF-spectrum (circles) with a help of asymptotic expansion (2.63) at 550 K

$$\phi_s^{(l)}(t) = \frac{3}{\pi}\frac{k_B T}{m_L}\int_0^\infty \frac{du}{u^2}\left(\cos u - \frac{\sin u}{u}\right)^2 e^{-\sigma\theta(u)\,u^2 t/r_L^2}\cos\left(c\frac{u}{r_L}t\right) \qquad (2.66)$$

and $p = 1 - u^2$, $r_L = 2\sqrt{\nu\tau_M}$ is the suitable radius of the Lagrange particle (see [15, 24]), $\sigma = \frac{1}{2}\left[\nu + \lambda(\gamma - 1)\right]$, $\lambda = \chi/\rho C_P$, $\gamma = C_P/C_V$, where C_P, C_V are isobaric and isochoric heat capacities and χ is the thermoconductivity coefficient, $\theta(u)$ is the step function.

The comparison of $\phi_V(\omega)$ given by the formulas (2.64)–(2.66) with the VACF-spectrum constructed with the help of MD-simulations is presented in the Fig. 2.3.

Trying for the best fitting of the low frequency part for the VACF-spectrum in the Fig. 2.3 we can determine the MRT for water. Obtained in such a way values of the MRT are gathered in the Table 2.2.

It is necessary to stress here that the values of the MRT satisfying to inequalities (2.60) and (2.62) in fact correspond to that temperature interval where the low-frequency VACF-spectra are determined by quasi-elastic transversal modes.

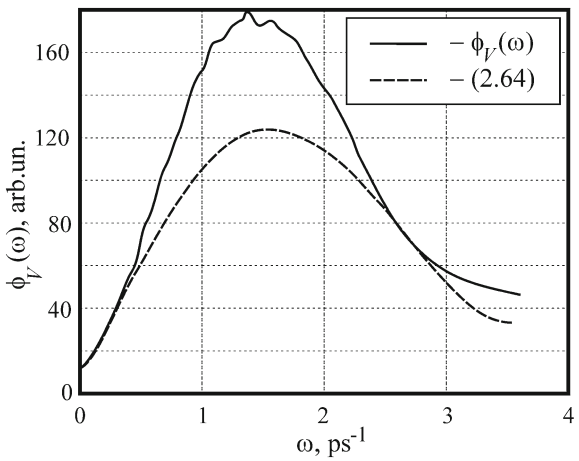

Fig. 2.3 The comparison of the VACF-spectrum (solid line) and that calculated according to (2.64)–(2.66) at 274 K (dashed line)

Table 2.2 Values of τ_M and the right boundary t_{osc} for the VACF oscillation region

P (MPa)	T (K)	τ_M (ps)	t_{osc} (ps)
0.001	274	0.98	1.96
0.0035	300	0.866	1.45
0.042	350	0.612	0.97
0.128	380	0.489	0.744
0.93	450		–

Table 2.3 Values of τ_M, $\zeta(T)$, t_{osc} and D_s for argon as functions of temperature

T (K)	τ_M (ps)	$\zeta(T)$	t_{osc} (ps)	D_s^{MD}(10^{-5}cm^2/s)
85	0.838	2.61	3.08	1.91
90	0.682	2.16	2.28	2.31
100	0.565	1.83	1.48	3.41
110	0.312	1.1	0.64	4.69

2.4.3 The MRT for Argon

In this case all main details of the procedure for the determination of the MRT are the same as for water. Corresponding values of τ_M, $\zeta(T)$, determined by (2.61), t_{osc} and D_s are gathered in the Table 2.3.

As we see from the Table 2.3 the characteristic temperature T_* for argon, determined by (2.60) and (2.62), is close to 110 K. For higher temperatures the MRT for argon loses its physical meaning, i.e. the elastic transversal modes disappear in a system.

2.5 Determination of the Ratio $\frac{D_c}{D_s}$ for Argon and Water

In this section we present results of our investigation of the ratio $\frac{D_c}{D_s}$ for argon and water.

2.5.1 The Ratio $\frac{D_c}{D_s}$ for Argon

In this subsection we present our results of determination of the ratio according to (2.21) and calculated immediately using D_c according to (2.16) and the MRT from the previous Section as well as experimental values for D_s.

Let us consider some details of determination of the ratio $\frac{D_c}{D_s}$ according to (2.21). The averaging of $F_{MD}(x)$ is carried out within time interval: $x_l < x < x_u$, where the lower limit satisfies the inequality: $x_l > 1$ and the upper limit—the one: $x_u < x_d$, where x_d determined by dynamic memory time. The behavior of $F_{MD}(x)$ inside such intervals for several temperatures is presented in the Fig. 2.4.

We see that the plateau in the behavior of $F_{MD}(x)$ is only observed for $T < 120$ K that is consistent with the existence of the MRT namely for these temperatures. Values of the ratio $\frac{D_c}{D_s}$ obtained in such a way are collected in the second column of the Table 2.4. Values of $\frac{D_c}{D_s}$ calculated immediately are placed in the third column.

Thus, the collective part of the self-diffusion coefficient (1) reaches approximately 10% at the triple point of argon; (2) increases with temperature taking its maximal

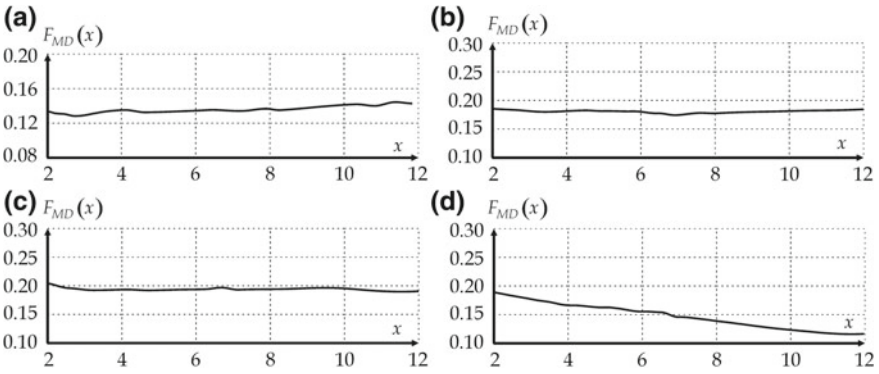

Fig. 2.4 Behavior of $F_{\mathrm{MD}}(x)$ for large enough x at several temperatures: $T = 85$, 100, 110, 120 K (**a**, **b**, **c**, **d** correspondingly)

Table 2.4 Comparative values of the ratio $D_{\mathrm{c}}/D_{\mathrm{s}}$ obtained according to (2.21) and calculated immediately. Experimental values of D_{s} barrowed from [46, 47]

T (K)	$D_{\mathrm{c}}/D_{\mathrm{s}}$ (2.21)	$D_{\mathrm{c}}/D_{\mathrm{s}}$ (immed.)
85	0.138	0.095
90	0.151	0.121
100	0.182	0.166
110	0.192	0.28

value at 110 K (about 25%) and (3) tends to zero with consequent increase of temperature. The last assertion reflects that fact that the MRT for argon becomes its incorrect characteristics for $T > 120$ K. There is a quite satisfactory correlation between values of $D_{\mathrm{c}}/D_{\mathrm{s}}$, obtained according to (2.21) and calculated immediately.

2.5.2 The Ratio $\frac{D_c}{D_s}$ for Water

In the Table 2.5 results of our calculations of D_{s} and $D_{\mathrm{c}}/D_{\mathrm{s}}$ for water are presented. They are obtained with the same procedure as for argon in Sect. 2.5.1.

Table 2.5 Values of D_{s} and $D_{\mathrm{c}}/D_{\mathrm{s}}$ for several temperatures. Experimental values taken from [48, 49]

T (K)	$D_{\mathrm{s}}^{\mathrm{MD}}$	$D_{\mathrm{s}}^{\mathrm{exp}}$	$D_{\mathrm{c}}/D_{\mathrm{s}}$ (2.21)	$D_{\mathrm{c}}/D_{\mathrm{s}}$ (immed)
274	1.529	1.18	0.022	0.036
300	2.779	2.41	0.081	0.076
350	7.04	6.28	0.157	0.133
380	11.07	9.33	0.243	0.182

2.6 MD-Modeling of the Spectrum for the ISF for Argon

In this Section we consider the applicability region of the diffusion approximation for the spectral density of the ISF.

2.6.1 Fitting of Computer Simulation Data with the Help of Diffusion Lorentzians

The behavior of the spectral density for the ISF for Argon in a low-frequency interval $0 < \tilde{\omega} < 3$, where $\tilde{\omega} = \omega/D_s\vec{k}^2$ and $a^2\vec{k}^2 \ll 1$, is presented in the Fig. 2.5.

As we see, (1) the spectral density of the ISF deviates from the Lorentzian already at $\tilde{\omega} \sim 1$ or ($\omega \sim D_s\vec{k}^2$) and (2) the contribution of the root square term in (2.25) is negligibly small, as it should be for small frequencies. The first fact is rather surprising and it should be taken into account at fitting experimental data with the help of Lorentzian. Below we will also give a rigorous theoretical substantiation of the restricted applicability of Lorentzian.

From the Table 2.6 it follows that the optimal fitting of the computer simulation data for the spectrum with the help of Lorentzian is observed for $\tilde{k}_l < \tilde{k} < \tilde{k}_u$ and $0 < \tilde{\omega} < \tilde{\omega}_u$, where the limit values of $\tilde{k}_l$, $\tilde{k}_u$ and $\tilde{\omega}_u$ are depending on density ρ. Speaking about the optimal fitting we suppose that values for the calculated self-diffusion coefficients D_s^{MD} are the closest to corresponding experimental data D_s^{exp}. The density dependence of $\tilde{k}_u$, presented in the Fig. 2.6, is close to the rectilinear one. The values of $\tilde{\omega}_u < 1.7$.

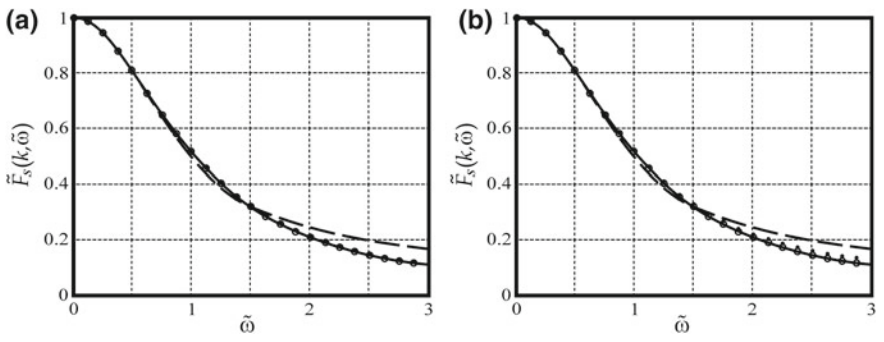

Fig. 2.5 The spectral density of the normalized ISF $\tilde{F}(\vec{k},\tilde{\omega}) = F(\vec{k},\omega)/F(\vec{k},0)$ for argon as a function of frequency $\tilde{\omega}$ at $\rho = 1.0\,\mathrm{g/cm^3}$ and $T = 90\,\mathrm{K}$: dashed line correspond to computer simulation data (CSD); open circles and points are the result of calculation according (2.25) at $b = 0$ and $b = 0.03$ (**a**), as well as $b = 0$ and $b = 0.1$ (**b**); solid curve corresponds to the Lorentzian: $\tilde{F}_L(\vec{k},\tilde{\omega}) = \frac{1}{\tilde{\omega}^2+1}$

Table 2.6 Values of D_s and the upper limit frequency $\tilde{\omega}_u$ for the applicability of Lorentzian for various densities and wave vectors $\tilde{k} = \frac{ak}{2\pi}$ at $T = 135$ K. Experimental values D_s^{exp} taken from [46, 47]

$\rho = 0.8\,g/cm^3$	$\tilde{k}$	0.10	0.22	0.24	0.28
	$D_s^{MD} \cdot 10^5$ (cm/s)	15.7	13.85	12.0	11.2
	$D_s^{exp} \cdot 10^5$ (cm/s)	14.27			
	$\tilde{\omega}_u$	–	1.65	1.5	–
$\rho = 1.0\,g/cm^3$	$\tilde{k}$	0.13	0.214	0.252	0.29
	$D_s^{MD} \cdot 10^5$ (cm/s)	10.61	9.97	8.81	8.3
	$D_s^{exp} \cdot 10^5$ (cm/s)	9.88			
	$\tilde{\omega}_u$	–	1.55	1.4	–
$\rho = 1.2\,g/cm^3$	$\tilde{k}$	0.17	0.26	0.29	0.32
	$D_s^{MD} \cdot 10^5$ (cm/s)	7.76	5.92	5.34	4.9
	$D_s^{exp} \cdot 10^5$ (cm/s)	6.02			
	$\tilde{\omega}_u$	–	1.5	1.3	–
$\rho = 1.4\,g/cm^3$	$\tilde{k}$	0.22	0.27	0.325	0.35
	$D_s^{MD} \cdot 10^5$ (cm/s)	4.71	3.53	3.14	2.88
	$D_s^{exp} \cdot 10^5$ (cm/s)	3.56			
	$\tilde{\omega}_u$	–	1.5	1.3	–

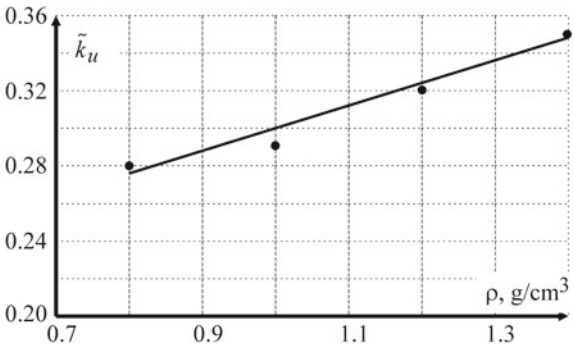

Fig. 2.6 The upper limit for wave vectors as a function of density

As it follows from the Table 2.7, the optimal fitting of experimental data with the help of Lorentzians becomes better for smaller wave vectors. At the same time values of $\tilde{\omega}_u$ a few increase.

Table 2.7 Values of D_s for water and the upper limit frequencies $\tilde{\omega}_u$ for different temperatures. Experimental values of D_s^{exp} barrowed from [48, 49]

$T = 278$ K	$\tilde{k}$	0.15	0.165	0.237	0.316
	$D_s^{MD} \cdot 10^5$ (cm/s)	1.47	1.22	1.17	1.1
	$D_s^{exp} \cdot 10^5$ (cm/s)	1.324			
	$\tilde{\omega}_u$	2.3	1.7	1.5	–
$T = 293$ K	$\tilde{k}$	0.157	0.209	0.25	
	$D_s^{MD} \cdot 10^5$ (cm/s)	2.072	1.864	1.51	
	$D_s^{exp} \cdot 10^5$ (cm/s)	2.02			
	$\tilde{\omega}_u$	2	1.6	–	
$T = 350$ K	$\tilde{k}$	0.073	0.11	0.146	
	$D_s^{MD} \cdot 10^5$ (cm/s)	7.2	5.845	5.5	
	$D_s^{exp} \cdot 10^5$ (cm/s)	6.41			
	$\tilde{\omega}_u$	2.4	1.6	–	

2.6.2 *The Applicability Region of the Diffusion Approximation for Liquids*

In order to establish the value of high frequency limit for description of the ISF spectrum with the help of Lorentzian

$$f_s(\vec{k}, \omega) = \frac{1}{\pi} \frac{\gamma(\vec{k}^2)}{\omega^2 + \gamma^2(\vec{k}^2)} \tag{2.67}$$

let us apply to the inequality:

$$\frac{1}{2} - \frac{1}{1 + \omega^2/\omega_m^2} \leq \frac{1}{m_0} \int_0^{\omega} I_A(\omega')\mathrm{d}\omega' \leq \frac{1}{2}, \quad \omega_m^2 = \frac{m_2}{m_0}, \tag{2.68}$$

having place in the spectral theory of moments [50–52]. Here, $I_A(\omega) \leq A^+(t)A(0) >_\omega$ is the spectrum for the correlation function $< A^+(t)A(0) >$, where the symbol "+" denotes the operation for Hermitian conjugation,

$$m_n = \int_{-\infty}^{\infty} I_A(\omega)\omega^n \mathrm{d}\omega, \quad n = 1, 2, \ldots. \tag{2.69}$$

are the frequency moments for the spectral density $I_A(\omega)$. If $I_A(\omega) \leq A^+(t)A(0) >_\omega$, only even moments are different on zero: $m_{2n} \neq 0$, $m_{2n+1} = 0$. If we will take into account greater number of even moments, the inequality (2.68) becomes more complicated [51, 52]. In accordance with [53, 54]:

$$m_{2n} = < A^{(n)}(t)A^{(n)}(t) >\big|_{t=0}, \tag{2.70}$$

where $A^{(n)}(t)$ is the n-th time derivative from $A(t)$.

In our case $F_s(\vec{k},\omega) = e^{2W}F_d(\vec{k},\omega)$, so $A(t) = \exp(i\vec{k}\vec{r}_d(t))$ and the zero-th frequency moments is equal to

$$m_0 = 1. \tag{2.71}$$

In order to find the second frequency moment let us define the averaged velocity $\dot{\vec{r}}_d(t)$ of a molecule during the time $t_D = 1/D_s\vec{k}^2$ characteristic for the diffusion motion:

$$\dot{\vec{r}}_D(t) = \frac{1}{t_D}\int\limits_{t-t_D/2}^{t+t_D/2} \vec{v}(t')\mathrm{d}t', \tag{2.72}$$

where $\vec{v}(t)$ is the usual velocity of a molecule. From here it follows that the second moment equals to

$$m_2 =< \dot{\vec{r}}_D^{\,2} > \vec{k}^2 \sim 6D_s\vec{k}^2/t_D. \tag{2.73}$$

In accordance with (2.71) and (2.73) the characteristic frequency ω_m takes the value:

$$\omega_m^{(\mathrm{dif})} \sim \sqrt{2}\omega_D,\ \ \omega_D = D_s\vec{k}^2, \tag{2.74}$$

As a result the inequality (2.68) with $I_A(\omega) = F_s(\vec{k},\omega)$ transforms to

$$\frac{1}{2} - \frac{1}{1+(1/2)\tilde{\omega}^2} \le \mathrm{arctg}\,\tilde{\omega} \le \frac{1}{2},\quad \tilde{\omega} = \omega/\omega_D. \tag{2.75}$$

If $\tilde{\omega} \ge 1$ the inequality (2.75) can be simplified:

$$\frac{1}{2} - \frac{1}{1+(1/2)\tilde{\omega}^2} \le \frac{1}{2} - \frac{1}{\pi\tilde{\omega}} + \frac{1}{3\pi\tilde{\omega}^2} + \cdots \le \frac{1}{2}. \tag{2.76}$$

The left inequalities is only correct for frequencies $\tilde{\omega} < \tilde{\omega}_*$ where

$$\tilde{\omega}_* \approx 2 \quad \text{or} \quad \omega_* \approx 2\,\gamma(\vec{k}^2). \tag{2.77}$$

Thus, our analysis allows us to conclude that the fitting of $F_s(\vec{k},\omega)$ by the diffusion Lorentzian (2.67) is satisfactory only for frequencies $\tilde{\omega} < \tilde{\omega}_*$ that is quite consistent with results of the Sect. 2.6.1. This circumstance is necessary to remember at processing of experimental data [55–60].

2.6.3 *Low Frequency Properties of the ISF-Spectrum for Water*

The thermal motion in water is more complicated in comparison with that in argon. In particular, here it is necessary to take into account the rotation of water molecules. At that, from the consideration [10–13] of the dipole relaxation in water it follows that this rotation is close to be quasi-free in the greater part of temperature interval for its liquid states: $0.49T_c < T < T_c$, $T_c = 649$ K.

Only in the narrow interval of liquid states: $0.42T_c < T < 0.49T_c$ and for supercooled ones the orientation correlations become essential. In connection with this we expect that the behavior of kinetic coefficients for water, in particular the self-diffusion coefficient, should noticeably change at $T_H \sim 0.49T_c$. At the same time, the structure of the diffusion peak should remain changeless. The last conclusion is fully supported by the Fig. 2.7.

The wave vector dependence for the half-width of diffusion peaks for water is presented in the Fig. 2.8. It is rectilinear as it should be.

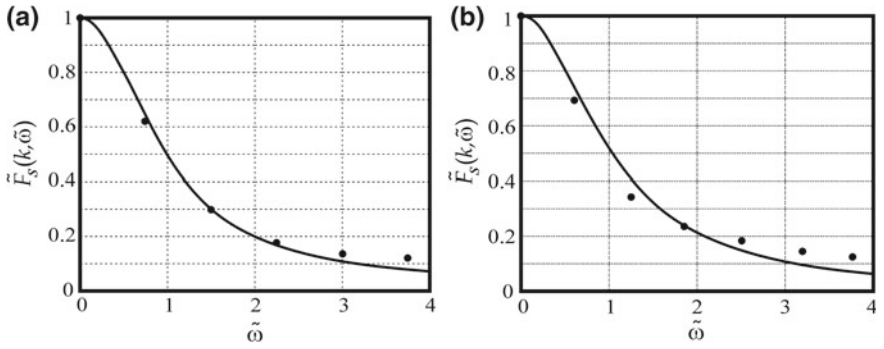

Fig. 2.7 The spectral density $\tilde{F}_s(k, \tilde{\omega})$ of the ISF as a function of $\tilde{\omega}$ at $\rho = 0.997 \text{g/cm}^3$, $T = 293$ K: points correspond to computer simulation data at $\tilde{k} = 0.1$ (**a**) and $\tilde{k} = 0.16$ (**b**), the solid curves correspond to the Lorentzian: $\tilde{F}_L(k, \tilde{\omega}) = \frac{1}{\tilde{\omega}^2+1}$

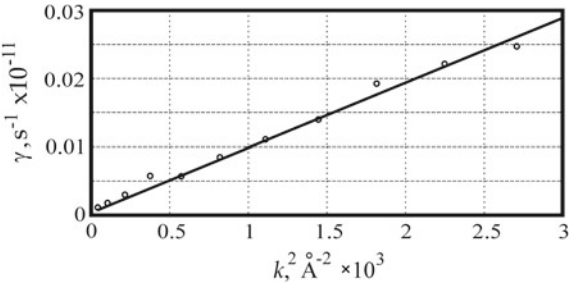

Fig. 2.8 The half-width of the diffusion peak for water as a function of k^2 at $T = 365$ K and small transferring wave vectors: open circles present values of $\gamma(\vec{k}^2)$ obtained with the help of MD-simulations, the solid line corresponds to the equation: $\gamma(\vec{k}^2) = D_s\vec{k}^2$

According to Fig. 2.8 the self-diffusion coefficient of water molecules equals to $D_s = 9.5 \cdot 10^{-5}$ cm^2/s that is close to its experimental value: $D_s = 8.48 \cdot 10^{-5}$ cm^2/s at $T = 365$ K.

Thus the similarity between argon and water spectra as well as the applicability of diffusion Lorentzian for their description is apparent. Therefore, in the following we will focus our attention on the character of wave vector dependence for the half-widths of the incoherent neutron scattering peaks (Fig. 2.9). This question had been experimentally studied in [55–59].

The curves for argon in the Fig. 2.9 correspond to temperatures T_{Ar} and densities n_{Ar} connected with those for water (T_w, n_w) by the similarity relations:

$$T_{Ar} = T_W \frac{T_c^{(Ar)}}{T_c^{(W)}}, \quad n_{Ar} = n_W \frac{n_c^{(Ar)}}{n_c^{(W)}}, \tag{2.78}$$

i.e. computer simulation data are compared for so called corresponding states [61]. Here $T_c^{(Ar)}$, $T_c^{(W)}$ and $n_c^{(Ar)}$, $n_c^{(W)}$ are the critical temperatures and densities for water

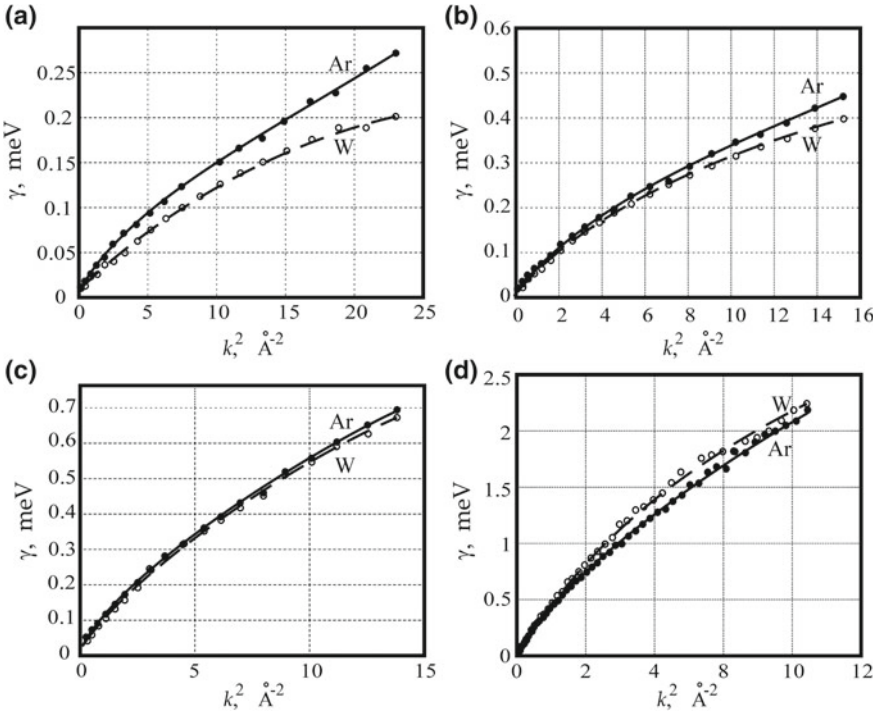

Fig. 2.9 The MD-calculated half-widths of the ISF spectra for water and argon as functions of k^2: open circles and solid lines correspond to argon, dark circles and dashed lines—to water. The curves are constructed at: $T_{Ar} = 59$ K, $T_w = 253$ K—**(a)**, $T_{Ar} = 64.7$ K, $T_w = 278$ K—**(b)**, $T_{Ar} = 68.2$ K, $T_w = 293$ K—**(c)**, $T_{Ar} = 84.5$ K, $T_w = 365$ K—**(d)**

and argon correspondingly. Note, that modeled argon and water remain stable in their supercooled states (see [62]).

Since values of wave vectors in the Fig. 2.9 change in wide limits, including $\tilde{k}^2 \gg (>)1$, shapes of the ISF spectra are very different from Lorentzians. In this case the half-width of peaks are determined by the equation:

$$\tilde{F}_s(\vec{k}, \tilde{\gamma}(\vec{k}^2)) = \frac{1}{2}, \quad \tilde{\gamma}(\vec{k}^2) = \frac{\gamma(\vec{k}^2)}{D_s\vec{k}^2}. \tag{2.79}$$

As we see the half-widths of the ISF peaks for water and argon are practically identical at $T_{Ar} = 68.2\,\mathrm{K}$, $T_w = 298\,\mathrm{K}$, where the last is close to the characteristic temperature $T_H \sim 0.485T_c = 315\,\mathrm{K}$ for water. For temperatures smaller and greater than T_H argon and water curves in Fig. 2.9 differ noticeably from each other. Due to clusterization of water for $T < T_H$ (see [10]) its self-diffusion coefficient additionally diminishes and the water curve in the Fig. 2.9a is shifted down relatively the argon one. If $T > T_H$ the situation is opposite since the self-diffusion coefficient of water is expected to be greater than that in argon. These reasons are also supported by the temperature dependence of the ratio $r_D(T_w) = D_s^{(w)}(T_w)/D_s^{(Ar)}(T_{Ar})$ presented in the Fig. 2.10.

Now we briefly concern an attempt in [3, 55, 56] to explain the $\vec{k}^2$-dependence of the half-width $\gamma(\vec{k}^2)$ for water on the base of hypothesis of rotational motion of molecules. The dotted line in the Fig. 2.11 presents the rotational contribution to the half-width.

It is clear that identical $\vec{k}^2$-dependences for $\gamma_{Ar}(\vec{k}^2)$ and $\gamma_w(\vec{k}^2)$ are not possible to explain assuming that $\vec{k}^2$-dependence of $\gamma_w(\vec{k}^2)$ for water is caused by another mechanism of thermal motion than in argon, in particular, by rotation of water molecules. Moreover, (1) the use of the expression: $\gamma(\vec{k}^2) = \frac{D_s\vec{k}^2}{1+\tau_r D_s\vec{k}^2}$ is incorrect in the diffusion approximation—in this case it is necessary to transform it to the expansion into series with respect to degrees of $\tau_r D_s\vec{k}^2$ similarly to (2.52) and (2) the numerical value of τ_r is too large. Thus, the nonlinear dependence of $\gamma_w(\vec{k}^2)$ on $\vec{k}^2$ is caused by translational motions of water molecules similarly to that in argon.

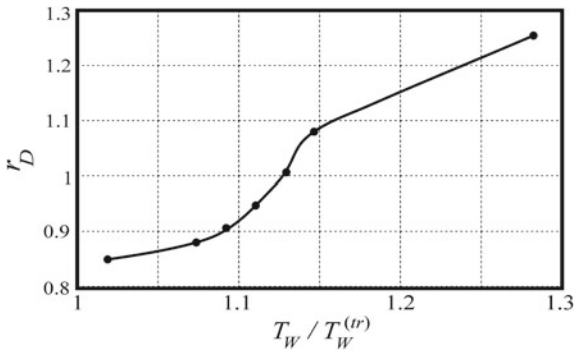

Fig. 2.10 The ratio $r_D(T_w/T_w^{(tr)})$ versus the normalized temperature: $T_w/T_w^{(tr)}$, where $T_w^{(tr)}$ is the temperature for the water triple point. Experimental values of the self-diffusion coefficients for water are taken from [48, 49], argon values are calculated according to the similarity principle

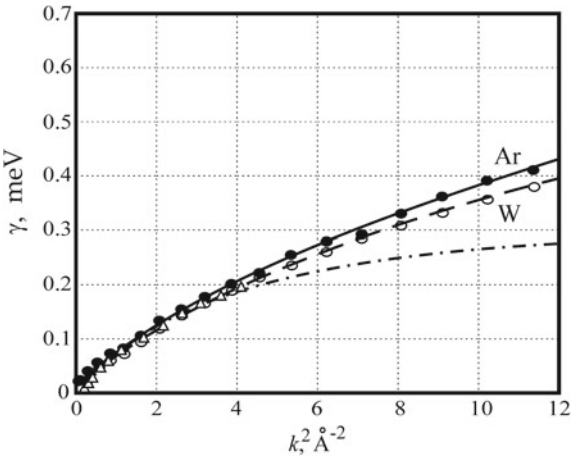

Fig. 2.11 The half-widths of the ISF spectra for water and argon versus $\vec{k}^2$: dark and open circles correspond to $\gamma(\vec{k}^2)$ at $T_{\mathrm{w}} = 278$ K, $T_{\mathrm{Ar}} = 64.7$ K, the solid and dashed curves are fitted with the help of the least-squares method. The dotted line corresponds to $\gamma(\vec{k}^2) = \frac{D_s\vec{k}^2}{1+\tau_r D_s\vec{k}^2}$ with $\tau_{\mathrm{r}} = 2.93 \cdot 10^{-12}$ s, triangles—to experimental data from [55, 56]

Now let us discuss the behavior of the half-width for $1 < \tilde{k}^2 < 10$. As it has been shown in [22] the half-width $\gamma(\tilde{k})$ is a quasi-linear function of the wave vector in this range (see the Fig. 2.12a, b). At that, the ISF is represented by Gaussian: $\tilde{F}(\tilde{k}, \tilde{\omega}) \sim \exp\left(-\tilde{\omega}^2/\gamma^2(\tilde{k})\right)$. As we see, the numerical values of $\gamma(\tilde{k})/\tilde{k}$ on the plateau (b) are close to $3 \cdot 10^4$ cm/s, that coincides with good accuracy with the average thermal velocity of a water molecule: $\upsilon_{\mathrm{T}} \approx 2.91 \cdot 10^4$ cm/s. It means, that main peculiarities of the ISF-spectra in the range: $1 < \tilde{k}^2 < 10$, are caused by quasi-free motion of water molecules. The similar behavior is also expected for argon and argon-like liquids, i.e. having the averaged potentials of argon-like type. As it had

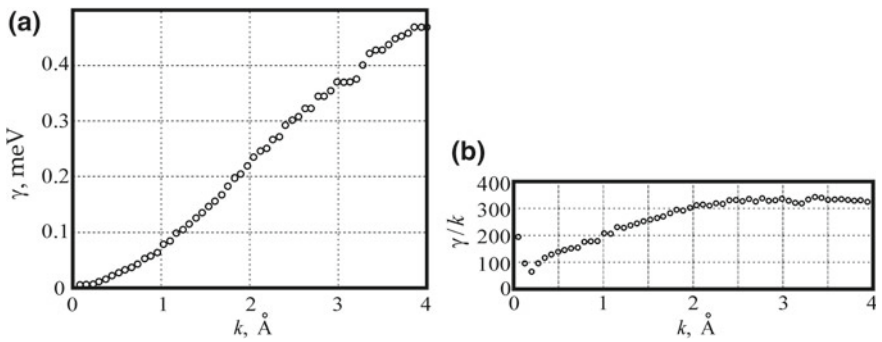

Fig. 2.12 The MD-calculated half-width of the incoherent neutron scattering peak for argon as function of k at $T = 64.7$ K (**a**) and the ratio $\gamma(k)/k$ (**b**)

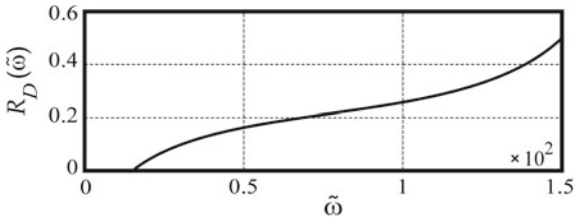

Fig. 2.13 The frequency dependence of $R_D(\tilde{\omega})$ for liquid argon at $k = 0.25\,\text{A}^{-1}$, and $T = 100\,\text{K}$, $\rho = 1.3\ \text{g/cm}^3$

been shown in [63, 64] the majority of low-molecular liquids, including water, belong to this class of similarity.

2.6.4 *Estimate of D_c/D_s for Argon According to Spectral Peculiarities*

In this subsection we will discuss peculiarities of frequency dependence for the ISF spectra at $50 < \tilde{\omega} < 100$ and wave vectors from the diffusion diapason. The behavior of the function $R_D(\tilde{\omega})$ connected with the spectral density of the ISF by the relations (2.30)–(2.32) is presented in the Fig. 2.13.

We see that $R_D(\tilde{\omega})$ monotonously increases although the consideration in the Sect. 2 allowed us to conclude that $R_D(\tilde{\omega})$ should be quasi-constant for $50 < \tilde{\omega} < 100$. In fact, one can say about the point of inflection near $\tilde{\omega}_I \sim 70$, where $R_D(\tilde{\omega}_I) \approx 0.2$. At that, the estimate for D_c/D_s:

$$D_c/D_s \sim R_D(\tilde{\omega}_I) \approx 0.2 \tag{2.80}$$

is quite consistent with that obtained in the Sect. 2.5 from the analysis of the VACF behavior. The absence of plateau in the behavior of $R_D(\tilde{\omega})$ near $\tilde{\omega}_I \sim 70$ is naturally explained by the taking into account of contributions caused by hard collisions between molecules (see details in [65–68]). These contributions, manifested in the ISF spectra, have high-frequency asymptote:

$$F_s(\vec{k}, \omega) \sim \exp\left(-\left(\tau(\vec{k}^2)\omega\right)^{2/3}\right) \tag{2.81}$$

for all wave vectors: $\tilde{k} \ll 1$ and $\tilde{k} \gg 1$ (see Fig. 2.14). The physical nature of this new phenomenon is not fully clear.

2.7 Discussion of the Questions Presented

In the present work we have consider the main peculiarities of the IFS-spectra for water and argon in the applicability region of the diffusion approximation as well as

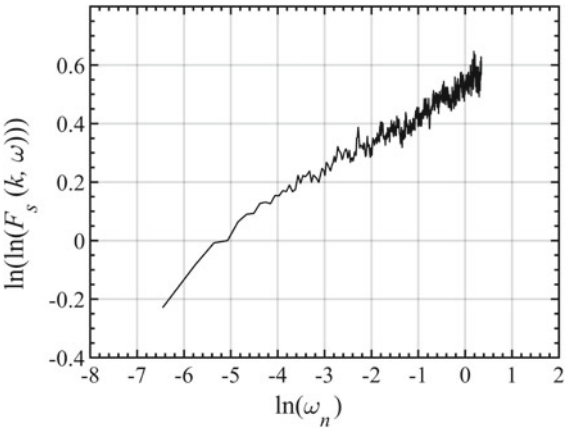

Fig. 2.14 $\ln\ln F_{\rm s}(\vec{k},\omega)$ versus $\ln(\omega_n)$, where $\omega_n = \omega/\omega_{\rm H},\ \omega_{\rm H} = k_{\rm B}T/\hbar$

outside it. At that, the determination of the self-diffusion coefficient $D_{\rm s}$ is regarded by us as well approved.

We have established that the quasi elastic incoherent neutron scattering can be used for the determination of

1. the residence time τ_0 and the collective part $D_{\rm r}$ for the self-diffusion coefficient caused by local displacements of small molecular groups. They can be found from the analysis of $\vec{k}^2$- dependence for the half-width of the diffusion peak (see the formula (2.52));
2. the collective contribution $D_{\rm c}$ to the self-diffusion coefficient caused by molecular drift in the field of velocity hydrodynamic fluctuations according to: $D_{\rm c} = D_{\rm s} - D_{\rm r}$, as well as the ratio $D_{\rm c}/D_{\rm s}$ from the analysis $F_{\rm MD}(x)$ (2.21) and frequency dependence of $R_D(\tilde{\omega})$ (the formula (2.32));
3. applicability region of the MRT. At that, it necessary to take into account that τ_M has only clear physical meaning for temperatures corresponding to the existence of quasi-elastic transversal modes. In fact, such a situation is only realized in a narrow temperature interval adjoining to the triple point of liquids.

It had been also shown that the investigation of the ISF-spectra for $\vec{k}^2a^2 \gg 1$, i.e. outside of the diffusion approximation, give us an important information about $\tau(\vec{k}^2)$ determining the high-frequency asymptotes for $F_{\rm s}(\vec{k},\omega)$. This question is especially important for establishment of peculiarities caused by hard interparticle collisions in molecular systems [65–67].

Using experimental results from [55–57] it had been shown in [4, 5, 15] that the ratio τ_0/τ_f, where $\tau_f \sim a/\upsilon_{\rm T}$, has very surprising temperature dependence (see the Fig. 2.15).

As we see, the inequality $\tau_0/\tau_f > (\gg)1$ takes only place for super-cooled states of ordinary water and its normal ones within the interval:

$$T_m < T < T_{\rm H}, \quad T_m = 273\,{\rm K}, \quad T_{\rm H} \approx 315\,{\rm K}. \tag{2.82}$$

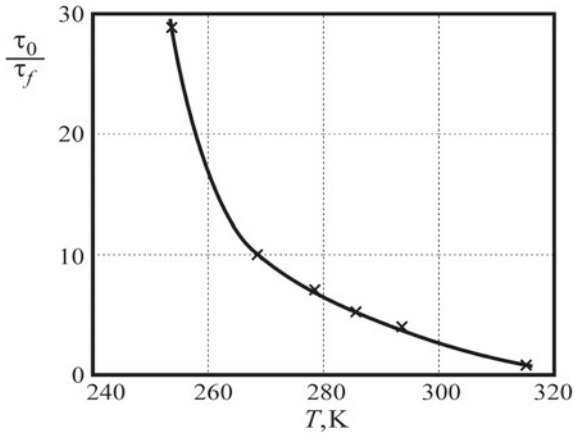

Fig. 2.15 The temperature dependence of the ratio $\frac{\tau_0}{\tau_f}$, where $\tau_f \approx 5 \cdot 10^{-13}$ s

Thus the crystal-like representation for water is only correct for normal and supercooled states corresponding to $T < T_{\mathrm{H}}$. The importance of this result for alive matter is discussed in [69, 70].

It is necessary to stress that our conclusion about the argon-like thermal motion in water for $T > T_{\mathrm{H}}$ is also supported by the temperature dependence of the ratio $\tilde{\tau}_{\mathrm{d}}(t) = \tau_{\mathrm{d}}(t)/\tau_{\mathrm{r}}$, where $\tau_{\mathrm{d}}(t)$ is the dipole relaxation time and τ_{r} is the period of free rotational motion. It is clear that $\tau_{\mathrm{r}} \sim 2\pi/\omega_{\mathrm{T}}$, where $\omega_{\mathrm{T}} \sim \sqrt{k_{\mathrm{B}}T/I}$ is the characteristic value for angular velocity, $I \sim m_{\mathrm{H}} r_{\mathrm{OH}}^2$ is the inertia moment for water molecule (m_{H} is the mass of hydrogen atom and r_{OH} is the distance between hydrogen and oxygen in water molecule). As it had been shown in [71] the nontrivial temperature dependence of $\tilde{\tau}_{\mathrm{d}}(t)$ is only observed for $T < T_{\mathrm{H}}$ (see the Fig. 2.16).

Thus, the quasi-free motion of water molecules is only observed for $T > T_{\mathrm{H}}$ corresponding to destructed crystal-like structure in liquid water.

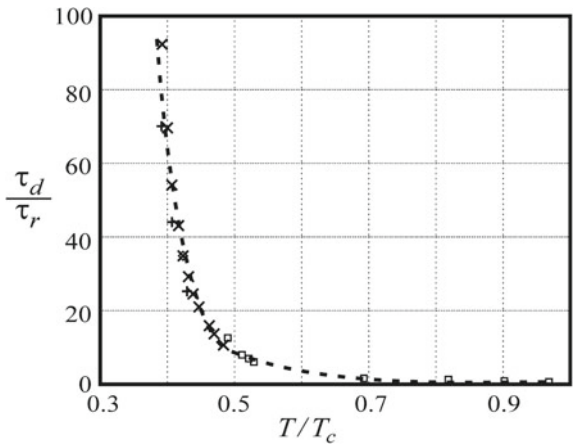

Fig. 2.16 Values of $\tilde{\tau}_{\mathrm{d}}(t)$ as a function of dimensionless temperature: $t = T/T_{\mathrm{c}}$, where T_{c} is the critical temperature. Experimental data are taken from the works: +—[10], □—[11], × —[12], ◊—[13]. The dot line corresponds to exponential dependence

Acknowledgements We cordially thanks Professor S. Magazu, Professor G. G. Malenkov, Professor G. E. Norman, Dr. V. Yu. Bardik and V. Sokolov for fruitfull discussion of our results.

References

1. I.I. Gurevich, L.V. Tarasov, *Low Energy Neutrons Physics* (North-Holland Publishing Co., 1968), p. 621
2. W. Marshall, S.W. Lovesey, *Theory of Thermal Neutron Scattering* (Clarendon Press, Oxford, 1971), p. 620
3. S.-H. Chen, in *Hydrogen-Bonded Liquids*, ed. by J.C. Dore, J. Teixeira (Kluwer Academic Publishers, Netherlands, 1991), p. 289
4. L.A. Bulavin, N.P. Malomuzh, K.N. Pankratov, Character of the thermal motion of water molecules according to the data on quasielastic incoherent scattering of slow neutrons. J. Struct. Chem. **47**, 48–55 (2006). https://doi.org/10.1007/s10947-006-0264-1
5. L.A. Bulavin, N.P. Malomuzh, K.N. Pankratov, Self-diffusion in water. J. Struct. Chem. **47**(Supplement 1), S50–S60 (2006). https://doi.org/10.1007/s10947-006-0377-6
6. J. Frenkel, *Kinetic Theory of Liquids* (Dover Publ, NY, 1955), p. 592
7. E.N. da C. Andrade, The viscosity of liquids. Nature. **125**, 309–310 (1930). http://dx.doi.org/10.1038/125309b0
8. K.S. Singwi, A. Sjolander, Diffusive motions in water and cold neutron scattering. Phys. Rev. **119**, 863–872 (1960). https://doi.org/10.1103/PhysRev.119.863
9. I.L. Fabelinskii, *Molecular Scattering of Light* (Plenum, New York, 1968), p. 622
10. D. Eisenberg, W. Kauzmann, *The Structure and Properties of Water* (Oxford University Press, Oxford, 2005), p. 308
11. K. Okada, M. Yao, Y. Hiejima, H. Kohno, Y. Kojihara, Dielectric relaxation of water and heavy water in the whole fluid phase. J. Chem. Phys. **110**, 3026–3037 (1999). https://doi.org/10.1063/1.477897
12. H.R. Pruppacher, Self-diffusion coefficient of supercooled water. J. Chem. Phys. **56**, 101–108 (1972). https://doi.org/10.1063/1.1676831
13. J.H. Simpson, H.Y. Carr, Diffusion and nuclear spin relaxation in water. Phys. Rev. **111**, 1201–1202 (1958). https://doi.org/10.1103/PhysRev.111.1201
14. T.V. Lokotosh, N.P. Malomuzh, Lagrange theory of thermal hydrodynamic fluctuations and collective diffusion in liquids. Phys. A **286**, 474–488 (2000). https://doi.org/10.1016/S0378-4371(00)00107-2
15. L.A. Bulavin, T.V. Lokotosh, N.P. Malomuzh, Role of the collective self- diffusion in water and other liquids. J. Mol. Liq. **137**, 1–24 (2008). https://doi.org/10.1016/j.molliq.2007.05.003
16. I.Z. Fisher, Gidrodinamicheskaya asimptotika avtokorrelyacionnoy funkcii skorosti molekuli v klassicheskoy zhidkosti (Hydrodynamic asymptotics of the velocity autocorrelation function of a molecule in a classical fluid). JETP (USSR) **61**, 1648–1659 (1971)
17. P.M. Morse, H. Feshbach, *Methods of Theoretical Physics.* Part 1 (McGraw-Hill, NY, 1953) p. 997
18. T.V. Lokotosh, N.P. Malomuzh, K.N. Pankratov, K.S. Shakun, New results in the theory of collective self-diffusion in liquids. Ukr. J. Phys. **60**, 697–707 (2015). http://dx.doi.org/10.15407/ujpe60.08.0697
19. L.A. Bulavin, N.P. Malomuzh, K.S. Shakun, MD-modeling of the intermediate scattering function for argon-like liquids and water. **263**, 200–208 (2018). http://dx.doi.org/10.1016/j.molliq.2018.04.142
20. G.G. Malenkov, Structural and dynamical heterogeneity of stable and metastable water. Phys. A **314**, 477–484 (2002). https://doi.org/10.1016/S0378-4371(02)01085-3

21. V.P. Voloshin, Y. Naberukhin, Hydrogen bond lifetime distributions in computer-simulated water. J. Struct. Chem. **50**, 78–89 (2009). https://doi.org/10.1007/s10947-009-0010-6
22. V.P. Voloshin, Y. Naberukhin, Distributions of hydrogen bond lifetimes in instantaneous and inherent structures of water. Z. Phys. Chem. **223**, 999–1011 (2009). https://doi.org/10.1524/zpch.2009.6062
23. N.P. Malomuzh, Nature of self-diffusion in fluids. Ukr. J. Phys, **63**, 1076–1087 (2018). https://doi.org/10.15407/ujpe63.12.1076
24. T.V. Lokotosh, N.P. Malomuzh, K.S. Shakun, Nature of oscillations for the autocorrelation functions for translational and angular velocities of a molecule. J. Mol. Liq. **96–97**, 245–263 (2002). https://doi.org/10.1016/S0167-7322(01)00351-8
25. T.V. Lokotosh, S. Magazù, G. Maisano, N.P. Malomuzh, Nature of self-diffusion and viscosity in supercooled liquid water. Phys. Rev. E **62**, 3572–3580 (2000). https://doi.org/10.1103/PhysRevE.62.3572
26. P.A. Egelstaff, *An Introduction to the Liquid state* (Academic Press, London, NY, 1967), p. 408
27. M.A. Gonzalez, J.L.F. Abascal, A flexible model for water based on TIP4P/2005. J. Chem. Phys. **135**, 224516(1–8) (2011). http://dx.doi.org/10.1063/1.3663219
28. C. Oostenbrink, A. Villa, A.E. Mark, W.F. van Gunsteren, A biomolecular force field based on the free enthalpy of hydration and solvation: The GROMOS forcefield parameter sets 53A5 and 53A6. J. Comput. Chem. **25**, 1656–1676 (2004). http://dx.doi.org/10.1002/jcc.20090
29. D. van der Spoel, E. Lindahl, B. Hess, G. Groenhof, A.E. Mark, H.J.C. Berendsen, Gromacs: fast, flexible and free. J. Comp. Chem. **26**, 1701–1718 (2005). https://doi.org/10.1002/jcc.20291
30. W.F. van Gunsteren, S.R. Billeter, A.A. Eising, P.H. Hunenberger, P. Kruger, A.E. Mark, W.R.P. Scott, I.G. Tironi, *Biomolecular Simulation: The GROMOS96 Manual and User Guide* (Hochschulverlag AG an der ETH, Zurich, 1996), p. 1044
31. U. Essman, L. Perera, M.L. Berkowitz, T. Darden, H. Lee, L.G. Pedersen, A smooth particle mesh Ewald method. J. Chem. Phys. **103**, 8577–8593 (1995). https://doi.org/10.1063/1.470117
32. S. Nose, A unified formulation of the constant temperature molecular dynamics methods. J. Chem. Phys. **81**, 511–519 (1984). https://doi.org/10.1063/1.447334
33. W.G. Hoover, Canonical dynamics: equilibrium phase-space distributions. Phys. Rev. A **31**, 1695–1697 (1985). https://doi.org/10.1103/PhysRevA.31.1695
34. G.J. Martyna, D.J. Tobias, M.L. Klein, Constant pressure molecular dynamics algorithms. J. Chem. Phys. **101**, 4177–4189 (1994). https://doi.org/10.1063/1.467468
35. G.J. Martyna, M.E. Tuckerman, D.J. Tobias, M.L. Klein, Explicit reversible integrators for extended systems dynamics. Mol. Phys. **87**, 1117–1157 (1996). https://doi.org/10.1080/00268979600100761
36. M.J. Abraham, D. van der Spoel, E. Lindahl, B. Hess, The GROMACS development team, GROMACS User Manual version 2018, www.gromacs.org (2018) 265 p., http://manual.gromacs.org/documentation/2018/manual-2018.pdf. Accessed 12 Dec 2018
37. AYu. Kuksin, I.V. Morozov, G.E. Norman, V.V. Stegailov, I.A. Valuev, Standards for molecular dynamics modelling and simulation of relaxation. Mol. Sim. **31**, 1005–1017 (2005). https://doi.org/10.1080/08927020500375259
38. D. Frenkel, B. Smit, *Understanding Molecular Simulation, Second Edition: From Algorithms to Applications* (Academic Press, San Diego, San Francisco, New York, 2001), p. 664
39. M. Charbit, G. Blanchet, *Digital Signal and Image Processing Using MATLAB* (ISTE Ltd, Telecom ParisTech, 2006), p. 512
40. S. Hess, M. Kroger, W.G. Hoover, Shear modulus of fluids and solids. Phys. A **239**, 449–466 (1997). https://doi.org/10.1016/S0378-4371(97)00045-9
41. C. Vogt, K. Laihem, C. Wiebusch, Speed of sound in bubble-free ice. J. Acoust. Soc. Am. **124**, 3613–8 (2009). https://doi.org/10.1121/1.2996304
42. NIST Standard Reference Database 69: NIST Chemistry WebBook, http://webbook.nist.gov/chemistry/fluid. Accessed 5 Dec 2018
43. A.R. Dexter, A.J. Matheson, Elastic moduli and stress relaxation times in liquid argon. J. Chem. Phys. **54**, 203–208 (1971). https://doi.org/10.1063/1.1674594

44. R. Hartkamp, P.J. Daivis, B.D. Todd, Density dependence of the stress relaxation function of a simple fluid. Phys. Rev. E **87**, 032155 (2013). https://doi.org/10.1103/PhysRevE.87.032155
45. P.S. van der Gulik, The linear pressure dependence of the viscosity at high densities. Phys. A **256**, 39–56 (1998). https://doi.org/10.1016/S0378-4371(98)00197-6
46. R. Laghaei, A.E. Nasrabad, B.C. Eu, Generic van der Waals equation of state, modified free volume theory of diffusion, and viscosity of simple liquids. J. Phys. Chem. B **109**, 5873–5883 (2005). http://dx.doi.org/10.1021/jp0448245
47. B.A. Younglove, H.J.M. Hanley, The viscosity and thermal conductivity coefficients of gaseous and liquid argon. J. Phys. Chem. Ref. Data **15**, 1323–1339 (1986). https://doi.org/10.1063/1.555765
48. R. Mills, Self-diffusion in normal and heavy water in the range 1–45°. J. Phy. Chem. **77**, 685–688 (1973). https://doi.org/10.1021/j100624a025
49. K.R. Harris, L.A. Woolf, Pressure and temperature dependence of the self diffusion coefficient of water and oxygen-18 water. J. Chem. Soc. Faraday Trans. 1. **76**, 377–385 (1980). http://dx.doi.org/10.1039/f19807600377
50. N.I. Akhiezer, M.G. Krein, *Some Questions in the Theory of Moments* (Providence, Amer. Math. Soc., 1962), p. 310
51. M.G. Krein, A.A. Nudelman, *The Markov Moment Problem and Extremal Problems. Translations of Mathematical Monographs*, vol. 50 (Amer. Math. Soc., 1977), p. 417
52. S.J. Karlin, W.J. Studden, *Tchebycheff Systems: With Applications in Analysis and Statistics* (Wiley, London, 1966), p. 586
53. L.D. Landau, E.M. Lifshitz, *Statistical Mechanics* (Pergamon Press, Oxford, 1980), p. 544
54. D. Zubarev, V. Morozov, G. Ropke, *Statistical Mechanics of Nonequilibrium Processes* (Wiley, 1997), p. 376
55. J. Teixeira, M.-C. Bellissent-Funel, S.-H. Chen, J. Dianoux, Experimental determination of the nature of diffusive motions of water molecules at low temperatures. Phys. Rev. A **31**, 1913–1918 (1985). https://doi.org/10.1103/PhysRevA.31.1913
56. J. Teixeira, J.-M. Zanotti, M.-C. Bellissent-Funel, S.-H. Chen, Water in confined geometries. Phys. B **234–236**, 370–374 (1997). https://doi.org/10.1016/S0921-4526(96)00991-X
57. P. Blanckenhagen, Intermolecular vibrations and diffusion in water investigated by scattering of cold neutrons. Ber. Bunsenges. Phys. Chem. **76**, 891–903 (1972). https://doi.org/10.1002/bbpc.19720760907
58. K.-E. Larsson, U. Dahlborg, Proton motion in some hydrogenous liquids studied by cold neutron scattering. Physica **30**, 1561–1599 (1964). https://doi.org/10.1016/0031-8914(64)90181-8
59. G.J. Safford, P.S. Leung, A.W. Naumann, P.C. Schaffer, Investigation of low-frequency motions of H2O molecules in ionic solutions by neutron inelastic scattering. J. Chem. Phys. **50**, 4444–4468 (1969). https://doi.org/10.1063/1.1670917
60. S. Magazu, G. Maisano, F. Migliardo, A. Benedetto, Elastic incoherent neutron scattering on systems of biophysical interest: mean square displacement evaluation from self-distribution function. J. Phys. Chem. **112**, 8936–8942 (2008). https://doi.org/10.1021/jp711930b
61. J.W. Tester, M. Modell, *Thermodynamics and Its Applications,* 3d edn. (Prentice Hall, 1997), p. 960
62. N.P. Malomuzh, K.S. Shakun, Specific properties of argon-like liquids near their spinodals. **235**, 155–162 (2017). https://doi.org/10.1016/j.molliq.2017.01.079
63. S.V. Lishchuk, N.P. Malomuzh, P.V. Makhlaichuk, Why thermodynamic properties of normal and heavy water are similar to those of argon-like liquids? Phys. Lett. A **374**, 2084–2088 (2010). https://doi.org/10.1016/j.physleta.2010.02.070
64. P.V. Makhlaichuk, V.N. Makhlaichuk, N.P. Malomuzh, Nature of the kinematic shear viscosity of low-molecular liquids with averaged potential of Lennard-Jones type. J. Mol. Liq. **225**, 577–584 (2017). https://doi.org/10.1016/j.molliq.2016.11.101
65. V.Yu. Bardic, L.A. Bulavin, V.M. Sysoev, N.P. Malomuzh, K.S. Shakun, in *Soft Matter Under Exogenic Impacts,* ed. by V.A. Mazur, S.J. Rzoska (Springer, 2007), p. 339
66. VYu. Bardic, N.P. Malomuzh, K.S. Shakun, V.M. Sysoev, Modification of an inverse-power potential for simple liquids and gases. J. Mol. Liq. **127**, 96–98 (2006). https://doi.org/10.1016/j.molliq.2006.03.026

67. V.Yu. Bardic, N.P. Malomuzh, V.M. Sysoe, Functional form of the repulsive potential in the high pressure region. J. Mol. Liq. **120**, 27–30 (2005). https://doi.org/10.1016/j.molliq.2004.07.020
68. V.Yu. Bardik, N.P. Malomuzh, K.S. Shakun, High-frequency asymptote for the velocity autocorrelation function spectrum of argon-like systems. J. Chem. Phys. **136**(24), 244511 (2012). http://dx.doi.org/10.1063/1.4729849
69. A.I. Fisenko, N.P. Malomuzh, To what extent is water responsible for the maintenance of the life for warm-blooded organisms? Int. J. Mol. Sci. **10**, 2383–2411 (2009). https://doi.org/10.3390/ijms10052383
70. A.I. Fisenko, N.P. Malomuzh, Role of the H-bond network in the creation of life-giving properties of water. Chem. Phys. **345**, 164–172 (2008). https://doi.org/10.1016/j.chemphys.2007.08.013
71. N.P. Malomuzh, V.N. Makhlaichuk, P.V. Makhlaichuk, K.N. Pankratov, Cluster structure of water in accordance with the data on dielectric permittivity and heat capacity. J. Struct. Chem. **54**, S205–S225 (2013). https://doi.org/10.1134/S0022476613080039

Chapter 3
Microscopic Study of Solid/Fluid Interface with Molecular Dynamics

Mykola Isaiev, Guillaume Castanet, Michel Gradeck, Fabrice Lemoine and Konstantinos Termentzidis

Abstract The aim of the chapter is to give physical insights regarding solid/liquid interfaces and solid/liquid nanocomposites via atomistic simulations and improved macroscopic analytical approaches. Particularly, the use of molecular dynamics for the study of a nanodroplet located on a solid substrate will be discussed. The impact of line tension, Tolman length and adsorption layer on the wetting characteristic will be considered in details.

3.1 Introduction

The interfaces between two or more different phases predominate a variety of physical and chemical properties. This is more pronounced at the nanometer scale, where the surface-to-volume fraction becomes very high. Interactions between different phases are crucial for the wettability, solubility, chemical reactions etc. The different phases interaction is an important challenge for a wide range of applications in several sectors as for example in chemical industry, catalysis, material science, microfluidics, pharmacology, medicine, etc.

Particularly, the heat and mass transfer across a nanostructured solid/fluid interface as well as the physical properties of the "solid-fluid" nanocomposite hybrid media are significant issues for the series of applications. Among them one can note photothermal theranostic (simultaneous therapy and diagnostic) of cancer dis-

M. Isaiev · G. Castanet · M. Gradeck · F. Lemoine
LEMTA, CNRS-UMR7563, Université de Lorraine, ENSEM, 2 avenue de la Forêt de Haye, 54505 Vandoeuvre les Nancy, France

M. Isaiev
Faculty of Physics, Taras Shevchenko National University of Kyiv, 64/13 Volodymyrska str, Kyiv 01601, Ukraine

K. Termentzidis (✉)
Univ Lyon, CNRS, INSA-Lyon, Université Claude Bernard Lyon 1, CETHIL UMR5008, 69621 Villeurbanne, France
e-mail: konstantinos.termentzidis@insa-lyon.fr

L. A. Bulavin and L. Xu (eds.), *Modern Problems of the Physics of Liquid Systems*, Springer Proceedings in Physics 223,
https://doi.org/10.1007/978-3-030-21755-6_3

eases, cooling and heat isolating technologies, fabrication of thermal based sensing elements, etc. The state and possible imperfections, oxidation or nanostructuration of the interface could drastically influence the thermal transport in a solid/liquid nanocomposite system. As an example, the impact of a dense adsorbed layer of the liquid on the solid substrate can lead to the significant alternation of the thermal conductivity of the nano-hybrid system.

Molecular dynamics (MD) is a powerful tool to study solid or multiphase systems and it can be used for the further improvement of different applied aspects related to the mentioned above areas. With the use of the MD approaches one can study physical properties of various nanohybrid systems such as nanofluids, colloidal solutions of the nanoparticles, nanoporous media filled with fluid, different interfaces between nanostructured surface/liquid. Atomistic simulations with the use of MD technique can give physical insights for the phenomena related to the heat transfer as well as thermal resistance at the interfaces of different phases. From the practical point of view, it can explain how the different types of modifications influence on the heat and mass transport in order to tune it.

In this chapter, we mainly focus on the consideration of atomistic approaches for the description of wetting properties of a nanoscale droplet on a solid substrate and features of heat and mass transport across nanostructured "solid/fluid" interface. Special attention will be dedicated to match nanoscale simulations with macroscale experiments and models.

3.2 Molecular Dynamics: Fundamentals

Molecular dynamics approach is based on the examination of a system with huge number of degrees of freedom evolution based on the Newton's law of motion. Molecular dynamics (MD) is proven to be a very useful technique to study adsorption and diffusion of small molecules as well heat transport properties at the micro and nanoscale. The above three fundamental properties are the main task of our current work here. With MD simulations one can study the evolution in time—typically some picoseconds—of a large system of atoms—typically some millions of atoms. If one is interest to study longer simulations times of the order of ns, then smaller systems of some thousands of atoms can be only accessed. Firstly, one should set a configuration of the system with initial positions of the atoms. As an example, to study a water nanodroplet on a solid substrate, one should initially add a crystalline water slab on a silicon substrate (see Fig. 3.1).

In classical MD, atoms are treated as hard spheres, and their motions are described by Newton second law:

$$\overrightarrow{F}_i(t) = m_i \overrightarrow{a}_i(t)$$

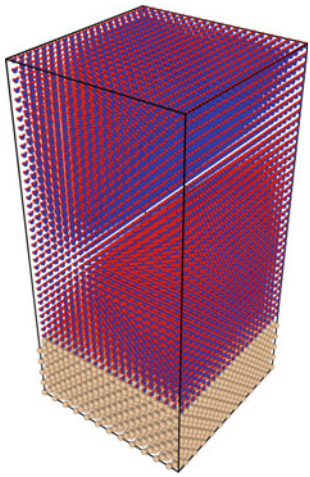

Fig. 3.1 An example of initial configuration: a water (red and blue atoms) crystalline slab located on a silicon (yellow atoms) substrate

where $\overrightarrow{F}_i$ is the force exerted on a particle i with mass m_i, while a_i is the accelation of the particle. On the other hand, the force can be written as the gradient of the potential energy V, else the interatomic potential for the MD friendly users;

$$\overrightarrow{F}_i = -\overrightarrow{\nabla}_i V$$

Combining the two equations, one has the following equation:

$$m_i \frac{\mathrm{d}^2 \overrightarrow{r_i}}{\mathrm{d}t^2} = \frac{-\partial V}{\partial \overrightarrow{r_i}}$$

where r_i is in general a 3N dimensional vector.

Then one uses an integration scheme to have the time evolution of the system. One very popular scheme is the Verlet algorithm, with which one can predict the position of all atoms at time $t + \mathrm{d}t$, knowing the positions at the two previous time steps (t and $t - \mathrm{d}t$). Several thermodynamics properties are connected to the trajectory of atoms. More details of MD simulations as the thermodynamic ensembles, the boundary conditions or the several interatomic potentials can be found in textbooks as "Computer Simulation of Liquids" by Allen and Tildesley [1], Haile [2], Wang [3], Termentzidis [4].

3.2.1 Water Models

The choice of the interatomic potential, which defines the way that atoms are interacting with each other, is an important step for performing meaningful simulations. Concerning water, there are several models, which are commonly used in the MD

simulations. In general, depending on the number of sites in a water molecule, one can distinguish one, two, three, four, five and six site water models.

The first two models belong to coarse-grain water models, which are started to be popular for acceleration of molecular dynamics simulations. Three and four sites water models are more widely used in molecular dynamics simulations because of reasonable computational costs and good physical description. In three sites water model each site corresponds to atom in a real water molecule—two sites for hydrogen atoms and one site for oxygen.

One of the simplest and intuitive three-point sites water model (Fig. 3.2a) is the simple point charge [5] (SPC) model and the transferable intermolecular potential for 3 points [6] (TIP3P) models. Each site in these models interact with Coulomb forces with respect to their charge (the values of a charge for oxygen $(q|O)$ and hydrogen $(q|H)$ atoms are mentioned in Table 3.1). Additionally, atoms of oxygen interact with each other with Lennard-Jones potential:

$$V(r) = 4\varepsilon\left(\left(\frac{\sigma}{r}\right)^{12} - \left(\frac{\sigma}{r}\right)^{6}\right),$$

where r is the distance between oxygen atoms, ε and σ is the energetic and the geometrical parameter of Lennard-Jones potential.

However, the density of liquid water calculated with SPC model is underestimated compared to the experiment one, while the density of vapor is overestimated compared to experimental data [7]. The discrepancy between the experimental and theoretical data arises from the nature of SPC potential [8]. SPC model can be significantly improved by adding self-energy correction term due to polarization [9]:

$$E = \frac{1}{2}\sum_i \frac{\left(\mu - \mu^0\right)^2}{\alpha_i},$$

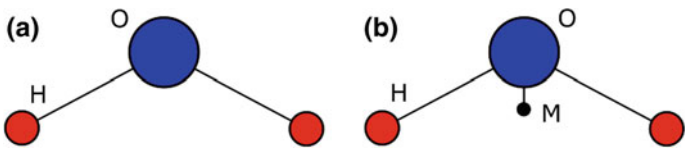

Fig. 3.2 Schematic representation of three (**a**) and four (**b**) sites water molecule

Table 3.1 Parameters for water models

Model	r_{OH} (Å)	$\angle_{HOH}$ (°)	ε (eV)	σ (Å)	q_O (e)	q_H (e)
SPC	1	109.47	$6.737 \cdot 10^{-3}$	3.166	−0.82	0.41
SPC/E	1	109.47	$6.737 \cdot 10^{-3}$	3.166	−0.8476	0.4238
TIP3P	0.9572	104.52	$6.596 \cdot 10^{-3}$	3.15061	−0.8340	0.4170

Table 3.2 Parameters for TIP4P based water model

Model	ε (meV)	σ (Å)	q_M (e)	q_H (e)	r_{OM} (Å)
TIP4P [6]	6.716	3.15365	−1.04	0.52	0.15
TIP4P-Ew [10]	7.0575	3.16435	−1.04844	0.52422	0.125
TIP4P/Ice [11]	9.1434	3.1668	−1.1794	0.5897	0.1577
TIP4P/2005 [12]	8.0313	3.1589	−1.1128	0.5564	0.1546

where μ is the dipole moment of an effectively polarized water molecule, μ^0 is the dipole moment of an isolated water molecule, and α_i is the polarizability constant. The water model which considers this term is called extended simple point charge water model (SPC/E). This water model is one of the most frequently used water models considering the reasonable computational costs.

In four sites water models, like transferable intermolecular potential for 4 points [6] (TIP4P), additional negative charged mass-less site (see Fig. 3.2b) is introducing to improve dipole moment of a water molecule. TIP4P has several parametrizations and it is widely used for description of water properties in various MD simulations. Parameters for some parametrizations based on TIP4P water model are presented in the Table 3.2. In all mentioned parametrizations the length of OH bond (l_{OH}) and angle HOH ($\angle$HOH) are equal to 0.9572 Å and 104.52° respectively.

3.3 Water Nanodroplet on a Solid Substrate

Molecular dynamics is a very useful tool for the description of solid-fluid interactions. It gives insights regarding numerous physical properties of and at the interface. However, for the correct use of MD for systems containing solid/liquid interfaces, one should also know the interatomic potentials between the water molecule and the substrate.

There are two main approaches to fit the parameters of interatomic potentials between atoms of solids and fluids: either based on experimental data or ab initio simulations. In the case of a substrate with electrically neutral atoms, conventionally the interactions between solid atoms and hydrogen of a water molecule are neglected. The simplest interaction between oxygen atoms and atoms of substrate is based on Lenard-Jones potential (see Fig. 3.3):

$$V = 4\varepsilon\left(\frac{\sigma^{12}}{r^{12}} - \frac{\sigma^{6}}{r^{6}}\right), \tag{3.1}$$

where ε and σ are the energetic and spatial parameters of Lenard-Jones potential, r is the distance between an oxygen atom and an atom of substrate. The energetic parameter defines the depth of potential well, while σ is the characteristic distance at which potential is equal to 0.

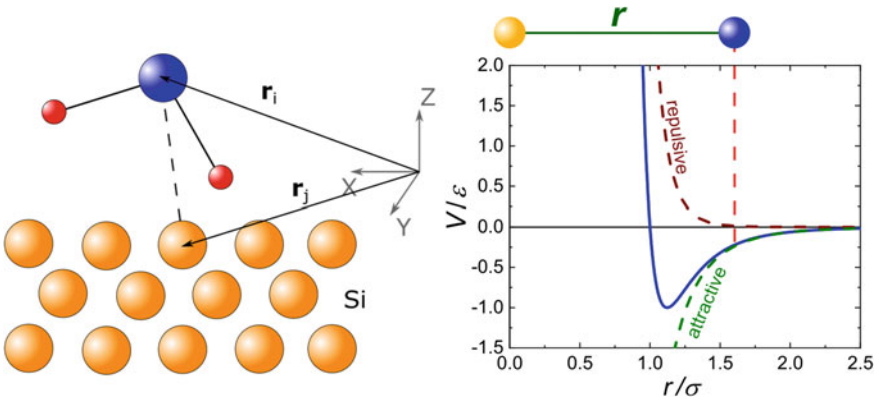

Fig. 3.3 Sketch representation of interaction between an oxygen atom of a water molecule and a silicon atom of a substrate

Often, mixing rules are used to estimate energetic and spatial parameters in Lenard-Jones potential for cross interactions. As an example of such rule the widely used Lorentz-Berthelot (LB) mixing rule can be mentioned:

$$\varepsilon_{OS} = \sqrt{\varepsilon_{OO} \cdot \varepsilon_{SS}},$$
$$\sigma_{OS} = \frac{1}{2}(\sigma_{OO} + \sigma_{SS}),$$

where indexes "OS", "OO" and "SS" mean cross interactions, intersections between oxygen atoms and interactions between atoms of substrate respectively.

However, as results of atomistic simulations show such approximation have rigid limitations [13].

In the following subsection, we will consider techniques to estimate LJ interaction parameters based on experimental values of the wetting angle. After, we will consider an example of application of these data for the study of adsorption of the liquid's atoms on the solid substrate in an external force field.

3.3.1 Solid/Fluid Interaction and Wetting Angle

For the simulation of a nanodroplet located on a solid substrate, one should start with the design of an initial configuration of atoms in a simulation domain. The most widely used configurations are spherical-cap and cylindrical-cap droplets on a smooth surface. Examples of corresponding initial configurations are presented in Figs. 3.1 and 3.4. Then, the system is equilibrated in appropriate thermostat and with chosen boundary conditions depending on required physics [13–15].

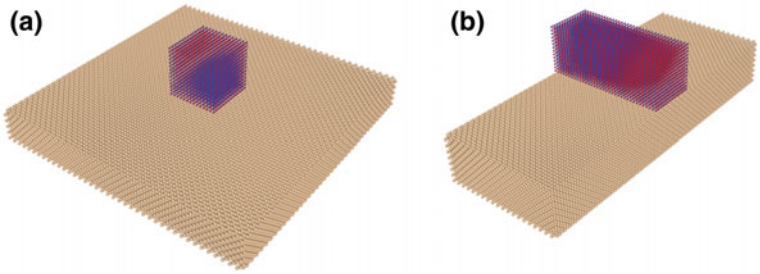

Fig. 3.4 Initial configurations of atoms to form spherical-cap (**a**) and cylindrical-cap (**b**) droplets

After the procedure of equilibration, one can obtain information about droplet properties for example shape, wetting angle, energetic and force characteristics for different input parameters like interaction parameters. As an example, Fig. 3.5 demonstrates the snapshots of the shapes of a water droplet located on a silicon substrate for different values of energetic parameter (ε). For evaluation of the wetting angle, one should take into account the presence of adsorption layer of a fluid on the solid substrate (so called layering effect). Therefore, one should approximate equimolar surface with the circular starting form some high above surface after which the impact of surface is negligible to estimate correctly the wetting angle.

The wetting properties of a liquid droplet on a solid substrate can be described with the simple Young's equation, which is a relation between the wetting angle θ and

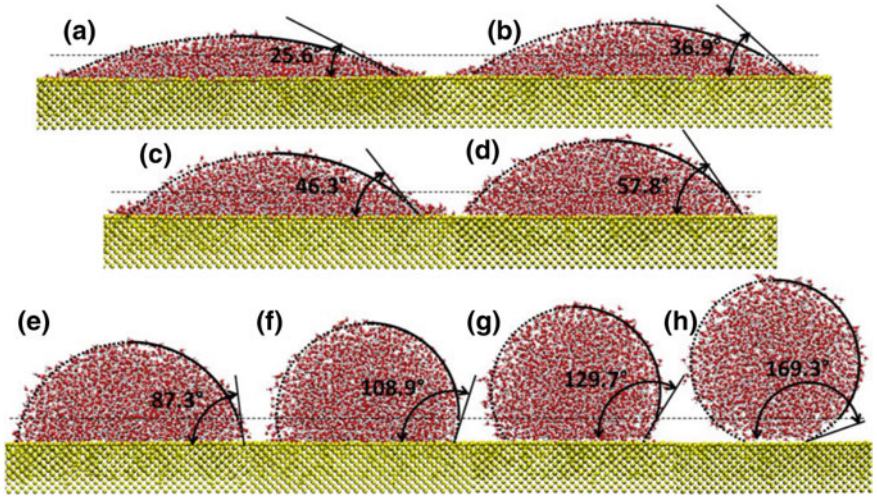

Fig. 3.5 Snapshots of spherical-cap water droplets on silicon substrate with the interaction strength values of 1 (**a**), 0.7 (**b**), 0.4 (**c**), 0.2 (**d**), 0.15 (**e**), 0.125 (**f**), 0.1 (**g**) and 0.05 (**h**) $\times$ ε_{SO} respectively, where $\varepsilon_{SO} = 0.12088$ eV is an energetic parameter of Lenard-Jones potential calculated with Lorentz–Berthelot mixing rule (reprinted with permission from Barisik and Beskok [13])

the surface tensions γ_{ij} between vapor/liquid (vl), liquid/solid (ls) and vapor/solid (vs):

$$\cos(\theta) = \frac{\gamma_{\mathrm{vs}} - \gamma_{\mathrm{ls}}}{\gamma_{\mathrm{vl}}}.$$

However, at the nanoscale, at typical scale at which MD can operate, one should consider the impact of the three-phase contact line [16, 17], between solid, liquid and vapor. Such impact can be expressed with the use of line tension τ, and the modified Young's equation in this case can be written as follows:

$$\cos(\theta) = \frac{\gamma_{\mathrm{vs}} - \gamma_{\mathrm{ls}}}{\gamma_{\mathrm{vl}}} - \frac{\tau}{\gamma_{\mathrm{vl}} r}, \tag{3.2}$$

where r is the radius of curvature of three phase contact line. Thus, the natural dependence of the wetting angle on the droplet size arises. Consequently, one should perform simulations for several sizes of droplet and then to make approximation for a large droplet to obtain correlation between macrosized experimental value of wetting angle and MD one.

As one can see from (2), the dependence of the cosines of a contact angle on the radius of curvature is linear. Thus, one can perform routine simulations for different parameters of interaction and for different droplet sizes. The macrosized wetting angle can be estimated as an approximation value when radius of curvature trends to infinity ($r \to \infty$). As an example, Fig. 3.6 presents the dependence of wetting angle of a water droplet on graphite substrate on the curvature of three-phase contact line for different energetic parameters of Lenard-Jones potential [13, 14].

Another simpler scenario as we will show in the following is to estimate the wetting angle by considering a cylindrical droplet. Figure 3.7a presents the MD

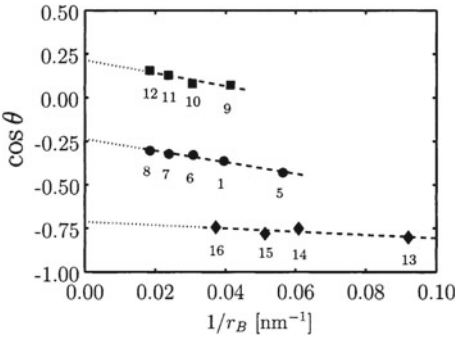

Fig. 3.6 Cosine of the contact angle θ as a function of the droplet base curvature $1/r$. The three series are computed using Lennard-Jones parameters of $\varepsilon = 3.25$ meV (circles), $\varepsilon = 4.55$ meV (squares), and $\varepsilon = 1.95$ meV (diamonds) for droplets with an increasing number of water molecules: 1000 (cases 5, 13, and 9), 2000 (cases 1, 14, and 10), 4000 (cases 6, 15, and 11), 8379 (case 7, 16, and 12), and 17576 (case 8) (reprinted with permission Werder et al. [14])

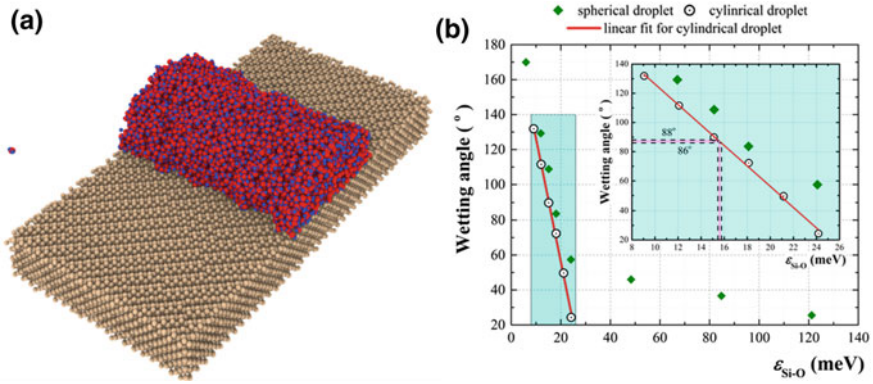

Fig. 3.7 **a** MD snapshot of cylindrical droplet on the silicon substrate; **b** the dependence of a wetting angle on energetic parameter for spherical (diamonds) and cylindrical (circles) droplets (reprinted with permission Isaiev et al. [18])

snapshots of a cylindrical droplet located on the silicon substrate. As one can see in this case that the curvature of three-phase contact line is trend to zero [15, 18].

The influence of line tension can be seen from the Fig. 3.7b, where the dependence of wetting angle on the energetic parameter of Lenard-Jones potential is presented for spherical (with diamonds) and for cylindrical (with circles) droplets on the silicon substrate. The data for spherical droplet was extracted from [13], and the figure was reprinted with permission from [18].

As one can see from the figure, the weeding angle for spherical droplet is bigger than the one for cylindrical for all values of ε. Such decreasing of wetting angle for cylindrical droplet arises because of the influence of linear tension.

Since the wetting angle depends on the surface tension in (2), one should take into account also size dependence of the surface tension which may also influence the wettability [19–21]. Such consideration may be performed in the frames of the Tolman formalism, which is based on the introduction of the following equation for the description of size dependence of surface tension [22]:

$$\gamma(R) = \frac{\gamma^{\infty}}{1 + \frac{(n-1)\delta}{R}} \approx \gamma^{\infty}\left(1 - \frac{(n-1)\delta}{R} + \cdots\right),$$

where γ^{∞} is the vapor/liquid surface tension (γ_{vl}) of a flat (un curved) surface; n is equal to 2 and 3 for cylindrical and spherical droplet respectively; R is the radius of the principle curvature; δ is the Tolman length—the distance between equimolar surface and surface of tension.

The dependence of surface tension on the curvature' radius can be seen in Fig. 3.8, where we depicted the results of simulations for spherical and cylindrical droplets.

Thus, the modified Young's equation with Tolman correction can be presented as follows

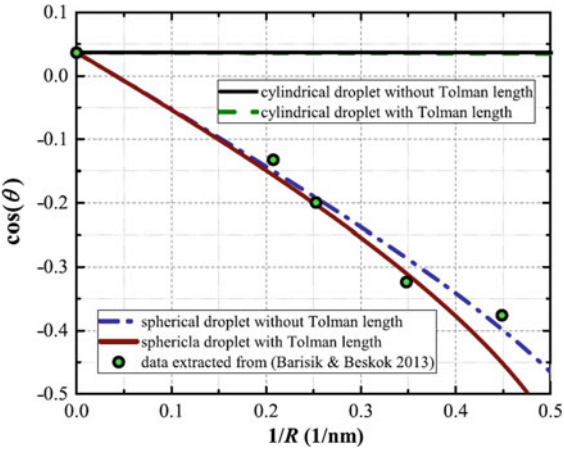

Fig. 3.8 Dependences of the cosine of the wetting angle on the inverse radius of the cylindrical and spherical droplets with Tolman correction (solid lines) and without Tolman correction (dash-dot lines) (reprinted with permission Isaiev et al. [18])

- for a spherical droplet:

$$\cos(\theta)\left(1-2\frac{\delta}{R}\right)+\frac{\tau}{\gamma^{\infty}}\frac{1}{R\sin(\theta)}=\frac{\gamma_{\mathrm{vs}}-\gamma_{\mathrm{ls}}}{\gamma_{\mathrm{vl}}}-\frac{\tau}{\gamma_{\mathrm{vl}}r},$$

- for a cylindrical droplet:

$$\cos(\theta)\left(1+\frac{\delta}{R}\right)=\frac{\gamma_{\mathrm{vs}}-\gamma_{\mathrm{ls}}}{\gamma_{\mathrm{vl}}}.$$

The impact of Tolman length on the wetting angle can be seen in Fig. 3.8, where the dependence of the wetting angle for cylindrical and spherical water droplets are presented taking into account the corrections or not of the impact of Tolman length.

As one can see from the last figure, the impact of the Tolman length on the wetting angle is less pronounced for the case of cylindrical droplets, while for spherical droplets the difference is important. In particular, the change of cosines of wetting angle caused by the size dependence of surface tension for a spherical droplet with radius 2.5 nm approximately equals to 7%.

Thus, the use of cylindrical droplets is more adequate for the correlation of molecular dynamics with macrosized experiments. However, as a recent study [23, 24] revealed; the wetting angle of cylindrical droplet also depends on the size of the droplet and this point should be studied more carefully in the future. This phenomenon may arise because of the contact area between solid and fluids and the more dense fluid layer close to the substrate due to adsorption, which will be considered in the following section.

3.3.2 Adsorption of Water Molecules on the Solid Substrate

As mentioned in a previous section, the thin layer of liquid with perturbed density arises between solid substrate and liquid, so called "layering effect". The presence of this adsorbed layer leads to variation [25] of droplet properties located on a solid substrate and may perturb experimental results [26]. As an example Fig. 3.9 demonstrates the presence of the adsorbed layer close to the solid/fluid interface for the case of a cylindrical droplet located on the silicon substrate. As one can see from the Fig. 3.9b, the density close to the interface is significant, and deviation from the density of bulk water is more than 20%. It is clear, that such density fluctuations lead to modifications of droplet properties.

It is clear that the quantity of water molecules adsorbed on a solid substrate is proportional to the contact area. Therefore, one way to study the influence of this layer is by increasing the droplet size. However, this will lead also to increase the number of "bulk molecules", and the effect of interface may be smoothed.

To study the influence of increasing the surface area, we introduce an external force field [25]. The magnitude of this external field should be from one side enough to deform a droplet shape, and from another side it should not be big to cause change of properties of a bulk/adsorbed water. The impact of such homogeneous force field can be seen in Fig. 3.10. As one can see, the application of such field leads to the deformation of the droplet, and in the same time the densities of bulk and adsorbed water were not changed compared to the case without external field.

Since the density of the adsorbed water layer is larger than the density of the bulk one, the increase of the contact area leads to the decrease of the droplet volume. The calculated dependence of the volume of a droplet on the contact area is presented in Fig. 3.11. The dependence is linear, and the slope of this line (ξ) depends on the portion of adsorbed molecules.

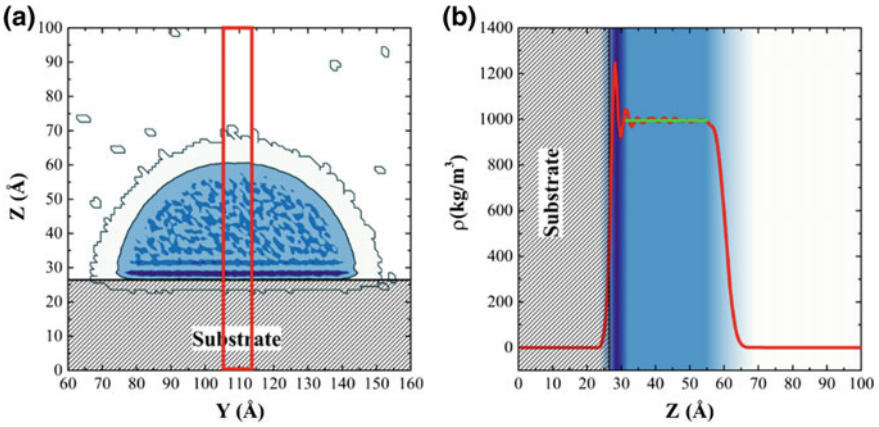

Fig. 3.9 **a** The spatial profile of the density of a cylindrical droplet on the silicon substrate. **b** Density variation of liquid close to solid/fluid interface (adopted from Isaiev et al. [25])

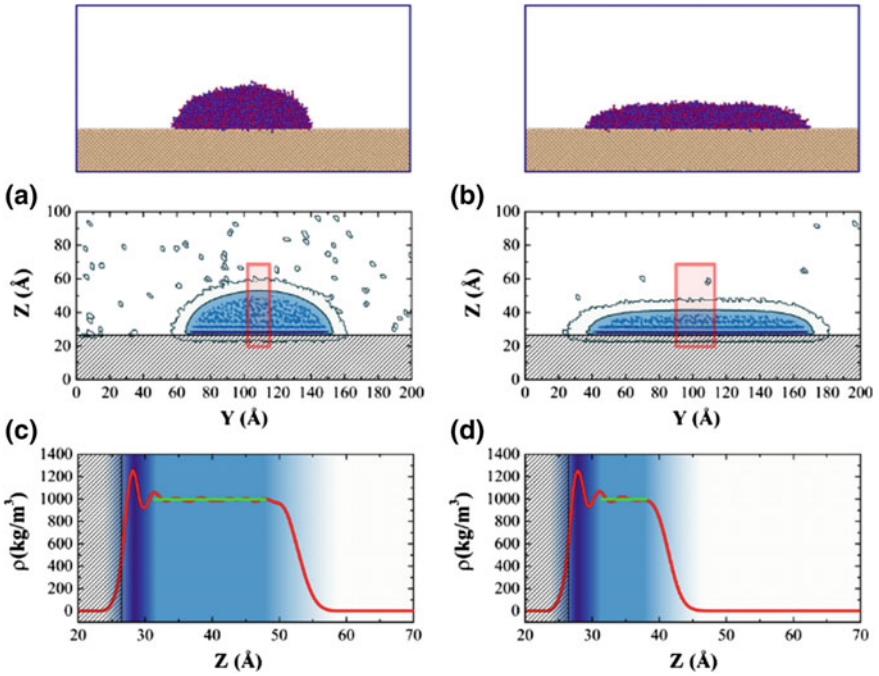

Fig. 3.10 Molecular dynamics snapshots (upper insets) and density profiles of the droplet density map in an external field with intensities of 19 (**a**) and 97 pN/Å (**b**) and corresponding density profiles in the middle of the water droplet for the same external field intensities (**c** and **d**) (reprinted with permission from Isaiev et al. [25])

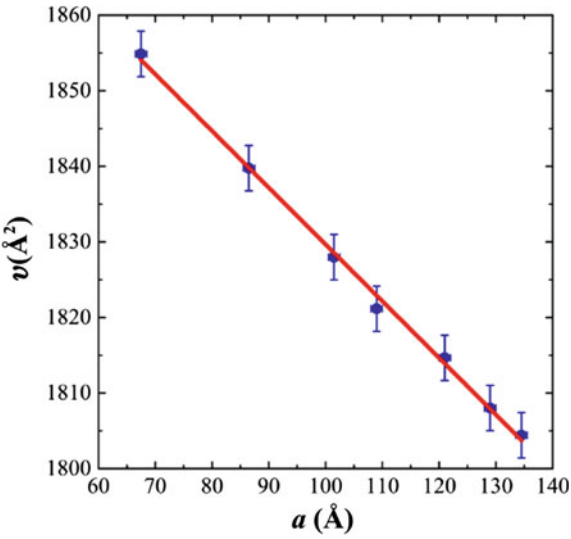

Fig. 3.11 Dependence of the droplet volume as a function of the contact area. The red lines are fitting curves with $\xi = 0.875$ Å (reprinted with permission from Isaiev et al. [25])

With the use of this value, one can estimate the value of the adsorption per unit area (in mol/m^2) with the following equation:

$$\Gamma = \frac{\xi \rho_b}{M_{H_2O}},$$

where ρ_b is the density of bulk water, M_{H_2O} is the molar mass of water. The founded value of the specific adsorption ($\Gamma = 4.8$ μ mol/m^2) for the case of SPC/E water on a silicon substrate is in a good agreement with experimental literature data [27]. Thus, the introduction of an external force field could be a promising way to evaluate several properties of the adsorbed thin water layer.

3.4 Phase Changing Phenomena

In the framework of coupled heat and mass exchanges, one point of attention is the efficiency of heat transfer from a hot surface (heated above temperature of liquid boiling) into a liquid that strongly depends on the temperature of the substrate. This dependence is usually analyzed in terms of the "heat flux vs temperature" curves (also called "boiling curve"), which describes the rate of the heat transfer from the substrate as a function of its temperature (see Fig. 3.12).

Among the different processes presented in Fig. 3.12, nucleate boiling is usually considered as the most desirable because of the high heat fluxes possible with moderate temperature differences. The thermal energy dissipation from the solid in contact with liquid due to nucleate boiling can be in several orders of magnitude bigger than the one resulting from convection heat transfer for a prescribed temperature difference between a solid and a liquid [28]. The efficiency of such thermal energy

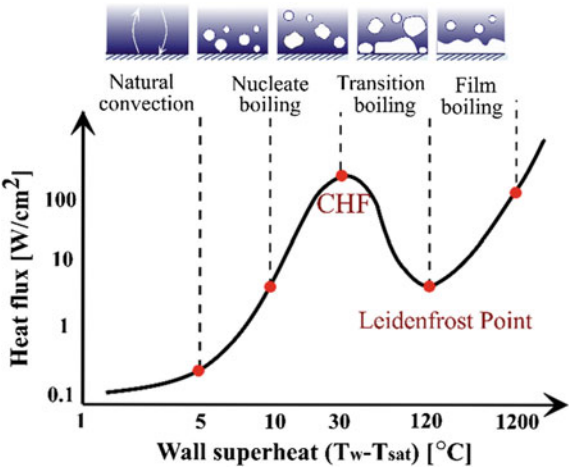

Fig. 3.12 Typical sketch of the boiling curve

dissipation increases with heat flux till the point called "critical heat flux" (CHF), which separates nucleate and transition boiling. In the latter regime, efficiency of heat dissipation from the solid in liquid is degraded as vapor essentially insulates the bulk liquid from the hot surface. Thus, the tuning of CHF is a significant technological issue for industrial applications based on heat exchanges [29] (dissipation of high thermal heat fluxes, waste heat recovery, condenser design, low/mid temperature heat exchangers, etc.) and heat management systems.

Till now there is a lack of a unified methodology for the description of heat and mass transfer, the elaborated models work mainly in narrow region of temperatures and pressures. Especially, the mentioned above approach is related with the case of a nanostrucred surface with a lot of nanoscale features. Molecular dynamics technique is a promising tool that can give physical insights regarding the impact of such features on heat and mass transfer across an interface.

3.4.1 Methodology of Simulations

Let us consider a system of a cold water slab on an overheated substrate. For such complex system, that has several applications (heat ex-changers, Leidenfrost effect, etc.), one can study its evolution from a molecular point of view with the following steps [30–32]. Firstly, one should set-up a simulation system with a water slab covering a solid substrate. As an example, in Fig. 3.13a, there is a situation where water slab is located on a crystalline silicon substrate. The following step is thermalization of the system to achieve a desire temperature for the water slab, typically 300 K (Fig. 3.13b). Then water slab is excluded from the updating velocities and positions (fixed), while the substrate can be heated up to the desired temperatures. Then, the

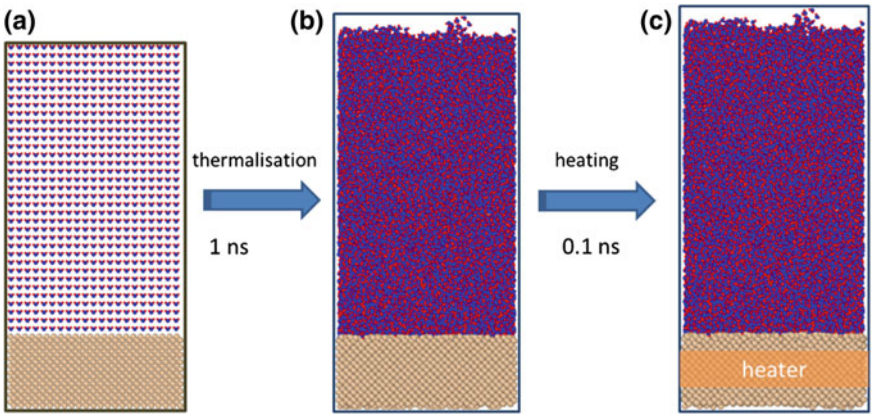

Fig. 3.13 Different stages of the simulation set-up to study a system of a cold water slab on an overheated substrate with MD approach

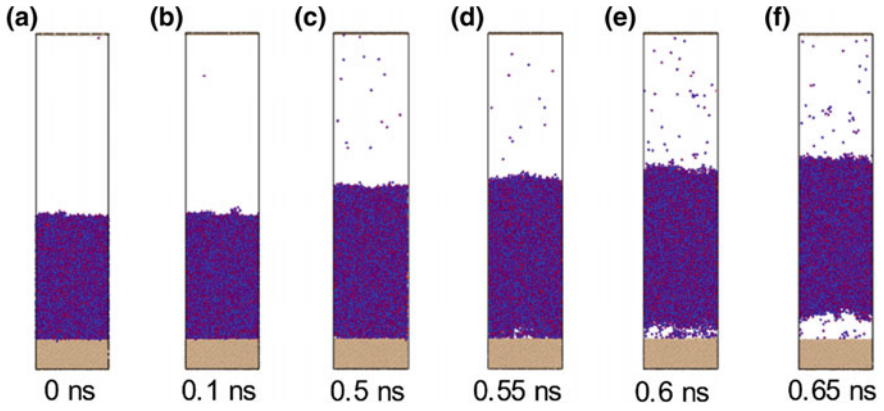

Fig. 3.14 MD time evolution snapshots of the system cold-water/heated-substrate

water film can be re-included in the numerical integration to study its interaction with the overheated slab.

Once the molecules of a water slab is free to change position and velocities (Fig. 3.14a, b), heat dissipation appears through the water/solid interface. First, the volume of the water film increases (Fig. 3.14c) because of the thermal expansion. Then the formation of rapidly grown nanobubble can be observed (Fig. 3.14d, e), and further fast phase separation at the interface is observed (Fig. 3.14f). The water film elevates fast from the overheated substrate and this could be infinite. Due to simulation time limitations, we are obliged to use periodic boundary conditions which oblige the water film to oscillate between the upper and lower solid substrate. Only the presence of an external field (which we have introduced in the previous paragraph) may stabilize such oscillation [33]. Once the water film stabilizes its position, we can study the so-called Leidenfrost effect, i.e. the thickness of the vapor layer between the water film and the overheated substrate depending the temperature of the solid substrate. Nevertheless, one should be careful, because such fast phase separation could be a spinodal decomposition instead of boiling in the macroscopic observed Leidenfrost effect.

The presence of the vapor film in the system leads to the appearance of a significant reduction of the heat flux from the overheated substrate. This can be observed in Fig. 3.15 which represents the time evolution of the energy which is necessary to give to the thermostated solid substrate to keep it under constant pressure and desired overheated temperature. Three regimes can be distinguished:

(i) initially the energy transfer from the solid substrate towards the water film is large, and therefore one needs to give to the system a lot of energy to keep the substrate thermostated;
(ii) the slope of the needed energy decreases when vapor nanobubles start to appear between the water film and the solid substrate;

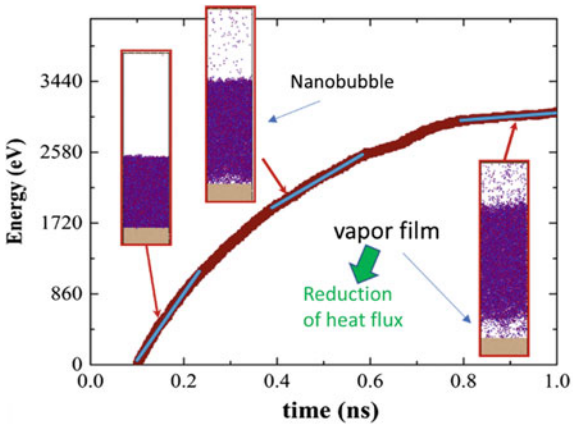

Fig. 3.15 Energy time-evolution for the cold-water/overheated-solid. This energy is what we should add to the thermostat to keep silicon slab under the desired constant overheated temperature

(iii) when the water film is detached totally from the substrate there is a saturation of energy, which means that the substrate is almost isolated from the water film, and the heat transport is now mainly through the vapor layer formed between the water film and the overheated substrate.

As mentioned before, one should be careful for possible spinodal decomposition and the total time of simulation. Different phenomena appears in different time scales. What we wanted to show here is that MD simulations could be used to study water/solid interactions at the small time and length scales and that it should be used with cautious for the description of the heat and mass transfer across nanostructured interface. It can give physical insights regarding such processes at the nanoscale [34, 35] and new solutions for heat and mass transfer enhancement, which is important for engineering of new generation of highly efficient substrates.

3.5 Conclusions

Molecular dynamics is a powerful tool which give physical impacts at the small scales to improve numerous technological applications in various applied fields. Particularly, in this chapter, we use molecular dynamics approach to study phenomena arising at the solid/fluid interface at the atomic scale. More specifically, the wetting properties of a water droplet on a solid substrate as well as heat/mass transfer across the interface were addressed in details and we found derivations from the classical macroscopic descriptions. The main issues connected with the features of consideration of nanoscale objects were underlined, like line tension, Tolman length and spinodal decomposition.

References

1. M.P. Allen, D.J. Tildesley, *Computer Simulation of Liquids*, 2nd edn. (Oxford University Press, Oxford, 2017)
2. J.M. Haile, *Molecular Dynamics Simulation: Elementary Methods* (Wiley, 1997)
3. L. Wang, (ed.), *Molecular Dynamics—Theoretical Developments and Applications in Nanotechnology and Energy* (InTech, 2012)
4. K. Termentzidis (ed.), *Nanostructured Semiconductors Amorphization and Thermal Properties*, 1st edn. (Pan Stanford, New York, 2017)
5. H.J.C. Berendsen, J.P.M. Postma, W.F. van Gunsteren, J. Hermans, in *Intermol. Forces* (1981), pp. 331–342
6. W.L. Jorgensen, J. Chandrasekhar, J.D. Madura, R.W. Impey, M.L. Klein, J. Chem. Phys. **79**, 926 (1983)
7. J.J. De Pablo, J.M. Prausnitz, H.J. Strauch, P.T. Cummings, J. Chem. Phys. **93**, 7355 (1990)
8. J. Alejandre, D.J. Tildesley, G.A. Chapela, J. Chem. Phys. **102**, 4574 (1995)
9. H.J.C. Berendsen, J.R. Grigera, T.P. Straatsma, J. Phys. Chem. **91**, 6269 (1987)
10. H.W. Horn, W.C. Swope, J.W. Pitera, J.D. Madura, T.J. Dick, G.L. Hura, T. Head-Gordon, J. Chem. Phys. **120**, 9665 (2004)
11. J.L.F. Abascal, E. Sanz, R. García Fernández, C. Vega, J. Chem. Phys. **122**, 234511 (2005)
12. J.L.F. Abascal, C. Vega, J. Chem. Phys. **123**, 234505 (2005)
13. M. Barisik, A. Beskok, Mol. Simul. **39**, 700 (2013)
14. T. Werder, J.H. Walther, R.L. Jaffe, T. Halicioglu, P. Koumoutsakos, J. Phys. Chem. B **107**, 1345 (2003)
15. H. Peng, G.R. Birkett, A.V. Nguyen, Mol. Simul. **40**, 934 (2013)
16. B.M. Law, S.P. McBride, J.Y. Wang, H.S. Wi, G. Paneru, S. Betelu, B. Ushijima, Y. Takata, B. Flanders, F. Bresme, H. Matsubara, T. Takiue, M. Aratono, Prog. Surf. Sci. **92**, 1 (2017)
17. P. Blecua, R. Lipowsky, J. Kierfeld, Langmuir **22**, 11041 (2006)
18. M. Isaiev, S. Burian, L. Bulavin, M. Gradeck, F. Lemoine, K. Termentzidis, Mol. Simul. **42**, 910 (2016)
19. S. Burian, M. Isaiev, K. Termentzidis, V. Sysoev, L. Bulavin, Phys. Rev. E **95**, 062801(1) (2017)
20. S.S. Rekhviashvili, E.V. Kishtikova, Prot. Met. Phys. Chem. Surfaces **48**, 402 (2012)
21. S.S. Rekhviashvili, E.V. Kishtikova, Tech. Phys. **56**, 143 (2011)
22. R.C. Tolman, J. Chem. Phys. **17**, 333 (1949)
23. M. Kanduč, J. Chem. Phys. **147** (2017)
24. M. Kanduč, L. Eixeres, S. Liese, R.R. Netz, Phys. Rev. E **98**, 1 (2018)
25. M. Isaiev, S. Burian, L. Bulavin, W. Chaze, M. Gradeck, G. Castanet, S. Merabia, P. Keblinski, K. Termentzidis, J. Phys. Chem. B **122**, 3176 (2018)
26. S.S. Rekhviashvili, B.A. Rozenberg, V.V. Dremov, JETP Lett. **88**, 772 (2008)
27. H. Nishino, T. Tanaka, K. Yoshida, J. Takatsubo, Ultrasonics **52**, 530 (2012)
28. V.S. Nikolayev, D. Chatain, Y. Garrabos, D. Beysens, Phys. Rev. Lett. **97**, 1 (2006)
29. N.S. Dhillon, J. Buongiorno, K.K. Varanasi, Nat. Commun. **6** (2015)
30. P. Yi, D. Poulikakos, J. Walther, G. Yadigaroglu, Int. J. Heat Mass Transf. **45**, 2087 (2002)
31. T.H. Yang, C. Pan, Int. J. Heat Mass Transf. **48**, 3516 (2005)
32. Y. Mao, Y. Zhang, Appl. Therm. Eng. **62**, 607 (2014)
33. M. Isaiev, M. Gradeck, K. Termentzidis, in *Proceedings Second Thermal and Fluids Engineering Conference* (Begellhouse, Connecticut, 2017), pp. 1997–2000
34. R. Diaz, Z. Guo, Numer. Heat Transf. Part A Appl. **72**, 891 (2017)
35. R. Diaz, Z. Guo, in *Proceedings Second Thermal and Fluids Engineering Conference* (Begellhouse, Connecticut, 2017), pp. 3199–3210

Part II
Physics–Chemistry Properties of Liquid Systems

Chapter 4
Oligomeric and Polymeric Ionic Liquids: Engineering Architecture and Morphology

Alexandr V. Stryutsky, Volodymyr F. Korolovych, Hansol Lee, Emily Mikan, Andrew Erwin, Oleh O. Sobko, Maryana A. Gumenna, Nina S. Klimenko, Valery V. Shevchenko, Leonid A. Bulavin and Vladimir V. Tsukruk

Abstract The series of amphiphilic anionic protic hyperbranched oligomeric and polymeric ionic liquids (HBP-OILs) with different terminal groups and an adjustable hydrophilic-hydrophobic balance which are sensitive to pH and ionic strength changes was obtained by neutralizing the carboxylic and sulfonic terminal acid groups of aliphatic hyperbranched core with N-methylimidazole (Im) and 1,2,4-1H-triazole (Tr). The introduction of long hydrophobic aliphatic tails to starting hydrophobic hyperbranched core influences more significantly on the size of micellar assemblies than the introduction of ionic groups does. The assembly of these compounds into core-corona micelles in aqueous media in a wide range of pH and ionic conditions was established. Regulation of HBP-OILs amphiphilicity can be realized by varying the extent of ionization of terminal groups by changing pH or ionic strength. The synthesis of the thermally responsive protic anionic hyperbranched poly(ionic liquid)s (HBP-PILs) was based on partial (50%) and full neutralization of carboxyl groups of aliphatic polyester core by monoamine-terminated poly(N-isopropylacrylamide)s (PNIPAM). Its linear oligoester analog was synthesized in a similar way. These compounds possess low critical solution temperature (LCST) behavior with a narrow LCST window and amorphous state in condensed matter. We found that HBP-PILs form smaller in comparison with linear analogues spherical

A. V. Stryutsky (✉) · O. O. Sobko · M. A. Gumenna · N. S. Klimenko · V. V. Shevchenko
Institute of Macromolecular Chemistry of the National Academy of Sciences of Ukraine, Kharkivske Shosse 48, Kyiv 02160, Ukraine
e-mail: striutskyi@gmail.com

V. V. Shevchenko
e-mail: valpshevchenko@gmail.com

V. F. Korolovych · H. Lee · E. Mikan · A. Erwin · V. V. Tsukruk
School of Materials Science and Engineering, Georgia Institute of Technology, Atlanta, GA 30332, USA
e-mail: vladimir@mse.gatech.edu

L. A. Bulavin
Taras Shevchenko National University of Kyiv, Volodymyrska Str. 64, Kyiv 01601, Ukraine
e-mail: bulavin221@gmail.com

L. A. Bulavin and L. Xu (eds.), *Modern Problems of the Physics of Liquid Systems*, Springer Proceedings in Physics 223,
https://doi.org/10.1007/978-3-030-21755-6_4

micelles and their aggregates of different morphologies depending on the content of PNIPAM. When temperature is higher than LCST the formation of spherical micelles, network-like aggregates and large vesicles is observed. In opposite to initial cores prone to form spherical domains the thermally responsive compounds are able to self-assemble into elongated unimolecular nanodomain. The complex self-assembling behavior and diverse morphology of resultant supramolecular assamblies of HBP-OILs and HBP-PILs might lead to unique ionic transport properties as a key point for creation of nanomaterials with tunable ion transport characteristics.

4.1 Introduction

Polymeric analogues of ionic liquids (PILs), obtained on the basis of reactive ionic liquids (ILs), are a new type of polyelectrolytes [1–7]. They combine the unique properties of classical ILs with the possibilities of varying the chemical structure and molecular architecture of polymers. However, these compounds are generally solids below 100 °C with rare exceptions [3–7]. Oligomeric ionic liquids (OILs), which occupy an intermediate state between ILs and PILs by molecular weight, retain the ability to exist in a liquid state at temperatures below 100 °C and combine the advantages of ILs with the peculiarities of the oligomeric state of a mater; in particular, a significant effect of end groups on their properties [3–7]. OILs as a separate class of polymer electrolytes were discussed by our recent study [6].

OILs in analogy with ILs are classified into protic and aprotic, and like PILs, they are also classified into cationic and anionic [2, 8]. In the case of PILs, regardless of the state of aggregation, the distinguishing feature is the presence of so-called ionic-liquid groups (functionalities) in their composition [2, 8, 9]. In terms of molecular architecture, currently existing OILs can be classified into linear, hyperbranched, and star-shaped (as a rule, silsesquioxane) [2, 8]. OILs with various molecular architectures also attract attention as anhydrous ion-conducting media for various electrochemical devices, nanoreactors, complexing agents, bioactive materials and components of optoelectronic devices [2, 8].

Among well-known OILs and PILs, hyperbranched compounds attract considerable attention [4–7]. Hyperbranched compounds are characterized by a globular core-shell structure and a high density of functional end groups on the shell, which opens up broad possibilities for a targeted change in their composition, structure and properties by changing the chemical nature of these groups. The globular structure of macromolecules gives the ability to form guest-host type complexes, provides low viscosity of melts and solutions, greater thermal stability and better solubility in comparison with linear analogues [4–7]. It should be emphasized that the hyperbranched compounds under consideration, as a rule, are oligomers in their nature and characteristics, however, they are known as “hyperbranched polymers” [10].

Introduction of ionic-liquid groups and fragments to the composition of hyperbranched compounds opens up significant opportunities for directional changes in their structure and properties [3]. The cationic protic and aprotic hyperbranched

OILs and PILs are discussed in the literature, while there is only a fragmentary information concerning the anionic representatives [3–7]. Hyperbranched OILs and PILs are capable of self-assembling and forming various hierarchical structures with unique morphology, which are inaccessible to classical ILs. One of the examples of these compounds is amphiphilic cationic hyperbranched OILs and PILs [3, 11]. This assembly behavior makes these compounds promising for the creation of supramolecular functional materials for various purposes [3, 12–14], in particular, membrane structures and liquid crystals [3–7]. Information on the use of these compounds in obtaining self-associated ultrathin films is fragmentary, and the use of the Langmuir-Blodgett (LB) method in obtaining such materials has not been described practically. At the same time, it is known, that such systems are promising in microelectronics, optics, sensor systems, various functionalized surfaces etc. [15, 16]. It should be noted that the LB method is a high-tech method for producing ultrathin films with unique characteristics and precisely adjustable thickness and structure, which opens up broad possibilities in the design of new functional nanomaterials [17–20]. Only a few works have been reported on obtaining the LB films based on linear [21–25] and star-like [25, 26] OILs and PILs. There is no information about LB films based on the OILs and PILs with dendrimeric and hyperbranched structures.

This chapter considers the works of the authors on the synthesis of amphiphilic protic OILs and PILs, the study of the features of formation of supramolecular structures in solution, at interphase boundary and in the condensed state, in particular ultrathin LB films, with response to pH and ionic strength of the environment, as well as temperature.

4.2 Assembly of Amphiphilic Hyperbranched Oligomeric Ionic Liquids in Aqueous Media at Different PH and Ionic Strength, at the Water/Air Interface

This section describes the synthesis of amphiphilic hyperbranched anionic OILs and PILs capable of self-assembling with the formation of various hierarchical structures with response to pH and ionic strength, which makes them promising for use in creating functional materials [3, 12–14]. It should be mentioned that such stimuli-responsive hierarchical structures are known in the absolute majority for non-ionic hyperbranched compounds [11]. However, the information on the application of this approach to hyperbranched OILs and PILs is missing in the literature.

4.2.1 *Synthesis of Amphiphilic Hyperbranched Olymeric Ionic Liquids*

The obtaining the anionic protic hyperbranched oligomeric ionic liquids (HBP-OILs) of amphiphilic type was realized through acylation of a commercially available polyesterpolyol Boltorn®H30 (HBP-OH) by the anhydrides of phthalic or 2-sulfobenzoic acids followed by neutralization of the resultant acidic oligomers with N-methylimidazole (Fig. 4.1) [6].

The hydrophobicity of the compounds was ensured by core type and the hydrophilicity was regulated using different ionic groups. We suggested a way of varying amphiphilicity of these compounds which is to introduce different amount of hydrophobic *n*-octadecylurethane tales to hyperbranched core [4, 5, 7] (Fig. 4.1).

The hydrophilic properties of HBP-OILs was varied by changing ionicity of ionic groups which is dependent on difference in pK_a values of an acid and base used; the ionicity degree increases as the pK_a difference gets larger [4–7]. In our study sulfonate and imidazolium ionic groups exhibited the highest ionicity. The amphiphilicity was controlled by the ratio of the components. Purification of the synthesized HBP-OILs was carried out by precipitation from alcohol into diethyl ether or acetonitrile (the heterocycles used are soluble in these solvents), followed by washing these compounds with the solvents mentioned.

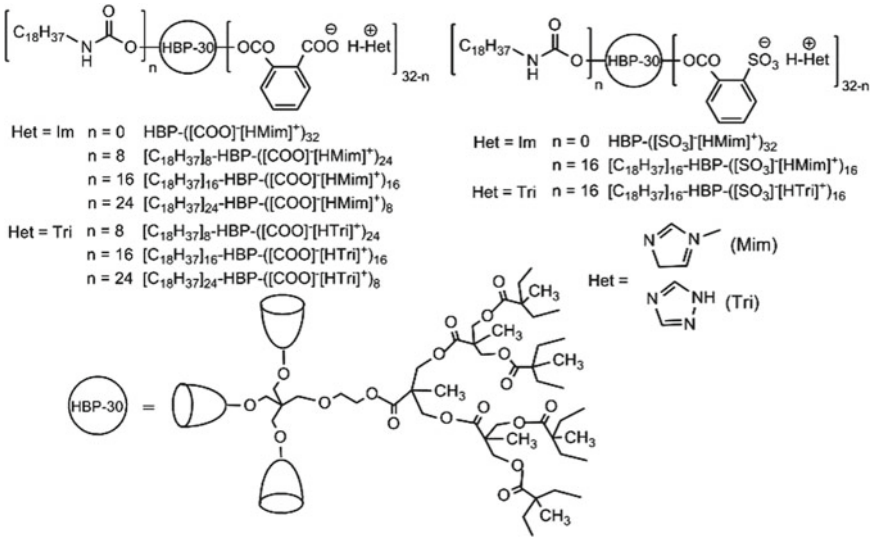

Fig. 4.1 The amphiphilic protic anionic HBP-OILs with adjustable content of different ionic groups and *n*-octadecyl tails. Adapted with permission from [4], copyright (2017) Chemical Society of Japan, [5], copyright (2016) American Chemical Society, and [7, 27], copyright (2017, 2018) Springer Nature

The chemical compositions of the synthesized HBP-OILs are represented in the Fig. 4.1. It should be mentioned that the incorporated alkylurethane substituents can be self-associated by means of Van der Waals interactions and hydrogen bonds. The obtained compounds are viscous liquids at room temperature except HBP-OILs enreached with alkylurethane substituents which are solid below 50–65 °C. The compounds are soluble in polar and insoluble in nonpolar organic solvents.

The experimentally found and calculated values of molecular weight (MW) for the synthesized compounds are in a good agreement (Table 4.1). M_w values obtained from GPC for the compounds $[C_{18}H_{37}]_{24}$-HBP-([COO]_[HMim]$^+$)$_8$ and $[C_{18}H_{37}]_{24}$-HBP-([COO]$^-$[HTri]$^+$)$_8$ are 12,033 g/mol (M_w/M_n = 1.62) and 12,318 g/mol (M_w/M_n = 1.59), respectively. Thermal stability of the synthesized compounds according to TGA data decreases with increase in the content of carboxylate IL groups (Table 4.1). This is due to the low thermal stability of carboxylate IL groups as evidenced by the significantly lower T_d (temperature of onset of thermal-oxidative destruction) value for the compound HBP-([COO]$^-$[HMim]$^+$)$_{32}$ containing only carboxylate imidazolium ionic groups, compared to that of its sulfonate analogue (HBP-([SO$_3$]$^-$[HMim]$^+$)$_{32}$). In accordance with [28], the lower thermal stability of carboxylate IL groups is due to their lower ionicity compared to sulfonate analogues.

As evidenced by DSC method the structure of the obtained compounds depends on the content of ionic groups and alkylurethane substituents (Table 4.1). The compounds with maxima content of ionic groups are amorphous and characterized by the lowest glass-transition temperature (T_g). The T_g value of the HBP-OILs decreases as the ionicity of the ionic groups gets lower (carboxylate-imidazolium HBP-OILs has a lowest T_g). The increase in the content of the aliphatic tales as well as ionicity of the ionic groups is accompanied by the rise in T_g values.

The exceeding of the alkylurethane fragments content above 8 leads to formation of crystalline phase due to the propensity of them to crystalize [7]. The melting point (T_m) of the crystalline phase is a little affected by changing the content of aliphatic tales and composition of ionic groups.

The proton conductivity of the obtained HBP-OILs was established by dielectric relaxation spectroscopy under unhydrous conditions and the highest values was $4.04 \cdot 10^{-4}$ S/cm at 40 °C and $3.22 \cdot 10^{-3}$ S/cm at 120 °C under anhydrous conditions for the compound HBP-([SO$_3$]$^-$[HMim]$^+$)$_{32}$ (Table 4.1) [6]. This is due to the highest content of ionic groups and their iconicity for that compound.

4.2.2 Colloid-Chemical Characteristics and Self-Assembling Peculiarities of Hyperbranched Oligomeric Ionic Liquids in Aqueous Media

Dynamic light scattering (DLS) and AFM data evidence that the obtained HBP-OILs are surfactants able to form micelles and characterized by CMC in the range of 2.4–5.5 mg/mL (Table 4.2). The CMC values of the sulfonate HBP-OILs are

Table 4.1 Characteristics of the synthesized HBP-OILs

Sample	MW		T_d (°C)	T_g (°C)	T_m (°C)	σ_{dc} (S/cm)	
	Found	Calculated				At 40 °C	At 120 °C
HBP-$([COO]^-[HMim]^+)_{32}$	10,112	10,932	145	−16.2	–	$5.60 \cdot 10^{-6}$	$6.95 \cdot 10^{-4}$
$[C_{18}H_{37}]_8$-HBP-$([COO]^-[HMim]^+)_{24}$	12,554	11,626	173	8.9	–	$5.90 \cdot 10^{-8}$	$1.90 \cdot 10^{-4}$
$[C_{18}H_{37}]_8$-HBP-$([COO]^-[HTri]^+)_{24}$	12,241	11,313	192	5.4	–	$7.59 \cdot 10^{-9}$	$5.17 \cdot 10^{-5}$
$[C_{18}H_{37}]_{16}$-HBP-$([COO]^-[HMim]^+)_{16}$	12,386	12,146	198	–	51.2	$4.10 \cdot 10^{-9}$	$1.73 \cdot 10^{-5}$
$[C_{18}H_{37}]_{16}$-HBP-$([COO]^-[HTri]^+)_{16}$	12,177	11,937	228	–	47.3	$1.90 \cdot 10^{-8}$	$3.40 \cdot 10^{-5}$
$[C_{18}H_{37}]_{24}$-HBP-$([COO]^-[HMim]^+)_8$	13,513	12,665	263	–	53.0	$1.30 \cdot 10^{-9}$	$3.70 \cdot 10^{-6}$
$[C_{18}H_{37}]_{24}$-HBP-$([COO]^-[HTri]^+)_8$	13,408	12,560	271	–	52.3	$1.20 \cdot 10^{-10}$	$1.90 \cdot 10^{-7}$
HBP-$([SO_3]^-[HMim]^+)_{32}$	12,951	12,296	270	−9.2	–	$4.04 \cdot 10^{-4}$	$3.22 \cdot 10^{-3}$
$[C_{18}H_{37}]_{16}$-HBP-$([SO_3]^-[HMim]^+)_{16}$	13,314	12,682	294	–	47.0	$1.40 \cdot 10^{-11}$	$1.62 \cdot 10^{-5}$
$[C_{18}H_{37}]_{16}$-HBP-$([SO_3]^-[HTri]^+)_{16}$	13,105	12,473	296	–	51.0	$1.20 \cdot 10^{-11}$	$5.40 \cdot 10^{-6}$

Adapted with permission from [4], copyright (2017) Chemical Society of Japan, [5], copyright (2016) American Chemical Society, and [7, 27], copyright (2017, 2018) Springer Nature

Table 4.2 Colloid-chemical properties of HBP-OILs

Compound	MMA* (nm^2/molecule)	CMC (mg/mL)	Sizes of micelles and their nanoassemblies (nm)				ξ-potential (mV)	
			pH 11.6		pH 5.2		pH 11.6	pH 5.2
			DLS	AFM	DLS	AFM		
$[C_{18}H_{37}]_{16}$-HBP-$([COO]^-[HMim]^+)_{16}$	13.8	$2.4 \cdot 10^{-4}$	12.8 ± 4	15 ± 6	160 ± 50	177 ± 30	−64 ± 7	−56 ± 4
$[C_{18}H_{37}]_{16}$-HBP-$([COO]^-[HTri]^+)_{16}$	14.5	$5.5 \cdot 10^{-4}$	13.7 ± 5	19 ± 8	197 ± 60	207 ± 40	−66 ± 8	−55 ± 4
$[C_{18}H_{37}]_{16}$-HBP-$([SO_3]^-[HMim]^+)_{16}$	16.8	$1.3 \cdot 10^{-4}$	14.0 ± 5	21 ± 10	27 ± 10	30 ± 12	−65 ± 7	−57 ± 4
$[C_{18}H_{37}]_{16}$-HBP-$([SO_3]^-[HTri]^+)_{16}$	18.6	$3.3 \cdot 10^{-4}$	16.4 ± 6	24 ± 12	33 ± 10	37 ± 14	−67 ± 7	−58 ± 4

*MMA is the limiting mean molecular area at water/air interface

Adapted with permission from [4], copyright (2017) Chemical Society of Japan, [5], copyright (2016) American Chemical Society, and [7, 27], copyright (2017, 2018) Springer Nature

40–50% lower compared to that of carboxylate analogs because of less folded state of macromolecules that facilitates hydrogen bonding between urethane groups and therefore stabilization of micelles [5].

It follows from DLS and AFM data that the HBP-OILs form micelles in neutral aqueous solutions two times larger compared to that of starting acid oligomers (12–16 nm vs. 5–7 nm correspondingly) [5]. An increase in pH of aqueous medium has almost no influence on size of micelles because acid groups are in ionized state under these conditions (Figs. 4.2e–h and 4.3, Table 4.2).

A decrease in pH causes micelles aggregation for carboxylate HBP-OILs resulting in formation of 100–250 nm assemblies (Figs. 4.2a, b and 4.3 a, b, Table 4.2).

It should be mentioned that imidazolium compounds form smaller micelles and micelle aggregates in comparison with triazolium analogs because of different ionicity and thus conformations of macromolecules.

The size distribution of the HBP-OILs assemblies in aqueous solutions at different pH is obtained from DLS (Fig. 4.3). DLS results showed that a narrow size

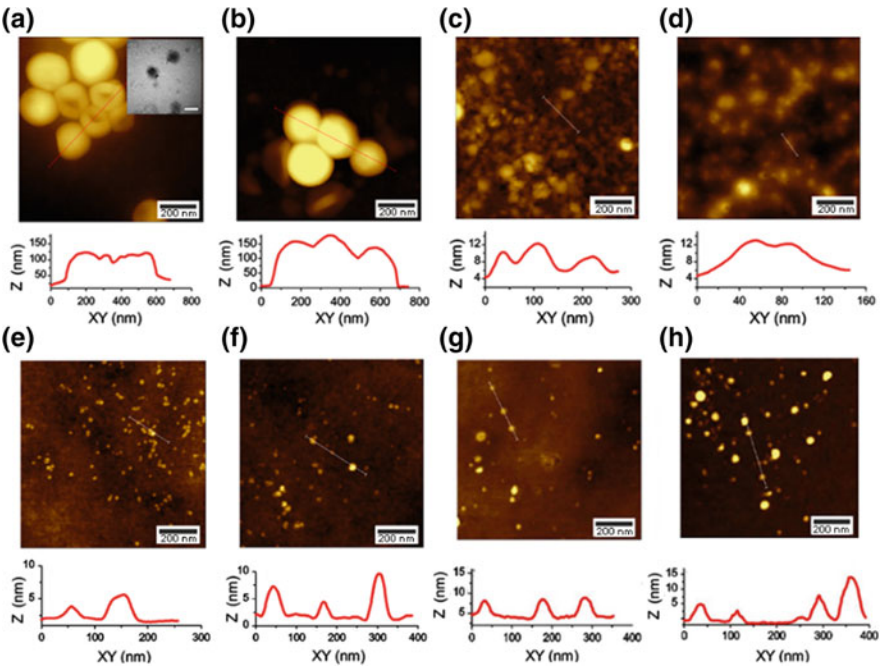

Fig. 4.2 AFM images of HBP-OILs $[C_{18}H_{37}]_{16}$-HBP-$([COO]^-[HMim]^+)_{16}$ (at pH 5.2 (**a**) and at pH 11.6 (**e**)), $[C_{18}H_{37}]_{16}$-HBP-$([COO]^-[HTri]^+)_{16}$ (at pH 5.2 (**b**) and at pH 11.6 (**f**)), $[C_{18}H_{37}]_{16}$-HBP-$([SO_3]^-[HMim]^+)_{16}$ (at pH 5.2 (**c**) and at pH 11.6 (**g**)) and $[C_{18}H_{37}]_{16}$-HBP-$([SO_3]^-[HTri]^+)_{16}$ (at pH 5.2 (**d**) and at pH 11.6 (**h**)) aqueous solutions deposited at pH 5.2 and pH 11.6 on silicon wafers and the corresponding height profiles along the lines. Scale bar is 200 nm. TEM image (insert on image (**a**)) of the HBP-OIL $[C_{18}H_{37}]_{16}$-HBP-$([COO]^-[HTri]^+)_{16}$ assemblies deposited from pH 5.2 solutions on carbon-formvar-coated copper grids. Reproduced with permission from [5], copyright (2016) American Chemical Society

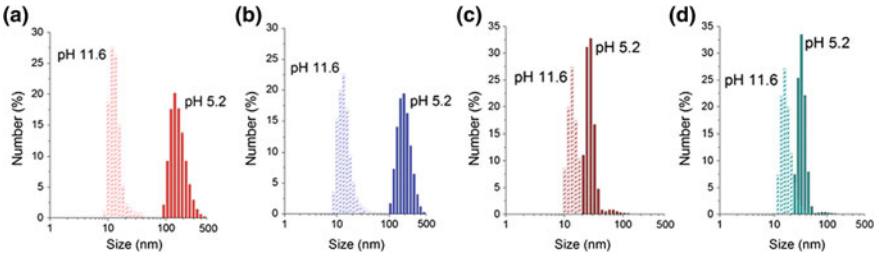

Fig. 4.3 Size distribution of micelles and their aggregates for HBP-OILs $[C_{18}H_{37}]_{16}$-HBP-$([COO]^-[HMim]^+)_{16}$ (**a**), $[C_{18}H_{37}]_{16}$-HBP-$([COO]^-[HTri]^+)_{16}$ (**b**) and $[C_{18}H_{37}]_{16}$-HBP-$([SO_3]^-[HMim]^+)_{16}$ (**c**), $[C_{18}H_{37}]_{16}$-HBP-$([SO_3]^-[HTri]^+)_{16}$ (**d**) in aqueous solution at different pH according to DLS data. Concentration of HBP-OILs is 0.2 mg/ml. Reproduced with permission from [5], copyright (2016) American Chemical Society

distribution (±4÷14 nm) is characteristic of the compounds with high ionicity of ionic groups (sulfonic HBP-OILs, Fig. 4.3c, d, Table 4.2) and high pH values of the medium (pH 11.6, Fig. 4.3a–d), while the assemblies formed by the carboxylate HBP-OILs in an acidic environment (pH 5.2) are characterized by a wide size distribution (±30÷60 nm) (Fig. 4.3a, b, Table 4.2).

Difference in the size distribution of the assemblies are also explained by the different extent of ionization of ionic groups; in particular, the wide distribution for carboxylic HBP-OILs at low pH is due to the low degree of ionization of ionic groups, which contributes to the micelle aggregation with large-sized supramolecular formation showing a corresponding statistical distribution.

Increasing the ionic strength of aqueous solutions via increase in NaCl concentration up to 0.1 M causes formation of micelles assemblies of 180–210 nm in size for carboxylate compounds $[C_{18}H_{37}]_{16}$-HBP-$([COO]^-[HMim]^+)_{16}$ and $[C_{18}H_{37}]_{16}$-HBP-$([COO]^-[HTri]^+)_{16}$ [5]. Further increase in the ionic strength leads to sedimentation. In case of sulfonate compounds ($[C_{18}H_{37}]_{16}$-HBP-$([SO_3]^-[HMim]^+)_{16}$ and $[C_{18}H_{37}]_{16}$-HBP-$([SO_3]^-[HTri]^+)_{16}$) the exceeding NaCl concentration of 0.6 M is accomplished by sedimentation [5]. The values of ζ-potentials for the compounds in aqueous solutions depends a little on pH and are in the range of −50 and −67 mV in accordance with electrophoretic light scattering (ELS) results (Table 4.2). The latter indicates high stability of micelles and their assemblies.

4.2.3 Assembly of Hyperbranched Oligomeric Ionic Liquids at Water/Air Interface

The values of the limiting mean molecular area (MMA) for the obtained HBP-OILs at water/air interface established by the LB method from the surface pressure-area isotherms are in the range of 13.8–18.6 nm^2/molecule (Fig. 4.4, Table 4.2).

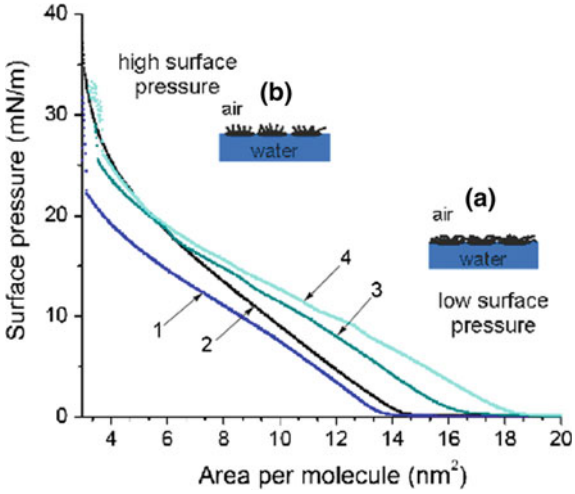

Fig. 4.4 Pressure-area isotherms for HBP-OILs $[C_{18}H_{37}]_{16}$-HBP-$([COO]^-[HMim]^+)_{16}$ (1), $[C_{18}H_{37}]_{16}$-HBP-$([COO]^-[HTri]^+)_{16}$ (2), $[C_{18}H_{37}]_{16}$-HBP-$([SO_3]^-[HMim]^+)_{16}$ (3) and $[C_{18}H_{37}]_{16}$-HBP-$([SO_3]^-[HTri]^+)_{16}$ (4) at water/air interface at 25 °C and sketches of molecular packing of monolayer at low (**a**) and high (**b**) surface pressures. Reproduced with permission from [5], copyright (2016) American Chemical Society

The sulfonate HBP-OILs are characterized by a larger MMA values compared to the carboxylate analogues due to more expanded conformation of sulfonate macromolecules as a result of their high ionicity. Also, the values of MMA for triazolium HBP-OILs are larger in comparison with those for imidazolium analogues due to solvation of imine group in triazolium ring by water molecules. In [4], we showed that when the number of ionic liquid groups in both imidazolium and triazolium carboxylate HBP-OILs are 24 and 16, the isotherms are characterized by the presence of the sections corresponding to gaseous and liquid states of Langmuir monolayers. Only when the content of ionic-liquid groups is minimum (8 groups) the isotherm sections corresponding to the solid state of the monolayer appeared.

The LB films of carboxylate imidazolium HBP-OILs with different content of ionic-liquid groups at a surface pressure in monolayers of 5 mN/m were obtained (Fig. 4.5) [4]. As the hydrophobic content is increased, the surface morphologies change from smooth featureless monolayers (compound $[C_{18}H_{37}]_8$-HBP-$([COO]^-[HMim]^+)_{24}$, Fig. 4.5a) to 2D surface micelles of 1–2 μm in diameter (compound $[C_{18}H_{37}]_{16}$-HBP-$([COO]^-[HMim]^+)_{16}$, Fig. 4.5b) and ultimately fractal-like aggregates (compound $[C_{18}H_{37}]_8$-HBP-$([COO]^-[HMim]^+)_{24}$, Fig. 4.5c). Surface aggregation will compromise interfacial stability.

4.3 Assembly of Linear and Hyperbranched Thermally Responsive Oligomeric and Polymeric Ionic Liquids in Aqueous Media and at the Water/Air Interface

The authors offered the direction of development of stimuli-responsive HBP-PILs, sensitive in terms of the structural organization of their supramolecular assemblies to

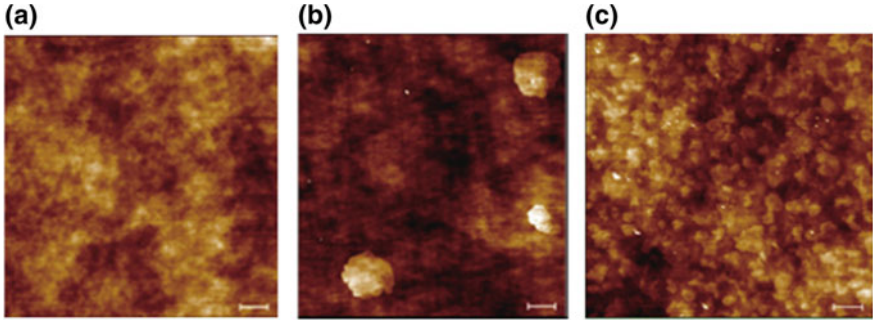

Fig. 4.5 AFM images of HBP-OILs $[C_{18}H_{37}]_8$-HBP-$([COO]^-[HMim]^+)_{24}$ (**a**), $[C_{18}H_{37}]_{16}$-HBP-$([COO]^-[HMim]^+)_{16}$ (**b**) and $[C_{18}H_{37}]_{24}$-HBP-$([COO]^-[HMim]^+)_8$ (**c**) LB films obtained at a surface pressure of 5 mN/m (scale bar 1 μm). Z-scale of all AFM images is 10 nm. Reproduced with permission from [4], copyright (2017) Chemical Society of Japan

temperature changes [29]. This direction was realized in the aspect of the synthesis of protic anionic HBP-PILs and their linear oligomeric analogs (OILs) with adjustable hydrophilic-hydrophobic balance, which contain thermally responsive macrocations showing LCST behavior.

These compounds are products of neutralization of linear and hyperbranched polyesters with terminal carboxyl groups by monoamine terminated poly(N-isopropylacrylamide) (PNIPAM) with $M_n = 2500$ g/mol. The synthesized compounds with ammonium thermally responsive PNIPAM macrocations are characterized by LCST at 33–35 °C [29]. This LCST behavior allows to adjust hydrophilic-hydrophobic properties of the compounds by temperature change and to control their self-organization in the aqueous solutions, at the water/air interface and in LB monomolecular ultrathin film. In addition, the hydrophilic-hydrophobic properties of these compounds were regulated by the content of ionic-liquid groups in their composition. It should be noted that the comparison of the self-assembling behavior of the synthesized HBP-PILs with their linear oligomeric analogs makes it possible to establish an understanding of the influence of the branched structure on their structuring process.

4.3.1 Synthesis of Thermally Responsive Linear and Hyperbranched Oligomeric and Polymeric Ionic Liquids

Poly(di(ethylene glycol) adipate) (PDA) $M_n = 800$ g/mol containing two terminal hydroxyl groups was used as an initial linear oligomer for synthesis of the linear OILs. This oligoester simulates chemical composition and amphiphilic properties of hyperbranched core of the HBP-PILs. A third-generation commercially available

HBP-OH Boltorn®H30, containing 32 terminal hydroxyl groups, was used as an initial oligomer for synthesis of the HBP-PILs. Introduction of terminal carboxyl groups into the composition of the above polyesters was carried out by reaction of acylation of the terminal hydroxyl groups with phthalic anhydride. The synthesized polycarboxylic acids were further used to produce the thermally responsive OILs and PILs by both partial (neutralization level 50%) and complete neutralization by the primary amino groups of PNIPAM (Fig. 4.6).

The abbreviation used to refer to the synthesized compounds reflects both the structure of macromolecules and the degree of neutralization of their terminal

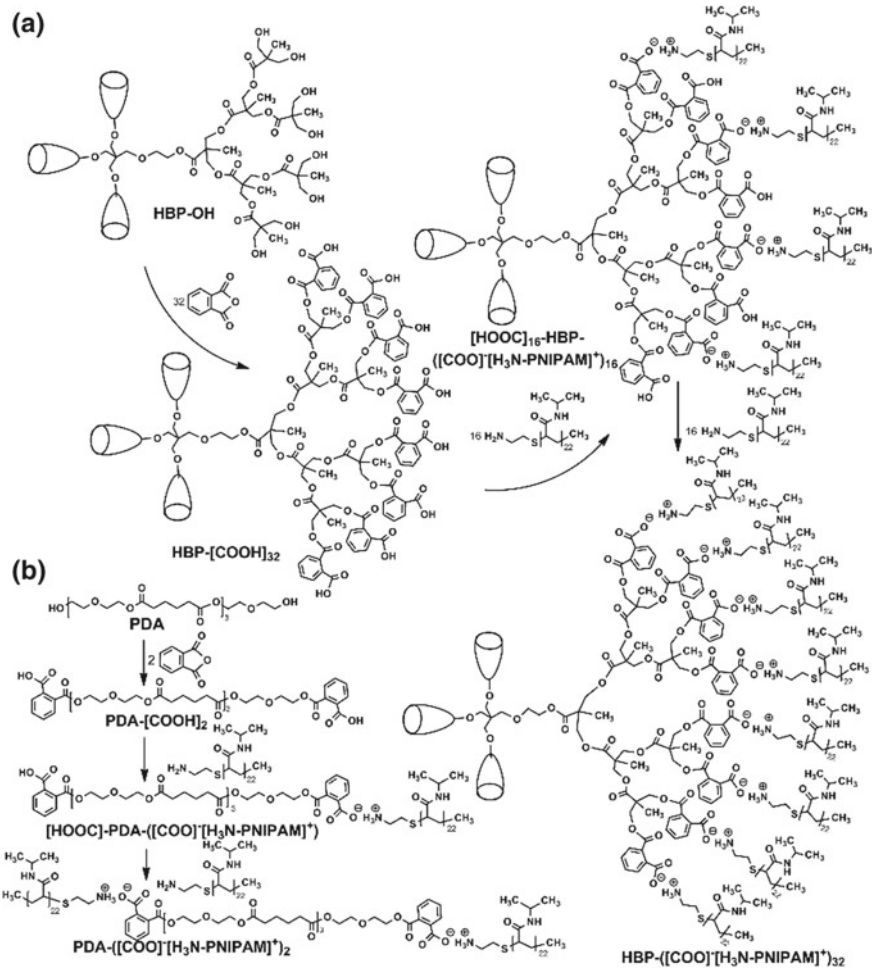

Fig. 4.6 Synthesis of the hyperbranched PILs (**a**) and the linear OILs (**b**) containing the thermally responsive PNIPAM macrocations. Reproduced with permission from [29], copyright (2018) American Chemical Society

carboxyl groups (Fig. 4.6). The linear oligomeric dicarboxylic acid and its partial (50%) and complete neutralized products are hereinafter referred to as PDA-$[COOH]_2$, [HOOC]-PDA-($[COO]^-[H_3N$-PNIPAM$]^+$) and PDA-($[COO]^-[H_3N$-PNIPAM$]^+)_2$ correspondingly and their hyperbranched analogues are referred to as HBP-$[COOH]_{32}$, $[HOOC]_{16}$-HBP-($[COO]^-[H_3N$-PNIPAM$]^+)_{16}$ and HBP-($[COO]^-[H_3N$-PNIPAM$]^+)_{32}$ respectively (Fig. 4.6). The compounds obtained were purified by reprecipitation from ethyl alcohol to diethyl ether.

The synthesized compounds are solid substances at room temperature, soluble in polar and insoluble in non-polar solvents. The solubility of these OILs and PILs in water is determined by the content of ionic groups in their composition: the increase in the content of ionic groups with PNIPAM fragments in the composition of the OILs and PILs favors their solubility in water at room temperature. Based on the content of carboxyl groups in the composition of initial oligomers, the degree of neutralization of carboxyl groups and the molecular weight (MW) of PNIPAM, the MW of synthesized linear OILs and hyperbranched PILs was determined (Table 4.3). The MW found and calculated on the basis of ideal compound formulas are close (Fig. 4.6).

According to DSC data the polycarboxylic acids, the OILs and the PILs are amorphous without any signs of crystallization which are characterized by high T_g (Table 4.3). T_g values of the synthesized compounds increase with increasing the content of the thermally responsive PNIPAM macrocation in their composition (Table 4.3), which is associated with the high rigidity of the PNIPAM macrocations (T_g values for PNIPAM are in the range of 110–140 °C) [30]). T_g values for the hyperbranched PILs is much higher than those for linear OILs. For example, T_g values of compounds $[HOOC]_{16}$-HBP-($[COO]^-[H_3N$-PNIPAM$]^+)_{16}$ and [HOOC]-

Table 4.3 MW characteristics and T_g values of the synthesized polycarboxylic acids, OILs and PILs

Sample	Peripheral groups (%)		MW (g/mol)		T_g (°C)
	–COOH	PNIPAM	Calculated	Found	
Linear architecture					
PDA-$[COOH]_2$	100	0	1096	1107	–
[HOOC]-PDA-($[COO]^-[H_3N$-PNIPAM$]^+$)	50	50	3596	3607	54
PDA-($[COO]^-[H_3N$-PNIPAM$]^+)_2$	3	97	6096	5957	77
Hyperbranched architecture					
HBP-$[COOH]_{32}$	100	0	8480	8471	34
$[HOOC]_{16}$-HBP-($[COO]^-[H_3N$-PNIPAM$]^+)_{16}$	51	49	48480	47671	94
HBP-($[COO]^-[H_3N$-PNIPAM$]^+)_{32}$	3	97	88480	86071	99

Adapted with permission from [29], copyright (2018) American Chemical Society

PDA-([COO]$^-$[H_3N-PNIPAM]$^+$) are 94 °C and 54 °C respectively (Table 4.3). The increase in T_g when the structure is changed from linear to hyperbranched is most likely related to an increase in the content of terminal functional groups and correspondingly rigid PNIPAM macrocations [3–7].

The turbidity experiment revealed that the LCST for the thermally responsive OILs and PILs is in the range of 33–35 °C (Table 4.4) and reduced by 1–3 °C compared to the values of typical PNIPAM containing OILs and PILs [31–33]. That is probably related to destabilization of salvating aqueous shell and salting out the PNIPAM fragments by ionic groups [34, 35]. Furthermore, the width of LCST transition for these compounds is within 1–2 °C which is narrower than usual LCST transition for PNIPAMs [5, 11, 29, 36, 37].

4.3.2 Assembly and Phase Transformations of Thermally Responsive Oligomeric and Polymeric Ionic Liquids in Aqueous Media

In aqueous media linear and hyperbranched compounds forms nanosized micellar assemblies with negative ζ-potential below LCST (Fig. 4.7, Table 4.4). According to DLS, the hydrodynamic diameter of micellar aggregates formed by the starting oligomeric polycarboxylic acids of linear and hyperbranched structure is 448 ± 55 nm (Fig. 4.7a) and 226 ± 109 nm, respectively (Fig. 4.7d). The size of the micellar aggregates from initial PDA-$[COOH]_2$ and HBP-$[COOH]_{32}$ is comparable with those for described in [38, 39] carboxylated hyperbranched polyesters. When the acids are neutralized by PNIPAM they form polydisperse assemblies with temperature dependent size (Fig. 4.7b, c, e, f, Table 4.4).

In this case, the size of such assemblies increases above LCST, which is associated with the transition of the PNIPAM macrocations into hydrophobic collapsed state, facilitating the coagulation of micelles and their aggregates [29, 40, 41]. It should be noted that the assemblies of compounds [HOOC]-PDA-([COO]$^-$[H_3N-PNIPAM]$^+$) and HBP-([COO]$^-$[H_3N-PNIPAM]$^+$)$_{32}$ are characterized by bimodal size distribution below (Fig. 4.7b) and above (Fig. 4.7f) LCST correspondingly, which can be related to ordering of macromolecules with various macrocation associations.

Completely neutralized linear oligomeric acid (compound PDA-([COO]$^-$[H_3N-PNIPAM]$^+$)$_2$) forms larger micellar aggregates (Fig. 7c, Table 4.4) than hyperbranched analogue (HBP-([COO]$^-$[H_3N-PNIPAM]$^+$)$_{32}$ does (Fig. 4.7f, Table 4.4). The decrease in size of such supramolecular structures is observed as a result of rise in content of PNIPAM component independently of the compounds architecture (Fig. 4.7a–f, Table 4.4). The size of micelles and micellar aggregates formed by linear OILs are in a good agreement with those for known thermally responsive polymers [42] and PILs [43] containing PNIPAM fragments.

Additional confirmation of spherical shape of OILs and PILs assemblies below LSCT comes from TEM images (Fig. 4.7g–l). TEM images evidence about larger

Table 4.4 Colloid-chemical characteristics of polycarboxylic acids, OILs and PILs assemblies

Sample	LCST (°C)	At 23 °C			At 38 °C		At 50 °C	
		D^{a}_{DLS} (nm)	D^{b}_{TEM} (nm)	ζ-pot. (mV)	D^{a}_{DLS} (nm)	ζ-pot. (mV)	D^{c}_{SEM} (μm)	ζ-pot. (mV)
Linear architecture								
PDA-$[COOH]_2$	–	448 ± 55	375 ± 40	−9.4 ± 4.6	520 ± 59	−15.0 ± 1.0	–	−22.1 ± 0.5
[HOOC]-PDA-($[COO]^-[H_3N$-PNIPAM$]^+$)	33.3 ± 0.1	10 ± 2, 380 ± 90	235 ± 60	−1.2 ± 0.2	2905 ± 210	−2.5 ± 0.2	4.2 ± 1.2	+8.9 ± 0.7
PDA-($[COO]^-[H_3N$-PNIPAM$]^+)_2$	34.0 ± 0.1	332 ± 74	170 ± 30	−2.6 ± 3.0	3299 ± 354	+1.4 ± 0.5	3.1 ± 0.8	+12.5 ± 1.0
Hyperbranched architecture								
HBP-$[COOH]_{32}$	–	226 ± 109	215 ± 60	−31.6 ± 1.6	220 ± 101	−35.9 ± 2.1	–	−32.7 ± 1.4
$[HOOC]_{16}$-HBP-($[COO]^-[H_3N$-PNIPAM$]^+)_{16}$	34.7 ± 0.1	253 ± 104	172 ± 57	−10.8 ± 2.7	2411 ± 306	−7.8 ± 1.9	7.2 ± 3.3	+1.9 ± 0.3
HBP-($[COO]^-[H_3N$-PNIPAM$]^+)_{32}$	34.3 ± 0.1	222 ± 60	70 ± 10	−10.2 ± 3.2	145 ± 30, 507 ± 119	−10.8 ± 1.7	1.3 ± 0.3	−1.1 ± 0.3

[a]Average size from DLS data; [b, c]Average size from TEM and SEM images, respectively
Adapted with permission from [29], copyright (2018) American Chemical Society

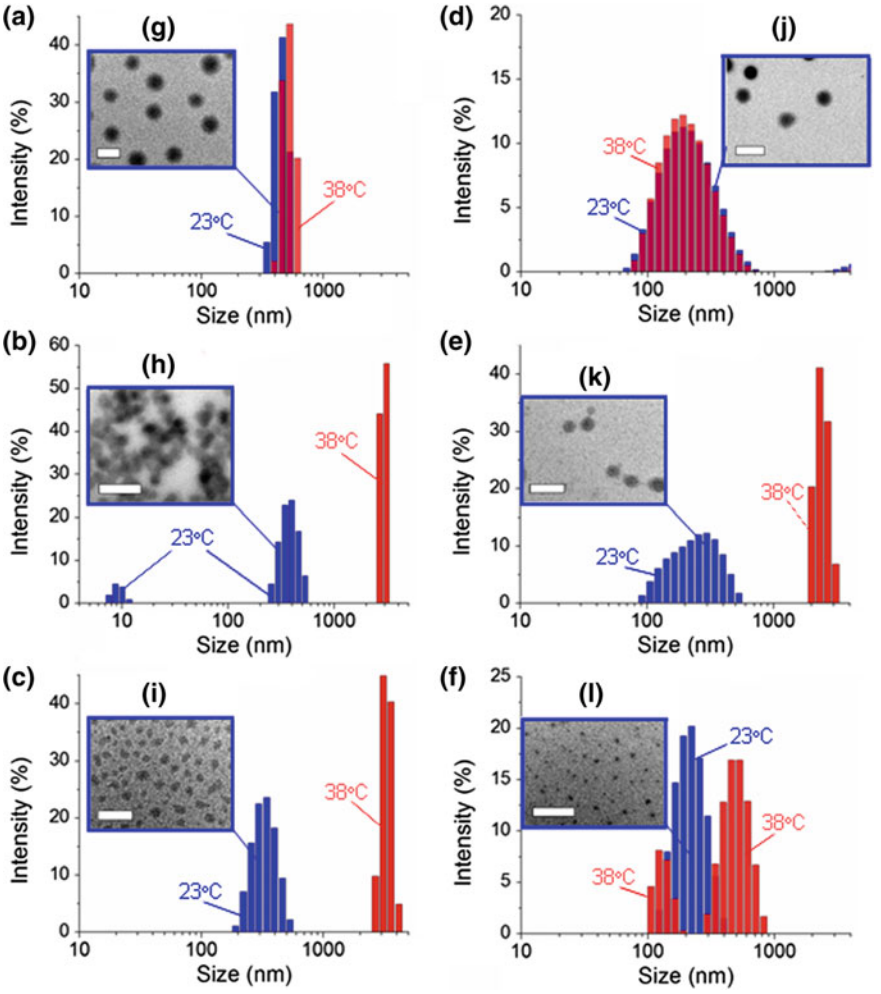

Fig. 4.7 Size distribution of micellar assemblies of linear compounds PDA-$[COOH]_2$ (**a**), [HOOC]-PDA-($[COO]^-[H_3N$-PNIPAM$]^+$) (**b**), PDA-($[COO]^-[H_3N$-PNIPAM$]^+)_2$ (**c**) and hyperbranched compounds HBP-$[COOH]_{32}$ (**d**), $[HOOC]_{16}$-HBP-($[COO]^-[H_3N$-PNIPAM$]^+)_{16}$ (**e**), and HBP-($[COO]^-[H_3N$-PNIPAM$]^+)_{32}$ (**f**) in aqueous media at 23 ± 0.2 °C and at 38 ± 0.2 °C according to DLS and corresponding TEM images (scale bar is 500 nm). Reproduced with permission from [29], copyright (2018) American Chemical Society

size of assemblies derived from compounds of linear architecture compared with those from hyperbranched analogues. (Fig. 4.7g–l, Table 4.4). Reducing size of the assemblies with rise in content of the thermally responsive component was also confirmed by TEM images (Fig. 4.7g–l, Table 4.4).

According to ELS data recorded at temperature below LCST, the initial hyperbranched oligomeric acid HBP-$[COOH]_{32}$ is characterized by the higher value of ζ-potential compared to the linear analogue PDA-$[COOH]_2$ (-31 ± 1.6 mV against -9.4 ± 4.6 mV correspondingly, Table 4.4) as a result of higher content of acidic groups [4]. Introduction of the PNIPAM component in composition of the oligomeric acids causes surface negative charge screening thereby significantly decreasing ζ-potential of assemblies independently of the compounds architecture (Table 4.4).

At the same time, the variation of the compound architecture (linear or hyperbranched) as well as the amount of PNIPAM macrocations plays a critical role in the design of multi-length scale micellar morphologies above LCST. When linear OILs [HOOC]-PDA-($[COO]^-[H_3N$-PNIPAM$]^+$) and PDA-($[COO]^-[H_3N$-PNIPAM$]^+)_2$ are deposited on silicon wafers above the LCST, they form micellar structures, namely submicron worm-like or network-like aggregates (Fig. 4.8a, b).

In contrast to the linear OILs, the branched PILs forms large vesicles (giant vesicles [44]) (Fig. 4.8c) or highly uniform, smaller spherical micelles above the LCST (Fig. 4.8d). Moreover, increasing the degree of neutralization up to 100% (compound

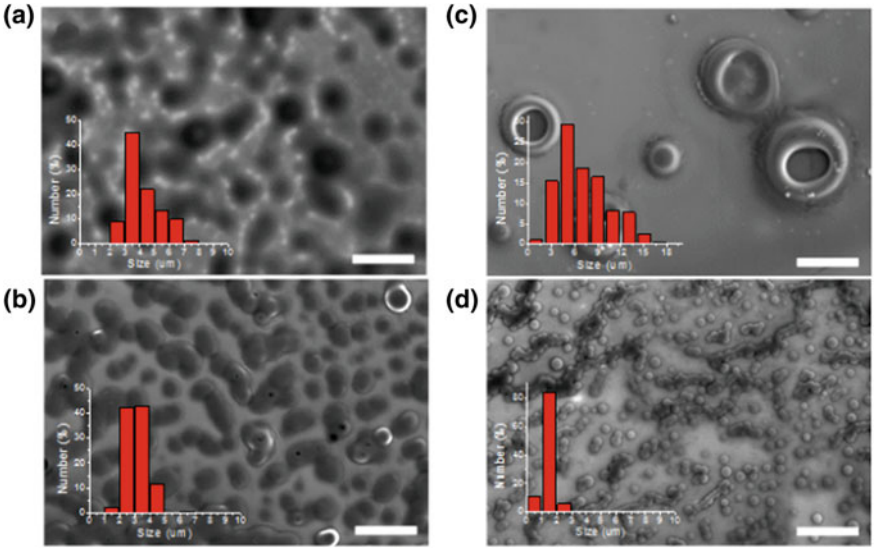

Fig. 4.8 SEM images of compounds [HOOC]-PDA-($[COO]^-[H_3N$-PNIPAM$]^+$) (**a**), PDA-($[COO]^-[H_3N$-PNIPAM$]^+)_2$ (**b**), $[HOOC]_{16}$-HBP-($[COO]^-[H_3N$-PNIPAM$]^+)_{16}$ (**c**) and HBP-($[COO]^-[H_3N$-PNIPAM$]^+)_{32}$ (**d**) deposited on silicon wafers from aqueous solutions at 50 ± 0.5 °C (scale bar is 20 μm) and corresponding size distributions of the assemblies (inserts). Reproduced with permission from [29], copyright (2018) American Chemical Society

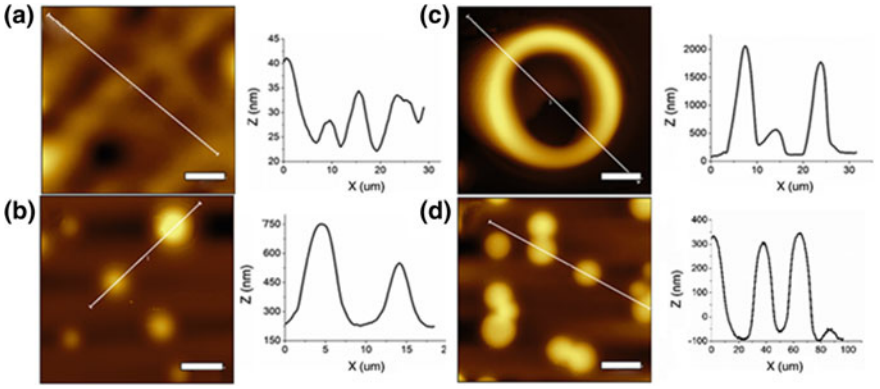

Fig. 4.9 AFM images of compounds [HOOC]-PDA-([COO]$^-$[H_3N-PNIPAM]$^+$) (**a**), PDA-([COO]$^-$[H_3N-PNIPAM]$^+$)$_2$ (**b**), [HOOC]$_{16}$-HBP-([COO]$^-$[H_3N-PNIPAM]$^+$)$_{16}$ (**c**) and HBP-([COO]$^-$[H_3N-PNIPAM]$^+$)$_{32}$ (**d**) deposited on silicon wafers from aqueous solutions at 50 ± 0.5 °C and corresponding height profiles along white lines (**e**–**h**). Scale bars are 5 μm for (**a**–**c**) and 2 μm for (**d**). Z scale is 70 nm (**a**), 800 nm (**b**), 2.3 μm (**c**), and 500 nm (**d**). Reproduced with permission from [29], copyright (2018) American Chemical Society

HBP-([COO]$^-$[H_3N-PNIPAM]$^+$)$_{32}$) leads to formation of chain-like aggregates of much smaller and highly uniform spherical micelles without fusion (Fig. 4.8d).

AFM images of dried micellar assemblies above the LCST confirm that [HOOC]-PDA-([COO]$^-$[H_3N-PNIPAM]$^+$) (Fig. 4.9a) and PDA-([COO]$^-$[H_3N-PNIPAM]$^+$)$_2$ (Fig. 4.9b) OILs form submicron aggregates with network-like and spherical morphology. On the other hand, HBP-PILs [HOOC]$_{16}$-HBP-([COO]$^-$[H_3N-PNIPAM]$^+$)$_{16}$ (Fig. 4.9c) and HBP-([COO]$^-$[H_3N-PNIPAM]$^+$)$_{32}$ (Fig. 4.9d) are assembled into giant vesicles and smaller spherical aggregates that correlates with SEM data (Fig. 4.8c and d correspondingly).

Furthermore, the temperature-triggered transformation of PNIPAM macrocations of the OILs and HBP-PILs at temperature above LCST shifts the ζ-potential of the assemblies from about −3 mV to +13 mV for the linear compounds and from −10 mV to ~0 mV for the hyperbranched compounds at maximum content of thermally responsive macrocations (Table 4.4). This shift indicates folding the PNIPAM fragments which screen the surface ionic groups of the assemblies that favors the compound aggregation above the LCST [5].

4.3.3 Assembly of Thermally Responsive Oligomeric and Polymeric Ionic Liquids at Water/Air Interface

The features of self-organization of the initial polycarboxylic acids (PDA-[COOH]$_2$, HBP-[COOH]$_{32}$), linear OILs ([HOOC]-PDA-([COO]$^-$[H_3N-PNIPAM]$^+$) and PDA-([COO]$^-$[H_3N-PNIPAM]$^+$)$_2$), and hyperbranched PILs ([HOOC]$_{16}$-HBP-

($[COO]^-[H_3N\text{-}PNIPAM]^+)_{16}$ and HBP-($[COO]^-[H_3N\text{-}PNIPAM]^+)_{32}$) in Langmuir monolayers at water/air interface and in LB films on silicon wafers were studied. The effect of the architecture and content of thermally responsive PNIPAM macrocations on the assembly at different temperatures was shown.

The pressure-area isotherms were found for all samples (PDA-$[COOH]_2$, [HOOC]-PDA-($[COO]^-[H_3N\text{-}PNIPAM]^+$), PDA-($[COO]^-[H_3N\text{-}PNIPAM]^+)_2$, HBP-$[COOH]_{32}$, $[HOOC]_{16}$-HBP-($[COO]^-[H_3N\text{-}PNIPAM]^+)_{16}$ and HBP-($[COO]^-[H_3N\text{-}PNIPAM]^+)_{32}$) at both 23 and at 37 °C using the LB trough (Fig. 4.10). The synthesized compounds form stable Langmuir monolayers at water/air interface and their compression isotherms are characterized by the presence of the sections corresponding to gaseous, liquid and solid state of monolayers [18, 19].

When heated, PNIPAM macrocations demonstrates LCST behavior while the oligoester component in aqueous media shows no temperature dependence [29, 34]. Therefore, no change in the isotherms between 23 and 37 °C for the oligomeric acids (samples PDA-$[COOH]_2$ and HBP-$[COOH]_{32}$) was expected (Fig. 4.10). In contrast to initial acids, there is a substantial difference (including MMA, see below Table 4.5) between the isotherms of the compounds containing PNIPAM macrocations (samples [HOOC]-PDA-($[COO]^-[H_3N\text{-}PNIPAM]^+$), PDA-($[COO]^-[H_3N\text{-}PNIPAM]^+)_2$, $[HOOC]_{16}$-HBP-($[COO]^-[H_3N\text{-}PNIPAM]^+)_{16}$ and HBP-($[COO]^-[H_3N\text{-}PNIPAM]^+)_{32}$) at 23 and 37 °C (Fig. 4.10). The profiles of the obtained curves indicate an increase in the critical pressure in monolayers, leading to their collapse, with increasing the content of ionic groups in

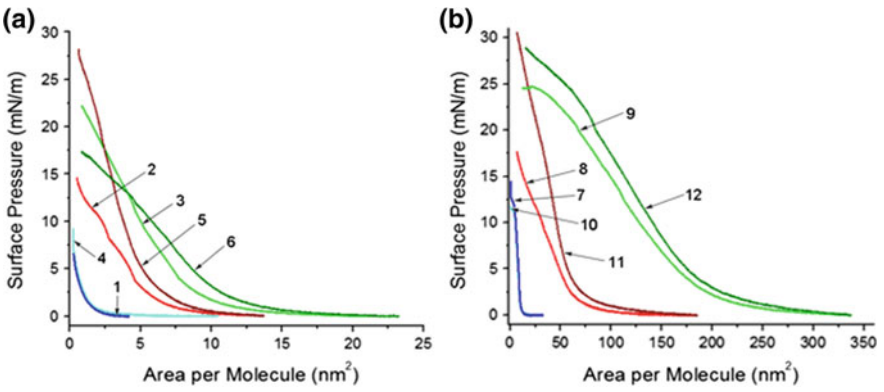

Fig. 4.10 Pressure-area isotherms for the polycarboxylic acids, the OILs and the HBP-PILs monolayers at water/air interface: **a** for linear compound PDA-$[COOH]_2$ (at room temperature (1) and at 37.9 °C (4)), [HOOC]-PDA-($[COO]^-[H_3N\text{-}PNIPAM]^+$) (at room temperature (2) and at 37.9 °C (5)) and PDA-($[COO]^-[H_3N\text{-}PNIPAM]^+)_2$ (at room temperature (3) and at 37.9 °C (6)); **b** for hyperbranched compound HBP-$[COOH]_{32}$ (at room temperature (7) and at 37.9 °C (10)), $[HOOC]_{16}$-HBP-($[COO]^-[H_3N\text{-}PNIPAM]^+)_{16}$ (at room temperature (8) and at 37.9 °C (11)) and HBP-($[COO]^-[H_3N\text{-}PNIPAM]^+)_{32}$ (at room temperature (9) and at 37.9 °C (12))

Table 4.5 Limiting MMA of the synthesized polycarboxylic acids, OILs and PILs at water/air interface and roughness of LB films based on them at room temperature and at 37 °C

Sample	MMA (nm^2/molecule)		Roughness[a] (nm)	
	At 23 °C	At 37 °C	At 23 °C	At 37 °C
Linear architecture				
PDA-$[COOH]_2$	1.4	0.9	1.13	1.32
[HOOC]-PDA-($[COO]^-[H_3N\text{-}PNIPAM]^+$)	6.4	5.3	1.35	1.29
PDA-($[COO]^-[H_3N\text{-}PNIPAM]^+)_2$	8.9	11.4	1.34	1.11
Hyperbranched arcitecture				
HBP-$[COOH]_{32}$	12.1	10.6	1.14	1.15
$[HOOC]_{16}$-HBP-($[COO]^-[H_3N\text{-}PNIPAM]^+)_{16}$	68.7	66.7	1.27	1.15
HBP-($[COO]^-[H_3N\text{-}PNIPAM]^+)_{32}$	191.2	204.4	1.43	1.23

[a] 10×10 μm surface area

the composition of the compounds, as well as temperature exceeding the LCST in the presence of thermally responsive component.

Using the pressure-area isotherms (Fig. 4.10), the limiting MMA was found for all samples (Table 4.5). The MMA values for the hyperbranched samples (HBP-$[COOH]_{32}$, $[HOOC]_{16}$-HBP-($[COO]^-[H_3N\text{-}PNIPAM]^+)_{16}$ and HBP-($[COO]^-[H_3N\text{-}PNIPAM]^+)_{32}$) are much higher than those for the linear analogues (PDA-$[COOH]_2$, [HOOC]-PDA-($[COO]^-[H_3N\text{-}PNIPAM]^+$) and PDA-($[COO]^-[H_3N\text{-}PNIPAM]^+)_2$) below LCST. In addition, a large increase in MMA can be seen with increasing PNIPAM content for all compounds studied here. For example, the MMA values of linear and hyperbranched compounds increase by ~270% and by ~30% when PNIPAM content increases from 50 to 100% (Table 4.5).

The decrease in limiting MMA for the initial oligomeric acids (by 36% and 12% for samples PDA-$[COOH]_2$ and HBP-$[COOH]_{32}$ correspondingly (Table 4.5)) can be promoted by slight rearrangement and better molecular packing of the hydrophobic parts of the molecules due to the higher energy from the increased temperature [45]. At the same time, the MMA values for the compounds with partially neutralized carboxylic groups (samples [HOOC]-PDA-($[COO]^-[H_3N\text{-}PNIPAM]^+$) and $[HOOC]_{16}$-HBP-($[COO]^-[H_3N\text{-}PNIPAM]^+)_{16}$) decreased less (by 17% and 3% correspondingly) in comparison with initial oligomeric acids as the temperature increased (Table 4.5). This trend of MMA of linear and hyperbranched compounds can be attributed to the rearrangement of the PNIPAM component as it changed from a swollen hydrophilic state below LCST to a condensed hydrophobic state above LCST. If the condensed hydrophobic PNIPAM fragments positioned themselves out of the water and above the oligoester hydrophobic component, only a small decrease in limiting MMA would be seen (Fig. 4.11).

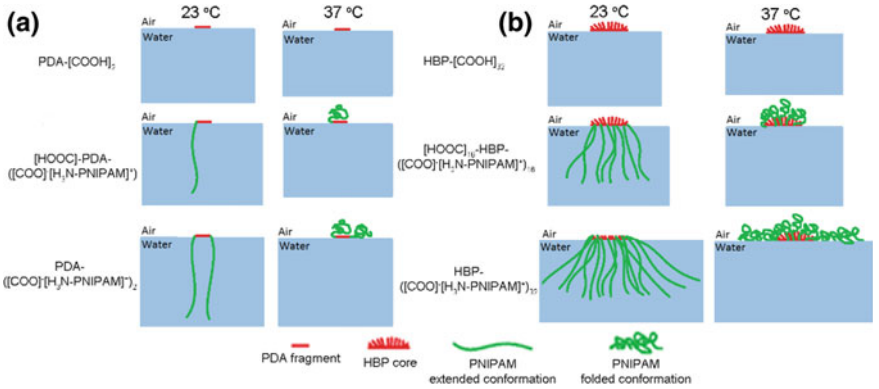

Fig. 4.11 Conformational behavior of the synthesized linear (**a**) and hyperbranched (**b**) polycarboxylic acids, OILs and PILs at water/air interface at both room temperature and 37 °C

Unlike the compounds with partially neutralized carboxylic groups ([HOOC]-PDA-([COO]$^-$[H_3N-PNIPAM]$^+$) and [HOOC]$_{16}$-HBP-([COO]$^-$[H_3N-PNIPAM]$^+$)$_{16}$) the limiting MMA for the fully neutralized compounds (PDA-([COO]$^-$[H_3N-PNIPAM]$^+$)$_2$ (Fig. 4.10a) and HBP-([COO]$^-$[H_3N-PNIPAM]$^+$)$_{32}$ (Fig. 4.10b) increased by 28% and 7% correspondingly as the temperature increased (Table 4.5). Because the size of hydrophobic oligoester component is limited, only a limited amount of condensed PNIPAM segments can position themselves directly above the oligoester hydrophobic component (Fig. 4.11), and the rest of the PNIPAM groups spread on the water surface. Therefore, the limiting MMA would increase if too many PNIPAM groups are added [46, 47].

The AFM images of LB films formed by initial oligomeric acids PDA-[COOH]$_2$ and HBP-[COOH]$_{32}$ at 23 and 37 °C at surface pressure of 5 mN/m which corresponds to solid state of Langmuir monolayer (Fig. 4.10) show no temperature dependence and no visible micelles (Fig. 4.12). The explanation for this result can be that these compounds do not have sufficient hydrophobic parts to form spheres with the correct proportions of hydrophobic centers and hydrophilic surfaces. No micelles were observed under the same conditions for any of the linear OILs.

In contrast to linear OILs, branched PILs (samples HBP-PILs [HOOC]16-HBP-([COO]-[H3N-PNIPAM]+)$_{16}$ and HBP-([COO]-[H_3N-PNIPAM]+)$_{32}$) form aggregates of 1–2 μm in size above LCST (Fig. 4.12b). We suggest that the aggregation of HBP-ILs can be explained by increasing hydrophobicity of the compounds as a result of PNIPAM folding [4, 5].

In addition, we found a slight increase in (~10%) surface microroughness (determined on area of 10 × 10 μm) of the obtained LB films with increasing PNIPAM content for HBP-ILs (Table 4.5). There is also a more significant decrease in the surface roughness of the films by 5–20% as temperature increased (Table 4.5). Such behavior of the compounds indicates the existence of spatial hindrances at temperatures below LCST caused by bulk PNIPAM substituents in the expanded state, which

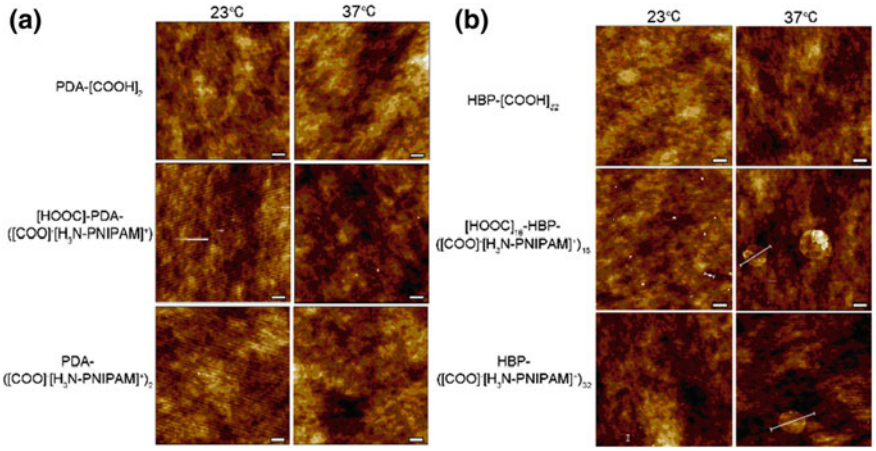

Fig. 4.12 AFM images of LB films formed by the polycarboxylic acids, the OILs and the PILs of linear (**a**) and hyperbranched (**b**) architecture at a surface pressure of 5 mN/m at 23 and 37 °C (scale bar is 1 μm)

prevents a dense packing of macromolecules. This results in rougher surface of the films. On the other hand, at temperatures above LCST the collapsed state causes a decrease in spatial hindrances and favors the formation of smoother films.

Overall, we demonstrated the variation of the content of ionic groups with PNIPAM macrocations in the composition of the synthesized linear and hyperbranched compounds allows us to obtain the smooth (microroughness <1.5 nm) ultrathin films with various morphologies which are promising for use as polyelectrolyte coatings with an adjustable thermally responsive structure in microelectronics, sensors, catalytic systems, and surface-orientation layers.

4.4 Conclusions

In this study, we summarize our recent efforts on synthesis and aqueous assembly of series of amphiphilic anionic protic oligomeric and polymeric ionic liquids based on hyperbranched polyfunctional acids core with various neutralization degrees of the peripheral carboxyl or sulfonic acid groups with N-methylimidazole (Im) and 1,2,4-1H-triazole (Tr) or monoamine-terminated poly(N-isopropylacrylamide)s, and their linear analogues. We find that introduction of long-chain aliphatic tails into the composition of the synthesized compounds enables them to form a crystalline phase. Moreover, these amphiphilic oligomeric and polymeric ionic liquids show unique chemically- and thermally-induced self-assembling behaviour with morphologies tuned by a chemical architecture, namely the content of hydrophilic ionic groups or hydrophobic long-chain aliphatic tails and linear or hyperbranched architecture of initial polycarboxylic acids.

The assembly of these compounds into core–corona micelles in aqueous media in a wide range of pH and ionic conditions was established. The introduction of long hydrophobic aliphatic tails to starting hydrophobic hyperbranched core influences more significantly on the size of micellar assemblies than the introduction of ionic groups does. Regulation of HBP-OILs amphiphilicity can be realized by varying the extent of ionization of terminal groups by changing pH or ionic strength. A more loose conformation of macromolecules at water/air interface is characteristic for the sulfonate HBP-OILs that is due to their higher ionicity compared to carboxylate analogues.

As the content of aliphatic long-chain hydrophobic tails is increased, the surface morphology of LB films of carboxylate imidazolium HBP-OILs is varied from smooth featureless monolayers to 2D surface micelles and ultimately fractal-like aggregates.

The thermally responsive HBP-PILs were obtained by neutralization of terminal carboxyl groups of aliphatic polyester core by monoamine-terminated PNIPAM (50 and 100%). These compounds possessed LCST behavior with a narrow LCST window and are amorphous in condensed state.

The OILs and PILs self-assemble into spherical micelles and their aggregates of different morphologies that is determined by their chemical structure. When temperature is higher than LCST the formation of spherical micelles, network-like aggregates and large vesicles is observed. In opposite to initial cores prone to form spherical domains the thermally responsive compounds are able to self-assemble into elongated unimolecular nanodomain. Increasing PNIPAN content in the composition of the compounds and exceeding LCST contribute to the increase in the area occupied by macromolecules at water/air interface. It was shown that the formation of large micellar aggregates of few μm in LB films was observed only for the HBP-PILs and at temperature above LCST.

Such a variation of chemical architecture of ionic compounds promotes multiscale tuning of the morphology of their assemblies which are not accessible to low molar mass ionic liquids. This novel morphological tunability can open a new pathway to compounds and materials with unique transport characteristics for ion-conducting media for different electrochemical devices, drug-delivery systems, tissue engineering, membrane and sensor technologies, catalytic systems, functional ultrathin coatings for optics, microelectronics and surface-orientation layers.

Acknowledgements This study was financially supported by the National Science Foundation DMR 150523 project (USA), and by program of fundamental studies of the NAS of Ukraine "Novel Functional Substances and Materials of Chemical Production" (project N 16-18).

References

1. T.E. Long, Y.A. Elabd, J. Yuan, Ionic liquids in polymer design. Macromol. Rapid Commun. **37**(14), 1105 (2016). https://doi.org/10.1002/marc.201600255
2. D. Mecerreyes, Polymeric ionic liquids: broadening the properties and applications of polyelectrolytes. Prog. Polym. Sci. **36**(12), 1629–1648 (2011). https://doi.org/10.1016/j.progpolymsci.2011.05.007
3. W. Xu, P.A. Ledin, V.V. Shevchenko, V.V. Tsukruk, Architecture, assembly, and emerging applications of branched functional polyelectrolytes and poly(ionic liquid)s. ACS Appl. Mater. Interfaces. **7**(23), 12570–12596 (2015). https://doi.org/10.1021/acsami.5b01833
4. V.F. Korolovych, A.J. Erwin, A. Stryutsky, E.K. Mikan, V.V. Shevchenko, V.V. Tsukruk, Self-assembly of hyperbranched protic poly(ionic liquid)s with variable peripheral amphiphilicity. Bull. Chem. Soc. Jpn **90**(8), 919–923 (2017). https://doi.org/10.1246/bcsj.20170121
5. V.F. Korolovych, P.A. Ledin, A. Stryutsky, V.V. Shevchenko, O. Sobko, W. Xu, L.A. Bulavin, V.V. Tsukruk, Assembly of amphiphilic hyperbranched polymeric ionic liquids in aqueous media at different pH and ionic strength. Macromolecules **49**(22), 8697–8710 (2016). https://doi.org/10.1021/acs.macromol.6b01562
6. V.V. Shevchenko, A.V. Stryutsky, N.S. Klymenko, M.A. Gumenna, A.A. Fomenko, V.N. Bliznyuk, V.V. Trachevsky, V.V. Davydenko, V.V. Tsukruk, Protic and aprotic anionic oligomeric ionic liquids. Polymer **55**(16), 3349–3359 (2014). https://doi.org/10.1016/j.polymer.2014.04.020
7. V.V. Shevchenko, A.V. Stryutsky, O.A. Sobko, V.F. Korolovich, N.S. Klimenko, M.A. Gumennaya, V.V. Klepko, Y.V. Yakovlev, V.V. Davidenko, Amphiphilic protic anionic oligomeric ionic liquids of hyperbranched structure. Polymer Sci. B **59**(4), 379–391 (2017). https://doi.org/10.1134/S1560090417040108
8. A.S. Shaplov, R. Marcilla, D. Mecerreyes, Recent advances in innovative polymer electrolytes based on poly(ionic liquid)s. Electrochim. Acta **175**, 18–34 (2015). https://doi.org/10.1016/j.electacta.2015.03.038
9. S. Prescher, F. Polzer, Y. Yang, M. Siebenbürger, M. Ballauff, J. Yuan, Polyelectrolyte as solvent and reaction medium. J. Am. Chem. Soc. **136**(1), 12–15 (2014). https://doi.org/10.1021/ja409395y
10. S. Peleshanko, V.V. Tsukruk, The architectures and surface behavior of highly branched molecules. Prog. Polym. Sci. **33**(5), 523–580 (2008). https://doi.org/10.1016/j.progpolymsci.2008.01.003
11. D. Wang, Y. Jin, X. Zhu, D. Yan, Synthesis and applications of stimuli-responsive hyperbranched polymers. Prog. Polym. Sci. **64**, 114–153 (2017). https://doi.org/10.1016/j.progpolymsci.2016.09.005
12. V.V. Tsukruk, Dendritic macromolecules at interfaces. Adv. Mater. **10**(3), 253–257 (1998). https://doi.org/10.1002/(SICI)1521-4095(199802)10:3%3c253:AID-ADMA253%3e3.0.CO;2-E
13. V.V. Tsukruk, F. Rinderspacher, V.N. Bliznyuk, Self-assembled multilayer films from dendrimers. Langmuir **13**(8), 2171–2176 (1997). https://doi.org/10.1021/la960603h
14. X. Zhai, S. Peleshanko, N.S. Klimenko, K.L. Genson, D. Vaknin, M.Y. Vortman, V.V. Shevchenko, V.V. Tsukruk, Amphiphilic dendritic molecules: hyperbranched polyesters with alkyl-terminated branches. Macromolecules **36**(9), 3101–3110 (2003). https://doi.org/10.1021/ma021383j
15. J. Cho, K. Char, J.-D. Hong, K.-B. Lee, Fabrication of highly ordered multilayer films using a spin self-assembly method. Adv. Mater. **13**(14), 1076–1078 (2001). https://doi.org/10.1002/1521-4095(200107)13:14%3c1076:AID-ADMA1076%3e3.0.CO;2-M
16. P. Bertrand, A. Jonas, A. Laschewsky, R. Legras, Ultrathin polymer coatings by complexation of polyelectrolytes at interfaces: suitable materials, structure and properties. Macromol. Rapid Commun. **21**(7), 319–348 (2000). https://doi.org/10.1002/(SICI)1521-3927(20000401)21:7%3c319:AID-MARC319%3e3.0.CO;2-7

17. J.A. Zasadzinski, R. Viswanathan, L. Madsen, J. Garnaes, D.K. Schwartz, Langmuir-Blodgett films. Science **263**(5154), 1726–1733 (1994)
18. S.A. Hussain, S. Deb, D. Bhattacharjee, Langmuir-Blodgett technique a unique tool for fabrication of ultrathin organic films. J. Environ. Sci. Res. **4**, 25–33 (2005)
19. V.V. Tsukruk, Assembly of supramolecular polymers in ultrathin films. Prog. Polym. Sci. **22**(2), 247–311 (1997). https://doi.org/10.1016/S0079-6700(96)00005-6
20. A. Kausar, Survey on Langmuir–Blodgett films of polymer and polymeric composite. *Polymer-Plastics Technology and Engineering*, vol. 56, no. 9, pp. 932–945. https://doi.org/10.1080/03602559.2016.1247282
21. V. Shembekar, A. Contractor, S. Major, S. Talwar, Photoisomerization of amphiphilic azobenzene derivatives in Langmuir Blodgett films prepared as polyion complexes, using ionic polymers. Thin Solid Films **510**, 297–304 (2006). https://doi.org/10.1016/j.tsf.2005.12.210
22. T. Yoshimi, M. Moriyama, S. Ujiie, Orientational behavior of ionic liquid crystal polymers and their nonionic family. Mol. Cryst. Liq. Cryst. **511**(1), 319/[1789]–1326/[1796]. https://doi.org/10.1080/15421400903054428
23. T. Yoshimi, S. Ujiie, Self-assembly and liquid crystalline properties of ionic polymers and their nonionic family. Macromol. Symp. **242**(1), 290–294 (2006). https://doi.org/10.1002/masy.200651040
24. A. Nayak, K.A. Suresh, Conductivity of Langmuir-Blodgett films of a disk-shaped liquid-crystalline molecule-DNA complex studied by current-sensing atomic force microscopy. Phys. Rev. E: Stat. Nonlin. Soft Matter Phys. **78**(2 Pt 1), 021606 (2008). https://doi.org/10.1103/PhysRevE.78.021606
25. A.J. Erwin, W. Xu, H. He, K. Matyjaszewski, V.V. Tsukruk, Linear and star poly(ionic liquid) assemblies: surface monolayers and multilayers. Langmuir **33**(13), 3187–3199 (2017). https://doi.org/10.1021/acs.langmuir.6b04622
26. V. Pérez-Gregorio, I. Giner, M.C. López, I. Gascón, E. Cavero, R. Giménez, Influence of the liquid crystal behaviour on the Langmuir and Langmuir-Blodgett film supramolecular architecture of an ionic liquid crystal. J. Colloid Interface Sci. **375**, 94–101 (2012). https://doi.org/10.1016/j.jcis.2012.02.049
27. V. Shevchenko, A.V. Stryutsky, O.O. Sobko, N.S. Klimenko, M.A. Gumenna, Peculiarities of self-organization of amphiphilic oligomeric protic ionic liquids of hyperbranched structure with the formation of various hierarchical nanostructures. Theor. Exp. Chem. **54** (2018). https://doi.org/10.1007/s11237-018-9555-9
28. U.A. Rana, I. Shakir, R. Vijayraghavan, D.R. MacFarlane, M. Watanabe, M. Forsyth, Proton transport in acid containing choline dihydrogen phosphate membranes for fuel cell. Electrochim. Acta **111**, 41–48 (2013). https://doi.org/10.1016/j.electacta.2013.07.144
29. V.F. Korolovych, A. Erwin, A. Stryutsky, H. Lee, W.T. Heller, V.V. Shevchenko, L.A. Bulavin, V.V. Tsukruk, Thermally responsive hyperbranched poly(ionic liquid)s: assembly and phase transformations. Macromolecules **51**(13), 4923–4937 (2018). https://doi.org/10.1021/acs.macromol.8b00845
30. E. Lizundia, E. Meaurio, J.M. Laza, J.L. Vilas, L.M. León Isidro, Study of the chain microstructure effects on the resulting thermal properties of poly(L-lactide)/poly(N-isopropylacrylamide) biomedical materials. Mater. Sci. Eng., C **50**, 97–106 (2015). https://doi.org/10.1016/j.msec.2015.01.097
31. J.-W. Seo, J.-Y. Hwang, U.S. Shin, Ionic liquid-doped and p-NIPAAm-based copolymer (p-NIBIm): extraordinary drug-entrapping and -releasing behaviors at 38–42 °C. RSC Adv. **4**(51), 26738–26747 (2014). https://doi.org/10.1039/C4RA03736G
32. J. Illescas, M. Casu, V. Alzari, D. Nuvoli, M.A. Scorciapino, R. Sanna, V. Sanna, A. Mariani, Poly(ionic liquid)s derived from 3-octyl-1-vinylimidazolium bromide and N-isopropylacrylamide with tunable properties. J. Polym. Sci. Part A Polym. Chem. **52**(24), 3521–3532 (2014). https://doi.org/10.1002/pola.27418
33. E. Karjalainen, N. Chenna, P. Laurinmäki, S.J. Butcher, H. Tenhu, Diblock copolymers consisting of a polymerized ionic liquid and poly(N-isopropylacrylamide). Effects of PNIPAM block length and counter ion on self-assembling and thermal properties. Polym. Chem. **4**(4), 1014–1024 (2013). https://doi.org/10.1039/c2py20815f

34. K. Jain, R. Vedarajan, M. Watanabe, M. Ishikiriyama, N. Matsumi, Tunable LCST behavior of poly(N-isopropylacrylamide/ionic liquid) copolymers. Polym. Chem. **6**(38), 6819–6825 (2015). https://doi.org/10.1039/C5PY00998G
35. S. Jung, K.I. MacConaghy, J.L. Kaar, M.P. Stoykovich, Enhanced optical sensitivity in thermoresponsive photonic crystal hydrogels by operating near the phase transition. ACS Appl. Mater. Interfaces **9**(33), 27927–27935 (2017). https://doi.org/10.1021/acsami.7b07179
36. Y. Men, H. Schlaad, J. Yuan, Cationic poly(ionic liquid) with tunable lower critical solution temperature-type phase transition. ACS Macro. Lett. **2**(5), 456–459 (2013). https://doi.org/10.1021/mz400155r
37. Y. Kohno, S. Saita, Y. Men, J. Yuan, H. Ohno, Thermoresponsive polyelectrolytes derived from ionic liquids. Polym. Chem. **6**(12), 2163–2178 (2015). https://doi.org/10.1039/C4PY01665C
38. Y. Zhou, W. Huang, J. Liu, X. Zhu, D. Yan, Self-assembly of hyperbranched polymers and its biomedical applications. Adv. Mater. **22**(41), 4567–4590 (2010). https://doi.org/10.1002/adma.201000369
39. L. Liu, L. Rui, Y. Gao, W. Zhang, Self-assembly and disassembly of a redox-responsive ferrocene-containing amphiphilic block copolymer for controlled release. Polym. Chem. **6**(10), 1817–1829 (2015). https://doi.org/10.1039/C4PY01289E
40. G. Li, S. Song, L. Guo, S. Ma, Self-assembly of thermo-and pH-responsive poly (acrylic acid)-b-poly (N-isopropylacrylamide) micelles for drug delivery. J. Polym. Sci. Part A Polym. Chem. **46**(15), 5028–5035 (2008)
41. G. Li, L. Shi, Y. An, W. Zhang, R. Ma, Double-responsive core–shell–corona micelles from self-assembly of diblock copolymer of poly(t-butyl acrylate-co-acrylic acid)-b-poly(N-isopropylacrylamide). Polymer **47**(13), 4581–4587 (2006). https://doi.org/10.1016/j.polymer.2006.04.041
42. J. Guo, Y. Zhou, L. Qiu, C. Yuan, F. Yan, Self-assembly of amphiphilic random co-poly(ionic liquid)s: the effect of anions, molecular weight, and molecular weight distribution. Polym. Chem. **4**(14), 4004–4009 (2013). https://doi.org/10.1039/C3PY00460K
43. M. Sahn, T. Yildirim, M. Dirauf, C. Weber, P. Sungur, S. Hoeppener, U.S. Schubert, LCST behavior of symmetrical PNiPAm-b-PEtOx-b-PNiPAm triblock copolymers. Macromolecules **49**(19), 7257–7267 (2016). https://doi.org/10.1021/acs.macromol.6b01371
44. Y. Zhou, D. Yan, Supramolecular self-assembly of giant polymer vesicles with controlled sizes. Angew. Chem. Int. Ed. **43**(37), 4896–4899 (2004). https://doi.org/10.1002/anie.200460325
45. M. Jaremko, Ł. Jaremko, H.-Y. Kim, M.-K. Cho, C.D. Schwieters, K. Giller, S. Becker, M. Zweckstetter, Cold denaturation of a protein dimer monitored at atomic resolution. Nat. Chem. Biol. **9**(4), 264–270 (2013). https://doi.org/10.1038/nchembio.1181
46. R.M. Richardson, R. Pelton, T. Cosgrove, J. Zhang, A neutron reflectivity study of poly(N-isopropylacrylamide) at the air–water interface with and without sodium dodecyl sulfate. Macromolecules **33**(17), 6269–6274 (2000). https://doi.org/10.1021/ma000095p
47. J. Zhang, R. Pelton, The dynamic behavior of poly (N-isopropylacrylamide) at the air/water interface. Colloids Surf. A **156**(1–3), 111–122 (1999)

Chapter 5
Vibrational Spectroscopy Applied to Solution and Metal/Solution Interface Chemistry Studies

Wagner A. Alves

Abstract Infrared (IR) and Raman experiments as well as SERS (Surface Enhanced Raman Scattering) and surface investigations were carried out in order to obtain detailed vibrational information on solution and metal/solution interface chemistry. For the former system, especial attention has been given to metal-catalyzed peptide bond cleavage reactions, in which the research of new and more efficient metal complexes is needed. A methodology based on the shifts of the ν_{CO} and ν_{CN} modes of a simple amide (formamide/FA) has shown to be useful for the prediction of the catalytic activity of metals and a data collection is presented. For the latter, the adsorption dynamics of different species on a copper electrode, in the presence of chloride anions, and the inhibition efficiency of a specific azole (imidazole/Imid) are analyzed and discussed. A proposal for the adsorption mechanism of Imid is suggested on the basis of potential-dependent spectra.

5.1 Introduction

5.1.1 Catalytic Activity of Metal Ions Toward Amide Bond Cleavage Reactions

It is well known that the electron delocalization on the OCN group imposes high stability to peptide bond so that its half-life is around 600 years at 25 °C and approximately neutral pH. Although certain metal ions are able to destabilize this kind of bond and to subsequently cleave it under physiological conditions, they are still limited in number and so the interest in the development of new and more efficient metal complexes has significantly increased in recent years [1, 2]. The cleavage of a peptide bond commonly takes place via oxidative, photooxidative and hydrolytic pathways, where the first two cause irreversible structural modifications into cleaved

W. A. Alves (✉)
Departamento de Química Inorgânica, Instituto de Química, Universidade Federal do Rio de Janeiro, Caixa Postal 68563, Rio de Janeiro, RJ 21941-909, Brazil
e-mail: wagner@iq.ufrj.br

L. A. Bulavin and L. Xu (eds.), *Modern Problems of the Physics of Liquid Systems*, Springer Proceedings in Physics 223,
https://doi.org/10.1007/978-3-030-21755-6_5

moiety and are hard to control. In contrast, the hydrolysis reaction can regenerate the carboxylic and amine functional groups and such a strategy has become very useful in protein sequencing, proteomics and protein engineering applications.

The most likely mechanisms to account for metal-catalyzed peptide hydrolysis are depicted in Fig. 5.1. At the first the metal polarizes the carbonyl group, which becomes susceptible to the attack of water (Fig. 5.1a). In the second, the attack to the carbonyl group occurs by means of a water molecule activated by the metal (Fig. 5.1b). The third is a combination between the first two mechanisms, in which the metal interacts to the oxygen atom while delivering a water molecule to the carbonyl group (Fig. 5.1c). The formation of a tetrahedral intermediate, which is considered as the active dipolar species, and regeneration of the carboxylic and amine functional groups are steps in common to the three pathways. A fourth mechanism has been proposed by Maslak and coworkers [3], in which coordination to the metal through the nitrogen atom would lead to the deconjugation of the carbonyl group followed by the attack of water. On the other hand, the rate of the hydrolysis products is substantially decreased if coordination through both O and N sites takes place, indicating that the chelating effect is critical for catalysis.

Formamide (FA) has been studied by various authors because it is the simplest molecule containing the OCNH moiety characteristic of the peptide bond. The most important conformational property corresponds to its planarity, which is usually interpreted on the basis of an equilibrium involving its two resonance forms (Fig. 5.2). Indeed, such a property is considered as the creative limitedness of peptide and protein

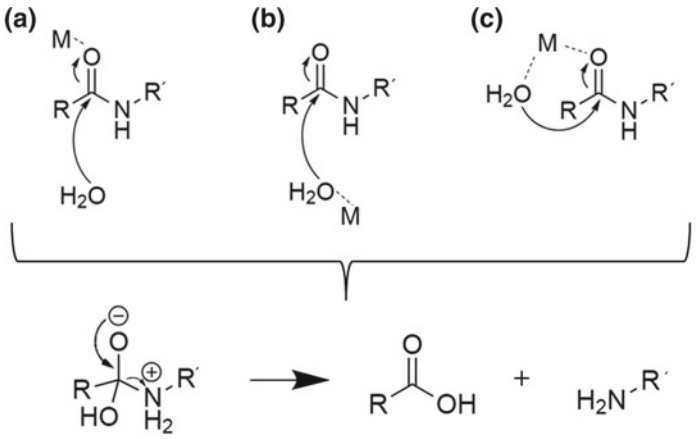

Fig. 5.1 Three mechanism proposals for metal-promoted amide bond hydrolysis

Fig. 5.2 Two canonical FA forms: **a** dipolar; **b** neutral

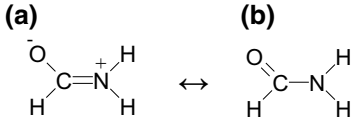

structures, even though deviations may occur for individual bonds, similarly to the behavior exhibited by liquid FA, in which the planarity of the cyclic dimer is lost as the acyclic one is formed [4]. From the vibrational point of view FA has been chosen due to the lowest mixture extent between the ν_{CN} mode and other vibrations, as compared to other simple amides [5]. My research group has taken advantage of this latter information and developed a methodology based on the band shifts observed at the ν_{CO} and ν_{CN} regions of this amide [6–14].

In this review, a collection of spectroscopic data clearly shows that the spectral pattern of FA changes as a function of the kind of metal ion. That is, some metals cause band shifts that can be associated with the stabilization of a molecular structure near the dipolar form (Fig. 5.2a), which is the active species in the amide bond cleavage process, whereas other metal ions provoke shifts that are related to the stabilization of a structure near the neutral form (Fig. 5.2b), which has low catalytic activity. In addition, the spectral pattern exhibited at the ν_{CO} and ν_{CN} regions of FA is also correlated to the metal-FA region in order to identify the coordination sites, in the absence of water, and to better evaluate the mechanism presented in Fig. 5.1a, in which this latter solvent has secondary effect.

5.1.2 Adsorbed Species on the Copper Surface and Their Relationship with Corrosion

Copper and its alloys are widely used because of their excellent electrical and thermal conductivities, workability, resistance, making them suitable for many different applications. In spite of all these properties, corrosion susceptibility is often observed when chloride ions are present in atmosphere, aqueous and soil media. For instance, the use of this metal in seawater distribution and thermal exchange systems makes the issue more interesting since appreciable amounts of chloride are found in the former whereas the second system is cleaned from time to time by the acid pickling process using HCl. In this sense, ongoing efforts have been done in the attempt of preventing the copper electrodissolution in chloride medium, in which CuCl/$CuCl_2^-$ and Cu_2O species are commonly formed [15–23]. Indeed, corrosion is a crucial problem in several areas and among the alternatives available to control it, inhibitors stand out due to their low cost and satisfactory results.

Azole compounds are still the most recommended corrosion inhibitors for copper and its alloys, being benzotriazole (BTAH) one of the most efficient due to its action mode, which is based on the formation of a passive film. However, its high toxicity has led many workers to look for environmentally friendly compounds and so imidazole (Imid) has arisen as an option [24, 25]. So far, the limitedness of using the latter is due to its lower inhibition efficiency (IE), which may be related to the protection mechanism varying from physisorption to chemisorption [26, 27]. The performance becomes even worse in acidic medium due to presence of appreciable amounts of imidazolium ($ImidH^+$), which weakly adsorbs on the surface [28, 29]. Indeed, the

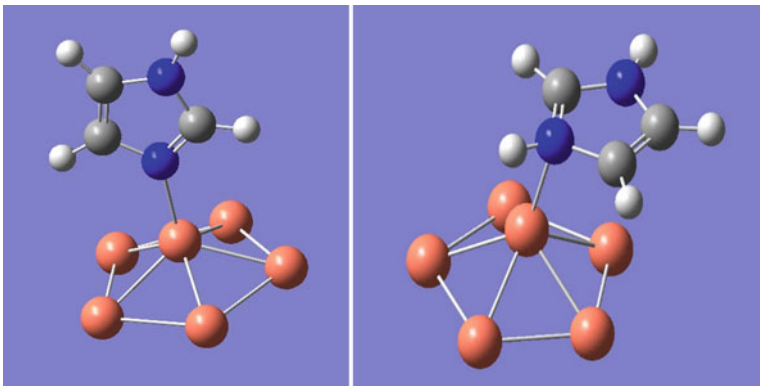

Fig. 5.3 Perpendicular (left panel) and parallel (right panel) orientations of Imid and $ImidH^+$, respectively, on a cluster containing six copper atoms

neutral molecule typically employs the pyridine-type N atom in the interaction with the metal whereas the cation uses its π electrons (Fig. 5.3).

The adsorption of different species onto metal surfaces may be studied by using Surface Enhanced Raman Scattering (SERS), which is a successful analytical technique due to the huge amplification of the Raman signal and achievement of detailed information on the vibrational behavior of the adsorbates as well as the participation of their active sites. Although SERS studies on the adsorption dynamics of the Imid:$ImidH^+$ pair have already been published, controversies with regard to molecular orientation and band assignments are still seen [30–33]. Here, the spectral data are devoted to clarify these issues and evidence the simultaneous adsorption of the neutral molecule and its protonated form on the copper surface, where the quantity of each species shows strong dependence on the solution pH and applied potential. Furthermore, the experiments were carried out in the presence of chloride ions in order to better evaluate the competitive adsorption between the inhibitor and the species formed during the corrosion process. To do this, spectra acquired from more negative to more positive potentials are presented as well as a proposal for the action mode of the inhibitor.

5.2 Materials and Methods

All chemicals were purchased from Sigma-Aldrich and metal halides and perchlorates were used without any additional purification. In order to eliminate water content, formamide was distilled under reduced pressure, discarding the first and last portions of distillate, and its solutions were prepared by weight (mol kg^{-1}). Ultra grade Imidazole was employed in order to avoid the arising of impurity bands in the SERS spectra, as already reported [32]. At this case, all solutions were prepared

using deionized water and the concentrations are expressed as molarities (mol L^{-1}). Values of pH were adjusted by using HCl and KOH solutions if needed.

Vibrational data were obtained from Bruker spectrometers. IR spectra were acquired on an FT-IR Vertex 70 equipment using NaCl windows. Normal Raman experiments were carried out on either an FT-Raman RAM (II) Module using the 1064 nm line or a SENTERRA confocal Raman microscope, using the 532 nm excitation line. SERS spectra were recorded on the latter instrument, but a 785 nm line was employed due to the good relationship with the copper plasmon, which provided an excellent band-enhancement factor. Details on the acquisition of all spectra, specification of the electrochemical cell used for the SERS experiments as well as cleaning and activation processes of the working electrode may be found in recent works [6–14, 23].

The curve-fitting analyses were done using OMNIC 7.3 software and each component under the band envelopes at the ν_{CO} and ν_{CN} regions was considered as a Voigt function. A systematic series of manual adjustment of band parameters was performed until contours in the spectra of different solutions were matched by changing only the height of the components and ending with computer refinement within the constraints of the established information. The results also showed excellent agreement with those obtained from the second derivatives of the original spectra.

5.3 Results and Discussion

5.3.1 Raman and IR Spectra Patterns of FA as a Function of the Metal Ion

Figure 5.4 illustrates Raman spectra of liquid FA and its solutions containing different concentrations of a Zn(II) salt in the 1780–1200 cm^{-1} range. For the pure solvent (Fig. 5.4a), the ν_{CO} region is characterized by two bands at 1710 and 1680 cm^{-1}, which are often ascribed to the respective monomers and dimers of FA. Bands at 1595, 1390 and 1310 cm^{-1} also compose the spectral range and correspond to the δ_{HNH}, δ_{CH} and ν_{CN} modes, respectively [4, 34, 35]. Asymmetry on the higher wavenumber side referring to the latter band can be seen as the solute is added until only one feature at 1340 cm^{-1} is then observed in the spectrum for the highest salt concentration and has been assigned to the ν_{CN} vibration of FA bound to the metal ion (Fig. 5.4b–d). On the other hand, the ν_{CO} region does not show any significant change, but it is well known that rich information can be achieved by using IR spectroscopy at this case. Indeed, Fig. 5.5a clearly shows that the I_{1680}/I_{1595} ratio is larger than the one found from the Raman spectrum of the solvent (Fig. 5.4a). The addition of a Cu(II) salt makes smaller this intensity ratio due to the arising of a new band at 1645 cm^{-1}, which is then attributed to the ν_{CO} mode of FA coordinated to the metal ion (Fig. 5.5b). It is important to stress that the shifts reported for the ν_{CO} and ν_{CN} regions of FA, in the

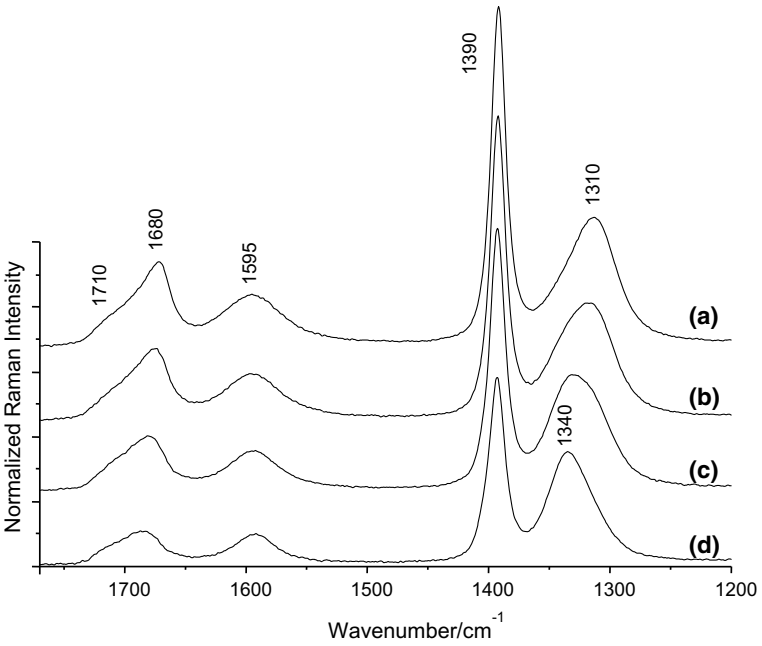

Fig. 5.4 Raman spectra of FA and its solutions with different molal concentrations of Zn(II): **a** FA; **b** 0.5; **c** 1.0; **d** 1.5. Spectra are identical to divalent (Mg, Ni, Fe, Cu, Co) and trivalent (Co, Cr, Ce) ions

presence of Zn and Cu(II), are identical to those observed as Ni, Mg, Fe and Co(II) as well as Cr, Ce and Co(III) salts are used.

As clearly seen the ν_{CO} band of FA is downshifted while the ν_{CN} feature suffers an upshift, as compared to the original FA signals. Such shifts suggest that a molecular structure near the dipolar FA form (Fig. 5.2a) is stabilized. Furthermore, one observes that the O atom is the only coordination site in this resonance hybrid and, indeed, bonding to the metal is evidenced in Fig. 5.6, where a band at 313 cm^{-1} is present in the Raman spectra and is typically ascribed to the $\nu_{Cu\text{-}O}$ mode.

The spectral pattern of FA is fully modified in the presence of Al(III), Fe(III) and Zr(IV) ions. At this case the perturbation provoked by these metals to electronic structure of FA causes upshifts of both ν_{CO} and ν_{CN} modes, as can be seen in Fig. 5.7 for the former ion. The ν_{CO} mode of coordinated FA is now observed at 1747 cm^{-1} whereas the ν_{CN} vibration of FA bound to Al(III) is present at 1349 cm^{-1}. One can still observe a new band at 1376 cm^{-1}, which shows good relationship with the two new features and so it has been attributed to the δ_{CH} vibration of complexed FA. Although this oscillator is not a binding site, such a spectral change may be easily interpreted on the basis of the electronic delocalization in the coordinated FA structure, which seems to be different as a molecular structure near the neutral FA form (Fig. 5.2b) is stabilized. This resonance hybrid can now use both O and N

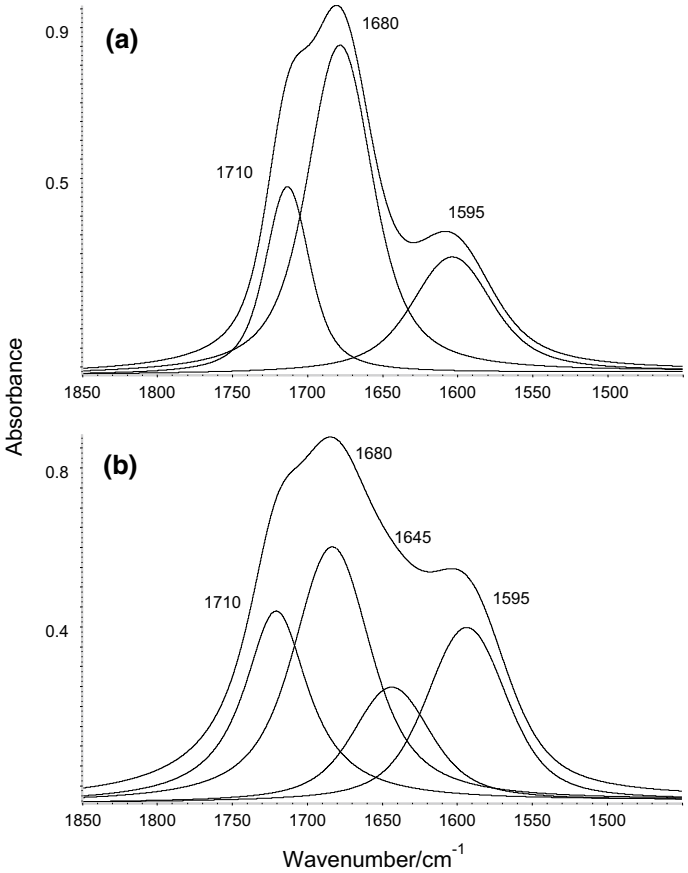

Fig. 5.5 IR curve fits for the ν_{CO} and δ_{HNH} modes of liquid FA (**a**) and its 1.0 mol kg^{-1} solution of Cu(II) ions (**b**). Spectra are identical to divalent (Mg, Ni, Fe, Zn, Co) and trivalent (Co, Cr, Ce) ions

atoms in the coordination process, as very well corroborated by the arising of bands at 547 and 295 cm^{-1}, which correspond to the $\nu_{Al\text{-}O}$ and $\nu_{Al\text{-}N}$ modes, respectively (Fig. 5.8).

In light of all these results, it would be now advisable to present an explanation for the two spectral patterns of FA in the presence of the selected ions. My research group has observed good relationship between the spectroscopic data and the electrostatic potential, φ, which is calculated from the (1):

$$\varphi = Z/4\pi\varepsilon_0 r' \tag{1}$$

where Z is the ionic charge, r' is the ionic radius and ε_0 is the permittivity of free space. Table 5.1 shows the φ values for all ions studied so far, the shifts observed

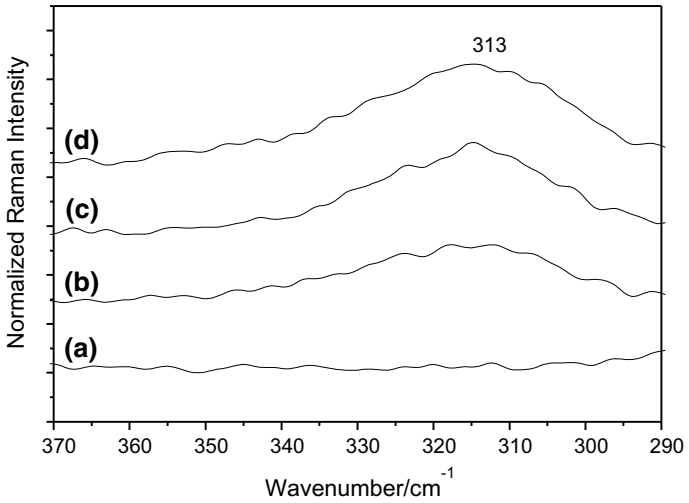

Fig. 5.6 Raman spectra of FA and its solutions with different molal concentrations of Cu(II) at the region characteristic of the copper-oxygen vibration: **a** solvent; **b** 1.0; **c** 2.0; **d** 3.0

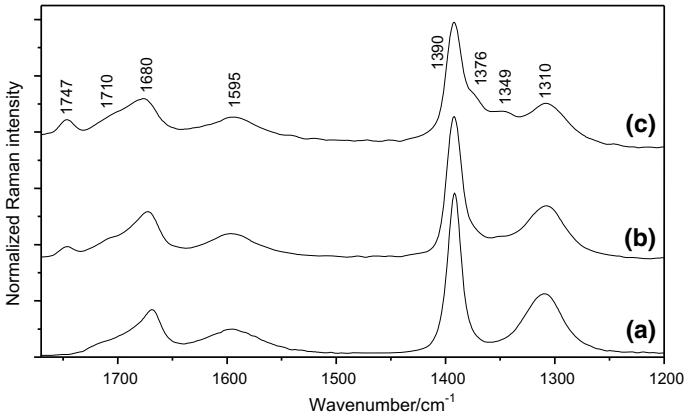

Fig. 5.7 Raman spectra of FA and its Al(III) solutions. Molal concentrations: **a** solvent; **b** 0.7; **c** 1.2. Spectra are identical to Fe(III) and Zr(IV) ions

for the ν_{CO} and ν_{CN} modes, and the ionic radius of each metal as a function of the Coordination Number (CN). This latter has been determined from the resolved Raman spectra at the ν_{CO} and ν_{CN} regions of FA [6–14]. The φ values in the 1.95–3.59 $\times$ 10^{20} J C^{-1} range are in line with the polarization provoked by the metal to the O atom of a molecular structure near the dipolar FA form (Fig. 5.2a), resulting in the ν_{CO} downshift much greater than the ν_{CN} upshift. However, the electron cloud on the N atom begins taking part in the interaction process as higher φ metal ions are present, thus stabilizing a molecular structure near the neutral FA form (Fig. 5.2b),

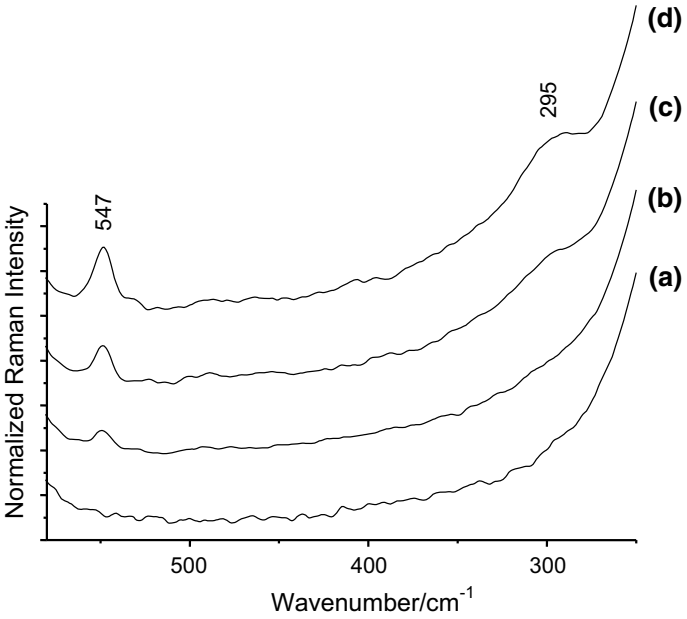

Fig. 5.8 Raman spectra of FA and its solutions with different molal concentrations of Al(III) ions in the low wavenumber region: **a** solvent; **b** 0.3; **c** 0.7; **d** 1.2

Table 5.1 Electrostatic potential, φ, at the surface of the coordinated ion

Metal	CN	r'(pm)	φ (J C^{-1})/$\times$ 10^{20}	$\Delta\nu_{CO}$ (cm^{-1})	$\Delta\nu_{CN}$ (cm^{-1})
Fe(II)	6	92	1.95	−50	+30
Zn(II)	6	88	2.04	−53	+28
Mg(II)	6	86	2.09	−59	+30
Ni(II)	6	83	2.16	−55	+29
Co(II)	4/5	72/81	2.49/2.22	−52	+31
Cu(II)	4/6	71/87	2.53/2.06	−50/−55	+26/+ 28
Ce(III)	8	128	2.11	−52	+26
Cr(III)	6	76	3.55	−67	+32
Co(III)	5/6	NF/75	3.59	−50	+34
Fe(III)	6	69	3.91	+50	+40
Al(III)	6	68	3.96	+50	+50
Zr(IV)	6	86	4.18	+51	+43

NF = Not Found; an average wavenumber value was used for obtaining $\Delta\nu_{CO}$

which may act as a bidentate ligand. Indeed, the chelating ring could be the reason for the upshifts of both ν_{CO} and ν_{CN} vibrations, in which the relatively symmetric charge delocalization on the OCN oscillator would justify the near band shifts. A few examples should be given at this point in order to validate the current methodology: (i) the catalytic activity of Fe(II) is well known, but its oxidation to Fe(III) causes low cleavage product levels so that the addition of a reducing agent is needed to recycle the whole process [36]; (ii) from the biological point of view, no information about the catalytic power of Al(III) has been reported in the literature so far; (iii) although moderate cleavage product levels are formed, the most likely hydrolysis pathway involving Zr(IV) is based on the mechanism 2, in which water acts primarily [1].

5.3.2 *SERS and Surface Raman Spectra of Adsorbed Species on the Copper Electrode*

Aqueous solutions of Imid exhibit pH >7 due to a basic hydrolysis reaction with formation of $ImidH^+$ (2). The equilibrium between such azole forms is well established in the literature, where a pK_{a1} value equal to 6.99 can be found [32, 33, 37].

$$Imid + H_2O = ImidH^+ + OH^- \tag{2}$$

The coexistence of both Imid and $ImidH^+$ species has been sometimes omitted so that the neutral molecule is commonly regarded as the major component in the solutions, as reported by spectroscopic, electrochemical and gravimetric analyses [26, 27, 30, 38]. However, the c_{Imid}:c_{ImidH+} ratio may be controlled by adjusting the solution pH according to the (3):

$$pH = pK_{a1} + \log c_{Imid}/c_{ImidH+} \tag{3}$$

where c is the concentration of each azole form in the equilibrium.

Thus, aqueous Imid solutions of pH = 8.3; 7.0 and 5.7 were prepared and provided c_{Imid}:c_{ImidH+} ratios equal to 20:1; 1:1 and 1:20, respectively. At these conditions, the Imid:$Imid^-$ (imidazolate) equilibrium may be neglected since the pK_{a2} is equal to 14.4 [33, 37]. Figure 5.9 illustrates the potential dependence on the SERS spectra acquired from these solutions, where the bands above 950 cm^{-1} are assigned to in-plane vibrations of the imidazole ring, whereas the ones from 950 to around 640 cm^{-1} are due to out-of-plane modes. The spectra are quite similar to each other and to another reported by Loo and coworkers [33] on a copper electrode and from an ultra grade Imid sample, in which impurity bands at 1026 and 1350 cm^{-1} are not present [32]. The most intense bands located in the 1277–1260 and 1177–1155 cm^{-1} ranges belong to the neutral molecule and their assignment is shown in Table 5.2 along with other band parameters. The δ_{NH} mode is typically observed in the second range and its presence in all SERS spectra confirms that the $Imid^-$ concentration is

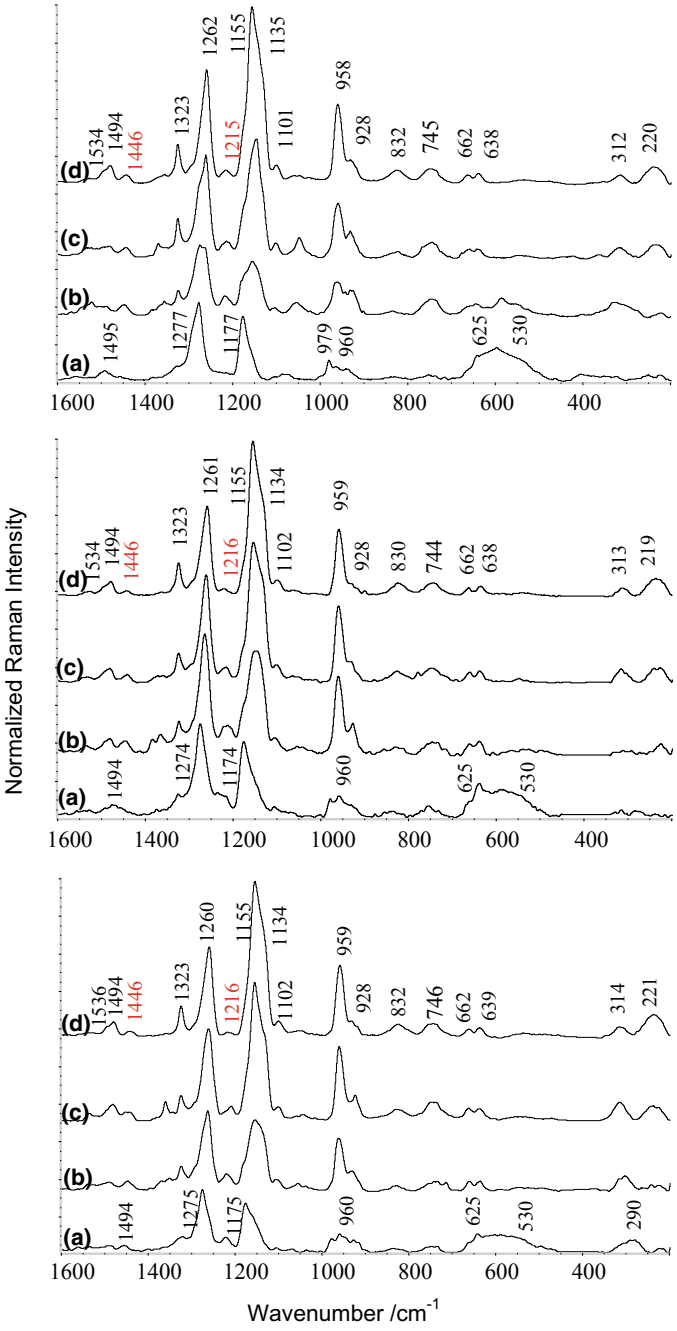

Fig. 5.9 SERS spectra of a 0.001 mol L^{-1} Imid solution at different pH and potential values: (top) pH = 8.3; (middle) pH = 7.0; (bottom) pH = 5.7 − *E* (V): **a** −0.3; **b** −0.6; **c** −1.0; **d** −1.2. Main $ImidH^+$ bands are highlighted in red

Table 5.2 SERS band assignment for different species adsorbed on a copper electrode as a function of the pH and potential values

pH = 8.3			pH = 7.0			pH = 5.7			Assignment [32]
−1.0 V	−0.6 V	−0.3 V	−1.0 V	−0.6 V	−0.3 V	−1.0 V	−0.6 V	−0.3 V	
220 (4)[a]	219 (2)/217	217	219 (5)	221 (4)/217	217	221 (4)	223 (2)/217	217	$\delta^{b}_{\text{Cu-N-C}}$
312 (4)	312 (4)/293	293	313 (5)	312 (2)/292	290	314 (5)	314 (4)/292	290	$\nu_{\text{Cu-N}} + \nu^{b}_{\text{Cu-Cl}}$
638 (3)	641 (4)	642	638 (4)	639 (5)	639	639 (3)	637 (3)	641	γ_{ring}; A″[c,d]
662 (3)	663 (3)	664	662 (4)	662 (4)	664	662 (3)	662 (3)	663	γ_{ring}; A″
745 (5)	746 (5)	750 (2)	744 (5)	746 (5)	754 (3)	746 (5)	742 (3)	747 (2)	γ_{CH}; A″
832 (3)	833 (2)	836 (1)	830 (4)	831 (3)	835 (2)	832 (3)	831 (2)	834 (1)	γ_{CH}; A″
928 (8)	931 (8)	941 (3)	928 (8)	929 (10)	932 (4)	928 (7)	930 (6)	927 (4)	γ_{CH}; A″
958 (15)	961 (10)	963 (4)	959 (27)	960 (25)	958 (6)	959 (20)	961 (14)	960 (5)	δ_{ring}; A′
1055 (5)	1056 (4)	1070 (2)	1057 (3)	1056 (4)	1071 (2)	1056 (3)	1056 (2)	–	δ_{CH}; A′
1101 (4)	1103 (3)	1104 (1)	1102 (7)	1104 (6)	1104 (3)	1101 (4)	1103 (3)	1104 (2)	$\delta_{\text{CH}} + \nu_{\text{ring}}$; A′
1135 (20)	1136 (13)	–	1134 (37)	1134 (28)	–	1134 (23)	1136 (15)	–	ν_{ring}; A′
1155 (32)	1154 (16)	1177 (17)	1155 (49)	1154 (33)	1174 (20)	1155 (37)	1154 (19)	1175 (13)	δ_{NH}; A′
1215 (5)	1215 (4)	–	1216 (6)	1216 (8)	1216 (6)	1216 (5)	1215 (6)	1219 (4)	δ_{CH} ImidH^{+}; A_1
1262 (27)	1263 (23)/ 1274 (19)	1277 (21)	1261 (38)	1263 (38)	1274 (25)	1260 (25)	1263 (22)	1275 (17)	δ_{CH}; A′
1323 (11)	1323 (7)	1330 (4)	1323 (11)	1322 (11)	1328 (6)	1323 (7)	1324 (7)	1324 (5)	ν_{ring}; A′
1446 (3)	1445 (3)	–	1446 (4)	1446 (6)	1447 (3)	1446 (3)	1446 (4)	1447 (2)	ν_{ring} ImidH^{+}; A_1
1494 (3)	1493 (3)	1495 (3)	1493 (4)	1493 (4)	1494 (2)	1494 (4)	1492 (3)	1494 (2)	ν_{ring}; A′
1534 (3)	1534 (4)	1552 (1)	1534 (3)	1534 (3)	1537 (2)	1536 (3)	1537 (2)	1535 (2)	ν_{ring}; A′

[a]Relative intensities are reported between brackets; [b]Assignment of this work; [c]A′ and A″ are the symmetry species belonging to the C_s point group of Imid and A_1 is related to the C_{2v} point group of ImidH^{+}; [d]ν is due to stretching vibration whereas δ and γ correspond to the in-plane and out-of-plane angular deformation modes, respectively

negligible, indeed. The band positioned in the former range (δ_{CH}) is more intense than the one observed in the second as the potential (E) varies from −0.3 to −0.6 V. At more negative E their intensities are inverted and the band assigned to the δ_{NH} mode is substantially enhanced. Other bands belonging to the neutral species are observed at around 1323 (ν_{ring}) and 960 cm^{-1} (δ_{ring}), and are also enhanced at more cathodic E. These spectral changes may be interpreted in the followings. At $E = -0.3$ V the metal has appreciable Cu_2O quantities, as revealed by the bands at 625 and 530 cm^{-1} [39, 40], which make irregular the electrode surface, resulting in a weak interaction with the Imid molecule. Some oxide level is still present at $E = -0.6$ V and such a statement is more easily observed at basic pH. As E is made more negative, Imid adsorbs on the oxide-free surface in a way similar to the arrangement depicted in Fig. 5.3 (left panel). In other words, the N-H bond begins aligning itself with the surface normal and so the corresponding band is rather enhanced. The orientation perpendicular to the Cu electrode also causes the enhancement of the other bands assigned to in-plane vibrations of the imidazole ring, in full agreement with the surface selection rules [41–44]. As a result, the interaction between the reduced Cu surface and Imid leads to the appearance of a new band at around 312 cm^{-1}, which is commonly assigned to the $\nu_{Cu\text{-}N}$ mode [45, 46]. Another one located at around 220 cm^{-1} composes this region and is then attributed to the $\delta_{Cu\text{-}N\text{-}C}$ vibration [23].

It is worth emphasizing the pH dependence on the bands observed at the region characteristic of the metal-ligand vibrations and at less cathodic E. That is, the band at ca. 312 cm^{-1} becomes a shoulder on another one located at around 290 cm^{-1}, which is typically ascribed to the $\nu_{Cu\text{-}Cl}$ vibration [47, 48]. Such a spectral change may be clearly seen at acidic pH because the oxide level is smaller as compared to the other media. The partial removal of the Cu_2O layer allows better observing the presence of CuCl on the electrode surface at E in going from −0.6 to −0.3 V.

A closer look at the SERS spectra allows one observes the presence of two weak signals at 1215 and 1446 cm^{-1}. They correspond to the in-plane modes of $ImidH^+$ and are its most intense bands [32, 49]. In fact, regardless of the c_{Imid}:c_{ImidH+} ratios in the probed solutions, the spectra clearly show that the neutral molecule is the dominant species on the Cu surface for the whole applied potential window. The weak intensity of these two bands may be then explained by the flat orientation of the protonated form, similar to the one illustrated in Fig. 5.3 (right panel), in which the in-plane modes are parallel to the Cu surface and no enhancement is seen at the SERS spectra, as expected from the selection rules [41–44]. Carter and Pemberton [32] investigated the adsorption of $ImidH^+$ on an Ag electrode and observed that the cation is desorbed from the surface along with chloride ion as E is made more negative. Such a finding was interpreted in terms of the ion pair formation between $ImidH^+$ and initially adsorbed Cl^-. In the present study, one can clearly observe that the cation is still on the Cu surface even when the anion is fully desorbed at more cathodic E.

In the attempt to obtain a SERS spectrum containing essentially the $ImidH^+$ bands, a solution of pH = 2 was prepared so that the c_{Imid}:c_{ImidH+} proportion is now equal to 1:ca. 98000. Figure 5.10 presents potential-dependent spectra where one observes a totally different pattern in relation to Fig. 5.9 at $E = -0.3$ V. Undoubtedly, the

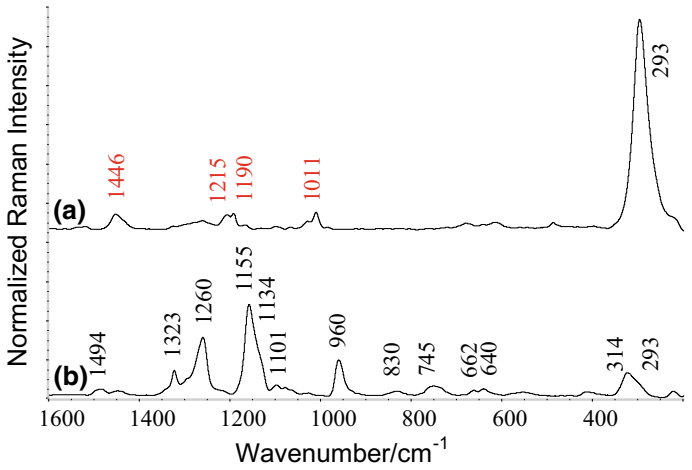

Fig. 5.10 SERS spectra of a 0.1 mol L^{-1} Imid solution (pH = 2.0) at two selected potentials (V): **a** $E = -0.3$; **b** $E = -1.0$. $ImidH^+$ bands are highlighted in red

oxide bands were drastically vanished and the cation seems to be the only azole form on the Cu electrode, whose its main bands are accompanied by others at 1190 and 1011 cm^{-1}, which were also seen in solution and on a silver electrode [32]. The extremely intense band at 293 cm^{-1} ($\nu_{Cu\text{-}Cl}$) strongly indicates that $ImidH^+$ is not able to protect the copper surface and such a result may be due to its weak adsorption through the π-electron cloud. Indeed, no band related to the $\nu_{Cu\text{-}N}$ mode can be observed at this potential, in contrast to the spectrum acquired at $E = -1.0$ V, in which the 314 cm^{-1} band is present and mixed with the 293 cm^{-1} band because there is still Cl^- on the surface. The presence of the former band is so corroborated by the main Imid features, which are now dominant even when its concentration is extremely low, and the largest enhancement of the 1155 cm^{-1} band (δ_{NH}) again points out to the perpendicular orientation of the neutral molecule.

The SERS experiments carried out in an strongly acidic medium and, particularly, at a less cathodic E are in line with investigations performed by using other characterization techniques [28, 29]. The low performance at this case seems to be the main reason for the use of this inhibitor in alkaline media. Furthermore, it is known that IE should be evaluated close to the corrosion potential. Hence, armed with these information, surface spectra at open circuit potential ($E_{OCP} = -0.07$ V) and at higher anodic potentials were measured for a solution of pH = 8.3 and are shown in Fig. 5.11. One can clearly observe that at $E_{OCP} = -0.07$ V the electrode surface is dominated by the corrosion products and the larger distance of Imid from the copper surface leads to a smaller contribution from the chemical enhancement mechanism of SERS. As a result, the main Imid features have now intensities comparable to the ones belonging to Cu_2O and CuCl. The irregular electrode surface is then responsible for the weak adsorption of the neutral species, which seems to occur through a physisorption mechanism. At $E \geq 0.0$ V a reaction between Imid

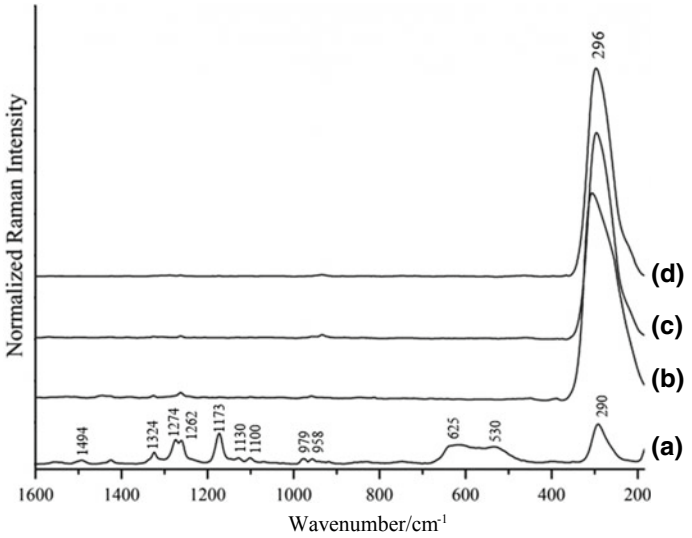

Fig. 5.11 SERS spectra of a 1×10^{-3} mol L^{-1} Imid solution (pH = 8.3) at different applied E (V): **a** −0.07; **b** 0.0; **c** 0.2; **d** 0.4

and Cu_2O begins taking place since their signals practically disappear, in contrast to the enhancement observed for the band ascribed to the ν_{CuCl} mode. The formation of a soluble complex, which makes easier the chloride attack to the surface, could be an explanation for such a finding. Indeed, a slightly blue solution has been observed and is always associated to presence of cupric ions, according to the disproportionation reaction below:

$$2\text{CuImid}^{+}_{(aq)} = \text{CuImid}^{2+}_{(aq)} + \text{Cu}_{(s)} + \text{Imid}_{(aq)} \tag{4}$$

For end, these latter spectral data reveal low IE of Imid even at an alkaline solution, where a better performance would be expected [22, 26, 27]. As can be also seen the action mode of this azole greatly differs from that reported for BTAH, in which the oxidized surface is needed for the formation of the passive Cu(I)BTA film.

5.4 Conclusions

The results presented in this study confirm the characterization power of vibrational spectroscopy to investigate solution and metal/solution interface chemistry. The shifts observed at the ν_{CO} and ν_{CN} regions of FA may be useful for the development of new metal complexes with applications in protein sequencing and proteomics. So far, metal ions with φ varying from low to moderate ($1.9–3.6 \times 10^{20}$ J C^{-1}) cause ν_{CO} downshift and ν_{CN} upshift, and stabilize a molecular structure near the dipolar FA

form, which is more susceptible to the hydrolysis reaction than a structure near the neutral FA form. This latter is stabilized by higher φ metal ions (3.9×10^{20} J C^{-1}), which provoke ν_{CO} and ν_{CN} upshifts in the spectra.

The adsorption of both Imid and $ImidH^+$ on a copper electrode has been simultaneously identified by SERS experiments, where the neutral molecule, which is the major chemisorbed species on the surface, employs the pyridine-type N atom in the interaction with the metal and its orientation varies from tilted to perpendicular as the potential is made more negative. On the other hand, the protonated form adsorbs flat on the metal surface, its orientation is not affected by potential changes and it is the minor component on the electrode at pH's equal to 8.3, 7.0 and 5.7. A SERS spectrum containing essentially the cation bands is only observed at pH equal to 2.0 and in a less cathodic *E*. Nevertheless, the strong Cl^- adsorption confirms the low IE of $ImidH^+$, which uses its π electrons in the interaction with the metal. Surface spectra acquired at OCP and higher anodic polarizations were very useful to evidence the action mode of Imid, in going from a physisorption mechanism to formation of a soluble complex at positive potentials. Such a finding also confirms the lower IE of Imid as compared to BTAH.

Acknowledgements This project was sponsored by Conselho Nacional de Desenvolvimento Científico e Tecnológico-CNPq and partly by the Coordenação de Aperfeiçoamento de Pessoal de Nível Superior—Brazil (CAPES)—Finance Code 001. The author thanks all collaborators for fruitful discussions and Laboratório de Ensaios Não-Destrutivos, Corrosão e Soldagem (LNDC) for the Raman facilities.

References

1. K.B. Grant, M. Kassai, Curr. Org. Chem. **10**, 1035 (2006)
2. N.E. Wezynfeld, T. Fraczyk, W. Bal, Coord. Chem. Rev. **327–328**, 166 (2016)
3. P. Maslak, J.J. Sczepanski, M. Parvez, J. Am. Chem. Soc. **113**, 1062 (1991)
4. A.C.G. Marigliano, E.I. Varetti, J. Phys. Chem. A **106**, 1100 (2002)
5. A.I. Freire, W.A. Alves, Spectrochim. Acta A **135**, 883 (2015)
6. L.M. Pereira, W.A. Alves, Vib. Spectrosc. **56**, 250 (2011)
7. A.I. Freire, W.A. Alves, Spectrochim. Acta A **89**, 259 (2012)
8. E.F. Silva, W.A. Alves, Vib. Spectrosc. **62**, 264 (2012)
9. T.B.C. Campos, E.F. Silva, W.A. Alves, Vib. Spectrosc. **65**, 24 (2013)
10. A.I. Freire, W.A. Alves, Vib. Spectrosc. **73**, 73 (2014)
11. F.G. Camacho, W.A. Alves, Spectrochim. Acta A **151**, 11 (2015)
12. T.B.C. Campos, W.A. Alves, Vib. Spectrosc. **80**, 86 (2015)
13. T.B.C. Campos, W.A. Alves, Vib. Spectrosc. **85**, 134 (2016)
14. A.K.M.S. Gomes, W.A. Alves, Vib. Spectrosc. **89**, 57 (2017)
15. C. Deslouis, B. Tribollet, G. Musiani, M.M. Musiani, J. Appl. Electrochem. **18**, 374 (1988)
16. C. Deslouis, B. Tribollet, G. Musiani, M.M. Musiani, J. Appl. Electrochem. **18**, 384 (1988)
17. O.E. Barcia, O.R. Mattos, N. Pebere, B. Tribollet, J. Electrochem. Soc. **140**, 2825 (1993)
18. J.B. Matos, E. D'Elia, O.E. Barcia, O.R. Mattos, N. Pebere, B. Tribollet, Electrochim. Acta **46**, 1377 (2001)
19. G.G.O. Cordeiro, O.E. Barcia, O.R. Mattos, Electrochim. Acta **38**, 319 (1993)
20. M.M. Antonijevic, S.M. Milic, M.B. Petrovic, Corros. Sci. **51**, 1228 (2009)

21. H.O. Curkovic, E. Stupnisek-Lisac, H. Takenouti, Corros. Sci. **52**, 398 (2010)
22. M.B.P. Mihajlovic, M.M. Antonijevic, Int. J. Electrochem. Sci. **10**, 1027 (2015)
23. E.F. Silva, M.C.E. Bandeira, W.A. Alves, O.R. Mattos, J. Electrochem. Soc. **165**, C375 (2018)
24. Y. Liu, G.G. Ying, A. Shareef, R.S. Kookana, Water Res. **45**, 5005 (2011)
25. E. Stupnisek-Lisac, A. Loncaric-Bozic, I. Cafuk, Corrosion **54**, 713 (1998)
26. H. Otmacic, E. Stupnisek-Lisac, Electrochim. Acta **48**, 985 (2003)
27. I. Milosev, N. Kovacevic, J. Kovac, A. Kokalj, Corros. Sci. **98**, 107 (2015)
28. R. Gasparac, E. Stupnisek-Lisac, Corrosion **55**, 1031 (1999)
29. R. Gasparac, C.R. Martin, E. Stupnisek-Lisac, J. Electrochem. Soc. **147**, 548 (2000)
30. D. Thierry, C. Leygraf, J. Electrochem. Soc. **133**, 2236 (1986)
31. B.H. Loo, Y.G. Lee, A. El-Hage, *Laser Applications to Chemical Dynamics*, vol. 742 (SPIE, 1987), p. 143
32. D.A. Carter, J.E. Pemberton, Langmuir **8**, 1218 (1992)
33. B.H. Loo, Y. Tse, K. Parsons, C. Adelman, A. El-Hage, Y.G. Lee, J. Raman Spectrosc. **37**, 299 (2006)
34. A. Mortensen, O.F. Nielsen, J. Yarwood, V. Shelley, Vib. Spectrosc. **8**, 37 (1994)
35. A. Mortensen, O.F. Nielsen, J. Yarwood, V. Shelley, J. Phys. Chem. **98**, 5221 (1994)
36. S. Soundar, R.F. Colman, J. Biol. Chem. **268**, 5264 (1993)
37. P. Cao, R. Gu, Z.Q. Tian, J. Phys. Chem. B **107**, 769 (2003)
38. M.C.S.S. Macedo, O.E. Barcia, E.C. da Silva, J. de O. Mendes, O.R. Mattos, J. Electrochem. Soc. **159**, C160 (2012)
39. H.Y.H. Chan, C.G. Takoudis, M.J. Weaver, J. Phys. Chem. B **103**, 357 (1999)
40. M. Muniz-Miranda, F. Muniz-Miranda, S. Caporali, Beilstein J. Nanotechnol. **5**, 2489 (2014)
41. M. Moskovits, J. Chem. Phys. **77**, 4408 (1982)
42. M. Moskovits, J.S. Suh, J. Phys. Chem. **88**, 5526 (1984)
43. M. Moskovits, Rev. Mod. Phys. **57**, 783 (1985)
44. J.A. Creighton, Surf. Sci. **158**, 211 (1985)
45. M.M. Campos-Vallete, R.E. Clavijo, F. Mendizabal, W. Zamudio, R. Baraona, G. Diaz, Vib. Spectrosc. **12**, 37 (1996)
46. G. Xue, J. Dong, Y. Sun, Langmuir **10**, 1477 (1994)
47. G. Niaura, A. Malinauskas, Chem. Phys. Lett. **207**, 455 (1993)
48. K.A. See, K.W. Chapman, L. Zhu, K.M. Wiaderek, O.J. Borkiewicz, C.J. Barile, P.J. Chupas, A.A. Gewirth, J. Am. Chem. Soc. **138**, 328 (2016)
49. A.M. Bellocq, C.G. Lagrange, Spectrochim. Acta A **27**, 1091 (1971)

Chapter 6
Organization of Nano-disks of Laponite® in Soft Colloidal Systems

Nikolai Lebovka, Longin Lisetski and Leonid A. Bulavin

Abstract The structure and properties of soft colloidal systems filled by nano-disks of Laponite® (Lap) are critically reviewed. The known Lap grades, chemical structure and physical properties are described. Various phases formed by exfoliated surface-charged Lap discs in aqueous media are analyzed, accounting for the kinetics of phase transformations and aging processes. The emerging interfacial structures are considered, as well as interactions of Lap discs with surfactants. Special attention is paid to formation of organically modified Lap (LapO). The latter can form homogeneous dispersions in non-aqueous media (organic solvents, soft non-ionic polymers, nematic and liquid crystals (LC)). LapO platelets exhibit various behavior patterns in ordered LC media, with specific effects emerging from interactions of disc-like LapO and rod-like LC molecules and carbon nanotubes. Promising practical applications of Lap based suspensions and nanomaterials based thereon are also outlined.

N. Lebovka (✉)
Department of Physical Chemistry of Disperse Minerals, Biocolloidal Chemistry Institute, 42, Vernadsky av, Kyiv 03142, Ukraine
e-mail: lebovka@gmail.com

L. Lisetski
Institute for Scintillation Materials of STC "Institute for Single Crystals", NAS of Ukraine, 60, Nauky Ave, Kharkiv 61001, Ukraine
e-mail: lisetski@isma.kharkov.ua

L. A. Bulavin
Department of Molecular Physics, Taras Shevchenko National University of Kyiv, 2, Prosp. Academician Glushkov, Kyiv 03022, Ukraine
e-mail: bulavin221@gmail.com

L. A. Bulavin and L. Xu (eds.), *Modern Problems of the Physics of Liquid Systems*, Springer Proceedings in Physics 223,
https://doi.org/10.1007/978-3-030-21755-6_6

List of Abbreviations and Chemical Substances

Abbreviations

BET	Brunauer–Emmett–Teller adsorption theory
CEC	cation exchange capacity
CNTs	carbon nanotubes
DLS	dynamic light scattering
DSC	differential scanning calorimetry
Lap	Laponite®
LapO	organo-modified Lap
LC	liquid crystal
LLC	lyotropic liquid crystal
NMR	nuclear magnetic resonance
SANS	small-angle neutron scattering
SAXS	small-angle X-ray scattering
SEM	scanning electron microscopy
TEB	transient electrically-induced birefringence
TEM	transmission electron microscopy
XRD	X-ray diffraction

Chemical substances

Liquid crystals

5CB	4-pentyl-4′-cyanobiphenyl, $CH_3(CH_2)_4C_6H_4C_6H_4CN$
M5	A mixture of cholesterol esters consisting of 30% cholesteryl formate ($C_{28}H_{46}O_2$), 5% cholesteryl butyrate ($C_{31}H_{52}O_2$) and 65% cholesteryl nonanoate $C_{36}H_{62}O_2$

Surfactants

Anionics

SDS	sodium dodecyl sulfate, $NaC_{12}H_{25}SO_4$
PSS-Na	sodium polystyrene sulfonate, $(CH_2CHC_6H_4SO_3Na)_n$

Cationics

CTAB	hexadecyltrimethylammonium bromide, $C_{19}H_{42}N^+Br^-$
CTAC	hexadecyltrimethylammonium chloride, $C_{19}H_{42}N^+Cl^-$
DODAB	dimethydioctodecylammonium bromide, $C_{38}H_{80}N^+Br^-$
DODAC	dimethydioctodecylammonium chloride, $C_{38}H_{80}N^+Cl^-$

Nonionics

Brij 30	polyoxyethylene(4)lauryl ether, $C_{12}H_{25}(OCH_2CH_2)_4OH$
Brij 35	polyethylene glycol dodecyl ether, $C_{12}H_{25}(OCH_2CH_2)_nOH$, $n \sim 23$

Others

PEG/PEO	polyethylene glycol/oxide, $H(OCH_2CH_2)_nOH$, PEG: $M_w < 20 \times 10^3$ g/mol, PEO: $M_w > 20 \times 10^3$ g/mol
SAP	oly(isobutylene) based stabilizer SAP 230TP (Infineum, UK)

6.1 Introduction

Laponite® (Lap) is a synthetic 2-dimensional (2D) nanomaterial that was invented in 1962 by B. S. Neumann from Laporte Industries Ltd. [1]. It is composed of disk-shaped crystals with large negative charges on their faces. In recent years, the soft materials filled by Lap disks have been attracted increasing attention. The fundamental studies revealed exotic phase behavior of aqueous suspensions of Lap, presence of aging and surprising states [2–4]. Moreover, Lap-based materials demonstrated useful technological properties promising for application as the drilling fluids [5, 6], rheology modifiers [7], film formers smart hydrogels [8, 9], for production of the high performance low-cost supercapacitors and thin film electrodes for electrochemical energy storage applications [10], materials for personal care, surface coatings, polymers, paper films, building, agriculture products [11], barrier layer-by-layer films for biomedical applications [12], and materials for pharmaceutical and cosmetic applications [13].

This chapter critically reviews properties of Lap, its applications and behavior in different dispersing media.

6.2 General Information on Lap

6.2.1 Grades of Lap

The Lap products from BYK Additives, Inc. (United Kingdom) can be divided into groups of sol forming and gel forming grades [11]. Lap is totally synthetic and has none of the contaminants that might typically be found in a natural products. It is free of crystalline silica and has low content of transition metals and other impurities. Under intensive agitation, Lap products of both grades disperse readily in water. The sol forming grades include additives that delay the formation of gels, and even at large concentration $C \approx 30\%$ wt the low viscosity liquid sols can be obtained. The produced sol forming grades can be of temporary type (short time of stability) and permanent type (long time of stability). The gel forming grades can form thixotropic gels even at small concentration of Lap in water, $C \approx 2\%$ wt.

The important sol forming grades are represented by products RDS, XLS, S482, and JS (fluorohectorite). The RDS is the general purpose sol grade recommended for applications in formulations with low content of free water. The XLS is a high purity personal care grade. The S482 and JS are designed as high sol stability grades used for production of electrically conductive, antistatic and barrier films. The composition, properties and applications of RDS, XLS, JS and S482 grades as stabilizers in Pickering emulsion polymerization have been recently studied [14].

The important gel forming grades are represented by products RD, XLG, D, XL21 (fluorohectorite). The RD and XLG grades are chemically identical in every respect, but Lap XLG is a purer (personal care) grade with certified low heavy metal and low microbiological content. The D and XL21 products also belong to the high purity personal care grades. The D grade is optimized for rapid dispersion in sorbitol solution, and XL21 grade is a sodium magnesium fluorosilicate for application in skincare formulations.

Among producers/suppliers of Lap products, we can also refer the companies Hemmelrath Lackfabrik (www.hemmelrath.de), Eckart Effect Pigments GmbH (www.eckart.net), Huizhi Jiangsu Fine Chemical Co., Ltd. (huizhichemical.lookchem.com), and Kremer Pigmente (www.kremer-pigmente.com).

The most investigated in different studies is a general purpose grade product Lap RD (hereinafter Lap) and in the following consideration we should pay attention to the properties of this product.

6.2.2 Chemical Structure

Lap has the structure of synthetic 2:1 crystals composed of one trioctahedral inner magnesium layer sandwiched by two tetrahedral silica layers (Fig. 6.1).

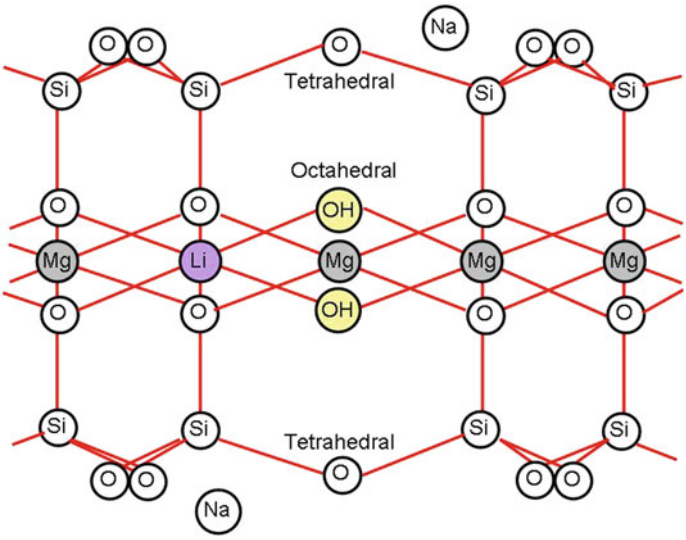

Fig. 6.1 Chemical structure of Lap

These groups are balanced by 20 atoms of O and 4 OH groups. In real systems in the central sheet some divalent Mg^{2+} ions (5–10 %mol) are randomly substituted by monovalent ions of Li^{+}. The chemical structure for OH-hectorites can be represented by the following formula

$$Na_{\alpha}\left[Mg_{6-\alpha}Li_{\alpha}Si_8O_{20}(OH)_4\right],$$

where α corresponds to the degree of the substitution.

As a result of the substitution the faces of the disks bear a negative charge balanced by the positive charge of the sodium ions.

In practice, some positions may be empty and in general case the empirical formula is

$$Na_{\alpha}\left[Mg_{\beta}Li_{\gamma}Si_8O_{20}(OH)_4\right],$$

where $\alpha = 0.8$, $\beta = 5.4$ and $\gamma = 0.4$ [15] or $\alpha = 0.7$, $\beta = 5.5$ and $\gamma = 50.3$ [16].

In powder state the disks of Lap are grouped in stacks (tactoids) and electroneutrality is insured by interlayer Na^{+} ions. The single disk is composed of about 1500 unit cells.

In fluorohectorites some OH groups are substituted by F atoms.

6.2.3 Properties

Lap is composed of disk-shaped crystals with a thickness of $h \approx 1$ nm (0.92 nm), diameter of $d \approx 25$ nm and high aspect ratio of $a = d/h \approx 25$. It has density of $\rho = 2.53$ g/cm^3 [11]. For Lap suspension in liquid medium the relation between volume concentration, φ, and weigh concentration, C, can be represents as

$$\varphi = 1/(1 + (1/C - 1)\rho/\rho_s) \text{ or } C = 1/(1 + (1/\varphi - 1)\rho_s/\rho)$$

where ρ_s is a density of solvent.

For aqueous suspensions $\rho_s \approx 1$ g/cm^3 and at small concentrations ($C \approx 1\%$ wt) we have the following approximate relation

$$C \approx 2.53\varphi.$$

A specific area of disk faces can be theoretically estimated as [17]

$$S = 2/(\rho h) \approx 430 \text{ m}^2/\text{g}.$$

This value exceeds the experimental values determined by the Harkins and Jura technique (87.9 m^2/g), gravimetric studies of H_2O adsorption (345.1 m^2/g) and BET studies of N_2 adsorption (358.5 m^2/g) [18]. It can be explained by partial inaccessibility of the surface of disks, due to their aggregation into stacks, and exposing only the external surface to the adsorbates.

6.3 Aqueous Systems

6.3.1 Chemical Stability

In aqueous media Lap has tendency to degrade (dissolve), particularly under acidic conditions [15, 16, 19, 20]. The observed significant dissolution of Lap below the pH 9 was explained by leaching of magnesium Mg^{+2} ions [15] and H^+ ion attacks [16]. Degradation can be described by the following chemical schema

$$Na_\alpha[Mg_\beta Li_\gamma Si_8 O_{20}(OH)_4] + 12H^+ + 8H_20 \rightarrow \alpha Na^+ + \beta Mg^{2+} + \gamma Li^+ + 8Si(OH)_4$$

The rate of chemical degradation is higher at low pH (below 10), low salt and low Lap concentrations [16, 20]. The process of degradation can be delayed using nitrogen atmosphere that was attributed to the reduction of dissolution of CO_2 from ambient air and formation of carbonic acid [19]. It was also speculated that the octahedral magnesia layers at the edges are more vulnerable for the attack. Increase

in concentration of Lap as well as that of salt resulted in stabilizing effect against degradation [16].

6.3.2 *Surface Charge*

When Lap is dispersed in water it acts as a base, capturing protons from solution with the resulting pH in suspension increasing (Fig. 6.2).

The Lap disks are charged highly heterogeneously. Their faces have large negative charges. The maximum possible negative charge of one disk face is estimated as ≈1500e [21]. The negative charge increases noticeably with an increase of pH from pH ≈ 2 to pH ≈ 8 and is stabilized in basic medium (at pH ≥ 8) [22]. The disks edges have exposed hydroxyl groups, and the edges can show a positive charge with MgOH groups at low pH and a negative charge with MgOH groups at high pH. The point of zero charge at edges was reported to be at pH of approximately 11 [21].

At room temperature (25 °C) and concentration of Lap in deionized water over the range 0.05–0.2% wt the estimations gave ≈−500e and ≈+50e for face and edge charges, respectively [21] (Fig. 6.2). So, surface charge of edges represents ~10% of the total charge. The concentration of negative charges can be evaluated through the cation exchange capacity and it is equal to ≈0.75 meq/g for pH above 8.0 [15].

The experimentally measured values of electrokinetic potential, ζ, were ≈−52 mV [23, 24], ≈−40 to 45 mV [25], ≈−58 mV [26], ≈−45 mV [22] that confirms net negative surface charge of the Lap disks.

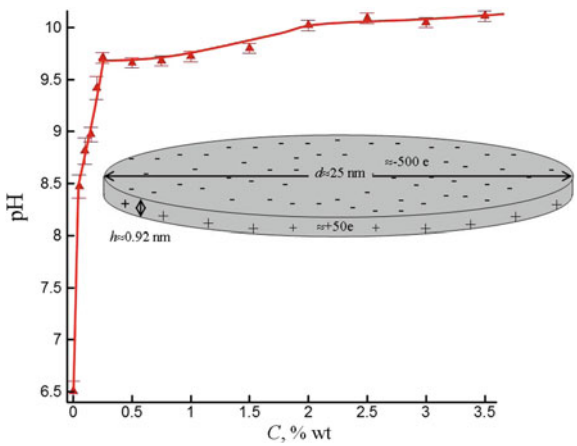

Fig. 6.2 pH versus Lap concentration, *C*, in water. Inset: Schematic presentation of Lap disk (Adopted from [83])

6.3.3 Exfoliation

In powder state disks of Lap are grouped in clusters of tactoids. The process of exfoliation in water includes the swelling and dispersion of these tactoids starting from the highly oriented packed disks, partially oriented disks in a viscoelastic gel and final fragmentation of tactoids with randomly oriented disks [27]. The duration of exfoliation process can depend upon details of suspension preparation (e.g., intensity of stirring), concentration of particles, temperature, pH, presence of electrolytes, and other factors.

Different experimental studies have demonstrated that even in dilute suspensions the fragmentation of the tactoids can be incomplete and a substantial fraction of the platelet aggregates can exist in aqueous suspensions. The tactoid size distributions depend on the concentration of particles, C. For example, a combination of light scattering data with membrane filtration and electron microscopy demonstrated the existence of tactoids containing 2–4 Lap disks with an average diameter of ≈30 nm in suspensions with concentration of $C \leq 0.5\%$ wt [28]. The light scattering data in diluted suspensions ($C = 0.1$–0.2% wt) show that the exfoliation process takes more than 5 h to reach the final state of dispersion [29]. The results evidenced presence of a distribution of individual particles and small oligomers. However, at low concentration, $C = 0.025\%$ wt, the complete fragmentation of the tactoids and dispersion into individual discs was observed in the final state. A transient electrically induced birefringence (TEB) studies revealed the presence of polydisperse particles and increase in the tactoid size with concentration of particles in a concentration range of $C = 0.1$–0.8% wt [30]. The data obtained by means of ultrasound attenuation spectroscopy demonstrated that at relatively high concentration (above 1.5% wt) the fragmentation of the clay tactoids is incomplete and a substantial fraction of the platelet aggregates in suspension still exists [31]. Moreover, at $C = 3\%$ wt the polydispersity of tactoid sizes decreases substantially with age. The exfoliation in a concentration range of $C = 0.5$–3.0% wt has been studied by NMR relaxometry [32]. Surprisingly, more concentrated suspensions demonstrated faster exfoliation dynamics.

6.3.4 Phase Diagram

Aqueous suspensions of Lap disks exhibit a very complex aging dynamic, non ergodic arrested states, and rich phase diagrams [2, 33, 34]. Such behavior reflects the high shape anisotropy of disks and presence of competing attractive and repulsive interactions between charged faces and edges.

The phase diagram of Lap has been extensively discussed in the literature (for a review see [33]). In general, it can be specified in terms of three variables: concentration of Lap, C, concentration of ionic component, C_i, and time of gelling (aging),

t_g. The recent knowledge on the phase diagram and aging in aqueous suspensions of Lap are summarized in the Fig. 6.3.

In salt-free water conditions ($C_i < 10^{-4}$ M) with increase in disk concentration, the four main states with different aging time were observed (Fig. 6.3a):

- mixed state of separated sol (disk poor) and gel (disk rich) phases ($C < 1\%$ wt),
- stable gel, equilibrium gel ($1\% < C < 2\%$ wt),
- repulsive glass or Wigner glass ($2\% < C < 3\%$ wt), and
- nematic gel, ordered phase ($C > 3\%$ wt).

The presence of strong correlations in suspensions even at small concentrations can reflect the shape anisotropy of disks and presence electrical double layers around disks of Lap. These correlations can be expected for critical volume concentrations above [35]

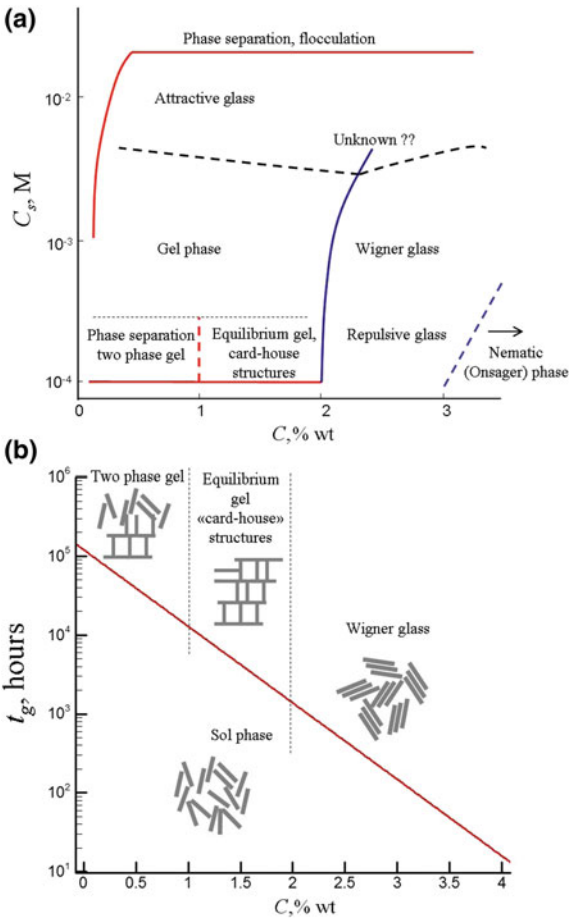

Fig. 6.3 Phase diagram (**a**) and aging (**b**) of aqueous suspensions of Lap (Schematic presentations adopted from [33, 37, 38])

$$\varphi^* \approx 0.64 \frac{3h}{2d(1+2\lambda/d)} \approx \frac{0.96}{a(1+2\lambda/d)},$$

where the value of 0.64 corresponds to the volume fraction of random dense packing of spherical particles, a is the aspect ratio and λ is the Debye screening length. This formula was obtained using the excluded volume considerations and for Lap ($a \approx 25$) it predicts $\varphi^* \approx 3.5\%$ v ($C^* \approx 8.4\%$ wt) at small concentration of electrolyte (in salt-free water conditions, $C_i < 10^{-4}$ M, i.e., $\lambda \approx d$) and $\varphi^* \approx 1.2\%$ v ($C^* \approx 3\%$ wt) at high concentration of electrolyte (i.e., at $\lambda \approx 0$).

The experiments revealed that at small concentrations of Lap in water, $C < 1\%$ wt, the gel phase is non-equilibrium and with the time it separates into two zones [36]. The upper zone phase is transparent and is depleted with particles whereas the bottom one is cloudy and is enriched with particles. The volume of bottom phase is proportional to the concentration C, and at $C \geq 1\%$ wt the bottom phase completely occupies the total volume [37]. Accounting for its stability, the phase in the concentration range $1\% < C < 2\%$ wt was called equilibrium gel.

The processes of structural aging (gelling or glass formation) may be rather long lasting and strongly depend upon the concentration of Lap [38]. At $C < 1\%$ wt the process of separation can take months and years (Fig. 6.3b). The gelling time, t_a, increases noticeably as the concentration of Lap, C, decreases. For example, for $C = 2\%$ wt, $t_g \approx 1500$ h (≈63 days), for $C = 2.8\%$ wt, $t_g \approx 200$ h (≈8.3 days), for $C = 3.2\%$ wt, $t_g \approx 97$ h (≈4 days), and extrapolation gives for $C = 4.0\%$ wt, $t_g \approx$ 17 h.

At higher concentrations (above 3–4% wt) the formation of nematic phase with parallel orientation of disks is expected. Nematic ordering has been predicted in the 40s by Onsager's theory [39]. It was explained using purely entropic reasons. The theory predicted the first order nematic/isotropic transition, i.e., with the phase coexistence and jump of the order parameter.

Figure 6.4 presents a phase diagram for the hard disk fluid obtained by the numerical solutions of the Onsager virial approximation theory [40]. Monte Carlo (MC) simulations also evidence a transition to the nematic phase for the particle number density above $\rho_n \approx 4/d^3$ [41–43]. It corresponds to the volume fraction of $\varphi_n \approx \pi/a$. For Lap disks ($a \approx 25$) in the absence of electrostatic interactions, disks should undergo the isotropic to nematic transition at $\varphi_n \approx 12.6\%$ v (26.7 wt).

However, the various kinetically trapped and liquid crystalline states were realized in Lap suspensions at the significantly smaller concentrations ($C > 2$–3% wt). For example, the macroscopically oriented domains of the nematic phase were grown by slowly drying isotropic suspensions of Lap [44]. Viewed between crossed polarizers, the concentrated gels at $C = 2\%$ wt shown optical birefringence with texture typical for nematic phase. The formation of such phase at $C > 3\%$ wt was also experimentally confirmed by birefringence studies [45]. Small-angle X-ray scattering (SAXS) experiments allowed determine value of order parameter, $S = 0.55$, for oriented samples of Lap ($C = 2\%$ wt) obtained by slow evaporation [46]. The existence of nematic-like orientational correlations in this low density bonded networks can reflect significance of the directional face-edge attractions [33].

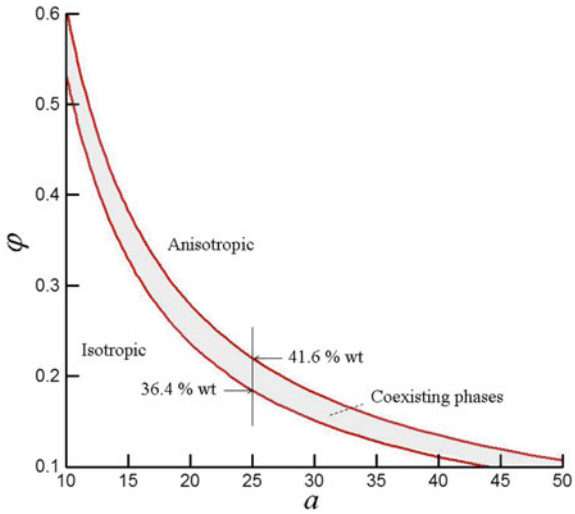

Fig. 6.4 Volume fraction, φ, versus the aspect ratio of disks, a. At a given aspect ratio, a, an increase in the volume fraction of the disks, φ, corresponds to the transition from the isotropic phase through the coexistence region to the anisotropic phase with nematic ordering (Adopted from [40]). Here, the values of weight fractions for Lap disks with $a \approx 25$ are shown

The aging dynamics and time of transition from a liquid phase to an arrested state can depend on the values of C and C_i, and even H/D isotopic substitution in water [47]. Addition of ionic components intensifies the aging and decreases the time of transition into the arrested state. For example, addition of NaCl accelerated aggregation and suspensions became turbid even at low concentrations of Lap (0.05–02% wt) [48]. The formation of glasses, strong and weak gels with prevailing edge-to-face or face-to-face contacts and aging in different arrested states in dependence of Lap content, electrolyte concentration and pH have been recently discussed in details [3].

For description of structure of aqueous Lap suspensions, different models based on formation of perpendicular edge-to-face (so-called T bonds) and parallel face-to-face (so-called partially overlapped configurations) contacts were proposed [49, 50] (Fig. 6.5). The T bonds form between positive and negative charges on the edges and

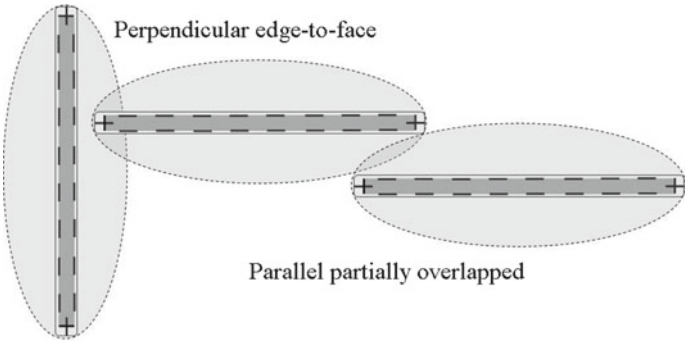

Fig. 6.5 Perpendicular edge-to-face and parallel face-to-face contacts in aqueous suspensions of Lap [49, 50]

faces, respectively. Monte Carlo simulations have shown that the disks tend to form wormlike elongated clusters, connected by T bonds, even at diluted suspensions [45].

In the equilibrium gel (at $1\% < C < 2\%$ wt), the T-bonded clusters of disks organize during aging into a spanning network with a "house-of-cards" structure. At concentrations above 2% wt more rapid formation of glassy state dominated by repulsive interactions was observed [33]). Particularly, 3% wt suspension arrested as a repulsive Wigner glass in a few days. In this state the electrostatic repulsion can originate formation of the partially overlapped configurations that hamper formation of T bonds.

6.3.5 Anomalous Interfacial Structures

The various examples of anomalous interfacial structures realized in aqueous suspensions of Lap have been demonstrated [51–53]. By the optical birefringence [51] and light scattering [52] techniques the presence of the induced nematic-like ordering was observed near the Lap suspension-air interface. In concentrated suspensions (3% wt), the ordering propagated into the bulk phase for long distances (of the order of 0.5 mm) [52]. Dilution of the concentrated suspensions destroyed the ordering. This effect was explained by the impact of Lap on the surface energy of the water-air interface [51]. It was speculated that the Lap particles could be repelled from the water-air interface with formation of depleted layers. Similar effects of exclusion of platelets of montmorillonite and bentonite from the air–water interface were also observed [54]. Colloid partitioning at gas–water interfaces can be explained by the negative charge of the air–water interface attributed to hydrogen bonding of hydroxyl ions to interfacial water molecules. The water-air is characterized by rather high negative zeta potential, $\zeta \approx -64$ mV [54], and the surface exclusion can be explained by strong repulsion between the negatively charged Lap faces and similarly charged water-air interface [52].

The orientational order of Lap disks near the upper air–water interface was observed in concentrated suspensions ($C = 3\%$ wt) when a concentration gradient is imposed through water evaporation [55]. The birefringence in samples was explained by plastic deformations of the colloidal glass in response to compression caused by evaporation. Recent Monte Carlo simulations of evaporation of suspensions of anisotropic particles evidenced about tendency of particle ordering in the interface zone [56].

The anomalous self-organization in aqueous suspensions of Lap disks near the gold surface was revealed using the surface plasmon resonance technique [53]. The changes in an effective refractive index at the Au/aqueous Lap interface were precisely estimated at the Lap concentration over the range $C = 1$–4% wt. The data evidenced the formation of depleted Lap architecture with anomalously small effective value of refractive index. Such anomaly can reflect the repelling of hydrated Lap disks from the gold surface. Moreover, the properties of water in depleted interfacial layer between the bulk Lap suspension and gold surface can be greatly affected by

competitive interactions between water molecules and gold/laponite surfaces. The significant impacts of both the gold [57] and Lap [58] surfaces on the interfacial structure of water have been reported. For example, X-ray absorption spectroscopy tests evidenced that near the gold surface the coordination of water molecules and structure of hydrogen bonds can be strongly distorted [57]. Neutron scattering tests in both liquid and arrested states of Lap aqueous suspensions evidenced a greater degree of orientational and translational order and higher local density compared to pure bulk water in the interfacial layers [58, 59]. This order maps into the periodicity of crystalline structure of Lap. However, no significant dependence of water structure on the Lap concentration and age was observed. Moreover, no indication of strong hydrogen bonding between water and Lap was found, and this can reflect a hydrophobic-like character of the surface of Lap.

6.3.6 Binary Aqueous Systems

Behavior of Lap disks in binary aqueous alcohol systems was investigated using dynamic laser light scattering and measurements of zeta potential, viscosity, and surface tension [52, 60]. Introduction of alcohols (methanol, ethanol and propanol) promoted colloidal aggregation of Lap disks and formation of clusters with the size of hundreds of nanometers. It was speculated that these clusters could be formed through face-edge electrostatic contacts. Universal power law scaling of physical properties such as zeta potential, effective aggregate size, viscosity and surface tension versus the relative solvent polarity was observed [52].

Viscosimetry, Raman spectroscopy and image analysis by transmission electron microscopy were used to characterize behavior of Lap disks (0.3% wt) in binary aqueous ionic liquid systems [61]. Spontaneous liquid–liquid phase separation under gravity into a Lap-poor (upper) and Lap-rich (bottom) phases was observed. The observed phase separation was a surface induced phenomenon (the surface exclusion of Lap particles) at the water–air interface.

6.3.7 Interactions with Surfactants

The interactions of Lap disks in aqueous suspensions with different surfactants, e.g., CTAB [26, 62], CTAC [63], DODAB [64], DODAC [65] and Brij [66] have been studied. The structural formulas of these surfactants are presented in Fig. 6.6.

As for cationic surfactants CTAB/CTAC and DODAB/DODAC, their polar parts strongly interact with negatively charged faces of Lap disks. Typically, at low concentrations of the surfactants, C_s, (much below of the monolayer coverage of Lap disks) the hydrophobic shells are formed on the surface of disks. For example, adsorption studies of CTAC on the surface of Lap in 1% wt suspension revealed that up to 50% CEC coverage of Lap, stable suspensions are formed [63]. Similar observations were

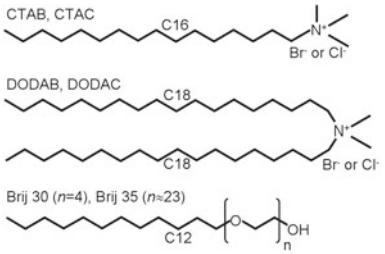

Fig. 6.6 Structural formulas of different surfactants: CTAB/CTAC (hexadecyltrimethylammonium bromide/chloride, $C_{19}H_{42}N^+Br^-/C_{19}H_{42}N^+Cl^-$), DODAB/DODAC (dimethydioctodecylammonium bromide/chloride, $C_{38}H_{80}N^+Br^-/Cl^-$), Brij 30 (polyoxyethylene(4)lauryl ether, $C_{12}H_{25}(OCH_2CH_2)_4OH$), and Brij 35 (polyethylene glycol dodecyl ether ($C_{12}H_{25}(OCH_2CH_2)_nOH$, $n \sim 23$)

made using different alkyltrimethylammonium bromide surfactants [67]. The studies by small-angle neutron scattering (SANS) and dynamic light scattering (DLS) have revealed that Lap disks can be covered by CTAB on both faces [62]. Moreover, CTAB/clay complex in water retains disk morphology.

The increase in surfactant concentration caused fast aggregation of Lap disks and led to precipitation of the particles (due to neutralization of the anionic charge) [26]. The separation of suspensions into clear upper (U) and turbid bottom (B) layers was observed at a certain threshold concentration of CTAB (≈0.3 CEC, where CEC is the cation exchange capacity of Lap). Then at large concentration the resuspension and formation of surfactant "double layer" can be observed [63]. The overcharging of the Lap surface by adsorption of different alkyltrimethylammonium bromide surfactants was confirmed by the zeta potential measurements [67]. For example, in 2.0% wt suspension the ζ-potential changed the sign from negative to positive value at CTAB concentration of ≈1 CEC and then it increased with increasing CTAB content [26].

The sedimentation stability and aging of aqueous suspensions of Lap (2% wt) in the presence of CTAB were studied using analytical centrifugation (AC) and dynamic light scattering (DLS) techniques [68]. The DLS data revealed noticeable changes in the aging dynamics of the U layer even at small concentration of CTAB (≈3% CEC). The phenomenon was explained by slow equilibration of CTAB molecules non-uniformly distributed between different Lap disks. Analysis of sedimentation regimes allowed proposing a model of disk interactions in presence of CTAB. In the presence of CTAB, the faces of disks become patchy, partially covered by hydrophobic spots. These spots strongly interact between each other and form hydrophobic contacts (H bonds). Decoration of Lap by CTAB increased hydrophobicity [68] and noticeably influenced the surface charge of Lap disks [69]. Addition of CTAB destabilized the Lap suspensions, and different types of Lap aggregates with three types of contacts between discs could be realized (Fig. 6.7):

- perpendicular edge-to-face contacts between charges (T bonds)
- parallel face-to-face contacts between hydrophobic spots (H bonds)
- mixed T&H bonds.

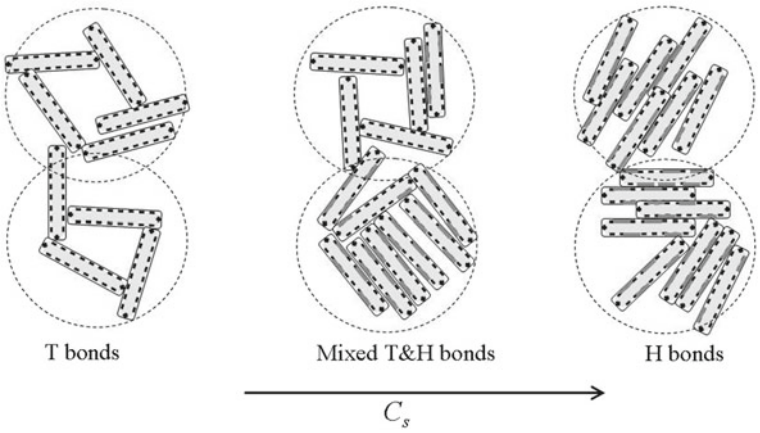

Fig. 6.7 Model of disk configurations in aqueous suspensions of Lap in the presence of CTAB for T, mixed T&H, and H bonds (Adopted from [68])

The face-to-face bonds are particularly important at small concentration of Lap ($\leq$0.5% wt), while suspensions of large Lap concentration (2% wt) contains both edge-to-face and face-to-face bonds [68]. Note that H bonds also hamper formation of T bonds and formation of mixed T-and-H bonds is possible (Fig. 6.7). These aggregates can change considerably in size and composition in dependence on CTAB concentration C_s. It was speculated that observed variety of sedimentation regimes can reflect the competition between T and H bonds and formation of structures with domination of T aggregates in U layers, H aggregates in B layers, and T-and-H aggregates in intermediate layers [68].

Treatment of Lap disks by cationic surfactants with the cations on the surface of disks can be used for preparation of *organically modified* Lap (LapO). Various methods for preparation of LapO have been proposed [65, 70, 71]. Typically, the preparation procedure includes temperature incubation of a mixture of Lap and ionic surfactant in water [72, 73] or in water/propanol solution [64, 74] for a long time (several hours). The quantity of surfactant corresponds to the required surface coverage accounting for the CEC value of Lap. Then the treated Lap disks are cleaned by repeated washing and dried (lyophilized). The incubation was done at room [64, 74–76] and elevated (233–253 K) [17, 65, 72, 73, 77, 78] temperatures. The other details on preparation of LapO can be found in literature (e.g., see [78–80]).

Note that details of preparation procedure and especially incubation time and temperature can be crucial in determination of the characteristics of LapO. Even for very popular CTAB modifiers the mechanism of its adsorption on the surface of Lap disks is rather complex and still unclear [62, 68].

Figure 6.8 present examples of X-ray powder diffraction spectra for untreated and CTAB treated Lap (LapO) samples. At high content of CTAB (four multiples of the Lap CEC) the derived interlayer distances were about 1.26 and 4.71 nm for Lap and LapO samples, respectively [62]. The increase in interlayer distance Δd in

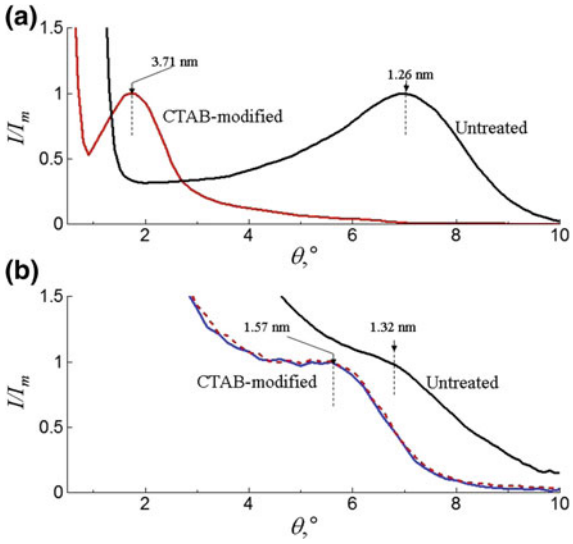

Fig. 6.8 X-ray powder diffraction spectra for untreated and CTAB treated (LapO) samples in powder air-dry state. $T = 298$ K for different CTAB amounts: about four multiples of the Lap CEC (**a**) and one CEC of the Lap CEC (**b**) (Adopted from the data presented in [62, 80] (**b**))

LapO ($\Delta d \approx 3.75$ nm) evidenced that Lap disks can be covered by four multiples of the Lap CEC. At small content of CTAB (one CEC) the increase in interlayer distance Δd was significantly smaller ($\Delta d \approx 0.25$ nm). It corresponds to successful penetration of CTAB into the clay interlayer.

In some works the covalent modification of the edges of Lap with organic groups [81, 82] or anionic surfactants [83–85] was reported. Modification with organic groups allowed affecting the gelation behavior of Lap [82]. Rheological (small amplitude oscillatory shear) and small-angle X-ray scattering techniques were applied to study the effects of anionic surfactants sodium dodecyl sulfate (SDS) [83] and sodium polystyrene sulfonate (PSS-Na) [85] on aqueous Lap suspensions. It was demonstrated that introduction of SDS resulted in acceleration of aging dynamics and increase in the mean distance between Lap disks [83]. For polyelectrolyte surfactant PSS-Na the interactions between adsorbed PSS-Na macroions can affect the structure of suspension [85] (Fig. 6.9). The adding of PSS-Na significantly accelerated the aging of 2.5% wt suspension. The systems were stable against sedimentation, and flocculation was not observed. It was speculated that acceleration of the aggregation may reflect not only a decrease of the Debye length, but also the cross-linking of Lap particles by PSS-Na macroions. Moreover, the adding of PSS-Na induced the transition from a homogeneous Wigner glass state to a gel network with a fractal structure.

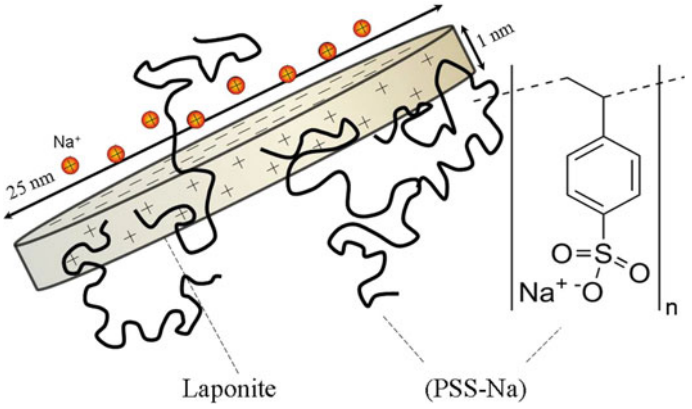

Fig. 6.9 Adsorption of PSS-Na on Lap disks (Adopted from [85])

6.3.8 Interactions with Water Soluble Polymers

Aqueous systems including Lap disks and poly(ethylene glycol/oxide) (PEG/PEO) attract great practical and scientific attention. Both the Lap disks and PEO neutral/non-ionic polymers can be well dispersed in the water. At room temperatures the PEO polymers are soluble in water. This solubility is due to a hydration of the ether oxygens. The PEO is often used as a simple model to simulate colloidal behaviour in aqueous polymer systems. Moreover, the PEO attracts great technological interest for using as lubricant, dispersant, plasticizer, recovery agent of tertiary oils and drag reducers in the flow of water trough ducts and channels [86].

Among promising practical applications we can refer the hydrogels with thermoresponsive sol-gel transition (a mixture of Lap with PEG-based copolymer with a high PEG ratio) [87], transparent hydrogels and films for biomedical applications [88], and shake-gel aqueous mixtures of Lap + PEO [89–92]. Many intriguing properties of the aqueous Lap + PEO systems have been also revealed by small-angle neutron scattering (SANS) [93–98], Raman spectroscopy [99], rheological and dynamic light scattering (DLS) [100–108], and electrokinetic [109] experiments. Detailed SANS studies of the aqueous Lap + PEO systems revealed a weak power law relationship between the adsorbed amount of PEO and its molecular weight ($M_w = (20–965) \times 10^3$ g/mol) [93]. Some fraction of PEO chains were adsorbed on the surface of the Lap (on the edge, as well as the face) and some remained as free chains in solution. The thickness of the polymer layer on the face was much smaller than on the edge, and it remained practically constant over the studied range of Mw, whereas the thickness on the edge grew with a power law dependence on the molecular weight. The critical concentration of PEO chains (for $M_w = 20 \times 10^3$ g mol^{-1}) needed to saturate the Lap surface was estimated through PEO/Lap ratio $X_p = m_p/m_l \approx 0.54$ g/g [110]. It is expected that content of free chains in solution increases above this critical concentration. Further studies by SANS for PEO with molecular weights within the

range of $M_w = 200$–35,000 g/mol revealed that the apparent radius of gyration of the hybrid aggregates increases in the region of low M_w ($\leq$400 g/mol) and decreases for high M_w polymers [94]. The results evidenced the presence of attractive interactions between Lap particles for PEO with small M_w and repulsive for PEO with large M_w. Moreover, the M_w influenced the thickness of the adsorbed PEO and the fraction of the PEO in the interfacial shells around the Lap particles was nearly independent of M_w.

Impact of PEO on the aggregation of Lap disks has been investigated [102]. With increase of M_w, the aggregation rate went through a minimum at $M_w \approx 1000$ g/mol. The decrease of the aggregation rate was explained by an increase in the activation energy for face–edge association due to steric hindrance of adsorbed PEO. The increase of the aggregation at $M_w \approx 1000$ g/mol was explained by bridging effects. The formation of lamellar structures (tactoids) by PEG bridges was suggested [97, 98]. In the tactoids the face-to-face Lap structures are realized.

Effect of PEO on aging dynamics of Lap suspensions was studied [101–103, 111–113]. For 2% wt Lap concentration the retardation of aging was observed at $M_w <$ 83,000 g/mol as a result of steric effects, but faster aging for larger M_w was explained by polymer bridging effects [101]. The slowing down of the aging dynamics with increasing PEO concentration ($M_w = 2 \times 10^5$ g mol^{-1}) was also explained by steric stabilization [114]. The strong effects of concentration of PEO and its molecular mass on the colloidal behavior and aging dynamics in the aqueous Lap + PEO systems were also revealed [103, 110].

The electrokinetic data can give useful information on the effective charge of Lap particles, electrostatic interaction between them and the effects caused by the adsorbed layers of PEO. However, the existing data on ζ-potential in aqueous Lap + PEO systems are not numerous. In the aqueous systems with 0.01% wt Lap (Laponite XLG) and different concentrations of PEO (0–0.2% wt, $M_w = 5100$ g/mol), the value of ζ in absence of PEO was $\zeta \approx -35$ mV, it decreased with adding of PEO, an overcharging was observed at PEO/Lap $\approx$1.25 and the value of ζ became positive at higher concentration of PEO [115]. The overcharging was in correspondence with observed dispersion stability evaluated by the turbidity at 500 nm as a function of PEO/Lap ratio. In later study the ζ-potential in the aqueous systems with 1% wt Lap and different concentrations of PEO (0–4% wt, $M_w = 10^4$ g/mol) was investigated [109]. In absence of PEO the measured value was $\zeta \approx -30$ mV and with increased PEO content the negative charge of Lap particles decreased. It was explained by covering of Lap surface by adsorbed PEO chains.

6.4 Nonaqueous Systems

The non-aqueous systems including the Lap particles represent interest for application in inks, paints, emulsions for biomedical applications, and cosmetic formulations [116]. However, Lap particles are practically non-dispersible in organic media. The dispersing of Lap disks in non-aqueous systems can be realized through the

adsorption of surfactants or polymers, and for this purposes the organo-modified Lap particles are commonly used. The studied dispersing media include simple organic solvents, polymers and liquid crystalline systems.

6.4.1 Organic Solvents

Rheometry and small-angle X-ray scattering were applied to study the stability of organo-modified Lap (treated by DODAB, polymer stabilizer SAP or their combination) in toluene [17]. The DODAB-treated disks formed gels at 2% wt, for SAP-treated disks long term stability (for months) was noted, and for DODAB + SAP-treated disks the unstable suspensions were obtained. For the DODAB-treated disks the basal layer spacings were 0.22 nm and 0.48 nm in dry powder state and in toluene, respectively. The structural and physical properties of the DODAB-treated Lap in different solvents (1-octanol, 1-dodecanol, toluene, xylene, propylene carbonate, and benzyl alcohol) were studied using small-angle X-ray scattering [70]. In the dry powder state, the DODAB molecules were densely packed between the Lap sheets. In organic solvents, the disks formed small stacks of disks (≈1.1–2.1 disks) with different basal spacing for each solvent. The maximum basal spacing (0.395 nm) was in non-polar xylene and minimum was in polar octanol (0.342 nm). It is explained by different swelling ability of the nonpolar region of the surfactant molecules in dependence of solvent polarity.

6.4.2 Non-ionic Polymers

Poly(ethylene glycol/oxide) (PEG/PEO) and Lap composites have been considered as promising materials with applications as Li ion conductors [117, 118] and for production of functional flexible and transparent hybrid films with good flame-resistant and fire-shielding properties [119, 120]. The composites can be prepared by direct introduction of Lap into polymers according to the melt-compounding procedure [79] or using the solution preparation and air drying [117, 118, 121] or freeze-drying [122] techniques.

The unusual multilayered structure on the micron length scale of transparent PEO and Lap composite films with high orientation of Lap disks and suppressed polymer crystallinity was observed [121]. These films with high Lap contents may be used as precursors for ceramic materials or microelectronics. In order to enhance the compatibility between Lap and PEO, different approaches were attempted. The disks can be organically modified with low molar mass PEG components with different end groups [79]. It was demonstrated that the composites based on the pure Lap as well as the modified LapO display an intercalated structure. In presence of Lap and LapO the inhibition of crystallization was observed. The composites based on the modified LapO displayed good thermal stability. In the other way, the endo-alkoxysilyl PEG

derivatives were used to modify silanol groups on the sidewalls of Lap [119, 123]. The cross linking of Lap by silanol agents allowed producing of flexible films with high solvent resistance and a disco-nematic liquid-crystalline-like structure. Effects of Lap disks modifications on dispersion of Lap in PEO matrix has been investigated [122]. At the initial step the Lap disks were protected with an adsorbed or a grafted layer of PEO chains, then freeze-dried, and finally introduced into the PEO-10,000 matrix in the molten state. The state of Lap dispersions was dependent upon the surface coverage of the disks, and it was better for saturated particles bearing grafted chains rather than adsorbed ones.

The structure and properties of composites based on PEG-1000 doped with LapO treated by CTAB were studied in detail using X-ray diffraction, differential scanning calorimetry (DSC), and impedance spectroscopy [124]. The crystalline reflexes were absent for PEG-1000 + LapO composite. It evidences the complete exfoliation of LapO disks inside PEG-1000 matrix. The both DSC and X-ray methods gave rather similar results about degree of crystallinity χ. The introduction of Lap resulted in disordering, i.e., a noticeable decrease in χ. It was explained by the steric restrictions created by a layered silicate surface. It can be explained by the deep integration and exfoliation inside PEG of LapO.

The percolation behavior of polypropylene glycol (PPG-400) doped with Lap and LapO and multiwalled carbon nanotubes (CNTs) was studied by different experimental methods [73]. The Lap and LapO displayed different affinity to PPG-400. The data have evidenced limited PPG integration inside Lap and complete exfoliation of LapO stacks in a PPG matrix. The percolation was observed at concentration of nanotubes of $C_n \approx 0.2\%$ wt for PPG-400 + CNT + LapO systems. The observed behaviour was attributed to the effects exerted by LapO on the size of CNT aggregates, state of their dispersion and homogeneity of their spatial distribution [73].

The different models have been proposed for description of structure of intercalated PEO inside Lap [118]. In the helical structure model, the crown-ether-like association between the interlayer cations and the PEO oxygen atoms is assumed. The other model suggests that the PEO chains are organized in two extended trans-layers parallel to the silicate surface.

6.4.3 Liquid Crystalline Systems

In recent years, the great interest was attracted by LC colloids on the base of Lap disks. For example, the attractive applications of LC colloids include the reversible electro-optical memory effects [125], the effect of the widening of the blue phase range induced by LapO disks dispersed in a chiral liquid crystal CE8 [126], and the effect of stabilization of suspensions of carbon nanotubes (CNTs) in liquid crystalline media in presence of LapO [72].

Covering of Lap disks with surfactant stabilizing layer allows obtaining liquid crystalline (LC) colloids with good dispersion and long-term stability [17]. Small angle X-ray scattering (SAXS) has revealed that organically modified disks of Lap

(LapO) can be well delaminated in a nematic liquid crystal 5CB (4-*n*-pentyl-4′-cyanobiphenyl, K15) [64, 74, 127]. It was demonstrated that suspensions consist of mixtures of stacked and single disks. For example, in 0.1% wt suspensions the stacks include ≈2 plates [127]. All particles in the suspensions (stacked and single disks) form large-scale aggregates. The effects of LapO on the isotropic–nematic phase transition temperature in the 5CB were ascribed to the surface anchoring and confinement effects [128]. In external magnetic fields the effects of LapO alignment were insignificant. The effect of the widening of the blue phase range (by a factor of two) induced by LapO disks dispersed in a chiral liquid crystal CE8 have been observed [126]. The mechanism of stabilization accounting for the integration of the trapped disks on LC dislocations was discussed. The disks of LapO has been used to stabilize suspensions of carbon nanotubes (CNTs) in liquid crystalline media [72]. It was demonstrated that the LapO disks cover CNTs and hamper their aggregation.

The nematic (5CB) and cholesteric (the mixture of 5CB with chiral M5) liquid crystals (LC) doped with LapO treated by (CTAB) were studied by differential scanning calorimetry (DSC), X-ray diffraction (XRD), microscopic image analysis, and optical density measurements [80]. The "cold" and "hot" methods were applied for obtaining of LapO. The platelets of original Lap were modified by ion-exchange reactions with the surfactant CTAB for 6 h at $T = 293$ K ("cold" sample) and $T = 253$ K ("hot" sample). The data of DSC and XRD for nematic 5CB + LO compositions evidenced the presence of strong interactions between 5CB molecules and LapO disks. The better exfoliation for LaO was obtained by "cold" method. The obtained data evidenced the presence of strong interactions between LC (5CB and 5CB + M5) media and LapO particles. The XRD patterns of the 5CB + LapO samples evidenced the presence of stratification into the phase enriched by smectite disks and phase enriched by 5CB. The impact of doping on the nematic-isotropic phase transition temperature was rather small but clearly noted (≈0.05–0.1 °C). The observed optical behavior for cholesteric compositions reflects combination of initial perturbation of cholesteric matrix by LapO particles and initiation of formation of topological defects at small concentration of LapO, $C < 0.1\%$ wt,as well as the partial trapping of LapO by large scale oily streaks at higher concentrations, $C \geq 0.1\%$ wt.

6.5 Conclusions

Critical analysis of numerous experimental data, both taken from literature and obtained with participation of the authors, on organization of nano-disks of Laponite® in soft colloidal systems has been presented. These studies have emerged as vividly developing and highly promising. Exfoliated discs of Lap can be efficiently distributed within molecular structures of different matrices with controlled degrees of homogeneity and ordering, leading to formation of materials with sufficiently stable physical and physico-chemical characteristics.

For example, the current challenges in the field include different biomedical applications. We can refer recent comprehensive reviews on Lap-based materials

- bioactivity and applications for regenerative medicine and biomaterial design [129],
- different biomedical applications (targeted drug delivery, imaging, photothermal therapy, tissue engineering and regenerative medicine) [130],
- stimuli responsive hydrogels [131],
- injectable hydrogels for cartilage tissue engineering [132],
- hydrogel matrices for biorecognition and biosensors for clinical diagnosis and food analysis [133–135].

The further studies acquired through investigations of optimum compositions and appropriate preparation conditions will be base for the wide applications of nanostructured Lap-based materials in future.

Acknowledgements This work was partially supported by the funding from the National Academy of Sciences of Ukraine, Projects No. 0117U004046 and 43/19-H (NIL).

References

1. B.S. Neumann, *Synthetic Hectorite-Type Clay Minerals,* US patent # 3586478 (1962)
2. S. Jatav, Y.M. Joshi, Phase behavior of aqueous suspension of Laponite: new insights with microscopic evidence. Langmuir **33**, 2370–2377 (2017)
3. M. Pilavtepe, S.M. Recktenwald, R. Schuhmann et al., Macro-and microscale structure formation and aging in different arrested states of Laponite dispersions. J. Rheol. (N. Y. N. Y.) **62**, 593–605 (2018)
4. T.B. Becher, C.B. Braga, D.L. Bertuzzi et al., The Structure–property relationship in LAPONITE® materials: from wigner glasses to strong self-healing hydrogels formed by non-covalent interactions. Soft Matter. **15**, 1278–1289 (2019)
5. X. Huang, H. Shen, J. Sun et al., Nanoscale Laponite as a potential shale inhibitor in water-based drilling fluid for stabilization of wellbore stability and mechanism study. ACS Appl. Mater. Interfaces. **10**, 33252–33259 (2018)
6. F. Liu, G.-C. Jiang, K. Wang, J. Wang, Laponite nanoparticle as a multi-functional additive in water-based drilling fluids. J. Mater. Sci. **52**, 12266–12278 (2017)
7. J.L. Dávila, M.A. d'Ávila, Laponite as a rheology modifier of alginate solutions: physical gelation and aging evolution. Carbohydr. Polym. **157**, 1–8 (2017)
8. S. Mishra, P. Rani, G. Sen, K.P. Dey, Preparation, properties and application of hydrogels: a review, in *Hydrogels* (Springer, 2018), pp. 145–173
9. P. Liu, Z. Peng, Q. Zhang, Nanocomposite hydrogel with varying number of repeating oxyethylene units: adjustable pore structure and thermo-responsibility. React. Funct. Polym. **117**, 43–51 (2017)
10. M. Fatnassi, C.-H. Solterbeck, M. Es-Souni, Clay nanomaterial thin film electrodes for electrochemical energy storage applications. RSC Adv. **4**, 46976–46979 (2014)
11. Anonymous, Laponite. Performance Additives. BYK. Technical Information B-RI 21 (2018)
12. M. Ghadiri, W. Chrzanowski, R. Rohanizadeh, Biomedical applications of cationic clay minerals. RSC Adv. **5**, 29467–29481 (2015)
13. H. Tomás, C.S. Alves, J. Rodrigues, Laponite®: a key nanoplatform for biomedical applications? Nanomed. Nanotechnol. Biol. Med. **14**, 2407–2420 (2018)

14. B. Brunier, N. Sheibat-Othman, M. Chniguir et al., Investigation of four different Laponite clays as stabilizers in pickering emulsion polymerization. Langmuir **32**, 6046–6057 (2016)
15. D.W. Thompson, J.T. Butterworth, The nature of Laponite and its aqueous dispersions. J. Colloid Interface Sci. **151**, 236–243 (1992)
16. R.P. Mohanty, Y.M. Joshi, Chemical stability phase diagram of aqueous Laponite dispersions. Appl. Clay Sci. **119**, 243–248 (2016)
17. E.S.H. Leach, A. Hopkinson, K. Franklin, J.S. van Duijneveldt, Nonaqueous suspensions of Laponite and montmorillonite. Langmuir **21**, 3821–3830 (2005)
18. J.J. Fripiat, M. Letellier, J.M. Cases et al., Comportement microdynamique et thermodynamique de l'eau dans les suspensions argileuses, in *Studies in Surface Science and Catalysis*, ed. by J. Rouquerol, K.S.W. Sing (Elsevier, 1982), pp. 449–477
19. A. Mourchid, P. Levitz, Long-term gelation of Laponite aqueous dispersions. Phys. Rev. E **57**, R4887 (1998)
20. S. Jatav, Y.M. Joshi, Chemical stability of Laponite in aqueous media. Appl. Clay Sci. **97**, 72–77 (2014)
21. S.L. Tawari, D.L. Koch, C. Cohen, Electrical double-layer effects on the Brownian diffusivity and aggregation rate of Laponite clay particles. J. Colloid Interface Sci. **240**, 54–66 (2001)
22. M. Manilo, N. Lebovka, S. Barany, Characterization of the electric double layers of multi-walled carbon nanotubes, Laponite and nanotube + Laponite hybrids in aqueous suspensions. Colloids Surf. A Physicochem. Eng. Asp **462**, 211–216 (2014)
23. J. Labanda, J. Llorens, Influence of sodium polyacrylate on the rheology of aqueous Laponite dispersions. J. Colloid Interface Sci. **289**, 86–93 (2005)
24. J. Labanda, J. Sabaté, J. Llorens, Rheology changes of Laponite aqueous dispersions due to the addition of sodium polyacrylates of different molecular weights. Colloids Surf. A Physicochem. Eng. Asp **301**, 8–15 (2007)
25. A.Y. Huang, J.C. Berg, High-salt stabilization of Laponite clay particles. J. Colloid Interface Sci. **296**, 159–164 (2006)
26. S. Zhang, Q. Lan, Q. Liu et al., Aqueous foams stabilized by Laponite and CTAB. Colloids Surf. A Physicochem. Eng. Asp **317**, 406–413 (2008)
27. J.D.F. Ramsay, S.W. Swanton, J. Bunce, Swelling and dispersion of smectite clay colloids: determination of structure by neutron diffraction and small-angle neutron scattering. J. Chem. Soc., Faraday Trans. **86**, 3919–3926 (1990)
28. L. Rosta, H.R. Von Gunten, Light scattering characterization of laporite sols. J. Colloid Interface Sci. **134**, 397–406 (1990)
29. T. Nicolai, S. Cocard, Light scattering study of the dispersion of Laponite. Langmuir **16**, 8189–8193 (2000)
30. A. Bakk, J.O. Fossum, G.J. da Silva et al., Viscosity and transient electric birefringence study of clay colloidal aggregation. Phys. Rev. E **65**, 21407 (2002)
31. S. Ali, R. Bandyopadhyay, Use of ultrasound attenuation spectroscopy to determine the size distribution of clay tactoids in aqueous suspensions. Langmuir **29**, 12663–12669 (2013)
32. A. Karpovich, M. Vlasova, N. Sapronova et al., Exfoliation dynamics of Laponite clay in aqueous suspensions studied by NMR relaxometry. Orient. J. Chem. **32**, 1679–1683 (2016)
33. B. Ruzicka, E. Zaccarelli, A fresh look at the Laponite phase diagram. Soft Matter **7**, 1268–1286 (2011)
34. H. Iwase, T. Ogura, H. Sakuma et al., Structural investigation of hectorite aqueous suspensions by dielectric microscopy and small-angle neutron scattering coupling with rheological measurement. Appl. Clay Sci. **157**, 24–30 (2018)
35. S. Jogun, C.F. Zukoski, Rheology of dense suspensions of platelike particles. J. Rheol. (N. Y. N. Y.) **40**, 1211–1232 (1996)
36. B. Ruzicka, E. Zaccarelli, L. Zulian et al., A phase separation in diluted Laponite suspensions: evidence of empty liquid and equilibrium gel states. ArXiv e-prints (2010)
37. W.K. Kegel, H.N.W. Lekkerkerker, Colloidal gels: clay goes patchy. Nat. Mater. **10**, 5 (2011)
38. J. Yu, O. Andersson, G.P. Johari, Effects of nanometer-size Laponite disks on thermal conductivity and specific heat of water and ice, and the gelation time. Colloid Polym. Sci. **293**, 901–911 (2015)

39. L. Onsager, The effects of shape on the interaction of colloidal particles. Ann. N. Y. Acad. Sci. **51**, 627–659 (1949). https://doi.org/10.1111/j.1749-6632.1949.tb27296.x
40. P.A. Forsyth, S. Marčelja, D.J. Mitchell, B.W. Ninham, Onsager transition in hard plate fluid. J. Chem. Soc. Faraday Trans. 2 Mol. Chem. Phys. **73**, 84–88 (1977)
41. R. Eppenga, D. Frenkel, Monte Carlo study of the isotropic and nematic phases of infinitely thin hard platelets. Mol. Phys. **52**, 1303–1334 (1984)
42. J.A.C. Veerman, D. Frenkel, Phase behavior of disklike hard-core mesogens. Phys. Rev. A **45**, 5632 (1992)
43. H.H. Wensink, H.N.W. Lekkerkerker, Phase diagram of hard colloidal platelets: a theoretical account. Mol. Phys. **107**, 2111–2118 (2009)
44. J.-C.P. Gabriel, C. Sanchez, P. Davidson, Observation of nematic liquid-crystal textures in aqueous gels of smectite clays. J. Phys. Chem. **100**, 11139–11143 (1996)
45. M. Dijkstra, J.-P. Hansen, P.A. Madden, Statistical model for the structure and gelation of smectite clay suspensions. Phys. Rev. E **55**, 3044 (1997)
46. B.J. Lemaire, P. Panine, J.C.P. Gabriel, P. Davidson, The measurement by SAXS of the nematic order parameter of Laponite gels. EPLEurophys. Lett. **59**, 55 (2002)
47. F.A.M. Marques, R. Angelini, G. Ruocco, B. Ruzicka, Isotopic effect on the gel and glass formation of a charged colloidal clay: Laponite. J. Phys. Chem. B **121**, 4576–4582 (2017)
48. N. Taco, C. Sthane, Structure of gels and aggregates of disk-like colloids. Eur. Phys. J. E **5**, 221–227 (2001)
49. B. Jonsson, C. Labbez, B. Cabane, Interaction of nanometric clay platelets. Langmuir **24**, 11406–11413 (2008)
50. A. Shahin, Y.M. Joshi, Physicochemical effects in aging aqueous Laponite suspensions. Langmuir **28**, 15674–15686 (2012)
51. A. Shahin, Y.M. Joshi, S.A. Ramakrishna, Interface-induced anisotropy and the nematic glass/gel state in jammed aqueous Laponite suspensions. Langmuir **27**, 14045–14052 (2011)
52. R.K. Pujala, H.B. Bohidar, Kinetics of anisotropic ordering in Laponite dispersions induced by a water-air interface. Phys. Rev. E **88**, 52310 (2013)
53. M. Manilo, P. Boltovets, B. Snopok et al., Anomalous interfacial architecture in Laponite aqueous suspensions on a gold surface. Colloids Surf. A Physicochem. Eng. Asp **520**, 883–891 (2017)
54. J. Wan, T.K. Tokunaga, Partitioning of clay colloids at air–water interfaces. J. Colloid Interface Sci. **247**, 54–61 (2002)
55. E.L. Hansen, S. Jabbari-Farouji, H. Mauroy et al., Orientational order in a glass of charged platelets with a concentration gradient. Soft Matter **9**, 9999–10004 (2013)
56. N.I. Lebovka, Y.Y. Tarasevich, N.V. Vygornitskii, Vertical drying of a suspension of sticks: Monte Carlo simulation for continuous two-dimensional problem. Phys. Rev. E **97**, 22136 (2018)
57. J.J. Velasco-Velez, C.H. Wu, T.A. Pascal et al., The structure of interfacial water on gold electrodes studied by x-ray absorption spectroscopy. Science **80**, 1259437 (2014)
58. M.A. Ricci, V. Tudisca, F. Bruni et al., The structure of water near a charged crystalline surface. J. Non Cryst. Solids **407**, 418–422 (2015)
59. V. Tudisca, F. Bruni, E. Scoppola et al., Neutron diffraction study of aqueous Laponite suspensions at the NIMROD diffractometer. Phys. Rev. E **90**, 32301 (2014)
60. N. Pawar, H.B. Bohidar, Hydrophobic hydration mediated universal self-association of colloidal nanoclay particles. Colloids Surf. A Physicochem. Eng. Asp **333**, 120–125 (2009)
61. N. Joshi, K. Rawat, R.K. Pujala, H.B. Bohidar, Ionic liquid induced surface exclusion and anomalous first-order phase transition in Laponite dispersions. J. Mol. Liq. **207**, 177–184 (2015)
62. H.J.M. Hanley, C.D. Muzny, B.D. Butler, Surfactant adsorption on a clay mineral: application of radiation scattering. Langmuir **13**, 5276–5282 (1997)
63. T. Nakamura, J.K. Thomas, Formation of surfactant double layers on Laponite clay colloids. Langmuir **3**, 234–239 (1987)

64. C. Pizzey, S. Klein, E. Leach et al., Suspensions of colloidal plates in a nematic liquid crystal: a small angle x-ray scattering study. J. Phys.: Condens. Matter **16**, 2479 (2004)
65. S. Borsacchi, M. Geppi, L. Ricci et al., Interactions at the surface of organophilic-modified Laponites: a multinuclear solid-state NMR study. Langmuir **23**, 3953–3960 (2007)
66. C.-F. Li, S.-Y. Zhang, J. Wang et al., Interactions between Brij surfactants and Laponite nanoparticles and emulsions stabilized by their mixtures. Acta Chim. Sin. **66**, 2313–2320 (2008)
67. Q. Liu, S. Zhang, D. Sun, J. Xu, Foams stabilized by Laponite nanoparticles and alkylammonium bromides with different alkyl chain lengths. Colloids Surf. A Physicochem. Eng. Asp **355**, 151–157 (2010)
68. V. Savenko, L. Bulavin, M. Rawiso et al., Sedimentation stability and aging of aqueous dispersions of Laponite in the presence of cetyltrimethylammonium bromide. Phys. Rev. E **88**, 52301 (2013)
69. M.V. Manilo, N. Lebovka, S. Barany, Combined effect of cetyltrimethylammonium bromide and Laponite platelets on colloidal stability of carbon nanotubes in aqueous suspensions. J. Mol. Liq. **235**, 104–110 (2017)
70. J. Connolly, J.S. van Duijneveldt, S. Klein et al., Effect of surfactant and solvent properties on the stacking behavior of non-aqueous suspensions of organically modified clays. Langmuir **22**, 6531–6538 (2006)
71. Y. Lambert, D.R. Le, Y. Mugnier et al., Second-harmonic generation imaging of LiIO 3/Laponite nanocomposite waveguides. Jpn. J. Appl. Phys. **45**, 7525 (2006)
72. O. Yaroshchuk, S. Tomylko, O. Kovalchuk, N. Lebovka, Liquid crystal suspensions of carbon nanotubes assisted by organically modified Laponite nanoplatelets. Carbon N. Y. **68**, 389–398 (2014)
73. E.A. Lysenkov, N.I. Lebovka, Y.V. Yakovlev et al., Percolation behaviour of polypropylene glycol filled with multiwalled carbon nanotubes and Laponite. Compos. Sci. Technol. **72**, 1191–1195 (2012)
74. C. Pizzey, J. Van Duijneveldt, S. Klein, Liquid crystal clay composites. Mol. Cryst. Liq. Cryst. **409**, 51–57 (2004)
75. W. Li, L. Yu, G. Liu et al., Oil-in-water emulsions stabilized by Laponite particles modified with short-chain aliphatic amines. Colloids Surf. A Physicochem. Eng. Asp **400**, 44–51 (2012)
76. T.J. Bruno, A. Lewandowska, F. Tsvetkov et al., Wall-coated open-tubular column chromatography on an organo–clay stationary phase. J. Chromatogr. A **973**, 143–149 (2002)
77. P.A. Mirau, J.L. Serres, D. Jacobs et al., Structure and dynamics of surfactant interfaces in organically modified clays. J. Phys. Chem. B **112**, 10544–10551 (2008)
78. B. Wang, M. Zhou, Z. Rozynek, J.O. Fossum, Electrorheological properties of organically modified nanolayered Laponite: influence of intercalation, adsorption and wettability. J. Mater. Chem. **19**, 1816–1828 (2009)
79. W. Loyens, P. Jannasch, F.H.J. Maurer, Poly (ethylene oxide)/Laponite nanocomposites via melt-compounding: effect of clay modification and matrix molar mass. Polymer (Guildf) **46**, 915–928 (2005)
80. L.A. Bulavin, L.N. Lisetski, S.S. Minenko et al., Microstructure and optical properties of nematic and cholesteric liquid crystals doped with organo-modified platelets. J. Mol. Liq. **267**, 279–285 (2018)
81. L.M. Daniel, R.L. Frost, H.Y. Zhu, Edge-modification of Laponite with dimethyloctylmethoxysilane. J. Colloid Interface Sci. **321**, 302–309 (2008)
82. S.P. Patil, R. Mathew, T.G. Ajithkumar et al., Gelation of covalently edge-modified Laponites in aqueous media. 1. Rheology and nuclear magnetic resonance. J. Phys. Chem. B **112**, 4536–4544 (2008)
83. V.S. Savenko, Aging of Laponite aqueous suspensions in presence of anionic surfactant. Bull. Taras. Shevchenko Natl. Univ. Kyiv. Ser. Phys. Math. **2**, 277–282 (2014)
84. R.-M. Guillermic, A. Salonen, J. Emile, A. Saint-Jalmes, Surfactant foams doped with Laponite: unusual behaviors induced by aging and confinement. Soft Matter **5**, 4975–4982 (2009)

85. V. Savenko, L. Bulavin, M. Rawiso, N. Lebovka, Aging of aqueous Laponite dispersions in the presence of sodium polystyrene sulfonate. Ukr Phys. J. **59**, 589–595 (2014)
86. Y. Aray, M. Marquez, J. Rodríguez et al., Electrostatics for exploring the nature of the hydrogen bonding in polyethylene oxide hydration. J. Phys. Chem. B **108**, 2418–2424 (2004)
87. M. Miyazaki, T. Maeda, K. Hirashima et al., PEG-based nanocomposite hydrogel: thermoresponsive sol-gel transition controlled by PLGA-PEG-PLGA molecular weight and solute concentration. Polymer (Guildf) **115**, 246–254 (2017). https://doi.org/10.1016/j.polymer.2017.03.016
88. A.K. Gaharwar, C.P. Rivera, C.-J. Wu, G. Schmidt, Transparent, elastomeric and tough hydrogels from poly (ethylene glycol) and silicate nanoparticles. Acta Biomater. **7**, 4139–4148 (2011)
89. J. Zebrowski, V. Prasad, W. Zhang et al., Shake-gels: shear-induced gelation of Laponite–PEO mixtures. Colloids Surf. A Physicochem. Eng. Asp **213**, 189–197 (2003)
90. D.C. Pozzo, L.M. Walker, Reversible shear gelation of polymer–clay dispersions. Colloids Surf. A Physicochem. Eng. Asp **240**, 187–198 (2004)
91. V. Can, O. Okay, Shake gels based on Laponite–PEO mixtures: effect of polymer molecular weight. Des. Monomers Polym. **8**, 453–462 (2005)
92. M.M. Ramos-Tejada, P.F. Luckham, Shaken but not stirred: The formation of reversible particle—polymer gels under shear. Colloids Surf. A Physicochem. Eng. Asp **471**, 164–169 (2015). https://doi.org/10.1016/j.colsurfa.2015.02.021
93. A. Nelson, T. Cosgrove, A small-angle neutron scattering study of adsorbed poly (ethylene oxide) on Laponite. Langmuir **20**, 2298–2304 (2004)
94. R. De Lisi, M. Gradzielski, G. Lazzara et al., Aqueous Laponite clay dispersions in the presence of poly (ethylene oxide) or poly (propylene oxide) oligomers and their triblock copolymers. J. Phys. Chem. B **112**, 9328–9336 (2008)
95. J. Lal, L. Auvray, Interaction of polymer with clays. J. Appl. Crystallogr. **33**, 673–676 (2000)
96. J. Lal, L. Auvray, Interaction of polymer with discotic clay particles. Mol. Cryst. Liq. Cryst. **356**, 503–515 (2001)
97. A. Thuresson, M. Segad, T.S. Plivelic, M. Skepö, Flocculated Laponite-PEG/peo dispersions with multivalent salt: a SAXS, Cryo-TEM, and computer simulation study. J. Phys. Chem. C **121**, 7387–7396 (2017)
98. A. Thuresson, M. Segad, M. Turesson, M. Skepö, Flocculated Laponite–PEG/PEO dispersions with monovalent salt, a SAXS and simulation study. J. Colloid Interface Sci. **466**, 330–342 (2016)
99. S. Morikubo, Y. Sekine, T. Ikeda-Fukazawa, Structure and dynamics of water in mixed solutions including Laponite and PEO. J. Chem. Phys. **134**, 44905 (2011)
100. A. Nelson, T. Cosgrove, Dynamic light scattering studies of poly (ethylene oxide) adsorbed on Laponite: Layer conformation and its effect on particle stability. Langmuir **20**, 10382–10388 (2004)
101. H.A. Baghdadi, H. Sardinha, S.R. Bhatia, Rheology and gelation kinetics in Laponite dispersions containing poly (ethylene oxide). J. Polym. Sci., Part B: Polym. Phys. **43**, 233–240 (2005)
102. P. Mongondry, T. Nicolai, J.-F. Tassin, Influence of pyrophosphate or polyethylene oxide on the aggregation and gelation of aqueous Laponite dispersions. J. Colloid Interface Sci. **275**, 191–196 (2004)
103. S. Kishore, Y. Chen, P. Ravindra, S.R. Bhatia, The effect of particle-scale dynamics on the macroscopic properties of disk-shaped colloid–polymer systems. Colloids Surf. A Physicochem. Eng. Asp **482**, 585–595 (2015)
104. S. Morariu, M. Bercea, Flow behavior of poly (ethylene oxide)-Laponite nanocomposite solutions. J. Optoelectron. Adv. Mater. **9**, 1005–1009 (2007)
105. S. Morariu, M. Bercea, Influence of poly (ethylene oxide) on the aggregation and gelation of Laponite dispersions in water. Rev. Roum. Chim. **52**, 147–152 (2007)
106. S. Morariu, M. Bercea, Effect of temperature and aging time on the rheological behavior of aqueous poly (ethylene glycol)/Laponite RD dispersions. J. Phys. Chem. B **116**, 48–54 (2011)

107. S. Morariu, M. Bercea, Gels based poly (ethylene oxide)-Laponite mixtures. Rev. Roum. Chim. **51**, 435 (2006)
108. S. Morariu, M. Bercea, Viscoelastic properties of Laponite RD dispersions containing PEO with different molecular weights. Rev. Roum. Chim. **60**, 777–785 (2015)
109. S. Morariu, M. Bercea, Effect of addition of polymer on the rheology and electrokinetic features of Laponite RD aqueous dispersions. J. Chem. Eng. Data **54**, 54–59 (2009)
110. A.K. Atmuri, G.A. Peklaris, S. Kishore, S.R. Bhatia, A re-entrant glass transition in colloidal disks with adsorbing polymer. Soft Matter **8**, 8965–8971 (2012)
111. H.A. Baghdadi, E.C. Jensen, N. Easwar, S.R. Bhatia, Evidence for re-entrant behavior in Laponite–PEO systems. Rheol. Acta **47**, 121–127 (2008)
112. H.A. Baghdadi, J. Parrella, S.R. Bhatia, Long-term aging effects on the rheology of neat Laponite and Laponite–PEO dispersions. Rheol. Acta **47**, 349–357 (2008)
113. H. Baghdadi, S.R. Bhatia, E.E.C. Jensen, N. Easwar, Evidence of re-entrant behavior in Laponite-PEO systems. MRS Online Proc. Libr. Arch. **899** (2005)
114. L. Zulian, F.A. de Melo Marques, E. Emilitri et al., Dual aging behaviour in a clay–polymer dispersion. Soft Matter **10**, 4513–4521 (2014)
115. T. Takahashi, Y. Yamada, K. Kataoka, Y. Nagasaki, Preparation of a novel PEG-clay hybrid as a DDS material: dispersion stability and sustained release profiles. J. Control Release **107**, 408–416 (2005). https://doi.org/10.1016/j.jconrel.2005.03.031
116. A.K.F. Dyab, H.N. Al-Haque, Particle-stabilised non-aqueous systems. RSC Adv. **3**, 13101–13105 (2013)
117. M.M. Doeff, J.S. Reed, Li ion conductors based on Laponite/poly (ethylene oxide) composites. Solid State Ionics **113**, 109–115 (1998)
118. J. Bujdák, E. Hackett, E.P. Giannelis, Effect of layer charge on the intercalation of poly (ethylene oxide) in layered silicates: implications on nanocomposite polymer electrolytes. Chem. Mater. **12**, 2168–2174 (2000)
119. K. Shikinaka, K. Aizawa, Y. Murakami et al., Structural and mechanical properties of Laponite–PEG hybrid films. J. Colloid Interface Sci. **369**, 470–476 (2012)
120. K. Shikinaka, K. Aizawa, K. Shigehara, Strengthening and structural ordering of Laponite-poly (ethylene glycol) hybrid films. Clay Sci. **21**, 7–12 (2017)
121. A. Dundigalla, S. Lin-Gibson, V. Ferreiro et al., Unusual multilayered structures in poly (ethylene oxide)/Laponite nanocomposite films. Macromol. Rapid Commun. **26**, 143–149 (2005)
122. A. Loiseau, J.-F. Tassin, Model nanocomposites based on Laponite and poly (ethylene oxide): preparation and rheology. Macromolecules **39**, 9185–9191 (2006)
123. K. Shikinaka, K. Aizawa, N. Fujii et al., Flexible, transparent nanocomposite film with a large clay component and ordered structure obtained by a simple solution-casting method. Langmuir **26**, 12493–12495 (2010)
124. E.A. Lysenkov, Y.P. Gomza, V.V. Klepko et al., Influence of mineral fillers on the structure and properties of nanocomposites based on polyethylene glycol. Nanosyst. Nanomater Nanotechnol. (Kiev, Ukr.) **8**(3), 677–692 (2010)
125. M. Kawasumi, N. Hasegawa, A. Usuki, A. Okada, Liquid crystal/clay mineral composites. Appl. Clay Sci. **15**, 93–108 (1999)
126. M. Lavrič, V. Tzitzios, G. Cordoyiannis et al., Blue phase range widening induced by Laponite nanoplatelets in the chiral liquid crystal CE8. Mol. Cryst. Liq. Cryst. **615**, 14–18 (2015)
127. J.S. Van Duijneveldt, S. Klein, E. Leach et al., Large scale structures in liquid crystal/clay colloids. J. Phys.: Condens. Matter **17**, 2255 (2005)
128. Z. Zhang, J.S. van Duijneveldt, Effect of suspended clay particles on isotropic–nematic phase transition of liquid crystal. Soft Matter **3**, 596–604 (2007)
129. M. Mousa, N.D. Evans, R.O.C. Oreffo, J.I. Dawson, Clay nanoparticles for regenerative medicine and biomaterial design: a review of clay bioactivity. Biomaterials **159**, 204–214 (2018)
130. A. Jayakumar, A. Surendranath, P.V. Mohanan, 2D materials for next generation healthcare applications. Int. J. Pharm. (2018)

131. M.A. Haq, Y. Su, D. Wang, Mechanical properties of PNIPAM based hydrogels: a review. Mater. Sci. Eng., C **70**, 842–855 (2017)
132. N. Asadi, E. Alizadeh, R. Salehi et al., Nanocomposite hydrogels for cartilage tissue engineering: a review. Artif. Cells Nanomed. Biotechnol. **46**, 465–471 (2018)
133. K. Rathee, V. Dhull, R. Dhull, S. Singh, Biosensors based on electrochemical lactate detection: a comprehensive review. Biochem. Biophys. Rep. **5**, 35–54 (2016)
134. P. Kanyong, F.D. Krampa, Y. Aniweh, G.A. Awandare, Enzyme-based amperometric galactose biosensors: a review. Microchim. Acta **184**, 3663–3671 (2017)
135. C.S. Pundir, V. Narwal, B. Batra, Determination of lactic acid with special emphasis on biosensing methods: a review. Biosens. Bioelectron. **86**, 777–790 (2016)

Chapter 7
The Techniques of Surface Alignment of Liquid Crystals

Greta Babakhanova and Oleg D. Lavrentovich

Abstract Alignment of liquid crystal (LC) molecules is an important topic of physics of anisotropic fluids. The boundary conditions and the surface properties of the material in contact with an LC dictate the preferred orientation of the molecules at the interface.

7.1 Introduction

Alignment of liquid crystal (LC) molecules is an important topic of physics of anisotropic fluids. The boundary conditions and the surface properties of the material in contact with an LC dictate the preferred orientation of the molecules at the interface. Several factors that affect the LC alignment include dipolar interactions, chemical bonding, van der Waals interactions, steric factors and surface topographies [61, 76].

There are three main types of director alignment: planar, tilted, and homeotropic (or perpendicular). The nomenclature reflects how the director $\hat{\mathbf{n}}$ that specifies the average molecular orientation of the LC is aligned at the surface, Fig. 7.1. In the planar case, $\hat{\mathbf{n}}$ is parallel to a single direction in the plane of the interface, so that the polar angle θ between the normal to the interface and $\hat{\mathbf{n}}$ is 90° and there is a well-defined direction in the plane, specified by some azimuthal angle φ, Fig. 7.1. A degenerate case, when $\hat{\mathbf{n}}$ is free to be along any direction in the plane, so that φ is not fixed, is called a tangential alignment. Tilted alignment $0 < \theta < 90^{\circ}$ can be along a single direction or conically degenerate. In the homeotropic alignment, $\hat{\mathbf{n}}$ is perpendicular to the interface, $\theta = 0$. Numerous techniques have been employed

G. Babakhanova · O. D. Lavrentovich (✉)
Advanced Materials and Liquid Crystal Institute, Kent State University, Kent, OH 44242, USA
e-mail: olavrent@kent.edu

Chemical Physics Interdisciplinary Program, Kent State University, Kent, OH 44242, USA
e-mail: gbabakha@kent.edu

O. D. Lavrentovich
Department of Physics, Kent State University, Kent, OH 44242, USA

L. A. Bulavin and L. Xu (eds.), *Modern Problems of the Physics of Liquid Systems*, Springer Proceedings in Physics 223,
https://doi.org/10.1007/978-3-030-21755-6_7

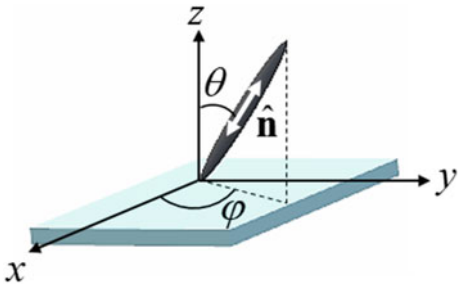

Fig. 7.1 Schematic representation of LC molecule depicting the polar (θ) and the azimuthal (φ) angles

to align rod-like calamitic LCs [28]. The challenge, however, is to align LCs with molecules of complex shapes, such as bent-core and flexible dimer molecules, for which alignment is not always trivial [35, 57]. Orienting water-based lyotropic LC systems is also difficult, but it is of great significance as this class of materials is often biocompatible. The stability of the alignment is one of the essential factors when assessing proposed methods, as environmental factors such as temperature, light polarization or humidity often affect the desired orientation. Though LCs are predominantly used in display technologies, the trend has now shifted towards biological application. Reports on LC alignment methods are vast. Therefore, in this chapter, we aim to briefly overview some of the widely used effective alignment approaches, report on the recently developed methods and extend on alignment techniques for non-calamitic LCs with molecules of complex shape. We conclude with discussing the advances, challenges and significance of using ordered, anisotropic LCs as templates for guiding biological matter.

7.2 Planar Alignment

Below we discuss the most popular approaches to planar alignment and tilted alignment with a small "pretilt" angle, measured as $\alpha = 90^{\circ} - \theta$, $0 < \alpha < 10^{\circ}$.

7.3 Grooved Surfaces

One mechanism of alignment proposed by Berreman is based primarily on geometrical factors that arise from elastic energy if the surface in contact with LC is grooved [12, 13]. There are many methods that can be implemented to produce grooved surface topography, which include rubbing/polishing the substrate, deposition of material by evaporation, ion beam etching and lithographic techniques. Berreman considered the grooved surface as a sinusoidal wave $z \approx A \sin qx$ defined with an amplitude A and wavelength $\lambda = \frac{2\pi}{q}$ (Fig. 7.2) [12].

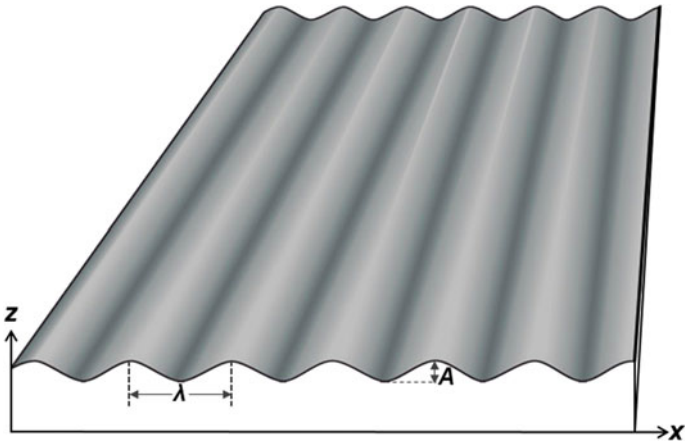

Fig. 7.2 Schematic representation of a sinusoidal grooved surface

Theoretical calculations of elastic energy of a liquid crystal in contact with such a substrate, assuming that the director is always tangential to the modulated surface and is aligned along a certain azimuthal direction φ, leads to the following elastic energy per unit area

$$F_{\mathrm{d}} = \frac{K}{4} A^2 q^3 \cos^2 \varphi, \tag{1}$$

where K is the elastic constant of the LC in the so-called one-constant approximation. As clear from (1), the equilibrium alignment of $\hat{\mathbf{n}}$ is along the grooves, i.e., along the y-axis in Fig. 7.2, as this is the only direction of alignment that causes no elastic distortions of the LC.

7.4 Deposition of Polymeric Coating

A typical LC cell is comprised of two sandwiched glass plates separated by spacers. Prior the assembly, the inner side of each glass plate is treated with an aligning agent, such as a thin polymer layer, to induce the desired LC director orientation [28, 41]. Appropriate polymer coatings such as polyimides (PIs) are optically transparent, stable and can withstand relatively high temperatures (>200 °C). The PI coating alone yields tangential anchoring of LCs, however, rubbing it with a velvet cloth, for example, will cause the rubbed surface to become unidirectionally anisotropic [80]. Thus, rubbed PI layer induces a preferred azimuthal direction of LCs [24]. Van Aerle explored the degree of orientation of the rubbed polymer layer in terms of Hermans' orientation factor f and determined that $0.5 < f < 1$, which indicates that rubbing process is an effective way to induce molecular orientation of a polymer layer [149].

Table 7.1 lists commercially available PI layers that produce the indicated pretilt angles [145].

Rubbing generates grooves and scratches on the polymer surface [182]. On that account, some suggest that surface topography may cause long-range elastic effects and orient the long axes of LC molecules in the grooves parallel to the rubbing direction, as in the Berreman's model [12, 13, 77, 182]. Another plausible mechanism is reorientation of polymer chains during rubbing [21, 41, 79, 80, 95, 147, 149, 152]. X-Ray scattering measurements demonstrate that rubbing a PI film causes near surface alignment of the polymer molecules parallel to the rubbing direction [147]. Buffing-induced birefringence measurements by Geary et al. and the Langmuir-Blodgett aligning films (nonrubbed) developed by Murata et al. also show that the orientation of polymer molecules is the primary driving mechanism of the LC alignment, and not the nanogrooves [41, 95].

The schematic representation of the rubbing process and generated molecular reorientation of polymer chains is illustrated in Fig. 7.3. Intermolecular forces between the polymer and LC molecules are of great importance in aligning such buffed system and favor parallel alignment [70, 164]. Even though rubbing PI layers results in good alignment of rod-like and bent shape LC molecules, a significant shortcoming of this technique is the accumulation of static charges and formation of fine dust particles which may deteriorate performance of LC displays [76].

The strength of alignment is determined by using anchoring energy concept [32]. The anchoring energy, $W(\theta, \varphi)$, is defined as a measure of work per unit area needed to deviate the director from the so-called "easy axis" (θ_0, φ_0) that corresponds to the director orientation that sets the minimum of the surface energy: $W = \frac{1}{2} W_\theta (\theta - \theta_0)^2$ or $W = \frac{1}{2} W_\varphi (\varphi - \varphi_0)^2$, where W_θ and W_φ is the polar and azimuthal anchoring coefficients. For small director deviations from the easy axis, the surface anchoring potential for tangentially anchored substrates may be approximated by Rapini-Papoular expression [121]:

$$W = \frac{1}{2} W_\theta \sin^2(\theta - \theta_0) + \frac{1}{2} W_\varphi \sin^2(\varphi - \varphi_0). \tag{2}$$

Anchoring strength is considered weak, when $W \sim \left(10^{-7} - 10^{-5}\right) \mathrm{J/m^2}$ and strong, when $W \sim 10^{-3}$ J/m^2; typically, $W_\theta > W_\varphi$ by one or two orders of magnitude [15, 70, 96, 164].

7.5 Carbon Nanotube Films

Carbon nanotubes (CNTs) are hollow cylindrical molecules which consist of rolled sheet of single-layer carbon atoms. Their aspect ratios may reach up to ~10^7, owing to their nanometer diameter and length that may extend up to centimeters [123]. CNTs are a subject of intense research due to their extraordinary physical properties such as high tensile strength, high electrical and thermal conductivities, high ductility,

Table 7.1 Commercially available polyimide alignment materials that generally yield planar alignment for conventional rod-like liquid crystals [145]

Name	Pretilt angle	Manufacturer	Name	Pretilt angle	Manufacturer
AL1454	0.7°	JSR	AL1J508	4.7°	JSR
LQ-2200	0.8°	Hitachi Chem. Dupont	SE-150	4–5°	Nissan Chem. Corp.
JALS-146-R39	1°	JSR	SE-3310	4–5°	Nissan Chem. Corp.
AL5056	2°	JSR	SE7992	4–5°	Nissan Chem. Corp.
SE2555	2°	Nissan Chemicals Corp.	JALS-1024-R1	4–5°	JSR
SE-410	2°	Nissan Chemicals Corp.	JALS-9800-R1	4–5°	JSR
SE-130	2°	Nissan Chemicals Corp.	JALS-1077-R2	5°	JSR
SE-2170	2°	Nissan Chemicals Corp.	SE3140	5–6°	Nissan Chem. Corp.
LX-1400	2.6°	Hitachi Chem. Dupont	SE5291	5–6°	Nissan Chem. Corp.
AL8254	3°	JSR	JALS-9005-R1	5–6°	JSR
LQ-C100	3.1°	Hitachi Chem. Dupont	SE7492	6–7°	Nissan Chem. Corp.
AL3408	3–4°	JSR	LQ-T120-04	6.8°	Hitachi Chem. Dupont
AL3046	3.5°	JSR	SE-610	7–8°	Nissan Chem. Corp.
LQ-T120-03	3.5°	Hitachi Chem. Dupont	SE3510	7–8°	Nissan Chem. Corp.
JALS-1068-R2	4.3°	JSR	LQ-1800	8.0°	Hitachi Chem. Dupont
AL1F408	4.5°	JSR			

high chemical and thermal stability [123]. CNTs also exhibit anisotropic physical properties [123].

Single-layer CNT sheets have attracted a lot of interest, since these highly optical transparent coatings may simultaneously serve as both a LC alignment layer and a conductive layer [38, 120, 129, 148]. Single-layer sheet can be drawn continuously from a vertically grown CNT forest, which facilitates mass production of these sheets at a commercial level [148]. Russell et al. generated aligned single-walled CNT films via self-assembly as well as dip-coating methods and achieved uniform planar alignment of nematic LCs on the scale of centimeters [129]. Their inherent conductive property eliminates the need of additional costly transparent electrodes for electro-optical applications. The surface topography of aligned CNTs observed via atomic force microscopy shows parallel grooved structures with an amplitude on the order of ~10^2 nm, much larger than grooves resulted from rubbed PI layers described in the previous section [38, 148]. It is proposed that since the long-chain structure at the surface does not exist, the mechanism of LC alignment is realized via grooved surface roughness of unidirectionally aligned CNTs [38, 129].

CNTs are attractive aligning materials because they may be implemented in flexible/foldable electro-optical systems [120]. The current issue which is being addressed is the difficulty of attaining good adhesion between CNTs and substrate while keeping the orientational order as high as possible [120]. Truong and co-workers have recently explored this issue and reported that the hydrophobic treatment of the substrate using hexamethyldisilazane prior to the deposition of CNT sheet improved the adhesion between aligned CNT bundles and the glass substrate [148]. The authors also eliminated the problem of short-circuit failure of the sandwich LC cell due to floating CNT nanofibrils that unintentionally connect two facing CNT-sheet electrodes by depositing an alumina passivation layer [148].

7.6 Photoalignment

One of the most powerful alignment methods employs light-matter interaction to induce controlled LC alignment. Contact-free photoinduced alignment technique eliminates undesired contaminants such as electrostatic charges, impurities as well as mechanical damage of the surface which may be caused by conventional rubbing

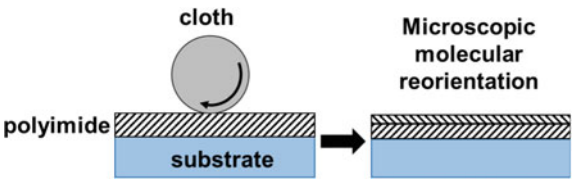

Fig. 7.3 Schematic diagram of polyimide rubbing process resulting in microscopic molecular reorientation. Adapted with permission from [80]. Copyright (1996) American Chemical Society

of PI films [26, 34, 43, 56, 108, 131]. Some of the greatest assets of this method is the ability to achieve rewritable, complex and nonuniform spatial patterns of the director field on flat or curved substrates, which are otherwise impossible to realize [116]. Additionally, photoalignment systems have an ability to achieve nano-scale alignment [137]. Photopatterning is widely used in LC display applications, however, recently this alignment method became extensively used to fabricate functional materials such as stimuli-responsive films/coatings (Fig. 7.4), sorting systems and optical elements [9, 19, 40, 91, 110, 111, 140, 154, 157, 158].

One can distinguish at least four types of photoalignment mechanisms: (1) photochemically reversible *trans-cis* isomerization in materials containing azobenzene dyes, (2) reorientation of azo-dye chromophore molecules under the action of polarized light, (3) photodegradation and orientational bond breaking in polyimides, and (4) photochemical crosslinking in preferred directions of polymer precursors, such as cinnamoyl side-chain polymers [25, 26, 168]. The first two mechanisms are reversible, whereas the other two processes involve irreversible photochemical changes [26].

Azobenzene molecules have two conformations: *trans* and *cis* (Fig. 7.5a), where the *trans* rod-like isomer is thermodynamically more stable than its bent (*cis*) counterpart [3]. Azobenzenes undergo reversible *trans-cis* isomerization when irradiated in their absorption bands [3, 10]. Usually, UV irradiation creates an excess of *cis*-isomers, while visible light converts most of the molecules into *trans* form. Ichimura and coworkers used azobenzene molecules attached to a substrate as a "commanding layer" of photoalignment: rod-like trans-isomers would align the adjacent LC molecules perpendicularly to the surface, while bent cis-isomers would support tangential alignment. The alignment can thus be switched by light driven isomerization from homeotropic to tangential and back (Fig. 7.5b) [56]. It is important to note that the degradation of the dye layer may impact the number of possible reversible cycles from *trans* to *cis* conformation.

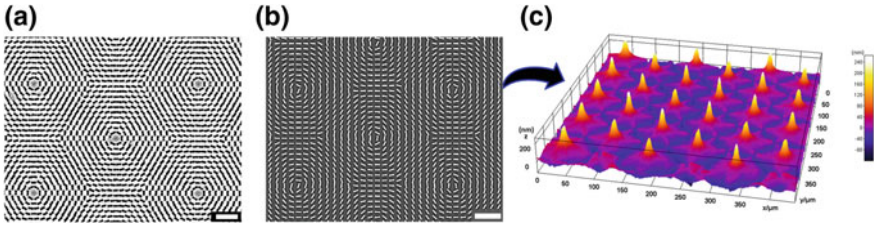

Fig. 7.4 **a** Scanning electron microscopy (Quanta 450) image of a plasmonic metamask made of nanoaperture arrays in Al film exhibiting an array of topological defects, (scale bar 1 μm), **b** LC PolScope (Abrio Imaging Systems) image of the director field of a photopatterned liquid crystal elastomer coating that closely follows the nanoaperture orientations in the plasmonic metamask in panel (**a**), (scale bar 50 μm), **c** digital holographic microscopy (DHM) image of a photopatterned thermoresponsive liquid crystal elastomer coating at $T = 100\,^{\circ}\mathrm{C}$ forming nanometer surface profiles composed of hills/valleys in controlled locations preprogrammed by the director field orientation in (**a**, **b**). Bend deformations shown in (**a**, **b**) result in hills illustrated in (**c**) as described in [9]

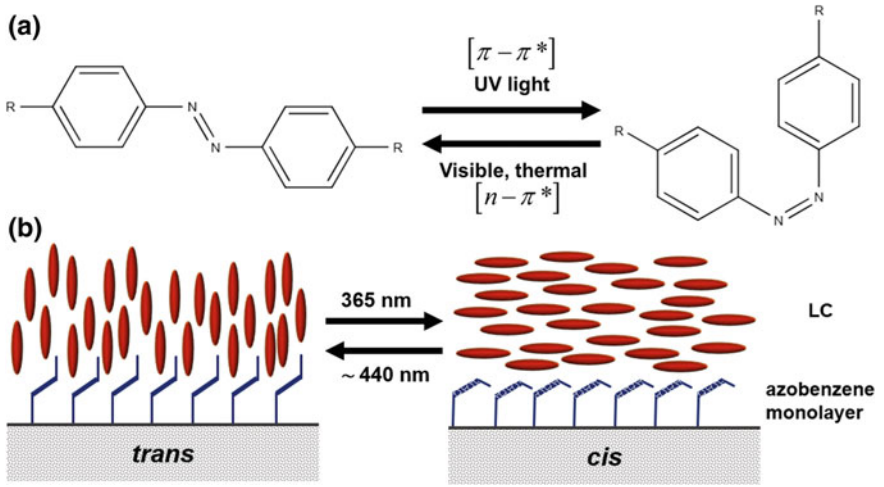

Fig. 7.5 **a** Schematic representation of an azobenzene unit that changes from trans conformation to cis upon illumination of UV light ($\lambda = 365$ nm), while visible light ($\lambda > 400$ nm) restores the trans form, **b** cartoon image of photoinduced homeotropic to planar alignments of LCs using trans-cis conformational changes of azo-dye moieties. Adapted with permission from [56]. Copyright (1988) American Chemical Society

The second photoalignment mechanism is the pure reorientation of azo-dye molecules due to polarized light [11, 72]. The azo-dyes strongly absorb light if the exciting optical field polarization is parallel to the dipole transition moment [78]. Azobenzenes in *trans* conformation with their transition moments parallel to the polarization direction of the incident light undergo reversible isomerization to *cis* state, where the probability of absorption is $\cos^2 \varsigma$; ς is the angle between the transition moment of an azobenzene and the linear polarization direction of the irradiating light [3, 84]. Thus, the isomers whose transition moments are perpendicular to the linear polarized light have a very low probability of undergoing photoisomerization [10]. Photodriven alignment of azobenzene chromophores perpendicular to the UV light polarization, also known as Weigert effect, is realized as the net population of azobenzene moieties reorient perpendicularly to the linearly polarized light [84].

One of the recently developed methods utilizing pure azo-dye reorientation is the plasmonic photoalignment technique that utilizes plasmonic metamasks (PMMs). The PMM represents a thin Al film with an array of rectangular 100 nm $\times$ 220 nm nanoapertures (Fig. 7.4a) [44]. Unpolarized light transmitted through a PMM acquires linear polarization that is perpendicular to the long axis of the nanoapertures. Thus, a transmitted light with a pattern of both intensity and polarization is produced, which is then projected onto an azo-dye coated photosensitive materials that is previously spin-coated onto a glass substrate. Guo et al. used Brilliant Yellow (BY) (Sigma Aldrich) and PAAD-72 (BeamCo) photoalignment materials [44]. Once polarized light irradiates the azo-dye molecules, photochemical reaction is induced that results in the reorientation of their long axes perpendicularly to the

local light polarization. When LC is in contact with prepatterned photoaligned coating, the director closely follows the orientation inscribed into the alignment of dye molecules; in other words, the orientational pattern of the liquid crystal is the same as that one of nanoapertures in the PMM (see Fig. 7.4a, b) [44].

One of the major drawbacks of photoalignment using azo-dyes is the sensitivity of the photoalignment materials to humidity [155]. Humidity may effect the wetting of the photoresponsive film during the spin-coating process [47]. Wang et al. explored the effect of relative humidity (RH) levels at different stages of photoalignment preparation using dichroic azo-dye BY: at the stage of substrate storage before coating, during the spin-coating process, between film coating and exposure, and after exposure [155]. The greatest effect of RH on the order parameter of the photoalignment layer was at the time of spin-coating process of the dimethylformamide/BY solution, the results in Fig. 7.6 indicate that the best alignment is achieved at RH levels <45%, and no alignment is achieved at RH levels >50% [155]. The absorption spectra of the prepared BY films (prepared at different RH levels at the time of spin-coating) shows a red-shift with increase in RH, possibly, due to the change in BY aggregation [155]. Grazing incidence X-ray diffraction patterns in the case of BY dispersed in triacetyl cellulose show that humidity triggers restructuring of the BY assembly from 1D nematic-like order to 2D rectangular lattice composed of columnar order of BY molecules, resulting in the dramatic increase in the order parameter [89]. During the humidification process, hydration might occur site-selectively around the sodium sulfonate hydrophilic functional groups that may enhance the lyotropic liquid crystalline property of BY which facilitates the reordering of the molecules into columnar assemblies [89]. Storing conditions before polarized light exposure also greatly effect the photoalignment. Wang et al. show that unexposed BY films kept at high humidity (80–90% RH) for 2.5 h show no alignment ($S = 0.01$–0.11), while films kept at moderate humidity (40–45% RH) show relatively constant order parameter ($S = 0.76$–0.79) [155]. Thus RH levels need to be taken into consideration as humidity absorption plays an important part during the photopatterning process.

Another photoinduced alignment mechanism involves breaking polyimide chains with UV light [46]. Initially, the PI chains are randomly oriented in the plane of the film. Upon UV irradiation, the PI chains that are parallel to the UV polarization

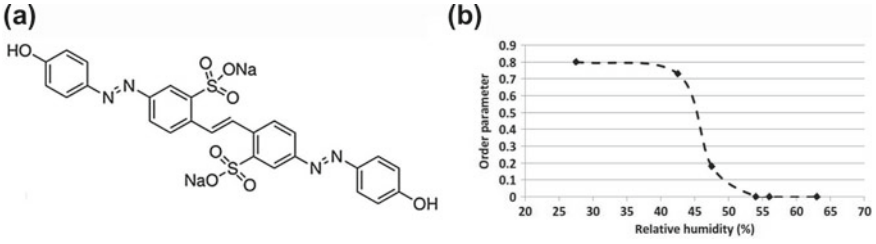

Fig. 7.6 **a** Azo-dye BY, **b** Order parameter (S) as a function of relative humidity levels during the spin-coating photosensitive layer BY. Reprinted by permission of the publisher Taylor & Francis Ltd., [155]

decompose. The remaining chains oriented perpendicular to the polarization of light remain intact. Thus, the direction of LC alignment due to van der Waals forces is parallel to the maximum density of unbroken polyimide chains [26]. One of the major limitation of photodegradation is the small value of the orientational order parameter, its accurate control and high sensitivity to UV exposure time (Fig. 7.7) [26, 144]. Additionally, the by-products may contaminate the system by reducing the thermal stability of the alignment layer, producing ions that may cause image sticking or flickers [156, 166].

The photoalignment mechanism developed by Schadt and coworkers is based on a different class of photoresponsive materials (typically used as a negative photoresist), called polyvinyl 4-methoxy-cinnamate (PVMC) [131]. The UV irradiation causes a topochemical reaction between the side chains of prepolymer containing cinnamate [27]. The optical excitation of π-electrons in double-bonds of cinnamoyl moieties is polarization dependent [130]. Thus, under linear photo-polymerization (LPP) the prepolymer undergoes [2 + 2] cycloaddition of cinnamic acid side chains that belong to different main chains, where parallel double bonds, one from each molecule, are broken and reform as single bonds between molecules (Figs. 7.8 and 7.9) [102, 131]. LPP leads to a preferred depletion of cinnamic acid side chain along linearly polarized UV light ($\lambda = 320$ nm). Consecutively, LPP causes anisotropic distribution of cyclobutane molecules with their long axis perpendicular to the polarization direction of the incident polarized UV light [26, 131]. When in contact with PVMC films, LCs align along the long axis of cyclobutane molecules due to van der Waals forces. LPP-photoalignment technology allows generation of pre-tilt angles ranging from 0°–90° and simultaneously fixation of the alignment [131]. The major drawback of this technique is the low thermal stability.

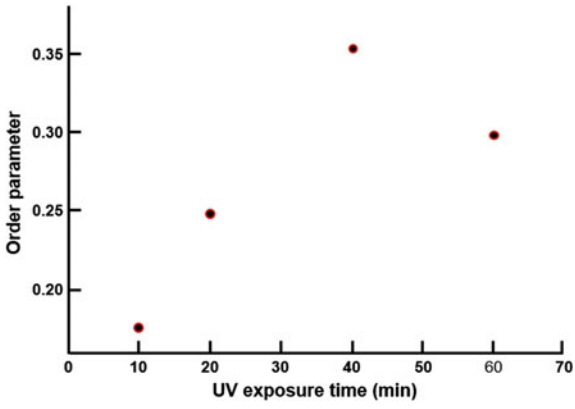

Fig. 7.7 Order parameter of LC cells as a function of UV exposure time. Adapted from [144]. Copyright (2001) Elsevier

Fig. 7.8 [2 + 2] cycloaddition; a model for polymerization

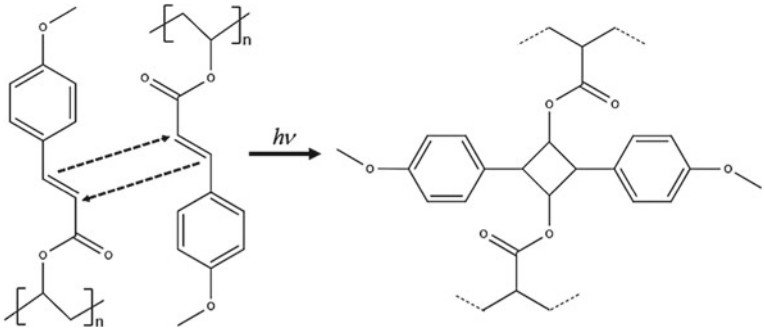

Fig. 7.9 Two poly(vinyl 4-methoxycinnamate) side chains undergo intermolecular photo-induced [2 + 2] cycloaddition. Adapted from [131]

There are other light-driven techniques that achieve LC alignment without involving any dyes. Scanning wave photopolymerization (SWaP) is a dye-free alignment method that does not require polarized light [49, 50]. SWaP allows to achieve arbitrary, complex 2D alignment patterns over large areas without any prior surface treatments with resolution down to ~ 2 μm [49]. SWaP uses spatiotemporal scanning of focused guided light and is triggered by mass flow in the film arising from molecular diffusion in the light intensity gradient as the polymerization reaction propagates [4, 49]. This single step process results in LC alignment parallel to the incident light patterns. The limiting factor of SWaP is that it is currently applicable to aligning photopolymerizable LCs with thicknesses below tens of micrometers [49].

7.7 Tilted Alignment

Generally, buffed polymer main chains described in the earlier section result in small pretilt angles (see Table 7.1). The alkyl branches in a PI layer affect the magnitude of the pretilt angle. For example, in the absence of the alkyl branches, the pretilt is very small: $\alpha \sim 2°$, whereas low and high density of alkyl chains results in an increase of the tilt angle (~5°–20°) [108]. Control of the tilt angle is crucial in applications in which there is a pre-requisite of molecular realignment along a single predetermined direction [28]. In order to achieve relatively high pretilt (~30°), generally, an oblique evaporation of silicon oxides (SiO_x) is used [59, 93]. Depending on the angle between the substrate plane and the direction of the incident beam (Fig. 7.10), tilt angles ranging from 0° to 90° may be obtained [28]. The incident angle of evaporation (β) causes the film to "grow" in the preferred direction forming micro-columnar structures on the surface of the substrate via self-shadowing mechanism [59, 74, 86, 109, 139, 145]. When in contact with such a surface, LCs orient in the direction of the film growth (defined by the azimuthal angle of the evaporation direction) [59].

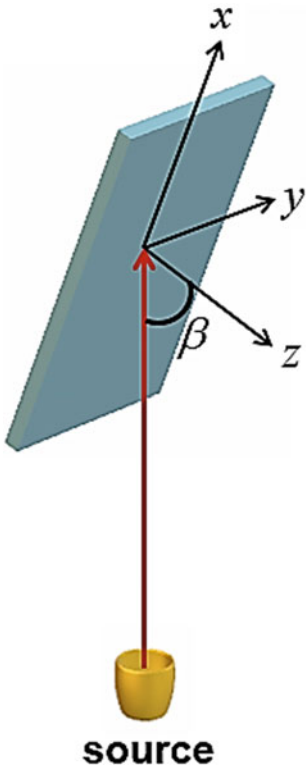

Fig. 7.10 Schematic representation of oblique evaporation system, where z-axis represents the surface normal, β is an angle between the surface normal and the evaporation direction. Adapted from [139]

The features of the surface structures of the oblique evaporated film change with β [86, 105, 145].

In order to achieve high in-plane uniformity of the film as well as high accuracy of the evaporation angle, the source must be placed at a large distance from the target substrate. The drawback of this technique is the cost of the vacuum equipment. Another considerable disadvantage is the need of large chambers to accommodate bigger substrates, which may pose a problem for high volume production.

Alternatively, another approach to control the pretilt is to mix planar and homeotropic polyimides. The mixing ratio, baking temperature and rubbing strength influence the pretilt angle [51, 63, 153, 160, 169, 170]. This technique allows achieving pretilt angles ranging from 0° to 90°, where the pretilt angle increases monotonically with the increasing concentration of homeotropic PI (Fig. 7.11a) [51, 160, 169]. The pretilt drops with the lower concentration of homeotropic PI due to the decline in the concentration of alkyl side chains associated with homeotropic PI [153]. Increasing the baking temperature also results in monotonous decline of pretilt angle (Fig. 7.11b). This observation is expected, since over-baking polyamic acids has two consequences: (1) it initiates imidization of the backbones of homeotropic PI promoting planar alignment, (2) cleaves away a fraction of the side chain of the homeotropic PI component which weakens the vertical alignment [153, 160]. Lastly, the pretilt

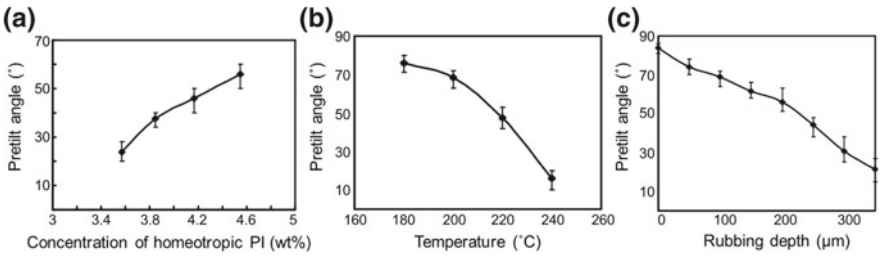

Fig. 7.11 Variation of pretilt angle as a function of **a** concentration of homeotropic PI in the mixture, **b** baking temperature, **c** rubbing strength. Adapted with permission from [160]. © The Optical Society

may also be affected by the strength of rubbing the homeotropic PI (Fig. 7.11c). When mixture of horizontal and vertical PIs is used, the tendency to align horizontally increases with increasing strength of rubbing, thus reducing the pretilt angle [160].

7.8 Vertical Alignment

Vertical, or homeotropic, alignment generally refers to LC molecular orientation such that $\theta = 0°$, although for some applications (such as electro-optical switching of LCs) a pre-tilt angle ($80° < \alpha < 90°$) might be essential. There is no single method of homeotropic alignment that would work for all LCs. Nevertheless, surfactants and homeotropic PIs are typically successful in aligning conventional rod-like molecules. Homeotropic alignment for nontrivial shape of LCs, however, is rather challenging. Realizing a durable homeotropic alignment is of great importance, since tilting of the uniaxial director due to anchoring transition in some cases might be misinterpreted as a biaxial nematic phase [65, 67, 68, 135]. Thus, we will introduce two alignment layers techniques which were successful in aligning rigid bent-core as well as flexible bent-core molecules.

7.9 Deposition of Surfactant

Surfactants are amphiphilic surface-active agents that are comprised of two parts: hydrophilic head group and hydrophobic hydrocarbon chain. The head and the tail of an amphiphile interact very differently with a polar or nonpolar media. Examples of popular surfactants that are generally used in LC alignment are lecithin (derived from eggs), hexadecyl-trimethylammonium bromide (HMAB), stearic acid, cetyl trimethylammonium bromide (CTAB) or dimethyloctadecyl[3-(trimethoxysilyl)propyl]ammonium chloride (DMOAP) (Fig. 7.12). Note here that

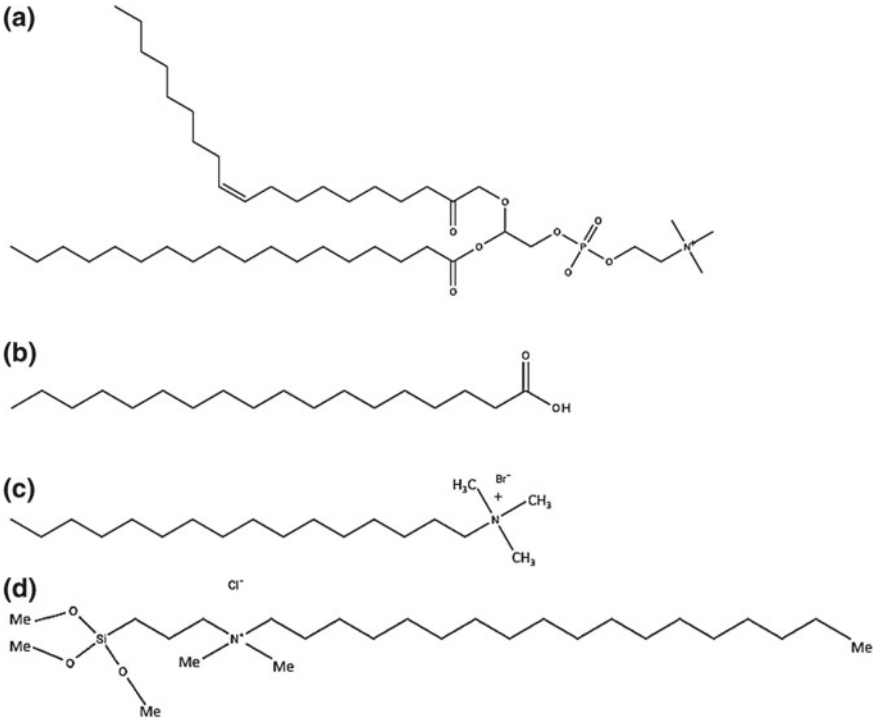

Fig. 7.12 Conventional surfactants used for homeotropic alignment of LCs: **a** lecithin, **b** stearic acid, **c** cetyl trimethylammonium bromide, **d** dimethyloctadecyl[3-(trimethoxysilyl)propyl]ammonium chloride

the quality of the homeotropic alignment via surfactants is highly dependent on the substrate and LC composition. Generally, (especially when using DMOAP) the cleanliness of the substrate is extremely important, since any organic residuals may hinder the desired alignment. Cleaning the glass substrates with piranha solution is very effective in removing organic residuals [181].

It is also worth mentioning that the longevity of the alignment layers using surfactants is less stable than hard-baked PI coatings, since the absorbed layer slowly dissolves in the LC, which may also affect the composition and properties of the system [28]. Thus, checking the isotropic—LC phase transition may be a convenient way to detect contamination due to an alignment layer, as doping LCs with small amounts of non-mesogenic compounds significantly alters the clearing points (by a few Kelvins) [33]. Humidity and heat may also damage the alignment [29, 173].

To set the homeotropic alignment using derivatives of lecithin, for example, clean glass substrates are typically treated with a weak solution of lecithin (0.1–2 wt%) in hexane by dipping or spin-coating methods. Dilution is important to avoid formation of unwanted spots [28]. The excess amounts of lecithin may be washed out with the solvent, after which the substrates are dried for 30 min at 80 °C [28]. The hydrophilic

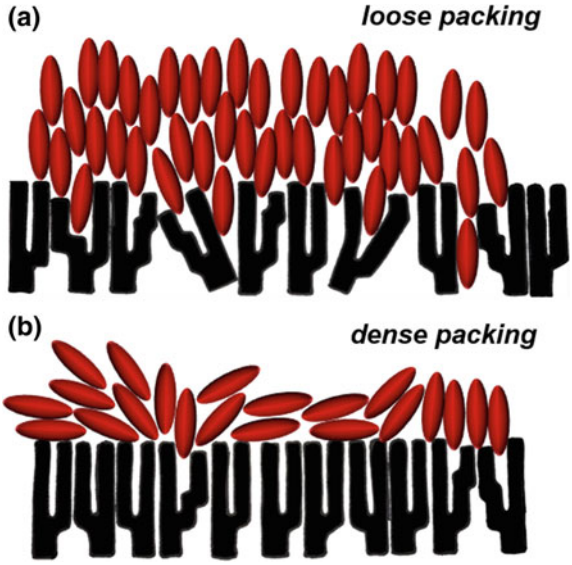

Fig. 7.13 Schematic representation of the model of interaction between nematic LCs and lecithin monolayer: **a** homeotropic alignment at low packing density, **b** lack of anchoring at high packing density resulting in distorted alignment. Adapted from [48]. Copyright (1978) Wiley-VCH and Bunsengesellschaft

head groups attach to the substrate, extending their long hydrophobic alkyl chains perpendicular to the surface, forming brush-like structure [48].

The alignment properties of LCs on lecithin monolayers depend on the packing density (PD), where, generally, the orienting power of amphiphiles decreases with PD [48]. One may precisely control PD by transferring a monomolecular layer of surfactants at the air-water interface onto a solid glass using Langmuir-Blodgett method [124]. At proper concentrations, the alkyl brushes form elongated holes of molecular dimensions which can accommodate rod-like LC molecules [48]. At low and high densities of alkyl chains, the steric interactions are not sufficient to induce homeotropic alignment, which results in random alignment. The model of steric interaction between surfactant layer and LC molecules that promotes vertical alignment proposed by Hiltrop et al. is shown in Fig. 7.13.

7.10 Homeotropic Polyimide Layers

Polyimides are generally mixed with a solvent, and the mixture is spin-coated onto a clean glass substrate to form a nano-layer coating [6]. The soft film then follows soft- and hard-baking procedures to generate a hard alignment layer. Each PI aligning agent has a unique curing temperature, though, generally the operational temperatures are very high to induce thermal imidization reaction (for example T_{curing} of the widely used SE-1211 and SE-7511L is 180 °C) [6]. The chemical structure of the homeotropic PIs is generally of side chain type, since the conventional rod-like LCs tend to align parallel to the side chain of the polymer [37, 53, 82, 103, 107, 145].

Typically, rubbing homeotropic PIs is also employed to generate a pre-tilt angle as the side chain tends to align towards the rubbing direction. Rubbing has to be extremely delicate, since a single rubbing-induced scratch in a projection display may be easily observed when the image is magnified by ~50–100× [6].

7.11 Rigid Bent-Core LCs

Note that the polyimide materials listed in Table 7.2 fail to produce homeotropic alignment of nematics formed by molecules of nontrivial shape, where Schlieren texture is observed instead [66, 68]. To stabilize the vertical alignment, a small amount of UV-curable reactive mesogen (RM) may be mixed with the homeotropic polyimide alignment layer [66, 68, 83, 134]. For instance, rigid oxadiazole bent-core mesogens, which could not be aligned via SE-1211, SE-7511, and SE-5661, were successfully aligned homeotropically using RM-doping technique following the procedure below [66].

The reactive mesogen RM-257 (Merck) was added to the polyimide SE5661 in a 1:50 weight proportion. A small amount (0.1 in weight proportion) of photoinitiator, Irgacure 651 (Ciba Chemicals), was then added. The mixture was spin coated on glass substrates and baked at $T = 170$ °C for one hour. Subsequently, RM-SE5661 coated substrates were exposed to UV irradiation using 6 W UV ($\lambda = 365$ nm) lamp for 90 min to polymerize the reactive mesogens [66]. Such aligning protocol was used to achieve stable homeotropic alignment and establish the uniaxial nematic nature of the oxadiazole bent-core mesogens on the macroscopic scale. Similar approaches employed different aligning layers mixed with RMs to achieve high-performance homeotropic alignment [81, 83, 141].

Table 7.2 Commercially available polyimide alignment materials that usually yield homeotropic alignment [145]

Name	Pretilt angle	Manufacturer
SE-1211	90°	Nissan Chemicals Corp.
SE-5661	90°	Nissan Chemicals Corp.
SE-7511L	90°	Nissan Chemicals Corp.
JALS-682-R6	88°	JSR
JALS-2021-R2	89°	JSR
JALS-2022-R2	82°	JSR
JALS-204	89°	JSR

7.12 Flexible Bent-Core LCs

Recently, flexible bent-core molecules were demonstrated in transmission electron microscopy studies to form a new nematic phase, called twist-bend nematic [16, 23]. The reports on unusual behavior of material properties found new applications in electro-optics [1, 8, 22, 30, 54, 87, 125, 126, 132, 133, 161–163, 174]. The characterization of material parameters such as dielectric anisotropy and elastic constants requires one to prepare both planar and homeotropic alignment. Planar alignment (Fig. 7.14a) is easily achieved with conventional methods of PI deposition (such as PI2555 in Table 7.1). Thus far, the homeotropic alignment, however, was only achieved for fluorinated flexible dimeric mesogens with negative dielectric anisotropy [16, 30, 58]. The deposition of conventional PIs or surfactants alone either results in characteristic misaligned Schlieren texture or weak homeotropic alignment stable for only few degrees, as upon cooling, LC experiences anchoring transition and homeotropic alignment is lost. A stable homeotropic alignment was achieved using DMOAP-SE5661 double-layer deposition method outlined below [30].

To realize stable homeotropic alignment of fluorinated dimers (Fig. 7.14b), first, the ITO-coated glass was cleaned in the ultrasonic bath, rinsed in deionized (DI) water and rinsed again with an Isopropyl Alcohol (IPA). To evaporate the solvent, the substrates were placed in an oven. After drying, the ITO glass was treated with UV ozone for 15 min. Subsequently, the substrates were immersed and agitated in 1 wt% aqueous solution of Dimethyloctadecyl[3-(trimethoxysilyl)propyl]ammonium chloride (DMOAP) (Sigma-Aldrich) for 25 min. The substrates were than rinsed with DI water for three minutes, dried with Nitrogen gas and cured in an oven at $T = 110$ °C. Lastly, the second alignment layer, SE5661 mixed with a thinner, Solvent 79, with 1:1 ratio (Nissan Chemical Industries), was

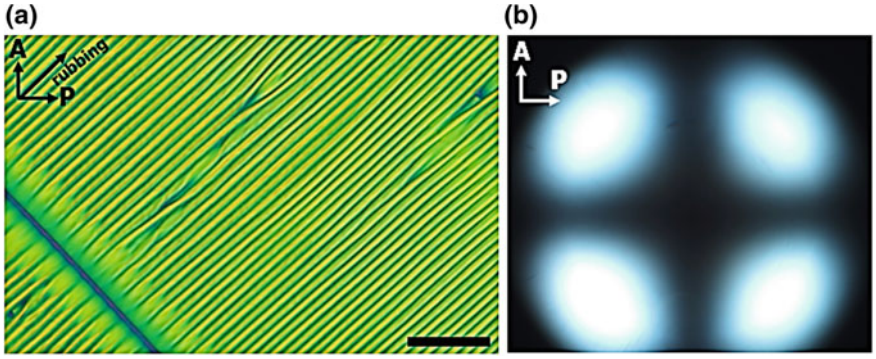

Fig. 7.14 Polarizing optical microscopy texture of **a** twist-bend nematic phase of 1,11-bis(2′,3′-difluoro-4″-pentyl-[1,1′:4′,1″-terphenyl]-4-yl)undecane (DTC5C11) in a homogeneous planar cell treated by PI2555 polyimide layer with characteristic striped texture oriented along the rubbing direction at 45°; **b** conoscopy pattern characteristic of a homeotropic uniaxial nematic; the glass substrates of the homeotropic cell were treated with DMOAP-SE5661 dual alignment layer. Scale bar 50 μm

spin-coated at 500 rpm (3 s), 3000 rpm (30 s), 50 rpm (1 s) on ITO substrates. After the spin-coating procedure, the substrates were soft-baked at $T = 80$ °C for 10 min, and, finally, baked at $T = 180$ °C for 55 min [30]. This procedure, however, does not align widely-used cyanobiphenyl-based flexible dimers. Therefore, further investigations will need to expand on alignment of other families of flexible dimers.

7.13 Electric/Magnetic Fields

Liquid crystals are highly susceptible to external fields. In this section, we will focus our discussion only on employing electric and magnetic fields as means to realign the director field. The reorientation of the director field occurs due to anisotropic LC electric polarization or magnetization. Under an applied external field and set boundary conditions at the boundaries that confine LCs, the equilibrium state of the director field will minimize the total free energy of the system (F) [165]. In case of an applied electric field, the mesogens with positive dielectric anisotropy ($\Delta\varepsilon > 0$) orient along the electric field (**E**) direction, while LCs with $\Delta\varepsilon < 0$ align perpendicular to **E**. The reorientation from uniform configuration to deformed state of the director is called the Frederiks effect. The distortion of the director field occurs only above a certain threshold electric field (E_{th}) which overcomes the surface anchoring and the elasticity of nematic bulk defined as

$$E_{\text{th}} = \frac{\pi}{d}\sqrt{\frac{K_{\text{ii}}}{\varepsilon_{\text{o}}|\Delta\varepsilon|}}, \tag{7}$$

where d is the thickness of a LC cell, K_{ii} is the splay, twist or bend elastic constant of LC, ε_{o} is the permittivity of free space, and $\Delta\varepsilon$ is the dielectric anisotropy of LC [15]. When the field is removed, surface anchoring restores the system to its original state [70]. Note that (7) is applied to a system with an assumption that the anchoring is infinitely strong. However, if the anchoring is weak, the director at the surface has a certain freedom to turn under the action of the elastic torque from the bulk [14]. Consequently, one needs to substitute d with $(d + 2b)$, where $b = K_{\text{ii}}/W^{\text{s}}$ is the surface extrapolation length, where W^{s} is the surface anchoring energy [14]. The schematic representation of cells filled with a LC with $\Delta\varepsilon > 0$ in three different geometries is presented in Fig. 7.15, where Frederiks transition above E_{th} induces splay, twist and bend deformations of the director field.

An application of magnetic field (**B**) is analogous, where LCs with positive diamagnetic anisotropy ($\Delta\chi > 0$) align parallel to applied (**B**), whereas LC with $\Delta\chi < 0$ align perpendicularly to (**B**). The threshold magnetic field is given by [15, 70]

$$B_{\text{th}} = \frac{\pi}{d}\sqrt{\frac{\mu_{\text{o}} K_{\text{ii}}}{\Delta\chi}}, \tag{8}$$

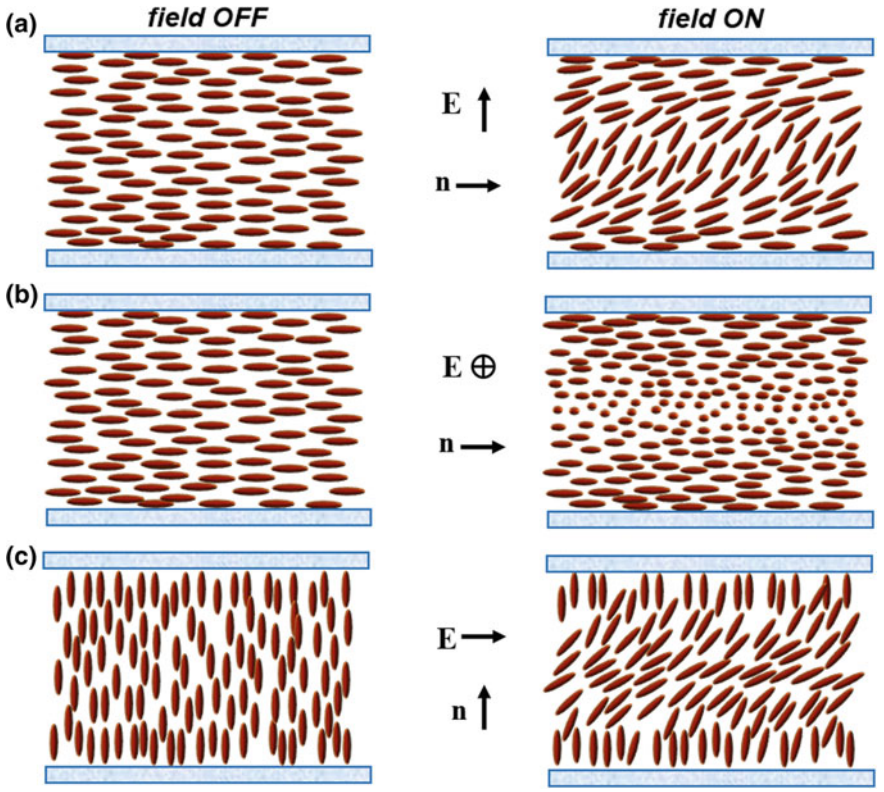

Fig. 7.15 Schematic representation of three different geometries of Frederiks effect inducing **a** splay, **b** twist or **c** bend deformations in a material with positive dielectric anisotropy which aligns parallel to the applied electric field. Adapted with permission from [70]. Copyright (2003) Springer

where $\mu_o = 4\pi \times 10^{-7}$ H m^{-1} is the magnetic permeability of vacuum.

Electric or magnetic field may be employed to (1) aligned an initially unaligned director field, or (2) realign a well aligned director configuration as in Fig. 7.15. The latter is the basis of many LC-based electro-optical applications. Commercial LC display companies exploit different switching modes (such as hybrid aligned nematic, vertical alignment, π-cell) by controlling the alignment at the boundaries of an LC-cell. Various modes yield different switching times, dark states, viewing-angle or contrast ratio [76].

7.14 Aligned LCs as Templates for Guiding Biological Matter

For decades LC alignment was primarily used for display applications. Yet, other fascinating interdisciplinary developments also emerge that use anisotropic nature of LC, molecular ordering and sensitivity to external factors to design sophisticated functional devices. For instance, it was demonstrated that LC-based constructs may be efficiently employed as an optical amplification medium, as well as chemical or biological sensors [17, 20, 36, 45, 52, 62, 69, 90, 115, 136]. In particular, macroscopic detection of the "adsorbate-induced anchoring transition" can be confirmed by observing the textural changes of the LC-based sensor [17]. This phenomenon occurs when amphiphiles adsorb to and alter the orientation ordering of LCs at aqueous-LC interfaces which changes the LC anchoring energy, where a coverage of the interface by adsorbate of 0.1–1 Langmuir (for example at least ~10 μg/ml solution concentrations of lipids) is usually required to change W to induce ordering transition [85, 94]. Another example of an antibody-antigen binding detection/amplification in the *bulk* was demonstrated using water-based lyotropic chromonic LC (LCLC) medium, where the immune complexes larger than R_c are detected optically due to director distortions around them, while individual antibodies that are too small to perturb $\hat{\mathbf{n}}$ remain unseen [136]. The balance of two energies, KR and $W_\theta R^2$ dictate the behavior of the system, as the small inclusions that are not recognized by antibodies, of a size below $R_c < \frac{K}{W_\theta}$, do not distort the director field, whereas the antigen-antibody biding that creates bigger aggregates of targeted microbes distorts LCLC and produces optical signal once $R_c > \frac{K}{W_\theta}$ condition is satisfied.

There is a growing interest in LCLCs due to their biocompatibility [73, 97–99, 113, 146, 159, 180, 181]. Chromonic molecules self-assemble into ordered structures through weak, noncovalent interactions ($\pi - \pi$ attraction), depending on factors such as ionic content, pH, temperature, concentration, and molecular structure [106]. The approaches to align LCLCs include rubbing glass, PI/graphene/silicon oxide deposition, photopatterning, micro-channel confinement, application of magnetic field, nanopatterning polymer films or self-assembling monolayers [39, 55, 60, 64, 75, 92, 101, 104, 112, 122, 128, 138, 150, 151, 167, 171, 172, 179]. Recent development of a dual-layer alignment technique to orient LCLC antiasthmatic drug, disodium cromoglycate (DSCG) [112] allows one to photopattern complex spatially-varying structures. Since *Bacillus subtilis* may be dispersed in non-toxic DSCG [178], such alignment layers were able to be control the distribution, geometry and polarity of bacteria trajectories (Fig. 7.16) [113]. Because the alignment layer and the implemented LC are both water-based, the method involves coating a protective RM layer over a preprogrammed director pattern generated by the azo-dye molecule SD1 [112]. The drawback of this method is the difficulty to assemble (uniform in thickness) LCLC cells using two glass plates with identical prepatterned director field under a polarizing optical microscope.

Another growing trend is to use liquid crystal based biocompatible surfaces or scaffolds for tissue growth [2, 71, 117–119]. Recently, Babakhanova and col-

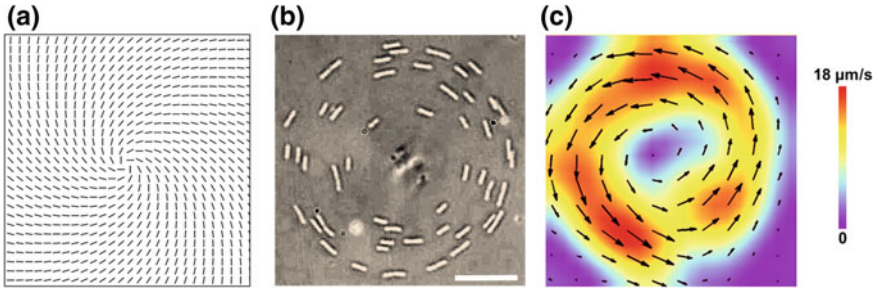

Fig. 7.16 Unipolar circular flow of bacteria around a spiraling vortex. **a** Prepatterned splay-bend deformations of the vortex, **b** circular bacterial swarm enclosing the vortex center, **c** map of bacterial velocities. Scale bar 25 μm. Peng et al. [113]. Reprinted with permission from AAAS

leagues developed nanogrooved surfaces (Fig. 7.17a) using commercially available 8OCB+RM82+photoinitiator Irgacure 651 materials [7]. The antagonistic boundary conditions at the air/homeotropic and unidirectional planar glass interfaces induce the formation of the 'oily streak' defects in the smectic A phase (inset of Fig. 7.17a) [42, 177]. To satisfy the anchoring, smectic layers deform into a series of hemicylinders and result in a texture that exhibits periodic light and dark linear stripes perpendicular to the easy axis (Fig. 7.17a) [42]. The mixture of LC reactive mesogen RM82+photoinitiator was used to fix the molecular orientation of the defect structures in SmA phase via photopolymerization, after which the non-reactive LC was washed out.

The atomic force microscopy shows nanometer topography of the periodic 'oily streak' polymerized defect structures (Fig. 7.17e). When human dermal fibroblasts (hDFs) are plated on these polymerized LC nanogrooved surfaces (Fig. 7.17d, e), the orientation of cells is guided by the topographical cues. Using the elongated nuclei of hDFs, the calculations of the orientational order parameter ($S \sim 0.75$) show the ability to achieve highly oriented alignment of cells using LC defect structures (Fig. 7.17b). Particularly, the cells orient their long axis predominantly parallel to the grooved direction (Fig. 7.17d). Note that when the cells are plated onto a flat glass substrate instead, the final state of the long axis of the cells shows random orientational distribution (Fig. 7.17b). Being able to guide cells in an orderly fashion is of extreme importance, since the cell migration plays a crucial role in chemotaxis, development, tumor invasion, immunity and tissue regeneration.

7.15 Conclusion and Outlook

In this chapter we summarized some of the conventional methods of liquid crystal alignment. The mechanisms of planar, homeotropic and tilted alignments were briefly discussed. One of the most important aligning techniques is the photoalignment method. One may generate all three kinds of (reversible) alignment types by

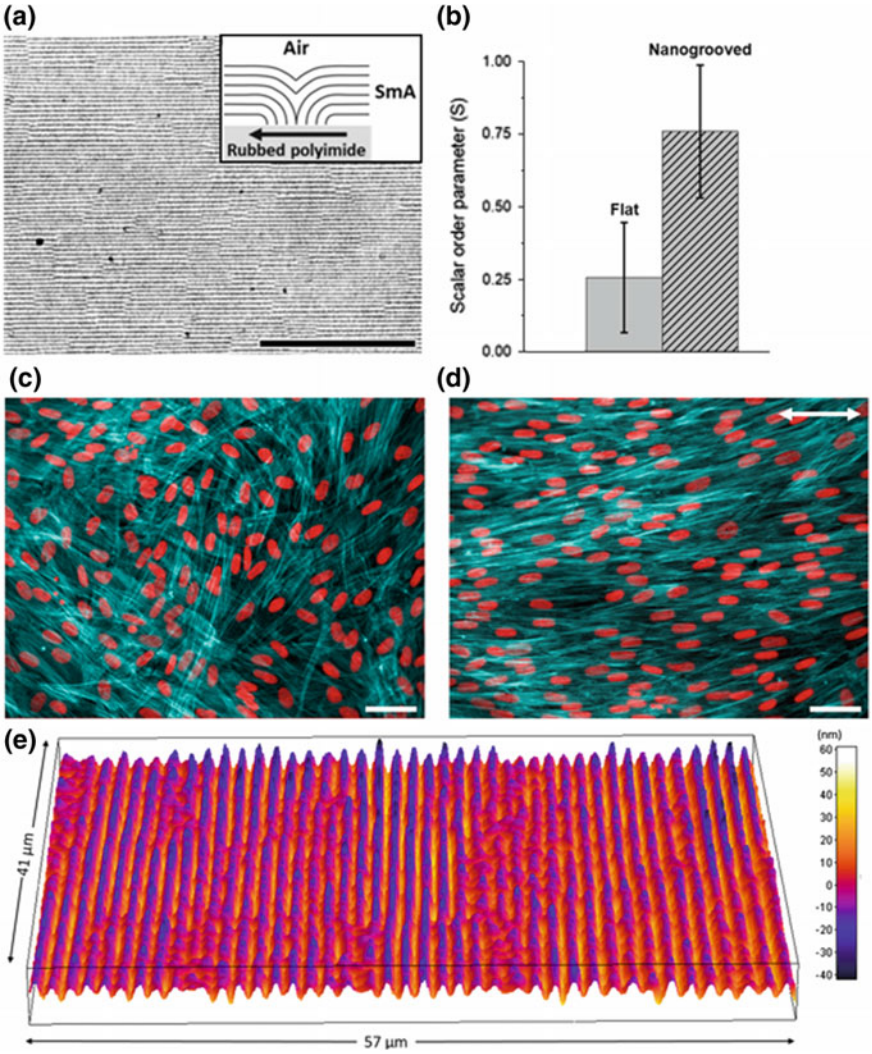

Fig. 7.17 **a** Bright field microscopy image of polymerized linear periodic SmA oily streak structures. The inset shows the formation of the oily streaks due to antagonistic boundary conditions, **b** orientational order parameter of the elongated nuclei (illustrated in red color in panels (**c**) and (**d**); fluorescence microscopy (Olympus IX-81) images of **c** hDF cells oriented randomly on flat glass plate, **d** hDF cells directed parallel to the SmA oily streak polymerized nanostructures. The arrow represents the direction of the nanogrooves, **e** DHM image of polymerized nanogrooved surface morphology of the reactive mesogens. Scale bars 50 µm

adjusting the conditions of the experiments. Importantly, this technique allows one to generate complex spatial patterns of the director with high accuracy. The major problem with this technique is the sensitivity of the alignment layer to environmental conditions at different stages of the preparation. Thus, there is a strong need to develop fast, inexpensive and stable alignment methods which are not too vulnerable to processing procedures for both thermotropic and lyotropic liquid crystals. We also address the importance of developing new alignment methods for non-trivially shaped LC molecules and introduce two methods of homeotropic alignment for rigid bent-core and flexible dimeric molecules.

An important research endeavor is in the ability to generate stable alignment of LC phases (such as chiral nematic or columnar) formed by DNA/RNA molecules of different lengths/sequences, G-quartets, proteins and other biological macromolecules [5, 18, 31, 88, 100, 114, 127, 142, 143, 175, 176]. The ability to tailor the surface properties and roughness of the polymerizable, responsive LCs (via photoalignment for example) may be useful in ordering variety of biological macromolecules.

Another exciting and promising area of exploration involves 'active liquid crystals' composed of self-propelling units. Both, artificial and living self-propelling matter is being investigated. The ability to deterministically control the motion of particles using alignment techniques poses an interesting challenge. Lyotropic and polymerizable liquid crystal systems give rise to vast opportunities to direct biological matter (such as bacteria, cells, sperm). We presented examples of two such reports: bacteria and cell guidance. Such controllable elements may be employed as micro-machines in biomedical engineering applications. The growing trend of using polymerizable LCs are promising not only in conventional LC applications, but also in developing intelligent biomaterials with pre-programmable abilities.

Acknowledgements The research is supported by the grant DE-SC0019105 funded by the U.S. Department of Energy, Office of Science.

References

1. K. Adlem, M. Copic, G.R. Luckhurst, A. Mertelj, O. Parri, R.M. Richardson, B.D. Snow, B.A. Timimi, R.P. Tuffin, D. Wilkes, Chemically induced twist-bend nematic liquid crystals, liquid crystal dimers, and negative elastic constants. Phys. Rev. E: Stat. Nonlinear Soft Matter Phys. **88**(2), 022503 (2013). https://doi.org/10.1103/PhysRevE.88.022503
2. A. Agrawal, O. Adetiba, H. Kim, H. Chen, J.G. Jacot, R. Verduzco, Stimuli-responsive liquid crystal elastomers for dynamic cell culture. J. Mater. Res. **30**(4), 453–462 (2015). https://doi.org/10.1557/jmr.2014.392
3. M.A.R. Aguilar, J. San Román, *Smart Polymers and Their Applications*. *Woodhead Publishing in Materials* (Woodhead Publishing, is an imprint of Elsevier, Cambridge, UK, 2014)
4. M. Aizawa, K. Hisano, M. Ishizu, N. Akamatsu, C.J. Barrett, A. Shishido, Unpolarized light-induced alignment of azobenzene by scanning wave photopolymerization. Polym. J. **50**(8), 753–759 (2018). https://doi.org/10.1038/s41428-018-0058-2
5. A. Annila, P. Permi, Weakly aligned biological macromolecules in dilute aqueous liquid crystals. Concept Magn. Reson. A **23a**(1), 22–37 (2004). https://doi.org/10.1002/cmr.a.20020

6. D. Armitage, I. Underwood, S.T. Wu, *Introduction to Microdisplays*. Wiley SID Series in Display Technology (Wiley, Chichester, England; Hoboken, NJ, 2006)
7. G. Babakhanova, J. Krieger, B.X. Li, M.H. Kim, O.D. Lavrentovich, *Surface Mediated Cell Alignment using Polymerized Liquid Crystal Nanostructures* (2019) (Manuscript in preparation)
8. G. Babakhanova, Z. Parsouzi, S. Paladugu, H. Wang, Y.A. Nastishin, S.V. Shiyanovskii, S. Sprunt, O.D. Lavrentovich, Elastic and viscous properties of the nematic dimer CB7CB. Phys. Rev. E **96**(6), 062704 (2017). https://doi.org/10.1103/PhysRevE.96.062704
9. G. Babakhanova, T. Turiv, Y. Guo, M. Hendrikx, Q.-H. Wei, A.P.H.J. Schenning, D.J. Broer, O.D. Lavrentovich, Liquid crystal elastomer coatings with programmed response of surface profile. Nat. Commun. **9**(1), 456 (2018). https://doi.org/10.1038/s41467-018-02895-9
10. H.M.D. Bandara, S.C. Burdette, Photoisomerization in different classes of azobenzene. Chem. Soc. Rev. **41**(5), 1809–1825 (2012). https://doi.org/10.1039/c1cs15179g
11. M. Barnik, V. Kozenkov, N. Shtykov, S. Palto, S. Yudin, Photoinduced optical anisotropy in Langmuir-Blodgett films. J. Mol. Electron. **5**(1), 53–56 (1989)
12. D.W. Berreman, Solid surface shape and alignment of an adjacent nematic liquid-crystal. Phys. Rev. Lett. **28**(26), 1683–1686 (1972). https://doi.org/10.1103/PhysRevLett.28.1683
13. D.W. Berreman, Alignment of liquid-crystals by grooved surfaces. Mol. Cryst. Liq. Cryst. **23**(3–4), 215–231 (1973). https://doi.org/10.1080/15421407308083374
14. L.M. Blinov, *Structure and Properties of Liquid Crystals* (Springer, Dordrecht Netherlands, New York, 2010)
15. L.M. Blinov, V.G. Chigrinov, *Electrooptic Effects in Liquid Crystal Materials*. Partially Ordered Systems (Springer, New York, 1994)
16. V. Borshch, Y.K. Kim, J. Xiang, M. Gao, A. Jakli, V.P. Panov, J.K. Vij, C.T. Imrie, M.G. Tamba, G.H. Mehl, O.D. Lavrentovich, Nematic twist-bend phase with nanoscale modulation of molecular orientation. Nat. Commun. **4**, 2635 (2013). https://doi.org/10.1038/ncomms3635
17. J.M. Brake, M.K. Daschner, Y.Y. Luk, N.L. Abbott, Biomolecular interactions at phospholipid-decorated surfaces of liquid crystals. Science **302**(5653), 2094–2097 (2003). https://doi.org/10.1126/science.1091749
18. R. Brandes, D.R. Kearns, Magnetic ordering of DNA liquid crystals. Biochemistry-Us **25**(20), 5890–5895 (1986). https://doi.org/10.1021/bi00368a008
19. O.S. Bushuyev, M. Aizawa, A. Shishido, C.J. Barrett, Shape-shifting azo dye polymers: towards sunlight-driven molecular devices. Macromol. Rapid Commun. **39**(1), 1700253 (2018). https://doi.org/10.1002/marc.201700253
20. R.J. Carlton, J.T. Hunter, D.S. Miller, R. Abbasi, P.C. Mushenheim, L.N. Tan, N.L. Abbott, Chemical and biological sensing using liquid crystals. Liq. Cryst. Rev. **1**(1), 29–51 (2013). https://doi.org/10.1080/21680396.2013.769310
21. J.A. Castellano, Surface anchoring of liquid-crystal molecules on various substrates. Mol. Cryst. Liq. Cryst. **94**(1–2), 33–41 (1983). https://doi.org/10.1080/00268948308084245
22. M. Cestari, S. Diez-Berart, D.A. Dunmur, A. Ferrarini, M.R. de la Fuente, D.J.B. Jackson, D.O. Lopez, G.R. Luckhurst, M.A. Perez-Jubindo, R.M. Richardson, J. Salud, B.A. Timimi, H. Zimmermann, Phase behavior and properties of the liquid-crystal dimer 1″,7″-bis(4-cyanobiphenyl-4′-yl) heptane: a twist-bend nematic liquid crystal. Phys. Rev. E **84**(3), 031704 (2011). https://doi.org/10.1103/PhysRevE.84.031704
23. D. Chen, J.H. Porada, J.B. Hooper, A. Klittnick, Y. Shen, M.R. Tuchband, E. Korblova, D. Bedrov, D.M. Walba, M.A. Glaser, J.E. Maclennan, N.A. Clark, Chiral heliconical ground state of nanoscale pitch in a nematic liquid crystal of achiral molecular dimers. Proc. Natl. Acad. Sci. USA **110**(40), 15931–15936 (2013). https://doi.org/10.1073/pnas.1314654110
24. J. Chen, *Handbook of Visual Display Technology* (Springer, Berlin Heidelberg, New York, NY, 2016)
25. V. Chigrinov, H.S. Kwok, H. Takada, H. Takatsu, Photo-aligning by azo-dyes: physics and applications. Liq. Cryst. Today **14**(4), 1–15 (2005). https://doi.org/10.1080/14645180600617908

26. V.G. Chigrinov, V.M. Kozenkov, H.S. Kwok *Photoalignment of Liquid Crystalline Materials: Physics and Applications*. Wiley SID Series in Display Technology (Wiley, Chichester, England; Hoboken, NJ, 2008)
27. M.M.Z.J. Chrzanowski, M. Olifierczuk, J. Kędzierski, E. Nowinowski-Kruszelnicki, Photoalignment—an alternative aligning technique for liquid crystal displays. J. Achiev. Mater. Manuf. Eng. **48**(1), 7–13 (2011)
28. J. Cognard, *Alignment of Nematic Liquid-Crystals and Their Mixtures. Molecular Crystals and Liquid Crystals* (Gordon and Breach Science Publishers, New York, 1982)
29. J. Cognard, *Lubrication with Liquid-Crystals*, vol. 441. *Tribology and the Liquid-Crystalline State*. ACS Symposium Series (Washington, D.C., 1990)
30. G. Cukrov, Y.M. Golestani, J. Xiang, Y.A. Nastishin, Z. Ahmed, C. Welch, G.H. Mehl, O.D. Lavrentovich, Comparative analysis of anisotropic material properties of uniaxial nematics formed by flexible dimers and rod-like monomers. Liq. Cryst. **44**(1), 219–231 (2017). https://doi.org/10.1080/02678292.2016.1240248
31. J.T. Davis, G.P. Spada, Supramolecular architectures generated by self-assembly of guanosine derivatives. Chem. Soc. Rev. **36**(2), 296–313 (2007). https://doi.org/10.1039/b600282j
32. P.G. de Gennes, J. Prost, *The Physics of Liquid Crystals*, 2nd edn. (Clarendon Press, Oxford, 1995)
33. I. Dierking, *Textures of Liquid Crystals* (Wiley-VCH, Weinheim, 2003)
34. A.G. Dyadyusha, T.Y. Marusii, Y.A. Reznikov, A.I. Khizhnyak, V.Y. Reshetnyak, Orientational effect due to a change in the anisotropy of the interaction between a liquid-crystal and a bounding surface. Jetp. Lett. **56**(1), 17–21 (1992)
35. O. Elamain, G. Hegde, L. Komitov, Alignment and alignment transition of bent core nematics. Appl. Phys. Lett. **103**(2), 023301 (2013). https://doi.org/10.1063/1.4813443
36. J.Y. Fang, W. Ma, J.V. Selinger, R. Shashidhar, Imaging biological cells using liquid crystals. Langmuir **19**(7), 2865–2869 (2003). https://doi.org/10.1021/la0264062
37. Y.Q. Fang, J.A. Wang, Q. Zhang, Y. Zeng, Y.H. Wang, Synthesis of soluble polyimides for vertical alignment of liquid crystal via one-step method. Eur. Polym. J. **46**(5), 1163–1167 (2010). https://doi.org/10.1016/j.eurpolymj.2009.12.021
38. W. Fu, L. Liu, K. Jiang, Q. Li, S. Fan, Super-aligned carbon nanotube films as aligning layers and transparent electrodes for liquid crystal displays. Carbon **48**(7), 1876–1879 (2010). https://doi.org/10.1016/j.carbon.2010.01.026
39. T. Fujiwara, K. Ichimura, Surface-assisted photoalignment control of lyotropic liquid crystals. Part 2. Photopatterning of aqueous solutions of a water-soluble anti-asthmatic drug as lyotropic liquid crystals. J. Mater. Chem. **12**(12), 3387–3391 (2002). https://doi.org/10.1039/b208311f
40. K. Gao, H.H. Cheng, A.K. Bhowmik, P.J. Bos, Thin-film pancharatnam lens with low f-number and high quality. Opt. Express **23**(20), 26086–26094 (2015). https://doi.org/10.1364/Oe.23.026086
41. J.M. Geary, J.W. Goodby, A.R. Kmetz, J.S. Patel, The mechanism of polymer alignment of liquid-crystal materials. J. Appl. Phys. **62**(10), 4100–4108 (1987). https://doi.org/10.1063/1.339124
42. I. Gharbi, A. Missaoui, D. Demaille, E. Lacaze, C. Rosenblatt, Persistence of smectic-a oily streaks into the nematic phase by UV irradiation of reactive mesogens. Crystals **7**(12), 358 (2017). https://doi.org/10.3390/cryst7120358
43. W.M. Gibbons, P.J. Shannon, S.T. Sun, B.J. Swetlin, Surface-mediated alignment of nematic liquid-crystals with polarized laser-light. Nature **351**(6321), 49–50 (1991). https://doi.org/10.1038/351049a0
44. Y. Guo, M. Jiang, C. Peng, K. Sun, O. Yaroshchuk, O. Lavrentovich, Q.H. Wei, High-resolution and high-throughput plasmonic photopatterning of complex molecular orientations in liquid crystals. Adv. Mater. **28**(12), 2353–2358 (2016). https://doi.org/10.1002/adma.201506002
45. V.K. Gupta, J.J. Skaife, T.B. Dubrovsky, N.L. Abbott, Optical amplification of ligand-receptor binding using liquid crystals. Science **279**(5359), 2077–2080 (1998). https://doi.org/10.1126/science.279.5359.2077

46. M. Hasegawa, Modeling of photoinduced optical anisotropy and anchoring energy of polyimide exposed to linearly polarized deep UV light. Jpn. J. Appl. Phys. Part 2-Lett. **38**(4b), L457–L460 (1999). https://doi.org/10.1143/jjap.38.l457
47. U. Hecht, C.M. Schilz, M. Stratmann, Influence of relative humidity during film formation processes on the structure of ultrathin polymeric films. Langmuir **14**(23), 6743–6748 (1998). https://doi.org/10.1021/la9804987
48. K. Hiltrop, H. Stegemeyer, Alignment of liquid crystals by amphiphilic monolayers. Ber. Bunsenges. Phys. Chem. **82**(9), 884–889 (1978). https://doi.org/10.1002/bbpc.19780820920
49. K. Hisano, M. Aizawa, M. Ishizu, Y. Kurata, W. Nakano, N. Akamatsu, C.J. Barrett, A. Shishido, Scanning wave photopolymerization enables dye-free alignment patterning of liquid crystals. Sci. Adv. **3**(11), e1701610 (2017). https://doi.org/10.1126/sciadv.1701610
50. K. Hisano, Y. Kurata, M. Aizawa, M. Ishizu, T. Sasaki, A. Shishido, Alignment layer-free molecular ordering induced by masked photopolymerization with non-polarized light. Appl. Phys. Express **9**(7), 072601 (2016). https://doi.org/10.7567/Apex.9.072601
51. J.Y.L. Ho, V.G. Chigrinov, H.S. Kwok, Variable liquid crystal pretilt angles generated by photoalignment of a mixed polyimide alignment layer. Appl. Phys. Lett. **90**(24), 243506 (2007). https://doi.org/10.1063/1.2748345
52. J.T. Hunter, N.L. Abbott, *Liquid Crystals Beyond Displays Chemistry, Physics, and Applications* (Wiley, Hoboken, N.J., 2012)
53. J.Y. Hwang, S.H. Lee, S.K. Paek, D.S. Seo, Tilt angle generation for nematic liquid crystal on blended homeotropic polyimide layer containing trifluoromethyl moieties. Jpn. J. Appl. Phys. Part 1-Regul. Pap. Short Notes Rev. Pap. **42**(4a), 1713–1714 (2003). https://doi.org/10.1143/jjap.42.1713
54. O.S. Iadlovska, G.R. Maxwell, G. Babakhanova, G.H. Mehl, C. Welch, S.V. Shiyanovskii, O.D. Lavrentovich, Tuning selective reflection of light by surface anchoring in cholesteric cells with oblique helicoidal structures. Opt. Lett. **43**(8), 1850–1853 (2018). https://doi.org/10.1364/Ol.43.001850
55. K. Ichimura, T. Fujiwara, M. Momose, D. Matsunaga, Surface-assisted photoalignment control of lyotropic liquid crystals. Part 1. Characterisation and photoalignment of aqueous solutions of a water-soluble dye as lyotropic liquid crystals. J. Mater. Chem. **12**(12), 3380–3386 (2002). https://doi.org/10.1039/b208310h
56. K. Ichimura, Y. Suzuki, T. Seki, A. Hosoki, K. Aoki, Reversible change in alignment mode of nematic liquid-crystals regulated photochemically by command surfaces modified with an azobenzene monolayer. Langmuir **4**(5), 1214–1216 (1988). https://doi.org/10.1021/la00083a030
57. W. Iglesias, T.J. Smith, P.B. Basnet, S.R. Stefanovic, C. Tschierske, D.J. Lacks, A. Jakli, E.K. Mann, Alignment by Langmuir/Schaefer monolayers of bent-core liquid crystals. Soft Matter **7**(19), 9043–9050 (2011). https://doi.org/10.1039/c1sm05546a
58. A. Jakli, O.D. Lavrentovich, J.V. Selinger, Physics of liquid crystals of bent-shaped molecules. Rev. Mod. Phys. **90**(4), 045004 (2018). https://doi.org/10.1103/RevModPhys.90.045004
59. J.L. Janning, Thin-Film surface orientation for liquid-crystals. Appl. Phys. Lett. **21**(4), 173 (1972). https://doi.org/10.1063/1.1654331
60. J.W. Jeong, G.H. Han, A.T.C. Johnson, P.J. Collings, T.C. Lubensky, A.G. Yodh, Homeotropic Alignment of lyotropic chromonic liquid crystals using noncovalent interactions. Langmuir **30**(10), 2914–2920 (2014). https://doi.org/10.1021/la404893t
61. F.J. Kahn, G.N. Taylor, H. Schonhorn, Surface-produced alignment of liquid-crystals. P IEEE **61**(7), 823–828 (1973). doi:https://doi.org/10.1109/proc.1973.9171
62. H.R. Kim, J.H. Kim, T.S. Kim, S.W. Oh, E.Y. Choi, Optical detection of deoxyribonucleic acid hybridization using an anchoring transition of liquid crystal alignment. Appl. Phys. Lett. **87**(14), 143901 (2005). https://doi.org/10.1063/1.2077859
63. J.B. Kim, K.C. Kim, H.J. Ahn, B.H. Hwang, J.T. Kim, S.J. Jo, C.S. Kim, H.K. Baik, C.J. Choi, M.K. Jo, Y.S. Kim, J.S. Park, D. Kang, No bias pi cell using a dual alignment layer with an intermediate pretilt angle. Appl. Phys. Lett. **91**(2), 023507 (2007). https://doi.org/10.1063/1.2757121

64. J.Y. Kim, K. Nayani, H.S. Jeong, H.J. Jeon, H.W. Yoo, E.H. Lee, J.O. Park, M. Srinivasarao, H.T. Jung, Macroscopic alignment of chromonic liquid crystals using patterned substrates. Phys. Chem. Chem. Phys. **18**(15), 10362–10366 (2016). https://doi.org/10.1039/c5cp07570j
65. Y.K. Kim, R. Breckon, S. Chakraborty, M. Gao, S.N. Sprunt, J.T. Gleeson, R.J. Twieg, A. Jakli, O.D. Lavrentovich, Properties of the broad-range nematic phase of a laterally linked H-shaped liquid crystal dimer. Liq. Cryst. **41**(9), 1345–1355 (2014). https://doi.org/10.1080/02678292.2014.920930
66. Y.K. Kim, G. Cukrov, F. Vita, E. Scharrer, E.T. Samulski, O. Francescangeli, O.D. Lavrentovich, Search for microscopic and macroscopic biaxiality in the cybotactic nematic phase of new oxadiazole bent-core mesogens. Phys. Rev. E **93**(6), 062701 (2016). https://doi.org/10.1103/PhysRevE.93.062701
67. Y.K. Kim, G. Cukrov, J. Xiang, S.T. Shin, O.D. Lavrentovich, Domain walls and anchoring transitions mimicking nematic biaxiality in the oxadiazole bent-core liquid crystal C7. Soft Matter **11**(20), 3963–3970 (2015). https://doi.org/10.1039/c5sm00580a
68. Y.K. Kim, B. Senyuk, S.T. Shin, A. Kohlmeier, G.H. Mehl, O.D. Lavrentovich, Surface alignment, anchoring transitions, optical properties, and topological defects in the thermotropic nematic phase of organo-siloxane tetrapodes. Soft Matter **10**(3), 500–509 (2014). https://doi.org/10.1039/c3sm52249k
69. Y.K. Kim, X.G. Wang, P. Mondkar, E. Bukusoglu, N.L. Abbott, Self-reporting and self-regulating liquid crystals. Nature **557**(7706), 539 (2018). https://doi.org/10.1038/s41586-018-0098-y
70. M. Kleman, O.D. Lavrentovich, *Soft Matter Physics: An Introduction* (Partially ordered systems, Springer, New York, 2003)
71. G. Kocer, J. ter Schiphorst, M. Hendrikx, H.G. Kassa, P. Leclere, A.P.H.J. Schenning, P. Jonkheijm, Light-responsive hierarchically structured liquid crystal polymer networks for harnessing cell adhesion and migration. Adv. Mater. **29**(27), 1606407 (2017). https://doi.org/10.1002/adma.201606407
72. V.M. Kozenkov, S.G. Yudin, E.G. Katyshev, S.P. Palto, V.T. Lazareva, V.A. Barachevskii, Photoinduced Optical Anisotropy in Multilayered Langmuir Films. Pisma. Zh. Tekh. Fiz. **12**(20), 1267–1272 (1986)
73. A. Kumar, S.K. Pattanayek, Imaging of bacteria using chromonic liquid crystals. Mol. Cryst. Liq. Cryst. **625**(1), 126–136 (2016). https://doi.org/10.1080/15421406.2015.1069441
74. A. Lakhtakia, R. Messier, *Sculptured Thin Films: Nanoengineered Morphology and Optics*. Press Monograph Series, vol. PM143 (SPIE Press, Bellingham, Wash, 2005)
75. O.D. Lavrentovich, T. Ishikawa, Bulk alignment of lyotropic chromonic liquid crystals. USA Patent US6411354B1 (2002)
76. C.C. Lee, *The Current Trends of Optics and Photonics* (Springer, Netherlands, 2014)
77. E.S. Lee, P. Vetter, T. Miyashita, T. Uchida, M. Kano, M. Abe, K. Sugawara, Control of liquid-crystal alignment using stamped-morphology method. Jpn. J. Appl. Phys. **32**(10a), L1436–L1438 (1993). https://doi.org/10.1143/jjap.32.l1436
78. K.S. Lee, *Polymers for photonics applications II,* vol. 2. *Nonlinear Optical, Photorefractive and Two-Photon Absorption Polymers*, vol. 158 (Springer, Berlin, 2003)
79. K.W. Lee, A. Lien, S.H. Paek, C. Durning, H. Fukuro, Relationship between alignment layer polymer surface structures and liquid crystal display parameters. Macromol. Symp. **118**, 505–512 (1997). https://doi.org/10.1002/masy.19971180168
80. K.W. Lee, S.H. Paek, A. Lien, C. Durning, H. Fukuro, Microscopic molecular reorientation of alignment layer polymer surfaces induced by rubbing and its effects on LC pretilt angles. Macromolecules **29**(27), 8894–8899 (1996). https://doi.org/10.1021/ma960683w
81. Y.J. Lee, J.H. Baek, Y. Kim, J.U. Heo, C.J. Yu, J.H. Kim, Enhanced surface anchoring energy for the photo-alignment layer with reactive mesogens for fast response time of liquid crystal displays. J. Phys. D Appl. Phys. **46**(14), 145305 (2013). https://doi.org/10.1088/0022-3727/46/14/145305
82. Y.J. Lee, Y.W. Kim, J. Du Ha, J.M. Oh, M.H. Yi, Synthesis and characterization of novel polyimides with 1-octadecyl side chains for liquid crystal alignment layers. Polym. Adv. Technol. **18**(3), 226–234 (2007). https://doi.org/10.1002/pat.862

83. Y.J. Lee, Y.K. Kim, S.I. Jo, A.R. Yoon, C.J. Yu, J.H. Kim, Liquid Crystal Alignment Control Using Reactive Mesogen Mixed with Alignment Layers, in *IDW* (San Diego, CA, USA, 2009)
84. Q. Li, *Intelligent Stimuli-Responsive Materials: From Well-Defined Nanostructures to Applications* (Wiley, Hoboken, New Jersey, 2013)
85. I.H. Lin, D.S. Miller, P.J. Bertics, C.J. Murphy, J.J. de Pablo, N.L. Abbott, Endotoxin-induced structural transformations in liquid crystalline droplets. Science **332**(6035), 1297–1300 (2011). https://doi.org/10.1126/science.1195639
86. W.R. Liou, C.Y. Chen, J.J. Ho, C.K. Hsu, C.C. Chang, R.Y. Hsiao, S.H. Chang, Improved alignment layer grown by oblique evaporation for liquid crystal devices. Displays **27**(2), 69–72 (2006). https://doi.org/10.1016/j.displa.2005.11.001
87. D.O. Lopez, B. Robles-Hernandez, J. Salud, M.R. de la Fuente, N. Sebastian, S. Diez-Berart, X. Jaen, D.A. Dunmur, G.R. Luckhurst, Miscibility studies of two twist-bend nematic liquid crystal dimers with different average molecular curvatures. A comparison between experimental data and predictions of a Landau mean-field theory for the N-TB-N phase transition. Phys. Chem. Chem. Phys. **18**(6), 4394–4404 (2016). https://doi.org/10.1039/c5cp07605f
88. M. Louhivuori, R. Otten, K. Lindorff-Larsen, A. Annila, Conformational fluctuations affect protein alignment in dilute liquid crystal media. J. Am. Chem. Soc. **128**(13), 4371–4376 (2006). https://doi.org/10.1021/ja0576334
89. M. Matsumori, A. Takahashi, Y. Tomioka, T. Hikima, M. Takata, T. Kajitani, T. Fukushima, Photoalignment of an azobenzene-based chromonic liquid crystal dispersed in triacetyl cellulose: single-layer alignment films with an exceptionally high order parameter. Acs. Appl. Mater. Inter. **7**(21), 11074–11078 (2015). https://doi.org/10.1021/acsami.5b02577
90. M.K. McCamley, G.P. Crawford, M. Ravnik, S. Zumer, A.W. Artenstein, S.M. Opal, Optical detection of anchoring at free and fluid surfaces using a nematic liquid crystal sensor. Appl. Phys. Lett. **91**(14), 141916 (2007). https://doi.org/10.1063/1.2795347
91. M.E. McConney, A. Martinez, V.P. Tondiglia, K.M. Lee, D. Langley, I.I. Smalyukh, T.J. White, Topography from topology: photoinduced surface features generated in liquid crystal polymer networks. Adv. Mater. **25**(41), 5880–5885 (2013). https://doi.org/10.1002/adma.201301891
92. C.K. McGinn, L.I. Laderman, N. Zimmermann, H.S. Kitzerow, P.J. Collings, Planar anchoring strength and pitch measurements in achiral and chiral chromonic liquid crystals using 90-degree twist cells. Phys. Rev. E **88**(6), 062513 (2013). https://doi.org/10.1103/PhysRevE.88.062513
93. D. Meyerhofer, New technique of aligning liquid-crystals on surfaces. Appl. Phys. Lett. **29**(11), 691–692 (1976). https://doi.org/10.1063/1.88928
94. D.S. Miller, X.G. Wang, N.L. Abbott, Design of functional materials based on liquid crystalline droplets. Chem. Mater. **26**(1), 496–506 (2014). https://doi.org/10.1021/cm4025028
95. M. Murata, M. Uekita, Y. Nakajima, K. Saitoh, Alignment of nematic liquid-crystal using polyimide langmuir-blodgett films-(Ii). Jpn. J. Appl. Phys. Part 2-Lett. **32**(5a), L679–L682. https://doi.org/10.1143/jjap.32.l679
96. I. Muševič, *Liquid Crystal Colloids* (Springer, Berlin Heidelberg, New York, NY, 2017)
97. P.C. Mushenheim, R.R. Trivedi, S.S. Roy, M.S. Arnold, D.B. Weibel, N.L. Abbott, Effects of confinement, surface-induced orientations and strain on dynamical behaviors of bacteria in thin liquid crystalline films. Soft Matter **11**(34), 6821–6831 (2015). https://doi.org/10.1039/c5sm01489a
98. P.C. Mushenheim, R.R. Trivedi, H.H. Tuson, D.B. Weibel, N.L. Abbott, Dynamic self-assembly of motile bacteria in liquid crystals. Soft Matter **10**(1), 88–95 (2014). https://doi.org/10.1039/c3sm52423j
99. P.C. Mushenheim, R.R. Trivedi, D.B. Weibel, N.L. Abbott, Using liquid crystals to reveal how mechanical anisotropy changes interfacial behaviors of motile bacteria. Biophys. J. **107**(1), 255–265 (2014). https://doi.org/10.1016/j.bpj.2014.04.047
100. M. Nakata, G. Zanchetta, B.D. Chapman, C.D. Jones, J.O. Cross, R. Pindak, T. Bellini, N.A. Clark, End-to-end stacking and liquid crystal condensation of 6-to 20-base pair DNA duplexes. Science **318**(5854), 1276–1279 (2007). https://doi.org/10.1126/science.1143826

101. A.Y. Nastishin, K. Neupane, A.R. Baldwin, O.D. Lavrentovich, S. Sprunt, *Elasticity and Viscosity of a Lyotropic Chromonic Nematic Studied with Dynamic Light Scattering* (2008). eprint arXiv:0807.2669
102. T. Ogawa, Y. Kanemitsu, *Optical Properties of Low-Dimensional Materials* (River Edge, NJ, World Scientific, Singapore, 1995)
103. M. Oh-e, H. Yokoyama, D. Kim, Mapping molecular conformation and orientation of polyimide surfaces for homeotropic liquid crystal alignment by nonlinear optical spectroscopy. Phys. Rev. E **69**(5), 051705 (2004). https://doi.org/10.1103/PhysRevE.69.051705
104. E. Oton, J.M. Escolano, X. Quintana, J.M. Oton, M.A. Geday, Aligning lyotropic liquid crystals with silicon oxides. Liq. Cryst. **42**(8), 1069–1075 (2015). https://doi.org/10.1080/02678292.2015.1024767
105. E. Oton, S. Lopez-Andres, N. Bennis, J.M. Oton, M.A. Geday, Silicon oxides as alignment surfaces for vertically-aligned nematics in photonic devices. Opto-Electron. Rev. **22**(2), 92–100 (2014). https://doi.org/10.2478/s11772-014-0182-2
106. H.-S. Park, O.D. Lavrentovich, *Liquid Crystals Beyond Displays Chemistry, Physics, and Applications* (Wiley, Hoboken, New Jersey, 2012)
107. J.C. Park, D.J. Park, K.C. Son, Y.B. Kim, The properties of homeotropic alignment materials as the side chain molecular structure in polyimides. Mol. Cryst. Liq. Cryst. **479**, 1229–1241 (2007). https://doi.org/10.1080/15421400701734056
108. S.V. Pasechnik, V.G. Chigrinov, D.V. Shmeliova, *Liquid Crystals: Viscous and Elastic Properties* (Wiley-VCH, Weinheim, 2009)
109. M. Pelliccione, T.M. Lu, *Evolution of Thin-Film Morphology Modeling and Simulations*. Springer Series in Materials Science (Springer, Berlin, 2008)
110. C. Peng, T. Turiv, Y. Guo, S.V. Shiyanovskii, Q.H. Wei, O.D. Lavrentovich, Control of colloidal placement by modulated molecular orientation in nematic cells. Sci. Adv. **2**(9), e1600932 (2016). https://doi.org/10.1126/sciadv.1600932
111. C. Peng, T. Turiv, R. Zhang, Y. Guo, S.V. Shiyanovskii, Q.H. Wei, J. de Pablo, O.D. Lavrentovich, Controlling placement of nonspherical (boomerang) colloids in nematic cells with photopatterned director. J. Phys.: Condens. Matter **29**(1), 014005 (2017). https://doi.org/10.1088/0953-8984/29/1/014005
112. C.H. Peng, Y.B. Guo, T. Turiv, M. Jiang, Q.H. Wei, O.D. Lavrentovich, Patterning of lyotropic chromonic liquid crystals by photoalignment with photonic metamasks. Adv. Mater. **29**(21), 1606112 (2017). https://doi.org/10.1002/adma.201606112
113. C.H. Peng, T. Turiv, Y.B. Guo, Q.H. Wei, O.D. Lavrentovich, Command of active matter by topological defects and patterns. Science **354**(6314), 882–885 (2016). https://doi.org/10.1126/science.aah6936
114. T. Pfohl, J.H. Kim, M. Yasa, H.P. Miller, G.C.L. Wong, F. Bringezu, Z. Wen, L. Wilson, M.W. Kim, Y. Li, C.R. Safinya, Controlled modification of microstructured silicon surfaces for confinement of biological macromolecules and liquid crystals. Langmuir **17**(17), 5343–5351 (2001). https://doi.org/10.1021/la010145z
115. N. Popov, L.W. Honaker, M. Popova, N. Usol'tseva, E.K. Mann, A. Jakli, P. Popov, Thermotropic liquid crystal-assisted chemical and biological sensors. Materials **11**(1), E20 (2018). https://doi.org/10.3390/ma11010020
116. V.V. Presnyakov, Z.J. Liu, V.G. Chigrinov, Infiltration of photonic crystal fiber with liquid crystals, in *Optics East 2005, SPIE* (2005), p. 7
117. M.E. Prevot, H. Andro, S.L.M. Alexander, S. Ustunel, C. Zhu, Z. Nikolov, S.T. Rafferty, M.T. Brannum, B. Kinsel, L.T.J. Korley, E.J. Freeman, J.A. McDonough, R.J. Clements, E. Hegmann, Liquid crystal elastomer foams with elastic properties specifically engineered as biodegradable brain tissue scaffolds. Soft Matter **14**(3), 354–360 (2018). https://doi.org/10.1039/c7sm01949a
118. M.E. Prevot, L.E. Bergquist, A. Sharma, T. Mori, Y. Gao, T. Bera, C. Zhu, M.T. Leslie, R. Cukelj, L.T.J. Korley, E.J. Freeman, J.A. McDonough, R.J. Clements, E. Hegmann, New developments in 3D liquid crystal elastomers scaffolds for tissue engineering: from physical template to responsive substrate. Liq. Cryst. Xxi **10361**, 103610T (2017). https://doi.org/10.1117/12.2275338

119. M.E. Prevot, S. Ustunel, E. Hegmann, Liquid crystal elastomers-A path to biocompatible and biodegradable 3D-LCE scaffolds for tissue regeneration. Materials **11**(3), 377 (2018). https://doi.org/10.3390/ma11030377
120. M.D.A. Rahman, H. Agha, T.-K. Truong, J.H. Park, D. Suh, G. Scalia, Incorporation and orientational order of aligned carbon nanotube sheets on polymer films for liquid crystal-aligning transparent electrodes. J. Mol. Liq. **267**, 363–366 (2018). https://doi.org/10.1016/j.molliq.2017.12.122
121. A. Rapini, M. Papoular, Distortion d'une lamelle nématique sous champ magnétique conditions d'ancrage aux parois. J. Phys. Colloq. **30**(C4), C4-54–C54-56 (1969)
122. A. Rapp, K. Ermolaev, B.M. Fung, The alignment of lyotropic liquid crystals formed by hexadecyltrimethylammonium bromide in D2O in a magnetic field. J. Phys. Chem. B **103**(10), 1705–1711 (1999). https://doi.org/10.1021/jp984021f
123. Z. Ren, Y. Lan, Y. Wang, *Aligned Carbon Nanotubes: Physics, Concepts, Fabrication and Devices. NanoScience and Technology* (Springer, Heidelberg, New York, 2013)
124. G.G. Roberts, *Langmuir-Blodgett Films* (Plenum Press, New York, 1990)
125. B. Robles-Hernandez, N. Sebastian, M.R. de la Fuente, D.O. Lopez, S. Diez-Berart, J. Salud, M.B. Ros, D.A. Dunmur, G.R. Luckhurst, B.A. Timimi, Twist, tilt, and orientational order at the nematic to twist-bend nematic phase transition of 1″,9″-bis(4-cyanobiphenyl-4′-yl) nonane: a dielectric, H-2 NMR, and calorimetric study. Phys. Rev. E **92**(6), 062505 (2015). https://doi.org/10.1103/PhysRevE.92.062505
126. B. Robles-Hernandez, N. Sebastian, J. Salud, S. Diez-Berart, D.A. Dunmur, G.R. Luckhurst, D.O. Lopez, M.R. de la Fuente, Molecular dynamics of a binary mixture of twist-bend nematic liquid crystal dimers studied by dielectric spectroscopy. Phys. Rev. E **93**(6), 062705 (2016). https://doi.org/10.1103/PhysRevE.93.062705
127. M. Ruckert, G. Otting, Alignment of biological macromolecules in novel nonionic liquid crystalline media for NMR experiments. J. Am. Chem. Soc. **122**(32), 7793–7797 (2000). https://doi.org/10.1021/ja001068h
128. C. Ruslim, M. Hashimoto, D. Matsunaga, T. Tamaki, K. Ichimura, Optical and surface morphological properties of polarizing films fabricated from a chromonic dye by the photoalignment technique. Langmuir **20**(1), 95–100 (2004). https://doi.org/10.1021/la035366e
129. J.M. Russell, S.J. Oh, I. LaRue, O. Zhou, E.T. Samulski, Alignment of nematic liquid crystals using carbon nanotube films. Thin Solid Films **509**(1–2), 53–57 (2006). https://doi.org/10.1016/j.tsf.2005.09.099
130. M. Schadt, Liquid crystal displays, LC-materials and LPP photo-alignment. Mol. Cryst. Liq. Cryst. **647**(1), 253–268 (2017). https://doi.org/10.1080/15421406.2017.1289604
131. M. Schadt, K. Schmitt, V. Kozinkov, V. Chigrinov, Surface-induced parallel alignment of liquid-crystals by linearly polymerized photopolymers. Jpn. J. App. Phys. Part 1-Reg. Pap. Short Notes Rev. Pap. **31**(7), 2155–2164 (1992). https://doi.org/10.1143/jjap.31.2155
132. N. Sebastian, B. Robles-Hernandezb, S. Diez-Berart, J. Saludc, G.R. Luckhurst, D.A. Dunmur, D.O. Lopez, M.R. La Fuente, Distinctive dielectric properties of nematic liquid crystal dimers. Liq. Cryst. **44**(1), 177–190 (2017). https://doi.org/10.1080/02678292.2016.1218963
133. N. Sebastian, M.G. Tamba, R. Stannarius, M.R. de la Fuente, M. Salamonczyk, G. Cukrov, J. Gleeson, S. Sprunt, A. Jakli, C. Welch, Z. Ahmed, G.H. Mehl, A. Eremin, Mesophase structure and behaviour in bulk and restricted geometry of a dimeric compound exhibiting a nematic-nematic transition. Phys. Chem. Chem. Phys. **18**(28), 19299–19308 (2016). https://doi.org/10.1039/c6cp03899a
134. B. Senyuk, Y.K. Kim, L. Tortora, S.T. Shin, S.V. Shiyanovskii, O.D. Lavrentovich, Surface alignment, anchoring transitions, optical properties and topological defects in nematic bent-core materials C7 and C12. Mol. Cryst. Liq. Cryst. **540**, 20–41 (2011). https://doi.org/10.1080/15421406.2011.568324
135. B. Senyuk, H. Wonderly, M. Mathews, Q. Li, S.V. Shiyanovskii, O.D. Lavrentovich, Surface alignment, anchoring transitions, optical properties, and topological defects in the nematic phase of thermotropic bent-core liquid crystal A131. Phys. Rev. E **82**(4), 041711 (2010). https://doi.org/10.1103/PhysRevE.82.041711

136. S.V. Shiyanovskii, T. Schneider, I.I. Smalyukh, T. Ishikawa, G.D. Niehaus, K.J. Doane, C.J. Woolverton, O.D. Lavrentovich, Real-time microbe detection based on director distortions around growing immune complexes in lyotropic chromonic liquid crystals. Phys. Rev. E **71**(2), 020702 (2005). https://doi.org/10.1103/PhysRevE.71.020702
137. E.A. Shteyner, A.K. Srivastava, V.G. Chigrinov, H.S. Kwok, A.D. Afanasyev, Submicron-scale liquid crystal photo-alignment. Soft Matter **9**(21), 5160–5165 (2013). https://doi.org/10.1039/c3sm50498k
138. K.A. Simon, E.A. Burton, F. Cheng, N. Varghese, E.R. Falcone, L. Wu, Y.Y. Luk, Controlling thread assemblies of pharmaceutical compounds in liquid crystal phase by using functionalized nanotopography. Chem. Mater. **22**(8), 2434–2441 (2010). https://doi.org/10.1021/cm901477a
139. K. Skarp, M. Matuszczyk, T. Matuszczyk, B. Bijlenga, A. Hornell, B. Stebler, S.T. Lagerwall, A $1'' \times 0.5''$ FLC bar-graph display with short-term memory. Ferroelectrics **85**, 313–325 (1988)
140. S. Slussarenko, A. Murauski, T. Du, V. Chigrinov, L. Marrucci, E. Santamato, Tunable liquid crystal q-plates with arbitrary topological charge. Opt. Express **19**(5), 4085–4090 (2011). https://doi.org/10.1364/Oe.19.004085
141. I. Son, J.H. Kim, B. Lee, C. Kim, J.Y. Yoo, C.H. Cho, J.H. Lee, Stabilization of in situ self-assembled homeotropic alignment layer for liquid crystals by photopolymerization of reactive monomer. Mol. Cryst. Liq. Cryst. **654**(1), 6–11 (2017). https://doi.org/10.1080/15421406.2017.1354665
142. H.H. Strey, V.A. Parsegian, R. Podgornik, Equation of state for DNA liquid crystals: Fluctuation enhanced electrostatic double layer repulsion. Phys. Rev. Lett. **78**(5), 895–898 (1997). https://doi.org/10.1103/PhysRevLett.78.895
143. T.E. Strzelecka, R.L. Rill, Solid-state P-31 Nmr-studies of DNA liquid-crystalline phases—the isotropic to cholesteric transition. J. Am. Chem. Soc. **109**(15), 4513–4518 (1987). https://doi.org/10.1021/ja00249a014
144. S.J. Sung, H.T. Kim, J.W. Lee, J.K. Park, Photo-induced liquid crystal alignment on polyimide containing fluorine group. Synth. Met. **117**(1–3), 277–279 (2001). https://doi.org/10.1016/S0379-6779(00)00385-4
145. K. Takatoh, *Alignment Technologies and Applications of Liquid Crystal Devices*. Liquid Crystals Book Series (2005)
146. J.G. Theis, G.P. Smith, Y. Yi, D.M. Walba, N.A. Clark, Liquid crystal phase behavior of a DNA dodecamer and the chromonic dye Sunset yellow. Phys. Rev. E **98**(4), 042701 (2018). https://doi.org/10.1103/PhysRevE.98.042701
147. M.F. Toney, T.P. Russell, J.A. Logan, H. Kikuchi, J.M. Sands, S.K. Kumar, Near-Surface alignment of polymers in rubbed films. Nature **374**(6524), 709–711 (1995). https://doi.org/10.1038/374709a0
148. T.-K. Truong, J.H. Park, M.D.A. Rahman, M. Urbanski, E.S. Kim, G. Scalia, D. Suh, Dynamic operation of liquid crystal cell with inherently nanogroove-featured aligned carbon nanotube sheets. Curr. Appl. Phys. **19**(2), 162–167 (2019). https://doi.org/10.1016/j.cap.2018.11.018
149. N.A.J.M. van Aerle, A.J.W. Tol, Molecular-orientation in rubbed polyimide alignment layers used for liquid-crystal displays. Macromolecules **27**(22), 6520–6526 (1994). https://doi.org/10.1021/ma00100a042
150. P. van der Asdonk, P.J. Collings, P.H.J. Kouwer, Fully stable and homogeneous lyotropic liquid crystal alignment on anisotropic surfaces. Adv. Funct. Mater. **27**(28), 1701209 (2017). https://doi.org/10.1002/adfm.201701209
151. P. van der Asdonk, H.C. Hendrikse, M.F.C. Romera, D. Voerman, B.E.I. Ramakers, D.W.P.M. Lowik, R.P. Sijbesma, P.H.J. Kouwer, Patterning of soft matter across multiple length scales. Adv. Funct. Mater. **26**(16), 2609–2616 (2016). https://doi.org/10.1002/adfm.201504945
152. N.A.J.M. Vanaerle, M. Barmentlo, R.W.J. Hollering, Effect of rubbing on the molecular-orientation within polyimide orienting layers of liquid-crystal displays. J. Appl. Phys. **74**(5), 3111–3120 (1993). https://doi.org/10.1063/1.354577

153. K.E. Vaughn, M. Sousa, D. Kang, C. Rosenblatt, Continuous control of liquid crystal pretilt angle from homeotropic to planar. Appl. Phys. Lett. **90**(19), 194102 (2007). https://doi.org/10.1063/1.2737427
154. A.M. Wai Tam, F. Fan, H.-S. Chen, T. Du, V.G. Chigrinov, Y.-H. Lin, H.-S. Kwok, 44-3: nanoscopic patterned photo-alignment for electrically switchable liquid crystal pancharatnam-berry phase diffractive lens. SID Symp. Dig. Techn. Pap. **47**(1), 599–601 (2016). https://doi.org/10.1002/sdtp.10751
155. J.R. Wang, C. McGinty, J. West, D. Bryant, V. Finnemeyer, R. Reich, S. Berry, H. Clark, O. Yaroshchuk, P. Bos, Effects of humidity and surface on photoalignment of brilliant yellow. Liq. Cryst. **44**(5), 863–872 (2017). https://doi.org/10.1080/02678292.2016.1247479
156. Y.H. Wang, C.Y. Xu, A. Kanazawa, T. Shiono, T. Ikeda, Y. Matsuki, Y. Takeuchi, Thermal stability of alignment of a nematic liquid crystal induced by polyimides exposed to linearly polarized light. Liq. Cryst. **28**(3), 473–475 (2001). https://doi.org/10.1080/02678290010017962
157. T.H. Ware, M.E. McConney, J.J. Wie, V.P. Tondiglia, T.J. White, Voxelated liquid crystal elastomers. Science **347**(6225), 982–984 (2015). https://doi.org/10.1126/science.1261019
158. T.J. White, D.J. Broer, Programmable and adaptive mechanics with liquid crystal polymer networks and elastomers. Nat. Mater. **14**(11), 1087–1098 (2015). https://doi.org/10.1038/Nmat4433
159. C.J. Woolverton, E. Gustely, L. Li, O.D. Lavrentovich, Liquid crystal effects on bacterial viability. Liq. Cryst. **32**(4), 417–423 (2005). https://doi.org/10.1080/02678290500074822
160. W.Y. Wu, C.C. Wang, A.Y.G. Fuh, Controlling pre-tilt angles of liquid crystal using mixed polyimide alignment layer. Opt. Express **16**(21), 17131–17137 (2008). https://doi.org/10.1364/Oe.16.017131
161. J. Xiang, Y. Li, Q. Li, D.A. Paterson, J.M. Storey, C.T. Imrie, O.D. Lavrentovich, Electrically tunable selective reflection of light from ultraviolet to visible and infrared by heliconical cholesterics. Adv. Mater. **27**(19), 3014–3018 (2015). https://doi.org/10.1002/adma.201500340
162. J. Xiang, S.V. Shiyanovskii, C.T. Imrie, O.D. Lavrentovich, Electrooptic response of chiral nematic liquid crystals with oblique helicoidal director. Phys. Rev. Lett. **112**(21), 217801 (2014). https://doi.org/10.1103/PhysRevLett.112.217801
163. J. Xiang, S.V. Shiyanovskii, Y.N. Li, C.T. Imrie, Q. Li, O.D. Lavrentovich, Electrooptics of chiral nematics formed by molecular dimers. Liq. Cryst. Xviii **9182**, 91820P-91821–91820P-91829 (2014b). https://doi.org/10.1117/12.2062737
164. D.K. Yang, S.T. Wu, *Fundamentals of Liquid Crystal Devices.* Wiley Series in Display Technology, 2nd edn. (Wiley, Chichester, West Sussex, United Kingdom, 2014)
165. D.K. Yang, S.T. Wu, *Fundamentals of Liquid Crystal Devices*. Wiley Series in Display Technology, 2nd edn. (Wiley, Chichester, West Sussex, United Kingdom, 2015)
166. K.H. Yang, K. Tajima, A. Takenaka, H. Takano, Charge trapping properties of uv-exposed polyimide films for the alignment of liquid crystals. Jpn. J. Appl. Phys. **35**(5a), L561–L563 (1996). https://doi.org/10.1143/jjap.35.l561
167. S.J. Yang, B. Wang, D.W. Cui, D. Kerwood, S. Wilkens, J.J. Han, Y.Y. Luk, Stereochemical control of nonamphiphilic lyotropic liquid crystals: chiral nematic phase of assemblies separated by six nanometers of aqueous solvents. J. Phys. Chem. B **117**(23), 7133–7143 (2013). https://doi.org/10.1021/jp401382h
168. O. Yaroshchuk, Y. Reznikov, Photoalignment of liquid crystals: basics and current trends. J. Mater. Chem. **22**(2), 286–300 (2012). https://doi.org/10.1039/c1jm13485j
169. F.S. Yeung, J.Y. Ho, Y.W. Li, F.C. Xie, O.K. Tsui, P. Sheng, H.S. Kwok, Variable liquid crystal pretilt angles by nanostructured surfaces. Appl. Phys. Lett. **88**(5), 051910 (2006). https://doi.org/10.1063/1.2171491
170. F.S.Y. Yeung, F.C. Xie, J.T.K. Wan, F.K. Lee, O.K.C. Tsui, P. Sheng, H.S. Kwok, Liquid crystal pretilt angle control using nanotextured surfaces. J. Appl. Phys. **99**(12), 124506 (2006). https://doi.org/10.1063/1.2206067
171. Y. Yi, N.A. Clark, Orientation of chromonic liquid crystals by topographic linear channels: multi-stable alignment and tactoid structure. Liq. Cryst. **40**(12), 1736–1747 (2013). https://doi.org/10.1080/02678292.2013.839831

172. D.K. Yoon, G.P. Smith, E. Tsai, M. Moran, D.M. Walba, T. Bellini, I.I. Smalyukh, N.A. Clark, Alignment of the columnar liquid crystal phase of nano-DNA by confinement in channels. Liq. Cryst. **39**(5), 571–577 (2012). https://doi.org/10.1080/02678292.2012.666809
173. H. Yoon, S.W. Kang, M. Lehmann, J.O. Park, M. Srinivasarao, S. Kumar, Homogeneous and homeotropic alignment of bent-core uniaxial and biaxial nematic liquid crystals. Soft Matter **7**(19), 8770–8775 (2011). https://doi.org/10.1039/c1sm05653k
174. C.-J. Yun, M.R. Vengatesan, J.K. Vij, J.-K. Song, Hierarchical elasticity of bimesogenic liquid crystals with twist-bend nematic phase. Appl. Phys. Lett. **106**(17), 173102 (2015). https://doi.org/10.1063/1.4919065
175. G. Zanchetta, Spontaneous self-assembly of nucleic acids: liquid crystal condensation of complementary sequences in mixtures of DNA and RNA oligomers. Liq. Cryst. Today **18**(2), 40–49 (2009). https://doi.org/10.1080/13583140903155093
176. G. Zanchetta, F. Giavazzi, M. Nakata, M. Buscaglia, R. Cerbino, N.A. Clark, T. Bellini, Right-handed double-helix ultrashort DNA yields chiral nematic phases with both right- and left-handed director twist. P. Natl. Acad. Sci. USA **107**(41), 17497–17502 (2010). https://doi.org/10.1073/pnas.1011199107
177. B. Zappone, E. Lacaze, Surface-frustrated periodic textures of smectic-A liquid crystals on crystalline surfaces. Phys. Rev. E **78**(6), 061704 (2008). https://doi.org/10.1103/PhysRevE.78.061704
178. S. Zhou, *Lyotropic Chromonic Liquid Crystals* (Springer, Berlin Heidelberg, New York, NY, 2017)
179. S. Zhou, Y.A. Nastishin, M.M. Omelchenko, L. Tortora, V.G. Nazarenko, O.P. Boiko, T. Ostapenko, T. Hu, C.C. Almasan, S.N. Sprunt, J.T. Gleeson, O.D. Lavrentovich, Elasticity of lyotropic chromonic liquid crystals probed by director reorientation in a magnetic field. Phys. Rev. Lett. **109**(3), 037801 (2012). https://doi.org/10.1103/PhysRevLett.109.037801
180. S. Zhou, A. Sokolov, O.D. Lavrentovich, I.S. Aranson, Living liquid crystals. P. Natl. Acad. Sci. USA **111**(4), 1265–1270 (2014). https://doi.org/10.1073/pnas.1321926111
181. S. Zhou, O. Tovkach, D. Golovaty, A. Sokolov, I.S. Aranson, O.D. Lavrentovich, Dynamic states of swimming bacteria in a nematic liquid crystal cell with homeotropic alignment. New J. Phys. **19**, 055006 (2017). https://doi.org/10.1088/1367-2630/aa695b
182. Y.M. Zhu, L. Wang, Z.H. Lu, Y. Wei, X.X. Chen, J.H. Tang, Atomic-force microscopic study of rubbed polyimide films. Appl. Phys. Lett. **65**(1), 49–51 (1994). https://doi.org/10.1063/1.113069

Part III
Aggregation in Liquid Systems

Chapter 8
Small-Angle Scattering in Structural Research of Nanodiamond Dispersions

O. V. Tomchuk, Leonid A. Bulavin, V. L. Aksenov and M. V. Avdeev

Abstract The general interest in carbon nanomaterials is related to the wide possibilities of their functionalization for a variety of practical, including biomedical, applications. This class of substances includes ultra-fine nanodiamonds of detonation synthesis, which are formed as a result of the explosion of oxygen-unbalanced explosives in an inert medium (Ōsawa, Pure Appl Chem 80:1365–1379, 2008) [1]. Recently, a number of methods for obtaining liquid systems with detonation nanodiamonds have been developed. Their large specific surface area and a non-uniform charge distribution over particle surface leads to the clusterization of these particles, which, nevertheless, in many cases, does not break the stability of the system. Despite the fact that there are many theoretical and experimental works on the study of liquid systems with nanodiamonds, the problem of the relationship between the structure and stability of such systems in a wide range of concentrations remains insufficiently studied today. The particle interaction and the structure of such liquid nanosystems are the subjects which are of current interest in modern molecular physics (Shenderova and McGuire, Biointerphases 10:030802, 2015; Bulavin and Chalyi, Modern problems of molecular physics, 2018) [2, 3]. The corresponding studies constitute the basis for improving the synthesis technology of highly stable nanodiamond suspensions with predefined properties and for the creation of new

O. V. Tomchuk · L. A. Bulavin
Faculty of Physics, Taras Shevchenko National University of Kyiv, Volodymyrska Str., 64, Kyiv 01601, Ukraine
e-mail: tomchuk@jinr.ru

L. A. Bulavin
e-mail: bulavin221@gmail.com

O. V. Tomchuk · V. L. Aksenov · M. V. Avdeev (✉)
Frank Laboratory of Neutron Physics, Joint Institute for Nuclear Research, Joliot-Curie 6, 141980 Dubna, Moscow, Russia
e-mail: avd@nf.jinr.ru

V. L. Aksenov
National Research Centre "Kurchatov Institute", Akademika Kurchatova pl. 1, 123182 Moscow, Russia
e-mail: aksenov@nf.jinr.ru

L. A. Bulavin and L. Xu (eds.), *Modern Problems of the Physics of Liquid Systems*, Springer Proceedings in Physics 223,
https://doi.org/10.1007/978-3-030-21755-6_8

liquid systems, better in general meaning. In recent decades, nuclear physics methods are becoming widespread in the research of nanosystems. Among these methods, small-angle scattering of thermal neutrons takes in important place (Feigin and Svergun, Structure analysis by small-angle X-ray and neutron scattering, 1987) [4]. The high penetrating power of this radiation, as well as the application of the neutron contrast variation technique, allow one to effectively investigate a supramolecular level of 1–1000 nm in multicomponent objects, including liquid systems with nanodiamonds.

8.1 Introduction

Nanodiamonds belong to allotropic forms of carbon. Discovered in the 1960s [1] nanodiamonds have attracted world-wide attention due to their low-cost industrial synthesis based on the detonation of carbon-containing explosives, the small size of primary particles (the order of units of nanometers), available surface functionalization, and high biocompatibility. A wide range of practical tasks requires the obtaining of suspensions with monomeric (non-aggregated) particles, since the tendency towards clusterization has a significant effect on the physical and chemical properties of liquid systems, including liquid systems with nanodiamonds. At the same time, branched clusters of nanodiamonds have found their specific applications too [2, 3]. Studies of the structure and cluster formation in nanodiamond liquid dispersions have both a fundamental and applied objectives. Such studies provide useful information on the equilibrium and kinetic properties of fluid systems characterized by cluster formation. The practical interest is primarily connected with the use of nanodiamonds in the development of advanced materials including superhard composites, anticorrosion coatings, polishing materials and terranostic agents, which are used both in medical diagnostics and therapy. For medical applications the researches are mainly concentrated on water-based systems. All applications requires detailed structural monitoring of various liquid dispersions of nanodiamonds, which prompts the development of experimental techniques for obtaining exact information on the structure of the nanosystems under study.

In the modern molecular physics, one of the actively employed structural methods for studying the structure of nano-sized objects is *Small-Angle Neutron Scattering* (SANS) [4]. The recent development of the SANS data analysis techniques in the case of multicomponent polydisperse nanoparticles and their clusters allows a more detailed structural study of these complex liquid systems. Along with the use of classical analysis, we have developed a number of new approaches to the data interpretation applied in practice in the studies of nanodiamond materials [5–7].

SANS is an elastic scattering from inhomogeneities whose size substantially exceed the de Broglie wavelength of a thermal neutron [4, 8–10]. Using SANS, objects with a characteristic size in the range of 1–1000 nm can be studied. In accordance with the Wolf-Bragg equation, to obtain information on the supramolecular structure it is necessary to detect the diffraction pattern in the region of small trans-

mitted wave vectors and, consequently, *small scattering angles*, from where got the name of the research method itself. The advantage of the method of small-angle neutron scattering over optical, X-ray, and electron analogues is the possibility of studying the structure in bulk due to high penetrating power of these uncharged particles. Due to a relatively large accessible length-scale in comparison with the interatomic distances, one can reasonably interpret the results of a SANS experiment in a continuous approximation in terms of the scattering length density (SLD) distribution [4]. SLD is essentially a tabular parameter and characterizes different materials in the same way as mass density spatial distribution, density distribution of electrical potential, etc. It is also worth noting that the effective way to obtain information on the internal heterogeneity of the particles is the possibility of varying the solvent SLD by applying isotopic substitution, followed by an analysis of the changes in the scattering curves, which is the basis of the so-called outer *contrast variation* technique. The intensity of the small-angle scattering at a certain solid angle, $I(q)$, is the differential cross-section of neutron scattering by an ensemble of particles per unit volume of the sample, averaged over the radial angle, φ, on a detector plane as a function of the scattering vector modulus, q (Fig. 8.1):

$$I(q) = n\frac{\mathrm{d}\sigma}{\mathrm{d}\Omega}(q), \tag{8.1a}$$

$$q = 4\pi \sin(\theta/2)\big/\lambda, \tag{8.1b}$$

where λ is the incident neutron wavelength, θ is the scattering angle and n is the number density of scattering units.

Diamond is a solid form of the carbon with its atoms arranged in a cubic-type crystal structure. Diamond has the highest hardness of any natural material. It withstands chemical corrosion, radiation load and high pressures. It also exhibits a unique combination of the highest electrical resistance and the best heat dissipation. Diamond

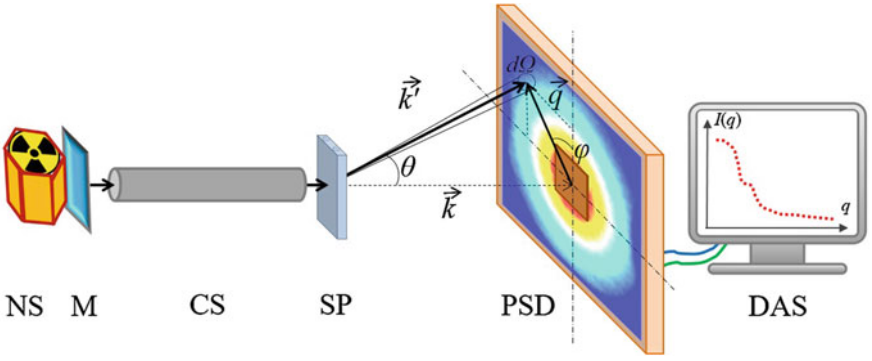

Fig. 8.1 Schematic of experiment on small-angle neutron scattering, where NS is the neutron source, M—moderator, CS—collimation system, SP—sample position, PSD—position-sensitive detector, DAS—data acquisition system

is transparent for ultraviolet radiation, X-rays, visible light and the vast majority of radiations with infrared spectrum. Thus, it is an ideal optical material that electromagnetic radiation can pass through in an extremely wide band from ultraviolet to far infrared rays. In addition to high strength, diamond has the highest atomic density. With the development of modern technologies, all of the above properties of diamonds are tested in practical applications of nanosized diamond particles.

Nanosized diamonds are characterized by high specific surface area, which is well employed in design of nanocomposite materials, selective catalysts, adsorbents, elements of nanoelectronics, as well as materials used in biology and medicine. Nanodiamonds are able to improve quality of magnetic recording systems, physical properties of rubbers, ceramics, polymeric composites, abrasive tools, lubricants, biocompatible materials and so on. In addition, nanodiamonds have demonstrated excellent optical and mechanical properties [2].

The analysis of the phase diagram of carbon (Fig. 8.2a) shows that the most stable carbon phase at low pressures is graphite, and at high pressures it is diamond; the melting point for both phases is about 4500 °C. For the nanosized carbon materials, the phase diagram is similar, however, the liquid phase takes place at lower temperatures [11, 12].

Methods of the synthesis of the diamond nanoparticles began to develop from the 60s of the XX century. They include chemical deposition from a gas medium [13], detonation synthesis with subsequent cooling in a gas or liquid medium [11, 14], synthesis in high-pressure/high-temperature chambers, chlorination of carbides [15], ion irradiation of graphite [16], electron irradiation of carbon onions (multilayered fullerenes) [17] et al. Moreover, astronomical studies show that up to 20% of carbon in the interstellar space is known to be in the nanodiamond state [18]. Figure 8.2b presents the structure of a diamond nanoparticle. *Detonation nanodiamonds* (DND) are one of the most common types of ultrafine diamonds with characteristic size of structural units of just a few nanometers. They are formed as a result of the explo-

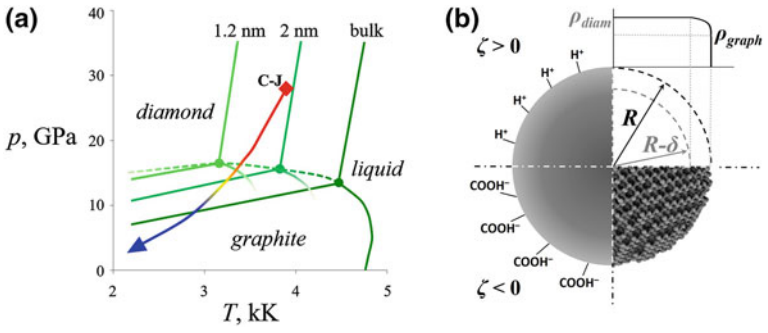

Fig. 8.2 **a** Carbon *p*-*T* phase diagram for different diamond crystal sizes; the arrow shows the adiabatic cooling process, in other words, the exit from the Chapman-Jouguet point (⬥). **b** Schematic representation of the structural organization of a nanodiamond particle with positive (top left) and negative (bottom left) stabilization. The SLD radial profile (top right), as well as the atomic model (bottom right) are shown

sion in the special cameras of condensed explosives with a negative oxygen balance, for example, from a mixture of trinitrotoluene ($C_6H_2(NO_2)_3CH_3$) and hexogen ($C_3H_6N_6O_6$) with the respective ratio of 3/2. During the explosion, the pressure and temperature in the chamber rapidly increase, reaching the Chapman-Jouguet point [19], which reflects the fact that the detonation wave propagates with the minimum possible speed and the speed of the reaction behind the detonation wave front is equal to the sound speed in detonation products. This point lays within the size range of 1–2 nm for many explosives. While the temperature in the chamber starts to decrease adiabatically, carbon atoms begin to gradually form diamond nanocrystals. After the pressure drops below the equilibrium line, the growth of nanodiamonds ceases and graphite phase begins to form. The nanodiamonds thus formed are preferably of a close to spherical shape with a variety of functional coatings. Functional groups can be partially destroyed, replaced by others, but they are always present on the surface of nanodiamonds. This fact reveals a wide range of functionalities for managing physical and chemical properties [20–22]. The non-equilibrium synthesis conditions and the finite volume of the explosive chamber determine the final size distribution of the nanoparticles produced. It is close to the lognormal type, because the process of the formation and growth of nanodiamonds is multiplicative [23]. The detonation synthesis is just the first stage in the production of nanodiamonds, since its result is a batch that, in addition to nanodiamonds, contains a significant amount of impurities. Primary purification of the batch allows obtaining nanodiamond powders. Nowadays, one considers nanodiamond powder to be a conglomerate of aggregates of various sizes, having in its core the most stable complex of covalently bound diamond crystallites with a size in the range of 60–200 nm—so-called 'agglutinates' [21, 22]. SANS studies of nano-diamond powders have shown that they have a branched porous structure [24], which can be re-organized with an increase in pressure up to hundreds of MPa (Fig. 8.3a). This fact reveals a principal possibility of disaggrega-

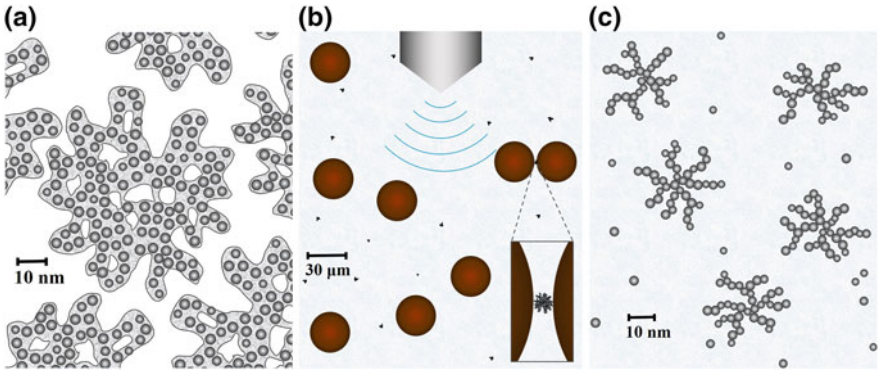

Fig. 8.3 **a** Initial powder of agglutinates which possess a developed pore fractal surface. Closed pores in agglutinates are observed. **b** Dispersing procedure using the powerful sonication together with milling by zirconia beads in wet conditions. **c** Resulting detonation nanodiamond suspensions with fractal clusters

tion of nanodiamond 'agglutinates', because the pore recombination is a result of mobility of nanodiamonds in the powder under pressure.

The agglutinate disaggregation is associated with dispersions in liquid carriers, followed by the use of powerful ultrasound, oxidation and milling using micrometric zirconia beads (Fig. 8.3b) [1, 21]. Various solvents were tested in preparation of stable suspensions (or sols) of nanodiamonds. It was concluded that in general the high polarity of the carrier fluid helps in dispersing procedures [25]. In particular, the production of a liquid system based on dimethylsulfoxide (DMSO, $(CH_3)_2SO$) is even more effective than those dealing with water. One of the reasons for this is that DMSO is one of the strongest acceptors of hydrogen bonds, which is several orders of magnitude stronger than water, and, at the same time, it is aprotic. Based on the data of dynamic light scattering, a conclusion was made about complete disaggregation of agglutinates resulted in separate nanodiamond particles [20, 25, 26]. However, a significant specific surface area of nanoparticles leads to a strong tendency to aggregation in concentrated solutions [27–30] (Fig. 8.3c). The cluster formation is determined not only by the thermodynamic conditions of the liquid system, but also by physical and chemical properties of the particle surface. The generated aggregates have a fractal (scale-invariant or self-similar) structure [29–31], which confirms the existence of a dipole moment in a nanosized diamond that promotes the formation of supramolecular structures. However, despite the formation of clusters, such suspensions have high stability ($\approx$1 year [30, 32]). The stabilization mechanism of such liquid systems is still under consideration [25, 33]. DND liquid dispersions reveal a number of interesting properties. Thus, thixotropy is an example of a reversible gelation in highly concentrated systems, when intensive shaking turns a gel back to sol for a relatively long time before it again transforms into gel [34].

In addition to neutron scattering experiments, a number of *Small-Angle X-ray Scattering* (SAXS) studies were also conducted. For example, [31] concerns the studies of the spatial structure of aggregates formed by detonation nanodiamonds in suspensions using both small-angle and wide-angle X-ray diffraction. The obtained results are consistent with the results of the neutron scatting studies in respect to the sizes and characteristics of the particle surface. The conclusion was that there is a primary clustering of 4–5 particles, which subsequently assembled into large aggregates.

The present paper reviews the works based on small-angle scattering application during last decade. The current possibilities of this method in the studies of the structure of liquid systems with detonation nanodiamonds are analyzed.

8.2 Structure of Diamond Nanoparticles by SANS

The particles of detonation nanodiamonds are characterized by a natural spatial transition from sp^3-hybridization of carbon in a diamond core to surface graphite states with sp^2-hybridization [35]. Taking into account the significant difference between the SLDs of diamond ($\rho_{\text{diam}} = 11.8 \cdot 10^{10}$ cm^{-2}) and graphite ($\rho_{\text{graph}} = 7.0 \cdot 10^{10}$

cm^{-2}), it can be supposed that, from the point of view of SANS, nanodiamond particles are essentially heterogeneous. In addition, suspensions of detonation nanodiamonds are highly dispersed systems that contain polydisperse nanoparticles and their aggregates. In the study of such systems in terms of small-angle scattering of X-rays and thermal neutrons, a question arises as to the effect of polydispersity on the determination of structural parameters of such systems [36].

Crystalline nature (and hence the multifaceted shape) of nanodiamond particles [35, 37] nonetheless allows one to consider them in the spherical approximation in a small-angle experiment, since the spherical approximation in small-angle neutron scattering for polyhedra is applicable up to $qR_g < 8$ [4], which is quite true for the following experiments.

The powerful tool in studying inhomogeneous nanoparticles by means of small-angle scattering is the contrast variation technique. In the SANS experiments with the contrast variation on detonation nanodiamond suspensions, the diamond-graphite interface was initially considered within the frame of the "core-shell" model [30] (Fig. 8.4). This made it possible to clarify the decrease in the mean SLD of ultrafine diamond particles in comparison with bulk diamond and gives an estimate of the graphite shell thickness δ of about 0.5 nm with a total particle size of 7 nm in a monodisperse approximation. However, the core-shell approach does not allow explaining the deviation from the Porod law:

$$I(q) \sim q^{-4} \tag{8.2}$$

to the higher power-law decay exponents, indicating to the diffusive surface [38]:

$$I(q) \sim q^{-(4+2\beta)}, \ \beta = 0 - 1. \tag{8.3}$$

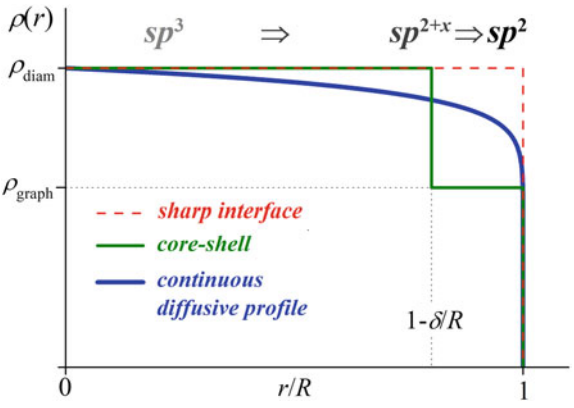

Fig. 8.4 Comparison of different SLD profiles of spherical particles (outer radius R restricts the solvent inaccessible volume) as a models of DND particle. For diffusive model $\beta = 0.07 \ll 1$

Therefore, it is necessary to introduce a wide interface to satisfy the observed dependence.

In [6], a special type of polydisperse heterogeneous particles was considered, the structure of which allows us to analyze the polydispersity without complex approximations by the integral functions. The heterogeneity of these particles is determined by their diffusive surface, which leads to the aforementioned deviation from the Porod law. Nanodiamonds in the powders and suspensions give such small-angle scattering behavior [5–7, 24, 30, 31, 39–42]. The radial SLD profile in this case has the form:

$$\rho(r) = \rho_{\text{diam}}(1 - r/R)^{\beta}, \tag{8.4}$$

where ρ_{diam} is SLD of the diamond core, R is the radius of the nanoparticle, β is the diffusivity parameter. First, for the detonation nanodiamonds, the parameter β should be small enough to describe the transition from the diamond in the center to the graphite on the periphery of the particle. For $\beta \ll 1$, the profiles corresponding to the (8.4) coincide with the "core-shell" model both for $r \approx 0$ and for $r \approx R$, therefore, the transition to ρ_{graph} is well described (Fig. 8.4). The values of β obtained in the experiment with nanodiamonds is varied around 0.1, which satisfies the condition of smallness. In addition, in the framework of the proposed model, the calculated volume-average SLD becomes independent of the particle radius and determined only by the core density ρ_{diam} and the β exponent, namely:

$$\bar{\rho}_e = \frac{6\rho_{\text{diam}}}{(\beta+1)(\beta+2)(\beta+3)}. \tag{8.5}$$

This relation is decisive for the contrast variation. In spite of the fact that the particles are heterogeneous, the average SLD does not depend on the size. This means that there will be no residual scattering at the match-point (minimum of the scattered intensity at zero angle as a function of the contrast), and the average SLD can be determined experimentally from [4, 6]:

$$I(q \to 0) \sim (\bar{\rho}_e - \rho_S)^2. \tag{8.6}$$

The developed analytical tool at the limit $\beta \to 0$ is reduced to expressions describing scattering by polydisperse homogeneous nanoparticles [4, 43].

Contrast variation SANS experiments on cluster suspensions of detonation nanodiamonds DUNCD in water (DND/water I) and dimethylsulfoxide (DND/DMSO) synthesized in the NanoCarbon Research Institute (Nagano, Japan) by the process of milling in a liquid carrier using a powerful ultrasonication and oxidation [1, 6]. Experiments were also carried out on aqueous suspensions of detonation nanodiamonds (DND/water II) synthesized at the Ioffe Institute of the Russian Academy of Sciences (St. Petersburg, Russia) [6, 44]. Besides, an experiment was conducted with the suspension of the RUDDM nanodiamonds (Real-Dzerzhinsk Ltd., Russia) in water (DND/water III) [7].

For the experiment on contrast variation, initial protonated systems were diluted with various isotopic mixtures of H- and D-solvents in order to cover an intervals of 20–100% and 50–100% for H_2O and H-DMSO, respectively. Thus, four series of samples with different neutron contrasts (the difference between the SLDs of the dispersed phase and the solvent) were obtained: DND/water I (5 wt%), DND/water II (1.8 wt%), DND/water III (2 wt%) DND/DMSO (5 wt%)

In addition, two types of initial concentrated DND hydrosols based on light (concentration is 5.05 wt%) and heavy (concentrations is 2.35 wt%) water were prepared according to the procedure described in [44]. The solutions were then diluted in different H_2O/D_2O mixtures so that the content of light water in the final solution varied at the same DND concentrations in the ranges of 30–100 v.% and 0–50 v.% in the first and second cases, respectively (DND/water IV) [42].

As an example, changes in scattering with varying the solvent SLD for the DND/water III system are shown in Fig. 8.5. A monotonous decrease in scattering with an increase in the solvent SLD across the measured q-range indicates clusters homogeneity at size-scale greater than 10 nm. In the curves, two scattering levels relate to the structural level of the particles (large q) and their clusters (small q). Both of them are characterized by power-law dependencies of $I(q)$. The nanodiamond particle scattering level gives the values of 4.1–4.2, which are evident to particles with a diffuse surface [38]. The absence of the diffraction peaks in scattering curves for large q indicates the polydisperse nature of particles of detonation nanodiamonds. The exponents found in the range of 2.3–2.5 for the cluster level for all systems stud-

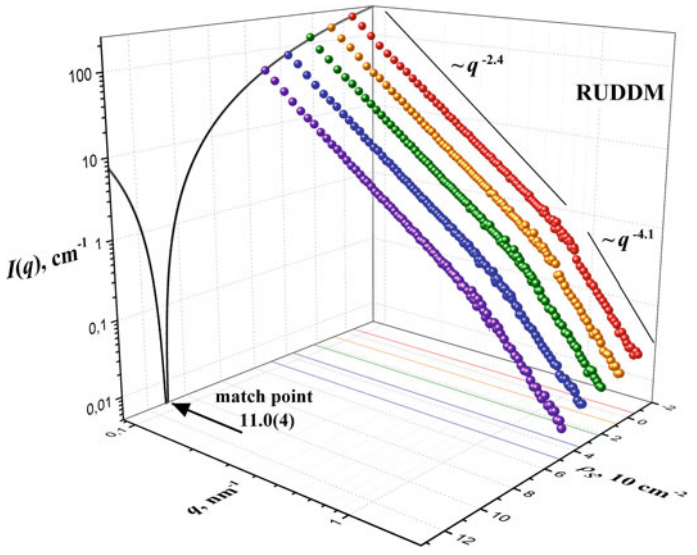

Fig. 8.5 SANS contrast variation for the DND/water system III, prepared from the initial 100 mg/ml dispersion diluted five times with different H_2O/D_2O mixtures. The specific power-law type scattering modes together with parabolic fit of $I(q_{\min})$ versus ρ_S are shown

ied indicate that clusters are mass fractals [45–49], because in this case, the intensity has the form:

$$I(q) \sim q^{-D}, \quad D = 1 - 3. \tag{8.7}$$

In order to avoid the effect of the residual incoherent scattering and find the match-point of the aggregates and, hence, their structural units, one can use the dependence of the scattering intensity at the minimum values of the scattering vector $I(q_{\min})$ on the solvent SLD. The data are well approximated by the quadratic dependence (8.6), the minimum of which is the match-point (Fig. 8.5), which gives the mean SLD of the nanodiamond particles shown in Table 8.1. The experimental values are well consistent with the calculated values obtained from the continuous approximation to radial SLD profile (8.5), using the density of diamond and the experimentally determined from the (8.3) diffusivity coefficient β of the nanoparticle surface.

Thus, there is a consistency of a continuous profile (8.4), which reflects the diffusive nature of the surface of particles, with mean particle scattering density. This cannot be achieved by using the "core-shell" approximation. This result confirms the previous conclusions: there is an identical content of the non-diamond component (preferably graphene) in the structure of the particles of detonation nanodiamond in suspensions with both low and high concentrations. Thus, the contrast variation indicates to the presence of graphene in the structural units of the clusters, which is likely to participate in the stabilization of the system.

It should also be noted that the level of clusters in suspensions of nanodiamonds of different origin is quite reproducible in relation to structural characteristics. The most stable in this sense is the parameter of fractal dimension of aggregates, which strongly suggests a common mechanism of cluster growth in such systems (see next section).

In paper [50] a method for analyzing the polydispersity of homogeneous particles based on small-angle scattering data was proposed. The idea was to use a polydisper-

Table 8.1 Comparison of experimentally obtained and calculated mean SLD together with polydispersity parameters[a] of DND particle for different suspensions

System	$\bar{\rho}_e$ (10^{10} cm^{-2})	$\bar{\rho}_c$ (10^{10} cm^{-2})	$\langle R \rangle$ (nm)	σ (nm)
DND/water I[b]	10.5(5)	10.4(3)	1.48(6)	0.62(3)
DND/water II[b]	10.8(6)	10.6(5)	1.3(1)	0.58(6)
DND/water III[c]	11.0(4)	10.8(3)	1.51(5)	0.57(2)
DND/water IV[d]	10.4(6)	10.2(3)	1.38(5)	0.49(2)
DND/DMSO[b]	10.2(4)	10.4(3)	1.52(4)	0.61(2)

[a]Parameters of the lognormal size distribution, $\langle R \rangle$ and σ, for DND particles are calculated based on the approach presented by authors in [6]
[b]Reference [6]
[c]Reference [7]
[d]Reference [42]

sity index PDI, a combination of parameters of the unified exponential/power-law approximation [51] to describe and compare the polydispersity of different systems. This approach combines the power-law mode (8.2) and Guinier approximation [4],

$$I(q) = G\,\exp\left(-q^2 R_g^2/3\right). \tag{8.8}$$

Each of fitting parameters, including forward scattering intensity G and radius of gyration R_g, is proportional to a certain moment of the size distribution function.

The situation is more complicated when the particles are heterogeneous. In [6], we consider nanoparticles with a diffusive surface (8.4) in a weakly scattering medium, that is, $\rho_S \approx 0$. These may be weakly scattering liquids or powders. The polydispersity index PDI for particles with diffusive surface has a similar form of dimensionless combination of parameters of the unified exponential/power-law approximation as a joint low-q/high-q model combining (8.8) and (8.3). The indicated polydispersity index can be used to compare the degree of polydispersity for systems with small β without specifying the size distribution function. The PDI index of the monodisperse system equals to 1 and increases with the increasing polydispersity.

For several important cases of size distribution, for example, for lognormal function, the approach allows to obtain the parameters of the particle size distribution function in an explicit form [6]. The verification of the proposed approach can be made for the limiting case $\beta \to 0$, when all expressions are transformed into corresponding analogs for a homogeneous model presented in [50].

Thus, for the profile (8.4), the concept of analyzing small-angle scattering data using the polydispersity index can be applied to spherical particles with a diffuse surface. It allows an analysis of the polydispersity of heterogeneous diamond nanoparticles (see Table 8.1). The results testify high polydispersity of nanodiamond particles ($\sigma/\langle R\rangle \approx 40\%$). The diameter of nanoparticles for all systems is ≈3 nm, and the degree of polydispersity in terms of the mean square deviation varies slightly for different manufacturers.

In summary, we note that the smallness of the β parameter for particles with diffusive surface allows to introduce a continuous radial profile of the scattering length density inside the particles (8.4) and to simplify greatly the interpretation of scattering data in polydisperse systems. This is especially true for the experiments on the contrast variation in SANS, where the scattering of neutrons by such particles is similar to scattering by monodisperse heterogeneous particles. In addition, an analysis of polydispersity can be carried out within the framework of the concept of a modified polydispersity index. As a result, the parameters of the DND particle size distribution function were obtained. Again, the experimentally observed parameter β for nanodiamonds well describes the spatial transition from inside diamond to surface graphene states of carbon. The aggregation in concentrated solutions allows to perform high-precision experiments on the contrast variation in small-angle neutron scattering. The analysis shows that the concept of a continuous profile of scattering density in nanodiamonds is preferred, because it combines the diffusive properties of the particle surface and the decrease of the mean scattering density detected by

SANS, which cannot be made within the framework of the "core-shell" model of nanoparticles. This is in line with the ab initio computer simulation [52] for diamond nanocrystals up to 3.3 nm, which suggests that the most stable structures require the presence of sp^{2+x} bonds, located mainly in the vicinity of crystallite edges. In some works, e.g. in [1], it was assumed that the process of milling using micron-sized beads can lead to the additional formation of sp^2-carbon on the DND surface under the mechanical influence, which should be chemically removed from the surface of nanodiamonds. However, we believe that sp^2-states, or graphene states, are an integral component of ultra-fine diamond particles and cannot be completely eliminated [5].

8.3 Study of Aggregation in Polar Liquid Systems with Nanodiamonds

The surface of detonation diamond particles is highly functionalized due to reactions with the surrounding media and gaseous side products. Varieties of functional groups have been identified already, such as carboxyl, ketone, hydroxyl, lactone and anhydride groups [21, 53–58]. That is why the material is an attractive candidate for enhanced surface functionalization. We have carried out a comparative analysis of the structure of clusters in different modified water suspensions of detonation nanodiamonds [40]. By the modifications we understand different ways of secondary treatment of nanodiamond suspensions. The problem of such systems is related to the relatively small concentrations of nanoparticles in the terminal product, defined by the preparation procedure for a number of modifications. The aim of conducted SANS experiments was to clarify possibilities of the method in respect of diluted suspensions (≈0.1 wt%) from the viewpoint of the detection of the structural parameters of the system based on analyzing small-angle scattering curves. At first sight, a low content of dispersed phase in the system decreases the SANS signal, insofar as the scattered intensity is directly proportional to the concentration. But high neutron contrast of the system—diamond SLD $11.8 \cdot 10^{10}$ cm^{-2} versus $-0.56 \cdot 10^{10}$ cm^{-2} for light water—allow registration of a curve with good statistics against the residual incoherent background scattering, since the differential cross-section of coherent scattering is proportional to square of the contrast [4].

Initial concentrated nanodiamond suspensions in water, produced according to the Osawa method [1], were provided by the NanoCarbon Research Institute (Nagano, Japan), hereinafter referred to as DUNCD, and purchased from PlasmaChem GmbH (Berlin, Germany)—UDD series. The modified system from the DUNCD series is obtained by ultrasonic treatment followed by centrifugation (>10^4 rpm) in order to remove the graphene shell. As a result, two fractions were obtained—a transparent supernatant and a gray-brown precipitate. The supernatant fluid was concentrated. The properties of resulting suspension were compared with the properties of diluted ten times the initial suspension. The UDD fluid system was subjected to additional purification and chemical treatment in accordance with [59], so that the remain-

ing functional covering of detonation nanodiamonds contained predominantly carboxyl groups. Thus, the suspension, which is the basis of the anticorrosive coatings described in [59], was synthesized.

The experimental SANS curves for the initial dispersion of detonation nanodiamonds DUNCD in water and dilute system are presented in Fig. 8.6. It has clearly seen from the qualitative behavior of scattering that the production of these systems is characterized by high reproducibility. Model power-law dependence with the exponent less than 3 (mass fractal) is shown in Fig. 8.6. Under dilution down to 0.1 wt%, the SANS curve does not change qualitatively. However, scattering for large q, which is responsible for scattering on structural units of clusters, cannot be detected in such experiments: low concentration of particles does not allow to obtain sufficient signal in comparison with incoherent background, the main source of which are the hydrogen nuclei. Thus, the low concentration of the system at the level of about 0.1 wt% somewhat limits the possibility for studying nanodiamond suspensions by neutron scattering and allows to obtain structural information only for clusters of size greater than 10 nm.

The experiments on small-angle neutron scattering with the liquid nanodiamond dispersions were made on the small-angle neutron spectrometer SANS-1 of the Helmholtz-Zentrum Geesthacht [40]. Experimental neutron scattering curves for UDD series are also shown in Fig. 8.6. As in the case of the DUNCD suspension, close to the linear behavior of curves both for initial and modified UDD systems in a double logarithmic scale indicates to the fractal organization of the structure of clusters of detonation nanodiamonds in water.

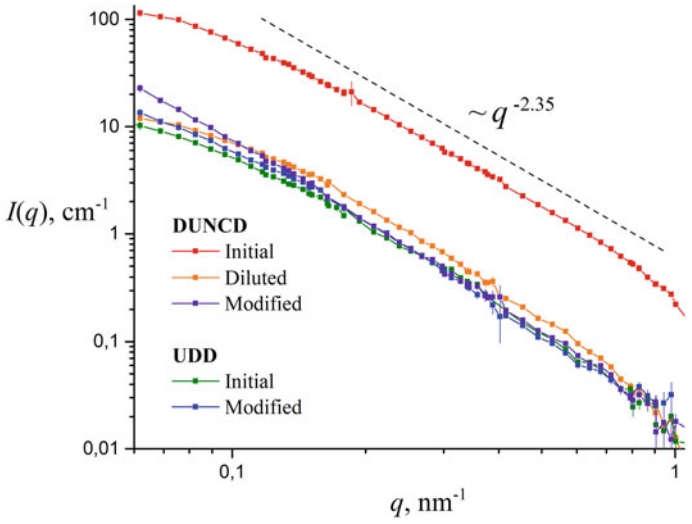

Fig. 8.6 SANS curves for DUNCD and UDD series of the DND/water liquid system. The specific mass fractal scattering regime is shown

Despite the different preparation conditions of the systems, their small-angle scattering curves have similar behavior. As we see, qualitative repetition of the previous results regarding the fractal dimension of clusters suggests a similar mechanism of cluster formation in liquid systems with nanodiamonds. In conclusion, the obtained D value indicates to the mechanism of diffusion limited aggregation in the formation of the investigated aggregates [60, 61]. Diffusion limited aggregation belongs to the "particle-cluster" aggregation mechanism class. Thus, the modification of the surface of nanodiamond particles does not have a critical effect on the structural organization of clusters in liquid systems. To a certain extent, the recently proposed model of the interaction of nanodiamonds based on surface modulations of the electrostatic potential confirms the presence of a unique mechanism for the growth of aggregates in suspensions of detonation nanodiamonds in liquid systems [62].

The weak kink in the scattering curves at $q \approx 0.15$ nm^{-1} (Fig. 8.6) makes it possible to obtain a lower estimate for the typical cluster size in these systems, taking into account the resolution in the configuration used, $L = 2\pi/q = 40$ nm. Qualitative changes in the scattering curve are observed for the modified liquid system DUNCD. Analysis of Fig. 8.6 shows that the discussed kink in the power-law behavior of the scattering curves disappears, which indicates an increase in the cluster size in this case, we get a lower estimate of the clusters' size of ≈120 nm. Thus, it is determined from the experiment that increasing the size of clusters after the application of the appropriate modification causes a destabilization of the suspension under study.

Consequently, the production of aqueous suspensions of detonation nanodiamonds by milling in liquids is rather reproducible. The differences relate mainly to the characteristic cluster size, which is sensitive to the initial concentration of nanodiamonds dispersed in the polar medium. Modifications of aqueous suspensions of detonation nanodiamonds have not principally influenced on resulting structural organization. The obtained range of values of the fractal dimension of clusters (2.3–2.5) in these systems, regardless of the series, indicates to a common mechanism of aggregation in the formation of clusters, namely, limited diffusion. Partial removal of the shell results in cluster size growth in water and loss of stability of the suspension.

The next question that arises in the study of nanodiamond suspensions: to what extent structural characteristics of aggregates, including size and shape, and the nature of the cluster-cluster interaction, vary in different samples and their fractions, i.e. for different size-scales [63]. To clarify this problem, SANS was applied for two types of nanodiamond suspensions based on commercial DND powders, namely RUDDM (Real-Dzerzhinsk Ltd., Russia) and SDND (PlasmaChem GmbH, Germany), and their two fractions (conditionally, "light" and "heavy") after centrifugation/fractionation procedure [7, 64].

The phase separation as a result of centrifugation is observed in Fig. 8.7, where SANS curves from light and heavy fractions of 10 wt% of RUDDM suspension after two different centrifugation times are given. The two fractions show a difference in neutron scattering at the aggregate level. The light fraction is characterized by significantly smaller aggregates; the corresponding scattering is well described by the Guinier approach (8.8) in the range of small q-values. In addition, longer cen-

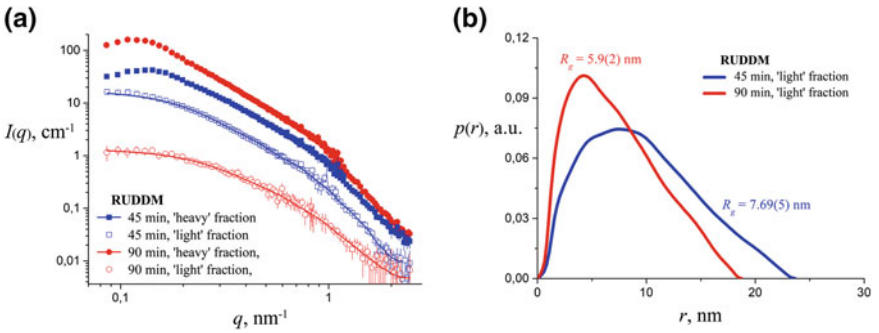

Fig. 8.7 **a** SANS curves from heavy and light fractions of 100 mg/ml RUDDM type DND/water suspension under centrifugation during 45 and 90 min. Solid lines show model curves obtained by indirect Fourier transform. **b** Corresponding pair distance distribution functions (calibrated to unit). Values of radii of gyration are indicated

trifugation leads to smaller aggregates in the light fraction. Despite the difference in the state of the aggregates in the RUDDM and SDND suspensions, the size characteristics of the light fractions after 90 min centrifugation become close for both types of suspensions [7].

The average aggregation number of clusters for light fractions is about 10. It is clear that fractal properties are not so noticeable for such small aggregation numbers, therefore there are significant deviations from the power-law scattering. In addition, a decrease in the average volume compared with heavy fractions leads to a decrease in the intensity of coherent neutron scattering. However, based on the detected values of the fractal dimension of the DND clusters, one can state that the mechanism of cluster growth is the same for clusters of different sizes in various dispersions. Regarding heavy fractions, the corresponding curves repeat the curves from initial suspensions for the most part of the interval of the transmitted wave vector q, which means that these fractions consist mostly of large branched clusters. Significant differences are observed only in the initial parts of the curves. One can see that the influence of the structure factor (the deviation from the power-law scattering at smallest values of q) in heavy fractions is more significant in comparison with the initial suspensions. The curve contains a peak at $q_{\text{peak}} < 0.2\ \text{nm}^{-1}$, which corresponds to a correlation length of $2\pi/q_{\text{peak}} \approx 45$ nm. This is a consequence of the higher concentration of nanoparticles after centrifugation, and it can be interpreted as the result of the interpenetration of fractal aggregates. This is in full agreement with the conclusions for concentrated solutions with branched clusters of detonation nanodiamond particles in DUNCD material [30].

Neutron data also indicate that the clusters are reproducible relative to the repeated dispersing and centrifugation procedures. From this, we can conclude that the clusters are formed during the synthesis of suspensions from nanodiamond powders. The synthesis involves the oxidation of particles of detonation nanodiamonds in liquid media, which leads to electro-static stabilization of suspensions. This process com-

petes with aggregation [1, 20, 25]. As a result, some distribution of clusters in a wide range of sizes is stabilized. Neutron research suggests a unique mechanism of aggregate formation in the process of synthesis and, consequently, the same structure of clusters in nanodiamond suspensions as a class of colloidal systems. The synthesis procedures from different manufacturers are characterized by different degree of stabilization, which leads to diverse distribution of clusters in size in liquid systems. Based on the analysis of dynamic light scattering and differential scanning calorimetry [63] it was shown that in SDND there is a fraction of non-aggregated DND particles that may be separated after 360 min of centrifugation. Nevertheless, the concentration of such particles is not enough to be detected by SANS due to the relatively high incoherent scattering from water. Indeed, the signal/background ratio in the small-angle neutron scattering is limited by the time of centrifugation to separate the light fraction in terms of size and concentration of clusters remaining in the fraction. Therefore, for neutron experiment the maximal time of centrifugation was chosen so that the intensity of small-angle neutron scattering at large q could be registered with acceptable statistics.

The effect of DND concentration on scattering was studied in the range of up to 10 wt%. With the increase in the number of particles in the system, the effect of the interaction between them becomes significant for scattering. In this case, the position and orientation of the particles can no longer be considered as independent. Thus, a correlation appears between the particles. In the case of isotropic interaction, the corresponding effect is factorized, that is, in addition to the scattering form-factor, the so-called structure factor $S(q)$ [4, 10] (the Fourier transform of the radial distribution function $g(r)$) is multiplicatively added. The $g(r)$ function is defined as the time-averaged on distribution of the density of the centers of particles around the selected one, depending on the radius measured from its center [2, 9]. In fact, $g(r)$ characterizes the modulation of density distribution because of particle interaction in the liquid systems (short-range order). The influence of the structure factor on the scattering is observed primarily in the region of small scattering vectors, since they correspond to distances (correlation lengths) that are comparable to the total particle size. The effect of cluster-cluster interaction on SANS intensity is observed both for primary suspensions DUNCD [30] and for redispersed suspensions SDND [7] (Fig. 8.8). As we can see, the nature of the curves of small-angle neutron scattering with the exception of the low-q parts, does not change with a concentration. This proves that the clusters of the light fraction after drying and subsequent redispersing in the liquid carrier retain their structure, indicating to a relatively strong bond between nanodiamonds in the clusters. The type of interaction between clusters was determined using the Zimm equation, which in this case takes the form [65]:

$$c/I(q_{\min}) = K_1 + K_2 B_2 c, \tag{8.9}$$

where c is the concentration of nanodiamonds; K_1 and K_2 are some positive constants, B_2 is the second viral coefficient, the sign of which determines the type of interaction. Shown in the insert to Fig. 8.8, Zimm plot has a positive slope, thus indicating to a repulsive type of interaction. An effective structure factor was evaluated as [66, 67]:

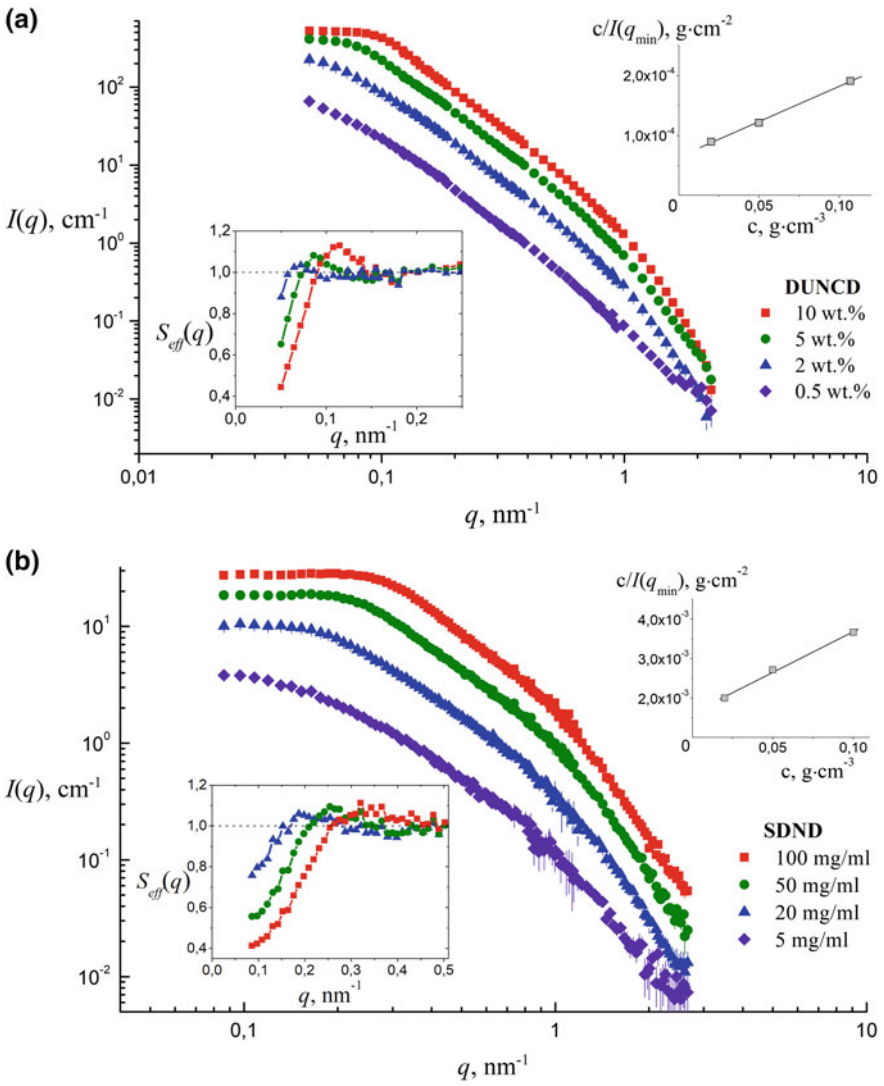

Fig. 8.8 SANS curves from DND water suspensions at different concentrations. Insets show effective structure factors according to (8.10) and Zimm plots with the corresponding linear fit according to (8.9). **a** DUNCD aqueous suspension. **b** Redispersions of the light fraction from the SDND water suspension

$$S_{\text{eff}}(q, \varphi) = (I(q, \varphi)) \Big/ (I(q, \varphi_{\min})), \tag{8.10}$$

where φ and $\varphi_{\min}$ are current and minimal mass fraction of nanodiamonds in water suspension, respectively. The system with lowest DND content is the case of non-interacting clusters.

The found $S_{\text{eff}}(q)$ functions (see inserted graph in Fig. 8.8) are characterized by the presence of a peak whose position, q_{peak}, increases with the growth of the concentration of nanodiamonds, thereby reducing the correlation length $\xi \approx 2\pi/q_{\text{peak}}$, which corresponds to the short-range cluster-cluster interaction. Modeling of the structure factor is complicated due to branchiness and high polydispersity of aggregates. An attempt to theoretically describe $S_{\text{eff}}(q)$ using the model of polydisperse spheres [68, 69] was failed. This may be due to the fact that the branched aggregates in the suspension are far from dense spherical objects (for example, see the asymmetry in the $p(r)$ functions in Fig. 8.7b), as well as the presence of an additional contribution to the interaction potential of the charge repulsion, partially screened in a polar solvent. At the highest DND concentration in the SDND system, the correlation length was approximately 20 nm that approaches the characteristic size, which, if one takes into account the fractality of the structure, exceeds 17 nm giving the size estimation of a densely packed spherical cluster. That is, aggregates can be relatively close to each other. Nevertheless, the charge on the surface of detonation nanodiamonds prevents further agglomeration. The effect of the structure factor is similar to that observed [30] for unfractionated suspensions DUNCD (aggregate size > 40 nm), which indicates to an even closer location and possible interpenetration of branched aggregates at concentrations of about 10 wt%.

From the obtained value of the power scattering exponent $D \approx 2.4 < 3$ at the cluster level for all investigated liquid systems, regardless of their origin, it follows that the organization of nanodiamond particles in aggregates results in mass fractals (branched clusters) with dimension D, which does not depend on the concentration of detonation nanodiamonds. Thus, the fractal organization once again testifies the specific mechanism of growth of aggregates in such systems, presumably the process of diffusion limited aggregation [7, 60]. In this case, the smoothed shape of the curves at the cluster scattering level suggests a wide distribution of cluster sizes [7, 61, 70–73]. The corresponding analysis confirms the broad size distribution not only for nanodiamond particles, but also for the clusters ($\sigma/\langle R\rangle \approx 30\%$) in polar suspensions [7].

Summing up, the data of small-angle neutron scattering indicate to the presence of fractal clusters of detonation nanodiamonds in aqueous systems. The clusters show high time stability and retain their structure after the suspensions are dried and the resulting powders are re-dispersed in water. All this testifies that clusters are formed during the synthesis of the initial suspensions of detonation nanodiamonds. For the investigated suspensions, the only principal structural difference concerns the size of the clusters depending on the preparation procedures and concentration. The obtained value for fractal dimension of the observed clusters indicates that the mechanism of growth is close to the model of diffusion limited aggregation. The effective correlation length of the interaction between nanodiamond clusters depends on the concentration

and size of the clusters. At high concentrations, the correlation is comparable with the cluster size, i.e., the slight interpenetration of the clusters takes place.

8.4 Conclusions

As was shown here, small-angle neutron scattering is a very informative tool for structural characterization of detonation nanodiamond particles in dry powders and in liquid systems with respect to size and shape, surface properties, aggregation degree and cluster-cluster interaction. Structural stability, fractality and polydispersity in polar nanodiamond suspensions were studied in details. The fractal nature of the studied clusters is discussed in terms of the unique growth mechanism in nanodiamond suspensions during their synthesis. Information on the structural parameters of nanodiamond cluster suspensions that was successfully obtained by small-angle neutron scattering is important in view of their practical applications, because the synthesis of these systems is the first step towards the creation of non-agglomerated aqueous nanodiamond dispersions for their further use.

Acknowledgements Experimental data demonstrated in this review were obtained by the authors in collaboration with a number of research groups from various research centers including Joint Institute for Nuclear Research (JINR) (Dubna, Russia), Taras Shevchenko National University of Kyiv (TSNUK) (Ukraine), NanoCarbon Research Institute (NCRI) (Ueda, Japan), Lomonosov Moscow State University (LMSU) (Russia), Ioffe Institute (St. Petersburg, Russia), Nuclear Physics Institute, Czech Academy of Sciences (NPI CAS) (Řež, Czech Republic), Budapest neutron center (BNC) (Hungary), Helmholtz Zentrum Geesthacht (HZG) (Germany).
The authors are grateful to Ōsawa E. (NCRI), Vul' A. Ya. (Ioffe institute), Korobov M. V. (LMSU), Rosta L. (BNC), Ivankov O. I. (JINR), Ryukhtin V. V. (NPI ASCR), Garamus V. M. (HZG), Nagorny A. V. (TSNUK, JINR) for the help in the preparation of DND samples, performing SANS experiments and useful discussions.
Tomchuk O. V. acknowledges the support from the Russian Science Foundation (Project No. 18-72-00099).

References

1. E. Ōsawa, Monodisperse single nanodiamond particulates. Pure Appl. Chem. **80**, 1365–1379 (2008). https://doi.org/10.1351/pac200880071365
2. O.A. Shenderova, G.E. McGuire, Science and engineering of nanodiamond particle surfaces for biological applications. Biointerphases **10**, 030802 (2015). https://doi.org/10.1116/1.4927679
3. L.A. Bulavin, A.V. Chalyi, *Modern Problems of Molecular Physics* (Springer International Publishing AG, 2018), 374 pp. https://doi.org/10.1007/978-3-319-61109-9
4. L.A. Feigin, D.I. Svergun, in *Structure Analysis by Small-Angle X-ray and Neutron Scattering*, ed. by G.W. Taylor (Plenum Press, New York, 1987), 335 pp. https://doi.org/10.1007/978-1-4757-6624-0
5. M.V. Avdeev, V.L. Aksenov, O.V. Tomchuk, L.A. Bulavin, V.M. Garamus, E. Ōsawa, The spatial diamond-graphite transition in detonation nanodiamond as revealed by small-angle neutron

scattering. J. Phys.: Condens. Matter. **25**, 445001 (2013). https://doi.org/10.1088/0953-8984/25/44/445001
6. O.V. Tomchuk, L.A. Bulavin, V.L. Aksenov, V.M. Garamus, O.I. Ivankov, A.Ya. Vul', A.T. Dideikin, M.V. Avdeev, Small-angle scattering from polydisperse particles with a diffusive surface. J. Appl. Cryst. **47**, 642–653 (2014). https://doi.org/10.1107/S1600576714001216
7. O.V. Tomchuk, D.S. Volkov, L.A. Bulavin, A.V. Rogachev, M.A. Proskurnin, M.V. Korobov, M.V. Avdeev, Structural characteristics of aqueous dispersions of detonation nanodiamond and their aggregate fractions as revealed by small-angle neutron scattering. J. Phys. Chem. C **119**, 794–802 (2015). https://doi.org/10.1021/jp510151b
8. A.I. Kuklin, A.V. Rogachev, D.V. Soloviov, O.I. Ivankov, Y.S. Kovalev, P.K. Utrobin, S.A. Kutuzov, A.G. Soloviev, M.I. Rulev, V.I. Gordeliy, Neutronographic investigations of supramolecular structures on upgraded small-angle spectrometer YuMO. J. Phys.: Conf. Ser. **848**, 012010 (2017). https://doi.org/10.1088/1742-6596/848/1/012010
9. A.I. Kuklin, A.Kh. Islamov, V.I. Gordeliy, Two-detector system for small-angle neutron scattering instrument. Neutron News **16**, 16–18 (2005). https://doi.org/10.1080/10448630500454361
10. H. Brumberger, *Modern Aspects of Small-Angle Scattering* (Kluwer Academic Publishers, Dordrecht, 1995), 463 pp. https://doi.org/10.1007/978-94-015-8457-9
11. V.N. Mochalin, O. Shenderova, D. Ho, Y. Gogotsi, The properties and applications of nanodiamonds. Nat. Nanotechnol. **7**, 11–23 (2012). https://doi.org/10.1038/nnano.2011.209
12. A.L. Vereshchagin, Phase diagram of ultrafine carbon. Combust. Explos. Shock Waves **38**, 358–359 (2002). https://doi.org/10.1023/A:1015618222919
13. D.M. Gruen, Nanocrystalline diamond films. Annu. Rev. Mater. Sci. **29**, 211–259 (1999). https://doi.org/10.1146/annurev.matsci.29.1.211
14. O.A. Shenderova, V.V. Zhirnov, D.W. Brenner, Carbon nanostructures. Crit. Rev. Solid State Mater. Sci. **27**, 227–356 (2002). https://doi.org/10.1080/10408430208500497
15. T.W. Ebbesen, P.M. Ajayan, Large-scale synthesis of carbon nanotubes. Nature **358**, 220–222 (1992). https://doi.org/10.1038/358220a0
16. L.-M. Peng, Z.L. Zhang, Z.Q. Xue, Q.D. Wu, Z.N. Gu, D.G. Pettifor, Stability of carbon nanotubes: how small can they be? Phys. Rev. Lett. **85**, 3249–3252 (2000). https://doi.org/10.1103/PhysRevLett.85.3249
17. Z. Mao, S.B. Sinnott, Separation of organic molecular mixtures in carbon nanotubes and bundles: molecular dynamics simulations. J. Phys. Chem. B **105**, 6916–6924 (2001). https://doi.org/10.1021/jp0103272
18. J.A. Nuth III, Small-particle physics and interstellar diamonds. Nature **329**, 589 (1987). https://doi.org/10.1038/329589b0
19. D.L. Chapman, On the rate of explosion in gases. Philos. Mag. **47**, 90–104 (1899). https://doi.org/10.1080/14786449908621243
20. A. Krueger, F. Kataoka, M. Ozawa, T. Fujino, Y. Suzuki, A.E. Aleksenskii, A.Y. Vul', E. Osawa, Unusually tight aggregation in detonation diamond: identification and disintegration. Carbon **43**, 1722–1730 (2005). https://doi.org/10.1016/j.carbon.2005.02.020
21. A. Krueger, M. Ozawa, G. Jarre, Y. Liang, J. Stegk, L. Lu, Deagglomeration and functionalisation of detonation diamond. Physica Status Solidi (A) Appl. Mater. Sci. **204**, 2881–2887 (2007). https://doi.org/10.1002/pssa.200776330
22. A. Krueger, The structure and reactivity of nanoscale diamond. J. Mater. Chem. **18**, 1485–1492 (2008). https://doi.org/10.1039/b716673g
23. J. Maul, E. Marosits, C. Sudek, T. Berg, U. Ott, Lognormal mass distributions of nanodiamonds from proportionate vapor growth. Phys. Rev. B **72**, 245401 (2005). https://doi.org/10.1103/PhysRevB.72.245401
24. M.V. Avdeev, V.L. Aksenov, L. Rosta, Pressure induced changes in fractal structure of detonation nanodiamond powder by small-angle neutron scattering. Diam. Relat. Mater. **16**, 2050–2053 (2007). https://doi.org/10.1016/j.diamond.2007.07.023
25. M. Ozawa, M. Inaguma, M. Takahashi, F. Kataoka, A. Krüger, E. Osawa, Preparation and behavior of brownish, clear nanodiamond colloids. Adv. Mater. **19**, 1201–1206 (2007). https://doi.org/10.1002/adma.200601452

26. E.D. Eidelman, V.I. Siklitsky, L.V. Sharonova, M.A. Yagovkina, A. Ya Vul', M. Takahashi, M. Inakuma, M. Ozawa, E. Ōsawa, A stable suspension of single ultrananocrystalline diamond particles. Diam. Relat. Mater. **14**, 1765–1769 (2005). https://doi.org/10.1016/j.diamond.2005.08.057
27. V. Pichot, M. Comet, E. Fousson, C. Baras, A. Senger, F. Le Normand, D. Spitzer, An efficient purification method for detonation nanodiamonds. Diam. Relat. Mater. **17**, 13–22 (2008). https://doi.org/10.1016/j.diamond.2007.09.011
28. V.Yu. Dolmatov, Detonation synthesis ultradispersed diamonds: properties and applications. Russ. Chem. Rev. **70**, 607 (2001). https://doi.org/10.1070/RC2001v070n07ABEH000665
29. I.I. Kulakova, Surface chemistry of nanodiamonds. Phys. Solid State **46**, 636–643 (2004). https://doi.org/10.1134/1.1711440
30. M.V. Avdeev, N.N. Rozhkova, V.L. Aksenov, V.M. Garamus, R. Willumeit, E. Ōsawa, Aggregate structure in concentrated liquid dispersions of ultrananocrystalline diamond by small-angle neutron scattering. J. Phys. Chem. C. **113**, 9473–9479 (2009). https://doi.org/10.1021/jp900424p
31. A.N. Ozerin, T.S. Kurkin, L.A. Ozerina, V.Yu. Dolmatov, X-ray diffraction study of the structure of detonation nanodiamonds. Crystallogr. Rep. **53**, 60–67 (2008). https://doi.org/10.1134/S1063774508010070
32. V.Yu. Dolmatov, Detonation nanodiamonds in oils and lubricants. J. Superhard Mater. **32**, 14–20 (2010). https://doi.org/10.3103/S1063457610010028
33. M.V. Korobov, N.V. Avramenko, N.N. Bogachev, N.N. Rozhkova, E. Osawa, Nanophase of water in nano-diamond gel. J. Phys. Chem. C **111**, 7330–7334 (2007). https://doi.org/10.1021/jp0683420
34. A.Ya. Vul, E.D. Eidelman, A.E. Aleksenskiy, A.V. Shvidchenko, A.T. Dideikin, V.S. Yuferev, V.T. Lebedev, Yu.V. Kul'velis, M.V. Avdeev, Transition sol-gel in nanodiamond hydrosols. Carbon **114**, 242–249 (2017). https://doi.org/10.1016/j.carbon.2016.12.007
35. J.Y. Raty, G. Galli, C. Bostedt, T.W. van Buuren, L.J. Terminello, Quantum confinement and fullerenelike surface reconstructions in nanodiamonds. Phys. Rev. Lett. **90**, 037401 (2003). https://doi.org/10.1103/PhysRevLett.90.037401
36. M. Zackrisson, A. Stradner, P. Schurtenberger, J. Bergenholtz, Small-angle neutron scattering on a core–shell colloidal system: a contrast-variation study. Langmuir **21**, 10835–10845 (2005). https://doi.org/10.1021/la051664v
37. A.S. Barnard, M. Sternberg, Crystallinity and surface electrostatics of diamond nanocrystals. J. Mater. Chem. **17**, 4811–4819 (2007). https://doi.org/10.1039/B710189A
38. P.W. Schmidt, D. Avnir, D. Levy, A. Höhr, M. Steiner, A. Röll, Small-angle X-ray scattering from the surfaces of reversed-phase silicas: power-law scattering exponents of magnitudes grater then four. J. Chem. Phys. **94**, 1474–1479 (1991). https://doi.org/10.1063/1.460006
39. O.V. Tomchuk, M.V. Avdeev, L.A. Bulavin, V.L. Aksenov, V.M. Garamus, Small-angle neutron scattering by fractal clusters in aqueous dispersions of nanodiamonds. Phys. Part. Nucl. Lett. **8**, 1046–1048 (2011). https://doi.org/10.1134/S1547477111100177
40. O.V. Tomchuk, M.V. Avdeev, V.L. Aksenov, V.M. Garamus, L.A. Bulavin, S.N. Ivashevskaya, N.N. Rozhkova, N. Schreiber, J. Schreiber, Comparative structural characterization of the water dispersions of detonation nanodiamonds by small-angle neutron scattering. J. Surf. Invest. X-ray Synchrotron Neutron Tech. **6**, 821–824 (2012). https://doi.org/10.1134/S1027451012100151
41. L.A. Bulavin, O.V. Tomchuk, M.V. Avdeev, Investigation of the cluster structure in aqueous suspensions of nanodiamonds by small-angle neutron scattering. Nucl. Phys. At. Energy **16**, 198–202 (2015). https://doi.org/10.15407/jnpae2015.02.198
42. M.V. Avdeev, O.V. Tomchuk, O.I. Ivankov, A.E. Alexenskii, A.T. Dideikin, A.Ya. Vul, On the structure of concentrated detonation nanodiamond hydrosols with a positive ζ potential: analysis of small-angle neutron scattering. Chem. Phys. Lett. **658**, 58–62 (2016). https://doi.org/10.1016/j.cplett.2016.06.010
43. M.V. Avdeev, Contrast variation in small-angle scattering experiments on polydisperse and superparamagnetic systems: basic function approach. J. Appl. Crystallogr. **40**, 56–70 (2007). https://doi.org/10.1107/S0021889806049491

44. A.E. Aleksenskiy, E.D. Eydelman, A.Ya. Vul', Deagglomeration of detonation nanodiamonds. Nanosci. Nanotechnol. Lett. **3**, 68–74 (2011). https://doi.org/10.1166/nnl.2011.1122
45. P.W. Schmidt, Small-angle scattering studies of disordered, porous and fractal systems. J. Appl. Crystallogr. **24**, 414–435 (1991). https://doi.org/10.1107/S0021889891003400
46. J. Feder, *Fractals* (Plenum Press, New York, 1989), p. 283. https://doi.org/10.1007/978-1-4899-2124-6
47. B.B. Mandelbrot, *The Fractal Geometry of Nature* (W.H. Freeman and Company, San Francisco, 1982), 656 pp. https://doi.org/10.1002/esp.3290080415
48. P.W. Schmidt, Use of scattering to determine the fractal dimension, in *The Fractal Approach to Heterogeneous Chemistry*, ed. by D. Avnir (Wiley, Chichester, 1989), pp. 67–79. https://doi.org/10.1002/adma.19900020913
49. G. Beaucage, Small-angle scattering from polymeric mass fractals of arbitrary mass-fractal dimension. J. Appl. Crystallogr. **29**, 134–149 (1996). https://doi.org/10.1107/S0021889895011605
50. G. Beaucage, H.K. Kammler, S.E. Pratsinis, Particle size distributions from small-angle scattering using global scattering functions. J. Appl. Crystallogr. **37**, 523–535 (2004). https://doi.org/10.1107/S0021889804008969
51. G. Beaucage, Approximations leading to a unified exponential/power-law approach to small-angle scattering. J. Appl. Crystallogr. **28**, 717–728 (1995). https://doi.org/10.1107/S0021889895005292
52. A.S. Barnard, S.P. Russo, I.K. Snook, Structural relaxation and relative stability of nanodiamond morphologies. Diam. Relat. Mater. **12**, 1867–1872 (2003). https://doi.org/10.1016/S0925-9635(03)00275-9
53. V.L. Kuznetsov, Yu.V. Butenko, Synthesis, in *Properties and Applications of Ultrananocrystalline Diamond*, ed. by D.M. Gruen, O.A. Shenderova, A.Ya. Vul' (Springer, Dordrecht, 2005), pp. 199–216. https://doi.org/10.1007/1-4020-3322-2_15
54. T. Jiang, K. Xu, FTIR study of ultradispersed diamond powder synthesized by explosive detonation. Carbon **33**, 1663–1671 (1995). https://doi.org/10.1016/0008-6223(95)00115-1
55. E. Mironov, A. Koretz, E. Petrov, Detonation synthesis ultradispersed diamond structural properties investigation by infrared absorption. Diam. Relat. Mater. **11**, 872–876 (2002). https://doi.org/10.1016/S0925-9635(01)00723-3
56. D. Mitev, R. Dimitrova, M. Spassova, C. Minchev, S. Stavrev, Surface peculiarities of detonation nanodiamonds in dependence of fabrication and purification methods. Diam. Relat. Mater. **16**, 776–780 (2007). https://doi.org/10.1016/j.diamond.2007.01.005
57. V.K. Kuznetsov, M.N. Aleksandrov, I.V. Zagoruiko, A.L. Chuvilin, E.M. Moroz, V.N. Kolomiichuk, V.A. Likholobov, P.N. Brvlvakov, G.V. Sakovitch, Study of ultradispersed diamond powders obtained using explosion energy. Carbon **29**, 665–668 (1991). https://doi.org/10.1016/0008-6223(91)90135-6
58. A. Barras, J. Lyskawa, S. Szunerits, P. Woisel, R. Boukherroub, Direct functionalization of nanodiamond particles using dopamine derivatives. Langmuir **27**, 12451–12457 (2011). https://doi.org/10.1021/la202571d
59. I. Hannstein, A.-K. Adler, V. Lapina, V. Osipov, J. Opitz, J. Schreiber, N. Meyendorf, Chemically activated nanodiamonds for aluminum alloy corrosion protection and monitoring, in *Proceedings of Conference on "Smart Sensor Phenomena, Technology, Networks, and Systems" (SPIE)* (San Diego, USA, 2009), p. 729300. https://doi.org/10.1117/12.815486
60. T.A. Witten, L.M. Sander, Diffusion-limited aggregation. Phys. Rev. B **27**, 5686–5697 (1983). https://doi.org/10.1103/PhysRevB.27.5686
61. C. Oh, C.M. Sorensen, Structure factor of diffusion-limited aggregation clusters: local structure and non-self-similarity. Phys. Rev. E **57**, 784–790 (1998). https://doi.org/10.1103/PhysRevE.57.784
62. A.S. Barnard, Self-assembly in nanodiamond agglutinates. J. Mater. Chem. **18**, 4038–4041 (2008). https://doi.org/10.1039/B809188A
63. M.V. Korobov, D.S. Volkov, N.V. Avramenko, L.A. Belyaeva, P.I. Semenyuk, M.A. Proskurnin, Improving the dispersity of detonation nanodiamond: differential scanning calorimetry as a new

method of controlling the aggregation state of nanodiamond powders. Nanoscale. **5**, 1529–1536 (2013). https://doi.org/10.1039/C2NR33512C
64. W. Peng, R. Mahfouz, J. Pan, Y. Hou, P.M. Beaujuge, O.M. Bakr, Gram-scale fractionation of nanodiamonds by density gradient ultracentrifugation. Nanoscale **5**, 5017–5026 (2013). https://doi.org/10.1039/C3NR00990D
65. B.H. Zimm, The scattering of light and the radial distribution function of high polymer solutions. J. Chem. Phys. **16**, 1093–1099 (1948). https://doi.org/10.1063/1.1746738
66. M.V. Avdeev, V.L. Aksenov, Small-angle neutron scattering in structure research of magnetic fluids. Phys. Usp. **53**(10), 971–993 (2010). https://doi.org/10.3367/UFNe.0180.201010a.1009
67. A.V. Nagornyi, L.A. Bulavin, V.I. Petrenko, O.I. Ivankov, O.V. Tomchuk, M.V. Avdeev, L. Vékás, Determination of the structure factor of interparticle interactions in the ferrofluid by small-angle neutron scattering. Nucl. Phys. At. Energy **15**, 59–65 (2014). In a public access: http://jnpae.kinr.kiev.ua/15.1/Articles_PDF/jnpae-2014-15-0059-Nagornyi.pdf
68. A. Vrij, Mixtures of hard spheres in the Percus-Yevick approximation. Light scattering at finite angles. J. Chem. Phys. **71**, 3267–3270 (1979). https://doi.org/10.1063/1.438756
69. D. Frenkel, R.J. Vos, C.G. de Kruif, A. Vrij, Structure factors of polydisperse systems of hard spheres: a comparison of Monte Carlo simulations and Percus-Yevick theory. J. Chem. Phys. **84**, 4625–4630 (1986). https://doi.org/10.1063/1.449987
70. B.B. Mandelbrot, Plane DLA is not self-similar; it is a fractal that becomes increasingly compact as it grows? Phys. A **191**, 95–107 (1992). https://doi.org/10.1016/0378-4371(92)90511-N
71. P. Meakin, Formation of fractal clusters and networks by irreversible diffusion-limited aggregation. Phys. Rev. Lett. **51**, 1119–1122 (1983). https://doi.org/10.1103/PhysRevLett.51.1119
72. O.A. Kyzyma, A.V. Tomchuk, M.V. Avdeev, T.V. Tropin, V.L. Aksenov, M.V. Korobov, Structural researches of carbonic fluid nanosystems. Ukr. J. Phys. **60**, 835–843 (2015). https://doi.org/10.15407/ujpe60.09.0835
73. O.V. Tomchuk, M.V. Avdeev, A.E. Aleksenskii, A.Ya. Vul, O.I. Ivankov, V.V. Ryukhtin, J. Füzi, V.M. Garamus, L.A. Bulavin, Sol–gel transition in nanodiamond aqueous dispersions by small-angle scattering. J. Phys. Chem. C 123(29), 18028–18036 (2019). https://doi.org/10.1021/acs.jpcc.9b03175

Chapter 9
Electron Structure and Optical Properties of Conjugated Systems in Solutions

O. L. Pavlenko, O. P. Dmytrenko, M. P. Kulish, V. A. Sendiuk, N. V. Obernikhina, Ya. O. Prostota, O. D. Kachkovsky and Leonid A. Bulavin

Abstract The review deals with the special type of the organic molecules which contain the collective system of π-electrons; the mobility of the electrons that determines both the electron structure and spectral properties of considered conjugated molecules. The classification of the linear conjugated systems is proposed: polymethine dyes, polyenes, donor-acceptor compounds and the differences between them. It is shown that the high mobility of the collective π-electron shell depends on the type of the conjugated system, chain length, symmetry, molecular constitution of the terminal groups, as well as the electron shell (neutral or charge system). Experimentally, the features of the electron structure of conjugated molecules are observed by spectral methods, especially, in various solvents. It is established that different molecular types show the different sensitivity to the solvent polarity. The work reviews principal results that were obtained by the quantum-chemical and spectral study of the linear conjugated systems.

9.1 Introduction

In the conjugated systems atoms of carbon in the sp^2-hybridization form 3 carbon—carbon σ-bonds while the residual $2p_z$ electrons can generate the collective systems of π-electrons (Fig. 9.1). Such systems form both 1-dimensional π-molecules and branched π-electron systems. According to the Daehne 's triad theory [1–4], the con-

O. L. Pavlenko (✉) · O. P. Dmytrenko · M. P. Kulish · V. A. Sendiuk · L. A. Bulavin
Faculty of Physics, Taras Shevchenko National University of Kyiv, Kyiv, Ukraine
e-mail: olpavl57@gmail.com

N. V. Obernikhina
Department of Bioorganic and Biological Chemistry, Bogomolets National Medical University, Kyiv, Ukraine

Ya. O. Prostota · O. D. Kachkovsky
Institute of Bioorganic Chemistry and Petrochemistry, NAS of Ukraine, Kyiv, Ukraine

L. A. Bulavin and L. Xu (eds.), *Modern Problems of the Physics of Liquid Systems*, Springer Proceedings in Physics 223,
https://doi.org/10.1007/978-3-030-21755-6_9

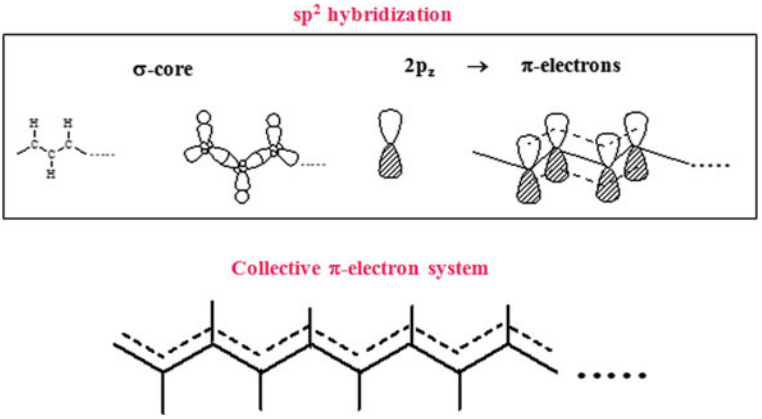

Fig. 9.1 Types of carbon branched π-electron systems

jugated systems are divided on cyclic molecules (or aromatics) and linear molecules (neutral polyenes and ionic polymethine dyes (PMD) as well as their derivatives including the donor-acceptor conjugated molecules).

Collective systems of π-electrons are formed by branched conjugated organic molecules are perspective as functional materials, sensors because of spectral properties (see reviews [5–8] and refers therein). In other hand, the molecules are convenient models for development of new conceptual theoretical approaches that take into consideration the electron properties and chemical topology correctly including both the simplest approaches (based on Hueckel approximation) [9–12] and modern TD DFT methods [13, 14] and soliton concept [15–19].

The similar collective systems of π-electrons are mobile and very sensitive to the various perturbations (injections of charge, deformation of σ-core, excitation by light quants) or/and to environment, including the solvent nature. The dependence electron structure deformation on the chemical constitution of the conjugated molecules could be investigated effectively by spectral methods so as the conjugated systems manifest the specific selective and highintensive bands both in the absorption and fluorescence spectra.

9.1.1 Classification

a. 1-Dimension Systems:
Linear conjugated systems (LCS) contain, as a rule, two terminal groups (TG) and polymethine chain (PC). In the general case, LCS with a non-branched PC can be represented as follows:

$$[G_1 - (CH)_m - G_2]^z, \qquad \mathbf{1}$$

where G_1 and G_2 are TG, m is the number of the methine groups, z is the charge ($z = 0; \pm 1$).

If $m = 2n + 1$, then neutral radicals ($z = 0$) are unstable; but the ionic systems ($z = \pm 1$) contrariwise system with closed electron shell are stable molecules with the oppositely charged counter ions; they are usually called as *polymethine dyes* (PDs). Of course, the stable cationic PDs contain the donor TGs; in the contrast, the stability of the anionic PDs is increased by introducing of acceptor end groups. The PDs with nitrogenous TGs trivially are called as *cyanine dyes* [20].

If number of methine component is even ($m = 2n$), such neutral molecules are treated as substituted *heteryl-polyenes* (HP) [1–4, 7]. The polyenes can contain both donor and acceptor TGs.

Symmetric PMD and HP differ substantially in several chemical and spectral properties. If linear conjugated systems have an asymmetric structure, the difference between PMD and HP decreases.

Besides, there exists another neutral 1-dimensional conjugated system containing simultaneously donor and acceptor terminal substituents **2**:

$$\text{Don} - (CH = CH)_n - \text{Ac}, \qquad \mathbf{2}$$

where Don is a donor TG while Ac is an acceptor TG; the n is denoted the number of the *vinylene* groups. Similar systems with extremely asymmetry are especially sensitive to the influence of various perturbations which could be registered by spectral measurements.

Here, we will regard two main types of the neutral donor-acceptor systems: merocyanines and cyanine bases, so as their spectral properties in the different solutions are studied in detail (see, for example, papers [21–24]).

Merocyanines. The first type of donor-acceptor compound can be presented by three resonance formulae **3–5**:

$$\underset{\mathbf{3}}{\text{Don} - (CH = CH)_n - CH = \text{Ac}} \leftrightarrow \underset{\mathbf{4}}{\text{Don}^+ = (CH - CH)_n = CH - \text{Ac}^-} \leftrightarrow$$

$$\leftrightarrow \underset{\mathbf{5.}}{\text{Don} - (CH \text{——} CH)^+_n - CH - \text{Ac}^-}$$

In contrast to non-charged response structure **3**, both other structures, **4** and **5**, are so-called "dipolar" contributing structures. In the first known merocyanines (in Brooker's papers [25, 26], the symbol Don was an amino group and Ac was oxygen. Many other terminal groups Don and Ac with similar functionality can be used in merocyanines retaining the characteristics and hence may also be treated under the

same name. In the structure **5**, the symbol A^- should formally treated as a donor group with high situated donor electronic level; there for merocyanines could be similar to the unsymmetrical polymethine dyes with two different terminal groups.

Cyanine bases: in contrast to merocyanines, the acceptor group in the cyanine dyes does not contain the high situated donor level, but low situated vacant level, and consequently they strongly differ on the related merocyanines. Neutral bases of cyanine dyes are obtained from cationic polymethines and hence are their dealkylated derivatives. For example, case of the simplest cationic streptocyanine **6** produces its base **7**:

$$\underset{\mathbf{6}}{(H_3C)_2N^+{=}CH{-}(CH=CH)_n-N(CH_3)_2} \Rightarrow \underset{\mathbf{7}}{H_3CN=CH-(CH=CH)_n-N(CH_3)_2}$$

Both merocyanines and bases as donor-acceptor compounds have high dipole moments that remain upon excitation and therefore they are effective sensors on the environment nature, especially, on the solution polarity.

b. Aggregates of PDs

It was observed, more than 70 years ago, an unusual behavior of some ionic cyanine dyes in aqueous solutions (see reviews [27, 28]). As regard to the solvent sensitivity, the absorption maximum was shifted bathochromically with increase of the concentration in water, and at high concentration the spectral bands became more intense and sharp. This tendency is typical for new absorption band: their sharpness with a small spectral wide and a very high absorption coefficient. Also, similar solutions demonstrate the strong fluorescence with small Stokes shift. This phenomenon of polymethine dyes in water solvents was explained by *aggregation*, and that the absorption spectrum was changed by the "vicinity effect" of adjacent molecules [28].

The dye aggregates that possess narrow absorption bands shifting bathochromically in comparison with monomer absorption band and nearly resonant fluorescence with small Stokes shift are generally termed Scheibe aggregates or J-aggregates, in the accordance with the name of their inventor (J denotes Jelley). Aggregates with hypsochromically shifted absorption bands are called H-aggregates (because of hypsochromic (H)) typically having low or absent fluorescence. Also, J-aggregates of other dyes, such as merocyanines, squaraines, etc. have been developed [27, 28]. Structural organization is important in considering of interaction between the dyes and carbon nanostructures, especially with fullerenes, antitumor agents [29–31]. The aggregation points in particular on the important influence of the solutions on the spectral properties of the linear conjugated systems.

9.1.2 Features of Electron Structure in Ground and Excited States

Electron Structure

According to Daehne' theoretical conception [1–4], in aromatic compounds, the C–C bond lengths are equalised while the carbon atoms have no noticeable charge, however the essential polarization of the C–H bonds causes to appearance of the appreciable positive charge at the carbon atoms and correspondingly charges with opposite sign at the hydrogen atom.

The polymethines and polyenes differ substantially on their electronic structure and hence on their chemical and physic properties. It is why, as a rule, they have been studied separately by the spectral methods [7, 8, 32, 33]. Particularly, the quantum-chemical calculation spectral data (^{13}CNMR) have shown that the considerable positive or negative charge alternates at neighboring carbon atoms in the extended chain of the polymethines in contrast to equalization of the bond lengths, that are approximately equal to 1.4 Å [4, 7, 8]. Going to the first excited state is accompanied by the little changes of the bond lengths, whereas the charges change significantly, even change their signs. In contrast, the atomic charges in the ground state in the polyenes are minimal (they appear by only C–H polarization), but the C–C bond lengths reach the maximum alternation, the amplitude of alternation in the long molecules reaching amounts to 0.08 Å. In the excited state, the bond lengths in the polyenes change significantly, so that following of the longer and shorter bonds is reversed (see, for example, the reviews [4, 7, 33] and the references therein).

In is to be noted that similar classification of linear conjugated systems with an open electron shell (radicals) becomes more complicated. Thus, in the ionic polyene-radicals, the bond lengths and the electron density at the atoms are simultaneously equalized [34, 35]. Also, the simultaneous equalization of both electron density at the atoms and bond lengths is reached in the neutral polymethine because of the appearance of the unpaired electron [36]. Consequently, the π-electronic structure of the chain in both types of conjugated system is similar.

There is specific interest concerning thy on injection of the electrons or holes in the collective π-electron, as far as the π-molecules can be used as semiconductors. According to the modern conception, similar injection of the charge (positive or negative) in the highly polarized conjugate molecule causes appearance of the specific solitonic or impurity level in the energy gap, both the conductive and valence bands to bottom and top are shifted considerably [15–19, 37–39]. Then the injected charge could be treated as an ionic defect. It was shown that this charge or defect is not uniformly delocalized along the whole extended π-electron system, but is rather localized within several atoms. I.e. charge in the collective system forms the finite wave or the soliton (neutral for the radical and charged for cationic or anionic molecules). Performed quantum-chemical calculations have showed that the charge wave in the ions of the linear conjugated molecules is of a finite width covering 15–17 carbon atoms. Also, similar numeral calculations have given that the soliton becomes mobile, so that it can move from one terminal group to another group along

the conjugated chain without a substantial change in the total energy of the molecule. It is to be noted that the similar movement of the solitonic wave is only possible when the length of the conjugated chain exceeds the dimension of the solitonic wave, what can accompanied by the symmetry breaking. It is logically, that the soliton-like wave of alternating bond lengths appears simultaneously with the charge alternation wave; it is treated as a geometrical soliton.

Thus, according to modern point view, the injected charge is neither localized in only one atom (π-center) nor uniformly delocalized along the conjugated system, but creates a solitonic wave of the alternating partial charges. Also, the quantum-chemical calculations have demonstrated that the multiple injections of the charges causes the generations of corresponding number of the solitons. It is important to notice that the location of the charge soliton depends on molecular topology and solvent polarity [8, 40].

Spectral Properties

The most specific feature of the conjugated systems is their comparatively narrow energy gap what enables the light absorption (and also fluorescence) in the different spectral regions (UV, visible and NIR). As regard to the linear systems, especially, PDs, the essential redistribution of the atomic charges and minimal changes in the lengths of bonds upon the light excitation provide the high intensive and narrow spectral bands (see, for example, reviews [5, 7, 8]).

Symmetrical cyanine dyes. The most intensive absorption is observed in the cationic PDs. As an impressive illustration, Fig. 9.2 presents the absorption spectra of the typical pyrylopolycycanines **8**:

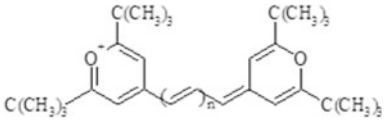

8

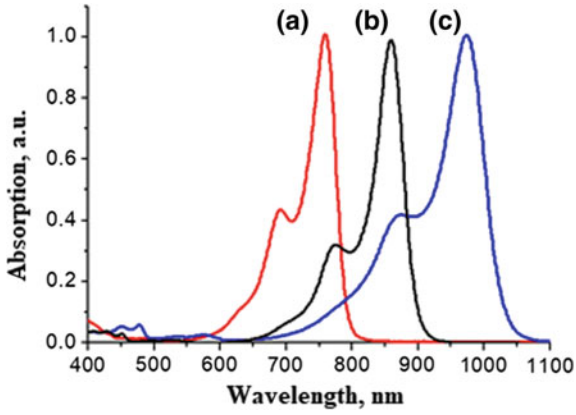

Fig. 9.2 Shift of maxima in the absorption spectra of dyes **8**; **a**: $n = 1$ (759 nm); **b**: $n = 2$ (860 nm), **c**: $n = 3$ (995 nm) (methanol) [8]

The PMD can undergo photoinduced geometrical isomerization in the excited state and hence to change essentially their absorption/fluorescence spectra what enable them to use widely as molecular switches [41–44], as well as fluorescence sensors, including biosensors [45–49]. PMDs have begun used in composites for solar cells, as far as they can convert light energy into electricity [50–52]. In this application, the dyes work as sensitizers, similarly to sensitization process in the photography.

Beside the ordinary electron transition from the ground state to the first excited state, $S_0 \rightarrow S_1$, there are the additionally possible high intensive transitions from the low excited states to the higher states, $S_n \rightarrow S_m$, as well as the effective two-photon absorption; these properties are perspective materials for the using of PMDs in non-linear optics [53–57].

Merocyanines. Since merocyanines as a D-A-conjugated compounds exhibit their intense absorption bands and the outstanding sensitivity of these bands to solvents, they attract high attention for different applications [55–58]. These features of the merocyanines are found to connect directly with their mobility of the electron density in collective conjugated system. It is supposed that merocyanines sensitivity of the absorption bands in the solvent could be simplest interpreted in terms of valence structures **3–5**, which assumes that the merocyanines the ground state (S_0) and excited state (S_1) are described by a linear combination of a non-charge-separated polyene-like structure **3** and charge-separated polyene-like structures **4**, **5**. In this model, increasing polarity of the solvent leads to increasing of the contribution of all charge-separated resonance structures, whereas the contribution of the neutral forms decreases. Experimental NMR spectroscopy confirms the redistribution of the atomic charges upon variation of solvent polarity [59]. When the balance of the contributions of the different valence structure is reached, this state is called as the "cyanine limit".

In is to be pointed that the transferring of the electron density along conjugation chain upon change of solvent polarity causes the essential change of the dipole moment direction and its value.

Cyanine bases. In another the donor-acceptor type, so-called cyanine bases, a donor and/or acceptor strength could be also varied regularly and purposefully to obtain the desired spectral characteristics. In these donor-acceptor molecules, the acceptor group is presented by nitrogen heterocycles that have more complex topology, the acceptor residues in merocyanines contain one-coordinated oxygen atom of the higher electronegativity [59]. Among the widest cyanine bases, styryl bases are most stable and hence are most studied (see review [60] and references therein). Going to the excited state is accompanied by the substantial intramolecular charge transfer, more often it is observed in the polar solvents.

As regard to spectral properties, bases exhibit, especially, in polar solvents, wide and structureless spectral bands, unlike the original cyanine dye with their narrow and high-intensive bands in the absorption and fluorescence spectra [24]; also bases show a considerable Stock's shift. This fact can be explained by is intramolecular charge transfer (ICT) process upon excitation, whereas an electron density in PMDs transfers only on the adjacent atoms (see, for example, [60] and refers therein). Nevertheless, the cyanine bases as a specific donor-acceptor conjugated molecules are the finest

fluorescent sensors; the cyanine bases in combination with a the crown complexing moiety, can be used as both the fluorescent quenchers so far the complexation with metal cations causes the drastic increasing of quantum yields, by a factor 100–1000 [59].

Both bases and chemically similar cationic cyanine dyes contain the same π-electron shell (the same number of π-electrons), however there the principal distinction between these two types of the donor-acceptor systems; it lies on the fact that the two-coordinated nitrogen atoms (for example, in the formulas **2**) have the electron configuration $N(tr^2trtr\pi)$ while the electron configuration of the three-coordinated nitrogen is $N(trtrtr\pi^2)$. It is fact, which one must take into consideration of the electron-electron interaction upon describing the features of the electron structure of the neutral bases and interpretation of their spectral data; they determine the specific nature of the electron transitions in the bases in comparison with the initial cationic cyanine dyes. Going from cyanines to its base is accompanied by the essential equalization of the atomic charges and increasing of the alternation of the bond lengths in the extended chain. So, the amplitude of the charge alternation in the chain middle of the bases **7** is less, practically by factor 5–7, than in the initial cationic cyanines **6**. Besides, the distribution of the electron densities in the cyanine dyes is symmetrical, whereas, the some charge alternation in the chain of the cyanine bases changes regularly along the chain from one terminal group to another that. This transformation of charge distribution in the chain of the bases is high sensitive to the donor strength of the donor group, especially, close to this group.

The essential difference between cyanine dyes and their bases manifests itself most pronounced in absorption spectra. For sake illustration, the spectra of the some vinylogs of thiacyanines **9** and corresponding bases **10** are pictured in Fig. 9.3.

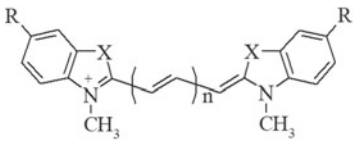

9

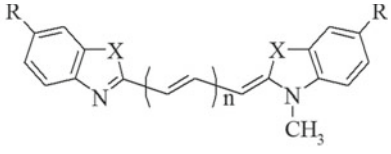

10

where X= S , R=H –**a**, $C(CH_3)_2$,R=H – **b**, $C(CH_3)_2$,R=NO_2 – **c**

Comparing spectra of cyanine dyes and related bases, one can see the considerable transformation of the longwavelength band. The cyanines **7** with different amount of vinilene groups from 0 to 2 possess high intensive and narrow spectral bands and the short wavelength shoulder corresponding to vibronical transitions, $0 \rightarrow 1'$ (Fig. 9.3a). The introducing of new vinylene, –CH=CH–groups in the chromophore (increasing of n) causes the bathochromic shift of the band maximum (so called vinylene shift) on 135 nm for $n = 0, 1$) and by 98 nm ($n = 1, 2$). Then the first vinylene shift (135 nm) is somewhat greater in compare with the usual value 100 nm; this can be explained

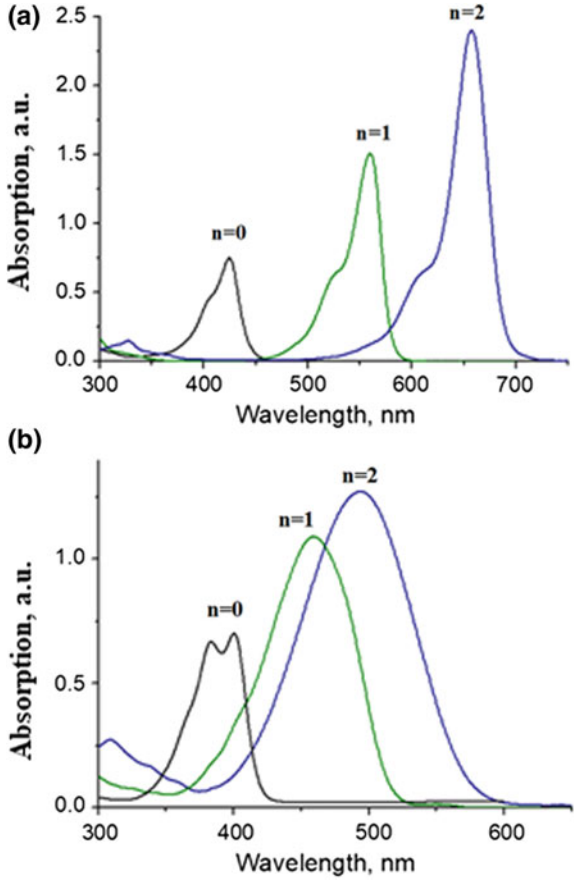

Fig. 9.3 Shift of the spectral maxima of the thiacyanines **9** (**a**) [81]; and base **10** (**b**), (concentrations $c = 1 \cdot 10^{-5}$ m/l, $c = 2 \cdot 10^{-5}$ m/l respectively, ethanol)

by an interaction between two sulfur atoms in the monomethinecyanine **7** ($n = 0$) which causes the hypsochromic shift of the band maximum [23, 24].

Figure 9.3b shows the transformation of the spectral bands of the bases in compare with spectra of the corresponding cyanine dyes; they are substantially wider and are hypsochromically shifted. Additionally, their vinylene shifts are lesser, 59 nm ($n = 0$, 1) and 34 ($n = 1$, 2); and decreases upon lengthening of the chain.

The shapes of spectral band of the dyes **10(a–c)** are similar and differ only by the position of the maxima and widths, especially in polar solvents (see Table 9.1, too).

Comparing of spectral data in ethanol and acetonitrile and toluene shows that the absorption spectra of the considered cyanine bases are not highly sensitive to solvent polarity. One can also see from Fig. 9.3 that the going to higher vinilogs is accompanied by the regular increasing of the intensity of the spectral bands in the both cyanine dyes and bases.

Table 9.1 Position of the maxima of the band, λ_{max} (nm) and bandwidths $\Delta\nu$ (cm^{-1}) in bases **10** in solvents *acetonitrile (1)*, *toluene (2), ethanol (3)*

Dye	*1*		*2*		*3*	
	λ_{max}	$\Delta\nu$	λ_{max}	$\Delta\nu$	λ_{max}	$\Delta\nu$
10-a	452	3721	449	3670	459	3607
10-b	435	4130	435	4092	447	4036
10-c	500	4057	488	3827	505	4073

9.1.3 Influence of Solutions and Spectral Sensitivity

The unique mobility of the π-electron shell of the conjugated systems determines their high sensitivity to the environment medium, firstly, to solvent nature. This is basis for the convenient high sensitive spectral methods for study of such π-electron mobility: one- and two-photon absorption (OPA and TPA), both steady and time-resolved fluorescence, excited state absorption (ESA), etc. There are series of the papers concerning of influence of the polarity of solvents on the spectral properties [26, 32, 58, 61–67]. So, Table 9.2 presents the solvation effects for the pyrylo-4-cyanines and their heteroanalogues **11a** obtained in two various solvents (low-polar dichloromethane and higher polar nitromethane). Recently, it was established that the symmetric PDs demonstrate the low sensitivity to solvent polarity. Besides, it was experimentally found that absorption spectra of the ionic polymethine dyes with the enough long chain (absorbing on 1000 nm) undergo substantial transformation: the shape of the longwavelength band becomes unusually broad [67–73]. In is to be noticed that the long-wavelength side of the absorption band remains the same as in dyes with the shorter chain, in contrast to broad shoulder at the short-wavelength side. The analysis shows that this spectral effect is not caused by the growing of vibronical structure, as far as increasing of the solvent polarity leads this additional peak to be shifted regularly hypsochromically, as well as its intensity increases simultaneously. Figure 9.4 presents the absorption spectra of typical long cationic dye **12** in solvents of different polarity.

Table 9.2 Position of the maxima of the band, $\lambda_{max,}$ (nm) of pyrylocyanines and their heteroanalogues in solvents CH_2Cl_2 *(1)*, CH_3NO_2 *(2)*

n	11-a (X = O)		11-b (X = S)		11-c (X = Se)	
	1	*2*	*1*	*2*	*1*	*2*
0	555	552	630	627	673	672
1	686	676	762	755	805	795
2	806	798	889	879	930	922
3	–	–	1016	1000	–	–

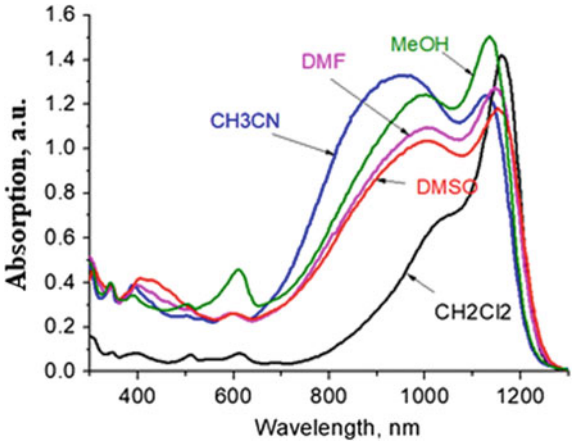

Fig. 9.4 Shape of spectral bands in various solvents [8]

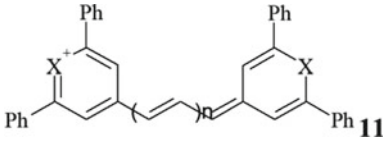

11

where X = O –**a;** X = S – **b;** X=Se – **c**

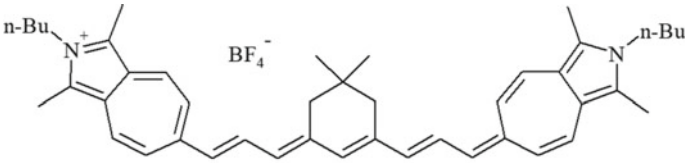

12

The dyes with the comparative short chain exhibit typical absorption spectra; their absorption bands in both more polar and less polar solvents are enough narrow. But the width of the spectral bans of long dyes increases progressively upon increasing of the solvent polarity. Such widening is firstly connected with the appearance of additional broad shoulder on the short-wavelength side of the band. Then, this spectral fact points directly on the strong polarsolvatochromism. Figure 9.4 demonstrates that the long-wavelength band preserves its shape as in the shorter dyes. Consequently, it was assumed that two different forms of the dye with the long chain coexist in the solution: the first dye form with a comparatively low dipole oriented perpendicularly the chain (similarly to the short dyes) and the second dye form with a high dipole moment oriented along the chain. Similar mobility of the electron density distribution was studied quantum-chemically and can be explained in the framework of the soliton

conception (see [8, 74] and numerous referrers therein). So, Painelli et al. [69] have shown the possible charge instability in polymethine dyes and their derivatives: they predicted the symmetry breaking in both the ground and the first excited state. Also, it was shown that quadrupolar chromophores can be classified as three types with different spectral properties. This theoretical model was illustrated by three representative quadrupolar chromophores: they exhibit the qualitatively different solvatochromic properties connected with the possibility of the symmetry breaking.

It should be pointed that the symmetry breaking can occur not only in ground state but also in the first excited state; this spectral effect was confirmed experimentally by time-dependent fluorescence upon the low-temperature [75, 76].

Basing on the spectral and quantum-chemical results, is was postulated that PDs with a polymethine chain containing crucial vinylene groups may exist in the ground state in two various charged forms, symmetrical and asymmetrical, correspondingly, with different distributions of the charge density [77]. Then appreciable difference between symmetrical and unsymmetrical forms of the dyes should display unambiguously the similar difference in their solvation effect, what agrees well with the measured spectral sensitivities of both forms to the solvent polarity.

Unsymmetrical Polymethine Dyes and Polyenes

Beside the symmetrical linear conjugated systems, the unsymmetrical compounds are also wide known; they are more sensitive to the solution nature [4, 5, 7, 32, 77, 78]. Traditionally, the unsymmetrical compounds are usually considered as derivatives of the corresponding symmetrical molecules which are usually referred to the *parent* compounds. In the construction of asymmetrical systems, a half of the molecule is taken from one symmetrical parent compound, the other half is taken from another parent compound.

In unsymmetrical molecules, the collective π-electron shell shifts from the chain middle, which is obtained from quantum-chemical calculations [77]; it was established that the minimum of the calculated charge alternation amplitude in unsymmetrical dye is shifted to the benzene ring and reach the practically the bond length equalization, similarly to the polyenes. The same distortion of charge distribution is experimentally confirmed by spectra NMR (^{13}C) [77]; the chemical shifts for the neighboring carbon atoms are considerably alternated along the polymethine chain. So, the measurements have given that the signals close to both terminal ends in the unsymmetrical as well as in the parent symmetrical dyes are appreciable shifted in the weak field because of the influence of terminal groups [77]. It is logically that increasing of asymmetry degree by using of the more basic variable terminal group causes the increasing of bond length alternation degree and of decreasing of charge alternation in the polymethine chain.

The spectra of the unsymmetrical dyes turn out to be more sensitive to asymmetry; namely absorption spectra were used for the estimation of the asymmetry degree [32]. As convenient asymmetry parameter, the deviation D was proposed. By definition, this parameter is calculated by comparing of the spectra of the unsymmetrical dye and its both parent dyes:

$$D = (\lambda_1 + \lambda_2)/2 - \lambda_{as} \tag{9.1}$$

Here λ_{as} is the absorption maximum for unsymmetrical dye whereas λ_1 and λ_2 are maxima of both symmetrical parent molecules. The systematic measurements have shown that for typical unsymmetrical cyanines, $D > 0$, i.e. the maximum for unsymmetrical dyes is hypsochromically shifted in comparison with the arithmetic mean value from the maxima of the parent dyes. This spectral effect was explained by the generation of the appreciable bond alternation along the polymethine chain when the terminal groups in the dye are non-equivalent [32]. It was found that the bond alternation in the excited state decreases considerably; as a result, the deviation in the fluorescence spectra (when electron transition occur upon the excited state relaxed geometry) of the unsymmetrical PDs decreases essentially [78]. Of course, the deviations depend strongly on the solvent polarity.

The opposite spectral effects are observed in the unsymmetrical polyenes [78]. It was shown the violation of symmetry in polyenes leads to the opposite change in bond orders as compared to that in PMD: bonds in asymmetrical polyenes are more equalized than in the corresponding parent compounds. Then, the deviations calculated from formula (9.1) should be negative, which was proved by experimental studies of vinylogous series of asymmetrical polyenes **13** with one constant nucleus and variable residues. The spectral characteristics are listed in Table 9.3.

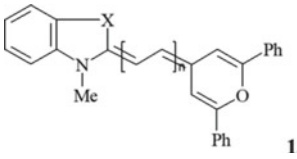

13

Where X:CMe_2 –**a;** X: S – **b;**
X: CH=CH – **c**

As one can see, the deviations in unsymmetrical polyenes are really negative. Their absorption maximum is bathochromically shifted in the comparison with the arithmetic mean $(\lambda_1 + \lambda_2)/2$ of both symmetrical parent polyenes.

Donor-Acceptor Molecules

Among various unsymmetrical linear conjugated systems, the spectral of the neutral donor-acceptor molecules are most sensitive to solvent media. The considerable spectral effects are, of course, observed for the merocyanines (see, for example,

Table 9.3 Position of the maxima of the band, $\lambda_{max,}$ (nm) for heteroanalogues **13**. D is deviation; $V = \boldsymbol{\lambda_{max}}(n) - \boldsymbol{\lambda_{max}}(n-1)$ is vinylne shift

n	13-a (X:CMe_2)			11-b (X:S)			11-c (X:CH=CH)		
	λ_{max}	V (nm)	D	λ_{max}	V (nm)	D	λ_{max}	V (nm)	D
0	442	–	−18	454	–	−24.5	456.5	–	−80.5
1	472	30	−8.5	483.5	29	−10	495	38.5	−36.5
2	495	23	−7.5	506	29.5	−13	515.5	20.5	−32.5

review [21] and refers therein) and related cyanine bases [24, 26, 79, 80]. Let us consider sequentially their spectra.

Merocyanines. As a worthwhile example, the absorption spectra of the merocyanines **14** derivatives of pyrole were examined; their spectra are pictured in [80].

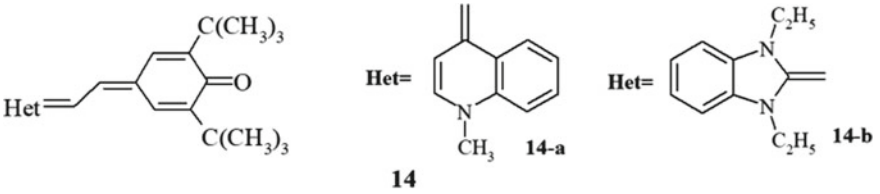

14

One can see that not only the band maximum but also band hope depend on solvent polarity, when vibrational transitions clearly observed (Fig. 9.5). The lowest $0 \rightarrow 0'$ vibrational transition could exhibits in the spectra by various ways: by the intensive peak or by less intensive second peak or even by shoulder at the longwavelength side

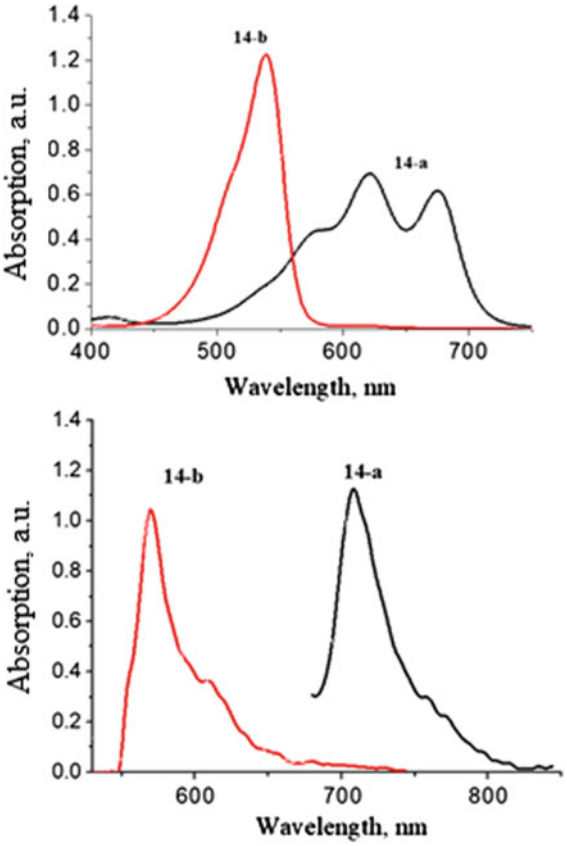

Fig. 9.5 Absorption (300 K) and fluorescence spectra (77 K) of the **14a–b** in acetonitrile ($\varepsilon \times 10^4$, l × mole^{-1} × cm^{-1})

of the band. The observed change in the relative intensities of vibrational transitions can be attributed to the changes of bond lengths within the chromophore upon its relaxation from the excited state. In dyes with an slight change of equilibrium molecular geometry upon excitation, the most probable transition occurs from the ground state 0-th vibrational level to the excited state 0′-th vibrational level, and hence the intensity of $0 \rightarrow 0'$ transitions should be the highest.

The occupation of higher vibrational level is less probable, therefore the corresponding intensities of $0 \rightarrow 1'$ and $0 \rightarrow 2'$ transitions should be lower. The intensity ratio of the vibrational peaks could be inverted when the substantial change of bond lengths in the dye chain happens upon relaxation in the excited state. One can see that vibrational structure (transitions to higher vibrational states) sharply changed in the fluorescence spectra measured upon the low temperature, especially, for merocyanine **14-b** (Table 9.4).

Donor-acceptor molecules; *cyaninebases*. In the absorption spectra of the cyanine bases, the separated bands connected with the first $\pi \rightarrow \pi^*$ electron transitions are also observed in the visible part. For sake illustration, the longwavelength bands of the dyes **15**a–e are pictured in Table 9.5.

Table 9.4 Spectral data of merocyanines **14**

	Absorbtion		Fluorescence			
	λ_{max} (nm)	$\varepsilon \times 10^4$ (l mole^{-1} cm^{-1})	λ_{max} (nm)	$\Delta\lambda$ (nm)	Stock's shift	
					$\Delta\lambda_S$ (nm)	$\Delta\nu_S$ (cm^{-1})
14-a	676	6.18	708	135	32	669
14-b	539	12.23	570	−3	31	1009

Table 9.5 Spectral data for cyanine base **15a–e**: a the absorption band maxima ($\lambda_{max,}$ nm), extinction (ε, $\mathbf{10^4}$) in solvents 1—dioxane, 2—toluene, 3—acetonitrile, 4—methanol. $\boldsymbol{\lambda^{theor}}$ (nm) is calculated wavelength of the first electron transition

	1		*2*		*3*		*4*		λ^{theor}
	ε	λ_{max}	ε	λ_{max}	ε	λ_{max}	ε	λ_{max}	
15a	1.58	569	1.85	567	5.57	571	9.70	523	522
15c	2.26	574	3.75	574	7.10	572	7.09	589	513
15b	3.57	582	3.21	583	7.01	584	6.76	569	531
15d	2.57	525	2.20	526	4.86	523	3.83	515	499
15e	2.20	519	2.08	520	4.06	515	2.88	508	472

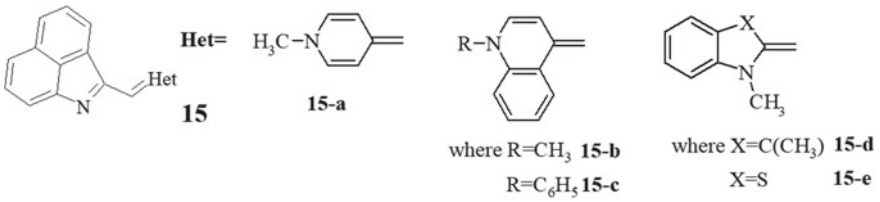

One can see that all presented spectra have wide bands with the vibronic structure in both polar and non-polar solvents. Their vibronical transitions are revealed as the spectral band shoulders. In non-polar toluene, the vibronic structure is most pronounced. The measured distance between vibronic transitions reaches the 1100–1400 cm^{-1}, what is close to the corresponding value in the spectra of polymethine dyes and derivatives. One could see from Fig. 9.6 that $0 \rightarrow 1'$ vibronic transition in the absorption spectra of the investigated cyanine bases is the most intensive.

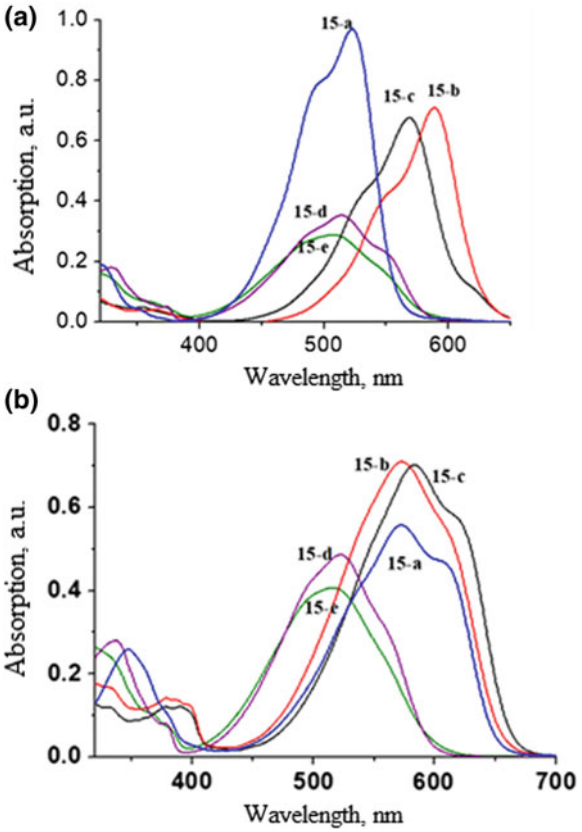

Fig. 9.6 Absorption spectra of bases **15a–e** at $c = 1 \times 10^{-5}$ M in different solvents: **a** methanol, **b** acetonitrile

The longwavelength separated comparative intensive band in all solvents corresponds to only the first $\pi \rightarrow \pi^*$-electron transition, whereas the higher transitions is observed in the spectral region shorter than 400–450 nm. The positions of the maxima of the longwavelength bands of the dyes **15**a–e are collected in Table 9.5.

Both Fig. 9.6 and Table 9.5 data testify that spectral characteristics of the cyanine bases are not very sensitive to the solvent polarity One can see from Fig. 9.6b that the spectral bands in the polar acetonitrile are rather wide and structural, so that the fine vibronic structure is observed and $0 \rightarrow 1'$ vibronic transition is the most intensive.

The careful study was shown that solutions of the cyanine bases **15a–e** are not stable. So, the intensity of absorption bands of the bases solutions upon exposure to air decreases regularly. Also, it was established that stability depends on the chemical constitution of the terminal donor group. The extinction coefficient decreases in serii: (in %) is: 15.71 (**15a**), 2.45 (**15b**), 5.45 (**15c**), 0.55 (**15d**) and 0.54 (**15e**).

Thus, Figs. 9.6 and 9.7 demonstrate appreciable influence of the polarity of the solvents on the spectral properties of the cyanine bases as the high sensitive neutral donor-acceptor compounds with the mobile collective system of the π-electrons.

At last, it has to be pointed that many cyanine bases can be weakly sensitive to the absorption spectra (i.e. electron transition upon the ground state equilibrium geometry), whereas are very sensitive to the fluorescence spectra, when electron transitions occur upon the excited state equilibrium geometry. As an illustration, the absorption and fluorescence spectra of cyanine bases **16** are pictured in Fig. 9.8. Also, spectral data collected in Table 9.6 testify about the high sensitivity of fluorescence maxima to the solvent polarity.

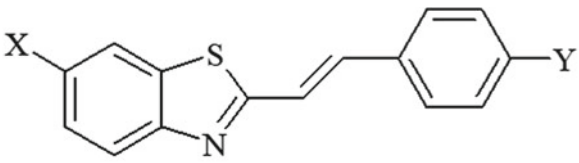

16

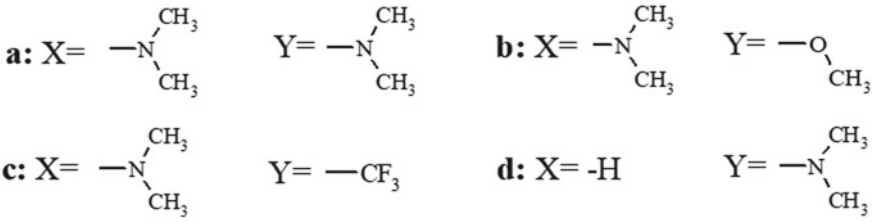

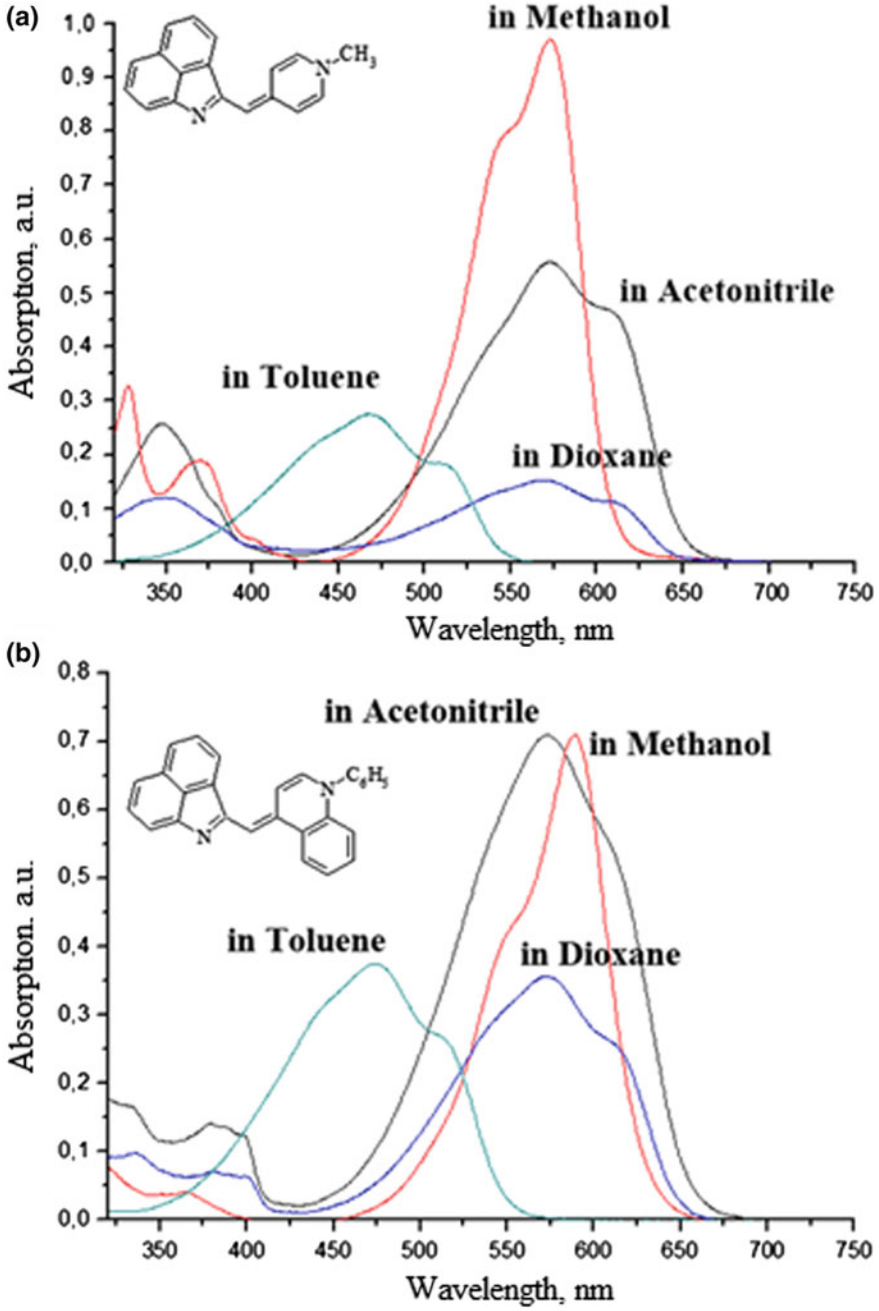

Fig. 9.7 Absorption spectra of bases, $c = 1 \times 10^{-5}$ M in different solvents: **a** 15a, **b** 15b

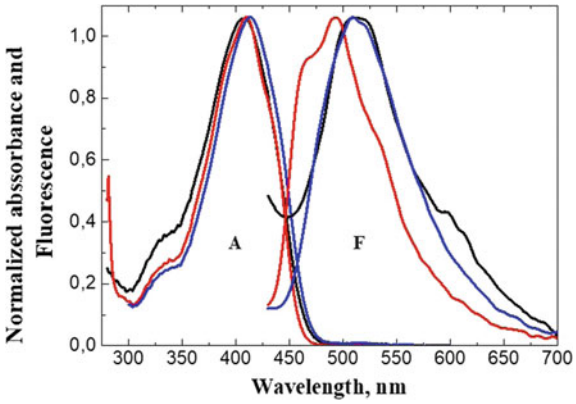

Fig. 9.8 Normalized absorbance (A) and fluorescence (F) spectra of **16a** (**a**) in toluene (red line), acetonitrile (black line) and methylene chloride (blue line)

Table 9.6 The main linear photophysical parameters of dyes **16 a–c**: absorption max λ_{ab} and fluorescence max λ_{fl} maxima, Stokes shifts (cm^{-1} (nm)), maximum extinction coefficients ε^{max} ($\times 10^{-3}$, M^{-1} cm^{-1}), calculated transition dipole moments $\mu_{\mathbf{01}}^{cal}$, D; fluorescence quantum yield Φ_{fl}, %; experimental τ_{fl}, ns (Ai)[a], (solvents with **c** with different polarity: 1—toluene, 2—DCM, 3—DMSO)

Solvent Comp.	1				2				3			
	16a	16b	16c	16d	16a	16b	16c	16d	16a	16b	16c	16d
λ_{ab}^{max} (nm)	410	393	410	395	414	394	410	400	419	399	416	408
λ_{fl}^{max} (nm)	491	480	499	491	506	496	531	497	515	525	590	522
Stokes shift	4020 (81)	4610 (87)	4350 (89)	4950 (96)	4390 (92)	5220 (102)	5560 (121)	4880 (97)	4450 (96)	6020 (126)	7090 (174)	5350 (114)
ε^{max}	35.9	26.8	26.9	25.2	27.0	29.5	26.0	32.3	33.7	26.8	24.5	26.1
$\mu_{\mathbf{01}}^{]textcal}$	7.9	6.8	7.2	6.4	7.1	7.6	7.4	7.4	8.6	7.4	7.2	6.8
Φ_{fl}	5	50	47	0.72	2.3	51	53	0.6	4	55	44	1.7
τ_{fl}	0.39	2.2	2.8	0.9	0.22	2.9	3.5	0.13	0.37	3.3	3.97	0.2

[a]Corresponding lifetime components

9.2 Conclusion

Thus, the high mobility of the collective π-electron shell in the linear conjugated molecules (and their ions) is confirmed by their spectral properties. This electron mobility depends on type of the conjugated system, chain length, symmetry, molecular constitution of the terminal groups, as well as the electron shell (neutral or charge system). Besides, different molecular types show the different sensitivity to the solvent polarity.

Acknowledgements Figures 9.2, 9.4 and 9.3, Table 9.1 are reprinted from: [8, 81]; Table 9.6 is reprinted from A.D. Kachkovsky, N.V. Pilipchuk, V.V. Kurdyukov, A.I. Tolmachev, Yu.L. Slominskii, V.Ya. Gayvoronsky, E.V. Shepelyavyy, S.V. Yakunin, M.S. Brodyn, Spectral and non-linear optical properties of cyanine bases' derivatives of benzo[c, d]indole, Dyes Pigments 74, 195–201 (2007) https://doi.org/10.1016/j.dyepig.2006.01.048, respectively with permission from Elsevier.

References

1. S. Daehne, Color and constitution. One hundred years of research. Science **199**, 1163–116
2. S. Daehne, K. Hoffmann, Colour and constitution: linear free energy relationships and/or polymethinic colour rules. J. Mol. Str. **219**, 403–409 (1990). https://doi.org/10.1016/0022-2860(90)80089-3
3. S. Daehne, Der ideale Polymethin zustand. Chimia **45**, 288–296 (1991). DOI: 200901100400230156
4. G. Bach, S. Daehne, Cyanine dyes and related compounds, in *ROOD'S Chemistry of Carbon Compounds*, 2nd suppl. to 2nd edn., vol. IVB, chapter 15, Heterocyclic Compounds, ed. by, M. Sainsbury (Elsevier Science, Amsterdam, 1997), pp. 383–481
5. A. Mishra, R.K. Behera, P.K. Behera, B.K. Mishra, G.B. Behera, Cyanine during the 1990s: a review. Chem. Rev. **100**, 1973–2011 (2000). https://doi.org/10.1021/cr990402t
6. G. Orlandi, F. Zerbetto, M.Z. Zgierski, Theoretical analysis of spectra of short polyenes. Chem. Rev. **91**, 867–891 (1991). https://doi.org/10.1021/cr00005a012
7. A.D. Kachkovsky, The nature of electronic transitions in linear conjugated systems. Russ. Chem. Rev. **66**, 647–664 (1997). https://doi.org/10.1070/RC1997v066n08ABEH000274
8. J.L. Bricks, A.D. Kachkovskii, Yu.L. Slominskii, A.O. Gerasov, S.V. Popov, Molecular design of near infrared polymethine dyes: a review. Dyes Pigments **121**, 238–255 (2015). https://doi.org/10.1016/j.dyepig.2015.05.016
9. H. Kuhn, A Quantum-mechanical theory of light absorption of organic dyes and similar compounds. J. Chem. Phys. **17**, 1098–1212 (1949). https://doi.org/10.1063/1.1747143
10. N.S. Bayliss, A "metalic" model for the spectra of conjugated polyenes. J. Chem. Phys. **16**, 287–292 (1948). https://doi.org/10.1021/bk-2013-1122.ch004
11. J.R. Platt, Wavelength formulas and configuration interaction in Brooker dyes and chain molecules. J. Chem. Phys. **25**, 80–105 (1956). https://doi.org/10.1063/1.1742852
12. M.L. Dekhtyar, Application of the quasi-long chain approximation to structural perturbation in polymethine dyes. Dyes & Pigments **28**, 261–274 (1995). https://doi.org/10.1016/0143-7208(95)00065-8
13. J. Fabian, TDDFT-calculations of Vis/NIR absorbing compounds. Dyes Pigments **84**, 36–53 (2010). https://doi.org/10.1016/j.dyepig.2009.06.008
14. S. Karaca, N. Elmaci, A computational study on the excited state properties of a cationic cyanine dye: TTBC. Comput. Theoret. Chem **964**, 160–168 (2011). https://doi.org/10.1016/j.comptc.2010.12.016
15. W.P. Su, J.R. Schrieffer, A.J. Heeger, Solitons in polyacetylene. Phys. Rev. Lett. **42**, 1698–1701 (2011). https://doi.org/10.1103/physrevlett.42.1698
16. W.P. Su, J.R. Schrieffer, A.J. Heeger, Solitons excitations in polyacetylene. Phys. Rev. **22**, 2099–2111 (1980). https://doi.org/10.1103/PhysRevB.22.2099
17. L.M. Tolbert, The photoexcited states of allyl anions. Acc. Chem. Res. **19**, 268–273 (1986). https://doi.org/10.1021/ar00129a002
18. L.M. Tolbert, Solitons in a box: the organic chemistry of electrically conducting polyenes. Acc. Chem. Res. **25**, 561–568 (1992). https://doi.org/10.1021/ar00024a003
19. A.D. Kachkovskii, The solitonic nature of ions of linear conjugated systems. Theoret. Exp. Chem. **41**, 139–164 (2005). DOI: 0040-5760/05/4103-0139

20. F.M. Hamer, *Cyanine Dyes and Related Compounds* (Interscience, New York, 1964), 790 pp.
21. A.V. Kulinich, A.A. Ishchenko, Merocyanine dyes: synthesis, structure, properties and applications Russ. Chem. Rev. **78**, 141–164 (2009). https://doi.org/10.1070/RC2009v078n02ABEH003900
22. A.V. Kulinich, N.A. Derevyanko, E.K. Mikitenko, A.A. Ishchenko, Merocyanines based on 1,3ω-indanedione: electronic structure and solvatochromism. J. Phys. Org. Chem. **24**, 732–742 (2011). https://doi.org/10.1002/poc.1821
23. H. Mustroph, K. Reiner, B. Senns, J. Mistol, S. Ernst, D. Keil, L. Hennig, The effects of substituents and solvents on the ground-state π-electronic structure and electronic absorption spectra of a series of model merocyanine dyes and their theoretical interpretation. Chem. Eur. J. **18**, 8140–8149 (2012). https://doi.org/10.1002/chem.201101830
24. J. Bricks, J. Slominskii, M. Kudinova, Syntheses and photophysical properties of a series of cation-sensitive polymethine and styryl dyes. J. Photochem. Photobiol. A: Chem. **132**, 193–208 (2000). https://doi.org/10.1016/S1010-6030(00)00208-2
25. L. Brooker, G. Keyes, R. Sprague, Studies in the cyanine dye series. XI. The merocyanines. J. Am. Chem. Soc. **73**, 5326–5332 (1951). https://doi.org/10.1021/ja01155a095
26. N.V. Pilipchuk, G.O. Kachkovsky, Yu.L. Slominskii, O.D. Kachkovsky, Electronic properties of polymethine systems. 11. Absorption spectra and nature of cationic oxystyryl and their neutral derivatives. Dyes Pigments **71**(1), 1–9 (2006). https://doi.org/10.1016/j.dyepig.2005.04.013
27. B.I. Shapiro, Molecular assemblies of polymethine dyes. Russ. Chem. Rev. **75**(5), 484–510 (2006). https://doi.org/10.1070/RC2006v075n05ABEH001208
28. F. Wurthner, T.E. Kaiser, C.R. Saha-Muller, J-Aggregates: from serendipitous discovery to supramolecular engineering of functional dye materials. Angew. Chem. Int. Ed. **50**, 3376–3410 (2011). https://doi.org/10.1002/anie.201002307
29. Y.I. Prylutskyy, V.V. Cherepanov, M.P. Evstigneev, O.A. Kyzyma, V.I. Petrenko, V.I. Styopkin, L.A. Bulavin, N.A. Davidenko, D. Wyrzykowski, A. Woziwodzka, J. Piosik, R. Kaźmierkiewicz, U. Ritter, Structural self-organization of C_{60} and cisplatin in physiological solution. Phys. Chem. Chem. Phys. **17**(39), 26084–26092 (2015). https://doi.org/10.1039/c5cp02688a.2
30. Y.I. Prylutskyy, M.P. Evstigneev, V.V. Cherepanov, O.A. Kyzyma, L.A. Bulavin, N.A. Davidenko, P. Scharff, Structural organization of C_{60} fullerene, doxorubicin, and their complex in physiological solution as promising antitumor agents. J. Nanopart. Res. **17**, 45 (2015). https://doi.org/10.1007/s11051-015-2867-y
31. O.A. Kyzyma, T.O. Kyrey, M.V. Avdeev, M.V. Korobov, L.A. Bulavin, V.L. Aksenov, Non-reversible solvatochromism in N-methyl-2-pyrrolidone/toluene mixed solutions of fullerene C_{60}. Chem. Phys. Lett. **556**, 178–181 (2013). https://doi.org/10.1016/j.cplett.2012.11.040
32. L.G.S. Brooker, Spectra of dye molecules. Absorbtion and resonance in dyes. Rev. Mod. Phys. **14**, 275–293 (1942). https://doi.org/10.1103/revmodphys.14.275
33. S. Huenig, H. Berneth, Two step reversible redox systems of the weitz type. Top. Curr. Chem. **92**, 1–44 (1980). https://doi.org/10.1007/BFb0034356
34. A.D. Kachkovskii, D.A. Yushchenko, G.A. Kachkovskii, Breaking of symmetry of solitons in the ion-radicals of α,ω-disubstituted polyenes. Teor. Éksp. Khim. **38**(6), 341–346 (2002). https://doi.org/10.1023/a:102221960
35. A.D. Kachkovskii, D.A. Yushchenko, G.A. Kachkovskii, D.M. Shut, Electronic properties of polymethine systems. 8. Geometry and electron structure of radicals. Dyes Pigments **66**, 211–221 (2005). https://doi.org/10.1016/j.dyepig.2004.06.020
36. H. Oeling, F. Baer, Radikaleaus Polymethin-Farbstoffen: III—Polymethinoxonole. Org. Magn. Reson. **8**, 623–627 (1976). https://doi.org/10.1002/mrc.1270081207
37. J.L. Bredas, G.B. Street, Polaron, bipolaron and solitons in conducting polymers. Acc. Chem. Res. **18**, 309–315 (1985). https://doi.org/10.1021/ar00118a005
38. A.O. Gerasov, I.H. Nayyar, A.E. Masunov, O.V. Przhonska, O.D. Kachkovsky, D.O. Melnyk, O.B. Ryabitsky, O.O. Viniychuk, Solitonic waves in polyenedications and principles of charge carrier localization in π-conjugated organic materials. Int. J. Quant. Chem. **112**, 2659 (2012). https://doi.org/10.1002/qua.23281

39. O.S. Nechyporenko, O.P. Melnyk, O.O. Viniychuk, T.M. Pinchuk-Rugal, V.A. Brusentsov, E.L. Pavlenko, Shape and location of multiple charge carriers in linear p-electron systems. Int. J. Quant. Chem. **114**, 416–428 (2014). https://doi.org/10.1002/qua.24585
40. A.E. Masunov, D. Anderson, A.Ya. Freidzon, A.A. Bagaturyants, Symmetry-breaking in cationic polymethine dyes: Part 2. Shape of electronic absorption bands explained by the thermal fluctuations of the solvent reaction field. J. Phys. Chem. A **119** (26), 6807–6815 (2015). https://doi.org/10.1021/acs.jpca.5b03877
41. M. Ikai, S. Tokito, Highly efficient phosphorescence from organic light-emitting devices with an exciton-block layer. Appl. Phys. Lett. **79**, 156–158 (2001). https://doi.org/10.1063/1.1385182
42. F. Koehn, J. Hofkens, R. Gronheid, M. Van der Auweraer, F.C. De Schryver, Parameters influencing the on- and off-times in the fluorescence intensity traces of single cyanine dye molecules. J. Phys. Chem. A **106**(19), 4808–4814 (2002). https://doi.org/10.1021/jp012959u
43. P.F.H. Schwab, J.R. Smith, J. Michl, Synthesis and properties of molecular rods. 2. Zig-Zag rods. Chem. Rev. **105**, 1197–279 (2005). https://doi.org/10.1021/cr040707u
44. D. Valeur, Principles of fluorescent probe design for ion recognition, in *Topics in Fluorescence Spectroscopy. Probe Design and Chemical Sensing*, vol. 4, ed. by, J.R. Lacowicz (New York, Plenum, 1994), pp. 21–48
45. G. Patonay, J. Salon, J. Sowell, L. Strekowski, Noncovalent labeling of bio-molecules with red and near-infrared dyes. Molecules **9**, 40–49 (2004). https://doi.org/10.3390/90300040
46. S.M. Borisov, O.S. Wolfbeis, Optical biosensors. Chem. Rev. **108**, 423–461 (2008). https://doi.org/10.1021/cr068105t
47. M.Y. Berezin, S. Achilefu, Fluorescence lifetime measurements and biological imaging. Chem. Rev. **110**(5), 2641–2684 (2010). https://doi.org/10.1021/cr900343z
48. H. Kobayashi, M. Ogawa, R. Alford, P.L. Choyke, Ya. Urano, New strategies for fluorescent probe design in medical diagnostic imaging. Chem. Rev. **110**, 2620–2640 (2010). https://doi.org/10.1021/cr900263j
49. A. Cravino, P. Leriche, O. Aleveque, S. Roquet, J. Roncali, Light-emitting organic solar cells based on a 3D conjugated system with internal charge transfer. Adv. Mater. **18**, 3033–3037 (2006). https://doi.org/10.1002/adma.200601230
50. Yo. Ooyama, Yu. Harima, Designs and syntheses of organic dyes for dye-sensitized solar cells. Eur. J. Org. Chem. **18**, 2903–2934 (2009). https://doi.org/10.1002/ejoc.200900236
51. G. Chen, D. Yokoyama, H. Sasabe, Z. Hong, Y. Yang, J. Kido, Optical and electrical properties of a squaraine dye in photovoltaic cells. Appl. Phys. Lett. **101**(8), 083904 (2012). https://doi.org/10.1063/1.4747623
52. O.V. Przhonska, J. Lim, D.J. Hagan, E.W. Van Stryland, M.V. Bondar, Yu.L. Slominsky, Nonlinear light absorption of polymethine dyes in liquid and solid media. J. Opt. Soc. Am. B. **15**(2), 802–809 (1998). https://doi.org/10.1364/josab.15.000802
53. W. Zhou, S.M. Kuebler, K.L. Braun, T.Yu.J.K. Cammack, C.K. Ober, J.W. Perry, S.R. Marder, An efficient two-photon-generated photoacid applied to positive-tone 3D microfabrication. Science **96**(5570), 1106–1109 (2002). https://doi.org/10.1126/science.296.5570.1106
54. S.R. Marder, Organic nonlinear optical materials: where we have been and where we are going. Chem. Commun. **2**, 131–134 (2006). https://doi.org/10.1039/b512646k
55. F. Terenziani, G. D'Avino, A. Painelli, Multichromophores for nonlinear optics: designing the material properties by electrostatic interactions. Chem. Phys. Phys. Chem. **8**(17), 2433–2444 (2007). https://doi.org/10.1002/cphc.200700368
56. M.G. Kuzyk, Using fundamental principles to understand and optimize nonlinear-optical materials. J. Mater. Chem. **19**, 7444–7465 (2009). https://doi.org/10.1039/b907364g
57. O.V. Przhonska, S. Webster, L.A. Padilha, H. Hu, A.D. Kachkovskii, D.J. Hagan, E.W. Van Stryland, Two-photon absorption in near-IR conjugated molecules: design strategy and structure-property relations, in *Advanced Fluorescence Reporters in Chemistry and Biology I*. Springer Series Fluorescence (Springer, Berlin, Heidelberg, 2010), pp. 105–148. https://doi.org/10.1007/978-3-642-04702-2_4
58. J. Griffiths, *Colour and Constitution of Organic Molecules* (Academic Press, London, 1976), 281 pp. https://doi.org/10.1002/col.5080030213

59. O. Ye, S.M. Shaydyuk, S.A. Levchenko, D. Kurhuzenkau, A.E. Anderson, O.D. Masunov, Yu.L. Kachkovsky, J.L. Slominsky, K.D. Bricks, M.V. Belfield, Bondar linear photophysics, two-photon absorption and femtosecond transient absorption spectroscopy of styryl dye bases. J. Lum. **183**, 360–367 (2017). https://doi.org/10.1016/j.jlumin.2016.11.073
60. K. Rurack, Flipping the light switch "ON"—the design of sensor molecules that show cation-induced fluorescence enhancement with heavy and transition meta ions. Spectrochim. Acta A Mol. Biomol. Spectrosc. **57**(11), 2161–2195 (2001). https://doi.org/10.1016/S1386-1425(01)00492-9
61. C. Reichardt, *Solvents and Solvent Effects in Organic Chemistry*, 3rd edn. (Wiley-VCH, Weinheim, 2003), 653 pp. ISBN 978–3-527-60567-5
62. F.L. Arbeloa, T.L. Arbeloa, I.L. Arbeloa, Electronic spectroscopy of pyrromethene. J. Photochem. Photobiol. A: Chem. **121**, 177–182 (1999). https://doi.org/10.1016/S1010-6030(98)00453-5
63. A. Toutchkine, W.-G. Han, M. Ullmann, T. Liu, D. Bashford, L. Noodleman, K.M. Hahn, Experimental and DFT studies: novel structural modifications greatly enhance the solvent sensitivity of live cell imaging dyes. J. Phys. Chem. A **111**, 10849–10860 (2007). https://doi.org/10.1021/jp073197r
64. M.A. Kudinova, N.A. Derevyanko, G.G. Dyadyusha, A.A. Ishchenko, A.I. Tolmachev, Pyrylocyanines. Symmetrical tetraphenyl-substituted pyrylo-2-cyanines. Chem. Het. Comp. **16**(7), 691–695 (1980). https://doi.org/10.1007/bf00557737
65. A.I. Tolmachev, N.A. Derevyanko, A.A. Ishchenko, Pyrylocyanines. 16. Tetraphenyl-substituted (pyrylo-2) (pyrylo-4) cyanines. Chem. Het. Comp. **18**(9), 897–902 (1982). https://doi.org/10.1007/bf00513426
66. K. Zyabrev, A. Doroshenko, E. Mikitenko, Yu. Slominskii, A. Tolmachev, Design, synthesis, and spectral luminescent properties of a novel polycarbocyanine series based on the 2,2-difluoro-1,3,2-dioxaborine nucleus. Eur. J. Org. Chem. **9**, 1550–1558 (2008). https://doi.org/10.1002/ejoc.200701012
67. P. Bouit, C. Aronica, L. Toupet, B.L. Guennic, C. Andraud, O. Maury, Continuous symmetry breaking induced by ion pairing effect in heptamethine cyanine dyes: beyond the cyanine limit. J. Am. Chem. Soc. **132**(12), 4328–4335 (2010). https://doi.org/10.1021/ja9100886
68. J. Fabian, Symmetry-lowering distortion of near-infrared polymethine dyes—a study by first-principles methods. J. Mol. Struct.: THEOCHEM **766**, 49–60 (2006). https://doi.org/10.1016/j.theochem.2006.02.003
69. F. Terenziani, A. Painelli, C. Katan, M. Charlot, M. Blanchard-Desce, Charge instability in quadrupolar chromophores: symmetry breaking and solvatochromism. J. Am. Chem. Soc. **128**(49), 15742–15755 (2006). https://doi.org/10.1021/ja064521j
70. S.V. Vasyluk, O.O. Viniychuk, Ye.M. Poronik, Yu.P. Kovtun, M.P. Shandura, V.M. Yashchuk, O.D. Kachkovsky, Breaking of symmetrical charge distribution in xanthylocyanine chromophores detecting by their absorption spectra. J. Mol. Struct. **990**, 6–13 (2011). DOI: 10.1016/j.molstruc.2010.12.047
71. A.D. Kachkovskii, A.I. Tolmachev, Yu.L. Slominskii, M.A. Kudinova, N.A. Derevyanko, O.O. Zhukova, Electronic properties of polymethine systems. 7. Soliton symmetry breaking and spectral features of dyes with a long chain. Dyes Pigments **64**, 207–217 (2005). https://doi.org/10.1016/j.dyepig.2004.04.003
72. R.S. Lepkowich, O.V. Przhonska, J.M. Hales, D.J. Hagan, E.W. Van Sryland, M.V. Bondar, Nature of electron transitions in thiacyanines with a long polymethine chain. Chem. Phys. **305**, 259–270 (2004). https://doi.org/10.1016/j.chemphys.2004.06.063
73. F. Terenziani, O.V. Przhonska, S. Webster, L.A. Padilha, Yu.L. Slominsky, I.G. Davydenko, A.O. Gerasov, YuP Kovtun, M.P. Shandura, A.D. Kachkovskii, J.D. Hagan, E.W. Van Stryland, A. Painelli, Essential-state model for polymethine dyes: symmetry breaking and optical spectra. J. Phys. Chem. Lett. **1**, 1800–1804 (2010). https://doi.org/10.1021/jz100430x
74. G.T. Dempsey, M. Bates, W.E. Kowtoniuk, D.R. Liu, R.Y. Tsien, X. Zwuang, Photoswitching mechanism of cyanine dyes. J. Am. Chem. Soc. **131**(51), 18192–18193 (2009). https://doi.org/10.1021/ja904588g

75. S.V. Vasyluk, V.M. Yashchuk, O.O. Viniychuk, Yu.P. Piryatinskii, M.M. Sevryukova, A.O. Gerasov, The investigation of relaxation paths in oxyborine anionic polymethine dyes detected by low-temperature time-resolved fluorescence. Mol. Cryst. Liq. Cryst. **535**, 123–131 (2011). https://doi.org/10.1080/15421406.2011.537959
76. P. Lutsyk, Yu. Piryatinski, O. Kachkovsky, A. Verbitsky, A. Rozhin, Unsymmetrical relaxation paths of the excited states in cyanine dyes detected by time-resolved fluorescence: polymethinic and polyenic forms. J. Phys. Chem. A **121**(43), 8236–8246 (2017). https://doi.org/10.1021/acs.jpca.7b08680
77. A.V. Stanova, A.B. Ryabitsky, V.M. Yashchuk, O.D. Kachkovsky, A.O. Gerasov, Ya.O. Prostota, O.V. Kropachev, Asymmetry in ground and excited states in styryls and methoxystyryls detected by NMR (13 C), absorption, fluorescence and fluorescence excitation spectroscopy. J. Mol. Struct. **988**, 102–110 (2011). https://doi.org/10.1016/j.molstruc.2010.12.038
78. M. Henary, A. Levitz, Synthesis and applications of unsymmetrical carbocyanine dyes. Dyes Pigments **99**, 1107–1116 (2013). https://doi.org/10.1016/j.dyepig.2013.08.001
79. PYu. Kobzar, E.L. Pavlenko, V.A. Brusentsov, O.P. Dmytrenko, N.P. Kulish, J.L. Bricks, Yu.L. Slominskii, V.V. Kurdyukov, O.I. Tolmachev, O.D. Kachkovsky, Comparative study of electronic structure cyanine bases versus parent cationic cyanines. J. Adv. Phys. **6**, 334–345 (2017). https://doi.org/10.1166/jap.2017.1347
80. E.L. Pavlenko, O.P. Dmytrenko, M.P. Kulish, V.V. Kurdyukov, O.I. Tolmachev, A.D. Kachkovsky, Spectral and quantum-chemical studies of the band shape in absorption of merocyanine derivatives of cyclohexadienone. J. Adv. Phys. **6**(4), 514–523 (2017). https://doi.org/10.1166/jap.2017.1365
81. A.D. Kachkovsky, N.V. Pilipchuk, V.V. Kurdyukov, A.I. Tolmachev, Electronic properties of polymethine systems. 10. Electron structure and absorption spectra of cyanine bases. Dyes Pigments **70**, 212–219 (2006). https://doi.org/10.1016/j.dyepig.2004.12.011
82. H. Mustroph, J. Mistol, B. Senns, D. Keil, M. Findeisen, L. Hennig, Relationship between the molecular structure of merocyanine dyes and the vibrational fine structure of their electronic absorption spectra. Angew. Chem. Int. Ed. **48**, 8773–8775 (2009). https://doi.org/10.1002/anie.200902687
83. A. Sanchez-Galvez, P. Hunt, M.A. Robb, M. Olivucci, T. Vreven, H.B. Schlegel, Ultrafast radiationless deactivation of organic dyes: evidence for a two-state two-mode pathway in polymethine cyanines. J. Am. Chem. Soc. **122**(12), 2911–2924 (2000). https://doi.org/10.1021/ja993985x
84. M.V. Bondar, N.A. Derevyanko, G.G. Dyadyusha, A.A. Ishchenko, Generation of light in the near infrared using solutions of asymmetric polymethine dyes. Sov. J. Quant. Electron. **14**(3), 317–322 (1984). https://doi.org/10.1070/qe1984v014n03abeh004888
85. Yu.L. Briks, Yu.A. Nesterenko, A.I. Tolmachev, A.D. Kachkovskii, Synthesis and spectral properties of vinylogs of heterylpolyenes based on pyran. Chem. Het. Comp. **26**(2), 218–221 (1990). https://doi.org/10.1007/bf00499420
86. O.M. Navozenko, A.P. Naumenko, V.M. Yashchuk, J.L. Bricks, Yu.L. Slominskii, A.B. Ryabitskii, O.D. Kachkovsky, Nature of the lowest electron transitions in styryl bases benzothiazole derivatives and analogues bearing para-methoxy and -trifluoromethyl substituents in phenylyne moiety. J. Mol. Struct. **1113**, 32–41 (2016). https://doi.org/10.1016/j.molstruc.2016.01.062

Chapter 10
Kinetics of Cluster Growth in Fullerene Solutions of Different Polarity

T. V. Tropin, M. V. Avdeev, N. Jargalan, M. O. Kuzmenko and V. L. Aksenov

Abstract Investigations of aggregation and associated kinetic effects, proceeding in various solutions of fullerenes C_{60} present a general interesting subject of research for the last 20–30 years. Since the discovery of fullerene solubility in liquids of different polarity, and also proposition of several methods for their dispersion in water media, these studies are considered particularly interesting from practical point of view. In this chapter we give a brief review of some experimental facts about kinetics of cluster growth in these systems, and present some theoretical models for their description. Most attention is given to such solvents as toluene, benzene and N-methylpyrrolidone (NMP). Some recent ultraviolet-visible (UV-Vis) spectroscopy studies of kinetics of fullerene dissolution, and C_{60}-NMP complexes formation are presented. While in case of low-polar solvents one can easily extract the kinetic constants by applying simple dissolution equations, for the polar solutions the Bouguer-Lambert-Beer law is not applicable and we propose a model for accounting of the complex formation. This allows, again, to extract the dissolution rate constants, and also the complex formation rates. The kinetic theory of cluster formation and growth is based on the nucleation theory. We develop additional suppositions that are required to account for change of fullerene state after interaction with solvents. For obtaining the evolution of the cluster-size distribution function for any stage of cluster growth in the solution, a specific method is applied. Finally, we propose a general model for describing the critical character of fullerenes clusters decomposition in polar solvent on addition of water. This model is based on the specific dependence of molecules solubility in binary mixture on the amount of added water.

T. V. Tropin (✉) · M. V. Avdeev · M. O. Kuzmenko · V. L. Aksenov
Frank Laboratory of Neutron Physics, Joint Institute for Nuclear Research, Joliot-Curie 6, 141980 Dubna, Moscow Reg., Russia
e-mail: ttv@jinr.ru

N. Jargalan
Institute of Physics and Technology, Mongolian Academy of Sciences, Ulaanbaatar, Mongolia

M. O. Kuzmenko
Faculty of Physics, Taras Shevchenko National University of Kyiv, Kyiv, Ukraine

V. L. Aksenov
National Research Centre "Kurchatov Institute", Moscow, Russia

L. A. Bulavin and L. Xu (eds.), *Modern Problems of the Physics of Liquid Systems*, Springer Proceedings in Physics 223,
https://doi.org/10.1007/978-3-030-21755-6_10

10.1 Introduction

The discovery of a new allotropic form of carbon, fullerenes, at the end of the last century [1], is regarded as one of the most important discoveries in the field of nanoscience. The scientific interest to these carbon nanoparticles is supported both by the discovery of new forms of carbon (carbon nanotubes and graphene), and by the prospects for their practical applications [2–5]. Partly, these prospects are related to the fact that fullerenes C_{60}, C_{70} dissolve relatively well in a wide class of organic and inorganic solvents. In solutions, fullerenes exhibit a number of interesting properties [6–8]. These are, for example, solvatochromism and the formation and growth of clusters. As a result of experimental studies of these phenomena, a classification of fullerene solutions according to the type of cluster formation was proposed [3]. The first class consists of non-polar solvents ($\varepsilon < 13$), where fullerenes were initially reported to dissolve in molecular form. The second class is composed of polar fullerene solutions ($\varepsilon \sim 13$–40), while the third one belongs to water and other high-polar liquids. The solutions of the third type are prepared by solvent substitution, or other special procedures required to transfer hydrophobic fullerene molecules to water media [9–12]. Their investigation is an important and regularly revisited subject for different researchers [13–17].

The study and description of the kinetics of formation and growth of clusters in various liquids is important from the point of view of practical applications, and is also an interesting task for applying the theory of cluster formation. Indeed, the character of fullerenes aggregation varies for different classes. For the non-polar solutions, some experimental results contradict one another even at the point of observation of growth of clusters [18–23]. This controversy of opinions regarding cluster formation and growth in low-polar solutions was analyzed in [6, 18] and the conclusion that aggregation is often caused by non-equilibrium conditions was drawn. Some new investigations of C_{60} solution in toluene are reported in [19], with cluster formation attributed to the photoinduced formation of $C_{60}O$ oxides. The dispersion forces between the oxides and fullerenes lead to reversible aggregation effect. These findings are generally in line with our classification [6] and conclusion on non-equilibrium conditions as the reason for cluster formation and growth.

Aggregation in solutions of second type is different: a kinetic transition of fullerene state from molecular to colloidal occurs [24–29]. Many measurements in polar liquids, especially in N-methylpyrrolidone (NMP) [26, 27, 30–32] and pyridine [33, 34] were performed. When modeling the growth of clusters in these solutions, it is necessary to take into account the influence of the formation of fullerene-solvent complexes on the aggregation of C_{60}.

The study and description of the kinetics of formation and growth of clusters in fullerene solutions is important from the point of view of practical applications. The low-polar and polar solutions can be regarded as model systems for studying fullerene aggregation [6, 35, 36], thus opening possibilities for controlling cluster state of C_{60} in water, which is important for perspective application in biomedicine.

Indeed, these systems are also quite interesting for applying the theory of cluster formation [37–40].

In this chapter, we present the results of investigations, both theoretical and experimental, of fullerene solutions in solvents of different polarity. First, a review of experimental investigations for low-polar and polar systems, with accent on our recent ultraviolet-visible spectroscopy (UV-Vis) measurements of kinetics of dissolution and complex formation is given. The second part of the chapter is dedicated to theoretical investigations of kinetics of cluster formation and growth of C_{60} clusters in solutions. A modified approach of the kinetic nucleation theory for describing the evolution of the cluster-size distribution function, $f(r,t)$, is developed. We present results for polar liquids and, finally, a model for mixtures of colloidal fullerene solutions with water is described. A discussion and some conclusions close the paper.

10.2 Experimental Study of Fullerene Aggregation in Solutions

Much research is concentrated on experimental investigations of fullerenes state and behavior in different solutions [6, 30, 41]. Let us briefly review important from our viewpoint findings in the field of clusters formation and growth. As expected, one of the effective and applicable methods here is the dynamic-light scattering (DLS), which was consequently applied for studies of fullerene aggregation in liquids of different polarity [4, 19, 21, 22, 24, 27, 29, 42, 43]. Summarizing, one can say, that in most of these cases, large clusters (size ~100 nm) are observed in such solvents, as benzene [21], toluene [19], pyridine [34], NMP [27, 42, 43], other polar solvents [24, 29] and water [11, 12]. In low-polar and polar solutions one can follow the kinetics of cluster growth [19, 21, 42, 43], it is also possible (in certain cases) to trace cluster decomposition on mechanical agitation of the vial [19, 21]. For the solutions in pyridine and NMP, investigations revealed the effect of cluster destruction on addition of water [33, 44, 45] or low-polar liquid [46, 47]. Finally, in water, fullerene colloidal solutions are very stable [11, 12, 15], this fact being reflected also by ζ-potential of the aggregates.

Big impact and valuable novel information was obtained by using small-angle X-ray and neutron scattering [14, 16, 18, 23, 44, 46, 48]. Method-specific information here is the structure of the clusters. For the case of fullerene-water solutions, for example, it was possible to distinguish one of three proposed shapes of aggregates [15]. For low-polar solutions, indications of two-level structure were reported, and the conclusion on the dense packing in aggregates was also drawn. In most cases, it was concluded, that the density of aggregates is similar to fullerene crystals [15, 44].

Electron microscopy was used for characterization of aggregates in the solution in several works [4, 9, 28, 49]. It must be mentioned, though, that the pre-measurements drying of the sample makes the solution pass through supersaturated state, which may lead to rapid aggregation effects [6, 18]. Thus one can investigate not the natural state

of nanoparticles in the liquid, but the effects occurring in the dried sample. On the other hand, if the clusters were initially formed and stabilized in the solution by certain interactions, the drying may not affect their state and the investigations may be plausible [4, 30].

UV-Vis spectroscopy studies also produce valuable information in this field. The spectrum of C_{60} molecular solution is characterized by an absorption peak at wavelength ~330 nm. Some other peaks at lower λ, and a small peak at ~408 nm may be found. Interactions in the solvent, indeed, affect the basic spectrum, hence new peaks may be detected, or bathochromic/hypsochromic effects observed. The temporal solvatochromic effect observed in solutions of fullerene in NMP or pyridine should be specifically mentioned [33, 50]. If the initial solution is prepared with due care, a characteristic "molecular" spectrum can be measured, yet as time passes the 330 nm peak is gradually smeared, the visual change of the solution color from purple to brown occurs. The final slope is a monotonically decreasing absorption spectrum. The UV-Vis spectrum of C_{60} colloidal solutions in water is similar to the one of a molecular solution, yet the peaks are broader and shifted to higher wavelengths [15, 51].

Recently, an investigation of kinetic processes occurring in fullerene solutions was made using the UV-Vis spectrophotometry method [31, 52]. Considering three solutions, benzene, toluene and NMP, the time evolution of light absorption coefficients was measured at different temperatures and rates of mechanical stirring.

Solubility of fullerene in toluene, benzene and NMP is 2.8 mg/ml, 1.7 mg/ml and 0.9 mg/ml, respectively [8, 53]. The temperature, concentration and dissolution conditions were varied. The equilibrium dissolution conditions and the magnetic stirring at different rates were applied. Measurements of temporal evolution of fullerene concentration in low-polar liquids were based on the Bouguer-Lambert-Beer law, which was applied to the absorption A peak at $\lambda = 408$ nm. An example of measurement results is presented on Fig. 10.1.

To analyze C_{60} dissolution kinetics in [52] the Noyes-Whitney equation was used [54]:

$$\frac{\mathrm{d}x}{\mathrm{d}t} = k(S - x), \tag{10.1}$$

where x is a function of t, reflecting the current solution concentration, S is the saturation concentration or the maximum solution concentration (in case there is no excess fullerene added), k is the dissolution constant. The parameters of (10.1) were determined for more than 10 samples, allowing to analyze their dependencies on preparation conditions [52]. In general, it was reconfirmed, that at equilibrium conditions, fullerene dissolution up to saturation concentration proceeds slowly (~7 days for toluene). On the opposite, in the unsaturated case and especially when stirring is applied, the process is much faster. The characteristic values of dissolution rate parameter k for C_{60} in two liquids are $\sim 2 \cdot 10^{-4}$ s^{-1} for toluene and $\sim 10^{-4}$ s^{-1} for benzene. The applied conditions vary k by an order of magnitude.

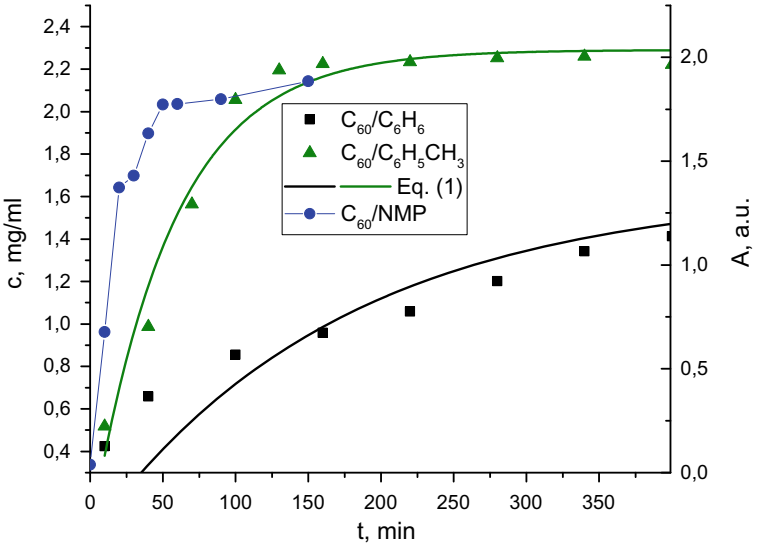

Fig. 10.1 Time evolution of fullerene C_{60} concentration in benzene (black squares) and toluene (green triangles) at different conditions, together with respective change of absorption coefficient A for C_{60}/NMP solution (blue circles) [52]. Bold black and green lines present a fit by dissolution kinetic equation

As it was already discussed, the evolution of the UV-Vis spectrum of the C_{60}/NMP solution is qualitatively different from the case of weakly polar solutions. Temporal solvatochromism is observed for the $A(\lambda,t)$ spectra [26, 30]. There is thus no direct relation between absorption and concentration, because it is affected by the formation of C_{60}-NMP complexes. The investigations of these complexes, occurring in polar C_{60}/NMP solution have been performed, for example, by fluorescence methods [55]. Some DFT calculations [56] also reveal their formation, and another extensive DFT study is underway.

To determine the concentration of the solution at a given point in time from the measured UV-Vis spectrum, we must propose a method for separating the complex formation and cluster growth contributions. In the evolution of the absorption coefficient of light with $\lambda = 330$ nm for a solution of C_{60}/NMP there is a non-monotonic dependence, the output to the equilibrium value occurs at a speed that does not depend on the speed of mixing in a certain range (<300 rpm). The maximum of the absorption coefficient seems to be associated with the disappearance of the characteristic "monomeric" peak and, thus, reflects the relaxation time of one of the processes occurring in the system—the formation of complexes. A rough estimate of this time gives a value of about 3000 s.

To extract the kinetic constants from the measurements, we suppose once again that the dissolution of fullerene is determined by the Noyes-Whitney equation (with the dissolution rate k_1) and that the complexes are formed simultaneously (the reaction rate k_2). Thus, it is possible to introduce a system of kinetic equations [31]:

$$\begin{cases} \frac{dc(t)}{dt} = k_1(C_s - c(t)) \\ \frac{dy(t)}{dt} = k_2(c(t) - y(t)) \end{cases} \tag{10.2}$$

where $c(t)$ is the concentration of "free" fullerene molecules in the solution (those that have not yet formed complexes), $y(t)$ is the concentration of C_{60}–NMP complexes in the system and C_s is the saturation concentration or available concentration of C_{60} (in case the unsaturated solution is prepared). For the considered experiments, when the initial stage is the addition of fullerene to NMP, the initial conditions for (10.18) should be: $c(0) = y(0) = 0$.

After most fullerene molecules form complexes with NMP in solution, the UV-Vis spectrum presents a monotonically decreasing curve. The observed peak at ~330 nm corresponds to the concentration of "free" C_{60} molecules. Thus, this height of the peaks at any time is proportional to $(\varepsilon_1 c(t) - \varepsilon_2 y(t))$, where ε_1 and ε_2 are the absorption coefficients for "free" molecules and complexes, respectively. The values of these coefficients are unknown, we will assume that they are of the same order. This assumption allows us to directly associate the peak height of ~330 nm over the monotonically decreasing type of the UV-Vis spectra with a concentration of "free" C_{60} molecules, equal to $(c(t) - y(t))$. Figure 10.2 shows a typical evolution of the corresponding peak heights for $T = 50$ °C, $v_s = 100$ rpm and $v_s = 400$ rpm. The absorption is normalized to the corresponding concentration of the solution, so it estimates the difference $(c(t) - y(t))$, which can be obtained directly from (10.2):

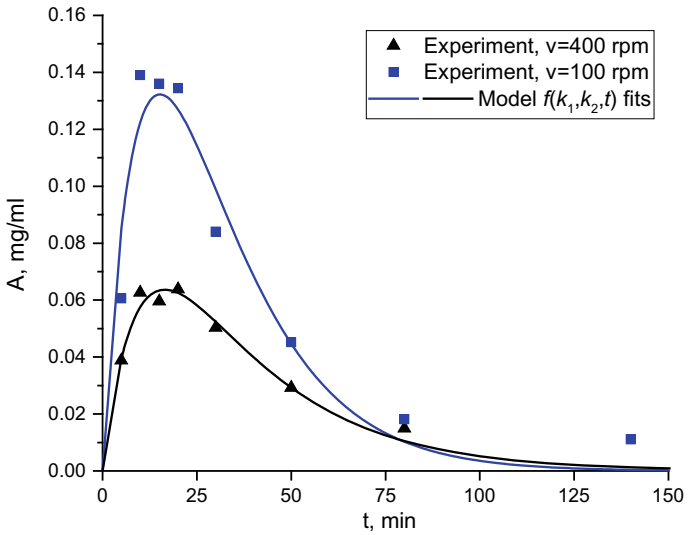

Fig. 10.2 Evolution of normalized peak $\lambda = 330$ nm height above monotonic UV-Vis slope at 50 °C and rotation speeds of 100 rpm (squares) and 400 rpm (triangles). Points represent measured data, lines—fits by using the proposed model [31]

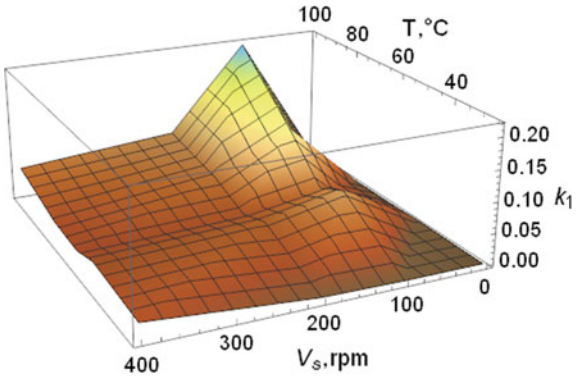

Fig. 10.3 Dependence of kinetic coefficient k_1, in 10^{-4} s^{-1} units, reflecting complex formation speed on solution temperature and stirring rate, obtained from model fitting of UV-Vis data

$$c(t) - y(t) = f(k_1, k_2, t) = \frac{C_s k_1 \left(e^{-k_1 t} - e^{-k_2 t}\right)}{k_2 - k_1} \tag{10.3}$$

The quality of the fit of the experimental data presented in Fig. 10.2 reflects the applicability of the proposed method and approximation. The resulting expression was used to fit various experimental curves to obtain k_1 and k_2 values for different temperatures and mixing rates. An example of the whole obtained 2D dependence of kinetic coefficient on both temperature and stirring rate is presented on Fig. 10.3.

Summarizing, the presented review and results of experimental research of kinetic processes shows, that in low-polar and polar solutions of fullerenes one regularly observes cluster formation and growth. This process is occurring simultaneously with changes of fullerene electronic state after certain interactions with the solvent or oxygen. In the next part of the chapter, we present an approach for theoretical description of kinetics of fullerene aggregation in polar solutions and their mixtures with water.

10.3 Theoretical Description of Kinetics of Fullerene Cluster Growth

10.3.1 C_{60} Aggregation in Polar Solutions

In order to theoretically describe the kinetics of cluster growth in polar (e.g. C_{60}/NMP) solutions, the approach previously developed to describe the nucleation processes and the corresponding segregation of particles during phase transitions is used [57]. The evolution of the cluster size distribution function $f(n,t)$ is obtained from a set of ordinary differential equations. The basic assumptions made to derive the equations are: clusters are quasispherical particles with densities as of a macroscopic solid phase; clusters grow or decompose only by joining and separating one particle (monomer) from the cluster. The second assumption works well for the ini-

tial stages of cluster formation and growth and can be revised for subsequent stages. Nevertheless, we will stay with this approach for the sake of simplicity of the results, thus obtaining a qualitative picture and some general estimates. Consequently, the following system of kinetic equations can be written [40, 57]:

$$\frac{\partial f(n,t)}{\partial t} = w^{(+)}_{n-1,n} f(n-1,t) + w^{(-)}_{n+1,n} f(n+1,t) - w^{(+)}_{n,n+1} f(n,t) - w^{(-)}_{n,n-1} f(n,t), \quad (10.4)$$

where $w^{(\pm)}_{n,m}$ are the probabilities that a monomer is attached/removed from the cluster, thus cluster size changes from n to m per unit time (m is $n+1$ or $n-1$). Hereinafter, the "cluster of size n" is a cluster consisting of n monomers. For comparison with experiments, we will further shift to $f(r,t)$ functions, were r is the cluster radius. The procedure of obtaining $f(r,t)$ from $f(n,t)$ is straightforward. Equation (10.4) with the boundary conditions and the introduction of some modifications will be the basis for calculating the evolution of $f(n,t)$.

From thermodynamic consideration, the ratio of the probabilities of monomer addition and decomposition from the cluster depends on the work of cluster formation, $\Delta G(n)$ [37, 38]:

$$\frac{w^{(+)}_{n-1,n}}{w^{(-)}_{n,n-1}} = \exp\left\{-\frac{\Delta G(n) - \Delta G(n-1)}{k_B T}\right\}. \quad (10.5)$$

In (10.5), $\Delta G(n)$ is the change in the Gibbs free energy of the solution if n monomers form a cluster (work of cluster formation). Thus, if a specific expression is given for $w^{(+)}_{n,n+1}$ and $\Delta G(n)$, then (10.4) are complete.

The expression for the probability of monomer addition is obtained from consideration of the diffusion of monomers from the bulk solution to the cluster surface of size n [57, 58]:

$$w^{(+)}_{n,n+1} = 4\pi D c \left(\frac{3v_s}{4\pi}\right)^{1/3} n^{1/3} \quad (10.6)$$

where D is the diffusion coefficient of the monomers in the solution, c is their concentration, v_s is the volume per particle in the cluster. For a kinetically limited aggregation regime, when the probability $w^{(+)}_{n,n+1}$ is determined by the time of addition of the monomer to the cluster, $w^{(+)}_{n,n+1}$ is proportional to $n^{2/3}$.

In previous works [35, 59, 60] it was shown that the classical liquid drop model is inapplicable for describing cluster growth in fullerene solutions. One of the ways to proceed is to modify the expression for the work of cluster formation $\Delta G(n)$, the so-called limited growth model [61–63]:

$$\Delta G(n) = -n\Delta\mu + \alpha_2 n^{2/3} + k n^{\beta} \quad (10.7)$$

In (10.7), the first two terms correspond to the classical model (the volume and surface terms, respectively). With the third term, as in (10.7), for $k > 0$, $\beta > 1$, cluster growth is limited (the clusters stabilize) at a certain size. This approach, however, requires to physically justify this third term and propose either an estimate or, better, some expressions for k and β values. While this can be done for growth limited by Coulomb interactions, or for nucleation and growth in pores, a straightforward approach for fullerene solutions has not been developed. We will proceed in a different way by modifying the probabilities of cluster growth and decomposition (see below).

The expression for the difference of the chemical potentials of the monomers in the bulk solution and in the cluster, $\Delta\mu$, is taken as for the ideal solution:

$$\Delta\mu = k_B T \ \ln\left(\frac{c}{c_{eq}}\right) \tag{10.8}$$

In (10.18), c is the time-dependent monomer concentration of the segregating phase (single fullerene molecules), and c_{eq} is the equilibrium concentration with respect to aggregation. If the concentration of the solution is higher than c_{eq} (supersaturated solution), then clusters grow. If c is below c_{eq} (unsaturated solution), then the molecular solution is stable. We consider c_{eq} here as an equilibrium concentration with respect to cluster growth. For polar solutions, c_{eq} may be unequal and even much lower than the saturation concentration of the solution, c_{sat}. The reason for this is considered to be interaction between C_{60} and solvent molecules in solution. As experimental studies show, this is a relatively slow kinetic process. Thus, c_{eq} here corresponds to C_{60} complexes with solvent molecules (which tend to aggregate), and c_{sat} corresponds to saturation concentration of unbound fullerene molecules. To some extent, the system under consideration can be compared with solutions of surfactants, where there are also various limiting concentrations, for example, first and second critical micelle concentrations (CMC). The established theory of the kinetics of the growth of micelles is given in [64]. Similarly to the above paper, the numerical approach can be found in [65]. Indeed, in this case, the aggregates in solution are not microcrystallites and qualitatively differ from the solid phase in some properties. Introducing the difference between c_{eq} and c_{sat}, we assume that a similar situation exists for fullerene solutions.

To describe the kinetics of aggregation in polar solutions of fullerenes, it is necessary to propose a modified model that takes into account the effect of the formation of fullerene-solvent complexes on cluster growth. As was shown in [30, 66, 67], the limitation of the processes of growth and decay of clusters due to complex formation can be qualitatively taken into account if the probabilities $w^{(+)}$ and $w^{(-)}$ are changed according to the formula:

$$w'^{(\pm)}_{n,m}(t) = w^{(\pm)}_{n,m}(t) e^{-\frac{t}{\tau}}, \tag{10.9}$$

where τ is the model parameter corresponding to the characteristic time of formation of complexes in the solution and $w'^{(\pm)}_{n,m}(t)$ are the modified probability functions.

Equations (10.4) are solved for a reduced time scale, where the scaling factor is $(4\pi D c_{eq} r_0)$. Further in the text, in most cases, by t we will mean this dimensionless time. In other case, units will be indicated to avoid confusion.

Obtaining a full evolution of $f(n,t)$ using numerical calculations is not possible (for $n \sim 10^8$ and more), so in [68] a method, based on the analytical calculation of the asymptotes of the late stages of cluster growth, developed by Slezov, Lifshitz and Sagalovich [69], is proposed. For the application of this method, it is shown that the distribution functions correspond to analytical functions, obtained by Slezov and colleagues, and the evolution of the average cluster size can be reduced to the $t^{1/3}$ law by transforming the time scale. This allows for any τ to obtain the functions $f(r,t)$ for any value of t. As an example, calculations are made further for the evolution of the cluster state of fullerenes C_{60} in a polar solution.

To simulate the aggregation of fullerene in a particular solvent, it is necessary to set the following system parameters: the surface tension energy, σ, the degree of supersaturation of the initial solution $c(t = 0)/c_{eq}$, the diffusion coefficient of C_{60} in the liquid D, as well as the formation time of the fullerene-solvent complex, τ. For polar solvents (NMP, pyridine, etc.), the values of the first three parameters of the model are unknown. Thus, a "model" solvent will be considered, for which σ is estimated from the calculations of the enthalpy of dissolution of C_{60} in $C_6H_5CH_3$ [70] $(\alpha_2/k_B T = 8)$; the diffusion coefficient is also taken for toluene, $D = 9.1 \cdot 10^{-10}$ m^2/s, the equilibrium concentration is estimated as 10% of the maximum concentration of the solution in NMP, $c_{eq} = 7.525 \cdot 10^{22}$ m^{-3}. An estimate of characteristic time of C_{60}-NMP complex formation was reported in previous section to be $\tau \sim 10^3$ s. The radius of the C_{60} molecule in a solution is $r_0 \sim 0.5$ nm. The transition coefficient for reduced to real time scale is, thus: $4\pi D c_{eq} r_0 \approx 4.3 \cdot 10^5$. It follows that $\tau \approx 4.3 \cdot 10^8$. It is necessary to obtain cluster distribution functions $f(r,t)$ for a given τ. For this, sequential calculations of $f(n,t)$ were performed for a set of τ values in the range from 10^4 to 10^6. This is sufficient to carry out a complete estimate of the evolution of the functions $f(r,t)$.

Analysis of the evolution of the cluster state in a solution we begin with the time dependence of the average particle radius in the solution:

$$\langle r \rangle = \frac{\sum_{n=n_{min}}^{n_{max}} f(n,t) r_0 (n\gamma)^{1/3}}{\sum_{n=n_{min}}^{n_{max}} f(n,t) n}, \tag{10.10}$$

where γ is the packing density of particles in a cluster, n_{max} is the maximum size of particles in the solution, and n_{min}, the minimum size from which the summation starts, is used to eliminate the effect on the <r> value of the equilibrium monomer concentration that is always present in the solution (in present work, $n_{min} = 10$). The calculated dependences <r> for different τ are presented in Fig. 10.4.

As can be seen, the dependence <r> is determined by the value of τ: at times t exceeding τ by two to three times, a stable particle size (and cluster distribution function) in the solution is achieved. In general, the growth of clusters takes place by four stages, the last is the stage of Ostwald ripening, where there is a steady growth

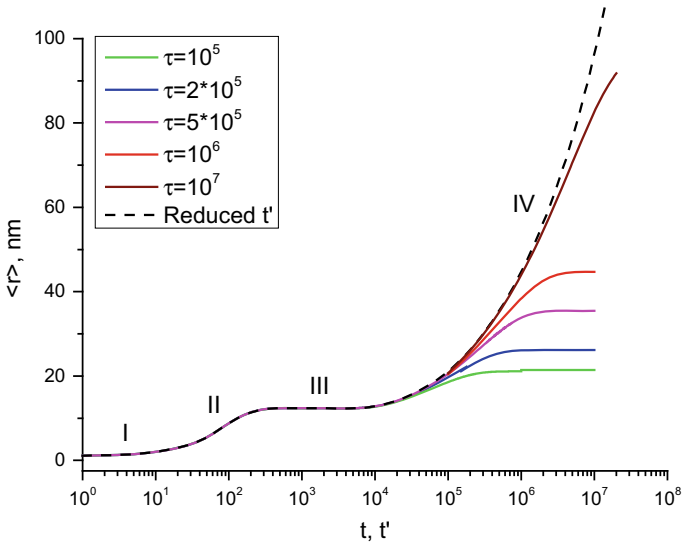

Fig. 10.4 Dependence of the average particle radius, <*r*> in the model solution on time for different values of the model parameter τ (bold curves), and for the case of a reduced time scale t' (dashed curve). Numerals denote different stages of the evolution of the system [68]. The values $\tau = 10^5$, $2 \cdot 10^5$, $5 \cdot 10^5$, 10^6, 10^7 consistently change from the bottom solid curve upwards

of large aggregates. In [71], it was shown that for aggregation limited by diffusion, the so-called "$t^{1/3}$ law" is implemented at this stage:

$$\bar{R}^3 = \bar{R}_0^3 + \frac{4}{9} D\alpha t, \quad \bar{R} >> \bar{R}_0, \tag{10.11}$$

where $\bar{R}_0$ is the average radius of clusters at stage III (independent growth stage). To reduce the dependence of the average particle size to the form (10.11) for a model of limited growth, we need to scale the time with regard to the parameter τ. It can be shown that the t' following expression should be used:

$$t' = \tau\left(1 - e^{-t/\tau}\right). \tag{10.12}$$

In terms of t', all curves <*r*>, regardless of the value of τ, coincide. Moreover, for a sufficiently large time value t', the law (10.11) will be satisfied. Thus, if we take the initial stages of cluster growth (I–III), as well as the transition stage between III and IV from the numerical calculations, then add an expression of the form (10.11), we will have the full dependence of <*r*> on t' at our disposal. For a given τ, the inverse transformation to the time scale t is performed by the formula:

$$t = -\tau \ \ln\left(1 - \frac{t'}{\tau}\right), \quad t' < \tau. \tag{10.13}$$

Similarly, calculations can be performed for the dependence of the number of monomers in a solution, for which an analogue of the "$t^{1/3}$ law" also exists. The monomer concentration in the system is required to calculate the exponentially decaying distribution function of small clusters in size (for $n < n_{\min}$). On Fig. 10.4 the dependency $<r>(t)$, obtained by the described method for $\tau = 10^7$, which roughly corresponds to 10^2 s—the 10% of time of formation of fullerene-NMP complexes in a C_{60}/NMP solution. The dash-dotted line on Fig. 10.4 represents the general dependence of $<r>$ on t' [before applying formula (10.18)]. Calculations for $\tau = 10^8$ are not shown on Fig. 10.4, because in the selected scale $<r>$ almost coincides with the dashed curve.

Since, after the time scale was transformed, the dependence of the basic parameters of the model system is similar to asymptotic calculations for classical kinetic nucleation theory, it can be expected that the cluster size distribution functions coincide with the function proposed in [69]:

$$f(R,t) = n(t)P\left(\frac{R}{\bar{R}}\right)\frac{1}{\bar{R}},$$
$$P(u) = \begin{cases} \frac{3^4 e}{2^{5/3}} \frac{u^2 \exp\left(-\frac{1}{1-(2/3)u}\right)}{(u+3)^{7/3}((3/2)-u)^{11/3}}, & 0 < u < 3/2, \\ 0, & u \geq 3/2 \end{cases} \tag{10.14}$$

where $n(t)$ is the time dependence of the number of particles in the system. For our model system, the cluster size distribution of type (10.14) is already applicable for $t > 2\tau$. Thus performing numerical calculations in the range $t = 0 - 2\tau$ and supplementing them with asymptotic approximations, described by (10.11)–(10.14), we will obtain the whole $f(r,t)$ evolution for a model C_{60} polar solution. The results of such procedure for $\tau = 4 \cdot 10^8$ are presented on Fig. 10.5. Indeed, $f(r,10^9)$ in this case is almost stabilized and will not change much further with time.

The method described here can be utilized for modeling the cluster growth in different polar solutions of fullerenes. A similar approach has been developed in [72] to describe the kinetics of AgCl separation in photochromic glasses already in 1990. In [72] the authors considered Ostwald ripening in a viscoelastic material, obtaining modifications for cluster growth equations with similar exponential decay, as introduced phenomenologically here in (10.9). Moreover, the same changes to the time scale, (10.12), were also considered.

In the next Section, we demonstrate the application of the model results for describing the critical effect of clusters decomposition on dilution of polar fullerene solutions by water.

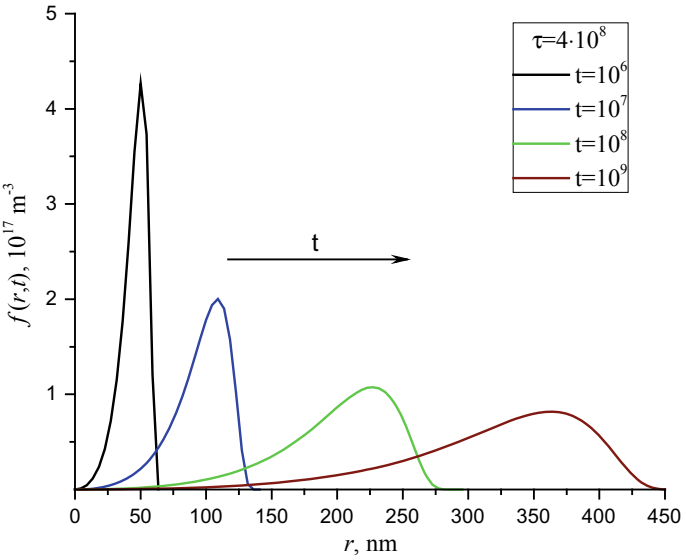

Fig. 10.5 Evolution of size distribution function of fullerene aggregates in a model polar solution, calculated via procedure described in the text and in [68]. The values of model parameters here are: $\alpha_2/k_BT = 8$, $D = 9.1 \cdot 10^{-10}$ m^2/s, $c_{eq} = 7.525 \cdot 10^{22}$ m^{-3}, $\tau = 4 \cdot 10^8$. The corresponding CSDs for $t = 10^7$, 10^8, 10^9 were multiplied by 10, 100 and 500 for better visualizing

10.3.2 Critical Effect of Cluster State Reorganization on Water Addition to C_{60} Polar Solutions

Using neutron scattering, an interesting from the point of view of cluster formation kinetics effect was discovered in [2]. Namely, it was found that when some C_{60} polar solutions are diluted with water, the size of clusters in a solution decreases: from sizes >100 nm to sizes in the range of 10–100 nm. The effect itself is of a threshold nature, and occurs when the volume fraction of added water exceeds ~0.4. The destruction of the clusters occurs immediately after dilution. For a long time, this effect remained unexplained, although this phenomenon seems to be of a general nature (for fullerene solutions, at least).

In [73] it was shown, that direct approach to dilution cannot explain the critical character of the effect. Here we shall recount a specific model of dilution of a colloidal solution with water for a qualitative explanation of this effect [74]. The key factor influencing the change in cluster sizes is the strong dependence of solubility on the composition of the mixture, characteristic of some binary liquids [75, 76]. Estimates of changes in cluster sizes at different stages of growth have been obtained for different volume fractions of added water.

Dilution of the considered colloidal solution with water changes the physico-chemical properties of the solvent, which affects the size distribution of clusters. To reflect this, a dimensionless parameter X, defining the proportion of added water is introduced:

$$X = \frac{V_{H_2O}}{V_{H_2O} + V_{SOL}}, \tag{10.15}$$

where V_{H_2O} is the volume of water added, and V_{SOL} is the volume of the initial solution before dilution. Thus, $X \in [0, 1]$, where 0 and 1 are the limiting values: $X = 0$ corresponds to the case when no water was added to the solution; $X = 1$—infinitely large volume of added water.

The evolution of the system at dilution, qualitatively, is the following. First, at the time of dilution, the values of the function $f(n,t)$ are scaled, since the addition of liquid to the solution changes the concentration of the solute:

$$f'(n, t) = f(n, t)\frac{1 - X}{1 + X}. \tag{10.16}$$

Secondly, the values of the parameters D, c_{eq}, α_2/k_BT and τ change. The ratio of the diffusion coefficients of particles in water and the initial solvent can be estimated by the Stokes-Einstein formula. As a rule, the diffusion coefficient does not change more than twice. Further, we assume that this parameter varies linearly:

$$D' = D_{SOL} + X(D_{H_2O} - D_{SOL}), \tag{10.17}$$

where D' is the value of the diffusion coefficient of the particles in the mixed solvent. The change in τ is not considered in this work; however, upon dilution with water, we restore the original values of the probabilities $\omega^{(+)}$ and $\omega^{(-)}$ [reset the exponent in (10.9)].

The main parameters that determine the behavior of the distribution function after dilution are surface tension (parameter α_2/k_BT) and the equilibrium concentration of c_{eq}. These parameters affect the shape of the potential, which determines the growth and decay of clusters in the solution. The first term in $\Delta G(n)$ changes not only with the cluster size, but also with a change in the concentration of monomers $c(t)$. The value of the α_2 parameter affects the size of the critical cluster in the system. We can approximately suppose that the ratio α_2 in the initial solvent and water is equal to the ratio of the dielectric permittivities of these liquids. In most cases in these calculations, the change in the surface term in $\Delta G(n)$ does not significantly affect the size of large clusters (hundreds of nanometers). We arrive at the conclusion that the main part in describing the effect of cluster decomposition upon dilution is played by the change in the value of c_{eq}.

For a complete formulation of the model, it is necessary to assume the nature of the change in c_{eq} when diluting the initial solvent with water. Fullerene is a hydrophobic molecule; however, its transfer from a polar liquid to water is not equivalent to direct dissolution. For example, in the case of NMP, upon mixing with water, the fullerene-NMP complexes are being transferred (thus, they have non-zero solubility in H_2O). Within the framework of the general model, we assume that the concentration of c_{eq} should continuously change from c_{eq}^{SOL} at $X = 0$ to some unknown value $c_{eq}^{H_2O}$ at $X = 1$. To select the dependence, let us use the results of [75, 76], which describe the use

of NMP as a liquid, which significantly improves the water solubility of drugs. The expression for the concentration that describes this property is:

$$\frac{c_{eq}^{MIX}}{c_{eq}^{SOL}} = \left(\frac{c_{eq}^{H_2O}}{c_{eq}^{SOL}}\right)^X \tag{10.18}$$

The value $c_{eq}^{H_2O} < c_{eq}^{SOL}$ is thus a parameter of the model. Further results will be analyzed in sense of a dimensionless parameter $S = c_{eq}^{SOL} \Big/ c_{eq}^{H_2O}$.

The investigation of effects of dilution on $f(n,t)$ via the proposed model was performed for a dimensionally small system, with maximum cluster sizes $n_{max} \sim 10^5$ particles and $\tau = 10^5$. As it was shown in the previous section, all the results can be extrapolated to the real-scale systems.

The dilution in the framework of the proposed approach was modeled for different values of the parameter $c_{eq}^{H_2O}$. In addition to expression (10.18), for the dependence on X, the linear dependence was also checked [74]. It was obtained that only the power-law dependence gives the qualitatively corresponding to the described effect results. For simplicity, t further corresponds to the second stage of the modeling (that is, after dilution) and reflects the elapsed time since the initial solution was diluted.

Figure 10.6 shows the calculated evolution of the average cluster size in a solution in a SOL–H_2O binary mixture for several values of X. Weak dilutions with water do not lead to a change in the cluster state. Starting from a certain, threshold value of X, cluster decomposition upon water addition is observed. For the case shown

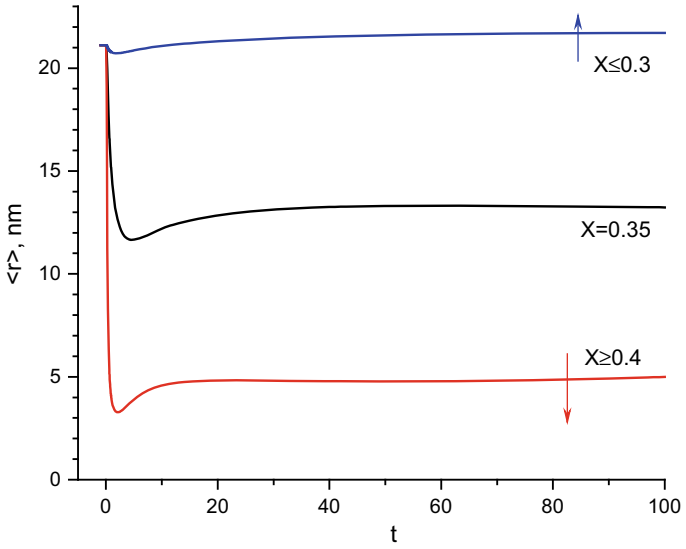

Fig. 10.6 Change of mean cluster size, <*r*>, of fullerenes in binary mixture after water addition to the polar liquid [74]

in Fig. 10.6 this occurs in the region $X_c = 0.35$. It is interesting to note that in the interval $X > 0.4$, the average cluster size drops to a certain value and does not further depend on X. Subsequent slow growth of the clusters is largely determined by the value of D'.

The threshold value X_c, at which cluster decomposition occurs, is determined by the ratio of the saturation concentrations $c_{eq}^{H_2O}$ and c_{eq}^{SOL}. To estimate the nature of this dependence, calculations were performed for different values of S, the results are presented in Fig. 10.7 in the form of the dependence of the average size of aggregates in a solution on X at $t = 1$ after dilution. The position and width of the region in which the transition to the cluster size reduction mode shifts left as S grows.

The cause of the observed in Fig. 10.7 behavior of the integral characteristics of the cluster state is the change of the ratio of the saturation concentration in the solvent mixture and the monomer concentration $f'(n = 1)$. Depending on the S values, there may be a region of X in which a strong supersaturation of the solution $\left(f'(n = 1) \gg c_{eq}^{MIX}\right)$ occurs. Thus, nucleation and growth of clusters rapidly undergoes the initial stages (I–III), which leads to the formation of a new peak in $f'(r,t)$. A bimodal distribution is formed (Fig. 10.8), in which both peaks slowly grow with time. At the same time, as reflected in Fig. 10.7, in this region the average cluster size, <*r*>, decreases in comparison with its value before dilution.

Let us also note, that in the region of large X values there is a threshold X value above which a bimodal distribution is not formed. For example, for $S \sim 10^4$, this

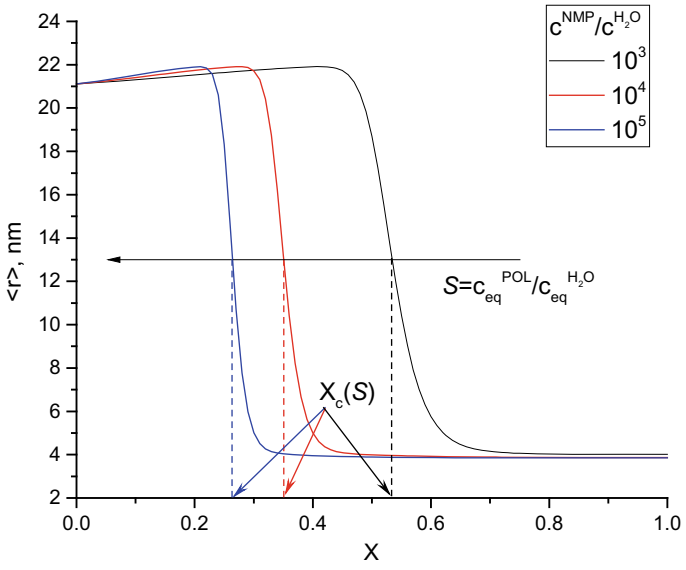

Fig. 10.7 Dependence of the mean cluster size in solution, at moment of time $t = 1$, after dilution by water on the value of X for different values of ratio $S = 10^3$, 10^4, 10^5 (lines from right to left) [74]. The procedure of definition of X_c is visualized

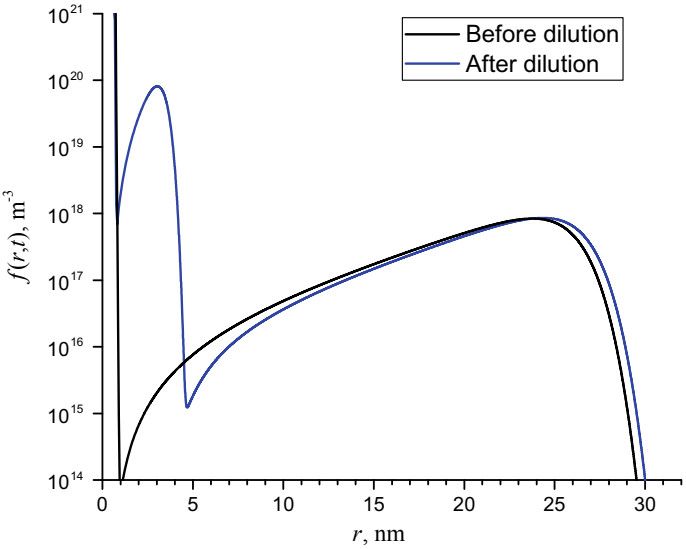

Fig. 10.8 Cluster size distribution functions of initial polar solution of fullerenes (black curve) and for the binary mixture after dilution (blue curve). The $f(r,t)$ after dilution was multiplied by $(1 + X)/(1 - X)$ factor [see (10.16)] for better comparison. Parameters: $S = 10^5$, $X = 0.6$

occurs in the region $X \approx 0.999$–0.9995. At $X > 0.9995$, the dilution transfers the solution to an unsaturated state, so that large clusters will decrease in size, emitting monomer particles into the liquid phase.

Summarizing, a model has been developed for describing the critical character of fullerenes cluster decomposition on water addition to C_{60} polar solution. Moreover, the simulated effect is of a general nature and can be observed in systems in which the stage of Ostwald ripening takes a long time. In these cases, the addition of a solvent to the system, in relation to which the particles are lyophobic, will lead to a significant decrease in the concentration of c_{eq}, and, consequently, the realization of bimodal particle size distributions.

10.4 Discussion

The reviewed investigations of cluster formation and growth, both experimental and theoretical, reveal the following general picture. It is evident that fullerene macromolecules have a tendency to aggregate in the liquids due to several different reasons. These can be solvent-nanoparticle interactions or excitations of fullerene oxidation by light. The size of C_{60} and C_{70} places them at the boundary between colloidal particles and atoms (and small molecules), thus leading to many intriguing effects. The interaction between fullerene molecules in solution occurs via van der Waals forces

(similar to C_{60} crystal) and is generally less or of the order of $k_B T$. Thus aggregation in non-polar liquids will not take place, until fullerene state is changed. In polar liquids lyophobic interactions may shift the state towards cluster growth, yet one can argue that if the equilibrium dissolution to molecular state is observed for some systems, then aggregation without additional effects is against the second law of thermodynamics. Thus most probably in these cases the aggregation also occurs via dispersion forces between fullerene-solvent complexes. The colloidal water solutions of fullerenes in this sense are standing separately, because they require either very intense treatment or transfer of already aggregated particles into water. A number of density-functional theory simulations is being performed presently, to enlighten additionally interactions of fullerenes in different media.

The developed theoretical models aim at describing the kinetics of fullerene aggregation from a general viewpoint. While initial attempts of considering low-polar solutions were made [36, 77], the obtained results are mostly applicable to polar C_{60}/NMP and similar systems. To some extent this is due to the basis of the theory on cluster formation and growth by nucleation in the liquid media [78]. We thus suppose the existence of a kinetic barrier, and also must define the value of c_{eq} as the equilibrium concentration of monomers with solid phase at a planar interface. For low-polar solutions, generally $c_{eq} \approx c_{sat}$, and thus aggregation via nucleation will proceed only if some non-equilibrium methods will be utilized to obtain the supersaturated solutions. For $c_{eq} \sim 2c_{sat}$, for example, the cluster growth will be quite limited in low-polar C_{60} solutions. On the other hand, one can imagine $c_{eq} \ll c_{sat}$ in polar solutions, where c_{eq} now corresponds to solubility of fullerene complexes with NMP. The additional models of confined growth were proposed for accounting of this effect.

On the other hand, a perspective for description of kinetics of fullerene aggregation in such solvents, as toluene and benzene, must be, from our viewpoint, based on applying segregation equations exploiting the hypothesis of binding of fullerene oxides with each other and C_{60} molecules in these media. For these types of modeling, a set of kinetic equations for two-dimensional cluster size distribution functions must be developed and solved numerically. This work is being performed at present.

Further, the developed method for obtaining cluster-size distribution functions for any stage of aggregation in the solution can be applied, for example, for modeling the small-angle scattering curves [71], or for comparison of the results with DLS measurements, which have been performed quite some time ago [28, 42] or recently [19], and are also underway for these and other liquids. The application of these models allows also to investigate such effects as dissolution by water [73, 74]. It is also possible to generalize the developed model of dissolution to account for addition of any other liquid to the system. Three different situations must be considered in this case: the addition of a low-polar liquid to the solution, $\varepsilon_{LIQ} < \varepsilon_{POL}$, addition of similar or the same liquid to the system, $\varepsilon_{LIQ} \sim \varepsilon_{POL}$, and, finally, addition of a high-polar liquid, with $\varepsilon_{LIQ} > \varepsilon_{POL}$. Thus we have to consequently consider a dissolution of polar liquid by each of three types of fullerene solutions, as proposed by the classification in [6]. In this work and in [74] we have considered only the third case, basing, moreover, on the experimental observation for water only [44].

Let us mention, that there exist several works, where similar effects were revealed and investigated for other types of relation between ε_{LIQ} and ε_{POL} [46, 47, 79]. The consideration of these effects and development of a generalized model of dissolution is an interesting research problem.

10.5 Conclusions

The present chapter consists of a review of investigations of fullerenes cluster growth in different solutions. The experimental investigations of these systems are based on a number of different methods, such as dynamic-light scattering, UV-Vis spectrophotometry, electron microscopy, small-angle neutron and X-ray scattering and others. A general classification of fullerene solutions with respect to cluster formation and growth properties can be given, revealing three distinctive classes of systems. We present the measurements of kinetic constants, namely the dissolution rate for low-polar systems at different temperatures and conditions. Additionally, a model-based UV-Vis investigation of kinetics of both dissolution and complex formation is reported, allowing to obtain both constants for these processes.

The theoretical description is based on the kinetic nucleation theory, with confined growth introduced additionally. Thus, the set of kinetic equations is modified to account for complexes formation and segregation in the solution. We have developed a method for obtaining the cluster-size distribution functions, $f(r,t)$ at any stage of systems evolution. The results of its application are used elsewhere, for example, to model the dependence of SANS curves on time of measurement. Here, on the other hand, we review the model of addition of water to polar C_{60} solution, which is developed for description of the critical character of the cluster state decomposition. In the final part of the paper we discuss the obtained results, reveal and propose further perspectives for developments in the field of investigation.

Acknowledgements This research is supported by RBFR (project no. 17-52-44024 Mong_a).

References

1. H.W. Kroto, J.R. Heath, S.C. O'Brien, R.F. Curl, R.E. Smalley, C_{60}: Buckminsterfullerene. Nature **318**, 162–163 (1985). https://doi.org/10.1038/318162a0
2. S. Bosi, T. Da Ros, G. Spalluto, M. Prato, Fullerene derivatives: an attractive tool for biological applications. Eur. J. Med. Chem. **38**, 913–923 (2003). https://doi.org/10.1016/j.ejmech.2003.09.005
3. B.C. Thompson, J.M.J. Fréchet, Polymer-fullerene composite solar cells. Angew. Chemie Int. Ed. **47**, 58–77 (2008). https://doi.org/10.1002/anie.200702506
4. L.A. Bulavin, Y. Prylutskyy, O. Kyzyma, M. Evstigneev, U. Ritter, P. Scharff, Self-organization of pristine C_{60} fullerene and its complexes with chemotherapy drugs in aqueous solution as promising anticancer agents (2018), pp. 3–22. https://doi.org/10.1007/978-3-319-61109-9_1

5. R. Bakry, R.M. Vallant, M. Najam-ul-Haq, M. Rainer, Z. Szabo, C.W. Huck, G.K. Bonn, Medicinal applications of fullerenes. Int. J. Nanomed. **2**, 639–649 (2007). http://www.pubmedcentral.nih.gov/articlerender.fcgi?artid=2676811&tool=pmcentrez&rendertype=abstract
6. M.V. Avdeev, V.L. Aksenov, T.V. Tropin, Models of cluster formation in solutions of fullerenes. Russ. J. Phys. Chem. A **84**, 1273–1283 (2010). https://doi.org/10.1134/S0036024410080017
7. V.N. Bezmel'nitsyn, A.V. Eletskii, M.V. Okun', Fullerenes in solutions, Uspekhi Fiz. Nauk. 168, 1195 (1998). https://doi.org/10.3367/ufnr.0168.199811b.1195
8. Y. Marcus, A.L. Smith, M.V. Korobov, A.L. Mirakyan, N.V. Avramenko, E.B. Stukalin, Solubility of C 60 fullerene. J. Phys. Chem. B. **105**, 2499–2506 (2001). https://doi.org/10.1021/jp0023720
9. G. Andrievsky, V. Klochkov, E. Karyakina, N. Mchedlov-Petrossyan, Studies of aqueous colloidal solutions of fullerene C_{60} by electron microscopy. Chem. Phys. Lett. **300**, 392–396 (1999). https://doi.org/10.1016/S0009-2614(98)01393-1
10. J.A. Brant, J. Labille, J.-Y. Bottero, M.R. Wiesner, Characterizing the impact of preparation method on fullerene cluster structure and chemistry. Langmuir **22**, 3878–3885 (2006). https://doi.org/10.1021/la053293o
11. S. Andreev, D. Purgina, E. Bashkatova, A. Garshev, A. Maerle, I. Andreev, N. Osipova, N. Shershakova, M. Khaitov, Study of fullerene aqueous dispersion prepared by novel dialysis method: simple way to fullerene aqueous solution, fullerenes. Nanotub. Carbon Nanostruct. **23**, 792–800 (2015). https://doi.org/10.1080/1536383X.2014.998758
12. M.E. Hilburn, B.S. Murdianti, R.D. Maples, J.S. Williams, J.T. Damron, S.I. Kuriyavar, K.D. Ausman, Synthesizing aqueous fullerene colloidal suspensions by new solvent-exchange methods. Colloids Surf A Physicochem. Eng. Asp. **401**, 48–53 (2012). https://doi.org/10.1016/j.colsurfa.2012.03.010
13. Y.I. Prylutskyy, V.I. Petrenko, O.I. Ivankov, O.A. Kyzyma, L.A. Bulavin, O.O. Litsis, M.P. Evstigneev, V.V Cherepanov, A G. Naumovets, U. Ritter, On the origin of C_{60} fullerene solubility in aqueous solution. Langmuir **30**, 3967–3970 (2014). https://doi.org/10.1021/la404976k
14. P. Scharff, K. Risch, L. Carta-Abelmann, I.M. Dmytruk, M.M. Bilyi, O.A. Golub, A.V. Khavryuchenko, E.V. Buzaneva, V.L. Aksenov, M.V. Avdeev, Y.I. Prylutskyy, S.S. Durov, Structure of C_{60} fullerene in water: spectroscopic data. Carbon N. Y. **42**, 1203–1206 (2004). https://doi.org/10.1016/j.carbon.2003.12.053
15. M.V. Avdeev, A.A. Khokhryakov, T.V. Tropin, G.V. Andrievsky, V.K. Klochkov, L.I. Derevyanchenko, L. Rosta, V.M. Garamus, V.B. Priezzhev, M.V. Korobov, V.L. Aksenov, Structural features of molecular-colloidal solutions of C_{60} fullerenes in water by small-angle neutron scattering. Langmuir **20**, 4363–4368 (2004). http://www.ncbi.nlm.nih.gov/pubmed/15969139
16. A.A. Khokhryakov, M.V. Avdeev, T.V. Tropin, G.V. Andrievskiĭ, L.A. Bulavin, Y.A. Osip'yan, V.L. Aksenov, Small-angle neutron scattering by colloidal solutions of fullerene C_{60} in water, Crystallogr. Reports **49**, S142–S147 (2004)
17. A.O. Khokhryakov, M.V. Avdeev, V.L. Aksenov, L.A. Bulavin, Structural organization of colloidal solution of fullerene C_{60} in water by data of small angle neutron scattering. J. Mol. Liq. **127**, 73–78 (2006). https://doi.org/10.1016/j.molliq.2006.03.019
18. M.V. Avdeev, T.V. Tropin, I.A. Bodnarchuk, S.P. Yaradaikin, L. Rosta, V.L. Aksenov, L.A. Bulavin, On structural features of fullerene C_{60} dissolved in carbon disulfide: complementary study by small-angle neutron scattering and molecular dynamic simulations. J. Chem. Phys. **132**, 164515 (2010). https://doi.org/10.1063/1.3415500
19. R. Dattani, K.F. Gibson, S. Few, A.J. Borg, P.A. DiMaggio, J. Nelson, S.G. Kazarian, J.T. Cabral, Fullerene oxidation and clustering in solution induced by light. J. Colloid Interface Sci. **446**, 24–30 (2015). https://doi.org/10.1016/j.jcis.2015.01.005
20. T. Tomiyama, S. Uchiyama, H. Shinohara, Solubility and partial specific volumes of C_{60} and C70. Chem. Phys. Lett. **264**, 143–148 (1997). https://doi.org/10.1016/S0009-2614(96)01290-0
21. Q. Ying, J. Marecek, B. Chu, Slow aggregation of buckminsterfullerene (C_{60}) in benzene solution. Chem. Phys. Lett. **219**, 214–218 (1994). https://doi.org/10.1016/0009-2614(94)87047-0

22. N.O. Mchedlov-Petrossyan, Fullerenes in molecular liquids. Solutions in "good" solvents: another view, J. Mol. Liq. **161**, 1–12 (2011). https://doi.org/10.1016/j.molliq.2011.04.001
23. G. Török, V.T. Lebedev, L. Cser, Small-angle neutron-scattering study of anomalous C_{60} clusterization in toluene. Phys. Solid State **44**, 572–573 (2002). https://doi.org/10.1134/1.1462711
24. S. Nath, H. Pal, A.V. Sapre, Effect of solvent polarity on the aggregation of C_{60}. Chem. Phys. Lett. **327**, 143–148 (2000). https://doi.org/10.1016/S0009-2614(00)00863-0
25. S. Nath, H. Pal, A.V. Sapre, Effect of solvent polarity on the aggregation of fullerenes: a comparison between C_{60} and C_{70}. Chem. Phys. Lett. **360**, 422–428 (2002). https://doi.org/10.1016/S0009-2614(02)00780-7
26. O.A. Kyzyma, M.V. Korobov, M.V. Avdeev, V.M. Garamus, V.I. Petrenko, V.L. Aksenov, L.A. Bulavin, Solvatochromism and fullerene cluster formation in C_{60}/N-methyl-2-pyrrolidone. Fuller. Nanotub. Carbon Nanostruct. **18**, 458–461 (2010). https://doi.org/10.1080/1536383x.2010.487778
27. N.P. Yevlampieva, Y.F. Biryulin, E.Y. Melenevskaja, V.N. Zgonnik, E.I. Rjumtsev, Aggregation of fullerene C_{60} in N-methylpyrrolidone. Colloids Surf. A Physicochem. Eng. Asp. **209**, 167–171 (2002). https://doi.org/10.1016/S0927-7757(02)00177-2
28. R.G. Alargova, S. Deguchi, K. Tsujii, Stable colloidal dispersions of fullerenes in polar organic solvents. J. Am. Chem. Soc. **123**, 10460–10467 (2001). http://www.ncbi.nlm.nih.gov/pubmed/11673976
29. N.O. Mchedlov-Petrossyan, N.N. Kamneva, Y.T.M. Al-Shuuchi, A.I. Marynin, O.S. Zozulia, Formation and ageing of the fullerene C_{60} colloids in polar organic solvents. J. Mol. Liq. **235**, 98–103 (2017). https://doi.org/10.1016/j.molliq.2016.10.113
30. T.V. Tropin, N. Jargalan, M.V. Avdeev, O.A. Kyzyma, R.A. Eremin, D. Sangaa, V.L. Aksenov, Kinetics of cluster growth in polar solutions of fullerene: experimental and theoretical study of C_{60}/NMP solution. J. Mol. Liq. **175**, 4–11 (2012). https://doi.org/10.1016/j.molliq.2012.08.003
31. N. Jargalan, T.V. Tropin, M.V. Avdeev, V.L. Aksenov, Investigation and modeling of evolution of C_{60}/NMP solution UV-Vis spectra. Nanosyst. Phys. Chem. Math. **7**, 99–103 (2016). https://doi.org/10.17586/2220-8054-2016-7-1-99-103
32. M. Baibarac, L. Mihut, N. Preda, I. Baltog, J.Y. Mevellec, S. Lefrant, Surface-enhanced Raman scattering studies on C_{60} fullerene self-assemblies. Carbon N. Y. **43**, 1–9 (2005). https://doi.org/10.1016/j.carbon.2004.08.020
33. A. Mrzel, A. Mertelj, A. Omerzu, M. Čopič, D. Mihailovic, Investigation of encapsulation and solvatochromism of fullerenes in binary solvent mixtures. J. Phys. Chem. B. **103**, 11256–11260 (1999). https://doi.org/10.1021/jp992637e
34. V.L. Aksenov, Study of fullerene aggregates in pyridine/water solutions, in *AIP Conference Proceedings, AIP*, pp. 66–69 (2001). https://doi.org/10.1063/1.1426823
35. V.L.L. Aksenov, M.V. Avdeev, T.V. Tropin, V.B. Priezzhev, J.W.P. Schmelzer, Model description of aggregation in fullerene solutions, in *AIP Conference Proceedings, AIP*, pp. 37–40 (2005). https://doi.org/10.1063/1.2103816
36. V.L. Aksenov, T.V. Tropin, M.V. Avdeev, V.B. Priezzhev, J.W.P. Schmelzer, Kinetics of cluster growth in fullerene molecular solutions. Phys. Part. Nucl. **36** (2005)
37. V.V. Slezov, J.W.P. Schmelzer, Comments on nucleation theory. J. Phys. Chem. Solids **59**, 1507–1519 (1998). https://doi.org/10.1016/S0022-3697(98)00079-1
38. V.V. Slezov, J. Schmelzer, Kinetics of formation and growth of a new phase with a definite stoichiometric composition. J. Phys. Chem. Solids **55**, 243–251 (1994). https://doi.org/10.1016/0022-3697(94)90139-2
39. V.V. Slezov, Y.J. Tkatch, J. Schmelzer, The kinetics of decomposition of solid solutions. J. Mater. Sci. **32**, 3739–3747 (1997)
40. R. Becker, W. Döring, Kinetische Behandlung der Keimbildung in übersättigten Dämpfen. Ann. Phys. **416**, 719–752 (1935). https://doi.org/10.1002/andp.19354160806

41. N.O. Mchedlov-Petrossyan, N.N. Kamneva, Y.T.M. Al-Shuuchi, A.I. Marynin, S.V. Shekhovtsov, The peculiar behavior of fullerene C_{60} in mixtures of 'good' and polar solvents: colloidal particles in the toluene–methanol mixtures and some other systems. Colloids Surf. A Physicochem. Eng. Asp. **509**, 631–637 (2016). https://doi.org/10.1016/j.colsurfa.2016.09.045
42. M. Alfè, B. Apicella, R. Barbella, A. Bruno, A. Ciajolo, Aggregation and interactions of C_{60} and C_{70} fullerenes in neat N-methylpyrrolidinone and in N-methylpyrrolidinone/toluene mixtures. Chem. Phys. Lett. **405**, 193–197 (2005). https://doi.org/10.1016/j.cplett.2005.02.030
43. M. Alfè, R. Barbella, A. Bruno, P. Minutolo, A. Ciajolo, Solution behaviour of C_{60} fullerene in N-Methylpyrrolidinone/toluene mixtures. Carbon N. Y. **43**, 665–667 (2005). https://doi.org/10.1016/j.carbon.2004.10.017
44. V.L. Aksenov, M.V. Avdeev, T.V. Tropin, M.V. Korobov, N.V. Kozhemyakina, N.V. Avramenko, L. Rosta, Formation of fullerene clusters in the system C_{60}/NMP/water by SANS. Phys. B Condens. Matter. **385–386**, 795–797 (2006). https://doi.org/10.1016/j.physb.2006.06.086
45. O.A. Kyzyma, M.V. Korobov, M.V. Avdeev, V.M. Garamus, S.V. Snegir, V.I. Petrenko, V.L. Aksenov, L.A. Bulavin, Aggregate development in C_{60}/N-methyl-2-pyrrolidone solution and its mixture with water as revealed by extraction and mass spectroscopy. Chem. Phys. Lett. **493**, 103–106 (2010). https://doi.org/10.1016/j.cplett.2010.04.076
46. T.V Tropin, T.O. Kyrey, O.A. Kyzyma, A.V. Feoktistov, M.V. Avdeev, L.A. Bulavin, L. Rosta, V.L. Aksenov, Experimental investigation of C_{60}/NMP/toluene solutions by UV-Vis spectroscopy and small angle neutron scattering. J. Surf. Investig. X-Ray, Synchrotron Neutron Tech. **7**, 5–8 (2013). https://doi.org/10.1134/s1027451013010199
47. O.A. Kyzyma, T.O. Kyrey, M.V. Avdeev, M.V. Korobov, L.A. Bulavin, V.L. Aksenov, Non-reversible solvatochromism in N-methyl-2-pyrrolidone/toluene mixed solutions of fullerene C_{60}. Chem. Phys. Lett. **556**, 178–181 (2013). https://doi.org/10.1016/j.cplett.2012.11.040
48. A.A. Kaznacheevskaya, O.A. Kizima, L.A. Bulavin, A. V. Tomchuk, V.M. Garamus, M.V. Avdeev, Reorganization of the cluster state in a C_{60}/N-Methylpyrrolidone/water solution: Comparative characteristics of dynamic light scattering and small-angle neutron scattering data. J. Surf. Investig. X-Ray, Synchrotron Neutron Tech. **7**, 1133–1136 (2013). https://doi.org/10.1134/s102745101306030x
49. A.D. Bokare, A. Patnaik, Evidence for C_{60} aggregation from solvent effects in [Ps–C_{60}] molecular complex formation. Carbon N. Y. **41**, 2643–2651 (2003). https://doi.org/10.1016/S0008-6223(03)00384-1
50. T.O. Kyrey, O.A. Kyzyma, M.V. Avdeev, T.V. Tropin, M.V. Korobov, V.L. Aksenov, L.A. Bulavin, Absorption characteristics of fullerene C_{60} in N-Methyl-2-Pirrolidone/Toluene mixture, fullerenes. Nanotub. Carbon Nanostruct. **20**, 341–344 (2012). https://doi.org/10.1080/1536383X.2012.655173
51. G.V. Andrievsky, V.K. Klochkov, A.B. Bordyuh, G.I. Dovbeshko, Comparative analysis of two aqueous-colloidal solutions of C_{60} fullerene with help of FTIR reflectance and UV–Vis spectroscopy. Chem. Phys. Lett. **364**, 8–17 (2002). https://doi.org/10.1016/S0009-2614(02)01305-2
52. N. Jargalan, T.V.V. Tropin, M.V.V. Avdeev, V.L.L. Aksenov, Investigation of the dissolution kinetics of fullerene C_{60} in solvents with different polarities by UV-Vis spectroscopy, J. Surf. Investig. X-Ray, Synchrotron Neutron Tech. **9,** 12–16 (2015). https://doi.org/10.1134/s102745101501019x
53. R.S. Ruoff, D.S. Tse, R. Malhotra, D.C. Lorents, Solubility of fullerene (C_{60}) in a variety of solvents. J. Phys. Chem. **97**, 3379–3383 (1993). https://doi.org/10.1021/j100115a049
54. A.A.A.A. Noyes, W.R.W.I. Whitney, The rate of solution of solid substances in their own solutions, J. Am. Chem. Soc. **19**, 930–934 (1897). https://doi.org/10.1021/ja02086a003
55. A. Naumenko, M. Biliy, V. Gubanov, A. Navozenko, Spectroscopic studies of fullerene clusters in N-methyl-2-pyrrolidone, J. Mol. Liq. 1–4 (2017). https://doi.org/10.1016/j.molliq.2017.01.035
56. O.B. Karpenko, V.V. Trachevskij, O.V. Filonenko, V.V. Lobanov, M.V. Avdeev, T.V. Tropin, O.A. Kyzyma, S.V. Snegir, Nmr study of non-equilibrium state of fullerene C_{60} in N-methyl-2-pyrrolidone. Ukr. J. Phys. **57**, 860–863 (2012)

57. J.W.P. Schmelzer, G. Ropke, V.B. Priezzhev, *Nucleation Theory and Applications*, in ed. by J.W.P. Schmelzer, G. Ropke, V.B. Priezzhev (JINR Publishing House, Dubna, 1999), pp. 1–525
58. V.V. Slezov, V.V. Sagalovich, Diffusive decomposition of solid solutions. Sov. Phys. Uspekhi. **30**, 23–45 (1987). https://doi.org/10.1070/PU1987v030n01ABEH002792
59. V.L.L. Aksenov, T.V.V. Tropin, M.V.V. Avdeev, V.B.B. Priezzhev, J.W.P.W.P. Schmelzer, Kinetics of cluster growth in fullerene molecular solutions. Phys. Part. Nucl. **36**, S52–S61 (2005)
60. T.V. Tropin, V.B. Priezzhev, M.V. Avdeev, J.W.P. Schmelzer, V.L. Aksenov, Fullerene cluster formation in carbon disulfide and toluene, fullerenes. Nanotub. Carbon Nanostruct. **14**, 481–488 (2006). https://doi.org/10.1080/15363830600666365
61. V.V. Slezov, J. Schmelzer, J. Möller, Ostwald ripening in porous materials. J. Cryst. Growth **132**, 419–426 (1993). https://doi.org/10.1016/0022-0248(93)90067-7
62. J. Schmelzer, J. Möller, V.V. Slezov, Ostwald ripening in porous materials: The case of arbitrary pore size distributions. J. Phys. Chem. Solids **56**, 1013–1022 (1995). https://doi.org/10.1016/0022-3697(95)00021-6
63. I.S. Gutzow, J.W.P. Schmelzer, *The Vitreous State: Thermodynamics, Structure, Rheology, and Crystallization* (1995)
64. F.M. Kuni, A.I. Rusanov, A.K. Shchekin, A.P. Grinin, Kinetics of aggregation in micellar solutions. Russ. J. Phys. Chem. A **79**, 833–853 (2005)
65. A.P. Grinin, D.S. Grebenkov, Study of relaxation in micellar solution by the numerical experiment. Colloid J. **65**, 552–561 (2003). https://doi.org/10.1023/A:1026111504241
66. T.V. Tropin, M.V. Avdeev, O.A. Kyzyma, V.L. Aksenov, Nucleation theory models for describing kinetics of cluster growth in C_{60}/NMP solutions. Phys. Status Solidi. **247**, 3022–3025 (2010). https://doi.org/10.1002/pssb.201000119
67. T.V. Tropin, M.V. Avdeev, O.A. Kyzyma, R.A. Yeremin, N. Jargalan, M.V. Korobov, V.L. Aksenov, Towards description of kinetics of dissolution and cluster growth in C_{60}/NMP solutions. Phys. Status Solidi. **248**, 2728–2731 (2011). https://doi.org/10.1002/pssb.201100099
68. T.V. Tropin, M.V. Avdeev, V.L. Aksenov, Modeling of the evolution of the cluster-size distribution functions in polar fullerene C_{60} solutions, J. Surf. Investig. X-Ray, Synchrotron Neutron Tech. **3** (2019). https://doi.org/10.1134/S102745101901035X
69. I.M. Lifshits, V.V. Slezov, Kinetics of the diffusion decomposition of supersaturated solid solutions. Zhurnal Eksp. i Teor. Fiz. **35**, 479–492 (1958)
70. A.L. Smith, E. Walter, M.V. Korobov, O.L. Gurvich, Some enthalpies of solution of C_{60} and C_{70}. Thermodynamics of the temperature dependence of fullerene solubility. J. Phys. Chem. **100,** 6775–6780 (1996). https://doi.org/10.1021/jp952873z
71. T.V. Tropin, N. Jargalan, M. V. Avdeev, O.A. Kyzyma, D. Sangaa, V.L. Aksenov, Calculation of the cluster size distribution functions and small-angle neutron scattering data for C_{60}/N-methylpyrrolidone. Phys. Solid State. **56,** 148–151 (2014). https://doi.org/10.1134/s1063783414010363
72. R. Pascova, I. Gutzow, J. Schmelzer, A model investigation of the process of phase formation in photochromic glasses. J. Mater. Sci. **25**, 921–931 (1990). https://doi.org/10.1007/BF03372180
73. V.L. Aksenov, T.V. Tropin, O.A. Kyzyma, M.V. Avdeev, M.V. Korobov, L. Rosta, Formation of C_{60} fullerene clusters in nitrogen-containing solvents. Phys. Solid State **52**, 1059–1062 (2010). https://doi.org/10.1134/S1063783410050367
74. T.V. Tropin, V.L. Aksenov, Theoretical investigation of the cluster size decrease effect on dilution of a solution by water. J. Exp. Theor. Phys. **128**, 274–280 (2019). https://doi.org/10.1134/S1063776119010187
75. P. Jain, S.H. Yalkowsky, Solubilization of poorly soluble compounds using 2-pyrrolidone. Int. J. Pharm. **342**, 1–5 (2007). https://doi.org/10.1016/j.ijpharm.2007.03.056
76. R. Sanghvi, R. Narazaki, S.G. Machatha, S.H. Yalkowsky, Solubility improvement of drugs using N-methyl pyrrolidone. Am. Assos. Pharm. Sci. **9**, 366–376 (2008). https://doi.org/10.1208/s12249-008-9050-z
77. V.L. Aksenov, M.V. Avdeev, T.V. Tropin, V.B. Priezzhev, J.W.P. Schmelzer, Model description of aggregation in fullerene solutions, in *AIP Conference Proceedings, AIP*, pp. 37–40 (2005). https://doi.org/10.1063/1.2103816

78. J. Bartels, U. Lembke, R. Pascova, J. Schmelzer, I. Gutzow, Evolution of cluster size distribution in nucleation and growth processes. J. Non. Cryst. Solids **136**, 181–197 (1991). https://doi.org/10.1016/0022-3093(91)90489-S
79. O.A. Kyzyma, L.A. Bulavin, V.L. Aksenov, T.V. Tropin, M.V. Avdeev, M.V. Korobov, S.V. Snegir, L. Rosta, Aggregation in C 60/NMP, C 60/NMP/water and C 60/NMP/toluene mixtures, fullerenes. Nanotub. Carbon Nanostruc. **16**, 610–615 (2008). https://doi.org/10.1080/15363830802312982

Part IV
Biological Aspects in Liquid Systems. Irradiation Influence on Liquid Systems

Chapter 11
Interactions of Heavy Ions with DNA and Radiative Aspects in Physics of Liquid Matter

Nan Zhang, Ming-Ru Li and Feng-Shou Zhang

Abstract Comparing with X/γ-rays cancer therapy, the heavy ion-beam therapy has unique physical properties such as high linear energy transfer (LET) and forming sharp energy loss peaks (Bragg peaks) during energy deposition. Heavy ion-beam cancer therapy technology is developing fast and has achieved significant clinical success. For radiation biology research, DNA as an important target biomolecule and irradiated by heavy ions to induce damages to genetic information. We will focus on understanding the precise mechanism of heavy ions-induced DNA damage under extremely physiological conditions (radiation therapy and mutagenesis). In this chapter, we summarize the microscopic processes of binding heavy ions to DNA fragments in liquid environment, especially the mechanism of DNA conformational transformation with varying liquid environment. With the energy deposition along the ionizing radiation path, the local ensemble conditions, such as solvent polarity, environment conditions (e.g. temperature), and the additional particles, will change dramatically. In the ion solutions, when normal water solvent are replaced by less polarized water, the Hofmeister serial of alkali metal ions is changed from $Li^+ > Na^+ \approx K^+ \approx Rb^+ \approx Cs^+$ to $Li^+ > Na^+ > K^+ > Rb^+ > Cs^+$. For less polarity solvent environment, the structure of DNA changes from the B to A form for Li^+, Na^+, and K^+ counterions.

N. Zhang · M.-R. Li · F.-S. Zhang (✉)
The Key Laboratory of Beam Technology and Material Modification of Ministry of Education, College of Nuclear Science and Technology, Beijing Normal University, Beijing 100875, China

Beijing Radiation Center, Beijing 100875, China
e-mail: fszhang@bnu.edu.cn

N. Zhang
e-mail: zhangnan@mail.bnu.edu.cn

M.-R. Li
e-mail: mruli@mail.bnu.edu.cn

F.-S. Zhang
National Laboratory of Heavy Ion Accelerator of Lanzhou, Center of Theoretical Nuclear Physics, Lanzhou 730000, China

L. A. Bulavin and L. Xu (eds.), *Modern Problems of the Physics of Liquid Systems*, Springer Proceedings in Physics 223,
https://doi.org/10.1007/978-3-030-21755-6_11

11.1 Introduction

As the world's second-largest non-communicable disease, more than 14 million people are diagnosed with cancer every year [1]. According to statistics, 8.8 million people died from cancer in 2015, accounting for one-sixth of deaths globally [2, 3]. The history of radiotherapy began in 1895, when Röntgen discovered X-rays, and in the following year, radiation was used for medical diagnosis and treatment [4]. Today about 50% of cancer patients require at least once radiation therapy to cure their cancer, increase the chance of cure or alleviate the symptoms [5]. The common sources of radiation are X/γ-rays, electrons, neutrons and heavy ions. The main contradiction in radiation therapy is to increase the radiation sensitivity of tumor cells while reducing the radiation sensitivity of normal cells. The energy deposition of heavy ions at a certain depth is a sharp energy peak, called Bragg peak, which provides a therapeutic dose to the tumor while minimizing unnecessary doses to healthy tissue [6–8]. Thus, the physical mechanism of heavy ion treatment of cancer has received extensive attention [9–12].

More than a century after the discovery of X-rays, heavy ions are currently also an essential component in mutation breeding, space radiation and environmental protection (nuclear facility accidents). In 1986, the Institute of Plasma Physics, Chinese Academy of Sciences, initial applied the low-energy ion implantation technology to the mutation breeding [13]. As a new induced-mutation method, a considerable number of mutants have been obtained such as wheat, rice, cotton, corn, peanuts, fruit trees, trees, pastures and microorganisms. College of Nuclear Science and Technology, Beijing Normal University and Beijing Radiation Center have done many researches in plant and microorganism induced-mutation breeding by ion implantation, and acquired some achievements.

Compared with traditional genetic breeding methods, the three main advantages of ion implantation breeding are as follows:

1. High mutation rate, more than 1000 times the probability of natural variation.
2. Wide variation spectrum, that is, the variety of mutations, can produce new types that have never been produced in nature.
3. Rapid mutations and high stability, which can greatly shorten the breeding cycle.

Crops implanted with different ions and different doses may have some valuable mutations in plant size, growth cycle, crop yield and so on. As an emerging source of radiation, heavy ion beams have high LET characteristics. In the plant mutation breeding, the mutagenic efficiency of unit dose is 10 times higher than that of low LET (X/γ-ray and electron beam). Different from interaction of other radiations and organisms, Low-energy heavy ion plantation of organism includes not only energy deposition process, but also mass deposition and charge exchanging processes, with a higher relative biological effect.

The biological target of ionization radiation in the cell is DNA. It has been observed that radiation can induce several types of DNA damage, such as base release, sugar ring damage, single strand breaks (SSBs), double strand breaks (DSBs) and cross-links [14, 15]. The accumulation of large amount of unrepaired DSBs, constitutes

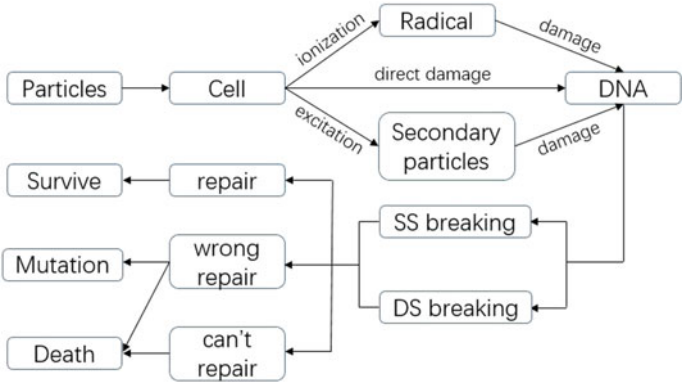

Fig. 11.1 The ionizing radiation mechanism of direct damage and indirect damage

the basis of anti-tumor radiotherapies, by inducing apoptosis, necrosis, mitotic catastrophe or permanent growth arrest [16].

According to the way of particle beams interact with DNA, it can also be divided into direct damage and indirect damage [17, 18]. Direct damage occurs when radiation beams directly interact with DNA molecule by ionizing or exciting electrons [19–21]. Indirect damage is initiated by the ionization of the surrounding medium, i.e. water, proteins, etc. As the incident radiation interacts with these components, a vast number of secondary species, mostly electrons and radicals, i.e. molecules with a missing electron (or containing a hole), are generated [22, 23]. These active secondary species will interact with and damage DNA consequently.

DNA damage varies with the type of incident particles, energy, velocity and cell type. High LET heavy ion radiation induces direct DNA damage, which is categorized into DSBs and non DSB oxidative clustered DNA lesions (OCDL), leading to cells apoptosis [24, 25]. Direct damage is an important aspect of radiation damage. Conversely, in the case of low LET, such as X/γ-rays and electrons, it can cause indirect DNA damage. The ionizing radiation mechanism is shown in Fig. 11.1.

Heavy ion-induced DNA damage is more complex than by X-rays, or γ-rays and leads to more serious biological consequences inducing apoptosis, necrosis, mitotic catastrophe or permanent growth arrest [26, 27]. Heavy ion can produce both DSBs and non-DSBs oxidative clustered DNA lesions [27, 28]. A general method for analyzing DSBs is pulsed or constant field gel electrophoresis, in which one takes the ratio of intact original size DNA to migrated broken DSBs after electrophoresis at a low voltage on agarose gels [29–31]. A DNA repair enzyme isolated from *E. coli* can be used as a damage probe to measure non-DSB oxidized cluster DNA damage [32]. Although the theoretical research on the mechanism of DNA damage induced by heavy ions has been made for many years, the research in this field is still in its infancy.

With the development of molecular biology, the molecular mechanism of interaction between ionizing radiation and biological macromolecules has been studied. Obviously, this process needs to be characterized from different time scales and spatial scales [33]. Taking the DNA damage process as an example, in the course of electron transfer between hydroxyl radicals and DNA molecules, the time scale required for electron transfer is fs, and the research object is electrons, which should be studied by time-dependent density functional theory (TDDFT). After electron transfer, the time scale required for DNA conformational transform is ns or μs. The research object is molecules, which should be studied by molecular dynamics (MD). The time scales required for biological processes such as cell repair varies from hours to days.

This chapter describes the mechanism of the interaction between heavy ion and biological macromolecules in a liquid environment, with extreme physical environment of radiotherapy and mutation breeding through molecular dynamics simulations. The structure of the chapter is as follows: Sect. 11.1 Introduction of the heavy ions interaction with DNA. Section 11.2 Simulation description and DNA structure parameters that need to be used in the discussion below. Section 11.3 DNA conformational transformation in different liquid environments and the underlying causes of these phenomena are studied. Section 11.4 The conclusion is presented at the end of the chapter.

11.2 Methods

11.2.1 Simulation Description

Classical molecular dynamics simulations are used to study the heavy ion interacts with DNA in liquid environments based on the GROMACS code packages [34]. The Drew-Dickerson dodecamer was selected as the initial state of DNA (PDB ID: 171d). Drew-Dickerson dodecamer contains the recognition site of the *EcoRI* restriction enzyme, commonly used in gene recombination techniques [35]. And Drew-Dickerson dodecamer was extensively studied by experiments and nanosecond-to-microsecond MD simulations [36–38]. What's more, Drew-Dickerson dodecamer contains 12 base pairs d(CGCGAATTCGCG) and the DNA duplex is long enough to maintain a complete B-helix. Stereo views of the initial 171d are given in Fig. 11.2.

The SPC model is adopted because its description is, generally, satisfactory under ambient conditions when compared with experiments [39]. PARMBSC1 force fields are used to describe oligonucleotide interactions in liquid environments [40]. Electrostatic interactions are dealt with by the particle mesh *Ewald* summation method using a cutoff of 1.2 nm for the interaction range, with the real-space cutoff set at 1.0 nm [41, 42] and the Lennard-Jones interactions cutoff set at 1.0 nm. LINCS is used to restrain all chemical bonds involving hydrogen atom [43].

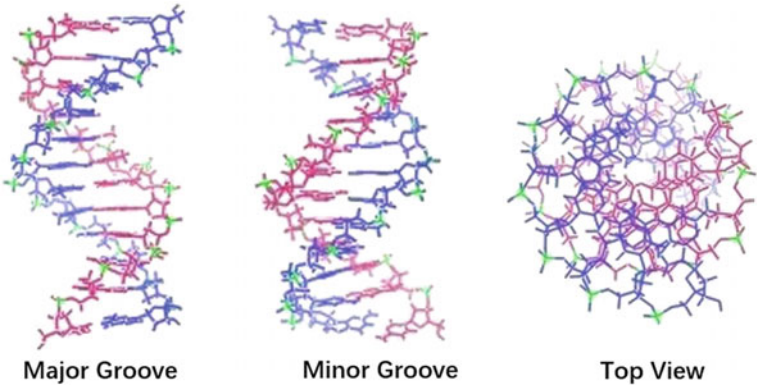

Fig. 11.2 Stereo views of the initial 171d structure. Presented here are three typical views from major, minor groove and top. The systems are treated with the PARMBCS1 force field

Table 11.1 The force field parameter for counter-ions in molecular dynamics simulations

	Li^+	Na^+	K^+	Rb^+	Cs^+
σ (Å)	2.37	2.73	3.36	3.57	3.92
ε (KJ/mol)	0.149	0.358	0.568	1.602	2.132
	Be^{2+}	Mg^{2+}	Ca^{2+}	Sr^{2+}	Ba^{2+}
σ (Å)	1.27	1.65	1.90	3.10	3.82
ε (KJ/mol)	0.500	3.470	1.881	0.495	0.197

One DNA dodecamer, 22 counter-ions and about 5080 solvent molecules (big enough to ensure the DNA does not interact with its periodic images) are contained in a periodic cubic box. The counter-ions force field parameters are present in Table 11.1. The aim of this work is to study the heavy ion effects on DNA conformation in the extreme physical liquid environment.

11.2.2 DNA Structure

The structure of DNA is very important in maintenance and alteration of biological inherited [44, 45]. Whether as a carrier of genetic information or a basic unit of emerging molecular devices, the correct structure is the basis for the realization of DNA functions [46, 47]. A introduction to the conformation of DNA as follows. B-DNA is a conformational form of DNA under physiological conditions or in an aqueous environment containing low salt. In living cell protoplasm, the vast majority of DNA is B-DNA. The distance between adjacent base pairs of B-DNA is about 0.34 nm, which is rotated by 36° along the helical axis, so that each helix has about 10 base pairs. In addition to the standard B-type right-handed helix structure, exper-

iments have found that DNA will have other different forms such as A-DNA [48], C-DNA, and left-handed Z-DNA [49]. In a sodium salt having a relative humidity of 75%, the DNA is in the A conformation. The distance between the A-DNA base pair plane is about 0.255 nm, the entire base pair plane is inclined by 20° to the helix axis, and each helix has about 11 base pairs. The major groove of A-DNA is narrow and deep, and the minor groove is wide and shallow. A-DNA does not generally exist in the body. Both A-DNA and B-DNA are right-handed helix that can be converted to each other [50, 51].

The details of structure parameters describing the Axis-base pair (X-displacement, Y-displacement, Inclination), Intra-base pair (Shear, Stretch, Stagger, Buckle, Propeller, Opening), Inter-base pair (Rise, Roll, Shift, Slide, Tilt Twist), Backbone torsion (BI/BII Population, Canonical $\alpha - \gamma$, Puckering) and Groove characters (MW, mW, MD, mD) of DNA are analyzed by programs Curves+ and Canal [52]. The X displacement (Xdisp) describes the displacement of a base pair along the X direction (the direction of the short axis of the base pair) of the base pair axis. Inclination (Incl) is defined as dihedral angle between the base pairs and the plane with the initial x and y axis. Twist and Roll ρ are relative rotation around the z axis and rotation around the y axis between two successive base pairs in an overall helix axis, respectively [53, 54]. The Width (MW for major groove and mW for minor groove) and Depth (MD for major groove and mD for minor groove) of the groove are defined in [53, 55, 56]. All of these parameters are analyzed continually for the precise values in our simulations. The B-DNA conformation can most easily be distinguished form the A conformation with these parameters.

11.3 Liquid Environment-Induced DNA Conformational Transition

Water is the most important life supporting solvent [57, 58]. It is both a solvent and a reactant, and an important component of biological macromolecules, accounting for two-thirds of human body [59–61]. A basic question of interest is which fundamental property of its molecule distinguishes water as the most important solvent in nature [62]. Under extreme conditions such as radiotherapy, mutation breeding, supra molecular chemistry, nanotechnology and molecular computing, if the nature of the water changes, what happens to the dissolution behavior of the biological macromolecules in water. An important property of water is that it dissolves charged ions and polar molecules easily. It is generally considered that polarity and hydrogen bonding are the distinguishing attributes of water when compared with other liquid [63–66]. This chapter investigates the effects of changes in polarity and hydrogen bond strength on DNA dissolution behavior in liquid environments.

There are two ways to change the polarity and hydrogen bond strength of an aqueous solution in the experiment. First, environmental conditions such as temperature and pressure can be changed to affect the thermodynamic fluctuation or hydrogen

bond distance of water molecules, thereby achieving the control of the hydrogen bond strength [67–69]. However, when temperature or pressure change, the interaction of other substances in the solution also varies. Another method is to adjust the polarity and hydrogen bond strength of the solution by mixing other molecules (e.g. salts and alcohols, etc.). The disadvantage of this method is to introduce the unnecessary interactions complicates the problem. In theory, the polarity and hydrogen bond strength of the solvent can be adjusted by modifying the water electron distribution and molecule structure.

Following the principle from simple to complex, the study sequence of polarity and hydrogen bond strength induced DNA conformational transition as follows:

1. Discuss the transforms about DNA conformation when the basic properties of water molecules (e.g. charge distribution and molecular structure) change.
2. The influence of environmental factors (e.g. temperature and pressure) on the secondary structure of DNA is described.
3. Study the effect of solution polarity on DNA conformation by adding other molecules (e.g. salts, alcohols).

11.3.1 Solvent Polarity-Induced DNA Conformational Transition

A water molecule contains two smaller hydrogen atoms and one oxygen atom. There is one electron outside the hydrogen nucleus, the oxygen atom has six outer electrons, these electrons form an eight-electron close shell structure in the water molecule. The charge distributed on the oxygen atom is about $-0.8\ |e|$, and the charge distributed on the hydrogen atom is about $0.4\ |e|$. Since the positive and negative centers of water molecules do not coincide, the water molecules have polarity. The polarity of the water molecules can be adjusted by changing the charge distribution between the hydrogen atoms and oxygen atoms in the water molecule or by changing the structure of the water molecule.

Solvent polarity induced DNA conformational transition have been studied as follows. Based on the SPC water model ($q_O = -0.82\ |e|$, $q_H = 0.41\ |e|$), the polarity of water molecules is changed by modifying the charge ratio $S(S = 0.6, 0.7, 0.8, 1.0, 1.2)$ of oxygen and hydrogen atoms in the water model.

For changes in the polarity of the solvent, the intermolecular structure of water is first affected. When $S < 0.8$, the intermolecular structure of water without local order is similar to Lennard-Jones liquid. For S belongs to 0.8 and 1, the solvent molecules are water-like structures forming tetrahedrons. As $S = 1.2$, the water molecules are more fixed by forming a strengthened tetrahedral structure, and the solvent is in a glassy state.

Solvent polarity modified also causes DNA conformational transition. The root mean square coordinate deviation (RMSD) (the DNA trajectories with respect to canonical B, canonical B and the initial PDB structure) and DNA structure parameter

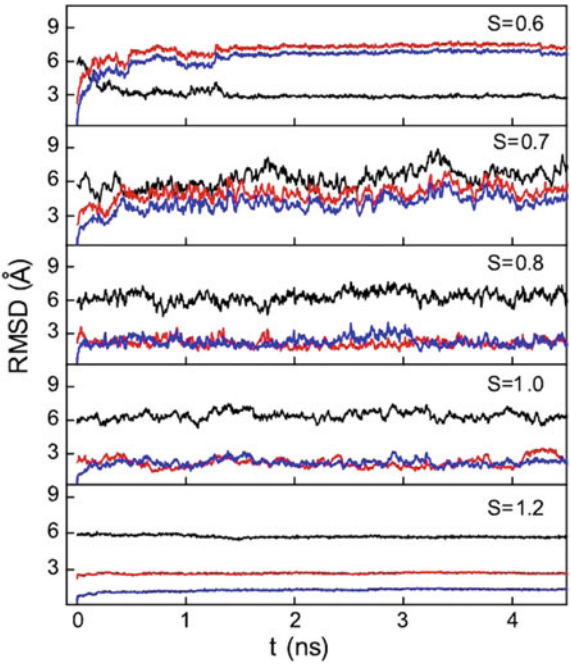

Fig. 11.3 RMSD of the DNA trajectories with respect to the canonical B (red or gray), A (black) forms, and the starting PDB structure [63]

detail analysis are given in Figs. 11.3 and 11.4. In a typical Lennard-Jones liquid with $S = 0.6$, the conformation of DNA is converted to stable A-DNA. However, when $S = 0.7$, the major groove of DNA remain close to the value of B form, the minor groove of DNA is close to the value of A form, while others DNA structural parameters in the middle area between A and B values. This state can be defined as an A–B mixed conformation. When $S = 1.0$ and 0.8, after molecular dynamics equilibrium, the DNA appears B conformation. In the over-polarized solvent of $S = 1.2$, the DNA maintains the initial conformation under the constraints of the glassy solvent.

There are many different perspectives on the physical mechanism of DNA conformational transformation. Solvent accessibility, base stacking interaction, phosphate hydration, minor groove spine of hydration, and the negatively charged phosphate groups screened are considered to be factors in DNA structural transition [70–75]. The most common factor is the different shielding mechanism between the negatively charged oxygen atoms of the phosphate groups [75]. Without the screening, the repulsive potential between the negative charges would causes the DNA to stretch and the helix axis to unwind. In this chapter, only the hydrated shell of the solvent and the sodium ion acting as a electrostatic balance can block the negative charge on the DNA phosphate group. To investigate the cause of the DNA structural change by solvent polarity, we investigated the distribution of hydration and counter ions around the phosphate groups on DNA helix [76].

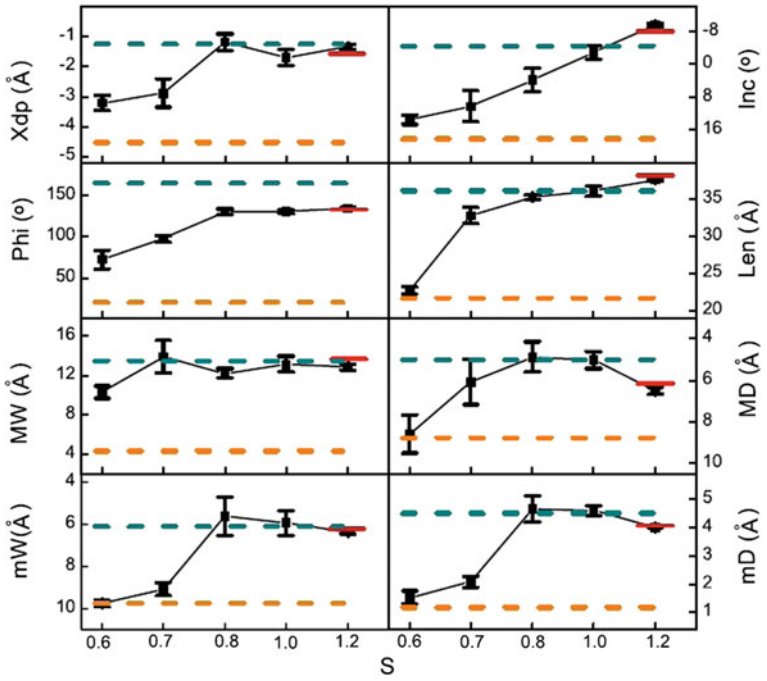

Fig. 11.4 Averaged DNA structure parameters during the last 2 ns simulations. The horizontal dashed lines indicate the reference values of type A (orange or light gray) and B (cyan or dark gray) forms and the short red or gray line shows the parameters of the starting PDB structure [63]

The radial distribution functions (RDF) and coordination numbers of Na^+ ions/modified H_2O molecules around the negatively charged oxygen atoms of phosphate groups are shown in Fig. 11.5. As the polarity of the solvent decreases, the binding of sodium ions to the phosphate groups becomes stronger. Conversely, the hydration around the phosphate oxygen atom is getting weaker. These situation demonstrates that the two different screening mechanisms of counter ions and hydration are competing with each other. In a weakly polar solution of $S = 0.6$, the phosphate oxygen atom is more likely to combine with the sodium ion, forming a strong chemical bond (Na^+–O^-(P)) to electrostatically shield the charge between the DNA backbones. Therefore DNA presents the shorter and more compact A type. When $S = 0.7$, the negative charge of oxygen atoms is balanced by ion coupling and solvent hydration to reach a relative equilibrium state, and the DNA exhibits a state of A–B mixing. In a state of the solvent polarity is close to normal water $S = 0.8$ and 1.0, the oxygen atom of the phosphate group mainly interacts with the positively charged hydrogen atoms in the solvent water molecule. A localized reorientation of the hydrated shell layer is formed around the phosphoric acid oxygen atom. This reorientation may redirect the neighboring water molecules through solvent-molecular hydrogen bonding interactions and ultimately transfer to the adjacent phosphate groups. In this way, there is

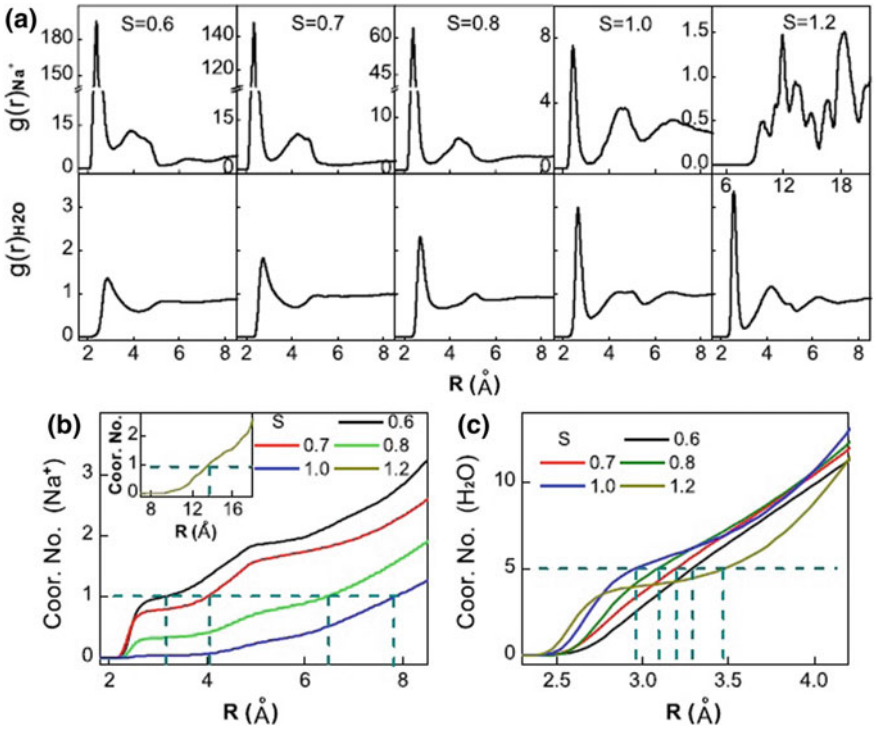

Fig. 11.5 **a** The radial distribution functions of ions/water around the negatively charged oxygen atoms of phosphate groups in a series of modified H_2O molecules. **b**, **c** The coordination numbers of ions/water around the negatively charged oxygen atoms of phosphate groups in a series of modified H_2O molecules. The blue (or dark gray) dashed lines show the radii in which the coordination numbers is 1 for Na^+ ions and 5 for solvent molecules [63]

an indirect interaction between adjacent phosphate groups, and the structure of DNA is closer to B-DNA. In the case of solvent molecules over polarized, because of the large charge of water molecules, only a small amount of water molecules are needed to screen the negative charge on the DNA backbone.

For DNA, specific structures have different functions. Whether as a carrier of genetic information or a basic unit of emerging molecular devices, the correct structure is the basis for the realization of DNA functions. The study, in this chapter, shows that when the polarity of the solution is reduced, the order of DNA conformational changes follow the B-form → (A–B) mix → A-form. A-DNA and B-DNA are common functional structures of double-stranded DNA. During the interaction of DNA with some proteins or RNA, some parts of DNA molecules will have a relatively stable (A–B) mixed state [77]. Analysis shows that ionic coupling and solvent hydration screen the negative charge on the phosphate group in two different ways, thereby achieving the effect of regulating the internal electrostatic interaction of the

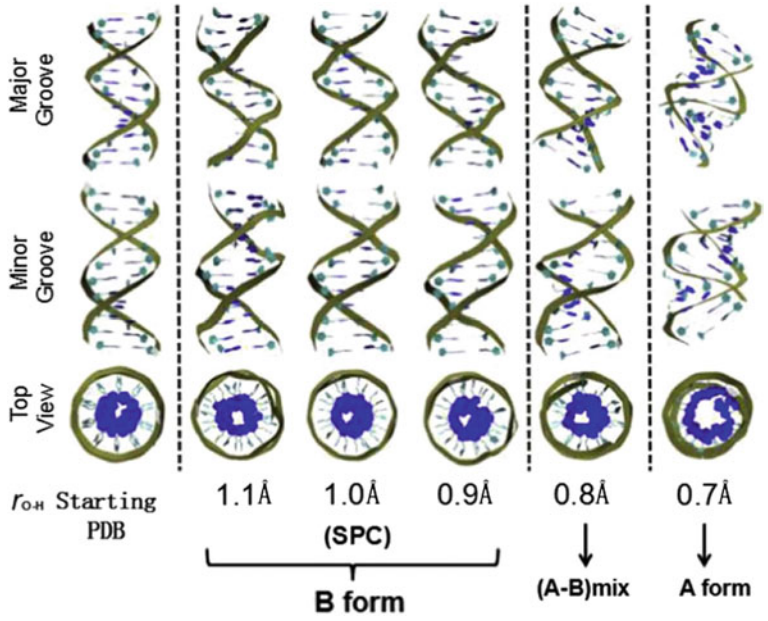

Fig. 11.6 Stereo views of the DNA make from the averaged resulting structures in the last 10 ns simulations for various O–H length models. Here, three typical views are presented: major, minor groove and top [78]

DNA double strand. The competition between these two different mechanisms is an important reason for the conformational transformation of DNA molecules.

Modified water models with different bond length are also be investigate in Fig. 11.6. The conformational transitions of constrained B to A as the water molecule bond length decreasing. The reason for conformational change of the DNA molecule in modified water model with different bond length is same as above describe, and will not be discussed herein.

11.3.2 Temperature-Induced DNA Conformational Transition

The hydrogen bond strength in liquid water usually does not exceed one-twentieth of the oxygen-hydrogen covalent bond, which is closely related to environmental conditions. At room temperature, the energy of hydrogen bonding is about 23 kJ/mol, which is five times the energy fluctuation caused by thermodynamic collision in water [79, 80]. Therefore hydrogen bonding is sufficiently stable to thermodynamic fluctuations at room temperature. When the temperature rises, hydrogen-oxygen covalent bonds change little in water molecules, and thermodynamic fluctuations

cause part of the hydrogen bonds to bend or break. In addition, pressure can cause hydrogen bond strength and structural changes [81]. The hydrogen bond strength of the water molecules can be adjusted by changing the temperature or pressure of the liquid environments.

Different environmental conditions—temperatures (200, 260, 298, 310, 343 K) are used to study the effects of hydrogen bonding thermodynamic fluctuations on DNA microstructure. The highest simulated temperature of 343 K is the melting temperature of the 171d DNA fragment.

For the solvent, when the temperature is 200 K, the solvent is in a glass-like state, and the molecular localized position is fixed, showing a strong tetrahedral structure. The fixed solvent structure becomes flexible at 260 K. When the temperature is between 298 and 310 K, the tetrahedral structure is maintained close to normal water. However, when the temperature rises to 343 K, the solution is close to the Lennard-Jones (LJ) liquid. In short, the solvent from the glass-like state to the water-like state, and finally to the LJ liquid, the local tetrahedral structure gradually disappears, when the temperature rise from 200 to 343 K.

Stereo views of the starting and averaged DNA structures during the last 30 ns are shown in Fig. 11.7, and the average values of inner eight base pairs are presented in Fig. 11.8. The effect of temperature changes on the microstructure of DNA, in the case of $T = 200$ K, the DNA remains in the same conformation as the original 171d, surrounded by glassy solvent. When the temperature is raised, the simulated DNA conformation is B-DNA with no apparent structural changes.

Significant structural changes occur at temperature of 343 K, DNA is an A–B hybrid structure, and the DNA structure undergoes a slight unwinding. This phenomenon is due to the fact that the temperature rise aggravates the thermal vibration of the molecules, resulting in hydrogen bonds breaks between base pairs. As shown in Fig. 11.7, when the temperature rises to 343 K, the hydrogen bond between the C-G base pairs at the terminal of DNA is broken, and the intermediate A-T base pair dose not exhibit hydrogen bond cleavage. Although the hydrogen bond number 2 of the A-T base pair is less than the hydrogen bond number 3 of the C-G base pair, the intermediate base pair A-T is more stable under the protection of the base stacking, the hydrated spine and the salt bridge.

Compared to the A form DNA in less-polar solvents as discussed above, DNA is an A–B hybrid structure at a temperature of 343 K, and has no obvious A-type structure. When the polarity of the water molecules is changed in the solvent, only the hydrogen bond strength in the water molecules is changed. However, the Na^+–O^-(P) bond strength between the Na^+ and phosphate oxygen atom does not changed, which makes the DNA appear a compact A form. And now the temperature changes not only affects the phosphate hydration, but also affects the shielding of the counter ion to the negative oxygen atom. Because of the ability of Na^+ shielding reduced, DNA only shows the mixed (A–B) state, no obvious A-DNA appears at high temperatures.

To explore the causes of temperature-induced DNA conformational changes, the distribution of sodium ions and water molecules around the DNA backbone is discussed in Fig. 11.9. For sodium ions, when the temperature is raised from 298 to 343 K, or decreased from 298 to 200 K, the coupling of sodium ions with phosphoric

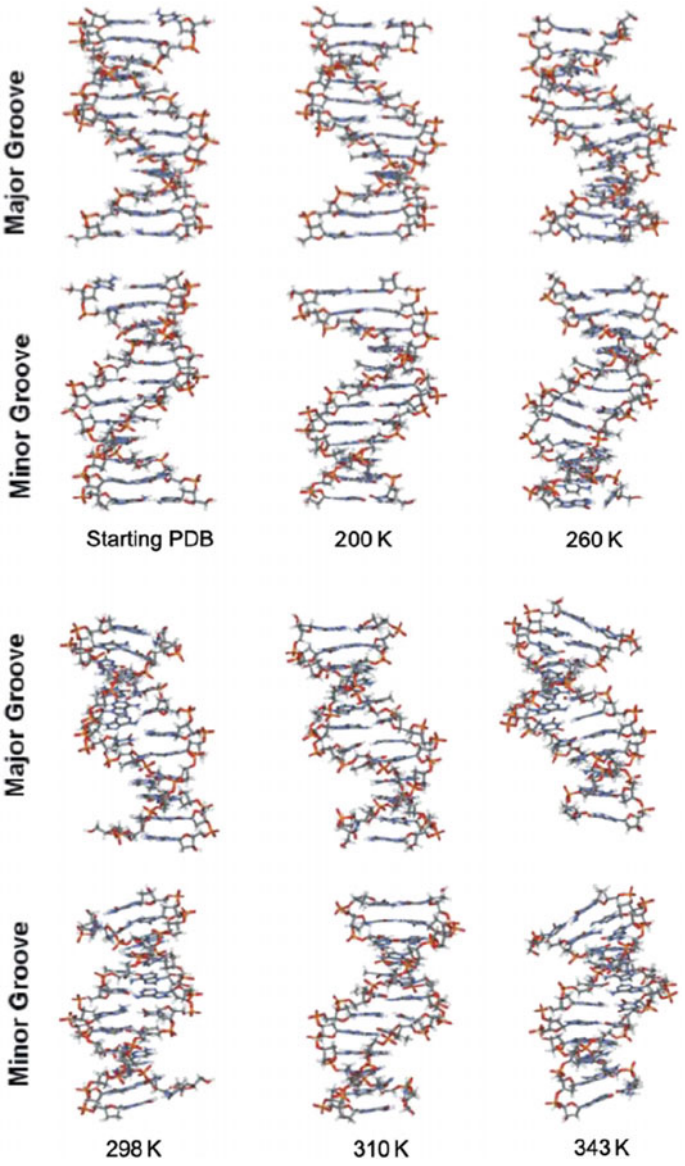

Fig. 11.7 Stereo views of the starting PDB structure and the generated configurations in different temperatures [82]

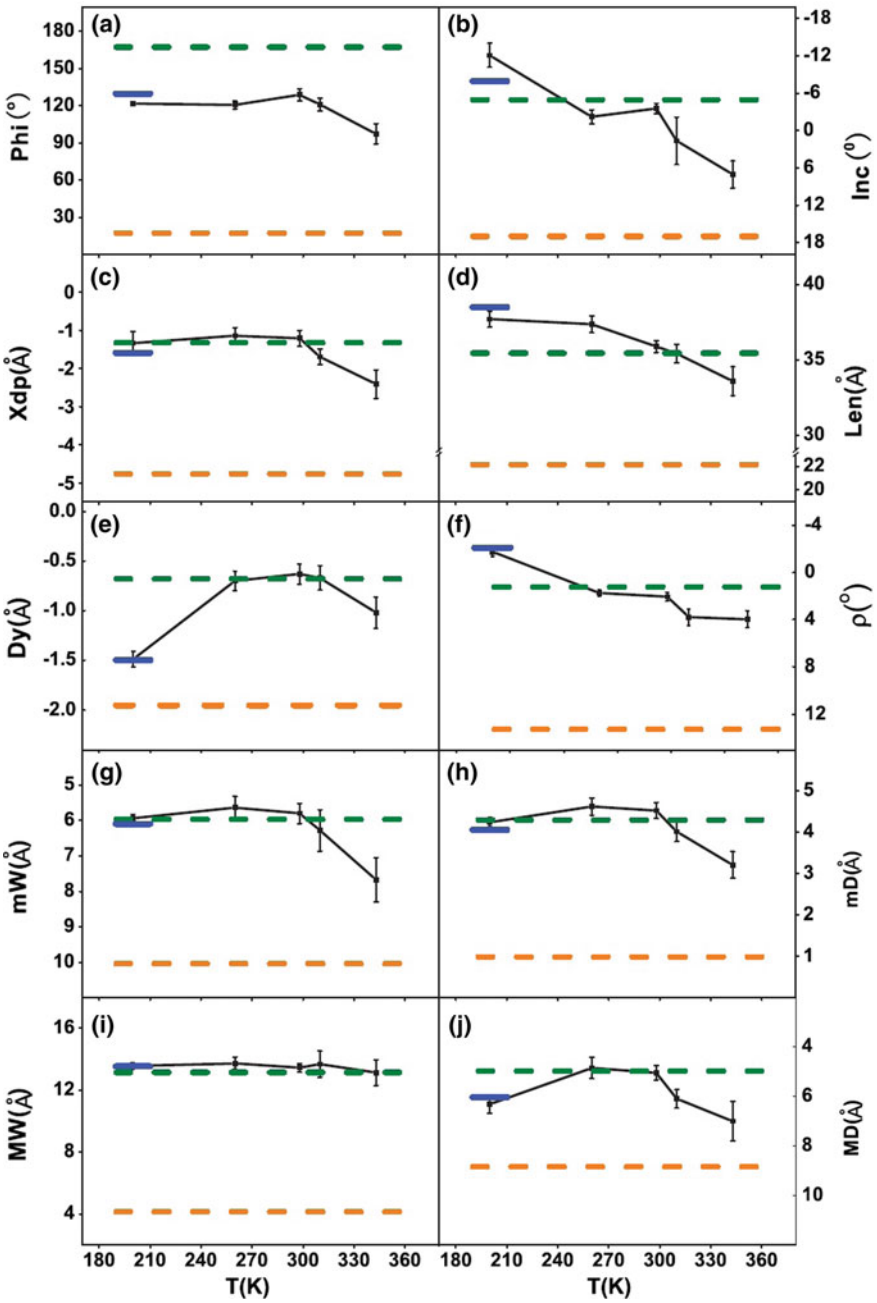

Fig. 11.8 Averaged DNA structure parameters during the last 30 ns simulations. The horizontal dashed lines indicate the reference values of type A (orange or light gray) and B (cyan or dark gray) forms and the short line shows the parameters of the starting PDB structure [82]

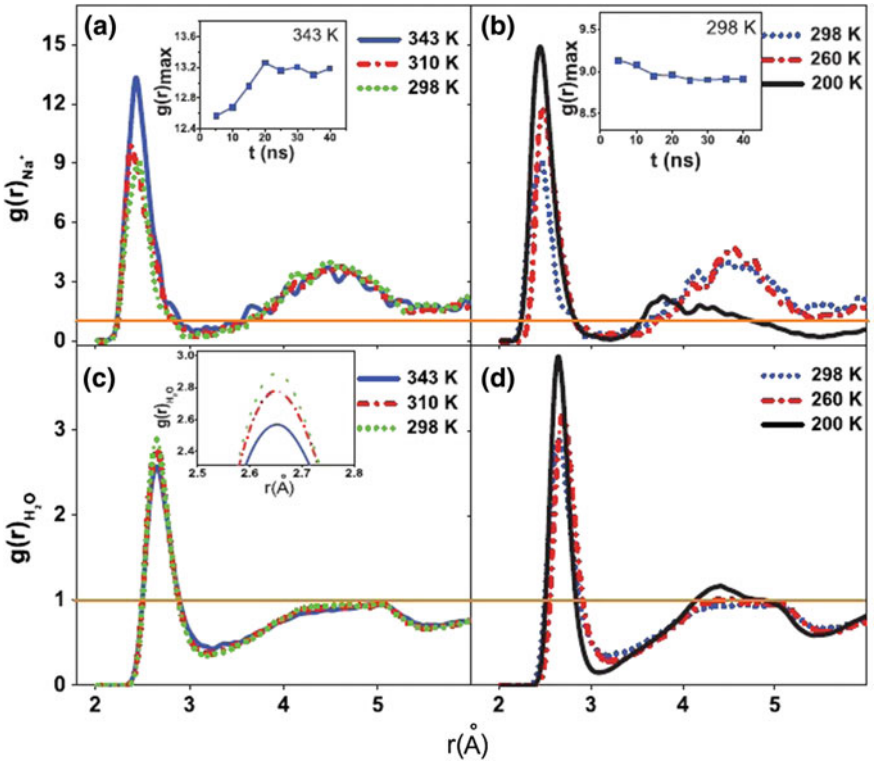

Fig. 11.9 Radial distribution functions (RDFs) of Na^+ ions (**a**), (**b**) and H_2O molecules (**c**), (**d**) around oxygen atoms of the phosphate groups on DNA backbones. The insets in (**a**) and (**b**) are maximums of the first peak of g(r) Na^+ as the function of simulation time at 343 K and 298 K, respectively. The inset in (**c**) is the local enlarging of g(r) H_2O [82]

acid oxygen atoms becomes stronger and stronger, with increasing or decreasing temperature. On the other hand, when the temperature is raised from 200 to 343 K, the distribution of water molecules around the phosphoric acid oxygen atom slightly decreases. It was found that at room temperature, DNA has the highest degree of hydration, that is, the most soluble in water. In the environment where the water molecule has a strong hydrogen bonding environment ($T < 298$ K), the original water-water molecular structure is difficult to be destroyed due to the enhancement of hydrogen bonding between solvent molecules, and the negative charge on the DNA molecule is more likely to be combined with sodium ions. However, in this case, the structure of the DNA is fixed by the glassy solvent to maintain the initial structure. As the temperature increases ($T > 298$ K), the solvent hydration capacity decreases, which makes the DNA less hydrated and tends to bind to sodium ions. The above discussion shows that DNA has the strongest solvency in water at room temperature. An increase or decrease in temperature reduces the ability of water to dissolve DNA.

A particular structure is crucial for DNA to perform its correct biological activity or any other novel function. Five temperatures (200, 260, 298, 310, 343 K) are chosen to study the environmental effect on a typical B form duplex d(CGCGAATTCGCG). With the increasing of temperature from 200 to 343 K, the structure of DNA changes from B-DNA to A–B mixed state. At 200 K, DNA was fixed at the initial PDB structure state in a glassy solvent. When $T = 260, 298$ and 310 K, the double-stranded DNA exhibits a flexible B form. At 343 K, near the melting temperature, in the Lennard-Jones-like solvent, the Na^+ ions showed a good distribution around the phosphate groups and invaded the shell of the solvent molecules. The balance between hydrogen bonding and counter-ion coupling and B-DNA becomes an intermediate mixed (A–B) structure in which the helical unwinding and base pair are open at the end of the DNA.

11.3.3 Salts and Alcohols-Induced DNA Conformational Transition

Another method to adjust the polarity and hydrogen bond strength of the solution is to mix other molecules (salts, alcohols) in proportion. When charged particles are added to the aqueous solution, the electrostatic interaction between the charged particles and the water molecules destroys the orientation of the water molecules, reducing the chance of hydrogen bonds between the water molecules, while the ions are surrounded by the hydrated layer. When neutral particles are added to an aqueous solution, the neutral particles prevent hydrogen bonding between the water molecules to form holes, and the neutral particles are confined in the holes by the van der Waals interaction. These neutral particles cluster to reduce the area of contact with water. Different solutes have a significant effect on solution polarity and hydrogen bonding.

For living system, currently about 30 elements are required, including 11 macro-elements (C, H, O, N, P, S, Cl, K, Na, Ca, Mg), three micro-elements (Fe, Zn, Cu) and 16 trace elements (F, I, Se, Si, As, B, Mn, Mo, Cr, V, Ni, Cf, Sn, Pb, Li). In this section, the polarity of the solution is changed by adding the alkali metal ions (organism necessary metal element) (Li^+, Na^+, K^+, Rb^+, Cs^+), and then the alkali metal ions induced DNA structure conversion is discussed. Normal and less polarized water model are used as the solvent to investigate Hofmeister effects and alkali mental ionic effects on dodecamer d(CGCGAATTCGCG) at room temperature.

In a normal aqueous solution, as the atomic size of the alkali metal ions increase, the distribution of the alkali metal ions in the first shell around the water molecule gradually decreases. For the secondary structure of DNA, although the distribution of alkali metal ions around DNA is different, the DNA is still in B form in normal water solution. Here, to study the effect of different alkali metal ions on DNA conformation, using the less polar water model mentioned above ($S = 0.6$), the influence of water molecules on DNA structure is weakened, and the main influencing factors are concentrated in alkali metal ions for discussion.

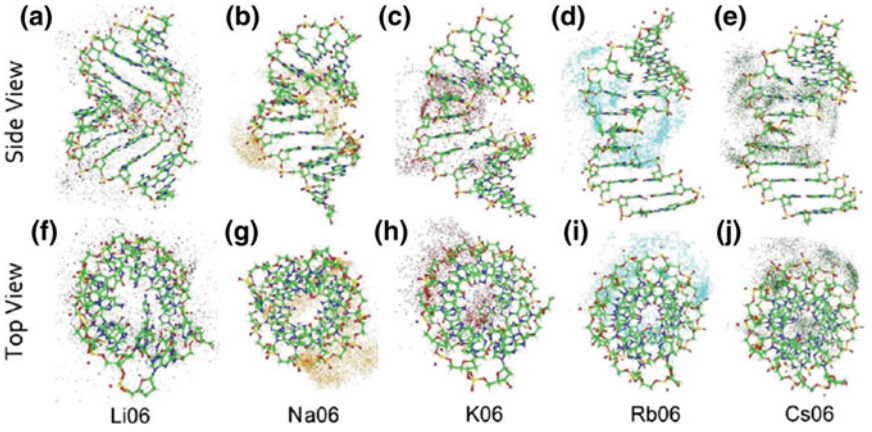

Fig. 11.10 Spatial distribution functions (SDFs) of Li^+ (black) (**a**, **f**), Na^+ (orange) (**b**, **g**), K^+ (dark grey) (**c**, **h**), Rb^+ (light blue) (**d**, **i**) and Cs^+ (dark blue) (**e**, **j**) around averaged DNA structures during the last 20 ns in less polarized solvent. The side stereo views are presented along the DNA helix axis with the minor groove at the upper half and the major groove at the lower half. SDFs of ions are drawn for densities > 10 particles/nm^3 [83]

In a less polar aqueous solution, the DNA exhibits an A form configuration in a lighter ions environment (Li^+, Na^+, K^+), while the DNA exhibits a B form conformation in a heavier ions (Rb^+, Cs^+) environment. In Fig. 11.10, spatial distribution functions (SDF) are used to study the distribution of alkali metal ions around DNA to explore the reasons for DNA conformational transitions. Li^+ ions are mainly distributed around the DNA backbone, Na^+ ions are around the intermediate phosphate backbone, and K^+ ions are distributed in the intermediate phosphate backbone and minor groove for A-DNA. For the Rb^+ ions, and Cs^+ ions concentrated in the minor groove. It can be indicated that as the mass number increases, the ionic radius raises, and the shielding of the alkali metal ions from the negative charges in the phosphate is gradually replaced by water molecules.

On the one hand, Li^+ ions, and Na^+ ions are distributed around the phosphoric acid to neutralize the Coulomb repulsion between the negative charges on the DNA backbone, at which time the DNA exhibits a A-type. On the other hand, Rb^+ ions, and Cs^+ ions are distributed in the groove to form salt bridge, and the negative charge on the DNA backbone is mainly shield by water molecules forming hydrated ridges, and the DNA exhibits form B.

For K^+ ions, Fig. 11.11 illustrates the evolution of the system over time from the initial stage to the stage of DNA structural stability. In the initial stage, around the original B-DNA, K^+ ions are mainly distributed around the phosphate group, and only a few K^+ ions are located in the minor groove. As the simulation progresses, K^+ ions are transferred to the minor groove, but part of the K^+ ions are still around the phosphoric acid, and the DNA is also converted to A-DNA. It seems that a small amount of K^+ ions can maintain stable A-DNA.

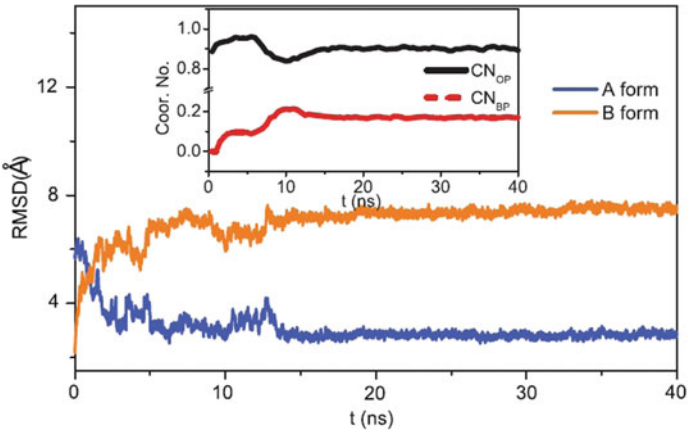

Fig. 11.11 Root mean square coordinate deviation (RMSD) of the DNA trajectories in K+ solution with respect to the canonical B (orange or light grey) and A (blue or dark gray) forms. The inset shows the changing of the coordination numbers with phosphate oxygen atoms C CNO(P) (solid line) and the coordination numbers with base pairs C CNBP (dashed line) with the simulation time in less polarised solvent [83]

Five alkali metal ions Li^+, Na^+, K^+, Rb^+, Cs^+ were used to study the effect of counter ions on the conformation of DNA in a less-polarized aqueous solution. In the less-polarized solution, as the mass number increases from Li^+ to Cs^+, the structure of the DNA becomes more and more flexible. For light ions, Li^+, Na^+, and K^+, DNA is converted from an initial conformation to a stable A-DNA during the simulation. As to Rb^+, and Cs^+ ions, the DNA remains stable B-DNA. The behaviors of K^+ ions are different with others that they both coordinate strongly with backbone and base pairs during DNA conformation transition. The competition between hydration and the ion coupling to the free phosphate oxygen atoms is dominant of the DNA conformation transitions. The Hofmeister series of alkali metal ions is $Li^+ > Na^+ > K^+ > Rb^+ > Cs^+$ in less polarized water.

In addition to alkali metal ions, alkaline earth metal ions are present in living organisms. This chapter also describes the effect of alkaline earth metal ions (Be^{2+}, Mg^{2+}, Ca^{2+}, Sr^{2+}, Ba^{2+}) on DNA conformation. Divalent alkaline earth metal ions have higher hydration in solution, and the interaction of the alkaline earth metal ions with the DNA is weaker than that of the alkali metal.

In a normal aqueous solution, as the ionic radius increases, the number of alkaline earth metal ions in the first shell around the water decreases, and the position of the first shell also moves backward, which is similar to the distribution of alkali metals in aqueous solution. However, Fig. 11.12 gives us a information that the Ba^{2+} with the weakest hydration ability in the alkaline earth metal is still stronger than the Li^+ in the alkali metal.

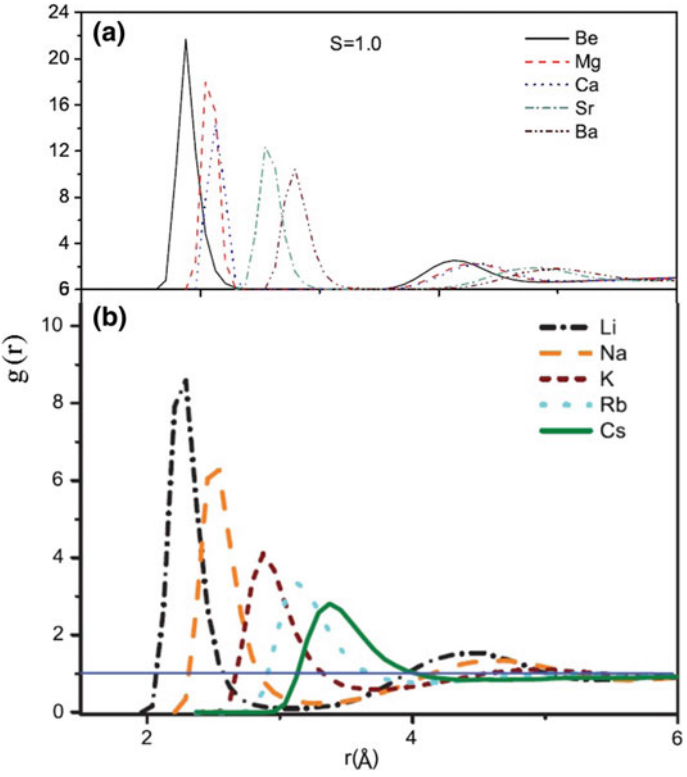

Fig. 11.12 Radial distribution functions (RDFs) of these 10 ions with solvent molecules [82, 83]

Due to the strong hydration of the alkaline earth metal ions in the normal aqueous solution, there is no direct interaction between the alkaline earth metal ions and the DNA molecules, and no DNA conformational transition occurs. Similar to the method mentioned above, the interaction of alkaline earth metal ions with DNA is studied using a sub-polarized solution ($S = 0.6$) instead of normal water. In the sub-polarized solution, due to the weakening of the hydrogen bond strength in the solution, the hydration structure around the DNA phosphate backbone and the hydrated ridge in the groove are easily destroyed by the alkaline earth metal ions, thereby causing the alkaline earth metal ions to interact with the DNA. When $S = 0.6$, in the lighter Be^{2+} ion solution, the DNA remains in the B conformation. Mg^{2+}, Ca^{2+}, and Sr^{2+} causes a shift of DNA from B to A. As for the unwinding of DNA in the Ba^{2+} solution, it will not be discussed in detail here. This trend is different from alkali metal ions.

By discovering the distribution of water molecules and alkaline earth metal ions around the DNA phosphate backbone, it is found that as the atomic number Z increases, both the distribution of water molecules and alkaline earth metal ions around the DNA phosphate cations decreases. This is in contrast to the competition between the water molecules and the alkali metal ions around the phosphate

groups in the alkali metal ions solution. The cause of this situation is that strong hydration between alkaline earth metal ions and water molecules, which makes the original water-ions interaction is difficult to destroy. In lighter ion solutions, water molecules are more likely to bind to phosphate groups. As the ionic radius raises, the hydration ability of the alkaline earth metal ions reduces. In this case, the part of alkaline earth metal ions bind to the negative valent phosphate groups in the DNA, causing a change in the conformation of the DNA from B to A. Here we can propose the sequence of the effect of alkaline earth metal ions on the conformation of DNA ($Be^{2+} < Mg^{2+} < Ca^{2+} < Sr^{2+}$) in less polarized water solution.

Here, the Hofmeister sequences between different kinds of alkali metals and alkaline earth metals in a less polarized aqueous solution are given, respectively. For alkali metals, as the ionic radius increases, the effect of ions on the DNA structure from Li^+ to Cs^+ is in the order of: $Li^+ > Na^+ > K^+ > Rb^+ > Cs^+$. As for alkaline earth metal ions, the order of ions influence on DNA conformation: $Be^{2+} < Mg^{2+} < Ca^{2+} < Sr^{2+}$. That is to say, in the alkali metal solution, as the mass number Z increases, phosphate hydration mainly occurs, and direct interaction between ions and phosphoric acid is shielded. In the alkaline earth metal solution, when heavier ions are added, the ions destroy the water molecule shell to be distributed around the DNA phosphate backbone. This opposite distribution trend is due to the strong hydration of divalent alkaline earth metal ions. Only when the mass number of the alkaline earth increases and the ion hydration is destroyed, some ions directly interact with the DNA backbone to change the DNA structure.

Unlike the addition of charged particles, the addition of alcohols can have different effects on the polarity and hydrogen bonding of the solution. Ethanol is the most common alcohols and can be mixed with water in any ratio. In a mixed solution of ethanol and water, how does the DNA configuration transform due to changes in the structure of the surrounding solution? We perform a series of simulation with the weight percent of ethanol of 0, 20, 40, 60, 80, and 95%.

The effects of different ethanol concentration on aqueous solution are discussed. The water-water, water-ethanol, and ethanol-ethanol intermolecular shell structures were enhanced with the addition of ethanol molecules in the mixed solution. When the proportion of ethanol in the solution is small, the ethanol molecules are almost completely surrounded by water. As the mass fraction of ethanol increases, the structure between the ethanol-ethanol molecules appears, but the ethanol molecules are still more likely to bind to water molecules through hydrogen bonds. However, in a solution with a large concentration of ethanol (95%), although the water-water tend to form clusters, large water clusters are not easily formed due to insufficient number of water molecules. The ethanol-ethanol intermolecular clusters increase.

Study of the conformational transformation of DNA in ethanol solution. In a 20% ethanol solution, the DNA structure changes little and remains in the B-DNA. When the mass fraction of ethanol in the solution reaches 40%, the terminals of the DNA double helix structure unwind, and the middle eight base pairs maintain the B-type structural features. In the mixed solution of 60%, the base pairs were destroyed except for the middle AATT sequence, and the middle four base pairs were present in the solution in an A-B mixed conformation. In an ethanol solution with a mass fraction

equal to or greater than 80%, due to the lack of water molecules in the solution, the DNA is in a pseudo-anhydrous environment, the hydrogen bonds between the DNA double strands are all broken, the DNA double helix structure is untwisted, which occurs denaturation.

For ethanol and water mixed solutions, the hydrogen bond strength between water molecules is enhanced with the addition of ethanol molecules. Water molecules tend to form cluster structures that are distributed around the DNA, and this cluster structure is also stabilized by the hydrogen bonding between water molecules in the solution. That is to say, the hydrated shell structure around the phosphate oxygen atom of DNA still exists and is more stable as the concentration of ethanol increases, so the direct interaction of ions with DNA is limited. When the concentration of ethanol increases to a certain range, there are not enough water molecules to maintain the hydrated structure, sodium ions enter the minor groove hydrated bridge, and the sodium ions directly interacts with the base, destroys the hydrogen bond between the base pairs. The DNA has an opportunity to change from the B conformation to the A–B mixed conformation.

The simulation results indicate the sensitivity of the DNA structure to solvent properties, and the concentration of ethanol in the solvent determines the change in DNA structure. As the concentration of ethanol increased, hydrogen bonds between DNA base pairs were broken, but A-DNA was not found in the simulation.

11.4 Conclusions

Molecular dynamics simulations have been used to study the interaction of heavy ions and DNA in liquid environments, with extreme physical environments for radiotherapy and mutation breeding. Whether as a carrier of genetic information or a basic unit of emerging molecular devices, the correct structure is the basis for the realization of DNA functions.

The transforms about DNA conformation are discussed, when the basic properties of water molecules (charge distribution and molecular structure) change. As the polarity of the solution is reduced, the order of DNA conformational changes is: B form—(A–B) mix—A form. During the interaction of DNA with some proteins or RNA, some parts of DNA molecules will have a relatively stable (A–B) mixed state [77]. Analysis shows that ionic coupling and solvent hydration screen the negative charge on the phosphate group in two different ways, thereby achieving the effect of regulating the internal electrostatic interaction of the DNA double strand. The competition between these two different mechanisms is an important reason for the conformational transformation of DNA molecules.

Different environmental conditions—temperatures (200, 260, 298, 310, 343 K) are used to study the effects of hydrogen bonding thermodynamic fluctuations on a typical B form duplex d(CGCGAATTCGCG). At 200 K, DNA was fixed at the initial PDB structure state in a glassy solvent. When $T = 260$, 298 and 310 K, the double-stranded DNA exhibits a flexible B form. At 343 K, near the melting temperature, in

the Lennard-Jones-like solvent, the Na^+ ions showed a good distribution around the phosphate groups and invaded the shell of the solvent molecules. The balance between hydrogen bonding and counter-ion coupling and B-DNA becomes an intermediate mixed (A–B) structure in which the helical unwinding and base pair are open at the end of the DNA.

Another method of adjusting the polarity and the hydrogen bond strength of the solution by mixing other molecules (salts, alcohols) in proportion was studied. In the less-polarized solution, as the mass number increases from Li^+ to Cs^+, the structure of the DNA becomes more and more flexible. For light ions, Li^+, Na^+, and K^+, DNA is converted from an initial conformation to a stable A-DNA during the simulation. As to Rb^+, and Cs^+ ions, the DNA remains stable B-DNA. The competition between hydration and the ion coupling to the free phosphate oxygen atoms is dominant of the DNA conformation transitions. The Hofmeister series of alkali metal ions is $Li^+ > Na^+ > K^+ > Rb^+ > Cs^+$ in less polarized water. As for alkaline earth metal ions, the order of ions influence on DNA conformation: $Be^{2+} < Mg^{2+} < Ca^{2+} < Sr^{2+}$. This opposite distribution trend is due to the strong hydration of divalent alkaline earth metal ions. Only when the mass number of the alkaline earth increases and the ion hydration is destroyed, some ions directly interact with the DNA backbone to change the DNA structure.

For neutral particles, the addition of ethanol have different effects on the polarity and hydrogen bonding of the solution. The hydrogen bond strength between water molecules is enhanced with the addition of ethanol molecules. Water molecules tend to form cluster structures that are distributed around the DNA, and this cluster structure is also stabilized by the hydrogen bonding between water molecules in the solution. When the concentration of ethanol increases to a certain range, there are not enough water molecules to maintain the hydrated structure, sodium ions enter the minor groove hydrated bridge, and the sodium ions directly interacts with the base, destroys the hydrogen bond between the base pairs. The DNA has an opportunity to change from the B conformation to the A–B mixed conformation.

Acknowledgements Thanks to Prof. L. Bulavin, N. Atamas, and K. Cherevko for the fruitful discussions. This work was supported by the National Natural Science Foundation of China under Grants No. 11635003, No. 11025524, No. 11161130520, the National Basic Research Program of China under Grant No. 2010CB832903, and the European Commission's 7th Framework Programme (Fp7-PEOPLE-2010-IRSES) under Grant Agreement Project No. 269131.

References

1. J. Ferlay, I. Soerjomataram, M. Ervik, R. Dikshit, S. Eser, C. Mathers et al., in *GLOBOCAN 2012 v1.0, Cancer Incidence and Mortality Worldwide: IARC CancerBase No. 11* (International Agency for Research on Cancer, Lyon, France, 2013). http://globocan.iarc.fr. Accessed 1 Oct 2018
2. *Global Health Observatory: The Data Repository* (World Health Organization, Geneva, 2017). http://www.who.int/gho/database/en. Accessed 1 Oct 2018
3. *Guide to Cancer Early Diagnosis* (World Health Organization, Geneva, 2017), pp. 4–8

4. E.C. Halperin, C.A. Perez, L.W. Brady, *Perez and Bradys Principles and Practice of Radiation Oncology*, 5th edn. (Lippincott Williams and Wilkins, Philadelphia, 2007)
5. E. Rosenblatt, E. Zubizarreta, *Radiotherapy in Cancer Care: Facing the Global Challenge* (International Atomic Energy Agency, Vienna, 2017), pp. 43–54
6. M. Brada, M. Pijls-Johannesma, D. De Ruysscher, J. Clin. Oncol. **25**, 965–970 (2007)
7. D. Schultz-Ertner, H. Tsujii, J. Clin. Oncol. **25**, 953–964 (2007)
8. T. Okada, T. Kamada, H. Tsuji, J.E. Mizoe, M. Baba, S. Kato, S. Yamada, S. Sugahara, S. Yasuda, N. Yamamoto, R. Imai, A. Hasegawa, H. Imada, H. Kiyohara, K. Jingu, M. Shinoto, H. Tsujii, J. Radiat. Res. **51**, 355–364 (2010)
9. R.M. Abolfath, P.K. Biswas, R. Rajnarayanam, T. Brabec, R. Kodym, L. Papiez, J. Phys. Chem. A **116**, 3940 (2012)
10. F. Merzel, F. Fontaine-Vive, M.R. Johnson, G.J. Kearley, Phys. Rev. E **76**, 031917 (2007)
11. D.A. Smirnov, M. Morley, E. Shin, R.S. Spielman, V.G. Cheung, Nature **459**, 587 (2009)
12. J. Rak, L. Chomicz, J. Wiczk, K. Westphal, M. Zdrowowicz, P. Wityk, M. Zyndul, S. Makurat, Ł. Golon, J. Phys. Chem. B **119**, 8227 (2015)
13. Z. L. Yu, Y. D. Yu, T. Vilaithong, *Introduction to Ion Beam Biotechnology* (trans. I.G. Brown) (Springer Science and Business Media Inc., New York, 2006)
14. P. Bennett, A.A. Ishchenko, J. Laval, B. Paap, B.M. Sutherland, Free Radic. Biol. Med. **45**, 1352–1359 (2008)
15. E. Gollapalle, R. Wang, R. Adetolu, D. Tsao, D. Francisco, G. Sigounas, A.G. Georgakilas, Radiat. Res. **167**, 207–216 (2007)
16. D.T. Goodhead, Int. J. Radiat. Biol. **61**, 7–17 (1994)
17. W.K. Pogozelski, T.D. Tullius, Chem. Rev. **98**, 1089 (1998)
18. T.D. Tullius, J.A. Greenbaum, Curr. Opin. Chem. Biol. **9**, 127 (2005)
19. B. Aydogan, W.E. Bolch, S.G. Swarts, J.E. Turner, T. David, Radiat. Res. **169**, 223 (2008)
20. W. Friedl, P. Jacob, H.G. Paretzke, M. Merzagora, A. Ottolenghi, Radiat. Environ. Biophys. **38**, 39 (1999)
21. R.M. Abolfath, P.K. Biswas, R. Rajnarayanam, T. Brabec, R. Kodym, L. Papiez, J. Phys. Chem. A **116**, 3940 (2012)
22. F. Merzel, F. Fontaine-Vive, M.R. Johnson, G.J. Kearley, Phys. Rev. E **76**, 031917 (2007)
23. W.K. Weyrather, G. Kraft, Radiother. Oncol. **73**, S161–CS169 (2004)
24. T. De Laney, H.M. Kooy, *Proton and Charged Particle Radiotherapy* (Lippincott Williams and Wilkins, Philadelphia, 2007)
25. B.M. Sutherland, P.V. Bennett, H. Schenk, O. Sidorkina, J. Laval, J. Trunk, D. Monteleone, J. Sutherland, Phys. Med. **17**, 202–204 (2001)
26. H. Terato, R. Tanaka, Y. Nakaarai, T. Nohara, Y. Doi, S. Iwai, R. Hirayama, Y. Furusawa, H. Ide, J. Radiat. Res. **49**, 133–46 (2008)
27. M. Hada, A.G. Georgakilas, J. Radiat. Res. **49**, 203–10 (2008)
28. A. Chatterjee, W.R. Holley, Adv. Space Res. **12**, 33–43 (1992)
29. N. Denko, A. Giaccia, B. Peters, T.D. Stamato, Anal. Biochem. **178**, 172–6 (1989)
30. G.E. Iliakis, L. Metzger, N. Denko, T.D. Stamato, Int. J. Radiat. Biol. **59**, 321–41 (1991)
31. D. Wlodek, J. Banath, P.L. Olive, Int. J. Radiat. Biol. **60**, 779–C90 (1991)
32. B.M. Sutherland, P.V. Bennett, O. Sidorkina, J. Laval, Proc. Natl. Acad. Sci. USA **97**, 103–8 (2000)
33. P.D. Dans, J. Walther, H. Gómez, M. Orozco, Curr. Opin. Struc. Biol. **37**, 29–45 (2015)
34. E. Lindahl, B. Hess, D. van der Spoel, Mol. Model. **7**, 306 (2001)
35. I. Barry, T. Mikita, G.W. Kellogg, K.H. Gardner, G.P. Beardsley, Biochemistry **33**, 11460 (1994)
36. P.D. Dans, L. Danilāne, I. Ivani, T. Dršata, F. Lankaš, A. Hospital, J. Walther, R.I. Pujagut, F. Battistini, J.L. Gelpí, R. Lavery, M. Orozco, Nucl. Acids Res. **44**, 4052 (2016)
37. A. Pérez, F.J. Luque, M. Orozco, J. Am. Chem. Soc. **129**, 14739 (2007)
38. T. Dršata, A. Pérez, M. Orozco, A.V. Morozov, J. Šponer, F. Lankaš, J. Chem. Theory Comput. **9**, 707 (2013)
39. H.J.C. Berendsen, R.J. Grigera, T.P. Straatsma, J. Phys. Chem. **91**, 6269–C6271 (1987)

40. I. Ivani, P.D. Dans, A. Noy, A. Pérez, I. Faustino, A. Hospital, J. Walther, P. Andrio, R. Goñi, A. Balaceanu, G. Portella, F. Battistini, J.L. Gelpí, C. González, M. Vendruscolo, C.A. Laughton, S.A. Harris, D.A. Case, M. Orozco, Nat. Methods **13**, 55 (2016)
41. T. Darden, D. York, L. Pedersen, J. Chem. Phys. **98**, 10089 (1993)
42. M.P. Allen, D.J. Tildesley, *Computer Simulation of Liquids* (Oxford University Press, 1989)
43. B. Hess, H. Bekker, H.J.C. Berendsen, J.G.E.M. Fraaije, J. Comput. Chem. **18**, 1463 (1997)
44. A.D. MacKerell, L. Nilsson, Curr. Opin. Struct. Biol. **18**, 194 (2008)
45. N. Huang, A.D. MacKerell Jr., J. Mol. Biol. **345**, 265 (2005)
46. Y. Qi, M.C. Spong, K. Nam, A. Banerjee, S. Jiralerspong, M. Karplus, G.L. Verdine, Nature **462**, 762 (2009)
47. E. Cubero, F.J. Luque, M. Orozco, Biophys. J. **90**, 1000 (2006)
48. B.N. Conner, T. Takano, S. Tanaka, K. Itakura, R.E. Dickerson, Nature (London) **295**, 294 (1982)
49. A.H. Wang, G.J. Quigley, F.J. Kolpak, J.L. Crawford, J.H. van Boom, G. van der Marel, A. Rich, Nature (London) **282**, 680 (1979)
50. A. Noy, A. Perez, C.A. Laughton, M. Orozco, Nucl. Acids Res. **35**, 3330 (2007)
51. M.A. Kastenholz, T.U. Schwartz, P.H. Hunenberger, Biophys. J. **91**, 2976 (2006)
52. R. Lavery, M. Moakher, J.H. Maddocks, D. Petkeviciute, K. Zakrzewska, Nucl. Acids Res. **37**, 5917 (2009)
53. R. Lavery, H. Sklenar, J. Biomol. Struct. Dyn. **6**, 655 (1989)
54. R. Lavery, J.H. Maddocks, M. Pasi, K. Zakrzewska, Nucl. Acids Res. **42**, 8130 (2014)
55. P.D. Dans, I. Faustino, F. Battistini, K. Zakrzewska, R. Lavery, M. Orozco, Nucl. Acids Res. **42**, 11304 (2014)
56. M. Pasi, J.H. Maddocks, R. Lavery, Nucl. Acids Res. **43**, 2412 (2015)
57. M. Chaplin, Nat. Rev. Mol. Cell Bio. **7**, 861 (2006)
58. L.J. Rothschild, R.L. Mancinelli, Nature **409**, 1092 (2001)
59. P. Ball, Chem. Rev. **108**, 74 (2008)
60. Y. Levy, J.N. Onuchic, Annu. Rev. Biophys. Biomol. Struct. **35**, 389 (2006)
61. R.M. Abolfath, A.C.T. van Duin, T. Brabec. J. Phys. Chem. A **115**, 11045 (2011)
62. P. Ball, Nature **436**, 1084 (2005)
63. B. Gu, F.S. Zhang, Z.P. Wang, H.Y. Zhou, Phys. Rev. Lett. **100**, 088104 (2008)
64. E. Arunan, G.R. Desiraju, R.A. Klein, J. Sadlej, S. Scheiner, I. Alkorta, D.C. Clary, R.H. Crabtree, J.J. Dannenberg, P. Hobza, H.G. Kjaergaard, A.C. Legon, B. Mennucci, D.J. Nesbitt, Pure Appl. Chem. **83**, 1619 (2011)
65. D. Chandler, Nature **437**, 640 (2005)
66. J.R. Errington, P.G. Debenedetti, Nature **409**, 318 (2001)
67. H.J. Bakker, J.L. Skinner, Chem. Rev. **110**, 1498 (2010)
68. E.T.J. Nibbering, T. Elsaesser, Chem. Rev. **104**, 1887 (2004)
69. D. Kraemer, M.L. Cowan, A. Paarmann, N. Huse, E.T.J. Nibbering, T. Elsaesser, R.J.D. Miller, Natl. Acad. Sci. USA **105**, 437 (2008)
70. W. Saenger, *Principles of Nucleic Acid Structure* (Springer, New York, 1984)
71. B. Jayaram, D. Sprous, M.A. Young, D.L. Beveridge, J. Am. Chem. Soc. **120**, 10629 (1998)
72. W. Saenger, W.N. Hunter, O. Kennard, Nature (London) **324**, 385 (1986)
73. K.J. McConnell, D.L. Beveridge, J. Mol. Biol. **304**, 803 (2000)
74. A. Madhumalar, M. Bansal, Biophys. J. **85**, 1805 (2003)
75. D. Jose, D. Porschke, J. Am. Chem. Soc. **127**, 16120 (2005)
76. P. Auffinger, E. Westhof, J. Mol. Biol. **300**, 1113 (2000)
77. R. Rohs, S.M. West, A. Sosinsky, P. Liu, R.S. Mann, B. Honig, Nature (London) **461**, 1248 (2009)
78. M.R. Li, N. Zhang, F.S. Zhang, J. Mol. Liq. https://doi.org/10.1016/j.molliq.2018.08.129
79. S.J. Suresh, V.M. Naik, J. Chem. Phys. **113**, 9727–C9732 (2000)

80. R. Ludwig, Phys. Chem. Chem. Phys. **4**, 5481 (2002)
81. N. Yoshii, S. Miura, S. Okazaki, Chem. Phys. Lett. **345**, 195–C200 (2001)
82. X. Shen, B. Gu, S.A. Che, F.S. Zhang, J. Chem Phys. **135**, 34509 (2011)
83. J. Wen, X. Shen, H. Shen, F.S. Zhang, Mol. Phys. **112**, 2707–2719 (2014)

Chapter 12
Radiative Aspects in Physics of Liquid Matter: Stable Magnetic Isotopes as New Trend in Anti-radiation Defense

V. K. Koltover

Abstract Once atomic power engineering has become a part of our everyday life; the special precautions should be taken to defend the people in case of chronic radiation. Novel anti-radiation protectors are required which would be non-toxic and suited to long-time applications. Of special interest, can be stable magnetic isotopes of some chemical elements which normally present in living nature. The so-called magnetic isotope effects (MIEs) have long been known in physics of liquid matter. Not long ago, MIEs were discovered in the experiments with living cells. In this review, I present the experimental results of our research group on searching in this direction. The striking effect of the magnetic isotope of magnesium, ^{25}Mg, has been revealed in the studies of post-radiation recovery of yeast cells irradiated by short UV light or ionizing radiation. The post-radiation recovery of the cells enriched with ^{25}Mg proceeds two times faster than the post-radiation recovery of the cells enriched with the nonmagnetic magnesium isotope. Furthermore, the striking beneficial effects of the magnetic ^{25}Mg were found in experiments with the isolated enzymes, muscle myosin and mitochondrial H^+-ATPase, the most important biomolecular motors of cell bioenergetics. A similar effect, i.e., the acceleration of chemo-mechanical cycle of myosin by the nuclear spin, has been discovered in experiments with the magnetic isotope of zinc, ^{67}Zn. Although physical mechanisms of the nuclear spin catalysis in molecular liquids and biomolecular nanoreactors require further investigations, there are the grounds to believe that pharmaceutical agents enriched with the magnetic isotopes will find use for creating novel anti-radiation protectors.

List of Abbreviations

MIE magnetic isotope effect,
ATP adenosine 5′-triphosphate,

V. K. Koltover (✉)
Institute of Problems of Chemical Physics, Russian Academy of Sciences, Chernogolovka, Moscow Region 142432, Russian Federation
e-mail: koltover@icp.ac.ru

L. A. Bulavin and L. Xu (eds.), *Modern Problems of the Physics of Liquid Systems*, Springer Proceedings in Physics 223,
https://doi.org/10.1007/978-3-030-21755-6_12

ADP adenosine 5′-diphosphate,
P_i inorganic phosphate

12.1 Introduction

Since the middle of last century, atomic power engineering has become a part of our everyday lives. Atomic catastrophes, like the catastrophes in Windscale (England, 1957), Three Mile Island (USA, 1979), Chernobyl (Ukraine, 1986), and Fukushima (Japan, 2011) may result from this kind of man's activity. Therefore, special precautions should be taken to reduce the harmful effects of radiation for specialists in atomic industry as well as for people in the contaminated territories. For emergency use, in the event of acute radiation, there are effective radio-protectors based on the biologically active amines and aminothiols [1, 2]. However, these compounds are rather toxic. To defend the people in case of chronic low-dose radiation, alternative drugs are required, which would be non-toxic and suited to long-time applications as nutrients.

In this regard, for preventive maintenance against radiation stress, some stable magnetic isotopes can be of interest as the basis of novel anti-stress medicine. There is a great variety of chemical elements which have both kinds of stable isotopes, nonmagnetic and magnetic, among them—carbon, oxygen, magnesium, calcium, iron, zinc, etc. For example, there are three stable isotopes of magnesium, ^{24}Mg, ^{25}Mg and ^{26}Mg with natural abundance, correspondingly, 78.7, 10.13 and 11.17%. Among them, only ^{25}Mg is magnetic one since it has the nuclear spin ($I = 5/2$) that produces the magnetic field. Two other Mg isotopes are non-magnetic since they are spinless ($I = 0$) and, hence, produce no magnetic fields [3]. Meanwhile, as one of the most abundant intracellular divalent ions, Mg^{2+} is the obligate cofactor of numerous cellular enzymes. Among the Mg-dependent enzymes, there are the enzymes of synthesis of ATP, the main source of energy in cells and tissues, and the enzymes which use the ATP energy, including the so-called "molecular motors" (see in [4]). Another important cell element, zinc, has five stable isotopes, ^{64}Zn, ^{66}Zn, ^{67}Zn, ^{68}Zn and ^{70}Zn with natural abundance 48.6, 27.9, 4.1, 18.8 and 0.6 atomic percents, from which ^{67}Zn is magnetic ($I = 5/2$) while the other isotopes are nonmagnetic [3]. The zinc ion, Zn^{2+}, serves as the cofactor for DNA-polymerase *I*, superoxide dismutase (Cu, Zn-SOD), carboanhydrase, performs the regulatory functions as the Zn-transcription factor ("zinc fingers") along with the signaling and redox-regulation functions in the cells [4].

Here, I present a review of the results on searching in this direction. In part, it has been revealed, the first time in the world, that the post-radiation recovery of the cells, enriched with ^{25}Mg, proceeds almost two times faster than the post-radiation recovery of the cells, enriched with the nonmagnetic magnesium isotope. Although physical mechanisms of the nuclear spin catalysis in molecular liquids and

biomolecular nanoreactors require further investigations, there are the grounds to believe that pharmaceutical agents enriched with the magnetic isotopes will find use in medicine for creating novel anti-radiation protectors, low toxic and suitable for the long-term use.

12.2 Magnetic-Isotope Effects in Post-radiation Recovery of Living Cells

The magnetic-isotope effects in living nature have been revealed, for the first time, in experiments with commonly accepted cell model, yeast cells *Saccharomyces cerevisiae* [5–7]. The experiments were performed in collaboration with Department of Radiation Biology of Institute of Cell Biology and Genetic Engineering, NAS of Ukraine, Kyiv (Ukraine) and Department of Molecular and Radiation Biology of Petersburg Institute of Nuclear Physics—National Research Center "Kurchatov Institute", Leningrad Region (Russia). In order to search for magnetic isotope effects, we developed procedures for growing living cells in a medium containing only one magnesium isotope, either the magnetic ^{25}Mg or the nonmagnetic ^{24}Mg, as $^{25}MgSO_4$ or $^{24}MgSO_4$, correspondingly.

Figure 12.1 represents the experimental data on influence of the different isotopes of magnesium on the kinetics of recovery of cells after irradiation with the short-wave UV light (λ = 240–260 nm). Survival of the cells transferred to nutrition agar immediately after irradiation was no more than a few percent. Upon getting so

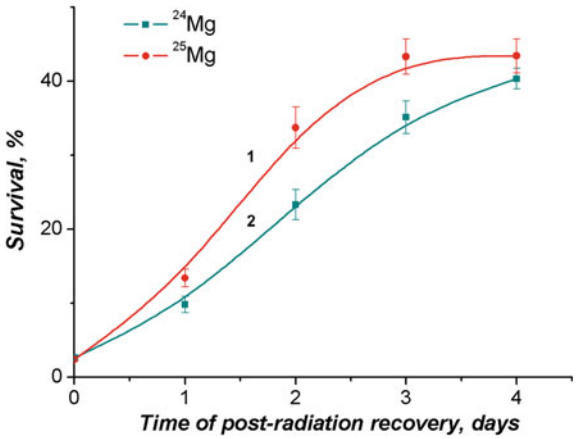

Fig. 12.1 Effects of different isotopes of magnesium, magnetic ^{25}Mg and nonmagnetic ^{24}Mg, on the post-radiation recovery of yeast cells, *S. cerevisiae*, after irradiation with the short-wave UV light (λ = 240–260 nm). Survival of the cells was estimated as the ability to form colonies on nutrition agar: 1—recovery of the cells enriched with ^{25}Mg; 2—recovery of the cells enriched with ^{24}Mg (compiled from [6, 7])

high radiation dose, most of the cells do not succeed to repair the injured genetic structures before mitosis and, as a result, the nonviable daughter cells are produced. Incubation in the nutrient-free media, in which the cells do not divide, provides them with more sufficient time for the repair processes and leads to the corresponding increase in survival. From the kinetics curves represented on this figure, one can see that the cells enriched with the magnetic isotope, ^{25}Mg, are recovered essentially more effectively than the cells enriched with the nonmagnetic ^{24}Mg. It was found that the recovery rate constant was 0.058 ± 0.004 h^{-1} for the cells enriched with ^{25}Mg and almost twice less, 0.032 ± 0.003 h^{-1}, for the cells enriched with ^{24}Mg (the difference between the means is statistically significant (the level of significance, $P = 0.02$). Thus, we have, for the first time, documented the magnetic-isotope effect in radiation biology [5–7].

Similar results have been recently obtained in studies of post-radiation recovery of the yeast cells irradiated by the ionizing radiation [8]. Two independent experimental sessions with three samples simultaneously tested for every kind of the isotope in the same experimental succession ($N = 3$) were performed. Figure 12.2 represents the kinetics of the post-radiation recovery. Table 12.1 represents the values of the kinetics parameters resulting from these experiments. One can see that the recovery

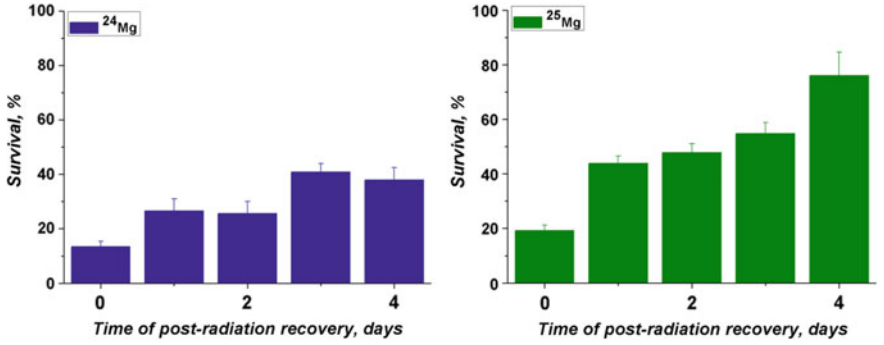

Fig. 12.2 Kinetics of the post-radiation recovery of yeast cells, *S. cerevisiae*, enriched with different isotopes of magnesium, magnetic ^{25}Mg or nonmagnetic ^{24}Mg, after ionizing irradiation (300 Gy). Survival of the cells was estimated as their ability to form colonies on nutrition agar: Left—recovery of the cells enriched with ^{25}Mg; Right—recovery of the cells enriched with ^{24}Mg [8]

Table 12.1 Kinetics parameters of the post-radiation recovery of yeast cells, *S. cerevisiae*, enriched with different isotopes of magnesium, magnetic ^{25}Mg or nonmagnetic ^{24}Mg, after ionizing irradiation (300 Gy) [8]

	β, h^{-1}	k
^{24}Mg	0.029 ± 0.003	0.81 ± 0.15
^{25}Mg	0.050 ± 0.004[a]	0.50 ± 0.17[b]

[a]The difference of the means for ^{25}Mg versus ^{24}Mg is statistically significant at $P = 0.02$
[b]The difference of the means for ^{25}Mg versus ^{24}Mg is statistically significant at $P = 0.5$

rate constant (β) is almost twice higher for the cells, enriched with the magnetic ^{25}Mg, than for the cells, enriched with the nonmagnetic ^{24}Mg. Besides, the fraction of the irreversible damages (k) after irradiation in the cells, enriched with ^{25}Mg, was about 60% less than in the cells, enriched with ^{24}Mg.

It might be suggested that the magnetic-isotope effects resulted from the differences in the levels of impurities in the growth media complemented with the different isotopes of magnesium, rather than the nuclear spin of ^{25}Mg. However, the possible influence of any trace elements is excluded by the data of analysis of the samples by atomic emission spectrometry and high-resolution mass spectrometry. It should be appreciated that not only magnesium oxides but other reagents required for experiments contain impurities which are introduced into the growth medium and other experimental media. Moreover, the amount of impurities coming from the main components is significantly greater than the amount of the same impurities coming into the medium with the different magnesium isotopes. Besides, it is also important that the impurities of the main components are added to each of the experimental media in the same amounts irrespective of the magnesium isotope contained in the medium. Hence, one can disregard impurities as a possible reason of the effect of acceleration of the post-radiation recovery of the cells enriched with magnetic ^{25}Mg.

Thus, the cells perceive the difference between magnetic and non-magnetic isotopes of magnesium. The enrichment of cells with the magnetic isotope gives the two-fold acceleration of the post-radiation recovery. In other words, the effect of nuclear spin catalysis has been discovered in the cited experiments [5–8].

12.3 Magnetic Isotope Effects in Biomolecular Motors

It is generally known that the main source of energy in cell bioenergetics is adenosine triphosphate (ATP) [4]. It is also generally known that Mg^{2+} serves the cofactor functions for the enzymes, biomolecular "fuel-energy nanoreactors", which perform the reactions of the ATP synthesis and hydrolysis [4]. Therefore, it was reasonable to suggest that the MIEs, which were discovered in the experiments with living cells, are stemming from the higher efficiency of the "fuel-energy nanoreactors" in the cells enriched with magnetic isotope of magnesium.

One of the most studied "molecular motors" is the muscle protein myosin. This Mg^{2+}-dependent enzyme provides the hydrolysis of the terminal phosphate bond in the ATP molecule: $ATP + H_2O \rightarrow ADP + P_i$. The energy released therewith (~0.54 eV under physiological conditions) is used to carry out the work—muscle contraction. The ATPase activity of myosin obligatorily depends on the presence of the Mg^{2+} ions required for ATP binding in the active site of the enzyme and playing the significant role in catalysis of ATP hydrolysis [4].

We studied effects of the different magnesium isotopes, magnetic ^{25}Mg and non-magnetic ^{24}Mg and ^{26}Mg, on Mg^{2+}-dependent ATP hydrolase activity of the catalytic fragment (subfragment-1) of myosin isolated from myometrium muscle [9–11]. The experiments were performed in cooperation with our Ukrainian colleagues in

Department of Muscle Biochemistry, A.V. Palladin Institute of Biochemistry, NAS of Ukraine, Kyiv. Myosin subfragment-1 is considered as the sufficiently functional unit of myosin since it possesses all native functional properties of myosin, namely, the ATPase activity and ability to interact with actin. Three independent experiments have been performed with three enzyme preparations isolated from three different animals (pigs) at different times.

Figure 12.3 shows the results of our experiments on the effect of different magnesium isotopes on ATPase activity of myosin subfragment 1. Several series of independent experiments with the enzyme isolated from smooth muscles of pigs at different times were carried out. Despite the variability in average values of the ATPase activity from one experimental series to the other, the same effect was observed in all experimental series. Namely, the enzyme activity in the presence of the magnetic isotope, ^{25}Mg, was 2.0–2.5 times higher than the activity of the same enzyme in the presence of the nonmagnetic isotopes, ^{24}Mg or ^{26}Mg, or the activity in the presence of a natural mixture of the magnesium isotopes. At the same time, no significant differences in activity were found in the case of nonmagnetic isotopes ^{24}Mg and ^{26}Mg. The effect is observed at physiological concentrations of magnesium chloride (5 mM). It is important to note that, in spontaneous ATP hydrolysis, i.e., in the absence of the enzyme, the magnetic isotope effect is not observed [9–11].

Furthermore, the effects of different isotopes of zinc on the ATP hydrolyze activity of the myosin subfragment-1 have been studied in two independent experiments with different enzyme preparations isolated from two different animals [11]. The same standard reaction media were used but supplemented with different isotopes of zinc, the magnetic isotope, ^{67}Zn, or the nonmagnetic isotopes, ^{64}Zn or ^{68}Zn, i.e., 5 mM of $^{67}ZnCl_2$ or $^{64}ZnCl_2$ or $^{68}ZnCl_2$, correspondingly. It has been found that ions of Zn^{2+}

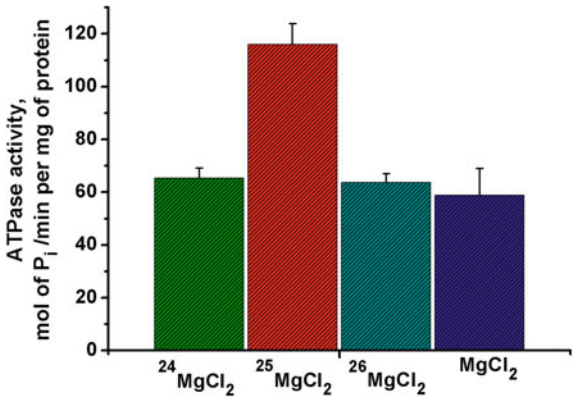

Fig. 12.3 Enzyme hydrolysis of ATP driven by the myosin subfragment-1 in the reaction solutions supplemented with different isotopes of magnesium. The rate of ATP hydrolysis was measured at 37 °C by the method of Fiske-Subbarow in the standard reaction solutions which contained 5 mM of $^{24}MgCl_2$, $^{25}MgCl_2$, $^{26}MgCl_2$ or $MgCl_2$ of the natural isotope abundance, The data are represented as mean values ± standard deviations ($m \pm SD$). The differences of the means for ^{25}Mg versus ^{24}Mg, or ^{26}Mg, or natural $MgCl_2$ are statistically significant at $P \leq 0.01$ (compiled from [9, 10])

perform the cofactor function less efficiently than ions of Mg^{2+}. However, the rate of the enzymatic ATP hydrolysis with ^{67}Zn has turned out to be 50–70% higher as compared to the nonmagnetic ^{64}Zn or ^{68}Zn (Fig. 12.4).

Next picture, Fig. 12.5, represents the results of the comparative studies of effects of different isotopes of magnesium on hydrolysis of ATP catalyzed by another important "molecular motor" of cell bioenergetics, the mitochondrial H^+-ATP hydrolase [12]. The experiments were performed in the Institute of Physical Chemistry, University of Freiburg, Freiburg (Germany). The enzyme, the so-called MF_0F_1 complex) was isolated from mitochondria of yeast cells, *S. cerevisiae*, and reconstituted into the liposome membrane ("proteoliposome"), as described in [13]. In order to eliminate initial $MgCl_2$ from the enzyme liposome complexes, they were pellet by centrifugation and then precipitated in the standard reaction solutions supplemented with 2.5 mM, 4 mM or 15 mM of $MgCl_2$ of different Mg-isotopes, as $^{24}MgCl_2$ or $^{25}MgCl_2$ or $MgCl_2$ of natural isotope abundance. To measure the ATP hydrolysis, ATP was added in the reaction solutions.

No MIEs have been found at physiological concentrations of $MgCl_2$. Obviously, there was not sufficient isotope replacement at 2.5 mM or 4 mM of $^{25}MgCl_2$. However, the small but statistically significant MIE has been revealed at 15 mM of $^{25}MgCl_2$. Namely, it was found that the initial rate of ATP hydrolysis with magnetic ^{25}Mg is about 20% higher as compared to the rate with nonmagnetic ^{24}Mg or Mg of natural isotope abundance [12]. Thus, similar to the myosin, the mitochondrial H^+-ATPase also demonstrate the catalytic effect of the magnetic isotope of magnesium, i.e., the nuclear spin catalysis in the reactions of ATP hydrolysis.

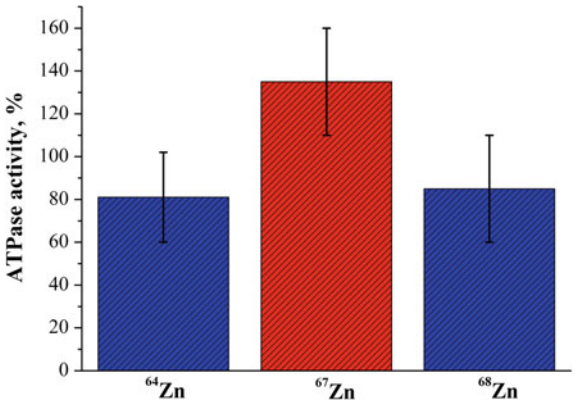

Fig. 12.4 Enzyme hydrolysis of ATP driven by the myosin subfragment-1 in the reaction solutions supplemented with different isotopes of zinc. The rate of ATP hydrolysis was measured at 37 °C by the method of Fiske-Subbarow in the standard reaction solutions which contained 5 mM of $^{64}ZnCl_2$, $^{67}ZnCl_2$ or $^{68}ZnCl_2$. The data ($m \pm SD$) are represented in percents to ATPase activity in the presence of 5 mM of $MgCl_2$ (natural isotope abundance) taken as 100%. The differences of the means for ^{67}Zn versus ^{64}Zn or ^{68}Zn are statistically significant at $P \leq 0.05$ [11]

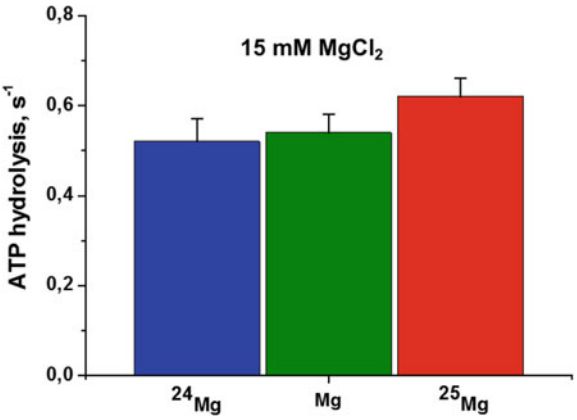

Fig. 12.5 Enzyme hydrolysis of ATP driven by the purified yeast H^+-ATPase in proteoliposomes. The rate of ATP hydrolysis was measured at 25 °C by the luciferin/luciferase assay in the standard reaction solutions containing 15 mM of magnesium chloride as $^{24}MgCl_2$ or $^{25}MgCl_2$ or natural $MgCl_2$ (natural isotope abundance). The data are represented as mean values ± standard deviations ($m \pm SD$). The differences of the means for ^{25}Mg versus ^{24}Mg or natural $MgCl_2$ are statistically significant at $P = 0.05$

12.4 Mechanisms of Nuclear Spin Catalysis: Back into Physics of Liquid Matter

Thus, we have documented the magnetic isotope effects of ^{25}Mg and ^{67}Zn in the enzymatic hydrolysis of ATP, driven by myosin, and the similar catalytic effect of ^{25}Mg in the ATP hydrolysis, driven by mitochondrial H^+-ATPase. In essence, there is the acceleration of the chemo-mechanical cycle of the enzyme via the nuclear spin of the magnetic isotope.

In chemistry and physics of liquid matter, magnetic isotope effects have long been known. MIE manifests itself experimentally by the fact that the reaction rate and the yield of products of the reaction involving free radicals and/or radical ion pairs substantially vary depending on whether the reactants contain magnetic or nonmagnetic isotope of the same element [14–17]. This effect is a direct consequence of the law of conservation of electron angular momentum. This law immediately follows from quantum mechanics, from the fundamental and universal Pauli principle: no two electrons may occupy the same quantum state simultaneously. This fundamental law of nature is as strict as the law of conservation of energy. Here, we are talking about the law of conservation of electron angular momentum, i.e—the electron spin. Namely, the total electron spin (S) of reaction products of any chemical reaction must be equal to the total electron spin of the initial reactants. Otherwise the reaction is forbidden.

To lift the ban on reactions forced by the spin conservation law, spins of the reactants must be changed and magnetic fields are the only means to change the spin state and, thereby, switch the reaction over the spin-forbidden and spin-allowed channels.

Accordingly, the probability of chemical reaction is a function of parameters of these interactions:

$$P = f(H; \omega; H_1; J; a; I; m_I; \mu_n)$$

In this equation H is an applied magnetic field; ω and H_1 are frequency and amplitude of microwave magnetic fields; J is exchange energy (exchange interaction). Correspondingly, acceleration of the free-radical reaction can be achieved through changes in the total electron spin of reactants by their interaction with external, applied, magnetic fields. The equation also contains parameters of hyperfine coupling a, nuclear spin I, nuclear spin projection m_I, and nuclear magnetic moment μ_n, i.e. the parameters of interactions of electron spins with magnetic nuclei. Correspondingly, the spin ban can be lift through the relevant changes in the total electron spin of reactants owing to interactions of the electron spins with magnetic fields of nuclear spins of the magnetic nuclei.

As a result, the reaction shows different reaction rates and different yields of products according to whether the reagents contain magnetic or nonmagnetic isotopes. In molecular liquids, MIEs have been discovered for a number of magnetic isotopes, among them, ^{13}C, ^{17}O, ^{29}Si, ^{33}S, ^{73}Ge, ^{117,119}Sn, ^{199,201}Hg, and ^{235}U (see [14–17] and references therein).

The similar spin bans arise at singlet-triplet transitions in molecules, both in small molecules and macromolecules [16]. Furthermore, in solid-state physics, the same spin effects are attributed to conduction by spin-dependent carriers trapped in shallow dislocation states, which are produced by the deformation potential [18, 19]. Similarly, external magnetic fields or magnetic fields of nuclear spins of the magnetic isotopes are the means to change the spin state, lift the ban and, thereby, accelerate the conductivity.

Thus, factual evidence of the magnetic isotope effects in the reactions of ATP hydrolysis, driven by myosin or H^+-ATPase, indicates that there is a spin-selective rate-limiting step in the reaction that is accelerated by the nuclear spin of ^{25}Mg or ^{67}Zn. Plausible explanations of the nuclear spin-catalysis in the enzymatic reactions of hydrolysis of ATP have been first presented in [20, 21]. In chemistry of molecular liquids, MIE unambiguously testifies a singlet-triplet conversion of a free-radical or radical-ion pair as the "bottle-neck" that is accelerated by the magnetic field of the nuclear spin. Yet, it is well known, however, that the exothermic reaction of ATP hydrolysis with formation of ADP and inorganic phosphate (P_i) follows the basic-acid mechanism [4]. If that is the case, a radical-ion pair as the reaction intermediate in ATP hydrolysis seems to be unlikely. Indeed, no magnetic-isotope effect has been detected in our experiments on non-enzymatic hydrolysis of ATP [9–11].

A different situation arises, however, in the case of enzymatic ATP hydrolysis. It was experimentally proved that ATP hydrolysis triggers electron-conformational interactions in the ATP-hydrolase active site thereby producing a conformational change in the enzyme macromolecule. In essence, there is a deformation excitation of macromolecule conformation, i.e—the strain owing to the energy released by ATP hydrolysis [22, 23]. Under the condition of the electron-conformational excitation

of the macromolecule, in the active site of the enzyme there may be a transfer of electron density from the OH^- group of bound water molecule, for example, or from NH_2 group of Glu459 to ADP^{3-} with formation of the corresponding radical-ion pair. Then, the oxy-anion exerts a nucleophilic attack on the phosphorus atom of inorganic phosphate with formation of ATP. However, the stable spin state of the product (ATP–Mg/Zn) should be singlet, i.e. the electron spin $S = 0$. Owing to the hyperfine interaction of the nuclear spin of ^{25}Mg or ^{67}Zn with the radical-ion pair's unpaired electron, the electron state of the pair is converted into the relatively long-lived triplet state ($S = 1$). Creating the spin ban, the magnetic isotope prevents the undesired reverse reaction of ATP synthesis, thereby promoting the direct ATP hydrolysis reaction. A hypothesis about the key-role of such a virtual radical-ion pair in ATP synthesis at oxidative phosphorylation was stated about 50 years ago [24].

Consider another possible explanation for the observed catalytic effect of the nuclear spin of $^{25}Mg/^{67}Zn$. The energy released during ATP hydrolysis (~0.54 eV) is not large enough for the electron-conformational excitation of the myosin macromolecule into the singlet exited state. This energy is sufficient to produce a low-level triplet state but the transition from the ground state ($S = 0$) to the triplet state ($S = 1$) is forbidden by the law of conservation of spin. The magnetic isotope makes a difference. The nuclear spin eliminates the problem of spin ban providing the required spin conversion to the triplet state (boson). A similar mechanism has been suggested to explain the effects of the magnetic field on mobility of dislocations in solids [18, 19]. The theoretical investigations hold that an elementary coherent deformation excitation, the so-called soliton, may arise in the quasi-one-dimensional protein molecules [25]. The low probability of loss of energy of the ATP hydrolysis into chaotic motion (incoherent heat phonons) is explained on the basis of high stability of the soliton so that the conformational energy can be transported along the protein molecule in the soliton form without heat losses [25].

Alternatively, in terms of physics of molecular liquids, the catalytic effect of the ^{25}Mg nuclear spin can be explained as follows. During the conformational transition, the positions of many atomic groups of the macromolecule undergo changes. At this, there occur processes of dehydration and rehydration related to the degree of ionization of the side aminoacid chains. Meanwhile, it is known that there are two isomers of water molecules differing in mutual orientation of the hydrogen nuclear spins, namely, *ortho*-H_2O with parallel orientation of proton spins (the summary nuclear spin of the protons $I = 1$) and *para*-H_2O with anti-parallel proton spins ($I = 0$). According to the quantum statistics, *ortho*-H_2O constitutes 75% of bulk H_2O at room temperatures [26]. There are the reasons to believe that *ortho*-H_2O molecules have a preferential affinity to *L*-aminoacid enantiomers as compared to *para*-H_2O [27]. If that is the case, when tightly bound in macromolecules, the molecules of *ortho*-H_2O are hard delivered to proper sites for proper processes. The spin-rotational interactions of protons are apparently weak to ensure adequate effectiveness of the *ortho* to *para* transitions. Again, the magnetic field of the nuclear spin of ^{25}Mg is able to make a difference by providing the required conversion rate of the water isomers. In this regard, the quantum theory of atoms with vibration spectroscopy of

intramolecular hydrogen bonds in molecules and the small-angle neutron scattering methods [28, 29] appear to have considerable promise.

In the "molecular motors" operating on the non-magnetic magnesium isotopes, the spin catalysis function can be carried out by the nuclear spins of phosphorus (^{31}P) and protons (^{1}H). The comparatively high catalytic effects of ^{25}Mg and ^{67}Zn are probably due to the fact that the spin of these nuclei, ^{25}Mg and ^{67}Zn, are 5 times higher than that of the nuclei of hydrogen or phosphorus. Another advantages of ^{25}Mg and ^{67}Zn stems from the beneficial localization features of the ion, Mg^{2+}/Zn^{2+}, just in the active site of the enzyme, resulting in a relatively large local magnetic field (hyperfine interaction constant ~21 mT) created by the nuclear spins of these isotopes.

12.5 Conclusions and Outlook

The results of studies of effects of different isotopes of magnesium on post-radiation recovery of yeast cells irradiated by short UV light or irradiated by ionizing radiation unambiguously evidence that the magnetic isotope, ^{25}Mg, essentially promotes the post-radiation recovery of the cells. The beneficial effects of the magnetic isotopes, ^{25}Mg and ^{67}Zn, were discovered in the reactions of ATP hydrolysis driven by the most important molecular motors of cell bioenergetics, myosin and mitochondrial H^+-ATPase. The nuclear spins of ^{25}Mg and ^{67}Zn accelerate the chemo-mechanical cycle of the enzyme. Detailed physical mechanisms of the nuclear spin catalysis in biomolecular motors, as well as biological mechanisms of enhancement of these effects in living cells, require further investigations. Nevertheless, the findings principally manifest the potential of the stable magnetic isotopes as the basis for creating novel effective anti-radiation protectors. As it was said, "Step by step, be steady in your purpose" (Mao Tsedun).

Acknowledgements This paper was prepared on the presentation given at 8th International Conference on Physics of Liquid Matter: Modern Problems (PLMMP-2018), May 18–22, 2018, in Kyiv, Ukraine. I am thankful to Organizers of PLMMP-2018 and personally to academician Leonid A. Bulavin who kindly invited me to take part in the conference, within the precincts of Physics Department of Kyiv Taras Shevchenko University, my Alma Mater. The work was realized in accordance with the state task (state registration No. 01201361868).

References

1. Z.M. Bacq, *Chemical Protection Against Ionizing Radiation* (Thomas, Springfield, USA, 1965)
2. J.C. Livesey, D.J. Reed, L.F. Adamson, *Radiation-Protective Drugs and Their Reaction Mechanisms* (Noyes Publications, Park Ridge, USA, 1985)
3. D.M. Grant, R.K. Harris (eds.), *Encyclopedia of Nuclear Magnetic Resonance* (Wiley, Chichester, USA, 1996)

4. D.L. Nelson, M.M. Cox, *Lehninger Principles of Biochemistry* (Freeman, New York, USA, 2008)
5. D.M. Grodzinsky, T.A. Evstyukhina, V.K. Koltover, V.G. Korolev, Y.A. Kutlakhmedov, Rep. Natl. Acad. Sci. Ukr. **12**, 153 (2011)
6. V.K. Koltover, V.G. Korolev, Y.A. Kutlakhmedov, *Ionizing Radiation: Applications, Sources and Biological Effects* (Nova Science Publishing, New York, USA, 2012), pp. 117–128
7. V.K. Koltover, Russ. Chem. Bull. **63**, 1029 (2014)
8. L.V. Avdeeva, T.A. Evstyukhina, V.K. Koltover, V.G. Korolev, Y.A. Kutlakhmedov, Nucl. Phys. At. Energy **20**(3) (2019) (in press)
9. V.K. Koltover, R.D. Labyntseva, A.A. Lul'ko, V.K. Karandashev, S.A. Kosterin, Rep. Natl. Acad. Sci. Ukr. **1**, 163 (2014)
10. V.K. Koltover, R.D. Labyntseva, V.K. Karandashev, S.A. Kosterin, Biophysics **61**, 200 (2016)
11. V.K. Koltover, R.D. Labyntseva, S.A. Kosterin, *Myosin*: *Biosynthesis, Classes and Function* (Nova Science Publishing, New York, USA, 2018), pp. 135–158
12. V.K. Koltover, P. Graber, V.K. Karandashev, I. Starke, P. Turina, *Abstracts of 11th International Conference "Biocatalysis: Fundamentals and Applications"* (Innovations and High Technologies, MSU Ltd., Moscow, 2017), pp. 50–51. ISBN 978-5-9500292-3-3
13. K. Forster, P. Turina, F. Drepper, W. Haehnel, S. Fischer, P. Graber, J. Petersen, Biochim. Biophys. Acta. Bioenergetics **1797**, 1828 (2010)
14. N.J. Turro, B. Kraeutler, Acc. Chem. Res. **13**, 369 (1980)
15. Y.B. Zeldovich, A.L. Buchachenko, E.L. Frankevich, Sov. Phys. Usp. **155**, 3 (1988)
16. B. Brocklenhurst, Chem. Soc. Rev. **31**, 301 (2002)
17. V.K. Koltover, *Physics of Liquid Matter: Modern Problems* (Springer Inter. Publ., Heidelberg et al., Germany, 2015), pp. 357–368
18. V.V. Kveder, Yu.A. Osip'yan, A.I. Shalynin, Zh. Eksp. Teor. Fiz. **83**, 699 (1982)
19. M.V. Badylevich, V.V. Kveder, V.I. Orlov, Y.A. Osipyan, Phys. Stat. Sol. **2**, 1869 (2005)
20. L.V. Avdeeva, V.K. Koltover, Moscow Univ. Chem. Bull. **7**, 160 (2016)
21. V.K. Koltover, J. Mol. Liq. **235**, 44 (2017)
22. V.K. Koltover, L.M. Reichman, A.A. Yasajtis, L.A. Blumenfeld, Biochim. et Biophys. Acta **234**, 296 (1971)
23. M.V. Volkenstein, *General Biophysics* (Academic Press, New York, USA, 1983)
24. V.K. Koltover, L.A. Blumenfeld, Mol. Biol. **6**, 130 (1972)
25. A.S. Davydov, Sov. Phys. Usp. **25**, 898 (1982)
26. V.I. Tikhonov, A.A. Volkov, Science **296**, 2363 (2002)
27. Y. Scolnik, I. Portnaya, U. Cogan, S. Tal, R. Haimovitz, M. Fridkin, A.C. Elitzur, D.W. Deamer, M. Shinitzky, Phys. Chem. Chem. Phys. **8**(3), 333 (2006)
28. T.Y. Nikolaienko, L.A. Bulavin, D.M. Hovorun, Phys. Chem. Chem. Phys. **14**, 7441 (2012)
29. N.A. Atamas, L.A. Bulavin, G.N. Verbinskaya, A.V. Brytan, Ukr. J. Phys. **60**, 503 (2015)

Chapter 13
On the Mechanism of the Radiation Influence Upon the Structure and Thermodynamic Properties of Water

Kostyantyn Cherevko, Dmytro Gavryushenko, Volodymyr Sysoev, Tetiana Vlasenko and Leonid A. Bulavin

Abstract In the current work the results of the study of the α-particle irradiation influence on water are presented. To quantify the changes in the structure and macroscopic parameters of water when irradiated by the α-particles with the energies in the range from 0.05 to 0.25 keV p/particle the molecular dynamic simulation is used. To interpret the obtained numerical results the theoretical model based on the fundamental Bogolyubov chain of equations is applied. Comparison of the current results with the existing simulation and experimental data confirms that the changes in the structural and thermodynamic properties of water under the irradiation in the stationary state are due to the distortion of the momentum distribution function of the system. The obtained results suggest that the proposed parameter "effective temperature" that is the analogue of the thermodynamic temperature for the case of the nonequilibrium system in the stationary state allows quantifying the changes in the structure and thermodynamic properties of water under the irradiation.

K. Cherevko (✉) · D. Gavryushenko · V. Sysoev · L. A. Bulavin
Physics Faculty, Taras Shevchenko National University of Kyiv,
64/13 Volodymyrska Street, Kyiv 01601, Ukraine
e-mail: k.cherevko@knu.ua

D. Gavryushenko
e-mail: dg@univ.kiev.ua

V. Sysoev
e-mail: sysoev@univ.kiev.ua

L. A. Bulavin
e-mail: bulavin221@gmail.com

T. Vlasenko · L. A. Bulavin
Institute for Safety Problems of Nuclear Power Plants, National Academy of Sciences of Ukraine, 12 Lysogirska St, Kyiv 03028, Ukraine
e-mail: vlasenko.tata@gmail.com

L. A. Bulavin and L. Xu (eds.), *Modern Problems of the Physics of Liquid Systems*, Springer Proceedings in Physics 223,
https://doi.org/10.1007/978-3-030-21755-6_13

13.1 Introduction

Nowadays, effects of the radiation influence on different physical systems are being intensively studied by the scientific community [1–7]. The available works cover the wide range from the fundamental questions of the energy transfer mechanisms to the applications in different fields. Among the main problems in focus there are two to mention. First deals with the influence of the irradiation on the solid state that is the fundamental question from the frontier of the radiation solid state physics [8–10]. Another interesting field is the one that covers different phenomena observed in the liquid systems under the irradiation [11, 12]. Such studies are especially important e.g. for nuclear energy. Since all the constructions surrounding the nuclear reactors are exposed to high doses of the irradiation, to keep the things safe it is crucial to understand the mechanisms of the changes that occur in different structural materials in such interaction. Combination of the radiation physics of solid state and of liquids is even more important for the design of the new Generation IV reactors such as molten salt or supercritical water reactors [13]. In that case it is necessary not only to know the properties of the surrounding materials under the irradiation, but to be able to predict the possible changes in the chemical and redox potential of liquid systems under the irradiation that can lead to the different corrosion rate in the highly radioactive medium.

The similar situation is in the case of liquid systems. The observed changes of the thermodynamic properties can be a key allowing to determine the correspondent structural changes [14]. Therefore, such studies can be helpful in the further development of the theory of the liquid systems. Among the applications that require understanding of the radiation influence on liquid systems one can mention medicine. Radiation therapy has been used for a long time. Recently, quite a lot of work have been done in developing techniques that involve the patients treatment with the proton or ion beams [15, 16]. Unfortunately, such treatment can still cause the negative effects on the healthy tissues as well. Knowing the mechanism leading to the changes of the thermodynamic properties of the biological fluids under the irradiation can give the possibility to improve the techniques in order to minimize the negative effects.

Another applied field to mention is genetics. Modern breeding techniques involve irradiating the seeds either in liquid medium or dry seeds with different water content [17, 18]. The existing studies suggest that the changes of the structure and thermodynamic properties of the liquid systems under irradiation can be a part of the explanation of the observed mutation and survival rates. Similar processes can be important for the studies of the irradiation influence on the complex biological objects, e.g. DNA [19, 20]. When the DNA double helix is broken by the ionizing beam it can recover either in a correct or in a abnormal way. In the alive organisms that process proceeds in a liquid medium. Therefore, knowing the thermodynamic properties of the biological liquids under the irradiation is important in order to predict the results of the recovery process.

From above description one can conclude that studying the influence of irradiation on different physical systems is extremely important. Therefore, it looks natural

that there exist quite a lot of works devoted to the studies of the mechanisms and consequences of the irradiation influence on solid systems [5, 10, 21, 22]. At the same time quite a number of the important applications involve irradiation of the liquid systems. This suggests that there should be many papers devoted to the study of this phenomena. In particular, it can be expected that there exist plenty of data on the radiation influence on water that is the basic component of many liquid systems. Surprisingly, it is not exactly the case. It can be seen from the literature that the studies of the radiation chemistry of water have quite a long history [23, 24]. Such studies are supported by the possibility to extract plenty of data from chemical experiments. Within classical approaches of the water chemistry it is possible to predict a number of the thermodynamic properties of water from the data on free-radical reactions such as H–OH bond dissociation energy, ionization potentials, etc. [25]. There exist quite many comprehensive models of the radiolysis of water [26–28]. They describe well the ionization of atoms and molecules, destruction of bonds and formation of the unstable ions and radicals that change the redox potential of the system. Some recent chemical studies address the problem of the molecular structure changes in the liquid systems under the irradiation [29]. At the same time, physical models able to give the reliable quantitative results regarding the structure and the thermodynamic properties of water under the irradiation are lacking.

There exist experiments [11, 30] that confirm the surface tension dependence on the irradiation (Fig. 13.1). The given absorbed dose rate of 1000 Gy s^{-1} suggests that if all the energy is absorbed by the droplet the temperature after the 80 s of irradiation can change for almost 20 K (assuming the heat capacity of water to be $C = 4.1809 \cdot 10^3$ J kg^{-1} K^{-1}) from $T_0 = 298.15$ K to $T_{\text{final}} = 317.29$ K. The corresponding surface tension coefficient is $\sigma = 6.89 \cdot 10^{-2}$ N m^{-1} [31]. Therefore, the observed in the experiment change in the surface tension can not be explained by the system heating. Moreover, the authors claim that the temperature remains almost constant during the experiment. This suggests some other mechanism to be responsible for

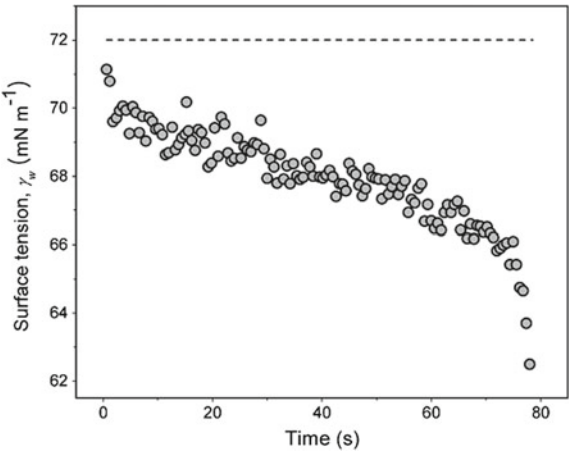

Fig. 13.1 Water surface tension dependence on the irradiation time. X-ray irradiation with the absorbed dose rate 1000 Gy s^{-1}. Irradiation time $\tau = 80$ s [11]

the observed changes. At this point one can recall the fact that surface tension is the property linked to the structure of the system. The well-known Fowler equation [32] links the surface tension σ with the radial distribution function $g(\mathbf{r}_{12})$, interaction potential $u(\mathbf{r}_{12})$ and density ρ_l:

$$\sigma = \frac{\pi}{8}\rho_l^2 \int_0^\infty d\mathbf{r}_{12}\mathbf{r}_{12}^4 u'(\mathbf{r}_{12})\, g(\mathbf{r}_{12}) \tag{13.1}$$

in the equilibrium system. Even though the system in the experiment [11] is hardly equilibrium one still can conclude that the observed changes in the surface tension necessarily require the modified radial distribution function [33] that is due to the changes in the structural part of the free energy. Therefore, studying the physical mechanisms of the radiation influence on water and the changes of the structural properties is an up to date task. Unfortunately, experiments to study the structure of water under the irradiation are quite complicated and the results might be difficult to interpret. The right choice might be the numerical experiment with the computer simulation of water under the influence of the irradiation. To support that approach one can mention that computer simulations are quite successfully used to predict the radiation influence on solids and biological molecules [34–36] as well as for studying the equilibrium and nonequilibrium liquid systems [37–41].

Our current study is aimed on revealing the mechanisms responsible for the changes of the thermophysical properties of water under the irradiation. To achieve the goal we run the computer simulation (molecular dynamics) of the water irradiation by α-particles. In order to interpret the obtained results we use the theoretical model developed recently [42] that explains the changes observed in the nonequilibrium liquid system under the irradiation in the stationary state. Within this model:

- Irradiation of the liquid system causes the changes in the momentum distribution function.
- The modified momentum distribution function leads to the changes in the structure of the system. Namely, it causes the changes in the radial radial distribution functions.
- It is suggested that in case of the nonequilibrium liquid system under the irradiation in the stationary state it is possible to quantify the changes in its thermodynamic properties by introducing new parameter "effective temperature" T_{eff} that is the analogue of the thermodynamic temperature of the equilibrium system.

The above model is obtained in the framework of the fundamental Bogolyubov chain of equations formalism [43]. The model suggests that for for the case of the nonequilibrium multicomponent system under the irradiation one can start from the Bogoliubov–Born–Green–Kirkwood–Yvon (BBGKY) chain of equations that has the form:

$$\frac{\partial F_{n_A+n_B+n_C+\cdots+n_Z}\left(\mathbf{r}^{A+B+C\cdots+Z},\mathbf{p}^{A+B+C+\cdots+Z},t\right)}{\partial t}=$$

$$=\left[\sum_{i=1}^{n_A}T_A\left(\mathbf{p}_i^A\right)+\sum_{i=1}^{n_B}T_B\left(\mathbf{p}_i^B\right)+\sum_{i=1}^{n_C}T_C\left(\mathbf{p}_i^C\right)+\cdots+\sum_{i=1}^{n_Z}T_Z\left(\mathbf{p}_i^Z\right)+\right.$$
$$+\sum_{\substack{i,j\\ j\succ i}}\Phi\left(\left|\mathbf{r}_i^A-\mathbf{r}_j^A\right|\right)+\sum_{\substack{i,j\\ j\succ i}}\Phi\left(\left|\mathbf{r}_i^B-\mathbf{r}_j^B\right|\right)+\cdots+\sum_{\substack{i,j\\ j\succ i}}\Phi\left(\left|\mathbf{r}_i^Z-\mathbf{r}_j^Z\right|\right)+$$
$$+\sum_{i,j}\Phi\left(\left|\mathbf{r}_i^A-\mathbf{r}_j^B\right|\right)+\cdots+\sum_{i,j}\Phi\left(\left|\mathbf{r}_i^A-\mathbf{r}_j^Z\right|\right)+\sum_{i,j}\Phi\left(\left|\mathbf{r}_i^B-\mathbf{r}_j^C\right|\right)+$$
$$\cdots\cdots\cdots\cdots\cdots\cdots\cdots\cdots\cdots\cdots\cdots\cdots\cdots\cdots\cdots\cdots\cdots\cdots$$
$$\left.+\sum_{i,j}\Phi\left(\left|\mathbf{r}_i^Y-\mathbf{r}_j^Z\right|\right),F_{n_A+n_B+n_C+\cdots+n_Z}\left(\mathbf{r}^{A+B+C+\cdots+Z},\mathbf{p}^{A+B+C+\cdots+Z},t\right)\right]+$$
$$+\rho_A\sum_{i=1}^{n_A}\int\frac{\partial\Phi\left(\left|\mathbf{r}_i^A-\mathbf{r}_{n+1}^A\right|\right)}{\partial\mathbf{r}_i^A}\frac{\partial F_{n_A+1}\left(\mathbf{r}^{A+B+C+\cdots+Z},\mathbf{p}^{A+B+C+\cdots+Z},t\right)}{\partial\mathbf{p}_i^A}d\mathbf{r}_{n+1}^A d\mathbf{p}_{n+1}^A$$
$$+\rho_B\sum_{i=1}^{n_A}\int\frac{\partial\Phi\left(\left|\mathbf{r}_i^A-\mathbf{r}_{n+1}^B\right|\right)}{\partial\mathbf{r}_i^A}\frac{\partial F_{n_B+1}\left(\mathbf{r}^{A+B+C+\cdots+Z},\mathbf{p}^{A+B+C+\cdots+Z},t\right)}{\partial\mathbf{p}_i^A}d\mathbf{r}_{n+1}^B d\mathbf{p}_{n+1}^B$$
$$\cdots\cdots\cdots\cdots\cdots\cdots\cdots\cdots\cdots\cdots\cdots\cdots\cdots\cdots\cdots\cdots\cdots\cdots$$
$$+\rho_Z\sum_{i=1}^{n_Z}\int\frac{\partial\Phi\left(\left|\mathbf{r}_i^Z-\mathbf{r}_{n+1}^Z\right|\right)}{\partial\mathbf{r}_i^Z}\frac{\partial F_{n_C+1}\left(\mathbf{r}^{A+B+C+\cdots+Z},\mathbf{p}^{A+B+C+\cdots+Z},t\right)}{\partial\mathbf{p}_i^Z}d\mathbf{r}_{n+1}^Z d\mathbf{p}_{n+1}^Z \tag{13.2}$$

where $F_{n_A+n_B+n_C+\cdots+n_Z}\left(\mathbf{r}^{A+B+C+\cdots+Z},\mathbf{p}^{A+B+C+\cdots+Z},t\right)$ is the nonequilibrium distribution function of the Z-component system depending on space coordinates $\mathbf{r}_1^A,\mathbf{r}_2^A,\ldots,\mathbf{r}_{n_Z}^Z$, momentum $\mathbf{p}_1^A,\mathbf{p}_2^A,\ldots,\mathbf{p}_{n_Z}^Z$ and time t, $A..Z$ stand for different components, $T_A\left(\mathbf{p}_i^A\right)$ is the kinetic energy of the particles of type A, $\Phi(|\mathbf{r}_i^A-\mathbf{r}_{n+1}^A|)$ is the potential of interaction between i-th and $(n+1)$-th particles of the component A, and $\rho_A=\frac{N_A}{V_A}$ is the numerical density of the component A.

It is important to mention here that comparison of the (13.2) to those for the two component system

$$\frac{\partial F_{n_A+n_B}\left(\mathbf{r}^{A+B},\mathbf{p}^{A+B},t\right)}{\partial t}=$$

$$=\left[\sum_{i=1}^{n_A}T_A\left(\mathbf{p}_i^A\right)+\sum_{i=1}^{n_B}T_B\left(\mathbf{p}_i^B\right)+\sum_{\substack{i,j\\ j\succ i}}\Phi\left(\left|\mathbf{r}_i^A-\mathbf{r}_j^A\right|\right)+\right.$$
$$\left.+\sum_{\substack{i,j\\ j\succ i}}\Phi\left(\left|\mathbf{r}_i^B-\mathbf{r}_j^B\right|\right)+\sum_{i,j}\Phi\left(\left|\mathbf{r}_i^A-\mathbf{r}_j^B\right|\right),F_{n_A+n_B}\left(\mathbf{r}^{A+B},\mathbf{p}^{A+B},t\right)\right]+ \tag{13.3}$$
$$+\rho_A\sum_{i=1}^{n_A}\int\frac{\partial\Phi\left(\left|\mathbf{r}_i^A-\mathbf{r}_{n+1}^A\right|\right)}{\partial\mathbf{r}_i^n}\frac{\partial F_{n_A+1}\left(\mathbf{r}^A,\mathbf{p}^A,t\right)}{\partial\mathbf{p}_i^n}d\mathbf{r}_{n+1}^A d\mathbf{p}_{n+1}^A+$$
$$+\rho_B\sum_{i=1}^{n_B}\int\frac{\partial\Phi\left(\left|\mathbf{r}_i^B-\mathbf{r}_{n+1}^B\right|\right)}{\partial\mathbf{r}_i^B}\frac{\partial F_{n_B+1}\left(\mathbf{r}^B,\mathbf{p}^B,t\right)}{\partial\mathbf{p}_i^B}d\mathbf{r}_{n+1}^B d\mathbf{p}_{n+1}^B$$

shows that adding the new component to the liquid system leads to just appearance of the new addend in the equations corresponding to the new subsystem. At the same time, the structure of the equations remains the same. This looks very convenient for the case of the liquid systems under the irradiation allowing to easily modify the governing equations when the new components appear due to the radiolysis process. From (13.2) assuming the system is in the stationary state one can define the "effective temperatures" T_{eff}^{kl} of the different subsystems in a form

$$kT_{\text{eff}}^{kl} = -\frac{\int \frac{\mathbf{p}_1^k}{m_k} f_2\left(\mathbf{p}_1^k, \mathbf{p}_2^l\right) d\mathbf{p}_1^k d\mathbf{p}_2^l}{\int \frac{\partial f_2\left(\mathbf{p}_1^k, \mathbf{p}_2^l\right)}{\partial \mathbf{p}_1^k} d\mathbf{p}_1^k d\mathbf{p}_2^l}$$
$$l, m = A \ldots Z \tag{13.4}$$

where $f_2\left(\mathbf{p}_1^k, \mathbf{p}_2^l\right)$ is the momentum part of the pair distribution function of the components l and k. The cross terms in the (13.4) are the same when the order of the components is changed ($T_{\text{eff}}^{kl} = T_{\text{eff}}^{lk}$).

For the current work we have chosen energies of the α-particles to be in the range 0.05–0.25 keV p/particle. Such a choice can make it easier to track the basic effects of the irradiation. It can be found from the literature [44] that when water is irradiated by the α-particles with the energies less than 1 keV p/particle the ionization cross section is almost zero and the probability of the inelastic collisions followed by the secondary electron emission is very low. Therefore, one can assume that for the chosen range of the irradiation energies the energy transfer process is dominated by the elastic collisions and water remains a single component system. Hence, to quantify the possible changes in the structure and thermodynamic properties we can simplify the model and use BBGKY chain of equations for the single component system

$$kT_{\text{eff}} \frac{\partial F_2(\mathbf{r}_1, \mathbf{r}_2)}{\partial \mathbf{r}_1} + \frac{\partial \Phi(|\mathbf{r}_1 - \mathbf{r}_2|)}{\partial \mathbf{r}_1} F_2(\mathbf{r}_1, \mathbf{r}_2)$$
$$+\rho \int \frac{\partial \Phi(|\mathbf{r}_1 - \mathbf{r}_3|)}{\partial \mathbf{r}_1} F_3(\mathbf{r}_1, \mathbf{r}_2, \mathbf{r}_3) d\mathbf{r}_3 = 0, \tag{13.5}$$

In that case the (13.4) can be reduced to the form:

$$kT_{\text{eff}} \int \frac{\partial f_2(\mathbf{p}_1, \mathbf{p}_2)}{\partial \mathbf{p}_1} d\mathbf{p}_1 d\mathbf{p}_2 = -\int \frac{\mathbf{p}_1}{m} f_2(\mathbf{p}_1, \mathbf{p}_2)\, d\mathbf{p}_1 d\mathbf{p}_2. \tag{13.6}$$

From (13.5) it can be seen that the "effective temperature" T_{eff} stands at the same position in the equation as the thermodynamic temperature for the equilibrium system in the familiar BBGKY equations. This fact suggests that for the nonequilibrium system under the irradiation in the stationary state T_{eff} plays the role of the temperature in respect to the structural and thermodynamic properties of the system. Therefore, one can expect that the properties of the nonequilibrium system with T_{eff}

are equal to those of the equilibrium system with the thermodynamic temperature $T = T_{\text{eff}}$. Another thing to mention is that according to the (13.5) and (13.6) the only reason for the T_{eff} to be different from the thermodynamic temperature is the disturbed momentum distribution function.

It should be emphasized that in current study we do not aim on studying the mechanisms of the high energy beams interaction with the particles forming the medium. That is a complicated process that involves different mechanisms of the energy transfer, excitation of the inner degrees of freedom, etc. Neither we are trying to study the changes in the chemical properties of the system. We are rather focused on the results of the interaction that can explain the changes in the structure and macroscopic parameters of water under the irradiation in the stationary state.

13.2 Molecular Dynamics Simulation Details and Protocol

Following the idea of the current work to study only the basic mechanisms of the radiation influence on water and to look at major effects we use several assumptions in order to make the numerical model as simple as possible. First to mention is the choice of the model of water. The SPC rigid model is used in our simulations as it gives structural and dynamic parameters of the bulk water that are in accord with the experimental data [45, 46] and at the same time it gives the results for the radial distribution functions (RDF) and momentum distribution functions that are not blurred by inclusion of the internal degrees of freedom. It seems to be attractive as we suggest that one of the main mechanisms responsible for the changes of the thermodynamic properties of the liquid systems under irradiation is the change in the momentum distribution function [42]. Therefore, using SPC model seems to be a reasonable choice as the first approximation. The geometric parameters of the SPC model used are given in Table 13.1.

Another important simplification used concerns the method to include the radiation in the simulation. In some recent works devoted to the simulations of the radiation influence on solids [5, 48] it was shown the possibility to assign the radiation energy to the heavy recoil atom rather then to introduce the α-particle in the system. In the current work it is suggested to use the same approach as in the chosen range for the α-particles energies the process is dominated by elastic collisions. Therefore, irradiation is included by accelerating the O atom originally present in the system. In order to reach the stationary state of the system we add energy in a discrete way with the step 0.05 keV. It is done by accelerating one O every 2 ps to have the total irradiation energy ranging from 0.05 to 0.25 keV. To have the scalar stationary

Table 13.1 Geometric parameters of the rigid SPC model used [47]

$\theta^o_{\angle \text{HOH}}$	109.47
r_{OH} (Å)	1
r_{HH} (Å)	1.63

state the O atom to be accelerated and the direction of the acceleration are chosen randomly at each step.

Apart from giving the possibility to use the model simplifying assumptions the expected qualitative picture of the phenomena sets some limitations on the molecular dynamics (MD) experiment. Namely, it requires the model to be able tracking the changes in the system that one expects to be crucial for explaining the changes in water under the irradiation. When providing the MD simulation of the liquid system it is convenient to use the NVT ensemble with some kind of thermostat that eliminates the energy drift due to the numerical errors. In that case all the existing MD thermostats make the momentum distribution function move towards the Maxwellian one and, hence, disturb the real physical picture in the momentum space. At the same time, the important hypothesis used in our study claims the changes in the momentum distribution function to be one of the main physical mechanisms of the radiation influence on the structural and thermodynamic properties of water. Therefore, using thermostats for our purposes is not acceptable. To deal with the problem it is suggested doing simulations in two steps with different ensembles. First, the system is equilibrated in the NVT ensemble using Berendsen thermostat and the box is fixed. In all the future simulation the box size remains unchanged. Next, the radiation is switched on. At this stage the simulation is performed in the NVE ensemble. Such an approach allows minimizing the energy drift during the equilibration process when keeping the correct picture in the momentum space during the irradiation stage.

To run the simulation the DL_POLY package (4.06 version) is used [49], with the Ewald particle mesh method for the evaluation of the Coulomb interactions. The intermolecular potential energy between atomic sites is calculated in a standard way by a sum of the Lennard-Jones (12-6) potential and the Coulomb electrostatic interaction

$$\begin{aligned} U\left(r_{ij}\right) &= U_{LJ}\left(r_{ij}\right) + U_{\text{Coul}}\left(r_{ij}\right) \\ &= \sum_{i \prec j} 4\varepsilon_{ij}\left(\left(\frac{\sigma_{ij}}{r_{ij}}\right)^{12} - \left(\frac{\sigma_{ij}}{r_{ij}}\right)^{6}\right) + \sum_{i \prec j} \frac{q_i q_j}{4\pi\varepsilon_0 r_{ij}} \end{aligned} \tag{13.7}$$

with the off-diagonal interaction parameters calculated using the Lorentz-Berthelot mixing rules [50, 51]

$$\sigma_{ij} = \frac{\sigma_i + \sigma_j}{2}, \tag{13.8a}$$

$$\varepsilon_{ij} = \sqrt{\varepsilon_i \varepsilon_j}. \tag{13.8b}$$

The parameters used are given in Table 13.2.

The simulation protocol is given in Table 13.3.

Table 13.2 Masses and intermolecular potential parameters of water [45, 52]

Atom	m (a.m.u.)	q (e)	ε (kJ mol^{-1})	σ (Å)
H	1	+0.41	0	0
O	16	−0.82	0.65	3.1656

Table 13.3 Simulation parameters

Number of water molecules	16,384
Box size (Å)	79
Density ρ (kg m^{-3}) [31]	992.27
Temperature T (K)	300
Equilibration time (NVT ensemble) (ps)	2000
Simulation time (NVE ensemble) (ps)	2–10
R_{cutoff} (Å)	14
Boundary conditions	Periodic
Simulation software	DL-POLY 4.06

13.3 Results and Discussion

In order to have the reliable data for the nonequilibrium system in the stationary state we have averaged the results of the three runs with the same initial equilibrated system. The g_{OO}, g_{OH}, and g_{HH} RDFs are shown at Figs. 13.2, 13.3 and 13.4 respectively.

The error bars in Figs. 13.2, 13.3 and 13.4 due to the averaging over the three runs are are comparable with the thickness of the lines. Therefore, one can conclude that the above graphs reflect well the structural changes in water under the irradiation. It can be seen from the figures that all the changes in the RDFs are quite small. At the same time for the case of liquid systems even such a small change in the structure can result in the non-negligible changes in the system properties. Another thing to mention about the Figs. 13.2, 13.3 and 13.4 is that there is the correlation in between the radiation energy and the changes in the RDFs. At the inset of Fig. 13.2 one can see the decrease of the height of the first peak with the increasing radiation energy. Such a behavior suggests the tendency to blurring of the first and second coordination spheres. At the same time its position remains the same at about 2.78 Å that corresponds to the geometric criteria for the hydrogen bond that is $R_{\text{OO}} \leq 3.3$ Å [40].

For $g_{\text{OH}}(r)$ the decrease of the height of the first peak with the increasing radiation energy (the inset at Fig. 13.3) is seen again. Its position at 1.8 Å corresponds to the geometric criteria for the hydrogen bond that is $R_{\text{OH}} \leq 2.6$ Å [40]. Such a behavior suggests the tendency of the radiation to destroy the net of hydrogen bonds.

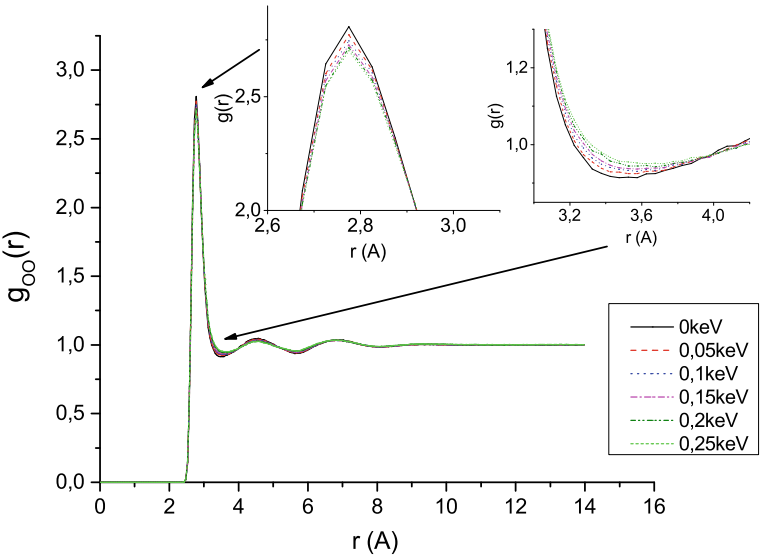

Fig. 13.2 Oxygen-oxygen RDFs for the radiation energies ranging from 0 to 0.25 KeV

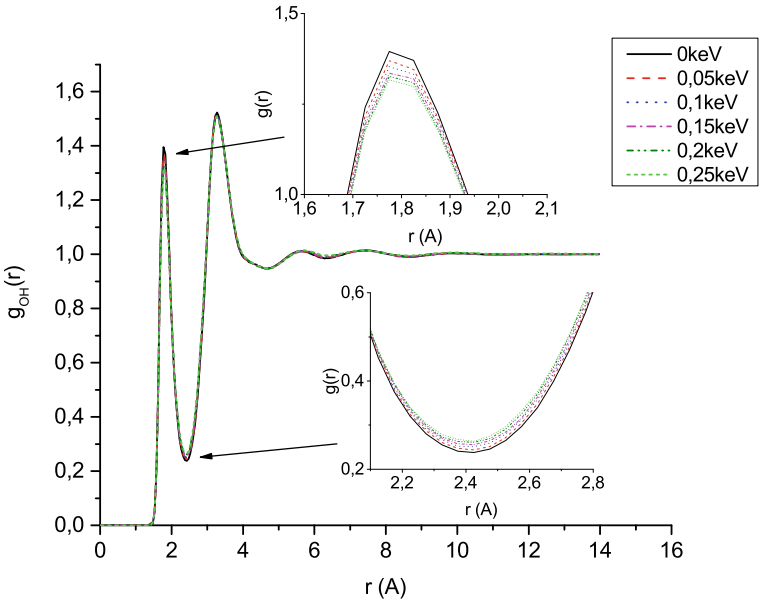

Fig. 13.3 Oxygen-hydrogen RDFs for the radiation energies ranging from 0 to 0.25 KeV

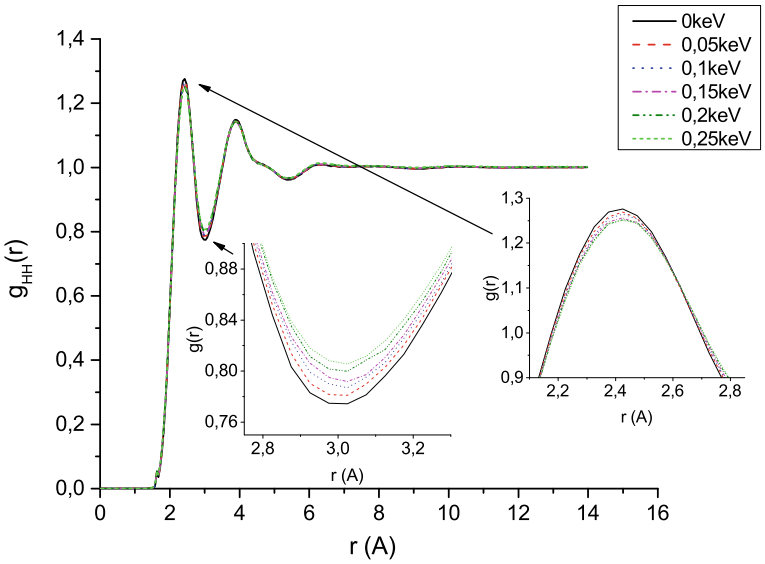

Fig. 13.4 Hydrogen-hydrogen RDFs for the radiation energies ranging from 0 to 0.25 KeV

Unfortunately, the changes in the $g_{\mathrm{HH}}(r)$ are hardly seen (Fig. 13.4). Still, the tendency of the first peak to decrease with the increasing radiation energy is also observed at the graph.

To confirm the statistic thermodynamic mechanism of the radiation influence on water causing the observed structural changes the obtained simulation results are interpreted within the theoretical model of the process developed earlier [42]. In order to calculate the "effective temperatures" that characterize the structural and thermophysical properties of the stationary nonequilibrium liquid system under irradiation the momentum distribution functions have been extracted from the simulation data for the different irradiation energies. To do this the whole interval of the particle velocities has been divided into the bins of 50 ms^{-1} and the number of particles in each bin has been calculated. The obtained distribution is then fitted with the Maxwell type functions $f(p) = Ap^2\exp(-\phi p^2)$. The correspondent graphs are shown at Fig. 13.5. One can see that the position of the maximum shifts toward the higher velocities and the peak broadens with the increasing radiation energy. Such a behavior qualitatively confirms the importance of the change of the velocity distribution function due to the momentum exchange between the active particles and the particles forming the liquid in explaining the effects of the irradiation influence on the properties of water.

According to the suggested model the above defined analytical expressions for the disturbed momentum distribution functions $f(|\,\mathbf{p}\,|)$ shown at Fig. 13.5 allow calculating the correspondent "effective temperature" T_{eff} from the (13.6). The resulting values are given in Table 13.4.

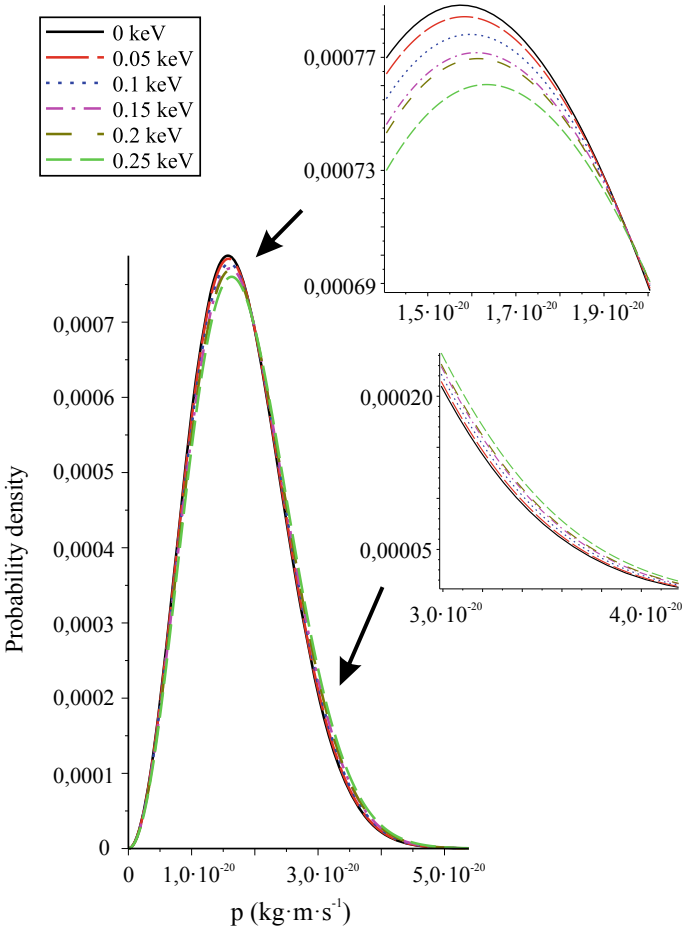

Fig. 13.5 Momentum distribution functions for the radiation energies ranging from 0 to 0.25 keV

Table 13.4 Effective temperatures for the different irradiation energies

Irradiation energy (keV)	0	0.05	0.1	0.15	0.2	0.25
T_{eff} (K)	300.2	303.4	308.3	313.5	315.2	322.8

As our system is in the stationary nonequilibrium state it is not possible to define the thermodynamic temperature of the system. At the same time it is important to mention that the RDFs of the equilibrium system calculated in the NVT ensemble at thermodynamic temperatures equal to T_{eff} given in Table 13.4 coincide with the RDFs shown at Figs. 13.2, 13.3 and 13.4 for the corresponding irradiation energies.

In order to confirm that it is the effective temperature that describes the thermophysical properties of the system under the irradiation one should compare the

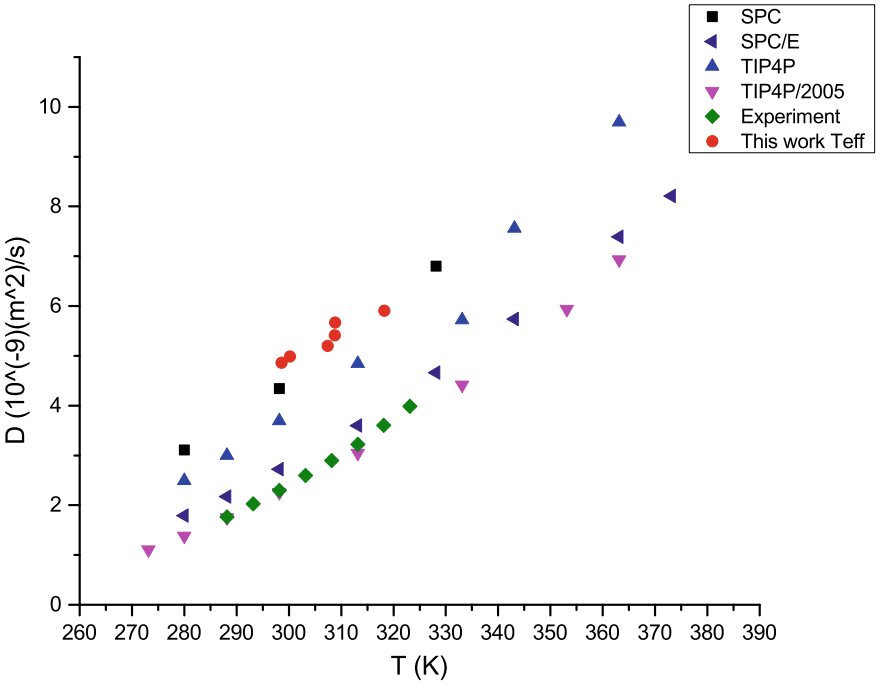

Fig. 13.6 Self-diffusion coefficient dependence on temperature: data from literature for the different models and experiment [53] (T at the x axis means thermodynamic temperature of the equilibrium system); dependence obtained in this work from T_{eff} (circles; T at the x axis means the introduced parameter T_{eff})

simulation results with the available experimental data. The effects might be seen in all the thermophysical properties that are defined by the structure of the system like the surface tension, self-diffusion coefficient, etc. We have analyzed the self-diffusion coefficient dependence on the effective temperature. The corresponding graph is shown at Fig. 13.6. At the same figure there are shown graphs of the self-diffusion coefficient dependence on thermodynamic temperature that can be found in the literature [53]. One can see from Fig. 13.6 that the obtained results for the self-diffusion coefficient plotted against the T_{eff} are in accord with the data available in the literature for the SPC rigid model. Therefore, the obtained results also confirm our suggestions regarding the physical meaning of the "effective temperature". Hence, for water under the irradiation it is T_{eff} that defines the observed behavior of the self-diffusion coefficient.

13.4 Conclusions

From the results obtained within the current study one can make several conclusions. First thing to mention is the confirmed possibility to study the changes in the structure and thermodynamic properties of water under the irradiation by the molecular dynamic simulations without specifying the mechanisms of the energy transfer from the projectiles to water molecules. More to say is that in order to reveal the basic mechanisms it is even not that important specifying the type of the high energy particles. They can rather be treated as some stationary external influence. Within such an approach the molecular dynamic simulations reveal the changes in the radial distribution functions that correlate with the changes of the radiation energies.

The results show that when water is irradiated by the α-particles with the energies lower than needed for the ionization the main structural effect is the destruction of the net of hydrogen bonds. The above phenomenon together with the observed blurring of the first and second coordination spheres suggest that the thermodynamic properties of water should also change under the irradiation.

The analysis of the obtained simulation results within the theoretical model of the process based on the fundamental Bogolyubov chain of equations shows that the calculated from the radial distribution functions new parameter the "effective temperature" can explain the "virtual heating" of the system and the correspondent changes in the thermodynamic properties. The comparison of the obtained data on the self-diffusion coefficients dependence on irradiation with the available in the literature experimental and simulation values on the temperature dependence confirms that the thermodynamic properties of water in the nonequilibrium stationary state under the irradiation are equal to those of water in the equilibrium state with the thermodynamic temperature equal to the "effective temperature".

Summarizing the above results for water under the irradiation it is possible to conclude that for the liquid system in case of the stationary process with the radiation energies low enough to keep the number of components in the liquid system constant the governing mechanism of the observed phenomena is the distortion of the momentum distribution function that leads to the changes of the structure. The knowledge of the radial distribution functions under the irradiation allows calculating the analogue of the thermodynamic temperature for the nonequilibrium liquid system in the stationary state that defines all the thermophysical properties of the system that depend on structure.

In this work we use the simplified model of the process. In order to have the comprehensive description of the phenomena it will be necessary to consider the possible ionization processes at higher energies, the possible excitations of the internal degrees of freedom, etc. At the same time, the model introduced appears to be successful in defining the basic mechanisms of the irradiation influence on water.

References

1. E.C. Montenegro, H. Luna, Braz. J. Phys. **35**(4A), 927 (2005)
2. M. Kreipl, V. Friedland, H. Paretzke, Radiat. Environ. Biophys. **48**, 11 (2009)
3. M. Qi, G. Wua, Q. Li, Y. Luo, Rad. Phys. Chem. **77**, 877–883 (2008). https://doi.org/10.1016/j.radphyschem.2007.12.007
4. B.M. Weon, J.S. Lee, J.H. Je, K. Fezzaa, Phys. Rev. E **84**, 032601 (2011). https://doi.org/10.1103/PhysRevE.84.032601
5. E. Zarkadoula, S.L. Daraszewicz, D.M. Duffy, M.A. Seaton, I.T. Todorov, K. Nordlund, M.T. Dove, K. Trachenko, J. Phys. Condens. Matter **25**, 125402 (2013). https://doi.org/10.1088/0953-8984/25/12/125402
6. W.J. Weber, R.C. Ewing, C.R.A. Catlow, T.D. de la Rubia, L.W. Hobbs, C. Kinoshita, H. Matzke, A.T. Motta, M. Nastasi, E.K.H. Salje, E.R. Vance, S.J. Zinkle, JMR **13**, 1434 (1998). https://doi.org/10.1557/JMR.1998.0205
7. E.M. Fielden, P. O'Neill (eds.), *The Early Effects of Radiation on DNA*, *NATO ASI Series H: Cell Biology*, vol. 54 (Springer, 1991). https://doi.org/10.1007/978-3-642-75148-6
8. K. Trachenko, J.M. Pruneda, E. Artacho, M.T. Dove, Phys. Rev. B **71**, 184104 (2005). https://doi.org/10.1103/PhysRevB.71.184104
9. K. Nordlund, M. Ghaly, R.S. Averback, M. Caturla, T. Diaz de la Rubia, J. Tarus, Phys. Rev. B **57**, 7556 (1998). https://doi.org/10.1103/PhysRevB.57.7556
10. L. Malerba, M. Marinica, N. Anento, C. Bjorkas, H. Nguyen, C. Domain, F. Djurabekova, P. Olsson, K. Nordlund, A. Serra, D. Terentyev, F. Willaime, C. Becquart, J. Nucl. Mater. **406**, 19 (2010). https://doi.org/10.1016/j.jnucmat.2010.05.017
11. B.M. Weon, J.H. Je, Y. Hwu, G. Margaritondo, Phys. Rev. Lett. **100**, 217403 (2008). https://doi.org/10.1103/PhysRevLett.100.217403
12. L. Yuan, J. Peng, L. Xu, M. Zhai, J. Li, G. Wei, J. Phys. Chem. B **113**, 8948–8952 (2009). https://doi.org/10.1021/jp9016079
13. K.D. Kok (ed.), *Nuclear Engineering Handbook* (Nuclear Engineering Handbook, 2016)
14. I.Z. Fisher, *Statistical Theory of Liquids* (University of Chicago Press, 1961)
15. A.J. Lomax, T. Boehringer, A. Coray, E. Egger, G. Goitein, M. Grossmann, P. Juelke, S. Lin, E. Pedroni, B. Rohrer, W. Roser, B. Rossi, B. Siegenthaler, O. Stadelmann, H. Stauble, C. Vetter, L. Wisser, Med. Phys. **28**(3), 317 (2001). https://doi.org/10.1118/1.1350587
16. O. Jäkel, C.P. Karger, J. Debus, Med. Phys. **35**(12), 5653 (2008)
17. T. Abe, Y. Kazama, T. Hirano, Nucl. Phys. News **25**(4), 30 (2015). https://doi.org/10.1080/10619127.2015.1104130
18. H. Ichida, R. Morita, Y. Shirakawa, Y. Hayashi, T. Abe, Plant J. (2019). https://doi.org/10.1111/tpj.14213
19. E. Alizadeh, A.G. Sanz, G. Garcia, L. Sanche, Phys. Chem. Lett. **4**(5), 820 (2013). https://doi.org/10.1021/jz4000998
20. M. Spotheim-Maurizot, M. Davidkova, J. Phys. Conf. Ser. **261**, 012010 (2011). https://doi.org/10.1088/1742-6596/261/1/012010
21. V.S. Urusov, A.E. Grechanovsky, N.N. Eremin, Glass Phys. Chem. **38**, 55 (2012)
22. K. Trachenko, E. Zarkadoula, I. Todorov, M. Dove, D. Dunstan, K. Nordlund, Nucl. Instr. Meth. Phys. Res. B **227**, 6 (2012). https://doi.org/10.1016/j.nimb.2011.12.058
23. H.A. Dewhurst, A.H. Samuel, J.L. Magee, Radiat. Res. **1**(1), 62 (1954). https://doi.org/10.2307/3570180
24. A.O. Allen, *The Radiation Chemistry of Water and Aqueous Solutions* (Princeton, NJ, Van Nostrand, 1961)
25. M.G. Evans, N.S. Hush, N. Uri, Q. Rev, Chem. Soc. **6**, 186 (1952). https://doi.org/10.1039/QR9520600186
26. A. Mozumder, *Fundamentals of Radiation Chemistry* (Academic Press, 1999)
27. A.H. Samuel, J.L. Magee, J. Chem. Phys. **21**, 1080 (1953)

28. M. Domae, Y. Katsumura, K. Ishigure, V.M. Byakov, Rad. Phys. Chem. **48**(4), 487 (1996). https://doi.org/10.1016/0969-806X(96)00060-6, http://www.sciencedirect.com/science/article/pii/0969806X96000606
29. A. Guleria, A.K. Singh, S. Adhikari, Phys. Chem. Chem. Phys. **17**, 11053 (2015). https://doi.org/10.1039/C4CP06070A
30. B.M. Weon, J.H. Je, Appl. Phys. Lett. **93**, 244105 (2008). https://doi.org/10.1063/1.3050528
31. E. Lemmon, M. Huber, M. McLinden, *REFPROP: Reference Fluid Thermodynamic and Transport Properties. Version 8.0*. NIST standard reference database (NIST, Gaithersburg, 2007)
32. R.H. Fowler, Proc. R. Soc. Lond. Ser. A Math. Phys. Sci. **159**(897), 229 (1937). https://doi.org/10.1098/rspa.1937.0069
33. J.S. Rowlinson, B. Widom, *Molecular Theory of Capillarity* (Clarendon, Oxford, 1982)
34. H. Christie, M. Robinson, D. Roach, D. Ross, I. Suarez-Martinez, N. Marks, Carbon **81**, 105–114 (2015). https://doi.org/10.1016/j.carbon.2014.09.031
35. G.R. Lumpkin, K.L. Smith, M.G. Blackford, B.S. Thomas, K.R. Whittle, N.A. Marks, N.J. Zaluzec, Phys. Rev. B **77**, 214201 (2008). https://doi.org/10.1103/PhysRevB.77.214201
36. K. Trachenko, M.T. Dove, E. Artacho, I.T. Todorov, W. Smith, Phys. Rev. B **73**, 174207 (2006). https://doi.org/10.1103/PhysRevB.73.174207, http://journals.aps.org/prb/abstract/10.1103/PhysRevB.73.174207
37. C. Valeriani, P.J. Camp, J.W. Zwanikken, R. van Roij, M. Dijkstra, Soft MatterD **6**(12), 2793 (2010). https://doi.org/10.1039/C001577F
38. L. Xu, S.V. Buldyrev, H.E. Stanley, G. Franzese, Phys. Rev. Lett. **109**, 095702 (2012). https://doi.org/10.1103/PhysRevLett.109.095702
39. S. Toxvaerd, Phys. Rev. E **58**, 704 (1998). https://doi.org/10.1103/PhysRevE.58.704
40. G.W. Robinson, S.B. Zhu, S. Singh, M.W. Evans, *Water in Biology, Chemistry and Physics: Experimental Overviews and Computational Methodologies, World Scientific Series in Contemporary Chemical Physics*, vol. 9 (World Scientific, Singapore, 1996)
41. J.O. Sindt, A.J. Alexander, P.J. Camp, J. Chem. Phys. **147**(21), 214506 (2017). https://doi.org/10.1063/1.5002002
42. L.A. Bulavin, K.V. Cherevko, D.A. Gavryushenko, V.M. Sysoev, T.S. Vlasenko, Phys. Rev. E **93**, 032133 (2016). https://doi.org/10.1103/PhysRevE.93.032133
43. N. Bogolyubov, Problems of dynamical theory in statistical physics. *Studies in Statistical Mechanics*, vol. 1 (North-Holland, 1962), p. 5
44. S. Uehara, H. Nikjoo, J. Phys. Chem. B **106**, 11051 (2002). https://doi.org/10.1021/jp014004h
45. J. Zielkiewicz, J. Chem. Phys. **123**, 104501 (2005). https://doi.org/10.1063/1.2018637
46. B. Guillot, J. Mol. Liq. **101**, 219 (2002). https://doi.org/10.1016/S0167-7322(02)00094-6
47. Y. Wu, H.L. Tepper, G.A. Voth, J. Chem. Phys. **124**, 024503 (2006). https://doi.org/10.1063/1.2136877
48. K. Trachenko, M.T. Dove, E.K.H. Salje, Phys. Rev. B **65**, 180102(R) (2002). https://doi.org/10.1103/PhysRevB.65.180102
49. I. Todorov, W. Smith, K. Trachenko, M. Dove, J. Mater. Chem. **16**, 1911 (2006). https://doi.org/10.1039/B517931A
50. H.A. Lorentz, Ann. Phys. **248**, 127–136 (1881). https://doi.org/10.1002/andp.18812480110
51. D. Berthelot, C.R. Acad. Sci. **126**, 1703–1855 (1898)
52. A.P. Lyubartsev, A. Laaksonen, J. Phys. Chem. **100**, 16410 (1996). https://doi.org/10.1021/jp961317h
53. G. Guevara-Carrion, J. Vrabec, H. Hasse, J. Chem. Phys. **134**, 074508 (2011). https://doi.org/10.1063/1.3515262